Transactions of the ASME®

Transactions of the ASME, Journal of Engineering for Gas Turbines and Power (ISSN 0022-0825) is published quarterly (Jan., Apr., July, Oct.,) for $120 per year by The American Society of Mechanical Engineers, 345 East 47th Street, New York, NY 10017. Second class postage paid at New York, NY and additional mailing offices. POSTMASTER: Send address change to Transactions of the ASME, Journal of Engineering for Gas Turbines and Power, c/o The AMERICAN SOCIETY OF MECHANICAL ENGINEERS, 22 Law Drive, Box 2300, Fairfield, NJ 07007-2300.
CHANGES OF ADDRESS must be received at Society headquarters seven weeks before they are to be effective. Please send old label and new address.
PRICES: To members, $29.00, annually; to nonmembers, $120.00.
Add $12.00 for postage to countries outside the United States and Canada.

INDEXED by Applied Mechanics Reviews and Engineering Information, Inc.

Journal of Engineering for Gas Turbines and Power

Published Quarterly by The American Society of Mechanical Engineers
VOLUME 111 • NUMBER 3 • JULY 1989

TECHNICAL PAPERS

(Contents continued on Inside Back Cover)

(Contents continued)

Diesel Lube Oils—Fourth Dimension of Diesel Particulate Control

K. J. Springer
Southwest Research Institute,
San Antonio, TX 78284

Particulate emission control, for the HD diesel engine, has previously been considered a three-dimensional problem involving: (1) combustion of the fuel by the engine, (2) fuel modification, and (3) exhaust aftertreatment. The lube oil contribution may be considered a fourth dimension of the problem. Historically, the heavy-duty engine manufacturer has met emission standards for smoke (1968 to present), CO, HC, and NO_x (1974 to present) and particulates (1988 to present) through changes in engine design. This paper uses the allocation method to estimate the reduction in lube oil consumption needed to meet 1991 and 1994 U.S. particulate emission standards. This analysis places the contribution of lube oil as a source of exhaust particulates into prospective with the contributions from fuel sulfur and fuel combustion. An emissions control strategy to meet future regulations is offered in which reductions from fuel modification, combustion improvement, reduced lube oil consumption, and exhaust particulate trap-catalysts are all involved.

Introduction

Heavy-duty diesel engines used in trucks and buses face a serious challenge in terms of stringent exhaust particulate and oxides of nitrogen levels required in 1991 and further in 1994. It appears that some engine manufacturers may manage to achieve the 1991 limits without use of an exhaust aftertreatment device such as a particulate trap. However, it is certain that those manufacturers with high oil consumption engines will seek ways to reduce oil consumption rate, as it occurs during the EPA transient cycle, in order to bring this source of measured particulates to a reasonable level without jeopardizing engine life. This poses a major challenge to all manufacturers since long engine life has been a major reason for the diesel engine's popularity. Starting in 1991, the engine manufacturer will expect help in fuel modification, through EPA regulation, and lubricant modification by the oil and additive supplier.

Engine Requirements

This is the first time the lube oil industry has been drawn directly into the argument regarding the ability of an engine to meet an emission standard. It may be helpful to define specifically what the engine manufacturer faces in trying to develop and certify engines. First, heavy duty (HD) means an engine used in a vehicle of over 8500 lb gross vehicle weight rating (GVWR) or a frontal area of over 45 square feet. The HD category of vehicles as defined by EPA [1] is all vehicles larger than the light-duty truck category and range from 1-ton type pick-ups to the largest Class VIII highway truck tractor trailer. Such tractor trailer trucks are typically 86,000 lb gross vehicle weight. Diesel engines used in HD vehicles vary from as low as 100 to over 400 horsepower. They may be direct or indirect injection, two-stroke or four-stroke cycle, unit or jerk pump injected. Some are normally aspirated while many are turbocharged with a variety of intake air cooling methods.

The future trend of some engines is to higher brake mean effective pressures causing an increase in piston ring zone temperatures. It is the temperature distribution in the ring zone that causes ring groove filling with deposits from the lube oil. Excessive deposits cause the ring to pack as it cannot move to effect an adequate seal. This, in turn, causes accelerated deposits in the top land area thay may cause bore polishing, scoring and eventual wear with attendant loss of power, high oil consumption rates, and a need to perform a major engine overhaul. This well-known lube oil–ring zone mechanism is repeated to emphasize the effect an increase in ring zone temperature has on the life of the diesel engine. The ring zone (piston-ring-liner) and lubricant (base stock plus additive package) combination is a result of over 40 years of continuous, evolutionary improvement by manufacturers and refiners working in harmony. They have achieved the long engine life the diesel is famous for through design, metallurgy, and chemistry. Some Class VIII truck diesels achieve over 600,000 miles before engine overhauls, a truly remarkable achievement.

The advent of stringent emission regulations for diesel particulates, shown in Table 1, is a serious threat to the long-life diesel, not so much for the expected increase in ring zone temperature, but because of the perceived need to reduce oil consumption drastically. Some of the oil consumed by an engine is not completely burned to CO_2 and water vapor, nor is it even possible to do so in the case of metallic additives. In-

Contributed by the Internal Combustion Engine Division and presented at the Internal Combustion Engine Division Technical Conference, San Antonio, Texas, October 2-5, 1988. Manuscript received by the Internal Combustion Engine Division June 1988.

Table 1 U.S. heavy duty diesel standards

			U.S.[2]	Calif.[3]
1985	HC		1.3	1.3
	CO		15.5	15.5
	NO_x		10.7	5.1
1987	NO_x		10.7	5.1 or 6.0
	Particulate		---	0.6
1988	Particulate		0.6	
1990	NO_x		6.0	
1991	NO_x		5.0	5.0
	Particulates	Truck	0.25	0.25
		Bus	0.10	0.10
1994	Particulates		0.10	0.10
Smoke Requirements		20% Accel,	15% Lug,	50% Peak

stead, these products of lube oil consumption/combustion exit the engine as particulates. The diesel engine manufacturer must meet particulate limits based on the following definition of particulates in order to sell engines in the U.S. HD vehicle market. "Whatever is collected on a 90 mm round plastic coated fiberglass filter at a temperature not to exceed 125°F and excluding condensed water droplets." This definition includes anything of a soot or carbonaceous nature as well as aerosols. It includes, for example, organics derived from partial combustion of fuel and lubricant as well as unburned, raw fuel and lubricant. It includes sulfuric acid and the water and organics that happen to be adsorbed during the test by the sulfuric acid collected on the filter. It includes metals and minerals from the consumption of lube oil additives as well as from the engine proper.

Test Procedure

Important to what is collected and measured as particulate emissions is the engine/vehicle test procedure employed. Unlike passenger cars, many HD diesel engines are sold as "loose engines" to a variety of truck makers and, therefore, an engine test is appropriate. Also, a HD engine is sold for its ability to provide power at the flywheel, not to move an average of 1.5 persons, as is the passenger car and many LD trucks. Accordingly, the exhaust emission regulations rely on an engine test in which a brake-specific emission rate is used to express an engine's contribution to air pollution. Brake Specific Particulate (BSP) is a common term that, if obtained by the EPA procedure, may be directly compared to the EPA limits. Its units are grams of particulate per brake horsepower-hour.

The HD category covers trucks used in city and suburban, as well as intercity, driving. The EPA transient cycle, used since 1985 to certify new HD engines intended for sale in the U.S., recognizes the variety of operation in and around large cities by including freeway (Los Angeles) and non-freeway type operation (Los Angeles and New York City). A transient cycle that includes engine start after overnight shutdown, idle, acceleration, deceleration, and a wide variety of different speed and load conditions, continuously connected, is used to simulate vehicle operation. It is not like any known oil test procedure and has few steady-state operating conditions aside from curb-idle. The duty factor is approximately 20–25 percent, defined as that fraction of the maximum power available from the engine at the speed operated. The 20 minute test is run once from "cold" start and once from "hot" start after 20 minute shutdown and emphasizes part-load, nonstabilized engine operation. A specially controlled, motoring, full electric dynamometer, capable of simulating any condition the engine might be typically called upon in actual operation, is

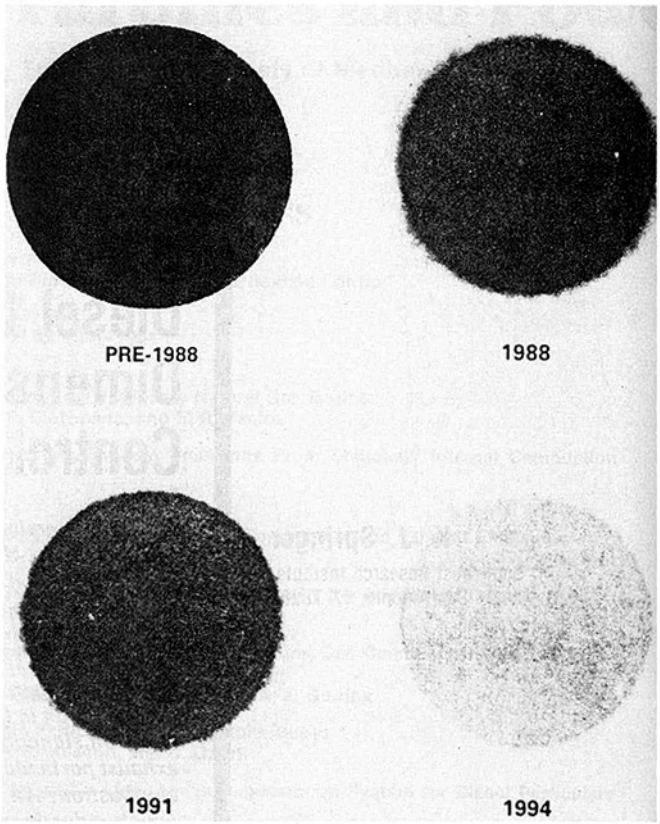

Fig. 1 Typical HD diesel engine particulate test filters

used. The average speed equivalent of the EPA transient cycle is taken to be 19.2 miles per hour and is based on a 6.4 mile equivalent length.

The method for collecting the particulates is described, as is the entire procedure, by the Code of Federal Regulations [4]. A large dilution tunnel is used to mix ambient air with the total engine exhaust and this flow is metered by a suitably sized constant volume blower. A second, much smaller, dilution tunnel is used to load the 90 mm test filter disk at an overall dilution of about 10 or 12 to 1. Although far from the 100:1 dilution of exhaust that occurs immediately on exit of exhaust into the atmosphere, the double dilution system is adequate to stabilize the exhaust pollutants and prevent water condensation. The relative appearance of typical diesel particulate on 90 mm test filters is shown in Fig. 1.

The filters in Fig. 1 illustrate the impact of particulate regulations on filter levels and appearance. All of this background on definition of particulate, the procedure, and conditions of sampling is important to the manufacturer and will be important to the lube oil maker in the future. In trying to meet particulate standards, "it's what's collected on the test filter that counts."

Oil Consumption Rates

A brief SwRI study confirmed earlier speculations that engine manufacturers may want to reduce oil consumption by as much as 80 percent, i.e., to 1/5th of that from some current engines. This study began with inquiries to manufacturers and truck lease companies to obtain general estimates of in-service oil consumption rates. Table 2 lists miles per quart values and an equivalent brake specific oil consumption (BSOC) rate in grams of oil consumed per bhp-h. It was assumed that there were no external leaks and all oil was consumed mostly via the ring zone, and some (a small part) by the intake valve guides and/or turbocharger seal. To calculate the miles/qt for Class

Table 2 Estimated in-service oil consumption rates

	Miles/Qt.	BSOC[a] Grams/Hp-Hr
Informal Industry Survey[b]		
Cummins	1060[d]	0.23
Caterpillar	890[d]	0.27
Mack	530[d]	0.45
DDA, 4-Stroke	1330[d]	0.18
Informal Lease Company Survey		
150[c], Class V-VI	500	0.94[d]
250, Class VI-VII	450	0.75[e]
350, Class VII-VIII	850	0.28[f]
CITY BUS, 3 BUS AVG		
DDA 6V92TA (Class VI)	570	0.27[g]

(a) Brake Specific Oil Consumption
(b) Class VIII
(c) ± 50 hp
(d) Class V-VI BSOC based on 25 mph average speed and 30% duty factor.
(e) Class VI-VII BSOC based on 40 mph average speed and 40% duty factor.
(f) Class VIII values based on 50 mph average speed and 50% duty factor.
(g) City Bus BSOC based on 13 mph average speed and 25% duty factor.

Table 3 Collectable fuel sulfur dependent particulate rates for several fuel sulfur contents

Fuel Sulfur Content, % Wt.		Brake Specific Sulfuric Acid Related Particulate, g/hp-hr: Sulfuric Acid Mist	Acid Mist Plus Water Vapor & HC
0.3	pre 1991	0.0375	0.075
0.1	1991	0.0125	0.025
0.05	1994	0.00625	0.0125

VIII industry values, a duty factor, percent of available power, and speed, miles per hour, was used for the appropriate engine-rated power. To convert lease vehicle data from miles/quart to BSOC, the duty factor and average speed given for the engine power and its typical vehicle class application was used. These values are given as notes at the bottom of Table 2. Since duty factor and average speed go together, the final BSOC values are not terribly sensitive to minor errors of generalization. However, the reader can perform additional calculations for a specific application. To estimate oil consumption in terms of qt/mi, use equation (1). For brake specific oil consumption, g/hp-h, use equation (2).

$$A = \frac{B \times C \times D}{E \times F \times 100 \text{ percent}} \text{ or} \tag{1}$$

$$B = \frac{A \times E \times F \times 100 \text{ percent}}{C \times D} \tag{2}$$

where

A is oil consumption, qt/mi
B is oil consumption, g/hp-h
C is rated engine power, hp
D is duty factor, percent
E is vehicle speed, mi/hr
F is 845 g/qt of oil

The average of the top three Class VIII engines on Table 2 is 828 mi/qt, which agrees well with the least company data for Class VII-VIII 850 mi/qt estimate. The four-stroke DDA engine was not included in the Class VIII average since it only recently was put into commercial use and is not yet reflected in the lease company experience. Based on this good agreement, it is through that the other values have some validity also.

Table 4 Speculated particulate budget

	Year 1988	1991	1991	1994[f]	1994
EPA Limit, g/hp-hr	0.6	0.25	0.25	0.10	0.10
Mfg Target, g/hp-hr	0.5	0.2	0.2	0.08	0.08
Fuel Sulfur, % wt	0.3	0.1	0.05	0.05	0.05
Catalytic Trap[a]	No	No	No	No	Yes
Fuel Sulfur[b], %[c]	15	12	6	16	20
g/hp-hr	0.0750	0.0250	0.0125	0.0125	0.0160[a]
Engine-Fuel Comb., %[c]	65	59	65	125	50
g/hp-hr	0.3250	0.1175	0.1300	0.1000[g]	0.0400[h]
Soot, %	45	30	30	55	30
Unb. Fuel, %	20	29	35	70	20
Fugitive[d], %[c]	5	9	9	22	12
g/hp-hr	0.0250	0.0175	0.0175	0.0175	0.0100[i]
Lube consump.[e], %[c]	15	20	20	35	18
g/hp-hr	0.0750	0.0400	0.0400	0.0280	0.0140[j]

Assumptions:
(a) Assumes 30% more H_2SO_4 due to $SO_2 \rightarrow SO_3$ by platinum oxidation catalyst.
(b) Half H_2SO_4, half adsorbed water and organics
(c) % based on Mfg target, rounded
(d) Half misc. metals, half misc. minerals, dust, silica, dirt
(e) Half ash, metals, additive residue, half unburned oil
(f) Budget is double Mfg target; requires trap.
(g) Assumed lowest level possible by Mfg by 1994 model year
(h) Assume 60% catalyst trap efficiency.
(i) Assumes 43% trap collection efficiency.
(j) Assumes 50% catalyst trap efficiency.

Fuel Sulfur Importance

Fuel sulfur content is important because during combustion some sulful is oxidized to SO_3 and this converts to H_2SO_4 (sulfuric acid aerosol) in the exhaust. In this form, it is easily collected as particulate on the test filter. During the EPA transient cycle test, the sulfuric acid on the filter collects water vapor and some hydrocarbons, further increasing the filter weight [5]. It is estimated that an equal amount of water and gaseous hydrocarbons are adsorbed by the sulfuric acid, regardless of the fuel sulfur content. This effectively doubles the fuel sulfur derived or dependent particulates.

Early sulfur balances [6] under steady-state conditions indicated that at least 95 percent of the fuel sulfur burned to SO_2 and the remainder exited the engine as SO_3, or a higher oxide form. Although the results were quite variable by condition and engine, it was concluded that about 2.5 percent of the fuel sulfur exited the engine as sulfate (H_2SO_4). More recent data indicate that 2 percent of the fuel sulfur content is collected as H_2SO_4 on the particulate filter during the EPA transient cycle. A 2 percent conversion will be assumed for calculations with the knowledge that as more engine data by the EPA transient cycle are reported, the value may change.

Type 2-D diesel fuel for on-highway trucks and buses can vary in sulfur content to a maximum of 0.5 percent by weight. The national average sulfur content is taken to be about 0.3 percent by weight. The following equation may be used to estimate the contribution of fuel sulfur to sulfuric acid. By doubling this value, because of the adsorbed water vapor and organic assumed, the importance of fuel sulfur to collectable particulates may be assessed.

$$G = \frac{H \times I \times J \times L}{K \times M} \tag{3}$$

where

G is grams H_2SO_4/hp-h
H is lb sulfur/lb of fuel, or percent S
I is transient cycle BSFC, estimated as 0.45 lb/hp-h
J is molecular weight H_2SO_4, 98
K is molecular weight sulfur, 32
L is 453.6 g/lb
M is percent conversion rate, S to H_2SO_4

Table 3 lists the fuel sulfur dependent particulates for three fuel sulfur contents. The 0.1 percent by weight sulfur content may be considered as a possible interim level for 1991 in the longer term reduction to 0.05 in 1994.

Table 5 Oil consumption reduction to achieve 1991 and 1994 particulate standards

Engine	BSOC[a]	Collect[b]	Reduction Needed 1991 g/Hp-Hr[c]	1991 Percent[d]	1994 g/Hp-Hr[c]	1994 Percent[d]
Cummins VII-VIII	0.227	0.0454	0.0054	11.9[e]	0.0174	38.3
Caterpillar VII-VIII	0.272	0.0544	0.0144	26.5	0.0264	48.5
Mack VII-VIII	0.454	0.0908	0.0508	55.9	0.0628	69.1
DDA (4ST) VII-VIII	0.181	0.0362	(0.0038)	(10.5)	0.0082	22.7
150 ± 50 V-VI	0.940	0.1880	0.1480	78.7	0.1600	85.1
250 ± 50 VI-VII	0.751	0.1500	0.1100	73.3	0.1220	81.3
350 ± 50 VII-VIII	0.284	0.0568	0.0168	29.6	0.0288	50.7
6V92TA Bus	0.270	0.1350	0.1070[f]	79.3	0.1070	79.3

(a) Brake Specific Oil Consumption, g/hp-hr from Table 2.
(b) Collect is fraction of BSOC considered collectable on test filter. 20 percent all engines except 2-stroke city bus assumed 50 percent.
(c) Reduction, g/hp-hr, is collect-budget from Table 4.
(d) Percent reduction is reduction needed divided by collect × 100%.
(e) ( ) means BSOC is lower than allocated, engine is considered "dry."
(f) City bus must meet 0.1 in 1991. Reduction in 1991 same as 1994.

Particulate Budget

One way an engine manufacturer might view the problem of meeting a particulate standard is to budget how much particulate is allowable from four major sources. Table 4 summarizes the amount of particulate collected on the test filter from fuel sulfur, fuel combustion, lubricant consumption, and fugitive metals and minerals.

Table 4 begins with a manufacturer's target certification engine particulate limit of 80 percent of the EPA standards for 1991 and 1994. This is to allow for increase in particulates with time and use (deterioration factor) and manufacturing tolerances encountered. This conservative target assumes the quality of future, more advanced components, engines, and systems remains at least as good as current engine manufacture.

The next item on Table 4 is the contribution by fuel sulfur, previously discussed. This is an interim sulfur level of 0.1 percent for 1991, which would increase the contribution of sulfur particulates by about 6 percent versus 0.05 sulfur fuel. It is thought that the manufacturer can tolerate no more than 10 to 15 percent particulates from fuel sulfur. References (7) and (8) contain expanded discussions of the importance of fuel sulfur.

Engine-Fuel Combustion

Improvements in engine combustion technology have simultaneously reduced hydrocarbons and oxides of nitrogen, as well as particulates. It is expected that manufacturers will continue to demonstrate further improvements, to about 0.13 g/hp-h in 1991. In conjunction with improvements in lube oil consumption and reduced fuel sulfur, this will permit engines to be sold in 1991 without need for exhaust particulate traps.

There is, however, a practical limit to such improvements in combustion system, injection system, electronic control, turbocharging, etc., within the time available to certify engines for 1994 production. Perhaps 0.10 g/hp-h from this source of particulates is the best one may expect from a laboratory prototype. As a result, it is anticipated that some type of catalytic aftertreatment must be used in 1994. Important to note from Table 4 is the split of soot versus unburned fuel. Soot has always been the predominant contribution to total particulate mass from the diesel engine. In 1991, the unburned fuel will be the major fraction of particulates from this category.

Fugitive Particulates

The next category in Table 4 is an allocation to miscellaneous particulates called "fugitive," for lack of a better term. This category includes dust, silica, and dirt, not collected by the engine intake air filter, and metals/minerals, which in the normal operation of an engine and exhaust system may be emitted. For 1991, 0.0175 g/hp-h is budgeted with reductions from use of a catalytic particulate trap expected.

Lube Oil-Derived Particulates

If the three categories already discussed (fuel sulfur, fuel combustion, and fugitive particulates) are summed, the remainder is allocated to particulate from the consumption of crankcase lubricant. This is the last category on Table 4 and is the subject of the remainder of this paper. Is it reasonable to allocate 20 percent of the filter-collected, EPA measured particulates to the products of lube oil consumption? This means only 0.04 grams of oil-derived particulate in 1991. Catalytic conversion of lube oil products by platinum catalyst is expected to be difficult. A 50 percent conversion-collection efficiency will require engine out lube oil particulates of 0.028 g/hp-h in 1994.

Oil Consumption Reductions Needed

Table 5 is a summary of the lube oil consumption reductions needed based on the brack specific oil consumption values in Table 2 and the lube oil allocations in Table 4. Important to these calculations is the observation and assumption that 20 percent of oil consumption from four-stroke cycle and 50 percent of oil consumption from two-stroke cycle HD diesel engines is considered filter collectable. A number of other notes are given on Table 5 to explain the calculations.

The significance of the percent reductions necessary is considered staggering for most engines. For 1991, the amount of reduction needed by this analysis is variable. Two of the four Class VIII engines are quite well developed in terms of lube oil control and may need little attention. Other engines, that are considered "moist," must be "dried up" as much as possible, or meeting the 1991 standard will be just that much more problematic. Aside from the two Class VIII truck engines, the needed reductions range from 30 to 80 percent, or about 50 percent in general.

With the use of a particulate catalyst-particulate trap in 1994, the oil fraction can be controlled with some additional improvements in oil consumption. All Class VIII engines from Table 5 now require reductions in oil consumption by 20 to 70 percent. The remaining engines on Table 5 appear to require up to 80 percent reductions. The engine manufacturer will want to investigate all possible technologies for mechanically "drying-up" his engine, while trying to find additives and lube oils will be expected to give the very long life of, say, 500,000 miles that is commonplace today in Class VIII truck engines. No doubt that lubricants will require new formulations and new additives to match new engine designs. Reference [9] describes the potential of low oil consumption engines and lubes.

The city bus with two-stroke diesel, at the bottom of Table 5, has a very special problem: the test-filterable form in which oil consumption products exit the engine (50 percent collectable versus, say, 20 percent for four-stroke). This problem is further aggravated for the city bus by having to meet the 1994 standard in 1991. As much as any other single factor, the form of the lube oil exhaust products plus the early standard has forced GM to the methanol alternative for city bus engines. It has also been a factor in discontinuing two-stroke cycle diesels in future on-highway vehicles. The Uniflow scavenging system of the modern two-stroke cycle diesel engine apparently entrains lube oil as partially or unburned oil mist and this mist is easily collectable as particulate by the test filter. The oil consumption rate is not considered high, however.

Lube Oil Consumption Targets for 1991-1994

For 1991, Table 4 listed an allocation to the test filter from lube oil of 0.04 grams per bhp-h. This was based on the consumed lube oil being 20 percent collectable on the filter, while the remainder burns to CO, CO_2, or uncollectable HC. This means that lube oil consumption should be limited to 0.2 grams of oil per bhp-h (0.04 divided by 0.2, the 20 percent collectability factor). For 1994, the use of a catalyzed trap oxidizer in the exhaust results in the need for less drastic reductions in lube oil consumption than would be the case otherwise. An oil consumption rate of 0.14 grams of oil per hp-h is speculated for 1994, based on 0.028 g/hp-h engine-out rate divided by 0.2, the 20 percent collectability factor. Thus the speculated oil consumption rates for 1991 and 1994 are listed as follows:

Year	Oil consumption rate targets, grams of oil per hp-h
1991	0.20
1994	0.14

These targets may be converted to oil consumption values in quarts per mile by use of equation (1) for a given engine size and duty factor. The basic assumptions of 20 percent filter collectability of oil consumption products and the 20 percent allowable for 1991 may be improved as experience indicates. For example, there is concern that more than 20 percent of the exhausted lube oil products are collected on the test filter due to ash and partially burned material. Also, some manufacturers may wish to reduce the oil products allowable to less than 20 percent in 1991 for one or more models. Readers are invited to investigate the sensitivity of the oil consumption rates using their own assumptions.

Control Strategies

Engine manufacturers must do everything possible in design and manufacturing tolerances to reduce oil consumption. The methods to do so are as varied as the engines and their designers. Most manufacturers know what to do to reduce ring zone oil consumption, and leakage through intake valve guides and the turbo seal.

Since no manufacturer has indicated plans to use an exhaust trap or catalyst to meet 1991 standards, some engines must be changed to consume less oil. Thus, major changes in engine design are anticipated to meet 1991 standards with a major reliance on further improvement from an aftertreatment device for 1994.

For 1991, it is assumed by some manufacturers that for those engines identified as needing major reductions in oil consumption, there will be suitable lubricants that will function properly and deliver the accustomed long engine life. This assumption needs further verification because it is not clear that such revolutionary reductions indicated on Table 5 for some engines are possible. In every engines' experience, there will come a point where further oil consumption reduction will begin to interfere with the delicate balance of piston-ring-liner design and the lube oil consumption rate required for acceptable life between overhauls.

When this point of oil consumption reduction versus desired engine life is reached, quite new and revolutionary lubrication systems, base oils, and additives may be necessary. Although two Class VIII diesel engines, listed on Table 5, appear to be within approximately 10 percent of the budget for 1991, it is uncertain how practically other engines can reach such oil consumption levels, especially for 1991 certification.

The EPA certification includes control of particulates and other emissions for up to 290,000 miles, in the case of Class VIII trucks, for example [10, 11]. It is possible that some models of four-stroke engines may not be offered in 1991 because of the difficulty factor in reducing oil consumption, along with other improvements that must be made. Low oil consumption engines for 1991 are possible, given the data on Table 2, in that some already meet the 1991 allocation.

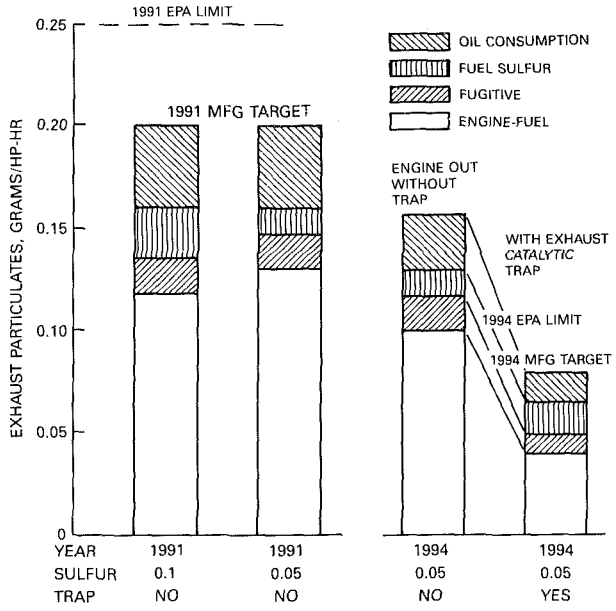

Fig. 2 Particulate budgets for 1991 and 1994 HD diesel emission limits

For 1994, the role of oil consumption on collected particulates is so significant that a catalyst trap oxidizer must be employed. This, however, does not eliminate the need to further reduce oil consumption. The catalyst trap system, considered 50 percent efficient on lube oil consumption products, will be needed in 1994 for soot, unburned fuel, and fugitive particulates as well. By taking advantage of the catalyst trap to collect a part of the lube oil emissions, it may be possible to use the 1991 low oil consumption engine configuration and lubricant with only incremental improvements. The assumed 50 percent efficiency could be realized and perhaps improved on by joint development of catalysts and lubricants that are compatible. The ability of a platinum catalyst formulation to convert oil additive organic residue to CO_2 and water vapor will require catalysts selective to certain hydrocarbons and, of course, lube oils that are compatible to improved catalytic combustion.

Figure 2 depicts the 1991 and 1994 allocations to exhaust particulates and the extent to which each source must be controlled. A catalyzed trap system that burns organics (unburned and partially burned fuel and oil) as well as collects soot, ash, and fugitive particles is necessary for 1994.

Summary

The role of oil consumption in diesel engine exhaust particulates is a complex yet fascinating phenomenon with far-reaching potential. The process by which oil is consumed, its products of combustion, and its collectability on a test filter under EPA transient test conditions are not well understood. The importance of lube oil base stock and various ash or ashless additives, metals, and other chemicals, is difficult to determine.

This paper has made informed assumptions regarding the unknowns, and then applied the logic of a test filter budget with allowances for the various sources of particulate. In this way, the relative importance and degree of control can be kept in overall perspective of realism and what might be practical.

From this, it is clear that reductions in oil consumption of perhaps as much as 80 percent for some engines may be necessary. Target oil consumption values for 1991 and 1994 were given as 0.20 and 0.14 grams of oil per hp-h, respectively.

Engine manufacturers need to reduce oil consumption to the extent practical as a means to help achieve 1991 and 1994 standards. There will come a point where further oil consumption reduction will endanger engine life. The advent of suitably catalyzed particulate traps can alleviate the problem of further reductions of lube oil consumption for 1994. The following are needed:

1 Confirmation of the 2 percent conversion rate of fuel sulfur to sulfuric acid during the EPA transient cycle.
2 Definition of the amount of water vapor and hydrocarbons adsorbed by the sulfuric acid in the test filter.
3 Discussin of the alternative of 0.1 percent fuel sulfur for 1991 as an interim step to the 0.05 percent level necessary for 1994 and for catalytic trap use.
4 Verification of trap-catalyst efficiency of 60 percent (50 percent on oil residue).
5 Confirmation of the estimate that 20 percent of lube oil consumption is filter collectable.
6 Evaluation of the estimated 0.10 g per ph-h as the practical minimum for engine-fuel combustion (excluding sulfur effect) by 1994 certification.

In summary, the on-road HD diesel engine is undergoing a revolutionary change in an attempt to achieve reduced exhaust particulates mandated by the U.S. EPA. There is little doubt that the diesel engine burning diesel fuel will continue as the preferred power plant in heavy-duty vehicles in the United States. Control strategies, however, must include the engine lubricating oil-derived particulate as the fourth dimension to the well-known dimensions of engine, fuel, and particulate trap.

References

1 40 CFR, Part 86, Subpart A, para. 86.082-2 Definitions, p. 265, 06-02-77, ed., *Protection of the Environment*.

2 40 CFR, Part 86, Subpart A, para. 86.085-11, 86.090-11, 86.091-11, and 86.094.11, p. 265, 06-02-77 ed., *Protection of the Environment*.

3 California New Vehicle Standards Summary, Passenger Cars and Heavy-Duty Engines and Vehicles, revised 6/9/86.

4 40 CRF, Part 86, Subpart N, para. 86.1310-88, 06-02-77, ed., *Protection of the Environment*.

5 Wall, J. S., and Hoekman, S. K., "Fuel Composition Effects on Heavy-Duty Diesel Particulate Emissions," SAE Paper No. 841346, 1984.

6 Springer, K. J., and Stahman, R. C., "Unregulated Emissions From Diesels Used in Trucks and Buses," SAE Paper No. 770258, 1977.

7 Richards, R. R., and Sibley, J. E., "Diesel Engine Emissions Control for the 1990s," SAE Paper No. 880346, 1988.

8 Gill, A., "Design Choices for 1990s Low Emission Diesel Engines," SAE Paper No. 880350, 1988.

9 Signer, M., and Steinke, R. E., "Future Trends in Diesel Engine Design and Their Impact on Lubricants," SAE Paper No. 871271, 1987.

10 40 CFR, Part 86, para. 68.085-2(d)(1), (2) and (3) p. 306, 07-01-86, ed., *Protection of the Environment*.

11 USEPA Advisory Circular No. 51C, Dec. 4, 1986, "Assigned Deterioration Factors for 1988 Model Year Light Duty Vehicles, Light Duty Trucks, and Heavy Duty Engines."

Low-Emission Diesel Fuel for 1991-1994

K. J. Springer
Southwest Research Institute,
San Antonio, TX 78284

A low-emission diesel fuel (LEDF) is proposed as a way to help the HD diesel engine manufacturer meet stringent U.S. particulate limits beginning in 1991. A new LEDF fuel specification would include sulfur reduction to less than 0.05 percent and a new specification putting a cap or maximum on aromatic content. Additive treatment to control injector deposits for less engine deterioration with time and a combustion improver could also be helpful. A two-fuel strategy would permit orderly phase-in of LEDF. As with unleaded gasoline, a smaller filler neck and nozzle and separate storage tank for dispensing would be required. Unlike the sale of unleaded fuel, the prices of DF-2 and LEDF must be equalized to prevent fuel switching.

Introduction

Diesel fuel composition is important to the manufacturers of heavy duty diesel engines in meeting U.S. emission standards for 1991–1994. Exhaust particulate standards of 0.25 (1991) and 0.1 (1994) g/hp-h are made more achievable by use of diesel fuel containing lower sulfur and aromatics. Less of these components will result in less smoke and fewer particulates. It is doubtful that a manufacturer can meet the 1991 limit through engine design change and combustion improvement alone. Thus, for the first time, refiners and suppliers of diesel fuel face new requirements, and very likely, new specifications for diesel fuel used in trucks and buses.

Background. Diesel fuel has traditionally been described as a distillate and even a residual fuel. Its specifications are broad to permit the maximum availability and lowest price possible. The ASTM specification D975 for type 2-D fuel [1] includes a fairly high maximum sulfur content of 0.5 percent by weight and no specification on aromatics content. The 90 percent distillation point can range from 282°C (540°F) to 338°C (640°F), and the minimum cetane number is 40.

It is intended that distillate fuel for on-road diesels be specified as loosely as possible to allow maximum flexibility in its manufacture by the approximately 140 refiners of such fuel in the U.S. The wide range of crude oils, the variety of refinery equipment to process and produce diesel fuel, and the product mix from these refineries requires minimal specifications and restrictions. This approach has served the industry well for many years inasmuch as engines operate successfully with satisfactory life and performance on such fuels. It has been the lowest cost approach to providing maximum availability of diesel fuel.

Low-Emission Diesel Fuel. The advent of strict pollution standards by the U.S. EPA [2] requires a new approach, namely, a low-emission diesel fuel. It is proposed that a new LEDF specification be considered for 1991 and later on-highway HD diesel trucks and buses. Such a specification would include lower sulfur content, a maximum aromatics, and use of additives to control injector deposits and improve combustion. Some consideration would be given to lowering the maximum 90 percent distilled point from 640 to 590°F, a 50°F reduction.

A modified or premium diesel fuel that permitted lower smoke has been used in Europe and on occasion in the U.S. with success. However, it was not mandatory nor made a requirement for engine/vehicle operation. As a result, its popularity in the U.S. varied and resulted usually from vigorous marketing efforts by the supplier. Such fuels were rarely specified by the manufacturer of the engine or vehicle and accordingly met with mixed reaction by the owner/operator of diesel vehicle(s). With regard to air pollution, the benefits were incremental at best and the manufacturer was always able to meet U.S. EPA or California regulations for new engines by engine modification and improvement.

However, the stringent 0.25 g/hp-h particulate regulations (0.1 g/hp-h city bus) for 1991 require the manufacturer to seek assistance from the fuel refiner/supplier. The alternative for certain makes and models will be a particulate trap or exhaust catalyst that, in its present form, will be noncompetitive in 1991.

Particulate Standards. Table 1 is a listing of U.S. Environmental Protection Agency [2] and California Air Resources Board [3] emission requirements. Although visible smoke from HD diesels has been subject to EPA regulation since 1970, exhaust particulates were controlled to 0.6 g per hp-h starting in 1988. In 1991, this limit will be reduced to 0.25 (0.1 for city buses) g/hp-h and joins a 5.0 g/hp-h NO_x standard. Taken together, the 0.25/5.0 combination is a formidable challenge to achieve. It is important to recognize that the EPA standards for HD diesel engines are based on a double dilution method, which obtains an integrated sample of particulates during en-

Contributed by the Internal Combustion Engine Division and presented at the Twelfth Annual Energy-Sources Technology Conference and Exhibition, Houston, Texas, January 22–25, 1989. Manuscript received by the Internal Combustion Engine Division October 1988.

Table 1 U.S. heavy duty diesel standards, g/hp-h

			U.S.	Calif.
1985	HC		1.3	1.3
	CO		15.5	15.5
	NOx		10.7	5.1
1987	NOx		10.7	5.1 or 6.0
	Particulates		---	0.6
1988	Particulates		0.6	
1990	NOx		6.0	
1991	NOx		5.0	5.0
	Particulates	Truck	0.25	0.25
		Bus	0.10	0.10
1994	Particulates		0.10	0.10

Smoke Requirements 20% Accel, 15% Lug, 50% Peak

gine operation thought representative of city-suburban type driving. The whole exhaust is sufficiently diluted in air to allow a sample to be passed across a plastic-coated fiberglass filter disk.

This test filter collects carbonaceous, soot-type particles as well as aerosols of unburned hydrocarbons, organics, sulfuric acid, and other condensibles, at a temperature not to exceed 125°F. Care is taken to dilute the exhaust sufficiently to prevent condensation of water droplets. The engine test procedure calls for engine start, acceleration, deceleration, idle, and a wide variety of part-load operations to yield a cycle duty factor of 20–25 percent of the maximum power available from the engine.

Strategies to Meet Emission Standards. Given the current state of development of particulate traps and the reluctance by manufacturers to offer such in 1991, the alternative is to achieve the limits principally through engine modification. Improvements in the combustion system, comprising the combustion chamber, injection equipment atomization, timing, mixing, etc., are a first priority to the manufacturers for basic reductions in particulate matter, i.e., carbon or soot and aerosols of various organics from partial or unburned fuel and lubricants.

A new dimension of electronic control of the injection and timing of the combustion event has been added. Further advances in computer control of the diesel engine await breakthroughs in sensor technology. Just as the gasoline automobile engine required a new type of exhaust sensor for an error signal to provide closed-loop control and eventual computer operation of the spark ignition engine, the diesel is expected to go through similar revolutionary change as it also becomes computer controlled.

However, there is a limit to just what is possible through such advances in engine technology in time for certification and sale in model year 1991. Reference [4] describes a particulate budget as might be viewed by a manufacturer. References [4, 5] illustrate the range of strategies and the possibilities of meeting standards through engine design/modification.

Figure 1 [6] illustrates the allocated particulates to various sources. As expected, combustion of the fuel results in most of the particulate being either sulfuric acid or carbonaceous or organic matter. Ignoring the contribution of sulfur, it is thought that combustion of the fuel will result in between 0.15 and 0.10 g/hp-h of particulates for 1991 engines. By 1994, the lowest practical emission rate from combustion of the fuel is thought to be about 0.10 g/hp-h. As manufacturers learn more about how to improve combustion, the relative amount of carbonaceous or soot content in the particulates will reduce in relation to the organic fraction on the filter. Regardless, aromatics has an effect on both soot and organics, while sulfur

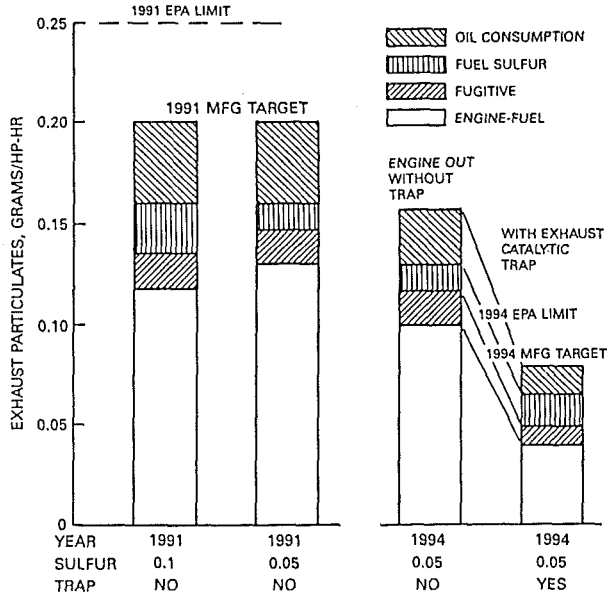

Fig. 1 Particulate budgets for 1991 and 1994 HD diesel emission limits (from [6])

in the fuel causes sulfuric acid aerosols. These two fuel components will be discussed next.

Importance of Fuel Sulfur Content

Sulfur in diesel fuel is important in meeting particulate standards for three major reasons:

1 About 2 percent of fuel S content burns to SO_3 and is collected as H_2SO_4 on test filter during EPA transient cycle.

2 An equal weight of water vapor and HC is thought to be collected during the test by H_2SO_4 on a particulate filter.

3 A platinum-catalyzed particulate trap is not feasible unless fuel sulfur is reduced to less than 0.05 percent.

Sulfur Combustion Products. The sulfur in the fuel contributes to the EPA test filter weight in two ways. First, during the combustion of diesel fuel, over 95 percent of the fuel sulfur is converted to SO_2 and the remainder exits the engine as sulfur trioxide (SO_3), sulfuric acid mist, H_2SO_4, or some other oxide form [7]. On the order of 2 percent of the fuel sulfur is collected during the EPA transient test cycle as sulfuric acid mist. Unpublished results were reported recently for a popularly used diesel truck engine of four-stroke cycle direct injected turbocharged design [6].

Reference [8] reports sulfur conversion rates to sulfate ($SO_4^=$), the analytical indicator of the presence of H_2SO_4 on the filter disk, of from 2 to 5.2 percent by the EPA cold-hot transient cycle. Other authoritative results by the certification test procedure [9] confirm the rate of conversion of about 2–3 percent. Experiments [9] also confirmed that conversion rate is not dependent on fuel sulfur content. Figure 2 [9] illustrates the range of conversion for a fuel sulfur content from over 0.5 to less than 0.1 percent by weight.

The sulfuric acid mist, now collected by the test filter, also acts as a drying agent to remove water vapor and certain hydrocarbons from the dilute exhaust during the remainder of the test period. It is estimated that water and gaseous hydrocarbons are adsorbed by the sulfuric acid in an amount equal to that of the sulfate collected regardless of fuel sulfur content. During collection of particulates on the test filter, the dilution is variable due to varying exhaust gas flows. The humidity of the diluted exhaust is thus quite variable. As it passes over the sulfuric acid, which is hygroscopic by nature, the weight increases. Reference [9] contains probably the best published

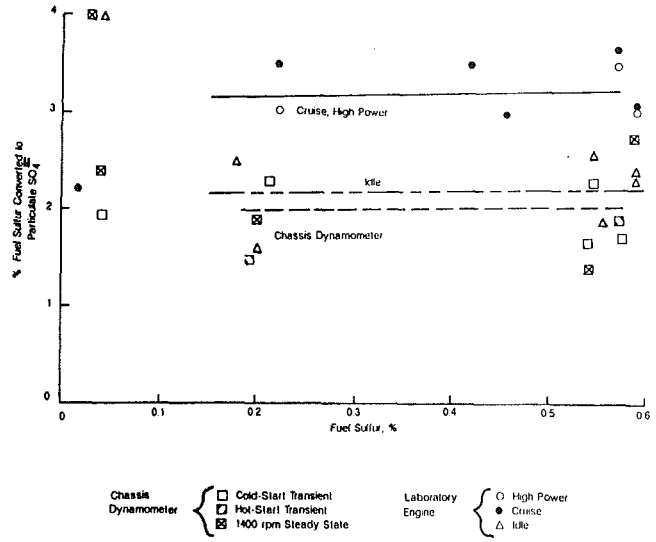

Fig. 2 Conversion rate of fuel sulfur to particulate sulfate versus fuel sulfur level for laboratory engine and chassis dynamometer experiments under different operating conditions (from [9])

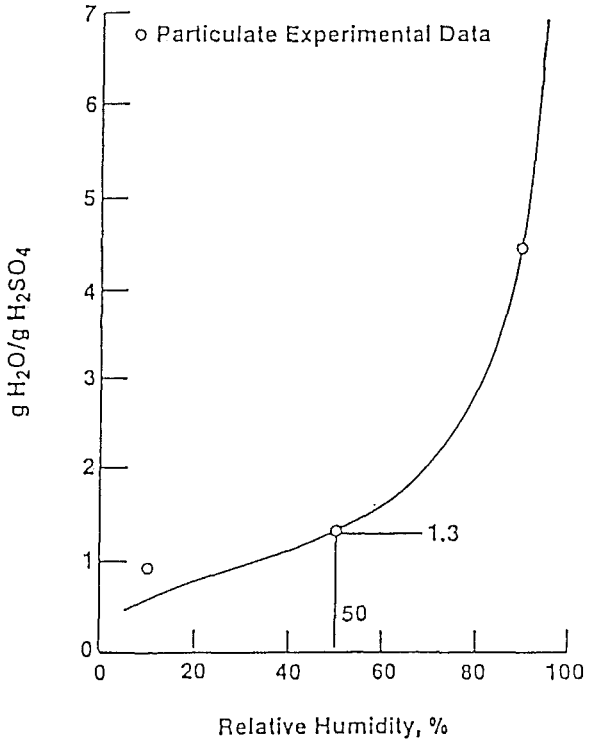

Fig. 3 Influence of relative humidity on "bound" water associated with sulfuric acid and results of changes in humidity on bound water in the particulate (from [9])

data on the subject of bound water and organics doubling the weight of directly filtered sulfuric acid mist.

Figure 3 [9] illustrates the effect of relative humidity on the weight of water to sulfuric acid equilibrium. Filters are weighed at a controlled humidity and use plastic-coated fiberglass media. Nevertheless, the water bound to the acid during the test is not easily reversed by the prescribed acclimation period of 1 hour minimum at controlled humidity condition.

The "scrubbing" of hydrocarbon compounds out of the gas phase due to reaction with sulfuric acid was also quantified by the pioneering work [9]. Solvent organic extraction with methylene chloride yields an increase in particulate weight when the filter was higher in sulfuric acid content than when not,

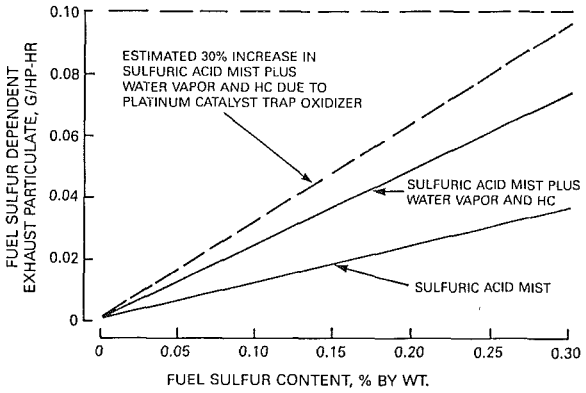

Fig. 4 Collectible fuel sulfur-dependent particulate as a function of fuel sulfur content

as would be the case with fuel containing high and low sulfur. For a change from 0.55 to 0.2 percent sulfur fuel, [9] showed roughly 90 percent less organic content in the collected particulates.

To place these two little-known, but pertinent, factors into perspective, the bound water accounts for about two thirds and scrubbed organics about one third of the increase in weight of fuel sulfur derived particulates. The sum total of these factors is roughly to double the weight of the sulfuric acid mist collected on the filter. As reported [9], this effect was found regardless of fuel sulfur content.

Sulfur-Dependent Particulates. Taking the most recent and respected value of 2 percent conversion over the combined EPA cold-hot test, it is possible to compute the importance of fuel sulfur to the manufacturer in his attempt to produce an engine to meet 1991 and 1994 limits. It should be noted that 2 percent is considered conservative. It may need to be revised slightly, perhaps upward, as more data are reported for a variety of engines operating on the EPA cycle. Figure 4 shows the relationship of fuel sulfur content to sulfuric acid mist and acid mist plus adsorbed water vapor and hydrocarbons.

The equation used to determine the particulate sulfuric acid is

$$\frac{\text{g } H_2SO_4}{\text{hp-h}} = (A)\,(B)\,(C)\,(D)\,(E) \qquad (1)$$

where A is $\dfrac{\text{lb sulfur}}{\text{lb fuel}} = \left(\dfrac{\text{percent S}}{\text{in fuel}}\right)\dfrac{(1)}{(100)}$

B is BSFC of engine on EPA cycle taken as

$$0.45\ \frac{\text{lb fuel}}{\text{hp-h}}$$

C is $\dfrac{\text{molecular weight } H_2SO_4}{\text{molecular weight S}} = \dfrac{98}{32}$

D is conversion rate of S to H_2SO_4 taken to be 2 percent, conservatively

E is conversion factor $= \dfrac{453\text{ g}}{\text{lb}}$

The above is then doubled to account for the weight of bound water and organics associated with the sulfuric acid. This is also shown in Fig. 4 over the range of 0.30 percent to the current national average sulfur content in type 2-D diesel fuel.

The third concern regarding fuel sulfur is that it makes the use of a highly active oxidation catalyst, such as the platinum material used in many automotive exhaust systems to reduce

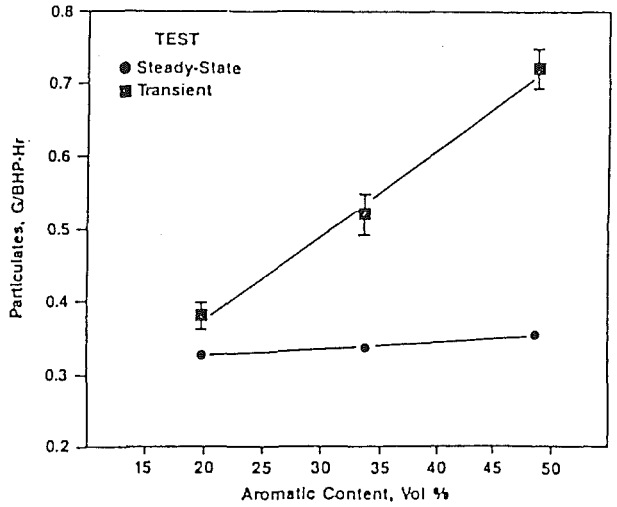

Fig. 5 Effects of fuel aromatic content on particulate emissions: steady-state versus transient tests on a heavy duty engine [13]

hydrocarbons and carbon monoxide, impractical. In 1991 and especially 1994, the nature of particulates is expected to become more organic in content than the carbonaceous soot typically thought of as particulate. This will happen as engine manufacturers are successful in improving combustion. As these improvements take place, the organics from idle, part load, and deceleration of the engine from incomplete combustion of the fuel will likely persist making the use of an oxidation type catalyst appropriate.

Catalyst Trap Oxidizer Needs Low Sulfur Fuel. It is not thought possible to meet the 0.1 g/hp-h 1994 standard for all HD trucks and buses without some type of exhaust aftertreatment device. This will take the form of a filter or trap device that could incorporate as an integral feature or, in tandem, an oxidation catalyst. The catalyst would principally work to burn hydrocarbon organics (unburned fuel and to some extent unburned lubricant). Some tests are in progress with promising results with low sulfur fuel. However, such efforts are not taken seriously because when used with exhaust from high-sulfur fuel, the conversion rate of the SO_3 to H_2SO_4 is sufficient to more than equal the reductions in hydrocarbon mass.

Accordingly, for exhaust aftertreatment devices that utilize precious metal catalysts to be used, low-sulfur fuel is absolutely required. Figure 4 shows the penalty estimated in sulfur-derived test filter particulate when a platinum catalyst trap oxidizer is used. This estimated 30 percent increase in collected weight is based on unpublished research using platinum washcoats containing materials that suppress the conversion of SO_3 to H_2SO_4. The so-called selective catalyst needs further development to demonstrate low conversions over the transient cycle. Incidentally, it has long been known that platinum in oxidation and three-way catalysts cause increases in H_2SO_4 even with unleaded gasoline (average sulfur content of 0.02 percent). Sulfur suppressed catalysts are not the rule for gasoline engines since there are no particulate regulations.

Fuel Sulfur Effect on Engine Wear. There is a fourth reason some use to reduce fuel sulfur, which is not universally true. The claim made in [10], for example, is that reducing fuel sulfur will reduce wear and increase engine life. This is based on the fact that SO_3 in piston blowby gases is converted to H_2SO_4 in the crankcase. This makes the lubricating oil acidic and leads to corrosion, etching, rapid bearing weight loss, accelerated wear, and short life. At one time, this was true. Before engine design, materials, and metallurgy, before the advent of lubricant base oils plus miracle lubricant additives, and before desulfurizing of diesel fuel, engine life was dependent somewhat on sulfur content of the fuel.

However, today's engines are capable of operating for extended mileage without major overhaul. It is not unusual for engines to achieve 500,000 miles in some of the largest trucks (Class VII and VIII) before major overhaul. Lubricants are capable of providing the superior protection needed against corrosive wear with fuel sulfur contents within the ASTM specification of 0.5 percent maximum sulfur content. When the manufacturers' recommendations for fuel, lubricant, maintenance, and operation are followed, engines usually wear out because of engine deposits in the ring zone, which in turn cause bore polishing, scoring, and wear.

Aromatics

What to do about the aromatic content in diesel fuel? Aromatics represent much of the usable heat value of the fuel, help the fuel to flow in winter, and allow the refiner flexibility in manufacture. Aromatics are not included in the ASTM specification. Aromatics are difficult to measure as a class and little is known about specific effects of the different subclasses or compounds that comprise the aromatics in diesel fuel.

Aromatics are directly related to visible smoke and particulates, both carbonaceous soot and organic content of particulates. It is the one fuel property that engine manufacturers feel strongly about as having sufficient incremental importance on diesel particulates to warrant its control and reduction. It is the aspect of diesel fuel the refiners feel most strongly about regarding the expected major adverse cost impact, and perhaps more importantly variable impact such control and reduction would have in specific refineries.

The literature has attempted to quantify the effect of aromatics on diesel engine emissions and performance with little universal success. Reference [11] is perhaps the most exhaustive series of tests to define the importance of aromatics on a group of light duty, indirect injection, diesel powered cars. This CRC light duty project was a forerunner to the current CRC VE-1 project on HD diesel engines. Reference [12] reports an attempt to relate statistically fuel-engine tests made prior to the CRC project [11]. Whereas [11] reported strong engine-fuel aromatics relationships in terms of increasing smoke, particulates, organics, and mutagenic activity with increased aromaticity, the results of [12] were confounded by several factors. The lack of appropriate experimental design and proper fuel preparation were contributing factors.

Effect on Transient Cycle Particulates. With regard to heavy duty diesel engines, [13] was one of the first to report fuel aromatic effect on transient cycle particulates. Figure 5 [13] shows the practical range of aromatic content from 20 to 50 percent in increasing particulates from 0.4 to 0.7 g/hp-h, a 75 percent increase. For the same fuels and engine, hydrocarbons likewise increased about 40 percent. Reference [13] also reported results of an effect of aromatics on NO_x. Probably more important was the total lack of agreement between steady state, or 13 mode test results, and the EPA transient cycle.

It may be speculated that aromatics influence engine combustion during transient acceleration and deceleration in greater proportion than at steady state. In any event, this work by Caterpillar and Mobil seems to have discredited all steady-state tests insofar as the effect of aromatics on particulates and hydrocarbons is concerned from transient cycles. This means that only data obtained since the inception of the transient cycle test, 1985, are useful in predicting the effect of aromatics in meeting the U.S. EPA limits for particulates.

Perhaps more fundamental is the definition of aromatics and its proper measurement. There are several methods used, but the ASTM D-1319, which uses the FIA method (hydrocarbon types in liquid petroleum products by Fluorescent In-

Table 2 EPA emissions test diesel fuel specifications [17]

Item	ASTM	Type 1-D	Type 2-D
Cetane	D613...	48-54	42-50
Distillation Range:			
IBF °F	D86....	330-390	340-400
10 percent point, °F	D86....	370-430	400-460
50 percent point, °F	D86....	410-480	470-540
90 percent point, °F	D86....	460-520	550-610
EP, °F	D86....	500-560	580-660
Gravity, API	D287...	40-44	33-37
Total Sulfur, percent	D129 or D2622.	0.05-0.20	0.2-0.5
Hydrocarbon composition:			
Aromatics, percent	D1319..	[1]8	[1]27
Paraffins, Napthenes, Olefins.	D1319..	([2])	([2])
Flashpoint, °F (minimum).	D93....	120	130
Viscosity, Centistokes	D445...	1.6-2.0	2.0-3.2

[1]Minimum
[2]Remainder

dicator Adsorption), is most popular. It is specified for gasolines yet is commonly used on distillate fuels with varying success. The precision is greatly dependent on operator and site so only with substantial care, calibration, and cross checking can the analyses by FIA be used with confidence. Any thought of controlling (reducing) aromatics must begin with a recognized, readily reproducible procedure with acceptable precision. It is hoped that it would be sanctioned by ASTM.

Effect on Organic Fraction of Particulates. The test filter collects organics from incomplete fuel combustion and products of lube oil consumption. These organics can be extracted from the filter by use of a solvent such as methylene chloride. In this way, increased organics due to a change in aromatic content can be measured, given no change in lube oil consumption.

The best and most comprehensive published work on this topic is that summarized in [11] using four passenger car diesels, the CRC projects CAPE 32-80 and 33-83 [14-16]. Fuel aromatic content increases were associated with large increases in extractables as well as increases in polynuclear aromatic hydrocarbon (PAH) emissions and mutagenic activity as measured by Ames Bioassay. Reference [9] included results for some steady-state HD diesel experiments with differing aromatic levels and reported modest PAH increases and some increases in extractables and hydrocarbons.

Although particulates, as previously defined, are what must be reduced, the PAH and mutagenic activity of the organic extractables is of major concern with the diesel engine. Reduction in "total particulates" is expected to bring with it a commensurate reduction in organics. However, there are, as yet, insufficient data to predict effect accurately or say with assurance the degree of aromatic reduction necessary. This is confounded somewhat by the lack of knowledge of the relative importance of various classes or subclasses of the fuel aromatics.

Certification Fuel Aromatics Specifications. The EPA emission test fuel specification was first published in support of 1968 regulations limiting visible smoke from diesel engines. This specification recognized the importance of aromatics to smoke emissions and required the test to be performed with a fuel that was considered to contain aromatics consistent with those sold in the U.S. For emission testing and engine development purposes, a fuel as described by Table 2 (reported from [17]) has become a standard type 2-D diesel fuel.

There is little argument that most engines under most conditions operating on fuels with higher aromatic content result in higher smoke, particulates, hydrocarbons, solvent extractable organics (from the particulate filter), PAH's and mutagenicity. The converse is also true. The argument regarding aromatics is over the amount of control or reduction and at what cost. There is little doubt that the manufacturers would like a fuel with controlled aromatics. Although the resolution of this issue is unclear at this time, it is apparent that in 1994, if not in 1991, some form of aromatic control of type 2-D diesel fuel will become a reality.

Distillation Range

The third variable of interest in a low emission diesel fuel is the upper end of the distillation range. Some believe that the distillation range, as described by the single 90 percent distilled point commonly known as T_{90}, should be decreased as much as 50°C. This somewhat arbitrary truncating is an attempt to eliminate the highest molecular weight portion of the fuel on the premise that this fraction is most difficult to ignite and burn in the high-speed automotive diesel and gives rise to PAH's and particulates.

The importance of T_{90} is, at present, less well understood than aromatics or sulfur, the other two properties of concern. Reference [9] reported that reducing T_{90} from 316 to 260°C resulted in an 8 percent reduction in particulates on top of (after) major reductions in fuel sulfur and aromatic content. While sulfur effects on particulates appear to stand alone, it is probable that the aromatic content and the T_{90} point of a diesel fuel are interrelated somewhat and that their effect on particulates cannot be easily separated. Aromatics are usually distributed throughout the full boiling range of a diesel fuel so that a reduction in the T_{90} point will affect both aromatic, paraffin, and to some extent the olefin class of hydrocarbons.

Reference [11] included analysis that attempted to correlate T_{90} to particulates but reported they were minor. Interactions between T_{90} and aromatics (as both increased) were shown to correlate strongly with polynuclear aromatic hydrocarbons and the Ames Bioassay test response increases. Even though [11] describes indirect injection passenger car engine fuel effects, it is indicative of the possibility that a reduction in T_{90} may be helpful in reduced exhaust emissions of concern to health. This effect was also discussed in [9].

At 50°C reduction in 90 percent point is equivalent to going from an ASTM type 2-D fuel to type 1-D fuel (based on max T_{90} [1]). Type 1-D fuels, also known as Jet A kerosene, were standard in city buses prior to the 1974 fuel embargo and were permitted by EPA in emissions certification. If type 1-D fuel were used, this would increase volatility because of the lower initial boiling point which controls fuel volatility. Reducing only the T_{90} point, assuming it could be done, by blending off everything about T_{90}, would not affect fuel volatility greatly. The use of type 1-D fuel will likely be limited to special circumstances such as city buses or vehicles in sensitive applications because of availability.

The justification for truncating the type 2-D boiling range, eliminating the last 25 to 50°C of the distillation curve, is not clear. The only reason, beyond that afforded by an aromatics reduction, might be further reduction in exhaust products of a carcinogenic nature. However, this needs much more study and should be of interest once aromatic control is effected. Then, the true need for control of T_{90}, if any, can be defined.

Low-Emission Diesel Fuel

A desire for a low-emission diesel fuel began with the advent of the first EPA smoke standard twenty years ago. It was known then that increasing aromatics content increased visible

Table 3 Speculated low emission diesel fuel for use in 1991 and later model year HD diesels

	1991		1994
	ALT. A	ALT. B	
Sulfur Max % Wt.	0.1	0.05	0.05
Aromatics Max %	30	30	20
Injector Deposit Control Additive	✓	✓	✓
Combustion Improver Additive		✓	✓
Incremental Cost(1)	6	7	9

(1) Sales Price must be equalized with Type 2-D Fuel

smoke from the engine. However, a reduction in aromatics reduced smoke only incrementally. Simpler, cheaper means through engine design were far more effective and fuel modification was abandoned. No amount of fuel modification could alone make most engines pass the limit.

With the advent of strict particulate emission standards, a case may now be made for a diesel fuel for HD vehicles that will result in lower air pollution. Such a fuel could result in lower smoke and particulates and keep them low longer. Manufacturers of HD engines need help from the fuel refiner to meet and keep on meeting the 1991 particulate standards.

Table 3 shows a speculated low-emission diesel fuel that embodies reduced sulfur, a cap on aromatics, and the use of chemical additives to control injector deposits and improve combustion. The timetable, levels and alternatives shown on Table 3 represent a plan for consideration.

Fuel Additives. Additives to improve combustion and reduce injector deposits are considered important parts of an LEDF plan. It has long been known that chemicals can improve the cetane number or ignition quality of diesel fuel and are used more or less in diesel fuel. Other chemicals are added to bring about better cold weather operation and include pour-point depressants and flow improvers, dewaxers, etc. For years, chemicals known as combustion improvers, utilizing some form of manganese, for example, have been sold in "premium diesel fuels." Chemicals to reduce injector deposits, coking, fouling, and malfunction have found favor as a means to achieve long life and reduced maintenance costs, and some even claim reduced fuel consumption. Chemical additives specific for visible smoke suppression, some containing barium or calcium, have been marketed, along with additives that when burned altered or modified the perceived exhaust odor. Some refiners, through refining and blending, have prepared premium diesel fuels that were to provide longer life, improved fuel economy, less smoke, and less maintenance. References [18–22] describe the performance advantages of various diesel fuel additives and specific field laboratory demonstrations of the performance claims.

Injector Deposits. Deterioration of fuel injection spray due to nozzle tip coking deposits is just one of several ways in which smoke and particulates are increased. Overlooked to date is the potential of fuel additives to maintain "like new" emission rates for long periods of operation by keeping the fuel injectors free of harmful tip deposits. The manufacturer must meet the stringent emission regulations for a long time, not just when new. For example, the EPA certification requires control of particulates and other emissions for up to 290,000 miles, in the case of the largest Class VIII vehicles/engines [23, 24].

Laboratory and/or field testing is performed by the manufacturer to determine the rate at which smoke, particulates, and gaseous emissions increase with service. Periodic transient emission tests are performed and the best fit "least-squares" line is drawn. From this, a deterioration factor DF is calculated that is additive (smoke) or multiplicative (all other emissions) to the certification engine value when new. This is the value that is compared to limits to determine whether the engine will be certified by the EPA.

The greater the increase in particulates with time, the larger the DF and the lower the emissions must be when new. The closer the DF is to 1.0, the better, and to the extent fuel additive treatment will permit this to happen, the more manufacturers could require such additive(s) to be included in a list of fuel modifications for use in 1991 low-emissions diesels. The ability to keep on meeting standards for the extended mileage/time now required by EPA is important to the manufacturer.

Combustion Improvers. Ignition quality of diesel fuel is typically associated with cetane number. Additives are effective in raising a fuel's cetane number and are used when necessary, but not as a rule. There is a range of other organic and organometallic additives that have been developed to aid the combustion process. As with injector deposit control additives, the available data are mostly from field trials or steady-state dynamometer engine testing with concentrations on demonstration of claims of lower fuel consumption, increased performance (power), better startability, better cold weather operation, and lower visible smoke.

The improvements with organic-based combustion improvers by the EPA transient cycle following prescribed EPA particulate and gaseous emissions procedures are not defined nor reported sufficiently to include in this paper. Thus it remains to demonstrate and quantify the importance of diesel combustion additives in terms of the EPA procedure. Many combustion improvers are organometallic. Metal-containing additives, though considered the most effective, have two problems.

One problem is the filter weight due to weight of the metal oxide or compound exhausted. An example of this is the use of barium or barium calcium containing compound to reduce visible smoke. The significant reduction in smoke resulted in a major increase in particulate weight [23]. The other problem is the resistance by California and U.S. authorities to sanction or permit introduction of a metal containing additive into diesel fuel. To do so could result in a long, expensive, testing program to demonstrate that the combustion products of the metal additive do not increase risk to health.

Two Fuel Strategy in 1991

The LEDF, described in Table 3, could be part of a two-fuel strategy. LEDF would be introduced, perhaps as early as 1991, for use with on-highway HD diesel powered vehicles that are certified to meet the 0.25 g/hp-h standard.

Low Emission Diesel Fuel Requirements. Two sulfur levels, 0.05 and 0.10 percent, are listed as alternatives for 1991 in Table 3. The engine emission control strategy speculated in Fig. 2 [6] illustrates the possibility of an interim 1991 fuel specification of 0.10 percent as sufficient. This alternative is listed to give more opportunity to the fuel refiner to use those options available in crude selection, refining, desulfurization, and blending until 1994 when the sulfur content needs to be below 0.05 percent by weight.

The cap or maximum on aromatics is a new requirement for diesel fuel. The levels for 1991 of 30 percent are arbitrary and speculative assumptions derived from the average aromatics sold in the U.S., on the order of 34 percent, and the emissions test fuel specification 27 percent minimum. The importance in 1991 is to put in place a specification for aromatics and to eliminate in LEDF variable aromatic levels that cause in-service

vehicles to exceed particulates HC and smoke levels over that when certified.

Type 2-D Fuel. The other fuel of the two-fuel approach would be essentially the same as that sold as type 2-D. It is conceivable that some refiners may attempt to achieve low sulfur/aromatics LEDF through selective blending and thereby shift the higher sulfur and/or aromatics to 2-D. This would be allowed until say 1994 to give refiners a period of transition and adjustment. As more engines enter the marketplace, however, refiners will have to modify their operations because type 2-D fuel could then exceed existing specification of 0.5 percent sulfur. In any event, some upper limit on type 2-D aromatics would be necessary in 1994 to prevent this fuel from becoming responsible for an increase in pre-1991 engine emissions. Selective blending, for those refiners who elect to do so, is not considered a problem for the first few years because of the relatively small quantities of LEDF needed at first.

Planned Phase-In of LEDF. Each year, more diesels would be sold that require LEDF until about 1997, when perhaps half of the diesel fuel sold would be LEDF. Newer trucks operate at higher mileage/year and it might not be until the year 2000 that half the trucks would require LEDF. In much the same way as unleaded gasoline was phased in, the same would occur with LEDF.

As with unleaded gasoline, small diameter tank filler openings and service station dispensing nozzles would be required to prevent using 2-D in vehicles powered by engines requiring LEDF. As with many service stations, many truck stops and private fleet fueling systems have multiple tanks. One tank would be devoted to LEDF along with the dispensing pump and nozzle. Although more trouble than a total switch to LEDF, it would permit early introduction to those vehicles/engines certified with LEDF and permit a phase-in over a period of time.

Price Equalization. Unlike unleaded–leaded gasoline policy, the Federal Government would *have* to require that LEDF be priced the same as 2-D. Only in this way will misfueling and avoidance of the price difference of LEDF be prevented. The Federal Government has many ways through energy/excise taxes to force the LEDF price to be no more than type 2-D fuel. The price of 2-D would not be fixed, but allowed to respond to the market. LEDF price would then move with the 2-D price. An added advantage of this strategy will be the increased voluntary use of LEDF in existing pre-1991 vehicles/engines. This will occur since diesel vehicle users recognize the importance of deposit control additives for long term injector performance. LEDF will offer the same types of improvements and advantages in all existing pre-1991 engines. Pre-1991 engines and vehicles will operate well on LEDF.

LEDF Incremental Cost. It is possible that the cost to prepare and market LEDF in 1991 could be as little as 6 cents per gallon more than type 2-D, before equalization. Perhaps 1 cent would be for sulfur removal, 3 cents for aromatics control, 1 cent for the additive package, and 1 cent for distribution and conversion of a pump and tank to LEDF. These prices/costs are guesses and unconfirmed. However, they help to place in perspective the essential elements of a LEDF and one way to get such a fuel into the market with not only changed composition, but also with an additive treatment to maintain low engine emissions for a longer period of time.

In 1994, the incremental cost increase, in 1988 pennies, could be on the order of 9 cents. This would provide reduced aromatics perhaps to 20 percent as well as trace sulfur at less than 0.05 percent by weight. Both deposit control and combustion improver additives would be required an in common use. A 10 percent increase in the cost of diesel fuel is thought to be about the maximum impact that many users of diesels would accept before considering use of gasoline engines, an option in most Class VI and smaller delivery trucks. However, the price equalization plan of this two-fuel strategy will result in spreading the incremental cost of LEDF across all highway diesel fuel. At most, diesel fuel used on-highway would see perhaps a 1/2 cent increase in 1991. Each year as more LEDF is used, the price for diesel motor fuel would increase, but in an orderly, phased-in plan.

Manufacturers' Responsibility

LEDF will occur when the manufacturers of HD diesel engines require it. Quite simply, the engine manufacturers must decide on the diesel fuel required to meet and keep on meeting the 1991 and later emission standards. The manufacturers are the affected party by the regulations and they have to decide on an overall strategy of emissions control, a strategy that will include one or more features of the proposed LEDF. The manufacturers must weigh the technical importance of the fuel against the cost and availability. They must not demand a fuel that cannot be made or is prohibitively costly to produce. However, once decided, they must press their requirements to the refiners and the EPA and make these requirements a part of the application for certification.

This can be accomplished through a continuing dialogue with the refiners and EPA while additional data are being obtained by the transient emissions test cycle to demonstrate further the sulfur, aromatic, and fuel additive effects. With respect to additives in certification fuel, there is ample precedent with intake system deposit control additives in EPA certification and durability gasolines. Incidentally, such additives are in widespread use to control injector and intake valve deposits in gasoline-powered vehicles.

Summary

There are those who will oppose this two-fuel, LEDF strategy and will wish the status quo to continue. Their arguments will be that diesel fuel is, after all, a residual fuel, which should continue to enjoy the widest possible specification for maximum availability, lowest price, and best overall system energy utilization of the barrel of crude. They will argue also that it may be cheaper to use a catalytic filter or trap to collect the particulates in the exhaust. Some will say that a further increase in fuel cost will drive customers away from diesel power to alternative fuels and engines.

There is an element of truth to each of the arguments. However, if one believes the mandate given Congress and EPA to reduce air pollution from diesel vehicles, then a strategy does exist by which this could occur. The strategy involves the engine manufacturer, first and foremost, to improve combustion efficiency as much as possible; second, the fuel maker to provide a modified low-emission diesel fuel; and third, for lube oil consumption to be severely reduced. For 1994, even these best efforts by all parties will require the addition of effective and durable exhaust particulate trap-catalyst systems.

There remain many issues to resolve, such as:

1 Confirm the 2 percent conversion of sulfur to H_2SO_4 during the EPA test and its proclivity to adsorb water vapor and organics once collected by the test filter.

2 Quantify the effect of aromatics on particulates and organics during the EPA test.

3 Demonstrate the effect of organic-based chemical additives by the EPA transient test on: (*a*) injector deposit control, and (*b*) combustion improvers.

4 Determine the importance of reducing the 90 percent distillation temperature specification.

5 Develop one or more strategies that result in price equalization between LEDF and conventional type 2-D fuel.

6 Establish estimated cost increments and determine price impact on on-highway diesel fuel from 1988 to say 2011.

This issue is at the point where arguments and debates can escalate to antagonism, lawsuits, and delaying tactics. Or, we can, for once, lock arms and decide to work together: EPA, manufacturers, and refiners, in the march to eliminate the diesel engine as a significant source of pollution. It is all a matter of our self-interest being one and the same as the national interest. When we become convinced that it is in our best interest to market a fuel that will promote lower emissions, then we will do so in the most practical, efficient, and timely way.

References

1 ASTM Designation: D 975-81, Standard Specification for Diesel Fuel Oils.

2 40 CFR, Part 86, Subpart A, para. 86.088-11, 86.091-11, 86.094-11, 07-01-87 edition, Protection of the Environment.

3 California New Vehicle Standards Summary, Passenger Cars and Heavy-Duty Engines and Vehicles, *revised 6/9/86.*

4 Richards, R. R., and Sibley, J. E., "Diesel Engine Emissions Control for the 1990's," SAE Paper No. 880346, 1988.

5 Gill, A., "Design Choices for 1990s Low Emission Diesel Engines," SAE Paper No. 880350, 1988.

6 Springer, K. J., "Diesel Lube Oils, 4th Dimension of Diesel Particulate Control," ASME JOURNAL OF ENGINEERING FOR GAS TURBINES AND POWER, this issue.

7 Springer, K. J., and Stahman, R. C., "Unregulated Emissions From Diesels Used in Trucks and Buses," SAE Paper No. 770258, 1977.

8 Wall, J. C., Shimpi, S. A., and Yu, M. L., "Fuel Sulfur Reduction for Control of Diesel Particulate Emissions," SAE Paper No. 872139, 1987.

9 Wall, J. S., and Hoekman, S. K., "Fuel Composition Effects on Heavy-Duty Diesel Particulate Emissions," SAE Paper No. 841364, 1984.

10 Weaver, C. S., Miller, C., Johnson, W. A., and Higgins, T. S., "Reducing the Sulfur and Aromatic Content of Diesel Fuel: Costs, Benefits, and Effectiveness for Emissions Control," SAE Paper No. 860622, 1986.

11 Hare, C. T., and Smith, L. R., "Light-Duty Diesel FTP Emissions as Functions of Fuel Volatility and Aromatic Content," SAE Paper No. 861120, 1986.

12 Bykowski, B. B., Hare, C. T., Mason, R. L., and Baines, T. M., "Comparison of Petroleum and Alternate-Source Diesel Fuel Effects on Light-Duty Diesel Emissions," SAE Paper No. 831712, 1983.

13 Barry, E. G., McCabe, L. J., Gerke, D. H., and Perez, J. M., "Heavy-Duty Diesel Engine/Fuels Combustion Performance and Emissions: A Cooperative Research Program," SAE Paper No. 852078 in: *Diesel Fuel Quality and Trends*, SP-639.

14 Hare, C. T., "Study of the Effects of Fuel Composition, and Injection and Combustion System Type and Adjustment, on Exhaust Emissions From Light-Duty Diesels," Final Report SwRI-6741 to The Coordinating Research Council, Inc. on project CAPE-32-80, Apr. 1985.

15 Hare, C. T., "Supplemental Study of Fuel Property and Injection and Combustion System Type Effects on Emissions From Light-Duty Diesels," Final Report SwRI-8515 to The Coordinating Research Council, Inc. on project CAPE-32-80, Nov. 1985.

16 Smith, L. R., "Study of the Effects of Fuel Composition, and Injection and Combustion System Type and Adjustment on Ames Bioassay, Nitroaromatics, and PNA Emissions from Light-Duty Diesels," Final Report SwRI-7658 to The Coordinating Research Council, Inc. on project CAPE-33-83, Aug. 1985.

17 40 CFR, Part 86, Subpart A, para. 86.1313-84 p. 688, 07-01-85 edition, *Protection of the Environment.*

18 Courtney, R. L., and Newhall, H. K., "Automotive Fuels for the 1980s," SAE Paper No. 790809, 1979.

19 Tupa, R. C., and Dorer, C. J., "Gasoline and Diesel Fuel Additives for Performance/Distribution/Quality," SAE Paper No. 841211, 1984.

20 Tupa, R. C., and Dorer, C. J., "Gasoline and Diesel Fuel Additives for Performance/Distribution Quality—II," SAE Paper No. 861179, 1986.

21 Coley, T. R., Rossi, F., Taylor, M. G., and Chandler, J. E., "Diesel Fuel Quality and Performance Additives," SAE Paper No. 861524, 1986.

22 Montagne, X., Herrier, D., and Guibet, J., "Fouling of Automotive Diesel Injectors—Test Procedure, Influence of Composition of Diesel Oil and Additives," SAE Paper No. 872118, 1987.

23 40 CFR, Part 86, para. 68.085-2(d) (1), (2) and (3) p. 306, 07-01-86 edition, Protection of the Environment.

24 USEPA Advisory Circular No. 51C, Dec. 4, 1986, Assigned Deterioration Factors for 1988 Model Year Light Duty Vehicles, Light Duty Trucks, and Heavy Duty Engines.

25 Hare, C. T., Springer, K. J., and Bradow, R. L., "Fuel and Additive Effects on Diesel Particulate Emissions—Development and Demonstration of Methodology," SAE Paper No. 760130, 1976.

C. M. Urban

H. E. Dietzmann

E. R. Fanick

Southwest Research Institute,
San Antonio, TX 78284

Emission Control Technology for Stationary Natural Gas Engines

This paper summarizes the status of NO_x emission control technology for stationary reciprocating natural gas engines. It provides information on most of the known methods of NO_x control for natural gas engines that are in use, are being considered for use, or may be considered for use.

Introduction

Interest in measurement and control of emissions from natural gas engines began in the early 1970s. In 1972, the Pipeline Research Committee (PRC) of the American Gas Association sponsored a project to measure exhaust emissions from reciprocating engines and gas turbines used in natural gas transmission [1]. Data collected in that program were then used to estimate the contributions of the natural gas utility industry to the total man-made HC, CO, and NO_x emissions emitted in the United States [2]. The status of emission control technology was summarized for the PRC in 1975 [2]. Subsequently, the PRC sponsored a number of other environmental research projects, with the PRC efforts terminating in a reissue of a compilation of all available exhaust emissions data for natural gas engines and gas turbines [3].

The U.S. Environmental Protection Agency proposed emission standards for stationary gas engines and gas turbines in the mid 1970s. Emission standards for gas turbines were promulgated, but national standards for stationary engines have not been enacted. Stringent emissions regulations for stationary engines, however, are currently in effect in air quality management and air pollution control districts in California and several other states.

Engine manufacturers, catalyst suppliers, and individual researchers have been successful in developing several NO_x emission control systems for gas engines (e.g., clean-burn engines, nonselective catalytic control, and prestratified combustion). Another system is currently under development (i.e., selective catalytic reduction), and a number of control concepts are under consideration (e.g., use of cyanuric acid and use of an electrochemical cell).

Over the past several years, the Gas Research Institute (GRI) has been sponsoring programs in NO_x reduction technology for natural-gas-fueled engines and gas turbines. These programs have included a study of catalytic control methods [4] and a special report on the current status of available NO_x reduction technology [5]. The information provided in this paper has primarily been compiled from information developed in the projects sponsored by the PRC and GRI.

Objective

This paper has been written in response to the numerous comments received regarding the special report on NO_x reduction technology [5]. Many of those comments stated the usefulness of concise compilations of information. The paper is an attempt to provide very concise, yet meaningful, information on most of the known methods of NO_x control for natural gas engines that are in use or may be considered for use.

Regulations

There are no national New Source Performance Standards (NSPS) for emissions from stationary reciprocating engines. There are, however, requirements for Prevention of Significant Deterioration (PSD) and for emission control in areas that do not meet National Ambient Air Quality Standards (NAAQS), and in some areas the control requirements are very stringent. Emission control requirements in a nonattainment area are illustrated by the simplification of the rules for control of NO_x emissions in the California South Coast Air Quality Management District (SCAQMD) given in Table 1 [6].

Gas Engines in Use

Compressing natural gas for pipeline transport is currently the major application for natural gas engines, and such engines range in size from under 100 to over 10,000 hp. The technology represented extends from the low-speed, horizontal reciprocating engines installed between 1900 and 1940 to modern low-No_x-emitting reciprocating engines presently being installed by the industry.

Table 1 Example SCAQMD NO_x emission rules [6]

Exhaust oxygen content	NO_x control requirements: Required reduction	or	Limit in ppm at 15 percent oxygen[c]	Approximate g/bhp-h
<4%[a]	90%		90	1.2
>4%[b]	80%		150	2

[a] Generally the naturally aspirated four-cycle engines.
[b] Generally, all of the two-cycle and many of the four-cycle turbocharged engines.
[c] NO_x emissions corrected to 15 percent oxygen.

Contributed by the Internal Combustion Engine Division and presented at the Twelfth Annual Energy-Sources Technology Conference and Exhibition, Houston, Texas, January 22–25, 1989. Manuscript received by the Internal Combustion Engine Division September 1988.

Engines used for compressing natural gas are summarized in Table 2 [7]. There are currently about 5900 units of 300 horsepower or more in service. These engines were produced by only 10 engine manufacturers, but there are about 350 different models or types. Makes of engines with over 100 units in service are Cooper, Clark, and Worthington for two-cycle engines and Ingersoll Rand, Waukesha, White, Cooper, Worthington, and Caterpillar for four-cycle engines. Other makes include Ajax, MEP, and Delaval. Most of these engines are designed for long service life, and engine life in excess of 50 years is not uncommon.

The overall average NO_x emissions from in-use natural gas engines is 11 to 12 g/bhp-h, with a range from a low of about 6 to a high of over 20 g/bhp-h [2]. Current production standard engines generally produce NO_x emissions near or below the overall average value. Low-emission engines (e.g., clean-burn) generally produce NO_x emissions below 2.5 g/bhp-h.

NO_x Emission Control Methods

Methods of NO_x emission control discussed in this paper are listed in Table 3. In this paper, NO_x control methods are divided into categories based on their current state of development for application to natural gas engines. Most of the NO_x emission control methods that have been or are being investigated are included in the table and described in this paper.

Commercially Available NO_x Controls

There are three commerically available NO_x emission reduction systems with major control potential: NSCR, Lean-Combustion, and Prestratified Charge Combustion. Another system with major control potential (SCR) has had some very limited field applications, but is not considered to be fully commercially available.

Table 2 Natural gas compressor engines [7]

Number of manufacturers	Number of engines by type[a]				
	Two-cycle			four-cycle	
	PS[b]	BS	TC	NA	TC
4(3)[c]	1400				
3(1)		700			
3(2)			1300		
7(4)				1500	
9(4)					1000
Cycle total	*3400*			*2500*	
Approximate hp	6,250,000			3,000,000	

[a]Excludes engine less than 300 hp (such engines are estimated to number about 1500).
[b]Abbreviations: PS = Piston Scavenged; BS = Blower Scavenged; TC = Turbocharged; NA = Naturally Aspirated.
[c]( ) denotes number of makes with more than 100 engines of the configuration designated.

Nonselective Catalytic Reduction [4]. Nonselective catalytic reduction (NSCR) systems have been used for over 20 years to convert engine exhaust into a nonreactive gas for use in pressurizing oil wells. Application of NSCR systems to the control of NO_x emissions from stationary gas engines began in the late 1970s, but systems that functioned acceptably for NO_x control in actual usage did not become available until a few years ago. NSCR requires that the engine exhaust be slightly fuel-rich of stoichiometric before being passed over a precious metal catalyst. The catalyst generally includes platinum and rhodium, and it can also include palladium. Basically, NSCR is the stationary application of the three-way catalyst system used in automotive applications.

The electrical signal from an exhaust oxygen sensor is processed in an air-fuel ratio controller to maintain the air-fuel ratio within a very narrow range, slightly fuel-rich of stoichiometric. Under this condition in the presence of the catalyst, the NO_x is reduced by carbon monoxide into nitrogen and carbon dioxide. The exhaust gas temperature range for NO_x reduction above 90 percent is about 800 to 1200°F, and the temperature of the exhaust from four-cycle natural gas-fuel engines is generally within this range. The catalyst will maintain a significant effectiveness within the range of about 700°F to 1500°F.

Practical application of NSCR is limited to natural gas engines that have very limited oxygen in their exhaust stream. Such engines include the four-cycle naturally aspirated and some of the four-cycle tubocharged types. This group of engines represents 30 to 40 percent of the in-service natural gas engines of 300 horsepower or greater (about 2000 of the engines used for compressing natural gas), but only 20 to 30 percent of the total natural gas engine horsepower.

A survey of NSCR suppliers in early 1986 indicated that there were about 1000 NSCR units in the field. Many of those units apparently used manual control of air-fuel ratio. Discussions with users and government regulatory personnel indicated that there were a number of problems with initial installations. The reported problems included inadequate catalyst housing design and support, failure of overtemperature protection systems, poisoning of the catalyst, and inadequate control systems. The two most important of the reported problems are considered to have been catalyst poisoning and inadequate control systems.

With natural gas engines, the primary source of catalyst poisoning is the lubricant. Running a new engine for several

Table 3 NO_x control methods

Control method	Status	Nominal reduction	Potential engine applications
Nonselective catalytic reduction [4]	Commercial	90%	4-cycle
Lean-combustion [8]	Commercial	80 to 90%	2- and 4-cycle
Prestratified charge combustion [9]	Commercial	80 to 90%	Some 4-cycle
Selective catalytic reduction [4]	Potential[b]	80%	2- and 4-cycle[c]
Exhaust gas recirculation [10]	Potential[b]	50%	2- and 4-cycle
Parameter optimization [11, 12]	Potential[b]	30%	2- and 4-cycle
Cyanuric acid ($RAPRENO_x$)	Research	Unknown	Unknown
Electrochemical cell	Research	Unknown	Unknown
Thermal $DeNO_x$	Boilers[d]	–	None apparent
Urea (NO_xOUT)	Boilers[d]	–	None apparent

[a]Reference(s) of primary information source(s).
[b]Potential is used where potential application has been demonstrated.
[c]And some turbocharged four-cycle engines.
[d]Currently applicable only to boilers.

hours prior to catalyst installation and use of low-ash oil have reduced the problems of catalyst poisoning. Suppliers and several users of air–fuel ratio controls for NSCR systems claim that problems with the control systems have been resolved.

Many four-stroke natural gas engines use a simple carburetor, and some older models of these carburetors are unsuitable for precise control near stoichiometric, especially when the load changes frequently. An additional limitation with retrofit of NSCR to in-use engines is insufficient space for mounting the catalyst. Another consideration is that many compressor stations are remote and unattended.

Considerable cost data were available from suppliers and users relative to NSCR systems. An equation developed in late 1985 for estimating the initial costs for an NSCR system with automatic air-fuel ratio control is as follows:

$$\text{System Costs} \simeq \$17{,}000 + \$15 \times \text{HP}$$

Note: HP is rated output, dollars are based on value in 1985, and costs given do not include any special requirements.

In 1985, the cost of an automatic air–fuel ratio control system was about $11,000, and the cost to replace the catalyst element was about $4 to $9 per horsepower of engine power output, depending on the type of catalyst involved. The guarantee period was generally two years, but the useful life of the catalyst was not well established. Costs for system installation and technical assistance in a specific situation can vary significantly.

A primary operating cost is any change in fuel consumption that occurs as a result of installing an NSCR system. A 1 percent change in fuel consumption of a 1000 hp engine, operating continuously for a year, is equivalent to about one million cubic feet of natural gas. There is about a 3 percent increase in fuel consumption in going from an air–fuel ratio that provides minimum fuel consumption to a stoichiometric air–fuel ratio. Conversely, there is about a 3 percent decrease in fuel consumption in going from an air–fuel ratio setting for best power to a stoichiometric air–fuel ratio. In actual usage, the effect of NSCR on fuel consumption has not been established. Other than replacement of the oxygen sensor several times a year and visual checks of the catalyst, there are generally no special maintenance requirements.

Lean-Combustion [8]. Lean-combustion technology (also known as lean-burn or clean-burn) involves a large increase in air–fuel ratio to reduce the combustion temperature, which reduces NO_x emissions. Burning high air–fuel ratio mixtures in an engine requires application of some method to increase the rate of combustion. This has been accomplished using a torch-cell igniter and by the application of controlled swirl. Lean combustion provides for reductions in NO_x emissions of up to 90 percent.

New lean-combustion engines often provide improved fuel economy in addition to reduction of NO_x emissions at a price not much greater than that of the standard engine. Initially, there were some problems with life of some torch-cell igniters. Currently, the primary shortcoming reported for lean-combustion engines is some reduction in spark-plug life.

Engine manufacturers are developing lean-combustion conversion kits. Retrofit applications generally require replacement of the turbocharger, power cylinders, cylinder heads, and engine control system. Lean-combustion retrofit has been applied to a number of engine models to date, most of which have been newer models. Based on costs reported for several conversions completed prior to 1988, an equation was developed for estimating the cost of lean-combustion retrofit to engines greater than 1500 hp:

$$\text{Lean-Combustion System Costs} \simeq \$20{,}000 + \$70 \times \text{HP}$$

Note: HP is rated power output and dollars are based on value in 1987.

Prestratified Charge Combustion [9]. Prestratified charge combustion (PSC) is a retrofit system that has been applied to four-cycle, carbureted, natural gas engines under 1500 hp. In this system, controlled amounts of air are introduced into the intake manifold of the engine in a prearranged sequence and quantity. This stratification provides a flame-cooling effect, resulting in reduced formation of NO_x.

PSC is being applied to engines in California to meet NO_x emission reduction requirements. It has been reported that reductions in NO_x emissions of up to 90 percent have been achieved without significant deterioration of fuel economy. Initially, minor mechanical difficulties were experienced, but subsequent adjustments corrected those problems, and no major problems have been reported.

Because the PSC system is relatively simple and consists of materials commonly available, costs are relatively low. Depending on the size and configuration of the engine, the costs reportedly vary from about $5000 to $25,000 per engine. In the Southern California area, the average cost to install PSC onto 1000 hp engines has been reported to be less than $15,000.

PSC has limitations to widespread application. A primary limitation is that it is applicable only to four-cycle, carbureted engines. Such engines represent a limited percentage of the total engines in use by the natural gas industry and a small percentage of the total horsepower. Another limitation is the need for increasing the intake air capacity or derating the maximum power output of the engine. Some engines are not readily adaptable to installation of a turbocharger or replacement of an existing turbocharger with one of higher capacity.

Potential NO_x Control Methods

Three NO_x emission control methods are considered to have potential application to natural gas engines but are not considered to be commercially available. These systems include SCR, EGR, and emissions optimization of engine operating parameters.

Selective Catalytic Reduction [4]. Selective catalytic reduction (SCR) is applicable to engines containing significant concentrations of oxygen in the exhaust. With SCR, gaseous ammonia is injected into the exhaust prior to being passed over a metal catalyst. There are a number of base metal oxides that can be used for the catalyst, and the efficiences of these catalysts are very dependent on the exhaust gas temperature.

In the current-design SCR systems, an NO_x analyzer is used to measure the concentration of NO_x in the exhaust and ammonia is injected at the rate necessary to attain maximum NO_x conversion efficiency in the catalyst. If less than an optimum amount of ammonia is injected into the exhaust gas, the efficiency of the catalyst decreases. Injection of excess ammonia results in ammonia breaking through the catalyst and discharging into the atmosphere.

Two programs were initiated in 1981 to evaluate application of SCR to natural gas engines. In a California South Coast AQMD demonstration test program, only one out of six SCR units successfully completed 4000 hours (six months) of operation. With that one system, the NO_x reduction efficiency was 75 percent initially and 72 percent at the end of 4000 hours of operation. That system was manually controlled. All other SCR systems evaluated in that demonstration experienced major difficulties. In an A.G.A. PRC sponsored test program, an SCR unit was installed on a two-cycle, 2500-hp natural gas engine. Major problems encountered in that study were frequent control equipment failures, catalyst poisoning, ammonia discharge to ambient air ("breakthrough"), and excessive engine backpressure.

In early 1986, one SCR system was reported in operation on a piston engine installation in Japan. This was a relatively large system used to treat the exhaust gases from two 7000-hp

diesel engines. Considerable daily maintenance was necessary to keep that catalyst system functioning at about 80 percent NO_x conversion efficiency. Five percent of the catalyst in the reactor was reported to be manually moved two to three times each day to remove dust accumulated on the catalyst. It was reported that this SCR unit had been operated for a number of years without major problems.

In early 1986, the primary supplier of SCR systems for stationary engines claimed to have about ten SCR units "in operation." Two other companies reported they had one or more units "in operation." Based on a site visit to observe an SCR system in San Diego, CA, and conversations with several other companies having SCR units, no system at that time appeared to be commercially operable. Contacts since that time indicate that the status concerning SCR for stationary engines has not undergone any really dramatic improvement. Problems reported with SCR units include fouling of the catalyst, settling of pelleted catalysts, ammonia vaporization in the supply lines upon shutdown, and a variety of control system failures.

Because the SCR catalyst will only operate over the narrow temperature range of about 600 to 800°F, locating the unit at the optimum temperature point in the exhaust stream is difficult. Accommodating an SCR catalyst in some existing units could require redesign of the exhaust system and facility. This could make retrofit of SCR on some existing units very difficult and costly.

Based on discussions with operators of engines having SCR systems, it appears that the basic system was provided by the supplier, and the complete system was then installed by some other organization. The operator then spent a considerable effort attempting to get the system to function properly. It was, therefore, very difficult to apply definite costs to those systems. However, a reasonable cost estimate for an SCR system installed on a stationary engine can be determined using the following equation:

$$\text{SCR System Costs} = \$120{,}000 + \$40 \times \text{HP}$$

Note: HP is the Rated Horsepower, dollars are based on values in 1985, and costs given do not include any special control requirements.

The cost of an SCR system with automatic controls for a 1000-hp engine is about five to six times the cost for an NSCR system.

Another type of SCR system (CER-NO_x process) uses aqueous ammonia and ceramic molecular sieve honeycomb catalyst modules. It has been stated to have a wider temperature operating range and to be more tolerant of contaminants in the exhaust gases [13]. Based on comments, however, the system appears to be even more expensive than conventional SCR for engine applications.

The operating costs for an SCR system involve significant maintenance and the cost of the ammonia. The ammonia requirement for an SCR system is about 0.4 lb for each lb of NO_x removed (with NO_x expressed as NO_2). The price of ammonia is subject to major price swings resulting from major perturbations in the price of feedstock.

Exhaust Gas Recirculation [10]. Recirculation of exhaust gases into the engine cylinder decreases the formation of NO_x by reducing the maximum combustion temperature. EGR has been used in automotive applications for over ten years and has been evaluated in stationary natural gas engines. One of the primary concerns with using EGR in stationary engines has been the potential detrimental effect on engine life.

In discussing EGR for engines with significant quantities of scavenging air in the exhaust, gross rate of exhaust recirculated is not very meaningful relative to the effects on combustion and NO_x emissions. Therefore, the concept of effective EGR (EEGR) was developed to adjust the gross rate of EGR properly for differences in concentrations of combustion products. The formula for converting the gross rate of EGR to the EEGR rate is as follows:

$$\text{EEGR} = \text{Gross EGR} \times (20.9 - \text{Exhaust Oxygen in \%})/20.9$$

Two factors limit the amount of reduction in NO_x emissions that can be achieved using homogeneous EGR without increasing the total amount of intake charge into the engine or derating the power output of the engine. One factor is the amount of excess oxygen available in the combustion chamber. If the amount of added exhaust gases exceeds the amount of excess oxygen, the resulting fuel-rich combustion increases the production of CO and fuel consumption. The second factor is that high rates of EEGR, generally between 10 and 15 percent, result in incomplete combustion and significant increase in fuel consumption.

A natural gas transmission company conducted an evaluation of EGR in which the recirculated exhaust gases were cooled and filtered before being reintroduced into the engine. Cooling and filtering the exhaust removes components that could be potentially harmful to the engine and also reduces the likelihood of engine detonation. A stainless steel heat exchanger was used to cool the exhaust, and filtration was accomplished by introducing the recirculated exhaust into the engine air intake.

Nominal reduction in NO_x emissions using EGR, with acceptable engine performance and without combustion system modifications to the engine, is about 40 to 50 percent. The minimum NO_x emission rate achievable with EGR appears to be about 6 g/bhp-h. Such levels of NO_x emissions attained with EGR are associated with about 2 percent increase in fuel consumption.

For two-cycle natural gas engines, the following equation is considered to be a reasonable estimate of the costs involved in applying EGR:

$$\text{Two-Cycle EGR System Costs} \simeq \$40{,}000 + \$25 \times \text{HP}$$

Note: HP is rated output and dollars are based on value in 1988.

Application of EGR to four-cycle natural gas engines is estimated to be about 10 percent lower in cost. If EGR systems were installed in significant numbers, some decrease in costs could be expected.

It is anticipated that the EGR system as described will have no measurable effect on engine maintenance or service life. A primary operating cost with EGR is increase in fuel consumption. A 2 percent increase in fuel consumption of a 1000-hp engine is equivalent to about two million cubic feet of natural gas per year.

Parameter Optimization [11, 12]. Baseline emissions of many in-use engines can be reduced by optimizing engine operating parameters, such as increasing air–fuel ratio and retarding ignition timing. Nominal reduction in NO_x emissions with parameter optimization is about 30 percent. The minimum NO_x emission rate achievable with parameter optimization appears to be about 8 g/bhp-h, and such reductions in NO_x emissions are generally associated with some increase in fuel consumption. Parameter optimization as a method for reducing NO_x emissions is primarily applicable only to older engines that are high NO_x emitters in the baseline configuration.

Engine NO_x Controls Under Research

Several other NO_x control concepts are currently being evaluated. The two concepts discussed in this paper are the use of cyanuric acid (RAPRENO$_x$) and an electrochemical cell. Another concept recently identified involves electromagnetic conversion.

Cyanuric Acid (RAPRENO$_x$). An NO_x control process has been developed that uses cyanuric acid as the source of a reducing agent. At exhaust temperatures above 630 to 680°F, cyanuric acid ($C_3H_3N_3O_3$) breaks down to cyanic acid (CHNO). The cyanic acid then apparently further breaks down into free radicals and compounds, which react with and break down NO. It has been reported that major reduction in NO concentrations has been achieved in exhaust flowing through a bed of cyanuric acid (cyanuric acid is a solid) at temperatures above 680°F.

The ideal consumption rate of cyanuric acid for complete reduction of the exhaust NO appears to be about one pound of cyanuric acid for each pound of NO (expressed as NO_2) reduced. The primary products of this reduction process are nitrogen, carbon dioxide, carbon monoxide, and water. Since the free radicals also can react with other free radicals and compounds, it is possible for this process also to produce nitrous oxide (N_2O), ammonia (NH_3), and hydrogen cyanide (HCN). In addition, some of the cyanic acid gas could pass through unreacted and be released. Cyanic acid gas is reported to be very toxic to certain types of barley and radishes.

Based on the dearth of any recently reported major progress in development of this process and comments made at several recent meetings, this process may not be living up to the early optimistic predictions. Although the future of this process can not be unequivocally predicted, it appears that any possible application would be at least years in coming.

Electrochemical NO_x Reduction [14]. Evaluation of a solid-state electrochemical reactor for reducing NO_x emissions has been initiated. This system uses a solid electrolyte, normally a high-surface-area ceramic oxide-ion conductor such as stabilized zirconia, ceria, or bismuth oxide. The electrodes can be of any material with good electric conductivity (e.g., porous high-surface-area silver).

Electrochemical reduction of NO takes place in the cathodic zone, yielding nitrogen gas and oxygen ions. The oxygen ions dissolve in the solid electrolyte, and an equivalent number of oxygen ions are released as oxygen gas in the anodic zone of the reactor.

The potential for reducing NO_x with an electrochemical reactor has been demonstrated in a laboratory system, using gases that did not contain oxygen. An electrocatalyst may be required to reduce NO in exhaust gases containing significant oxygen. At this stage of development, there are insufficient data to predict the commercial feasibility of using electrochemical reduction for control of NO_x emissions.

NO_x Control Methods for Boilers

A number of NO_x control methods have been developed for use on boilers that do not currently appear to have application to engines. Two methods are briefly discussed in this paper because of questions that have occasionally arisen concerning such methods. The methods discussed involve thermal $DeNO_x$ and use of urea.

Thermal $DeNO_x$. Under a limited range of conditions, ammonia can be used to reduce NO_x without the aid of a catalyst. Selective noncatalytic NO_x reduction (Thermal $DeNO_x$) is a patented process involving injection of ammonia into high-temperature flue gas without a catalyst. Flue gas temperatures over 1600°F are required for effective NO_x reduction. If hydrogen is injected along with the ammonia, the minimum temperature can be reduced to about 1300°F.

With the high overall air-fuel ratios in the exhaust of two-cycle gas engines, temperatures generally remain below even the 1300°F level. With four-cycle gas engines operating at overall air-fuel ratios nearer stoichiometric, exhaust temperatures are significantly higher and Thermal $DeNO_x$ could potentially become applicable. The systems, controls, and ammonia, however, tend to make Thermal $DeNO_x$ less attractive than combustion modifications or NSCR for four-cycle engine applications.

Urea (NO_x OUT). Injection of an aqueous solution of urea into hot exhaust, along with reaction enhancers, has achieved over 80 percent NO_x reduction in fossil-fuel-burning sources. Urea reacts with nitrogen oxides to form carbon dioxides, nitrogen, and water. Effective NO_x reductions have been demonstrated at exhaust temperatures of 1100 to 2000°F, and efforts are in process to reduce the minimum temperature to about 750°F. Trace amounts of ammonia are formed but can be removed by a scrubbing step. The cost of NO_x reduction using this technique is reported to be considerably less than than of conventional SCR systems on power plants.

Urea does not have the inherent potential hazards associated with liquid ammonia, nor does it require a catalyst. Also, there are no reported apparent concerns or toxic by-products (other than ammonia). The current requirement for high exhaust temperatures, however, makes application of this process to two-cycle gas engines unfeasible.

Costs for NO_x Reduction

Baseline NO_x emissions for natural gas engines range from about 6 to over 20 g/bhp-h, and engine sizes range from less than 300 to over 10,000 hp. Add to that the inadequately defined maintenance and fuel consumption associated with the various control methods. Then include the various capital recovery factors and computational methods used industry-wide for calculating costs, and one can conclude that calculated life-cycle costs or costs in terms of dollars per year or dollars per ton of NO_x removed are essentially a function of the specific assumptions used. Therefore, in this paper, presentation of costs has been limited to providing installation cost projections for several of the emission control systems.

Acknowledgments

The information summarized in this paper has primarily been obtained from programs sponsored by the Pipeline Research Committee (PRC) of the American Gas Association or by the Gas Research Institute (GRI). The authors would like to express their gratitude to the PRC for sponsoring numerous interesting programs over the past sixteen years and to the GRI for sponsoring a number of interesting program tasks over the past several years. We would also like to thank the members of the A.G.A. PRC Environmental Research Supervisory Committee and the Diesel Engine Manufacturers Association (DEMA), and all of the other natural gas transmission companies, engine manufacturers, and emission control companies who provided information for those programs.

References

1 Dietzmann, H. E., and Springer, K. J., "Exhaust Emissions From Piston and Gas Turbine Engines Used in Natural Gas Transmission," Final Report to the Pipeline Research Committee of the American Gas Association under Project No. PR-15-61, Jan. 1974 (A.G.A. Catalog No. L22274).

2 Urban, C. M., and Springer, K. J., "Study of Exhaust Emissions From Natural Gas Pipeline Compressor Engines," Final Report to the Pipeline Research Committee of the American Gas Association under Project No. PR-15-61, Feb. 1975 (A.G.A. Catalog No. L22276).

3 Urban, C. M., "Compilation of Emissions Data for Stationary Gas Engines and Gas Turbines in Use by the Natural Gas Pipeline Transmission Industry," prepared for the Pipeline Research Committee of the American Gas Association under Project PR-15-613, Reissued May 1988.

4 Urban, C. M., et al., "NO_x Control Technology Database for Gas-Fueled Prime Movers, Phase I," Gas Research Institute Topical Report No. GRI-87/0229, Project Period Mar. 1985 through Sept. 1986, published Apr. 1988.

5 Urban, C. M., "Evaluation of NO_x Reduction Technology for Natural Gas Industry Prime Movers," Special Report No. GRI-87/0257 for the Gas Research Institute. Sept. 1987.

6 Rules and Regulations, South Coast Air Quality Management District, Rule 1110.1. "Emissions From Stationary Internal Combustion Engines."

7 "Engines Turbines and Compressors Directory," prepared by Compressor Committee, Operating Section of the American Gas Association, published 1985 (A.G.A. Catalog No. XF0484).

8 Preliminary progress reports on work being conducted by SwRI under Task A.5 of the Gas Research Institute Contract No. 5084-251-1101.

9 Tice, J. K., et al., "Control of NO_x Emissions in Gas Engines Using Prestratified Charge," ASME Paper No. 88-ICE-11, Jan. 1988.

10 Urban, C. M., "Exhaust Gas Recirculation for Retrofit NO_x Reduction of Natural Gas Engines," Draft Topical Report for Gas Research Institute under Task C.7 of Contract No. 5084-251-1101, Apr. 1988.

11 Dietzmann, H. E., and Fanick, E. R., "Parametric NO_x Control Method for In-Use Engines," Final Report prepared for the Pipeline Research Committee of the American Gas Association under Project No. PR-15-425, Mar. 1986 (A.G.A. Catalog No. L51520).

12 Urban, C. M., "High Energy Ignition Systems for Spark-Ignited Natural Gas Engines," Final Report prepared for the Pipeline Research Committee of the American Gas Association under Project No. PR-15-523, July 1986 (A.G.A. Catalog No. L51528).

13 Grove, M., and Sturm, W., "NO_x Reduction With CER-NO_x (SCR) Process," *Engine Emissions Technology for the 1990's*, ASME ICE-Vol. 4, 1988, pp. 89–96.

14 Neyman, M., et al., "NO_x Abatement in Natural Gas Combustion Exhaust Gases by Solid-State Electrochemical Technology," Final Report No. GRI-87/0249 for the Gas Research Institute, Nov. 1987.

Current Regulations Impacting Exhaust Emissions From Stationary Internal Combustion Engines

D. W. Hall
Bay Area Air Quality Management District,
Permit Services Division,
San Francisco, CA 94109

The San Francisco Bay Area is in a nonattainment area for both ozone and carbon monoxide. A significant amount of air pollution emanates from the combustion of fuels in stationary internal combustion engines. The NO_x emissions output from stationary I.C. engines in the Bay Area Air Quality Management District (BAAQMD) is around 14.2 Mg/day (15.6 tons/day). The contributions from other pollutant factors are not nearly as large; nonetheless, they are still noteworthy. BAAQMD has imposed New Source Review (NSR) requirements and Best Available Control Technology (BACT) levels for new stationary I.C. engines. The purpose of BACT is to achieve the lowest level of engine exhaust emissions using today's proven control technology. The BACT level for NO_x is presently set at 0.00056 mg/J (1.5 g/bhp-hr) or less for stationary I.C. engines. The BACT level for each of the other exhaust pollutants has not been set since they seldom require a BACT determination. In the event BACT is triggered, a case-by-case BACT evaluation will be performed. The placement of BACT and NSR standards on stationay I.C. engines has aided the BAAQMD in achieving better local air quality. More stringent standards may be imposed as long as the need for better air quality exists.

Background

Since Congress passed the Air Quality Act in 1967, air quality in the U.S. Metropolitan areas has improved significantly. Major progress toward making the nation's air cleaner has been achieved through more stringent controls imposed on factories, refineries, utilities, vehicles, and small businesses at federal, state and local levels. In fact, most areas in the United States are in compliance 99 percent of the time with the air quality standards set by the Act [1]. Even though great strides have been accomplished, the nation's air quality is still in need of further improvement.

To fight air pollution in the San Francisco Bay Area, the District was formed in 1955 by the California Legislature. The District is a local agency, on a regional level, charged with controlling air pollution from stationary sources. The District is comprised of seven complete counties: San Francisco, Santa Clara, Alameda, Contra Costa, Napa, Marin, and San Mateo, and portions of two others: Southern Sonoma and Southwestern Solano. The District, whose control standards are among the most stringent in the nation, has made many inroads in reducing the Bay Area's ozone concentration. Since 1969, the number of days on which the one-hour federal ozone standard of 0.12 ppm was exceeded has been reduced from about 60 days/yr to fewer than 20 days/yr. Similar efforts are now being directed at controlling the release into the atmosphere of toxic contaminants such as benzene, which may cause adverse health effects.

Introduction

A major contributor to air pollution is the combustion of fuels in internal combustion engines. In the San Francisco Bay Area, about 42 percent of POC and 54 percent of NO_x comes from motor vehicles that are powered by internal combustion engines [2]. Fortunately, increasingly stringent standards imposed on automobiles and trucks have resulted in the development of more efficient control measures for reducing these pollutants.

Even though most internal combustion engines are used to power motor vehicles, a sizable number of them are utilized for industrial application. In the District, stationary I.C. engines are used by sewage treatment plants for pumping and cogeneration, oil companies in the field for natural gas recovery, refineries for gas compression, hospitals for standby electrical power, and many other useful applications. These engines are fired on various fuels: natural gas, refinery gas, digester gas, landfill gas, and diesel fuel. Their power output ranges from around 93 kW (125 hp) to 2.9 MW (3900 hp). These engines collectively produce significant quantities of gaseous exhaust emissions and particulate emissions. As shown in Table 1, nearly one eighth (12.5 percent) of the total

Contributed by the Internal Combustion Engine Division and presented at the Internal Combustion Engine Division Technical Conference, San Antonio, Texas, October 2-5, 1988. Manuscript received by the Internal Combustion Engine Division June 1988.

Table 1 Daily emissions from stationary sources[1]

Pollutant	District Total Mg (tons)	I.C. Engine Total Mg (tons)
NO_x	111.6 (123.0)	14.2 (15.6)
CO	59.9 (66.0)	3.4 (3.8)
POC	78.8 (86.9)	1.8 (2.0)
SO_2	68.0 (75.0)	0.8 (0.9)
Part.	43.5 (48.0)	0.8 (0.9)

[1]Emissions computed from point source information in the District's data bank as of June 1988.

NO_x emissions emitted from stationary sources in the District comes from I.C. engines.

This technical paper was prepared to acquaint industry, engine manufacturers, and the public with the current regulations established by the District for the control of exhaust emissions from stationary I.C. engines. It is not intended to be a step-by-step paraphrase of the regulations, which would be too cumbersome for this paper, but as an overview. Additional information pertaining to these regulations can be found in the District's Rules and Regulations document [3].

Exempt I.C. Engines

All stationary I.C. engines that have a capacity less than 190 kW (250 hp) output rating are exempt from District's permit requirements per Regulation 2-1-115.2. However, any engine that produces amounts in excess of 68 kg per day (150 lb/day) of any single pollutant is not exempt. Other exemptions, as documented in the Appendix A, apply to automobiles, agricultural operations, standby operations, laboratory engines, and portable I.C. engines.

District Regulatory Requirements

For any nonexempt source, an Authority to Construct and a Permit to Operate must be obtained from the District. The Authority to Construct grants the applicant the right to install the equipment in accordance with District's rules and regulations. This Authority to Construct must be obtained by the applicant in advance of any construction or the company would be in violation. When operational, the Permit to Operate is issued upon adherence with all said governing regulations and applicable conditions, if any.

The rules and regulations that apply to stationary I.C. engines require that they conform with the BACT and NSR requirements. These standards are elaborated upon in the subsequent sections.

Best Available Control Technology

BACT, which is defined in Appendix B, is the lowest level of exhaust emissions achievable with today's proven technology. BACT is required on all new and modified stationary I.C. engines that:

Table 2 BACT for NO_x spark-ignited reciprocating gas engines

YEAR	BACT NO_x LEVEL
1982-1984	-90% reduction[1]
1984-1985	0.00074 mg/J (2.0 g/bhp-hr)
1986-1988	0.00056 mg/J (1.5 g/bhp-hr)

[1]The catalyst was found to be inappropriate for I.C. engines fired on digester gas and landfill gas.

1 Reach, on any single day, more than 68 kg (150 lb) of POC, NO_x, SO_2, or particulate matter; or more than 249 kg (550 lb) of CO.

2 The increase in emissions from that new or modified source when added to the total for previously permitted sources has or will result in an increase for a specific pollutant in excess of any of the following amounts:

POC	22.7 Mg/yr (25 ton/yr)
NO_x	22.7 Mg/yr (25 ton/yr)
SO_2	22.7 Mg/yr (25 ton/yr)
Particulate matter	22.7 Mg/yr (25 ton/yr)
CO	90.7 Mg/yr (100 ton/yr)

I.C. engines that are subject to BACT for NO_x must presently meet a NO_x level of 0.00056 mg/J (1.5 g/bhp-h) or less. The BACT levels for other exhaust pollutants have not been set since they rarely trigger BACT. However, when BACT is triggered because of one of the other pollutants, a case-by-case BACT evaluation will be performed. Depending on the fuel, BACT for CO and POC could range from simply fine tuning the engine to installing an oxidation catalyst. For SO_2, BACT could be the use of very low-fuel oils containing as little as 0.05 percent sulfur, by weight. Table 2 shows the BACT NO_x level for stationary I.C. engines over the last 6 years.

Identification of available control technology for a source such as an I.C. engine is of extreme importance in making a BACT determination [4]. In the early 1980's, many manufacturers reported that rich-burning I.C. engines could achieve low levels of NO_x as well as substantial reductions in other pollutants with the use of a NSCR catalyst. NO_x levels were reported to drop from 0.0067 mg/J (18 g/bhp-h) for an uncontrolled engine to 0.00026 mg/J (0.7 g/bhp-h) using a catalyst with controls [5]. However, emissions from these engines when fired in the field on sewage treatment digester gas or landfill gas caused fouling of the catalyst. Digester gas and landfill gas are byproducts of the aneorobic biological decomposition of sewage or organic material. The two gases are typically comprised of about 50 percent methane and 50 percent carbon monoxide with some water vapor, hydrogen sulfide, and many other trace compounds. However, the percentages by volume of both methane and carbon monoxide can vary widely. The contaminants that caused the fouling were found to be sulfates from the fuel combustion, and phosphorus, copper, and silicon possibly from the lube oil,

Nomenclature

BAAQMD = Bay Area Air Quality Management District (referred to as District)
BACT = best available control technology
Mg = megagrams
mg = milligrams
NAAQS = national ambient air quality standards
NO_x = nitrogen oxides
NSCR = nonselective catalytic reduction
NSR = new source review
POC = precursor organic compounds (includes HC)
ppm = parts per million

engine gaskets, or airborne materials. Extensive research has been done to rectify this fouling problem and promising remedies are being evaluated.

In 1984, BACT for NO_x from stationary I.C. engines was deemed by the District to be 0.00074 mg/J (2.0 g/bhp-h). This BACT level was lowered in 1986 to 0.00056 mg/J (1.5 g/bhp-h). To meet the current BACT NO_x level, the operator is free to use any proven technology that can satisfy the BACT requirement. For instance, catalysts, stratified charge engines, and other properly developed lean burn combustion systems, to name a few, could be used.

Influence of New Technology on BACT

The BACT level for NO_x emissions is subject to being lowered incrementally in response to advances in proven engine control technology. Industry as a whole has spent countless hours and research dollars aimed at developing new technology to minimize air pollution from I.C. engines.

Considerable effort to control exhaust emissions from mobile and stationary I.C. engines has been expended in the areas of:

- Alternative fuels such as the widely discussed use of methanol fuel for diesel-powered buses.
- Engine modification retrofits, which may include changes in the pistons, camshaft, injector, cylinder head, etc., and EGR. Retrofits are expensive and may cost four times the capital cost of new controls [6].
- Electronic feedback controls for better optimization of the air/fuel mixture for ideal combustion.
- Fuel composition, such as a reduction in sulfur and aromatic content to control particulate matter from diesel engine exhaust. Also, the use of fuel additives to remove critical deposits formed in carburetors [7] and fuel injectors, which are known to upset the manufacturer's designed air/fuel metering properties.
- Three-way catalysts which reduce CO, POC, and NO_x emissions.
- Reduced peak combustion temperatures accomplished through retardation of the fuel injection timing, intercoolers to lower the inlet charge air temperature on turbocharged engines, and the recycling of exhaust gas products (EGR).

It is important to the District to be knowledgeable of existing control alternatives available for I.C. engines as it will augment the District's efforts in making a BACT determination. As new control technology enters the marketplace and is successfully operated for at least one year, the BACT level will be lowered accordingly.

New Source Review (NSR)

This rule applies to all new and modified stationary sources that are subject to the requirements of BACT. The purpose of this rule is to provide for the review of new and modified stationary sources and provide mechanisms by which permits may be granted. The NSR process might require an applicant to perform emissions modeling and to provide emission offsets. The NSR requirements of the District are contained in Regulation 2, Rule 2 [3].

Offsets for NO_x and POC

Offset is the process by which increases in plant emissions from new equipment are fully mitigated through decreases in plant emissions from, for the most part, discontinued sources. For the purpose of meeting the offset requirement, the District established a formal bank in 1984 to allow a plant to accrue partial emission credit from the permanent shutdown of equipment. Sources with a cumulative increase in emissions of 36.3 Mg/yr (40 tons/year) of POC or 90.7 Mg/yr (100 tons/yr) of NO_x will trigger the offset requirement. A cumulative increase, as defined by the District, is the sum of all increases in emissions of a specific pollutant from a new or modified stationary source occurring since Mar. 7, 1979, pursuant to the Authorities to Construct or Permits to Operate. When NSR is triggered, offsets must be provided for the entire cumulative increase at the ratios specified:

Distance from stationary source	Required offset ratio
On-site or off-site but not over 3.2 km (2 mi)	1.1
Off-site over 3.2 km (2 mi) but not over 24.1 km (15 mi)	1.2
Over 24.1 km (15 mi) but not over 48.3 km (10 mi)	2.0

This means that exhaust emissions from stationary I.C. engines, new or modified, which individually or on a cumulative basis exceed the set offset trigger limit, must comply with the offset requirement before any operation can begin. Offsets may be obtained from previously banked emissions credits by the plant and/or they may be acquired from other facilities holding credits. Purchasing NO_x credits can be expensive. In Santa Barbara County, NO_x credits have been bought for about $3000 to $10,000 per 0.907 Mg (ton) of NO_x.

CO and NO_x Modeling Requirement

Modeling is required for any stationary source with a cumulative increase in excess of 90.7 Mg/yr (100 tons/yr) for CO or in excess of 36.3 Mg/yr (40 tons/yr) for NO_x. By modeling, the applicant must demonstrate that the net air quality impact of the cumulative increase will not interfere with the attainment or maintenance of the NAAQS in the District or any contiguous air basin. In lieu of modeling, the applicant can offset the cumulative increase at a specified ratio.

Future Outlook

BACT and NSR standards will become more stringent as the need for cleaner air prevails. However, the District does not envision in the near future any major changes in the existing regulations that govern stationary I.C. engines.

Offshore Oil Development

One area of increasing attention is the possibility of offshore oil development in the outer continental shelf off San Francisco in California coastal waters. If permitted, this endeavor would involve the use of many pieces of emissions-producing equipment to explore, drill, and produce oil. To support platform operations, a number of marine vessels equipped with diesel engines for main propulsion and electrical output would be needed. Presently, no regulations exist for controlling exhaust emissions from marine vessels as the impact of offshore emissions on onshore air quality is still being quantified. However, if onshore air quality is anticipated to be adversely affected, some regulatory activity in this area may be warranted.

Measures for controlling NO_x emissions from marine vessels have been recently addressed in a study initiated by the Santa Barbara Air Quality Control District [8]. In that study, 4 deg retardation of the diesel engine's fuel injection timing in combination with enhanced seawater intercooling or "aftercooling" resulted in about a 40 percent reduction in NO_x emissions.

Summary

Control measures for regulating exhaust emissions from stationary I.C. engines in the District consist of BACT performance levels and NSR requirements. BACT requires that the engines use a proven and economical control technology that will provide the lowest level of exhaust emissions. It is imposed on all stationary I.C. engines that:

1 Emit on any single day more than 68 kg (150 lb) of POC, NO_x, SO_2, or particulate matter; or more than 249 kg (550 lb) of CO.

2 The increase in exhaust emissions has or will result in a cumulative increase in excess of 22.7 Mg/yr (25 tons/yr) for POC, NO_x, SO_2, or particulate matter; or 90.7 Mg/yr (100 tons/yr) for CO.

The current BACT level for controlling NO_x emissions from spark-ignited reciprocating gas engines is 0.00056 mg/J (1.5 g/bhp-h). BACT for other criteria pollutants will be determined on a case-by-case basis.

The NSR requirements place a cap on the overall quantity of exhaust emissions that can be emitted from a facility before offsets and emissions modeling are required. Offsets for NO_x and POC are triggered with a cumulative increase in excess of 90.7 Mg/yr (100 tons/yr) and 36.3 Mg/yr (40 tons/yr), respectively. At this point, the plant must provide emissions credits to fully offset the new cumulative increase total. Emissions modeling that may be done in conjunction with the offset requirement must demonstrate that air quality in the affected surrounding area will not interfere with the attainment or maintenance of the NAAQS.

Acknowledgments

The author wishes to express his deep appreciation to the members of the Permit Services Division who aided him in the development of this paper, especially Mr. John Swanson, Director of Permit Services Division, and Mr. Bill deBoisblanc, Manager of New Source Review Section.

References

1 *Issues and Actions, A Chevron Public Affairs Advisory*, Vol. 7, Spring 1988.

2 *Air Quality Handbook*, Bay Area Air Quality Management District, 1987-1988.

3 *Rules and Regulations*, Bay Area Air Quality Management District, Vol. 1, Regulations 1-8.

4 Weiss, S. M., "Best Available Control Technology," South Coast Air Quality Management District, May 1983.

5 Product Bulletin, "Emission Levels – Natural Gas Engines," Waukesha Distributors and OEM's, Aug. 18, 1980.

6 Muller, R., et al., Act for Stationary NO_x Sources, prepared for EPA, EPA-909/9-79-002, Dec. 1979.

7 Hall, D. W., and Gibbs, L. M., "Carburetor Deposits – Are Clean Throttle Bodies Enough?" presented at SAE National Fuels and Lubricants Meeting, Dearborn, MI, Oct. 1976.

8 "Crew and Supply Boat NO_x Control Development Program," prepared by Air Pollution Control District of Santa Barbara with Technical Assistance from Arthur D. Little, Inc., June 1987.

APPENDIX A

Exemption, Internal Combustion Equipment

The following equipment, per Regulation 2-1-115, is exempt from the Authority to Construct and Permit to Operate requirements. Equipment that produces air contaminants in excess of 68 kg per day (150 lb/day) of any single pollutant is not exempt.

115.1 Any internal combustion engine or gas turbine used for the purpose of propelling or powering a vehicle.

115.2 Internal combustion (I.C.) engines or gas turbines of less than 190 kW (250 hp) output rating.

115.3 Internal combustion (I.C.) engines directly used for agricultural operations necessary for the growing of crops, or the raising of fowl or animals.

115.4 Internal combustion engines that are laboratory engines used in research or teaching programs.

115.5 Internal combustion engines used solely as a source of standby power and that are operated less than 100 hours per year or (1) are only used for power when normal power line service fails, or (2) are only used for the emergency pumping of water.

115.6 Portable internal combustion engines used on a temporary basis of no more than 30 days per calendar year at any one facility.

APPENDIX B

Definition, Best Available Control Technology

For any stationary source, per Regulation 2-2-201, except cargo carriers, the more stringent of:

201.1 The most effective emission control device or technique that has been successfully utilized for at least one year for the type of equipment comprising such stationary source; or

201.2 The most stringent emission limitation achieved by an emission control device or technique for at least one year, for the type of equipment comprising such stationary source; or

201.3 Any emission control device or technique determined to be technologically feasible and cost-effective by the Air Pollution Control Officer (Chief Executive of the District); or

201.4 The most effective emission control limitation for the type of equipment comprising such stationary source, which the EPA states, prior to or during the public comment period, is contained in an approved implementation plan of any state, unless the applicant demonstrates to the satisfaction of the Air Pollution Control Officer that such limitations are not achievable. Under no circumstances shall the emission control required be less stringent than the emission control required by any applicable provision of District, state, or federal laws or regulations.

Evaluation of Some Factors Controlling DI Diesel Combustion and Exhaust Emissions

C. E. Hunter

H. A. Cikanek

T. P. Gardner

Ford Motor Company,
Research Staff,
Dearborn, MI 48121

The combined effects of turbocharging, high fuel injection pressure, and reduced oil consumption on diesel exhaust emissions were investigated using a single-cylinder research engine. The influence of these exhaust emission control concepts on particulate composition was determined using a new particulate analysis method. In addition, the dependence of particulate composition on engine load and air utilization was examined using the microfumigation technique. Simultaneous application of these emissions control concepts reduced exhaust particulates by 70 percent. High injection pressure reduced the insoluble component of particulates, while reducing oil consumption and turbocharging the engine lowered both soluble and insoluble particulates. Reductions in oil-derived particulates with increasing engine load were partially attributed to increases in volumetric air utilization. Ninety percent of the lube oil found in exhaust particulates was unburned; however, similar concentrations of unburned and partially oxidized components were observed in fuel-derived particulates.

Introduction

Stringent Federal emissions regulations governing light-duty and heavy-duty diesels for the 1990s have renewed interest in particulate reduction research. In-cylinder reduction of particulate emissions, using advanced technology that improves fuel-air mixing and reduces oil consumption, appears to be a more cost-efficient approach than after treatment devices. The effects of increasing fuel injection pressure on diesel smoke have been reported by Komiyama et al. [1] and a study using a rapid compression machine was reported by Kamimoto et al. [2]. The influence of reduced oil consumption on particulate emissions has also been studied [3, 4]. However, the combined effects of fuel injection pressure and oil control have not been investigated.

The primary purpose of this study was to investigate the combined effects of turbocharging, fuel injection pressure, and controlled lube oil reduction on total exhaust particulate emissions and particulate composition. The dependence of particulate, smoke, NO_x, and hydrocarbon emissions on changes in combustion was also examined.

Determination of Particulate Composition

Particulates are defined, by the Environmental Protection Agency, as any diesel exhaust effluent collected on a binderless glass fiber filter in a dilution tunnel at temperatures below 125°F [5]. Hence, particulates include not only solid carbon, but sulfate emissions and soluble organic fractions (SOF). The SOF found in diesel particulates are comprised of unburned fuel and lube oil, and partially oxidized fuel and lube oil.

The fuel and oil components of soluble particulates were determined using a modified chromatographic analysis technique. In some cases it was necessary to use several filters to obtain enough material to conduct detailed chromatographic analysis of the particulates. The number of filters required was determined by measuring the amount of soluble organics in each sample using thermogravimetric analysis (TGA). The accuracy of the TGA method was verified using soxhlet extraction.

Thermogravimetric Analysis. Thermogravimetric analysis was used as a method to determine the amounts of soluble organic in particulate samples, prior to performing the modified chromatographic analysis on the particulate sample. The TGA method required less analysis time than soxhlet extraction, which involves a laborious refluxing process using large quantities (500 ml) of methylene chloride solvent and requires approximately eight hours to complete. In addition, TGA was used as a survey diagnostic to estimate the amount of oil and fuel in diesel exhaust particulates. The analysis was performed in two parts. First, a small portion of the particulate sample ($<1/20$) was placed in a chamber and heated argon gas was passed over it. The volatile portion of the particulate sample was completely evaporated by increasing the temperature from 50°C to 700°C. The remaining carbon in the sample was then converted to CO_2 by passing oxygen through the sample cham-

Contributed by the Internal Combustion Engine Division and presented at the Twelfth Annual Energy-Sources Technology Conference and Exhibition, Houston, Texas, January 22-25, 1989. Manuscript received by the Internal Combustion Engine Division October 1988.

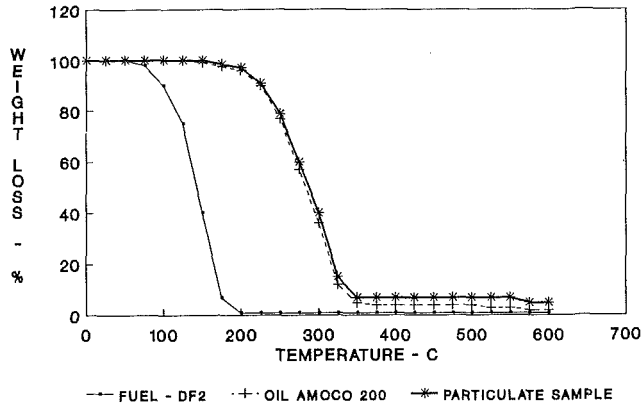

Fig. 1 Thermogravimetric analysis of diesel fuel, lube oil, and soluble particulates

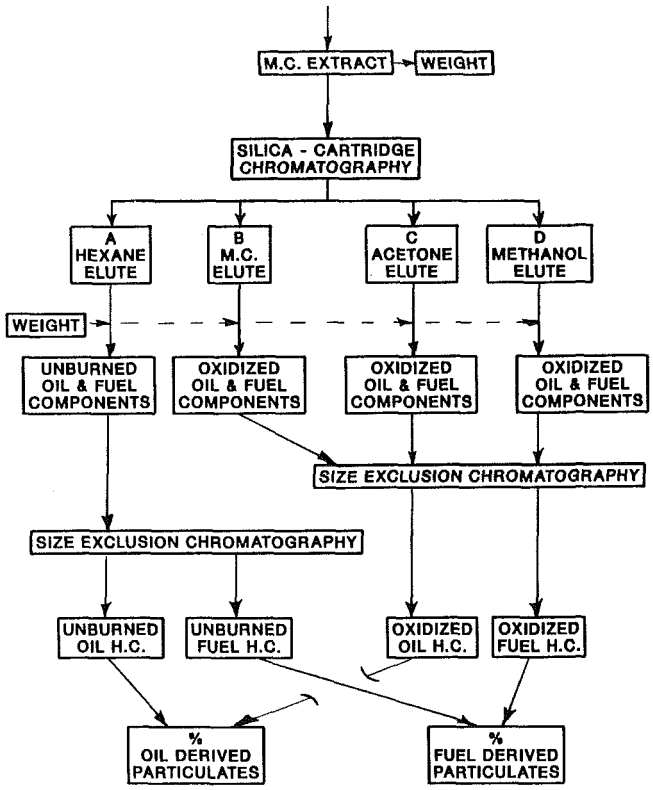

Fig. 2 Schematics of the modified particulate analysis method

ber. The thermograms for fuel, lube oil, and a typical particulate sample are shown in Fig. 1. These results showed that lube oil was the major constituent of the soluble organic portion of particulates for the exhaust sample analyzed, as indicated from the close match of thermograms. Comparison of soluble organics determined using TGA with those obtained from soxhlet extraction showed good agreement, as listed in Table 1.

Chromatographic Oil/Fuel Analyses. A modified chromatographic technique was used to determine the amounts of unburned and partially oxidized components of fuel and oil in the diesel particulate samples. The accuracy of chromatographic techniques currently used [6–8] to determine the contributions of oil and fuel to diesel particulates is restricted due to the overlap of the chromatograph of partially oxidized fuel with that of the unburned lube oil. To overcome this limitation

Table 1 Comparison of soluble organic determined using TGA and soxhlet extraction

SAMPLE NO.	SOLUBLE ORGANIC FRACTION (%)	
	SOXHLET	TGA
1	80.8	82.7
2	63.2	68.1
3	46.4	34.0
4	79.5	75.2
5	65.8	65.6
6	51.8	42.7
7	38.6	37.8
8	34.5	35.2
9	21.6	24.2
10	36.5	33.5
11	24.6	23.0
12	13.6	18.1

a modified chromatographic analytical procedure was developed and is illustrated in Fig. 2. First, soluble organics were repeatedly extracted from the particulate sample using 10-ml portions of methylene chloride solvent until the soluble organics were quantitatively removed from the filter. Second, the soluble organic material was then collected onto a silica cartridge. Third, hexane was used to extract the nonpolar unburned component from the silica cartridge, and methylene chloride (MC), acetone, and methanol solvents were used to extract the partially oxidized component. Fourth, each of these portions was subjected to size exclusion chromatography to determine the contribution of fuel and oil to soluble particulates. A more detailed description of this technique will be reported [9].

Experimental Apparatus

A research diesel engine equipped with an experimental fuel injection system was designed for this study. The test facility consisted of a dynamometer test bed and controls that were linked to an automated data acquisition system.

Test Engine and Steady-State Test Procedure. A single-cylinder direct-injection research diesel engine instrumented with combustion diagnostics was used. The specifications for the engine and fuel systems are listed in Table 2. The cylinder bore was 80 mm and the stroke was 88 mm. The engine had a helical intake port and a piston with a re-entrant-type bowl. For the reduced oil consumption tests, the tangential tension in the oil ring was increased 35 percent over the normal specification. This oil ring design reduced oil consumption by approximately 50 percent. It should be noted that the base oil consumption of this experimental engine was higher than that of a typical diesel engine. The baseline fuel injection system consisted of a Bosch VE distributor type fuel pump with a geometric fuel delivery rate of 17.3 mm^3/pump-deg. A Maximec, in-line pump (CAV) was used to achieve high injection pressure, with a geometric fuel delivery rate of 39.6 mm^3/pump-deg. For the high injection pressure tests, the nozzle orifices were reduced from 0.18 mm to 0.15 mm and injection

Table 2 Description of the baseline engine

Bore	(mm)	80
Stroke	(mm)	88
Displacement	(l)	.44
Compression Ratio		20.4
Fuel Injection		
Injection Pump		Bosch VE
Plunger Diameter	(mm)	10
Nozzle Holes (#)		4
Nozzle Orifice	(mm)	.18
Spray Angle	(deg)	150
Intake Port		
Swirl Ratio		2.2
Type		Helical
Piston		
Squish Area	(%)	81.2
Bowl Type		Re-entrant
Bowl Diameter	(mm)	37.8
Bowl Height	(mm)	17.5

Table 3 Steady-state operating conditions

STEADY STATE POINT	ENGINE SPEED (rpm)	ENGINE IMEP (psi)	AIR-FUEL RATIO	
			NA	TC
1	1000	40.0	87.0	115.7
2	1500	60.0	54.2	82.2
3	1500	88.0	34.3	52.4
4	2500	125.0	22.5	34.0

pressure was increased from 5500 to 12,000 psi at an IMEP of 88 psi and 10,500 to 17,500 psi at an IMEP of 125 psi. Four steady-state test points were used to represent the light-duty Federal Test Procedure and the smoke limited test point in these experiments. The four points are listed in Table 3. Start of combustion timing was adjusted to maintain a constant level of exhaust NO_x equivalent to 4.75 g/bhp-h. For each of these engine operating conditions, intake boost pressure and temperature settings were adjusted to simulate turbocharger conditions. The combined effects of test variables were determined using the following test configurations:

1 baseline pump
2 baseline pump with boosted intake
3 high injection pressure pump with boosted intake
4 high injection pressure, boosted intake, and high tension oil rings

Instrumentation and Test Facility. A Tektronix 4052 computer, coupled to a Fluke multichannel data logger, and a Norland 3001A digital oscilloscope were used to monitor and record high-speed and steady-state engine and emissions data. Gaseous emissions were measured using a Beckman emission console and Horiba hot hydrocarbon (FID) instruments. Particulates were measured with a mini-dilution tunnel. A Norland digital oscilloscope was used to sample cylinder pressure, injector needle lift, and fuel injection pressure data at one-crank-angle-deg intervals.

Air Utilization—Microfumigation

It is postulated by the authors that the oil burnup mechanism in diesel engines is governed by volumetric air utilization (VAU). Hence, the microfumigation technique was developed to measure the effects of engine designs and operating variables on volumetric air utilization.

Description of the Microfumigation Technique. The microfumigation technique is based on the premise that low concentrations of combustible substances located within the chamber of a diesel engine will be burned only by a bulk combustion phenomenon. The procedure used in this technique consisted of ingesting methane into the intake port at concentrations below its flammability limits and measuring the change in methane emitted through the exhaust. During the combustion event, methane residing in the volume occupied by the spray plumes and the surrounding volume is burned, as shown in Fig. 3. Methane located outside of the utilized air region, which is noted by the dotted region, is not consumed during the combustion event. Hence, the difference between ingested and exhausted methane concentrations is a direct measure of volumetric air utilization, as given in equation (1).

$$\text{VAU} = V_{\text{cyl}}*([\text{CH}_4]_{\text{int}} - [\text{CH}_4]_{\text{exh}})/[\text{CH}_4]_{\text{int}} \quad (1)$$

where V_{cyl} = volume of the combustion chamber at top dead center; $[\text{CH}_4]$ = concentration of methane in ppm.

Air Utilization/Microfumigation Measurements. Prior to using this technique to measure volumetric air utilization, it was necessary to address the following issues: (1) the residence time required to consume methane in the region of the combustion chamber where average cylinder pressures and temperatures exist, and (2) the maximum concentration of methane tracer gas that can be used without altering the combustion process.

First, the NASA chemical kinetics program [10] was used to compute the residence time required for oxidation of methane. The average temperature of the combustion chamber for the operating range of a diesel is 1250 to 1500 K. Although the temperatures of the regions between the spray plumes were significantly lower than the average combustion chamber temperature, methane burnup was computed at 1500 K to ensure a correct lower limit for the residence time of methane. The residence time required for 10 percent burnup of methane at a concentration of 600 ppm and chamber temperature of 1500 K was greater than 300 ms, which exceeds the combustion cycle duration at the lowest engine speed tested. This result confirmed the theory that low concentrations of methane located in regions of the combustion chamber where temperatures are equal to or less than the average chamber temperature will not be consumed.

For the second issue, intake methane concentrations were increased from 100 ppm to 6500 ppm to determine the optimum level to ingest into the intake port. Gas chromatography analyses were used to correlate cold FID hydrocarbon instrument measurements with actual methane concentrations. Exhaust methane was found to be proportional to intake methane between 300 and 6500 ppm, as shown in Fig. 4. At methane concentrations of 600 ppm and higher the slope was constant. Combustion analyses, based on cylinder pressure data, showed that microfumigation with methane had a minimal effect on combustion at a concentration of 600 ppm. For this reason, an intake methane concentration of 600 ppm was selected for the microfumigation tests.

Volumetric air utilization was measured at engine loads of 61 and 125 psi, and at three different compression ratios. It is generally assumed that the engine can only use the air in the piston bowl and that directly above it at top dead center. This volume is expressed as a fraction of the nominal clearance volume. The geometric K factor is equal to the sum of the piston bowl volume and that volume projected directly above the piston bowl divided by the total combustion chamber vol-

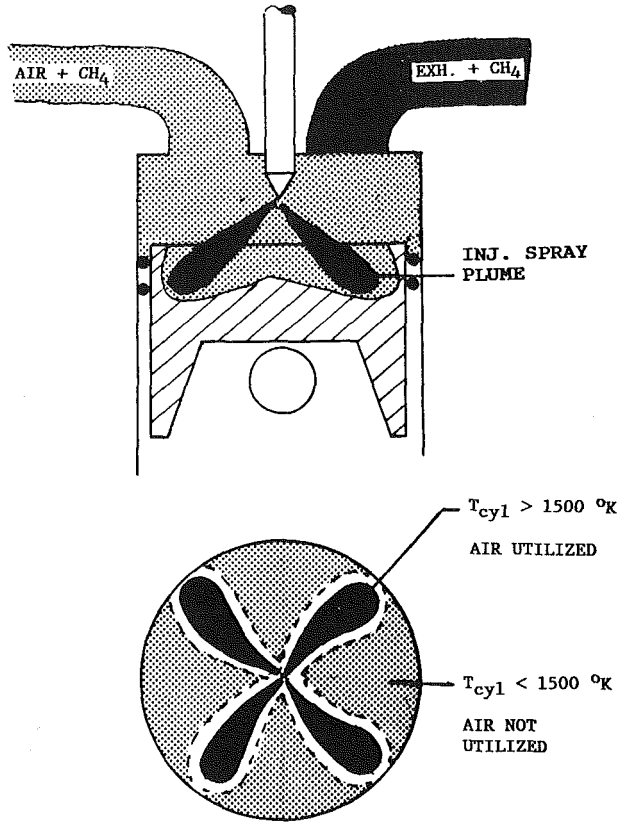

Fig. 3 Schematics of the microfumigation technique

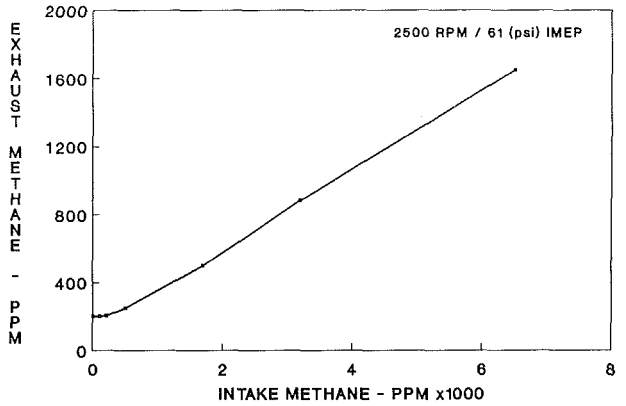

Fig. 4 Dependence of exhaust methane on intake methane concentration

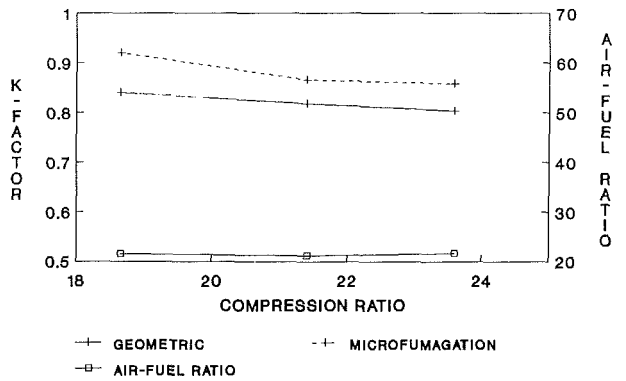

Fig. 5 Comparison of geometric and volumetric air utilization *K* factor

ume at top dead center. The geometric *K* factor computed using combustion chamber dimensions was compared with that determined using the microfumigation technique. The engine was operated at smoke limited power where maximum volumetric air utilization occurs. The difference observed between *K* factors computed using engine geometry and those determined from volumetric air utilization measurements for three compression ratios tested is shown in Fig. 5. These results suggested that the microfumigation technique may be a viable method for measuring volumetric air utilization.

To explore further the utility of the microfumigation technique, this experimental method was used to determine the dependence of volumetric air utilization on engine load. A comparison of volumetric air utilization derived from methane burnup with that computed from exhaust oxygen concentration was made and is shown in Fig. 6. The exhaust oxygen method indicated that 45 percent of the total available oxygen was used at an engine load of 88 psi. However, the microfumigation technique showed that almost twice as much air (83 percent) was involved in the combustion process. In contrast, the overall air-fuel ratio at an IMEP of 88 psi was 35:1, where it is implied that 100 percent of the air is involved in the combustion process. However, the equivalent (measured) air-fuel ratio computed from the product of the overall air-fuel ratio and volumetric air utilization for this engine load is richer and is equal to 29.0. It should be noted that the microfumigation technique does not differentiate between the methane-air mixture consumed in the flame and that re-entrained and burned by hot gases. Hence, the product of the overall air-fuel ratio and volumetric air utilization only provides an upper limit of the local air-fuel ratio in the combustion zone.

Particulates and Gaseous Emission Measurements

Exhaust particulates and smoke emissions decreased significantly with boosted intake pressure, increased fuel-injection pressure, and controlled reduction in oil consumption. Hydrocarbon emissions generally decreased with improved fuel-air mixing and oil control. Nitrogen oxide emissions were maintained at a constant level during these tests by adjusting the timing of the start of combustion. Ignition delay and the relative amounts of premixed and diffusion combustion varied with boost pressure and fuel injection pressure.

Total Particulates. The cumulative effects of simulated turbocharging, high injection pressure, and controlled reduction in oil consumption resulted in significant reductions in total exhaust particulates in this study. Simulated turbocharging and increased oil ring tension reduced particulates over the range of engine loads tested, as shown in Fig. 7. However, the higher injection pressures had a stronger effect on particulates at an IMEP of 125 psi. The effects of these engine modifications on particulates can be further understood by analysis of the particulates in terms of insoluble and soluble organic components, as shown in Fig. 8.

Insoluble Particulates. Higher boost, increased fuel injection pressure, and controlled reduction in oil consumption decreased the amount of insolubles in exhaust particulates at full load with slight reductions at part load.

The primary effect of increased boost pressures on emissions can be related to higher concentrations of oxygen in the combustion chamber at a fixed load. Increasing the oxygen concentration in this manner can reduce the formation of carbon in the early stages of combustion. In addition, the higher amount of oxygen associated with turbocharging increased the burnup of carbon insolubles during the latter stages of combustion. Increasing engine boost decreased insoluble particulates at IMEPs of 88 and 125 psi, as shown in Fig. 8. In addition, boosted intake reduced ignition delay, which increased the amount of diffusion burning. Although particulate formation may have been enhanced by such increases in the

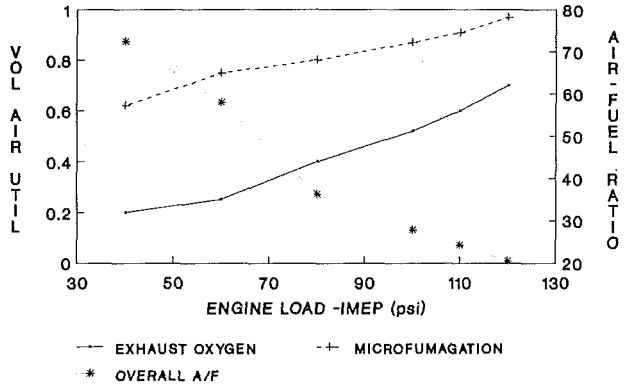

Fig. 6 Dependence of volumetric air utilization on engine load

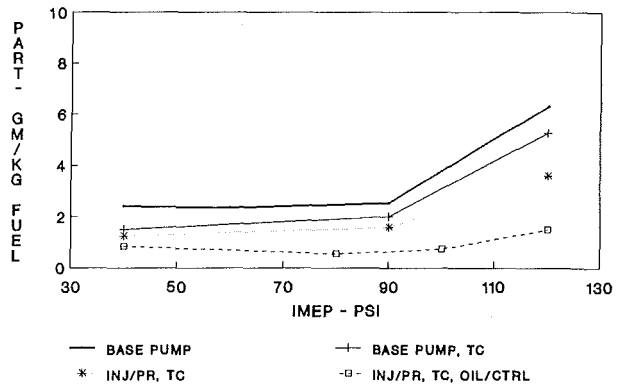

Fig. 7 Effects of turbocharging, injection pressure, and oil control on total particulates

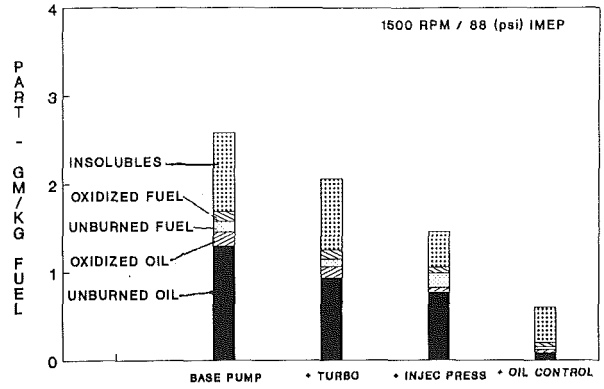

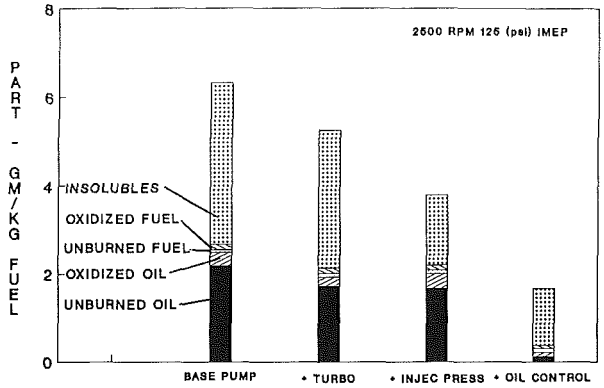

Fig. 8 Variation of particulate composition with experimental test variables

amount of diffusion burning with boost, particulate reduction processes related to increases in oxygen dominated. This resulted in a net reduction in insoluble particulates.

The effect of fuel injection pressure on insoluble particulate formation is related to improved fuel–air mixing. Increasing injection pressure has the potential to reduce droplet size, which improves fuel–air mixing, enhances burning, and shortens the combustion duration. In this study, increasing fuel injection pressure reduced insoluble particulates by 50 percent at IMEPs of 88 psi and 125 psi, as shown in Fig. 8. The reduction in particulates may have been associated with the change in combustion duration from 48 to 40 crank-angle deg. The shorter combustion duration increased the time between the end of combustion and the opening of the exhaust valve and provided a longer residence time for combustion of insoluble particulates at high combustion chamber temperatures. Changes in premixed and diffusion combustion for the two operating points were computed from cylinder pressure and engine geometry and are shown in Figs. 11 and 12.

Increasing the tension in the oil ring by 35 percent reduced insolubles by 25 percent at an IMEP of 125 psi but had very little effect on insolubles at an engine load of 88 psi, as shown in Fig. 8. This reduction in smoke may be related to decreases in the amount of lube oil available for pyrolysis. In laboratory tests, lube oil pyrolysis to carbon and soluble organics has been previously reported [10]. Reducing oil consumption in this manner did not alter the combustion process, as shown in Fig. 9.

Soluble Fuel-Derived Particulates. Fuel-derived particulates in the soluble organic fraction were distributed between unburned and partially oxidized components in similar amounts. Increasing oil ring tension and boosting intake pressure generally reduced the soluble organic fuel component of particulates. However, higher injection pressures increased fuel-derived particulates at an IMEP of 88 psi but only had a slight effect at full engine load. Fuel-derived particulates decreased with increasing oil ring tension, as shown in Appendices B and C. The unburned fuel-derived particulates were selectively reduced by operating the engine with a high tension oil ring during tests where the fuel injection pressure was increased, as shown in Fig. 8 and Appendix B. These results suggest that soluble organic, fuel-derived particulates may be linked to the amounts of oil present in the combustion chamber. Adsorption of fuel by oil is one plausible explanation for the decrease in fuel-derived particulates with controlled reduction in oil consumption. A similar mechanism was reported to have influenced gaseous hydrocarbons in spark-ignition engines by Kaiser [11]. Unburned and partially oxidized fuel-derived, soluble organic particulates were detected in nearly equal amounts regardless of the changes in the combustion environment with experimental test variables. The exception to this was the increase in unburned fuel with increased fuel injection pressure at an IMEP of 88 psi. Increasing fuel injection pressure can result in a larger quantity being injected early during the ignition delay period. Overmixing of the fuel with air during this period could result a mixture that is too lean to burn. This fuel can then be adsorbed by carbon particulates. An increase in fuel-derived particulates may also be caused by higher spray penetration and the subsequent wetting of the piston bowl wall. Although the above explanations are plausible, further study is required to understand this phenomenon fully.

Soluble, Oil-Derived Particulates. Increasing ring tension and raising boost pressure decreased soluble organic, oil-derived particulates, while higher injection pressure had only a minor effect on oil-derived particulates. Although oil consumption is reported [3, 13] to increase by a factor greater than two with changes in engine speeds and loads similar to those used in this study, the contribution of oil to soluble

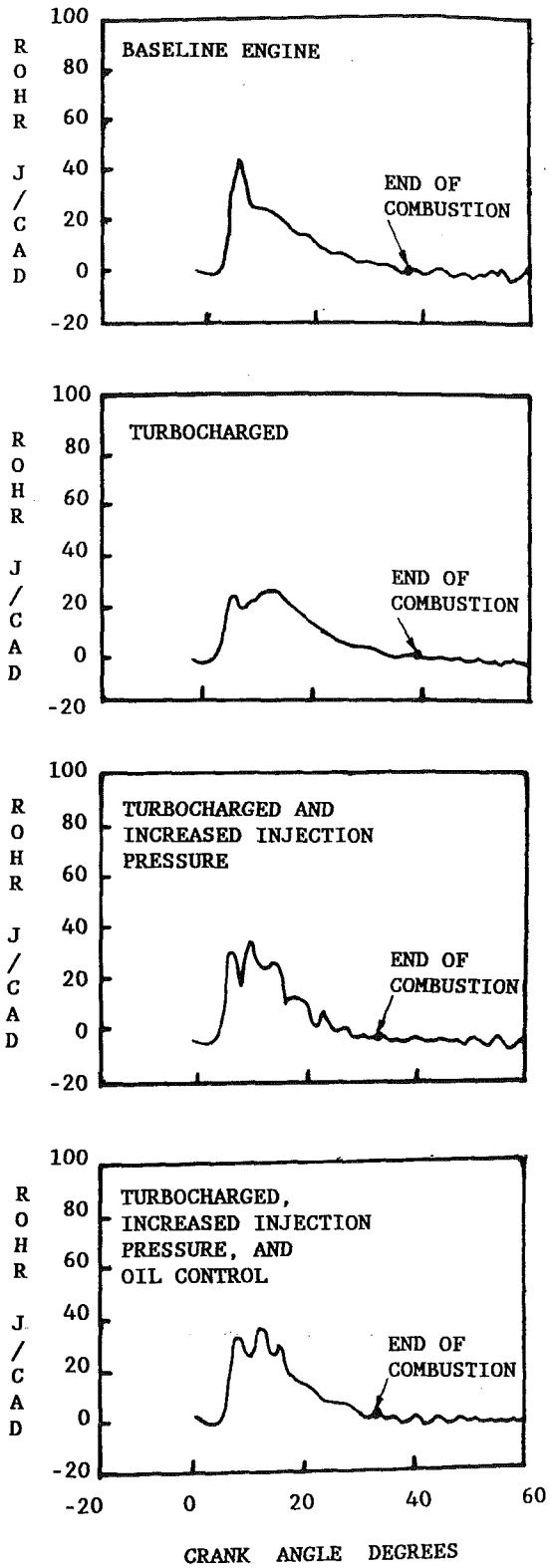

Fig. 9 Effects of intake boost, injection pressure, and oil control on apparent rate of heat release at 1500 rpm / 88 (psi) IMEP

particulates was only slightly higher for the 2500 rpm / 125 (psi) IMEP than that of the 1500 rpm / 88 (psi) IMEP speed load point. The small difference in the level of oil-derived particulates at the two speed load conditions shown in Fig. 8 suggested that the burnup of particulates increases significantly at the higher engine load.

Oil-derived particulates may be reduced by limiting the amount of oil consumption and by developing a more efficient method of burning the oil that reaches the combustion chamber. Increasing the tension in the oil ring by 35 percent reduced oil-derived particulates by a factor of ten, as shown in Fig. 8 and Appendices B and C. This method of reducing oil consumption was selected primarily for experimental investigations and its associated effects were not examined.

Increased air-fuel ratios and higher combustion temperatures can be achieved using higher boost pressures, which tend to increase the oxidation of particulates. Oil consumption may increase or decrease with intake boost pressure. Rulfs did not observe a significant change in oil consumption for intake boost pressure in the range of 2–3 bars [14]. Since the boost pressure used in this experiment was within this range, no significant increase in oil consumption with boost pressure was expected. Therefore, the reduction in oil-derived particulates with an increase in intake pressure may be related to an increase in the burnup process.

The relative concentrations of unburned and partially oxidized lube oil in particulates provide a basis for postulating an oil burnup mechanism. These experimental results suggest that oil resided in three regions of the combustion chamber, described as follows:

1 a flame region where complete combustion of oil occurred;
2 a high-temperature low oxygen concentration region where pyrolysis to carbon insolubles is prevalent; and
3 a low-temperature region where no reaction was detected.

The volume of the combustion chamber involved in the combustion phenomenon increased with engine loads, as discussed in the section on the microfumigation technique. Therefore, increasing engine load not only increases average combustion temperatures but more importantly it increased volumetric air utilization, which enhanced the burnup of oil-derived particulates, as shown in Fig. 8 and Appendices B and C. This oil burnup mechanism is also consistent with decreases in oil-derived particulates with engine load observed by Meyer et al. [3].

Exhaust Smoke. High fuel-injection pressure and simulated turbocharging conditions were used to improve fuel-air mixing. The effects of these changes were evaluated across a range of engine loads, as shown in Fig. 13. Increasing the intake pressure from 29.5 to 45.5 in. Hg and intake air temperature from 82 to 108°F increased the overall air-fuel ratio and reduced exhaust smoke from 2.8 to 1.7 Bosch number. However, intake air temperatures tested were lower than those of production turbocharged and intercooled systems. Boosting intake air increased the total air flow; therefore, a portion of the reduction in smoke must be attributed to the dilution of the exhaust. Smoke was also reduced at an IMEP of 88 psi. Peak fuel-injection pressure was increased from 10,500 to 17,500 psi to evaluate the effect of improved fuel atomization on fuel-air mixing. At an IMEP of 125 psi smoke was reduced from 1.7 to 1.2 Bosch number. The decrease in smoke with injection pressure may be related to the increase in the amount of premixed combustion and to the improved fuel-air mixing during the diffusion combustion period (reflected by the increase in the rate of diffusion burning), as shown in Figs. 10 and 12.

Gaseous Emissions. Hydrocarbon and NO_x were the gaseous emissions that were measurably affected by simulated turbocharging, increased fuel injection pressure, and reduced oil consumption.

Nitrogen Oxide Emissions. The exhaust emissions of NO_x were maintained at a constant level equivalent to 4.75 g/bhp-h by retarding or advancing the timing of the start of combustion. Oxides of nitrogen increased when the fuel injection

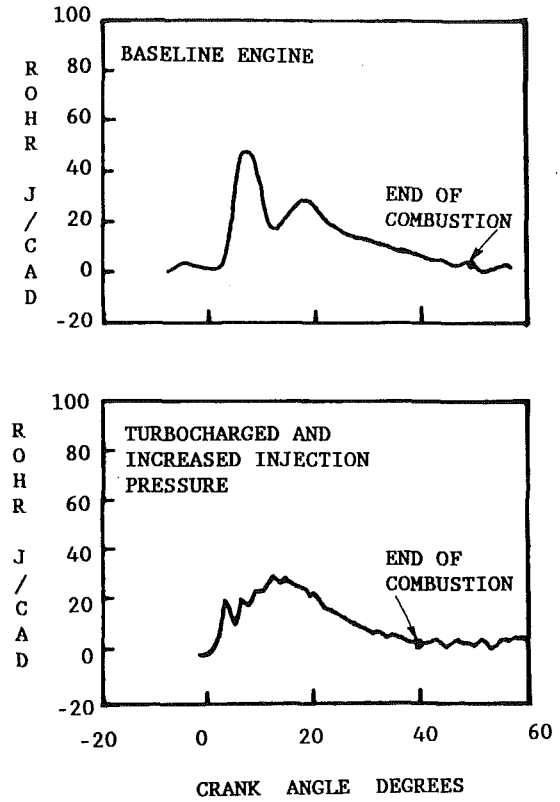

Fig. 10 Effects of intake boost, injection pressure, and oil control on apparent

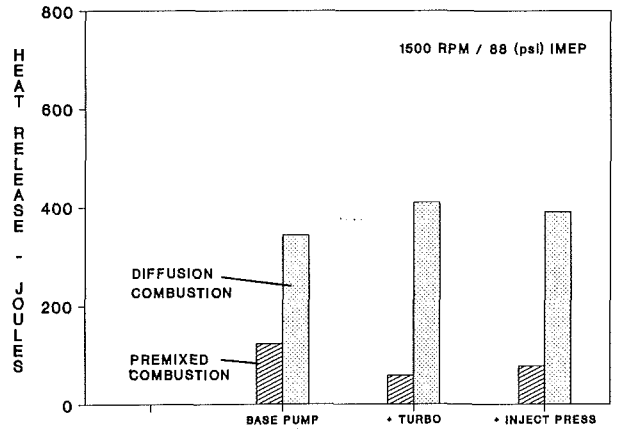

Fig. 11 Variation of premixed and diffusion combustion with turbocharging, injection pressure, and oil control at 1500 rpm / 88 (psi) IMEP

pressure was increased and timing of the start of combustion had to be retarded by 2–3 deg to maintain constant NO_x levels. These increases in NO_x may be related to the increases in the amount of premixed combustion with increased fuel-injection pressure and the reduction in combustion duration from 48 to 40 crank-angle deg. Oxides of nitrogen did not vary measurably with boosted intake air and with controlled reduction in oil consumption.

Hydrocarbon Emissions. Turbocharging the engine resulted in lower hydrocarbon exhaust emissions, as shown in Fig. 14. The effects of injection pressure and reduced oil consumption were mixed during these tests. The absence of a significant decrease in gaseous hydrocarbons with decreases in oil consumption was expected in view of the lack of a correlation between gaseous hydrocarbons and hydrocarbons adsorbed on particulates [3].

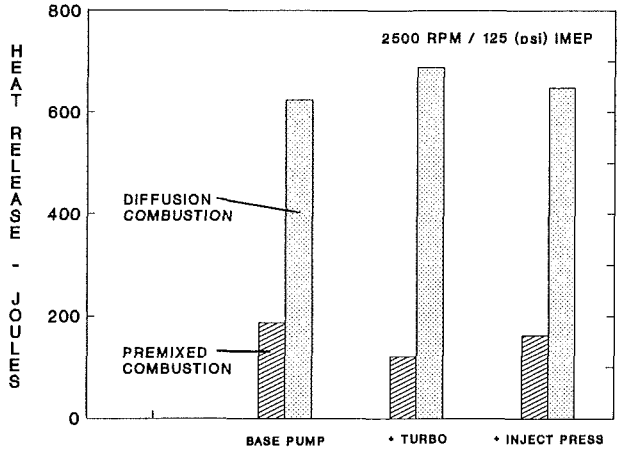

Fig. 12 Variation of premixed and diffusion combustion with turbocharging, injection pressure and oil control at 2500 rpm / 125 (psi) IMEP

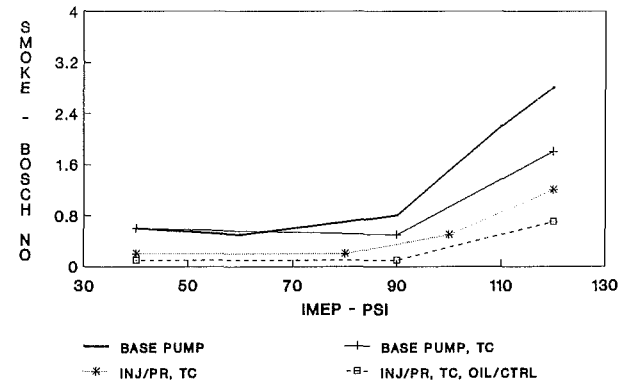

Fig. 13 Effects of turbocharging, injection pressure, and oil control on hydrocarbon

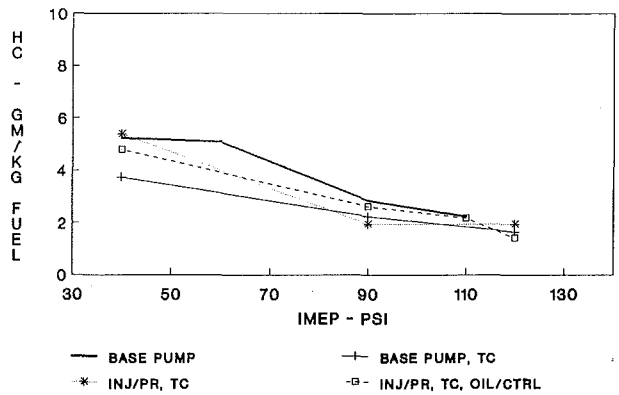

Fig. 14 Effects of turbocharging, injection pressure and oil control on smoke

Conclusions

The combined effects of turbocharging, fuel injection pressure, and controlled oil reduction on particulate composition, total particulates, gaseous emissions, and combustion were investigated using a single-cylinder, DI diesel engine. The conclusions from this work can be summarized as follows:

1. Operating the engine under simulated turbocharged conditions, without increasing fuel flow, reduced insoluble particulates and oil-derived soluble particulates and resulted in a decrease in ignition delay.
2. Higher pressure fuel injection significantly reduced in-

soluble particulates and smoke, and shortened the combustion duration.

3. Increased oil ring tension lowered oil consumption and decreased oil-derived particulates. Insoluble particulates were also reduced by the higher tension oil rings at the higher engine load.

4. The oil found in particulate emissions was primarily unburned. The small quantities of fuel found in particulates were distributed between unburned and partially burned components in similar amounts.

5. An oil burnup mechanism governed by volumetric air utilization may be used to explain the changes in oil-derived particulates with engine load and oil consumption.

References

1 Komiyama, K., Okazaki, T., Togashi, K., Jashimoto, H., and Takase, K., "Electronically Controlled High Pressure Injection System for Heavy Duty Diesel Engine—KOMPICS," SAE Paper No. 810997, 1981.

2 Kamimoto, T., Yokota, H., and Kobayashi, H., "Effect of High Pressure Injection on Soot Formation in a Rapid Compression Machine to Simulate Diesel Flames," SAE Paper No. 871610, 1987.

3 Mayer, W. J., Lechman, D. C., and Hilden, D. L., "The Contribution of Engine Oil to Diesel Exhaust Particulate Emissions," SAE Paper No. 80256, 1980.

4 Cartellieri, W., and Tritthart, P., "Particulate Analysis of Light Duty Diesel Engines (IDI & DI) With Particular Reference to the Lube Oil Particulate Fraction," SAE Paper No. 840418, 1984.

5 Federal Regulations, CFR 40, 86.110-82, "Exhaust Gas Sampling System; Diesel Engines," July 1984, pp. 495–500.

6 Kageyama, K., and Kinehara, N., "Characterization of Particulate Emission From Swirl Chamber Type Light-Duty Diesel Engine as a Function of Engine Parameters," SAE Paper No. 820181, 1982.

7 Black, F., and High, L., "Methodology for Determining Particulate and Gaseous Diesel Hydrocarbon Emissions," SAE Paper No. 790422, 1979.

8 Alkidas, A. C., "Combustion Characteristics of a Single-Cylinder Open-Chamber Diesel Engine," ASME JOURNAL OF ENGINEERING FOR GAS TURBINES AND POWER, Vol. 109, No. 4, 1987, pp. 419-427.

9 Zinbo, M., Hunter, C. E., and Schuetzle, D., "Determination of Lubricating Oil and Unburned Fuel in Diesel Particulates," to be published in *J. Anal. Sci.*, 1989.

10 Bittker, D. A., and Scullin, V. J., "General Chemical Kinetics Computer Program for Static and Flow Reactions With Application to Combustion and Shock-Tube Kinetics," NASA TN D-6586, 1972.

11 Lahaye, J., Prado, F., and Donnet, J. B., "Nucleation and Growth of Carbon Black Particles During Thermal Decomposition of Benzene," *Carbon*, Vol. 12, 1974, pp. 27-35.

12 Kaiser, E. W., Lorusso, J. A., Lavoie, G. A., and Adamczyk, A. A., "The Effect of Oil Layers on the Hydrocarbons Emissions From Spark-Ignited Engines," *Combustion Science Technology*, Vol. 28, 1982, pp. 69–73.

13 Warrick, F., and Dykehouse, R., "An Advanced Radiotracer Technique for Assessing and Plotting Oil Consumption in Diesel and Gasoline Engines," SAE Paper No. 700052, 1970.

14 Rulfs, H. W., "Investigation of Oil Consumption in Pressure-Charged Diesel Engines Using a Radioisotope Technique," *VDI Forschungsheft*, Vol. 601, 1980.

APPENDIX A

Experimental test configurations

TEST #	BASE PUMP	BOOSTED INTAKE	HIGH PRESSURE INJECTION PUMP	HIGH TENSION OIL RING
1	X	-	-	-
2	X	X	-	-
3	-	X	X	-
4	-	X	X	X

APPENDIX B

Effects of test variables on particulate composition at 1500 rpm / 88 psi IMEP

TEST #	TOTAL PART	INSOLUBLES	FUEL-DERIVED SOLUBLE		OIL-DERIVED SOLUBLE	
			UNBURNED	PARTIAL BURNED	UNBURNED	PARTIAL BURNED
	gm/kg-fuel					
1	2.581	0.890	.121	.111	1.297	.162
2	2.056	0.809	.089	.098	0.930	.129
3	1.458	0.405	.162	.065	0.769	.057
4	0.604	0.400	.032	.046	0.081	.040

APPENDIX C

Effects of test variables on particulate composition at 2500 rpm / 125 psi IMEP

TEST #	TOTAL PART	INSOLUBLES	FUEL-DERIVED SOLUBLE		OIL-DERIVED SOLUBLE	
			UNBURNED	PARTIAL BURNED	UNBURNED	PARTIAL BURNED
	gm/kg-fuel					
1	6.316	3.641	.065	.121	2.182	.307
2	5.242	3.115	.081	.119	1.723	.202
3	3.778	1.578	.083	.120	1.674	.324
4	1.675	1.294	.089	.073	0.121	.097

Reduction of Nitrogen Oxides in Engine Exhaust Gases by the Addition of Cyanuric Acid

J. A. Caton
Texas A&M University,
College Station, TX 77843-3123

D. L. Siebers
Combustion Research Facility,
Sandia National Laboratories,
Livermore, CA 94551-0969

Nitric oxide concentrations in a portion of the exhaust of a diesel engine operated with equivalence ratios between 0.25 and 0.75 were reduced by up to 98 percent by the addition of cyanuric acid. The cyanuric acid was combined with the exhaust gas in an electrically heated quartz flow reactor. The effects of the key process parameters (temperature, exhaust gas composition and residence time, and the overall engine equivalence ratio) on NO reduction by cyanuric acid were investigated. Nitric oxide reduction was evident at flow reactor temperatures above 700 K. The maximum nitric oxide reduction varied from 80 percent for a reactor temperature of 1180 K and an engine equivalence ratio of 0.25 to 98 percent for a temperature of 1120 K and an equivalence ratio of 0.75. The temperature range over which 60 percent or greater nitric oxide reduction was obtained was 1100 to 1340 K. Increasing the exhaust gas carbon monoxide concentration lowered the required reactor temperature and increased the temperature range for significant nitric oxide reduction. Increasing the exhaust gas nitric oxide concentration lowered the ratio of cyanuric acid to nitric oxide required for maximum nitric oxide reduction.

Introduction

Nitrogen oxides are one of the major pollutant species emitted from combustion sources. Nitrogen oxides that are currently regulated are nitric oxide (NO) and nitrogen dioxide (NO_2), which together are called nitrogen oxides (NO_x). The predominant nitrogen oxide from many combustion devices is nitric oxide. Nitric oxide is formed from the nitrogen and oxygen in the combustion air at the high temperatures (>2000 K) that occur during combustion. Another potential source of nitric oxide is the oxidation of fuel-bound nitrogen during combustion. A large fraction of the nitric oxide formed during combustion remains in the post-combustion gases and is exhausted as a pollutant.

Control strategies to minimize nitrogen oxide emissions may be divided into two categories: (1) combustion process modifications (e.g., Sarofim and Flagan, 1976) and (2) post-combustion gas treatments (e.g., Rosenberg et al., 1980). Combustion process modifications are most effective at reducing nitric oxide formed from the nitrogen in the combustion air. For example, combustion process modifications that reduce nitrogen oxide emissions from diesel engines include retarding the injection timing, reducing the inlet air temperature, and using exhaust gas recirculation (e.g., Wade, 1980). Other combustion devices such as gas turbines and furnaces also realize reduced nitrogen oxide emissions by the use of related combustion process modifications. Although combustion process modifications have been proven effective and economical for nitric oxide control, lower NO_x emission levels can be achieved with post-combustion gas treatment processes.

Post-combustion or flue gas treatments (FGT) to reduce nitrogen oxide emissions include a variety of methods that have been developed for specific classes of combustion devices. For example, automotive spark-ignited engines use reducing, noble-metal catalysts in conjunction with controlled combustion stoichiometry to reduce nitric oxides to nitrogen (Lester, 1983). Large stationary diesel engines, on the other hand, may use ammonia-based selective catalytic reduction (SCR) (Wasser and Perry, 1988a). Boilers and furnaces may be equipped with one of several different systems for post-combustion reduction of nitrogen oxides. In addition to SCR, boilers may use selective noncatalytic reduction (SNCR). An example of SNCR is the use of ammonia injection into high-temperature (~1225 K) post-combustion gases without a catalyst (Thermal DeNOx) to reduce NO_x (Lyon and Hardy, 1986). Another example of SNCR is the use of urea injection (NO_xOUT) into hot exhaust gases (Mansour et al., 1987). Other potential post-combustion gas treatments include the addition of ferrous ethylenediamine tetraacetic acid (Fe-EDTA process), the use of activated carbon, electron beam irradiation, wet scrubbers, dry absorption processes, and solid-state electrochemical techniques (Rosenberg et al., 1980).

Recently, a new exhaust gas treatment process that uses cyanuric acid (CA) to reduce nitrogen oxides was discovered (Perry and Siebers, 1986; Perry, 1988b). This patented process is called RAPRENOx for RAPid REduction of NO_x. Earlier work showed that this process was capable of reducing nitric

Contributed by the Internal Combustion Engine Division and presented at the Internal Combustion Engine Division Technical Conference, San Antonio, Texas, October 2-5, 1988. Manuscript received by the Internal Combustion Engine Division June 1988.

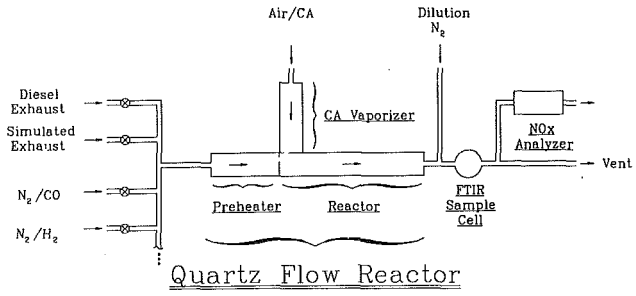

Fig. 1 Schematic of the experiment

oxide levels in exhaust gases. The process works by adding gaseous isocyanic acid (HNCO) to an exhaust gas stream. The HNCO is formed by sublimation and decomposition of CA at temperatures greater than 600 K. The HNCO then drives a series of reactions that lead to the reduction of NO.

Perry and Siebers (1986) established the effectiveness of this process in flow tube experiments using (1) simulated exhaust gas and (2) exhaust gas from a diesel engine. In the first set of experiments, the simulated exhaust gas results showed that this process reduced NO in a stainless steel flow reactor with no oxygen. The flow reactor temperature, the residence time, and the molar HNCO/NO ratio required to achieve NO reduction in excess of 90 percent were 920 K, one second, and unity, respectively. The second set of experiments, using exhaust from a diesel engine in a stainless steel flow reactor packed with chrome-steel bearings, demonstrated that the process reduced NO in the diesel exhaust gas with 12 percent oxygen. Nitric oxide reduction approaching 100 percent was achieved for a flow reactor temperature of between 720 and 1170 K, an HNCO source temperature of 600 K, and a residence time of one second.

Siebers and Caton (1988) studied the use of cyanuric acid to reduce nitric oxide in a portion of diesel engine exhaust. These experiments were conducted in a quartz flow reactor. They reported on the effects of reactor temperature, CA concentration, exhaust gas composition, and surfaces on the process. The results showed that reductions of NO up to 95 percent were possible at a reactor temperature of 1150 K. For lower reactor temperatures, the NO reduction was 20 percent or less. For higher reactor temperatures, the NO reduction slightly decreased with increasing temperature, reaching 80 percent at 1340 K. A byproduct noted in the above experiments under certain conditions was N_2O (Siebers and Caton, 1989). The results also showed that increasing the exhaust gas CO concentration lowered the temperature at which NO reduction became significant and that a molar CA/NO ratio of order one yielded the maximum NO reduction. Finally, the results indicated that lower temperature ($\sim$700 K) NO reduction is possible with surfaces such as Fe_2O_3. Some of these results will be reviewed in more detail in the Results and Discussion Section.

In summary, a potential NO reduction technique has been identified; however, the chemical mechanism of this reduction process in not completely understood nor has the entire operating domain for the process been investigated. Successful reduction of NO in an actual combustion system with cyanuric acid will depend on many factors. To gain a better understanding of the NO reduction process and to gain the information necessary to assess the practical application of this process in actual combustion systems, a series of additional experiments was conducted. The overall objective of the following experiments was to determine the major effects of the operating conditions on the NO reduction process. This was accomplished by investigating the effects of temperature, residence time, input carbon monoxide and nitric oxide concentrations, and engine equivalence ratio on the process.

Table 1 Engine specifications, operating conditions, and performance parameters for the baseline conditions

Engine	Onan IDI Diesel
No. of Cylinders	1
Bore (mm)	82.5
Stroke (mm)	92.1
Displacement (cc)	493.
Compression Ratio	19
Equivalence Ratio	0.5
Engine Speed (rpm)	800.
Inlet Air Temperature (°C)	22.
Inlet Air Pressure (kPa)	100.
Exhaust Gas Pressure (kPa)	100.
Brake Power (kW @ 800 rpm)	1.43
Brake MEP (kPa @ 800 rpm)	435.
Brake SFC (kg/kW·hr)	0.29
Brake Specific NO (g NO/kW·hr)	3.55 (396 ppm)
EINO (g NO/kg fuel)	12.3
Fuel	Phillips DF-2 Control
Cetane No.	46.2

Description of the Experiment

Figure 1 is a schematic of the experiment. The main components of the experiment are a diesel engine, a flow reactor, a chemiluminescent NO_x analyzer, and a Fourier transform infrared (FTIR) spectrometer. The engine is a single-cylinder, 5.6 kW (at 1800 rpm), prechamber Onan diesel engine. Table 1 lists the major engine specifications, operating conditions, and performance parameters. Although a diesel engine was used, the results of this work are believed to apply to most post-combustion gases.

The NO_x analyzer is a Thermo Electron model 10 A/R and the FTIR spectrometer is a Beckman model 1300. The flow reactor is made from quartz tube with a 1.65 cm i.d. The flow reactor has three sections: an exhaust gas preheater, a CA vaporizer, and a main reactor. Each section is electrically heated with independent temperature control. Quartz is used to minimize surface effects on the NO reduction chemistry. Table 2 lists the baseline conditions for the reactor system.

The experiments are conducted by continuously drawing a portion of the exhaust from the engine through a tube heated to 100°C into the 30-cm-long exhaust preheater. At the end of the preheater, the exhaust gas flows into the main reactor through a 1.6-mm orifice located near the top of the preheater tube and is mixed with the flow from the CA vaporizer. The effect of the exhaust preheater temperature on the NO reduction process is examined.

The CA vaporizer consists of a 24.1-cm-high vertical section and an 8.3-cm-long horizontal section. Solid CA is fed in at the top of the vertical section along with a 0.20 slpm (standard liters per minute at 0°C and one atmosphere of pressure) coflow of carrier gas (dry air). The CA is fed in by loading a gas-tight syringe feed system with CA particles and then advancing the syringe plunger at a controlled rate with a variable speed DC motor. As the plunger advances, CA particles fall into the vertical part of the heated CA vaporizer and sublime. Particles approximately 150 μm in diameter were used. This particle size along with vibration of the syringe feed system resulted in the smoothest CA feed rate. Table 3 lists the cyanuric acid (CA) specifications.

Any particles that do not fully sublime in the vertical section of the vaporizer fall onto the lower heated wall of the horizontal section and continue to sublime. As the vaporized CA is carried

Table 2 Baseline conditions for the reactor system

CA VAPORIZER	
CA Mass Flow Rate (mg/min)	3.2
Air Carrier Flow Rate (slpm)	0.2
Average Temperature (K)	620
Outlet Temperature (K)	740
Residence Time for 620 K (seconds)	5.2
EXHAUST PREHEATER	
Exhaust Flow Rate (slpm)	1.0
Average Temperature (K)	690
Outlet Temperature (K)	720
Residence Time for 690 K (seconds)	0.7
REACTOR	
Flow Rate (Preheater+Vaporizer) (slpm)	1.2
Average Temperature (K)	670-1340
Residence Time (seconds)	1.3-0.64
Input Species Concentrations (for ϕ=0.5):	
CO (ppm)	260
NO (ppm)	330 ±40.
CA (ppm)	470
H_2O (%)	5.2
CO_2 (%)	5.8
O_2 (%)	12.3

Table 3 Cyanuric acid (CA) specifications

Chemical Name	2,4,6 Trione-Symmetrical Triazine
Chemical Formula	$H_3C_3N_3O_3$
Molecular Mass	129.08
Purity (%)	>98.9
Ammeline-ammelide (max %)	0.6
Moisture (max %)	0.5
Ash (max ppm)	200.
Iron (max ppm)	35.
Chlorine (max ppm)	100.
pH (min)	2.7
Specified Bulk Density (g/cc)	0.8-0.9
Measured Density (g/cc)	0.838
Particle Diameter (μm)	125-180
Supplier	Monsanto Chemical Co.

through the vaporizer by the air flow it can begin decomposing, forming HNCO, if the residence time is long enough for the selected vaporizer temperature. At the end of the CA vaporizer, the vaporized CA, its decomposition products, and the air carrier gas flow into the main reactor through a second 1.6-mm orifice. The orifice is located off-center near the top of the reactor tube. The effect of the vaporizer temperature on the process is examined.

The jets from the exhaust preheater and CA vaporizer orifices impinge upon each other at a 90-deg angle at the inlet of the reactor. The impinging jets enhance the mixing of the exhaust gas with the HNCO carrier gas. In addition, the jets are off-center, which induces swirl that further enhances mixing.

The reactor is 52.1 cm long with the first 36.8 cm heated. The temperature of the reactor is uniform to ±4 percent over the last 80 percent of the heated section. This uniform temperature is the reported average reactor temperature. The initial 20 percent of the heated section is considered a preheat section,

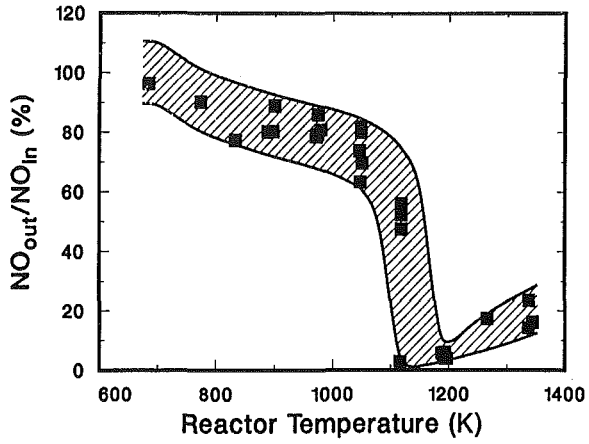

Fig. 2 The effect of the reactor temperature on the exhaust gas NO reduction

since its temperature is low enough that little NO reduction occurs.

After passing through the reactor the treated exhaust is diluted with nitrogen (N_2), passed through a particulate filter, and analyzed with the FTIR spectrometer and the NO_x analyzer. The amount of N_2 dilution is adjusted so that when dilution caused by the CA air carrier gas plus any other species added to the exhaust is taken into account, the total dilution of the original diesel exhaust is a factor of five. Water condensation in the unheated lines after the reactor was prevented and the interference of combustion products such as CO_2 and H_2O with the chemiluminescent NO_x analyzer was minimized by the use of N_2 dilution.

Discussion of the results from the FTIR spectrometer is in preparation (Siebers and Caton, 1989). Most of the results presented in this paper are based on NO measurements from the chemiluminescent NO_x analyzer. Note that the NO_2 concentrations were always less than 5 percent of the NO concentration in the treated or untreated exhaust as verified by the NO_x analyzer and the FTIR spectrometer. Because this level of NO_2 was difficult to measure accurately and because the stainless steel (NO_x) convertor on the NO_x analyzer responded to HNCO, as well as NO_2 (when HNCO and O_2 were present in the sample flow), the NO_2 concentrations are not presented.

Operating Conditions

The engine and flow reactor conditions listed in Tables 1 and 2 are defined as the baseline conditions. The effects of several key parameters on NO reduction with cyanuric acid will be demonstrated by comparing the NO reduction obtained for the baseline conditions in the two tables with the NO reduction obtained when one of the key parameters is perturbed.

The reactor inlet molar concentrations listed in Table 2 result when 1.0 slpm of engine exhaust is diluted by the 0.2 slpm flow of CA and its air carrier gas at the reactor inlet. The balance of the flow at the reactor inlet was primarily nitrogen; however, soot and other minor species formed by the diesel engine were also present. The reactor inlet CA concentration was calculated from the CA feed rate assuming no decomposition to HNCO in the vaporizer. The reactor residence time varied from 1.3 s at 670 K to 0.64 s at 1340 K for a total reactor flow of 1.2 slpm, since residence time is inversely proportional to temperature for a fixed mass flow rate. In summary, the baseline operating conditions included an engine equivalence ratio of 0.5, an average vaporizer temperature of 620 K, an average exhaust preheater temperature of 690 K, a

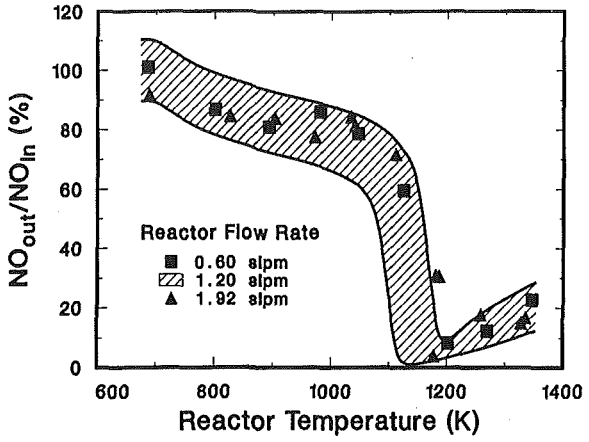

Fig. 3 The effect of the total reactor mass flow rate on the exhaust gas NO reduction

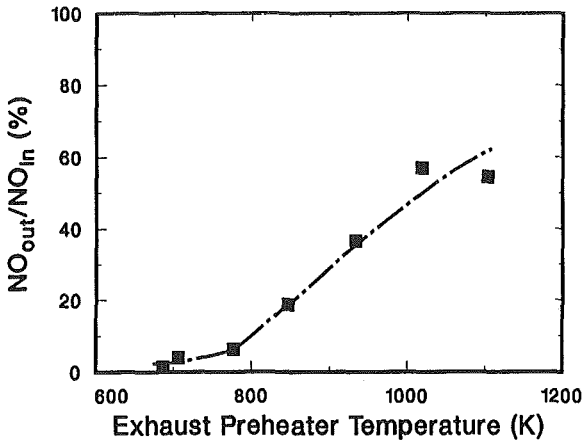

Fig. 5 The effect of the exhaust preheater temperature on the exhaust gas NO reduction

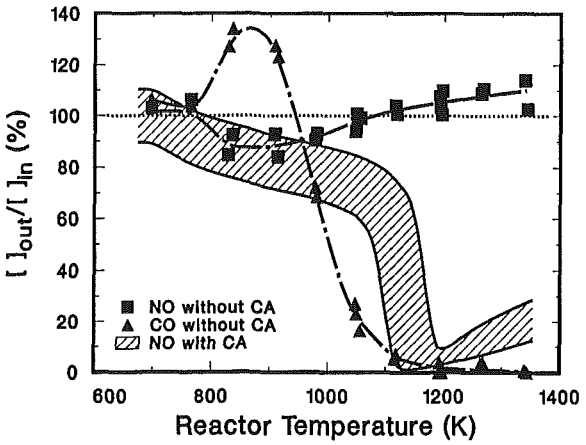

Fig. 4 The effect of the reactor temperature on the NO and CO concentrations without CA addition

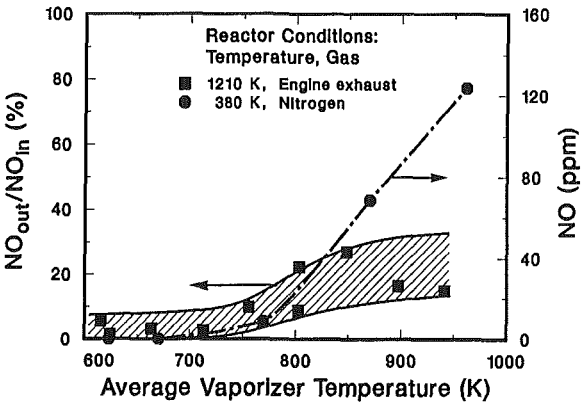

Fig. 6 The effect of the vaporizer temperature on the exhaust gas NO reduction (square symbols) for a reactor temperature of 1200 K and on NO production (triangular symbols) using N_2 instead of exhaust gas for a reactor temperature of 380 K

CA/NO ratio of 1.4, a total reactor flow of 1.2 slpm, and a residence time of order 1.0 s.

Results and Discussion

Figure 2, previously presented by Siebers and Caton (1988), shows the ratio of the reactor outlet NO concentration and the reactor inlet NO concentration (in percent) as a function of the average reactor temperature for the baseline engine and flow reactor conditions. The cross-hatched region bracketing the data set in Fig. 2 represents the spread in the data due to fluctuations of the exhaust NO concentration with time and the repeatability of the experiment. The exhaust NO fluctuation for a given day was as much as ±40 ppm. Figure 2 shows that NO reduction starts at a reactor temperature of 700 K. As the reactor temperature is increased, the reactor outlet NO slightly decreases until 1050 K. Above 1050 K, the reactor outlet NO decreases rapidly with increasing temperature, reaching a minimum at 1150 K. Beyond 1200 K, the outlet NO level slightly increases with increasing temperature. Similar effects of temperature on the process were noted by Perry (1988a) in another experiment for temperatures above 1200 K.

Figure 3 compares the NO reduction as a function of the average reactor temperature for three reactor mass flow rates. The cross-hatched region represents the data from Fig. 2 for the baseline mass flow rate of 1.2 slpm. The other two reactor flow rates are 0.6 slpm and 1.9 slpm, which are a factor of two lower and 1.6 higher than the baseline flow rate, respectively. The total reactor flow was varied by changing the exhaust gas, the CA, and the CA air carrier gas flow rates by the same factor. The reactor residence times varied from 0.8 to 2.6 s at 670 K and from 0.4 to 1.3 s at 1340 K for 0.6 slpm and 1.9 slpm, respectively.

The data in Fig. 3 show that the total reactor flow rate in the range of 0.6 to 1.9 slpm (the limits of the experiment) has no significant effect on the process, which means that residence time in the range of 0.4 to 2.6 s has no significant effect on the process. Relating this result to Fig. 2 demonstrates that the trends in Fig. 2 were the result of reactor temperature variation and were not influenced by the change in residence time accompanying a change in temperature for a fixed reactor mass flow rate.

Figure 4 shows the output concentrations of NO and CO relative to their input concentrations as a function of average reactor temperature when no CA is added to the reactor. Also shown for reference are the baseline NO reduction data from Fig. 2 (cross-hatched region). Without CA addition, the exhaust NO concentration declines with reactor temperature, similar to the case with CA addition, until a temperature of 850 K. The reduction at 850 K is 10 to 15 percent. As the reactor temperature increases above 850 K, the NO concentration steadily increases for the case without CA addition, diverging from the case with CA addition. These results suggest that the actual NO reduction as a result of CA addition does not begin until a temperature of 850 K. (Note: When no CA was added, the variations in NO_x and NO with temperature

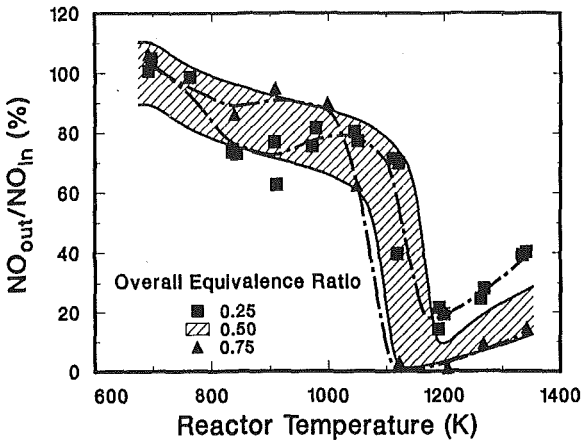

Fig. 7 The effect of the engine equivalence ratio on the exhaust gas NO reduction

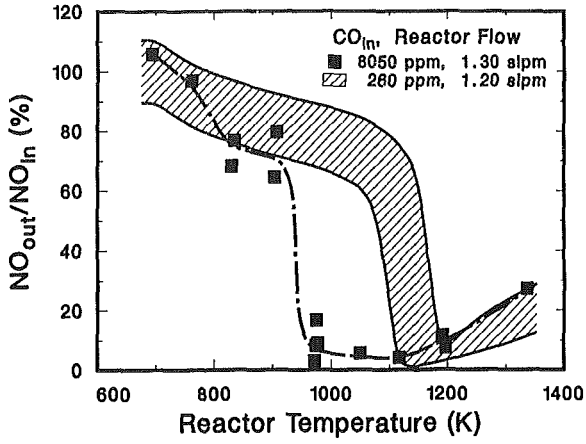

Fig. 8 The effect of the reactor temperature and increased exhaust CO concentration on the exhaust gas NO reduction

were similar indicating that the reduction in NO around 850 K is not the result of a shift from NO to NO_2.)

Figure 4 also shows that CO, measured with the FTIR spectrometer, increases for reactor temperatures between 750 and 850 K. Above 850 K, the CO concentration decreases steadily as the reactor temperature increases, approaching zero at 1200 K. The decline in the CO concentration starting at a temperature of 850 K is coincident with the divergence of the NO concentrations for the cases with and without CA addition. In other words, NO reduction as a result of CA addition is coincident with the decline in the CO concentration. The potential importance of CO to the NO reduction process will be discussed later.

The next two figures, 5 and 6, show the effects of the exhaust preheater and vaporizer temperatures on the NO reduction process for this experiment. Figure 5 shows the NO reduction as a function of the average exhaust preheater temperature for the baseline operating conditions and a reactor temperature of 1200 K. As the preheater temperature was increased above 775 K, the NO reduction steadily deteriorated. For example, for an average exhaust preheater temperature of 1000 K, the NO reduction is 50 percent as compared to 95 percent for the baseline average preheater temperature of 690 K. This deterioration in the process may be a result of oxidation of the exhaust gas CO or other key exhaust gas species in the preheater at temperatures above 800 K. Note that CO oxidation occurred in the reactor at temperatures above 850 K as shown in Fig. 4. Although the preheater temperature effects shown are specific to this reactor design, these results suggest that the composition of the exhaust gas has a significant impact on the NO reduction process.

Figure 6 shows the NO reduction (square symbols) as a function of the average CA-vaporizer temperature for the baseline operating conditions and a reactor temperature of 1210 K. The purpose of this series of tests was to determine the effect of the average vaporizer temperature on the overall NO reduction process. The band drawn around the data illustrates the fluctuations present in this experiment. The general trend is that as the vaporizer temperature increases above 700 K the NO reduction process deteriorates.

One explanation for the behavior illustrated in Fig. 6 is that when the higher vaporizer temperatures are coupled with the long vaporizer residence time, 5.2 s, the HNCO partially reacts in the vaporizer before entering the main reactor. To explore this possibility, nitrogen, instead of exhaust gas, was drawn through the exhaust preheater and the reactor while the same vaporizer CA and air carrier gas flows were maintained. The average temperature of the reactor was 380 K to insure that no water condensed in the reactor. The uses of nitrogen and a relatively low reactor temperature were expected to quench any further reaction of the HNCO in the reactor so that measurements at the reactor outlet would be representative of the vaporizer outlet. Figure 6 demonstrates that NO was produced in the vaporizer (triangular symbols) for temperatures above 750 K. The detection of NO indicates that the HNCO was reacting and forming NO as one product. As the vaporizer temperature increased above 750 K, the NO concentration steadily increased reaching 120 ppm at the outlet of the reactor or a level equal to approximately one-third of the NO in the engine exhaust for the baseline conditions. This result suggests that the CA will react in air and form NO when maintained at elevated temperatures for long residence times. Both the loss of HNCO and the formation of NO in the vaporizer adversely affect the efficiency of the process. These results show that long residence times at elevated temperatures when using air to deliver the HNCO should be avoided in the design of an HNCO delivery system.

Figure 7 shows NO reduction as a function of the average reactor temperature for overall engine equivalence ratios of 0.25, 0.5, and 0.75. The reactor inlet NO concentrations were 202, 330, and 286 ppm and the reactor inlet CA/NO ratios were 1.6, 1.4, and 1.6 for the equivalence ratios of 0.25, 0.5, and 0.75, respectively. The cross-hatched region represents the data from Fig. 2 for the baseline equivalence ratio of 0.5. As illustrated, the NO reduction is only weakly related to equivalence ratio in the equivalence ratio range of 0.25 to 0.75. The results suggest that above 1100 K the NO reduction process improves with increasing equivalence ratio in the range examined. This trend could be caused by changes in the concentrations of any one of several species that vary with equivalence ratio.

Figure 8 from Siebers and Caton (1988) shows the NO reduction as a function of the average reactor temperature for the baseline conditions with 260 ppm of CO at the reactor inlet (cross-hatched region) compared with a case for which the reactor inlet CO concentration was increased to 8050 ppm. All other conditions were the same for the two cases except for a slight increase in the overall reactor flow rate and the accompanying additional dilution of the exhaust caused by the CO addition (Siebers and Caton, 1988). The addition of CO to the reactor flow had a dramatic effect on the NO reduction chemistry. The temperature for maximum NO reduction decreased from 1150 K to 970 K by increasing the CO concentration from 260 ppm to 8050 ppm. A possible explanation of the effect of CO on the NO reduction chemistry is given in the reaction mechanism proposed by Perry and Siebers (1986). The CO may be acting as an indirect source of hydrogen (H) atoms through the reaction

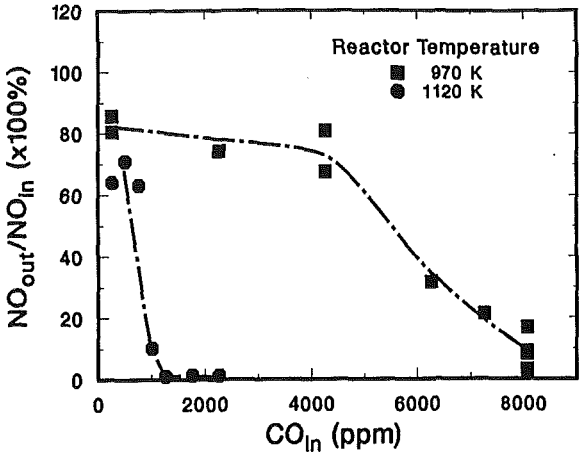

Fig. 9 The effect of the exhaust CO concentration on the exhaust gas NO reduction for two reactor temperatures

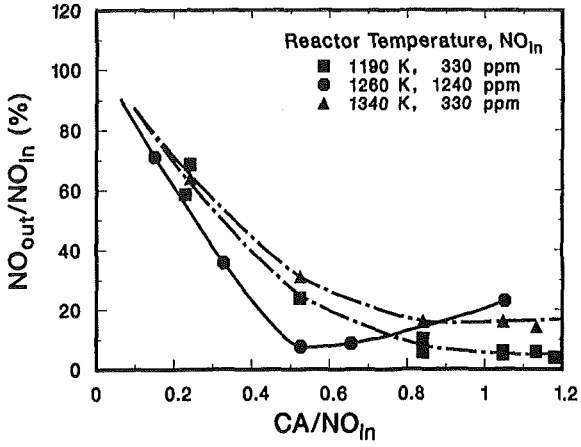

Fig. 10 The effect of the input NO concentration on the exhaust gas NO reduction

$$OH + CO = H + CO_2$$

Enhancing the concentration of H atoms would enhance reduction of NO based on the proposed mechanism.

For the results presented in Fig. 8, the concentration of CO was a constant 8050 ppm for all reactor temperautres. Figure 9 shows the NO reduciton as a function of the CO concentration at the reactor inlet for two reactor temperatures. The first temperature selected, 970 K, represented the minimum temperature for which significant (95 percent) reduction was noted with 8050 ppm of CO at the reactor inlet. As shown, not much effect was detected until over 4000 ppm of CO was used. Increasing the CO concentration beyond 4000 ppm resulted in a steady improvement in the NO reduction up to the maximum level of CO used, 8050 ppm. The second reactor temperature, 1120 K, represented a temperature slightly lower than the temperature required for significant NO reduction (95 percent), as shown in Fig. 2. For this reactor temperature (1120 K), much less CO was needed than for the lower temperature (970 K). Using a CO concentration of 1200 ppm provided an NO reduction of more than 95 percent.

Figure 10 shows NO reduction as a function of the reactor inlet CA concentration to NO concentration ratio for two inlet NO concentrations: 330 and 1240 ppm. For the inlet NO concentration of 330 ppm, data for two reactor temperatures that bracket the reactor temperature used for the 1240 ppm concentration are shown. The general trends in the results are similar for both concentrations. Namely, as the ratio of CA and inlet NO concentration increases, the NO reduction increases until a maximum NO reduction of 95 percent is reached. The important difference between the results obtained for the two inlet NO concentrations is that the reactor inlet CA/NO ratio is significantly lower for the higher inlet NO concentration: 0.5 as compared with 1.0. This result demonstrates that the process is more efficient in terms of CA usage for higher inlet NO concentrations and that the maximum NO reduction is not affected by the inlet NO concentration.

Summary and Conclusions

The addition of CA to a portion of diesel engine exhaust gases to reduce the NO exhaust concentrations was studied experimentally. The CA was combined with the exhaust gases in a quartz flow reactor and the mixture was heated to temperatures up to 1340 K. The baseline operating conditions included an engine equivalence ratio of 0.5, an average vaporizer temperature of 620 K, an average exhaust preheater temperature of 690 K, a CA/NO ratio of 1.4, and a total reactor flow of 1.2 slpm. The operating parameters that were varied in this study were the engine equivalence ratio, the reactor, vaporizer, and preheater temperatures, the reactor mass flow rate, and the exhaust gas CO and NO concentrations.

The findings and conclusions of this work include:

1 For the baseline operating conditions, the engine exhaust NO concentration was reduced by 95 percent for an average reactor temperature of 1150 K. The average NO reduction was 20 percent or less for lower reactor temperatures. As the reactor temperature was increased above 1200 K, the NO reduction deteriorated slightly. At a reactor temperature of 1340 K the NO reduction was 80 percent.

2 Varying the reactor mass flow rate from 0.5 to 1.9 slpm did not affect the NO reduction. This result implies that the baseline NO reduction results apply for reactor residence times of between 0.4 and 2.6 s for the range of conditions examined.

3 When the average exhaust preheater temperature was increased above 775 K or when the average vaporizer temperature was increased above 700 K, the NO reduction steadily deteriorated. A suggested cause of the preheater temperature effect is the oxidation of key species in the preheater such as CO. This result indirectly demonstrates the importance of the exhaust gas composition on the NO reduction process. The vaporizer temperature effect is most likely caused by reaction of HNCO in the vaporizer to form NO. This latter result demonstrates the need to control temperature and residence time in a cyanuric acid delivery system using air as a carrier gas.

4 The engine equivalence ratio in the range from 0.25 to 0.75 had a secondary effect on NO reduction with cyanuric acid. As the equivalence ratio was varied from 0.25 to 0.75 the maximum reduction increased from 80 to 98 percent.

5 Increasing the CO concentration at the reactor inlet both lowered the temperature required to achieve NO reduction and increased the temperature range over which significant NO reduction occurred.

6 Increasing the exhaust gas NO concentration from 330 to 1240 ppm improved the efficiency of the process. Although more absolute CA was needed, the amount relative to the input NO was 50 percent less.

Acknowledgments

Work performed at the Combustion Research Facility at Sandia National Laboratories and supported by the U.S. Department of Energy, Energy Conversion and Utilization Technologies Program.

References

Lester, G. R., 1983, "The Development of the Automotive Exhaust Catalysts," *Heterogeneous Catalysis—Selected American Histories*, B. H. Davis and

W. P. Hettinger, eds., American Chemical Society Symposium Series, Washington, DC, Vol. 222, pp. 415–433.

Lyon, R. K., and Hardy, J. E., 1986, "Discovery and Development of the Thermal DeNO$_x$ Process," *Industrial Engineering and Chemical Fundamentals*, Vol. 25, pp. 19–24.

Mansour, M. N., Nahas, S. N., Quartucy, G. C., Nylander, J. H., Kerry, H. A., Radak, L. J., Eskinazi, D., and Behrens, T. S., 1987, "Full Scale Evaluation of Urea Injection for NO Removal," Paper No. 7A-4, presented at the 1987 Joint Symposium on Stationary Combustion NO$_x$ Control, New Orleans, LA, Mar. 23–26.

Perry, R. A., and Siebers, D. L., 1986, "Rapid Reduction of Nitrogen Oxides in Exhaust Gas Streams," *Nature*, Vol. 324, pp. 657–658.

Perry, R. A., 1988a, "NO Reduction Using Cyanuric Acid: Pilot Scale Testing," Paper No. 88-68, Western States Section/The Combustion Institute Fall Technical Meeting, Dana Point, CA, Oct.

Perry, R. A., 1988b, "NO Reduction Using Sublimation of Cyanuric Acid," U.S. Patent No. 4,731,231, Mar. 15.

Rosenberg, H. S., Curran, L. M., Slack, A. V., Ando, J., and Oxley, J. H., 1980, "Post Combustion Methods for Control of NO$_x$ Emissions," *Progress in Energy and Combustion Sciences*, Vol. 6, p. 287–302.

Sarofim, A. S., and Flagan, R. C., 1976, "NO$_x$ Control for Stationary Combustion Sources," *Progress in Energy and Combustion Sciences*, Vol. 2, pp. 1–25.

Siebers, D. L., and Caton, J. A., 1988, "Reduction of Nitrogen Oxides by the RAPRENOx Process," *Proceedings of the Spring Meeting of the Central States Section/The Combustion Institute*, May.

Siebers, D. L., and Caton, J. A., 1989, "Removal of Nitric Oxide From Exhaust Gas With Cyanuric Acid," *Combustion and Flame*, in press.

Wade, W. R., 1980, "Light-Duty Diesel NO$_x$-HC-Particulate Trade-Off Studies," SAE Paper No. 800335.

Wasser, J. H., and Perry, R. B., 1987, "Diesel Engine NO$_x$ Control: Selective Catalytic Reduction and Methanol Emulsion," Paper No. 7b-2, presented at the 1987 Joint Symposium on Stationary Combustion NO$_x$ Control, New Orleans, LA, Mar. 23–26.

M. S. Hossain

M. Neyman

W. J. Cook

Helipump Corporation,
Cleveland, OH 44141

A. Z. Gordon

IGR Enterprises,
Beachwood, OH 44122

IGR Solid-State Electrochemical NO_x Control for Natural Gas Combustion Exhaust Gases

Solid-state electrochemical technology, embodied in the IGR process, is used to reduce nitrogen oxides (NO_x) to nitrogen and oxygen, and thereby control NO_x emissions from natural gas powered engines. The IGR deNO_x process is based on solid-state, flow-through, high surface area, porous oxygen ion conductive ceramic electrolytes. Recent bench-scale experiments conducted for the Gas Research Institute have demonstrated NO_x reduction in multicomponent gas streams, the inert portion of which simulate natural gas combustion products. The reduction products were analyzed by in situ gas chromatography to verify NO_x reduction rates inferred from electrochemical measurements. IGR process advantages compared with existing NO_x control technologies are reviewed.

Introduction

Oxides of nitrogen are receiving increased government regulation intended to reduce or eliminate these air pollutants. Out of a total NO_x (sum of NO and NO_2) emission of about 20 million tons per year, combustion of fuel (e.g., coal, oil, and natural gas) is by far the largest source of NO_x [1]. Virtually all NO_x produced during combustion is emitted in the form of NO (~95 percent) although it oxidizes in the atmosphere to NO_2.

NO_x is formed by two mechanisms: The first is oxidation of free nitrogen in combustion air (thermal NO_x), and the second is the oxidation of chemically bound nitrogen in fuel (fuel NO_x). Natural gas contains insignificant levels of chemically bound nitrogen, so NO_x produced from natural gas combustion is due almost solely to thermal NO_x. This thermally driven fixation of nitrogen is described by the following chemical equation:

$$N_2(P=0.8 \text{ atm}) + O_2(P=0\text{–}0.2 \text{ atm}) = 2O(P=0\text{–}0.005 \text{ atm})$$

where all of the species are gases and the partial pressures are given in atmospheres. The partial pressure of oxygen is an adjustable combustion parameter, and the maximum equilibrium partial pressure of nitric oxide in a natural gas flame is roughly 5000 ppm (0.5. vol percent).

Several techniques have been developed to prevent NO_x formation (NO_x abatement) by combustion modifications, or to control NO_x emissions by postcombustion flue gas treatment (FGT). Combustion parameters that can be modified to reduce NO_x formation are excess air, combustion temperature, water injection, burner design, and the like.

Several postcombustion approaches for NO_x reduction have been proposed. Among these, ammonia-based selective catalytic reduction (SCR) has received increasing attention. Under favorable conditions, SCR can reduce NO_x emissions by 80 to 90 percent. SCR suffers a number of disadvantages, however, such as high cost, uncertain catalyst life, waste disposal requirements, tight control of stoichiometry, and ammonia slip.

Another postcombustion technique is nonselective catalytic reduction (NSCR). NSCR is limited to exhaust gas streams with less than 4 percent oxygen.

Other postcombustion FGT techniques offering NO_x reduction of about 50 percent include selective noncatalytic reduction (SNCR), electron beam irradiation, wet scrubbers, and dry absorption processes. In general, all these techniques are limited by high cost or uncertain reliability.

This paper discusses the IGR deNO_x process, a solid-state electrochemical NO_x control technique conceived by IGR Enterprises [2] for natural gas combustion exhaust gases. Evaluation of technical feasibility on the basis of bench-scale experiments and advantages of IGR technology over existing NO_x control technologies are presented.

IGR Solid-State Electrochemical Reactor

IGR emissions control technology is based on a solid-state, flow-through, electrochemical reactor, which reduces NO_x to nitrogen and oxygen. There are no moving parts, consumable reagents, or byproduct sludges. Exhaust flue gas is the only fluid. The cell electrolyte is a solid, porous ceramic oxide-ion conductor such as stabilized zirconia (SZ), stabilized ceria (SC), or stabilized bismuth oxide (SB). The electrodes for the cell may be of any material(s) having sufficient electronic conductivity. In laboratory test cells, porous, high surface area silver has been used.

A schematic cross section of an IGR test cell is shown in Fig. 1. As shown, the cell is installed in a section of the exhaust gas piping between the combustion unit and the exhaust system.

Contributed by the Internal Combustion Engine Division and presented at the Energy-Sources Technology Conference and Exhibition, New Orleans, Louisiana, January 10–14, 1988. Manuscript received by the Internal Combustion Engine Division October 12, 1987. Paper No. 88-ICE-10.

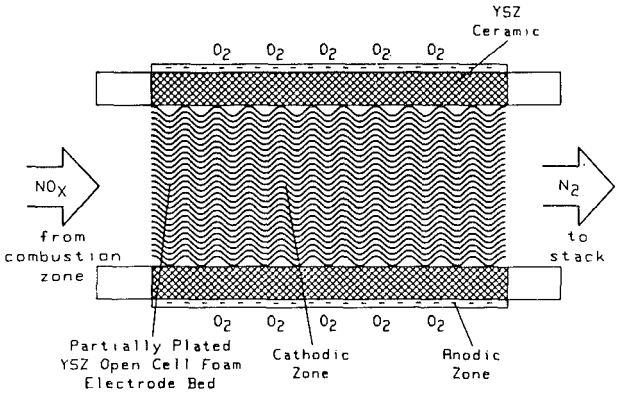

Fig. 1 Schematic cross section of IGR test cell

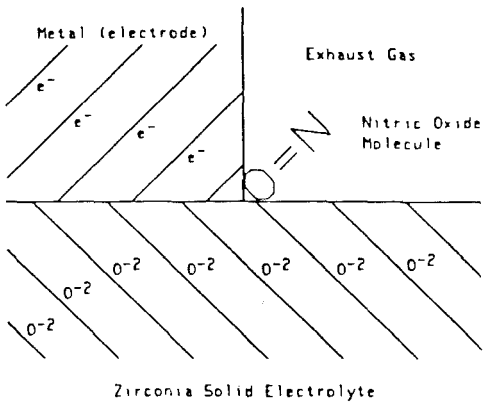

Fig. 2 Molecular scale representation of cathodic electrode reaction

The cathodic zone of the cell is a porous ceramic foam coated with silver paint. The outer shell of the cell is a gas-tight ceramic membrane of the same composition as the porous foam. The outer ceramic surface, coated with silver paint, is the cell anode.

Pancharatnam [3], Mason [4], and Gur and Huggins [5] have performed fundamental electrochemical kinetic measurements of NO decomposition with nonporous zirconia disk electrolytes. In these studies the authors have measured rates of reaction of NO on stabilized zirconia disk electrolytes as a function of such fundamental physical parameters as temperature, gas partial pressure, and voltage. Based on these measurements the authors, in conjunction with Amirnazmi and Boundart [6], who studied heterogeneous catalytic decomposition of NO, have proposed kinetics and mechanisms for the electrolytic reduction of NO on high-temperature stabilized zirconia electrolytes. Pancharatnam [3] also showed that it is the electrolyte and not the metal electrode material that plays the dominant role in the electroreduction of NO.

Electrode and Overall Process Reactions. Exhaust gas passes through the cell and contacts the high surface area, solid electrolyte. In the cathodic zone of the cell, electrochemical reduction of NO_x yields nitrogen gas and oxide ions. The nitrogen is swept along by the flue gas while the oxide ions dissolve in the solid electrolyte. Simultaneously, in the anodic zone, an equivalent number of oxide ions are converted to oxygen gas. The principal reactions are thought to be:

Cathode

$$2NO(gas) + 4e^-(Ag, \ldots) = N_2(gas) + 2O^{-2}(SZ,SC, \ldots)$$

$$2NO_2(gas) + 8e^-(Ag, \ldots) = N_2(gas) + 4O^{-2}(SZ,SC, \ldots)$$

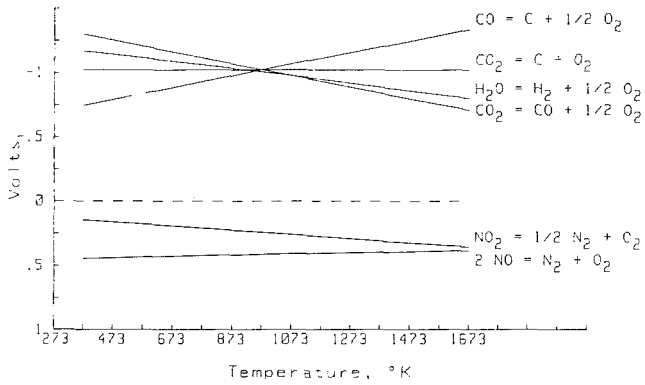

Fig. 3 Reduction potentials versus temperature

Anode

$$2 \text{ or } 4\,O^{-2}(SZ,SC, \ldots) = 1 \text{ or } 2\,O_2(gas) + 4 \text{ or } 8e^-(Ag, \ldots)$$

Overall

$$2NO(gas) = N_2(gas) + O_2(gas)$$

$$2NO_2(gas) = N_2(gas) + 2O_2(gas)$$

A molecular scale schematic believed to represent the cathodic electrode reaction process is shown in Fig. 2. The nitric oxide molecule reacts at the three phase boundary electrode–electrolyte–exhaust gas.

Electrical Measurements and NO_x Removal Rates. The observed current passing through the IGR reactor is the sum of two discrete currents:

$$i_{\text{observed}} = i_{\text{ionic}} + i_{\text{electronic}}$$

The ionic current results from transport of oxide ions and signals the removal of NO_x, while the electronic current is a background noise caused by impurities and defects in the electrolyte.

The value of i_{ionic} is related to the rate and efficiency of NO_x removal by Faraday's Law

$$i_{\text{ionic}} = (F)\,(N_{eq})(\text{gmoles } NO_x \text{removed/second})$$

where F = Faraday constant = 96,487 coulomb/equivalent; N_{eq} = number of electrons transferred per molecule of NO_x reacted; 2 for NO, 4 for NO_2, and in general 2 for each oxygen atom participating in the reaction. Each ampere of current in a given cell corresponds to an NO removal rate of 9.3 mg/min.

Selective Electrochemical Reduction. Exhaust gases contain a number of compounds that may, in principle, be reduced (or oxidized) within the IGR reactor. Additional exhaust gas reactions, such as the reduction of water, are undesirable power-consuming side reactions.

The standard potentials of several possible electrochemical reactions are displayed in Fig. 3 [7]. Chemical reactions that occur spontaneously have a negative Gibb's energy and a positive standard potential. All of the reductions listed in Fig. 3, except for the nitrogen fixations, have negative voltages. The oxides NO_2 and NO are thermodynamically unstable and therefore have positive voltages associated with their spontaneous decomposition. However, as the energy of activation for spontaneous NO decomposition is very high, the thermal decomposition kinetics are slow. Heterogeneous catalysts are available to reduce this activation energy considerably but reaction rates are still too low to be practical for NO_x emission control.

For the IGR reactor to reduce a compound, a potential

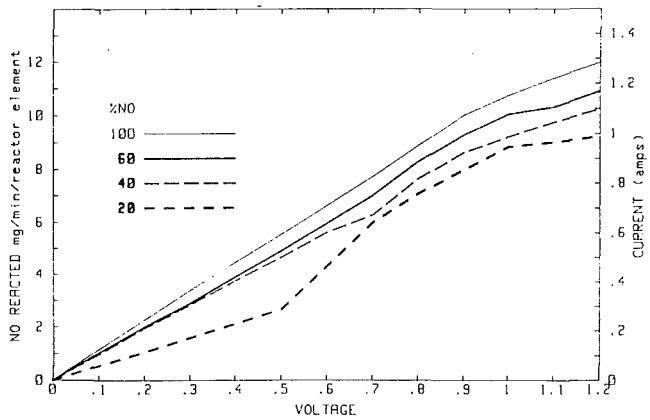

Fig. 4 Nitric oxide reduction polarization on yttria-stabilized zirconia (10 percent Y_2O_3) at 883 K; electrode material: Ag; flow rate of NO: 1 lpm

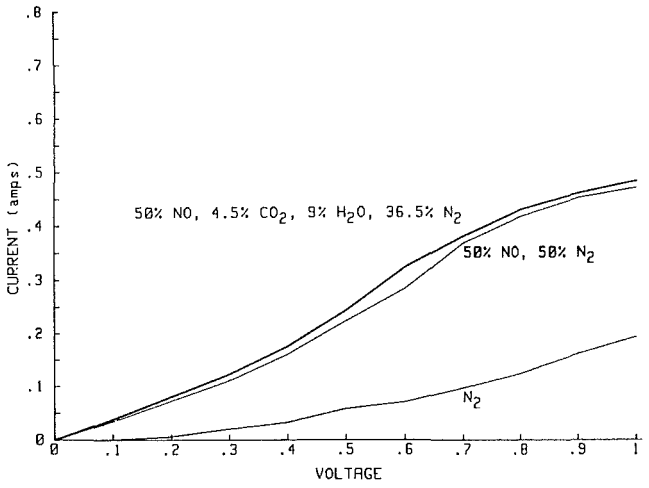

Fig. 5 Current versus voltage for a gas mixture on yttria-stabilized zirconia (10 percent Y_2O_3) at 878 K; electrode material; Ag; flow rate 1 lpm

greater than the thermodynamic potential for that compound must be applied across the cell. To achieve removal of the fundamentally unstable nitrogen oxides, any cathodic voltage will suffice. However, to reduce the more thermodynamically stable species such as CO_2 or H_2O, a potential greater than about 1 V must be applied. Accordingly, NO_x may be selectively removed from a combustion gas stream by maintaining the applied potential below that required to reduce the nonpolluting species.

Experimental Results

Electrochemical Measurements. Both laboratory and bench-scale experiments confirm the decomposition of NO_x with solid-state IGR electrochemical cells. The initial experiments were conducted with a binary gas mixture, generally nitrogen spiked with a NO concentration of 1000 ppm or less [2]. The electrochemical reactors used calcia- or yttria-stabilized zirconia (CSZ, YSZ) electrolytes in packed bed or reticulate foam configurations. Recent bench-scale experiments conducted for the Gas Research Institute (GRI) with YSZ reticulate electrolyte (volume ~ 32.8 cm^3) have achieved 130× scale-up for NO decomposition over initial laboratory experiments. Results are shown in Fig. 4 in the form of current versus voltage (current is directly proportional to the amount of NO decomposed) as a function of NO partial pressure. The decomposition kinetics seem to indicate that the rate is not very sensitive to the partial pressure of NO in the test mixture (the rate is approximately proportional to the 0.4 power of the NO partial pressure).

Electrochemical measurements have been made for a multicomponent gas mixture, the inert portion of which simulates a natural gas fired engine exhaust gas. Current versus voltage measurements using a YSZ electrolyte at 878 K for the multicomponent gas mixture, a binary mixture of NO and N_2, and for pure N_2 are shown in Fig. 5. The multicomponent gas mixture is 50 percent NO, 4.5 percent CO_2, 9 percent H_2O, and 36.5 percent N_2, where the CO_2: H_2O: N_2 ratio (1:2:8) is typical of natural gas combustion products. The binary mixture is 50 percent NO and 50 percent N_2. The results indicate that over the voltage range of the IGR deNO_x process CO_2, H_2O, and N_2 have an insignificant effect on the rates of NO decomposition.

Gas Chromatographic Measurements. In addition to the above electrochemical data, gas chromatographic (GC) data were taken on the gas stream passing through an IGR reactor element. The GC column packing was made with molecular sieve 13x[3]. Measurement of nitrogen formed in the reactor was used to infer the NO decomposed; 1 mole of N_2 is formed from the decomposition of 2 moles of NO. Measurements were made on 100 percent NO and 50 percent NO (diluted with helium) gas streams at 873 K under both open and closed-circuit conditions. At 1 V, from GC analysis, decomposition rates of 10.5 mg/min and 7.9 mg/min were obtained for 100 and 50 percent NO, respectively. These values are in reasonable agreement with decomposition rates obtained from electrochemical data using Faraday's law.

Preliminary Design and Economic Analysis

Preliminary Design Analysis. Combining the effects of NO concentration (experimental reaction rates were dependent on the NO concentration) and improved reactor geometry gives an estimated NO decomposition volumetric turnover rate (VTR) for a commerical reactor of 3×10^{-5} gmole NO reacted/min/cm^3 operating at an average NO concentration of 2475 ppm and 873 K. A preliminary sizing of an IGR deNO_x reactor is calculated for a 713-hp natural gas fired reciprocating engine, which powers a cogeneration system recently installed at the Medical Center del Oro, Houston, TX. (This cogeneration system is highlighted in GRI's 1984 Annual Report, page 10.) The engine is a model G398SITA Caterpillar with the following operating specifications:

- natural gas fuel, about 50,000 MCF/year
- exhaust gas manifold temperature 873 K
- exhaust gas flow 3280 cfm
- 15 grams of NO_x/hp/h (5.9 mole (as NO)/min) (inlet concentration to reactor is 4500 ppm NO)
- 713 hp reciprocating engine

The IGR deNO_x reactor volume necessary to remove 90 percent of the NO_x (outlet NO_x concentration of 450 ppm) for this hospital cogeneration system is therefore (at 1 V and 0.3 V DC):

Vol. = IGR Reactor Volume
= NO_x Emissions Rate/VTR
= (5.9 gmole NO_x/min (0.9 conversion)/(3×10^{-5})
= 178 liters/V
= 6.29 ft^3 @1 VDC (e.g., 2 ft diameter, 2 ft long)

or alternatively

= 21.0 ft^3@ 0.3 VDC
(e.g., 3 ft diameter, 3 ft long)

The VTR used in calculations is evaluated at the average of the inlet and outlet NO concentrations to the reactor ((4500+450)/2 or 2475 ppm NO).

Table 1 Capital cost estimates: NO_x control for 713-hp natural gas fired IC engine

	SCR (ammonia)	NSCR	IGR @0.3 V DC
Installation		6,000	6,000
Catalytic Converter		14,000	0
Automatic Controller		11,000	0
Electronics		0	4,355
Ceramic Reactor		0	10,876*
TOTAL CAPITAL COST	168,000	31,000	21,231
$/HP	236	43	30
Relative Cost	7.91	1.46	1.00

*based on information supplied by Dr. Morris, Hi-Tech Ceramics, Inc., Alfred Station, New York.

Table 2 Annual operating cost estimates: NO_x control for 713-hp natural gas fired IC engine

	SCR (ammonia)	NSCR	IGR @0.3 V DC
Catalyst Replacement		3,600	
Electricity			3,254
Maintenance		1,200	1,200
Overhead/G&A		600	600
Capital Charges		4,600	3,150
Annual Operating Cost	20,000	10,000	8,205
mil/HP-HR	3.20	1.60	1.31

electricity @ 6.00 cents per kw-hr

The IGR deNO$_x$ reactor power requirements are:

Power = (reactor voltage)(amps)/1000
= (voltage)(F)(N_{eq})(gmoles NO removed/s)/1000
= (1.0)(96,487)(2)(5.9/60)(0.9)/1000
= 17 kW (@1 V, 6.29 ft^3 reactor),

or alternatively,

= 5.1 kW (@0.3 V, 21.0 ft^3 reactor)

A portion of the oxygen present in the gas stream may also be pumped from the cathodic zone to the anodic zone in the reactor. Given a nominal oxygen concentration range of about 0.5 to 5 percent and an operational selectivity of 10 to 100 to 1 of NO over O_2 in the reactor, the reactor volume and power consumption would increase approximately 20 percent (a mole of O_2 causes twice as much current as a mole of NO) to 25.2 ft^3 and 6.2 kW at 0.3 volt and 7.6 ft^3 and 20.6 kW at 1 volt. Selectivity of NO over O_2 was not studied in this initial GRI research and will be the subject of future investigations. The literature on transition metal oxide electrocatalysis suggests that a practical level of selectivity may be achievable.

Hence, about 1 percent of engine output power is required to operate the NO_x electrochemical reduction reactor at 0.3 V DC. This power consumption might possibly be recouped by retuning the engine toward improved fuel economy.

Preliminary Economic Analysis. A preliminary economic analysis of the IGR deNO$_x$ technology applied to a 713-hp stationary reciprocating engine is presented in Table 1. IGR deNO$_x$ technology operating at 0.3 V per cell is compared with SCR and NSCR technology for postcombustion control of NO_x emissions. The assumptions and analysis format follow that of Urban [8]. The capital cost and operating cost comparisons are shown in Table 1 and Table 2, respectively. The IGR deNO$_x$ process economics compare favorably with SCR and NSCR.

Conclusions

IGR process has several attractive features:

- No moving parts
- No consumable reagents
- No byproducts
- Flue gas is the only fluid
- Preliminary economics are favorable

Although the IGR deNO$_x$ process will require long-term testing on engine exhaust streams before it can become commercially viable, from the analysis of bench-scale experiments, the process seems to be a very promising postcombustion NO_x control technique for natural gas fired prime movers.

Acknowledgments

The authors wish to acknowledge the financial support of the Gas Research Institute.

References

1 Hopper, T. G., and Marrone, W. A., "Impact of New Source Performance Standards on 1985 National Emissions From Stationary Sources," EPA 450/3-76-017, 1976.

2 Gordon, A. Z., "Solid-State Electrochemical Pollution Control Device," U.S. Patent No. 4,659,448, Apr. 21, 1987.

3 Pancharatnam, S., "Dissociation of Nitric Oxide on Platinum With Electrolytic Removal of Oxygen Using Stabilized Zirconia," Ph.D. Thesis, Stanford University, 1974.

4 Mason, D. M., "Methods and Apparatus for Catalytic Dissociation of NO," U.S. Patent No. 4,253,925, Mar. 3, 1981.

5 Gur, T. M., and Huggins, R. A., "Decomposition of Nitric Oxide on Zirconia in a Solid-State Electro-Chemical Cell," *J. Electrochem. Soc.*, Vol. 126, No. 6, 1979, p. 1067.

6 Amirnazmi, A., and Boudart, M., "Decomposition of Nitric Oxide on Platinum," *J. Cat.*, Vol. 39, 1975, p. 383.

7 Bulletin, 542, U.S. Bureau of Mines, CRC 1954, p. D-354.

8 Urban, C., "Evaluation of NO_x Reduction Technology for Natural Gas Industry Prime Movers," GRI Special Report, Aug. 1987.

Development of a Ceramic Particulate Trap for Urban Buses

G. M. Cornetti

P. P. Messori

C. Operti

IVECO Engineering,
Torino, Italy

Main aspects concerning the development of a burner-assisted ceramic particulate trap for diesel engines equipping urban buses have been examined. First of all the basic phenomena causing particulate accumulation inside the filter and chemical and physical parameters controlling regeneration have been studied. Then systematic measurements were performed in different running conditions on an urban bus equipped with a ceramic filter using a diesel fuel burner to start regeneration in order to verify the theoretical approach. These tests showed that: (1) The amount of particulate collected by the trap is a function of the different flat and/or hilly circuits inside the city; (2) regeneration has to be started with a proper amount of particulate collected (too little does not allow complete regeneration, too much is dangerous for trap life). Therefore an on-line continuous monitoring system of the particulate collected has been developed. When a certain level is exceeded, the filter is bypassed and regeneration starts. The system is based on the direct measurement of the exhaust flow by means of a Venturi and the pressure loss on the trap. The amount of particulate is defined by real time comparison of Venturi differential pressure and filter pressure loss. Urban buses were purposely designed in order to be equipped with a ceramic particulate trap plus the control unit. Tests of the system have been successfully performed on the buses operated on flat and hilly circuits inside the city.

1 Introduction

Over the past five years, two concomitant and certainly interdependent phenomena have taken place in Europe:

(*a*) A strong increase of urban mobility with both private and public transportation systems.

(*b*) The augmented "sensitivity" to the urban air pollution increase. "Sensitivity" is the right word for expressing the interest in the urban air pollution. In fact, from the atmospheric sampling in some Italian cities (e.g.,Torino), it appears that, relative to the early seventies, a real reduction of most pollutants has occurred as a consequence of the improved fuel quality used in domestic heating.

Apart from the real pollution levels, people who live in congested cities have developed a negative sensitivity to the problem, supported as well by the careful consideration devoted to it by mass media.

All this is extremely positive, for there is no doubt of the validity for the collective interest to have cities presenting improved life conditions.

These exigencies are now coagulating a need of change, which sometimes assumes the radical aspect "to want all at once," without taking into consideration the objective possibilities offered by the available technologies and without considering the risk associated with modifications not fully supported by correct experimentation; in this way there is no guarantee of obtaining the expected results.

As an example, much attention is presently paid to so-called alternative fuels, and in particular spark-ignited engines burning gaseous fuels, such as methane and propane. These engine configurations do not emit black smoke, but they exhibit much higher nitrogen oxides than the traditional diesel engines [1]. Furthermore methane-powered buses present a limited autonomy, due to the compressed gas bottle size, and only part of urban transportation could be converted to gas engines.

Based on these considerations, the approach to low urban pollution by an engine and vehicle manufacturer has to be as follows:

- To follow with interest only those tests that size, seriousness, and scientific completeness allow to give significant suggestions about the real advantages and disadvantages related to the innovative solutions.
- Not to expend human resources and facilities on different research activities, such as alternative fuels; but to concentrate on activities that promise to meet all the requirements necessary to be superior in the near future in comparison with all the other possible solutions.

The strategy of Iveco for reducing smoke opacity in diesel engines is represented by the particulate trap development. The description of this development is the objective of the paper.

2 How to Reduce Diesel Smoke

The reduction of diesel smoke opacity requires combined actions on the main parameters of the combustion system, such as the state of the air coming inside the cylinder and the

Contributed by the Internal Combustion Engine Division and presented at the Internal Combustion Engine Division Technical Conference, San Antonio, Texas, October 2-5, 1988. Manuscript received by the Internal Combustion Engine Division June 1988.

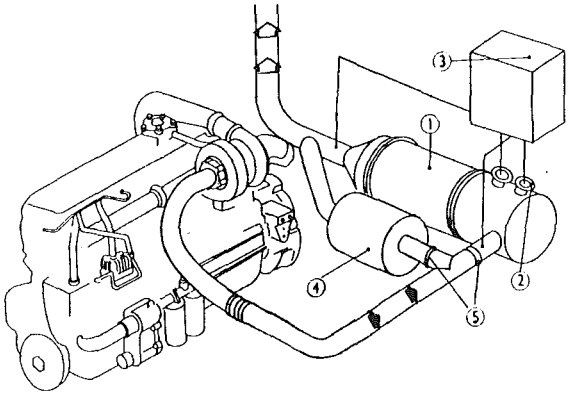

Fig. 1 Trap installation on the Iveco Turbocity Urban Bus

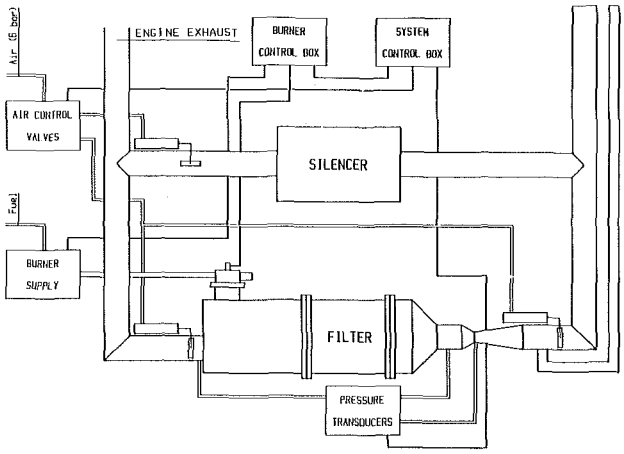

Fig. 2 Single filter with bypass configuration

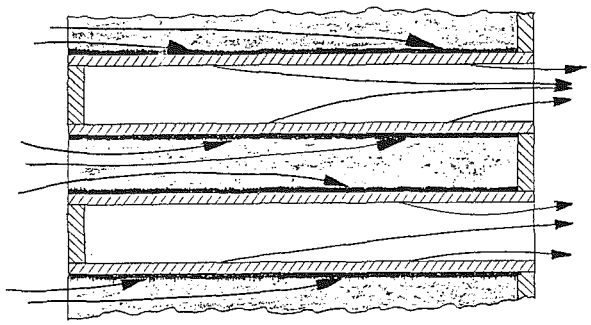

Fig. 3 Particulate deposition on the filter walls

atomization and distribution of the fuel injected by the pump, and on the exhaust system through particulate traps.

In the near future, turbocharging, new combustion chamber shapes, and high-capacity injection systems will allow great reduction of smoke and gaseous emissions, while maintaining the extremely high thermal efficiency level of diesel engines, efficiency that represents the best of thermal machinery.

On the other hand, development of particulate traps will allow immediate and dramatic reductions of particulates (and the associated visible smoke) with a collection efficiency up to 90 percent. With control of visible smoke, the other major engine targets, such as performance, emissions, and fuel consumption, will be met more easily.

This paper deals with the development of a particulate trap, i.e., a system placed on the engine exhaust pipe to collect particulates exhausted from diesel engines. The particulate trap is substantially based on an NGK cordierite ceramic wall-flow filter and a unique control system developed by Iveco.

After a short description of the basic trap components, the fundamental parameters of conditioning the accumulation of particulates inside filter, the main chemical and physical factors dominating the oxidation process, and trap regeneration, will be examined. Careful attention will be given to the analysis of the control system that, in a continuous way, is first able to detect the proper conditions for regeneration to be started; and secondly to follow regeneration in order to check the completion of the oxidation process.

3 Particulate Trap Description

The particulate trap under consideration is composed of (Fig. 1)

- an NGK ceramic monolith filter (1), 229 mm in diameter and 305 mm long, collecting particulates exhausted by the diesel engine;
- filter canning plus two fuel burners (2) manufactured by Eberspaecher;
- control system (3);
- bypass (4), which is included by means of the valves (5) when the filter is regenerating.

Two main processes characterize the mode of operation of the particulate trap:

- a first stage, called accumulation, where the filter is collecting particulates;
- a second stage, called regeneration, where particulates are burned and the filter is cleaned and ready for starting a new cycle.

When a ceramic cordierite wall-flow trap is employed, three different regeneration solutions can be adopted [2]:

- The first solution, consisting of a catalyzed ceramic, needs some artificial [3, 4] increase of the exhaust gas temperature in order to obtain temperatures of 500/550°C required for starting carbon oxidation. On-road bus tests have shown that these high exhaust temperatures do not occur under normal operating conditions.
- The second solution is based on a fuel additive or additives directly injected into the exhaust stream before the trap [5–7]. It still requires some artificial means in order to obtain temperatures of 300/350°C necessary to promote oxidation in the presence of additives.
- The third solution is the burner-assisted system proposed in the paper. It is able to promote carbon oxidation at all engine running conditions because of a burner, which can increase the temperature of an external air source up to level requested for carbon oxidation (600°C).

During regeneration using the third solution, exhaust gases do not flow into the filter, but external air enters the filter at high temperature, because of burners. In this way the thermal power supplied by burners (15 kW) is not as high as would be required by exhaust gases where the oxygen concentration is much lower than in the external air. On the other hand there is the need for two separate exhaust systems (Fig. 2); one for bypass of untreated exhaust during regeneration (20 min each 2/8 h).

4 Particulate Accumulation and Regeneration

Particulate accumulation is a function of their progressive deposition on the filter wall (Fig. 3). Filter channels are alternately closed and open. Gas entering the open channel is filtered on the walls, then is discharged on the contiguous channels that are open on the rear.

Filter pressure drop, sum of the pressure loss due to [8–11]

- channel inlet and outlet
- channel
- particulate layer
- pore,

can be expressed by the following function:

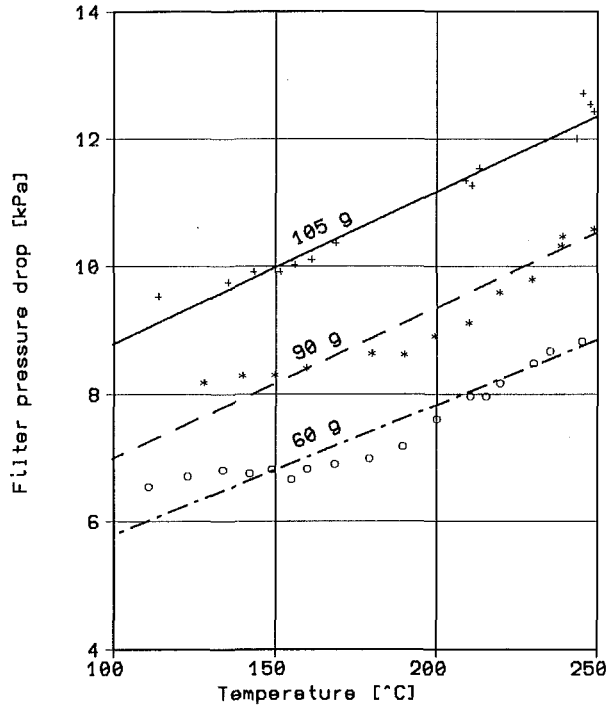

Fig. 4 Filter pressure drop as a function of collected particulate mass and gas temperature at the filter inlet

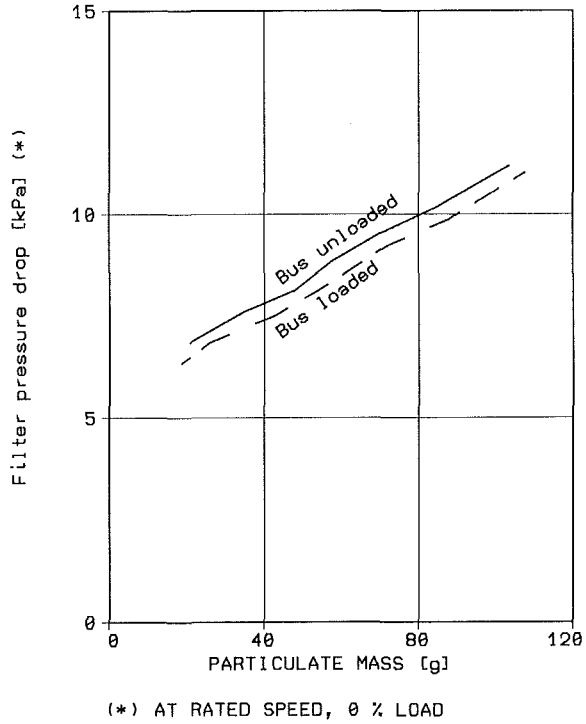

Fig. 5 Filter pressure drop at the engine-rated speed without load as a function of the collected particulate mass; two different driving conditions

$$\frac{\Delta p}{\frac{1}{2}\rho V_c^2} = f(\mathrm{Re}_c, \mathrm{Re}_p, d/L, s/d, s/d_p) \quad (1)$$

where

Δp = filter pressure drop
Re = Reynolds number
V_c = mean velocity in the channel *
V_p = mean velocity in the pore *
L = channel length
d = channel hydraulic diameter *
s = channel wall thickness *
d_p = mean pore diameter *
μ = gas viscosity
ρ = gas density

Parameters marked with (*) are a function of particulate mass collected by the filter.

The particulate accumulation, measured by weighing the filter at different times, was monitored by measuring:

- filter pressure drop
- temperature distribution inside the filter
- engine speed
- engine load

As shown in Fig. 4 the filter pressure drop is a function of the total amount of particulates collected on the filter, at a given filter inlet temperature. A multiple linear regression of the measured data was employed, at the beginning of the test program, for the prediction of the particulate mass collected by the filter.

By driving buses on different flat and/or hilly circuits inside the city, it was observed that the accumulated particulates depend on the type of diesel engine operation as expected. For instance, on a flat circuit the mass of particulate collected was more than 100 g during six hours with the bus completely loaded, while only 70 g were collected during eight hours when the bus was unloaded.

However, if data points related to the different test operations are plotted on a diagram with filter pressure loss (ordinate) and collected particulate mass (abscissa), the test points belong to the same straight line (Fig. 5). Then filter pressure loss, measured at the maximum engine speed without load and at an assigned inlet filter temperature, represents a useful criterion for the determination of the mass of the accumulated particulates.

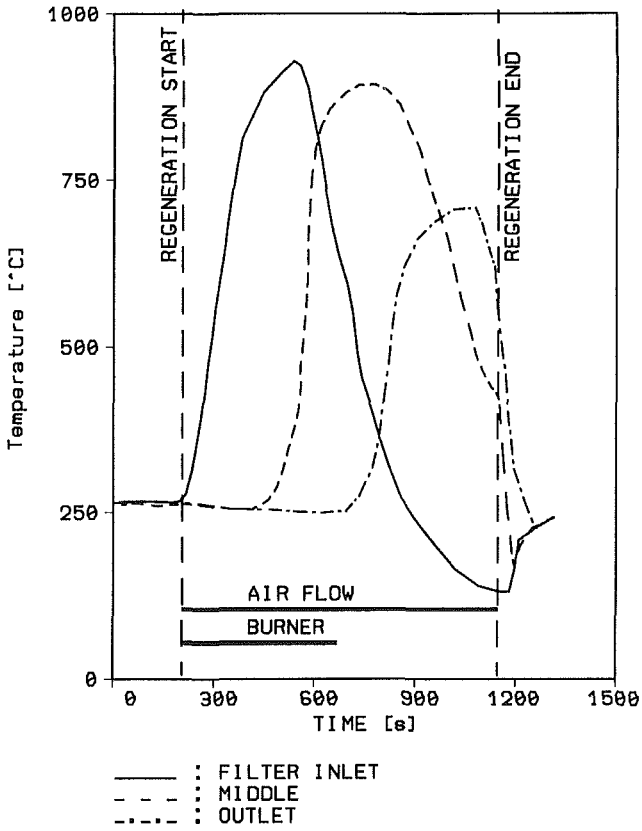

Fig. 6 Temperatures inside filter during regeneration

Let us now examine the regeneration mechanism (Fig. 6). At first, during a total time of eight minutes, burners increase the temperature of the air flow through the filter to a level high enough to start the process of particulate oxidation to carbon dioxide. When combustion is already stabilized, the burners are switched off, while the air flow is maintained. Energy supplied by the carbon oxidation is able to sustain the combusion because of thermal conduction, and propagates along the filter channels to the remaining carbon layers in twelve minutes. It is at this time that the regeneration is completed.

The regeneration process can be followed through the temperature signal supplied by three thermocopules located in the front, middle, and rear of the filter, respectively (Fig. 6). When regeneration starts, the first thermocouple placed at the filter inlet reads a progressive temperature increase, which, after a maximum, decreases as particulate combustion leaves the filter inlet. At this moment the second thermocouple, placed in the middle, starts to read its progressive temperature increase as the combustion wave approaches. Close to the maximum of the second thermocouple, burners are switched off, with combustion continuing to propagate along the filter channels as detected by the third thermocouple placed at the filter end. After regeneration is completed, exhaust gas begins flowing into the filter and temperatures of all three thermocouples converge.

Regeneration depends on three main factors:

1 amount of particulates collected by the filter;
2 temperature;
3 oxygen concentration.

The regeneration system is based on using a predetermined external air flow that is independent of the engine exhaust gas and guarantees a constant oxygen concentration. Furthermore the temperature level at the beginning (first eight minutes) is determined by the burner power; and after (second twelve minutes) by the amount of particulates collected on the filter. Therefore, the only true independent variable of the system is the mass of collected particulates; this is the variable that has to be controlled.

5 Need for a Control

The main problem of the particulate trap is the control of the periodic process of loading and regeneration. Control is needed in order to limit the negative effect of the pressure drop across the filter on the engine performance and to avoid filter damage during regeneration.

The filter pressure drop is strictly related to the collected particulate mass; this is the reason that an upper limit to filter loading is required. In urban bus applications, the increase in fuel specific consumption caused by the trap is negligible; in fact, the actual limit to the filter loading is related to the temperatures reached during regeneration and not to the filter pressure drop.

The ceramic monolith withstands temperatures up to 1000°C. It should be noted that a local melting and/or wall cracking, due to the thermal stresses, causes a strong decrease of filter efficiency (failure).

As stated above, the burner-assisted regeneration system assures constant properties of the gaseous stream. This leaves the particulate mass as the independent variable controlling the combustion rate. This rate must be confined to a certain range: not too high, in order to avoid over-temperatures, but sufficiently high to assure a stable flame propagation along the filter channels, and to guarantee a complete filter regeneration. This second condition is related to a minimum amount of particulates collected by the filter.

The completeness of the filter regeneration is required because local residue particulates, added to those collected in the subsequent loading phase, will produce over-temperatures in the next regeneration.

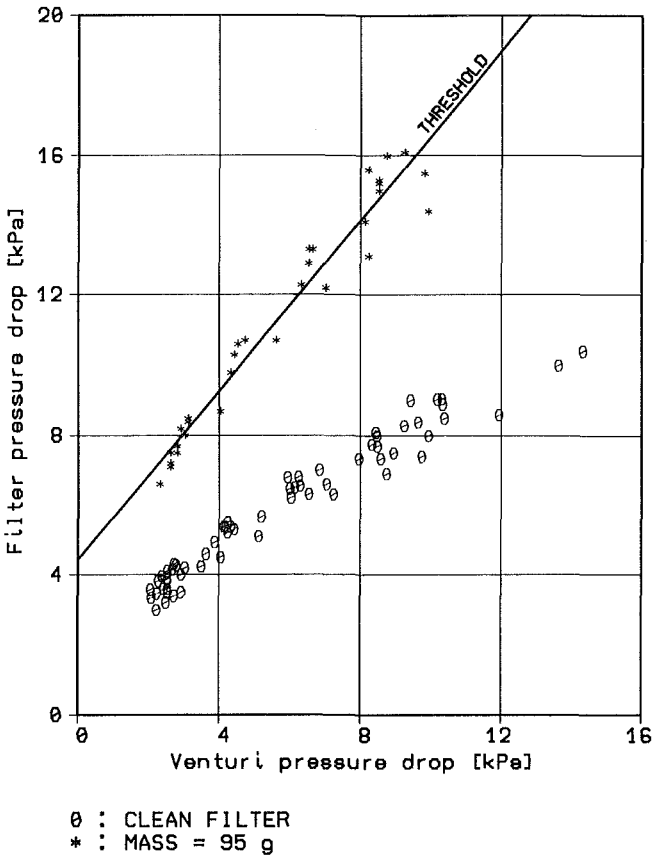

Fig. 7 Correlation between the particulate collected mass, the pressure drop across the filter, and the pressure drop across the venturi; different engine running conditions (speed and load)

Therefore, the basic concept of the control system is to start the regeneration when the proper filter loading level is achieved. The present system requires a collected particulate mass between 75 g and 95 g.

The problem is to know when this condition occurs, because the particulate production rate is not predictable, and is dependent on how the bus is exerted.

Benefits of the system are that both regeneration and control strategy are not affected by the engine characteristics and its operating conditions. In other words, the system can be installed on different vehicles with different engines, on new and in-use vehicles.

6 Control of the Collected Particulates

As pointed out by equation (1), filter pressure loss depends on the mass of particulates and the filter geometry, along with flow and density of exhaust gas. Flow and density are in turn determined by the diesel engine operations.

With the filter geometry assigned, the continuous monitoring of the particulate collected on the filter requires knowledge of three quantities: flow and density of the exhaust gas, and filter pressure loss.

This can be obtained through a double measurement of differential pressure: Δp_f across the filter; and Δp_v on a venturi, placed after the trap according to the scheme of Fig. 2.

In fact the basic equation of a venturi is analogous to equation (1)

$$\frac{\Delta p_v}{\frac{1}{2}\rho V^2} = const \tag{2}$$

where V is a characteristic gas velocity inside the duct.

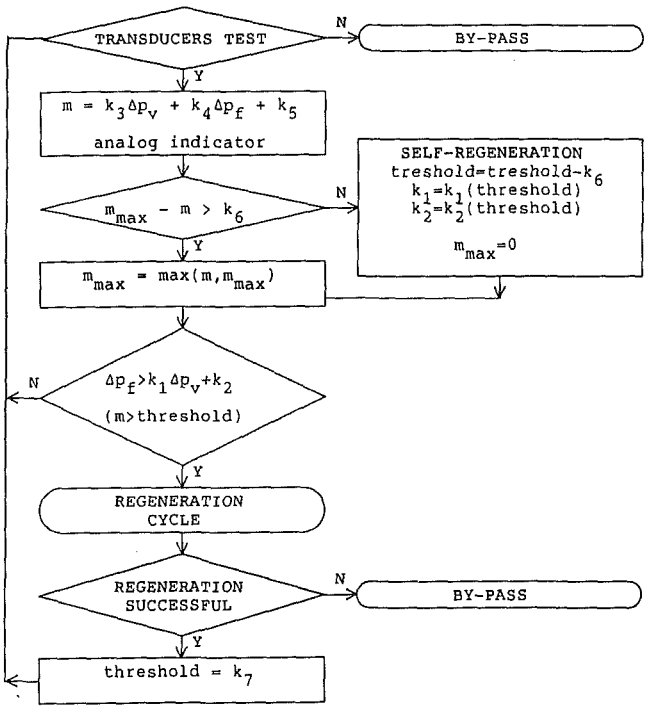

m = collected particulate mass

Δp_f = pressure drop across filter

Δp_v = pressure drop across venturi

k_1, k_2, k_3, k_4, k_5, k_6, k_7 = experimental constants

Fig. 8 Regeneration control logic

Figure 7 plots the different mass of particulate collected inside the filter, when engine speed and load are changed, versus Venturi differential pressure (abscissa) and filter pressure drop (ordinate). The figure shows the straight line of the particulate mass (100 g) that can not be exceeded in order to guarantee the life of the filter. An analogous limit exists for the minimum amount of particulate, below which any regeneration has to be avoided. It is inside this window, defined by the maximum and the minimum mass of particulate, where regeneration has to start.

The equation of the plane, obtained by doing a multiple linear correlation of all the collected data points, is

$$m = 11.9\ \Delta p_f - 11.1\ \Delta p_v + 0.49 \tag{3}$$

where m is the mass particulate, g; Δp_f is the filter pressure drop, kPa; Δp_v is the venturi differential pressure, kPa.

Equation (3) represents the relationship among the different variables and is mainly used for supplying an analog indication of accumulated particulates.

Regeneration has to start when the signal of filter pressure loss verifies the following inequality:

$$\Delta p_f > k_1 \Delta p_v + k_2 \tag{4}$$

where correlation constants $k_1 = 1.215$ and $k_2 = 4.4$ refer only to the threshold value of 95 g of particulates collected by the filter in order to guarantee a better accuracy of the prediction.

In this inequality, Δp_v has to be higher than a prefixed minimum value because, at low exhaust flow, the function is no longer valid. Besides that, the inequality (4), which triggers regeneration, has to be verified during several seconds in order to avoid untimely regenerations due to transient phenomena.

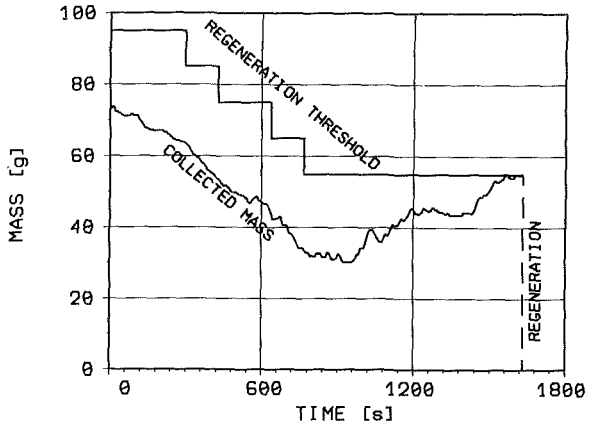

Fig. 9 Threshold reduction when a self-regeneration occurs

7 Control System

The decision of when regeneration is to be started is the main duty performed by the control system, but other functions are required in order to detect system failures or particular conditions dangerous to filter life.

Figure 8 shows a block diagram of the regeneration control. By means of internal cross-checking, pressure transducer failures can be detected. If this condition occurs, the control is no longer performed, the filter is bypassed, and the alarm lamp on the dashboard begins flashing.

During the loading phase at high exhaust gas temperatures, the collected particulate can be ignited causing a partial filter regeneration. Self-regeneration can occur when diesel engines, having high exhaust gas temperatures, run continuously at maximum load for several minutes. The particulate combustion rate is very high, but this is not a problem because the considerable gas flow forces the temperature of the filter to approach that of the exhaust gases.

Generally, such a condition is the most favorable to perform the regeneration for catalytic systems, but not for burner-assisted regeneration. In fact particulate residues of the self-regeneration can cause local over-temperatures during the next regeneration resulting in filter destruction.

The collected particulate mass is calculated from the pressure drops across the filter and the venturi and is displayed on the dashboard. If the accumulated particulate mass is decreasing, instead of increasing, a self-regeneration event is recognized by the control system and the regeneration threshold is reduced by an amount corresponding to the self-regenerated particulate mass as shown in the stepwise profile of Fig. 9. In order to avoid erroneous decisions caused by signal fluctuations, no action is taken for a mass decrease of less then 10 g. At the end of the normal regeneration phase, the original value of the threshold is restored.

A subsystem controls the burners and the blowers during the regeneration. If this is not successful, the filter is not inserted, so that engine exhaust is bypassed.

The valve actuators are constructed so that the system defaults to bypass. Then, if a control system failure occurs, no action is required by the driver.

8 Conclusions

1 The start of regeneration cannot be referred to a fixed time interval of urban bus driving (for instance a regeneration every 6 hours) because the amount of particulate collected is a function of the urban bus operations (e.g., loaded or unloaded, flat or hilly circuits).

2 Regeneration depends on three parameters: oxygen concentration, gas temperature, and amount of particulates. With the amount of oxygen fixed through a constant air flow during

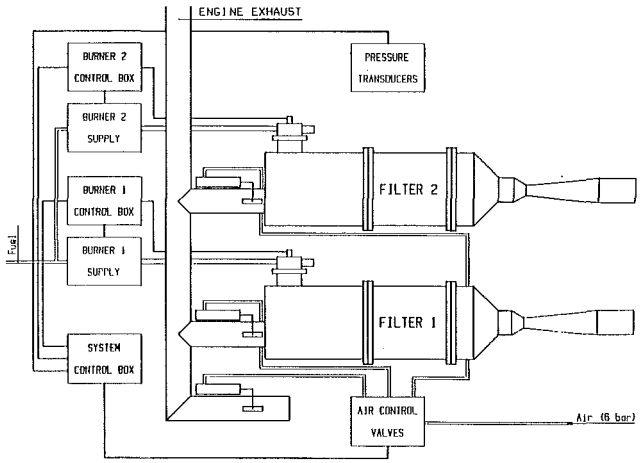

Fig. 10 Twin filter configuration

regeneration, and with the carbon burning temperature achieved by fuel burners, the key factor in process control remains the amount of particulates collected on the filter walls.

3 A detection of the accumulated particulate mass based on the double measurement of differential pressure across the filter and on the venturi has been developed. The continuous reading of the total collected mass allows the definition of the very moment to start regeneration. With the most critical points of the thermal regeneration solved, the burner bypass particulate trap can be used on diesel engines installed in urban buses. It offers the fundamental advantage of regenerating at all conditions, as opposed to the catalyst system.

4 The regeneration system and the associated control strategy are not affected by the engine characteristics and operating conditions, such as engine speed and boost pressure. Therefore, the system can be fitted on different vehicles with different engines, and also on existing in-use urban buses.

5 On the basis of favorable experimental results, during spring 1988, ten buses (Iveco 471) with single filter plus bypass configuration (Fig. 2) started tests in different Italian cities. At the beginning of 1989 50 additional buses (Iveco 480) will start tests in Italy. The new urban bus 480 is equipped with a second generation particulate trap configuration, consisting of a twin filter system (Fig. 10). When one filter is regenerating, the other one goes on working. In this way, the reduction of about 90 percent of the total particulates exhausted by a diesel engine can be achieved at any time of urban bus operations.

Acknowledgments

The authors are indebted to many Iveco people who gave their contribution to the success of this project. The authors' gratitude goes to Mauro Fabbri for preparing instrumentation and to Francesco Pidello for data acquisition and elaboration.

References

1 Goetz, W. A., Petheric, D., and Topaloglu, T., "Performance and Emissions of Propane, Natural Gas, and Methanol Fuelled Bus Engines," SAE Paper No. 880494, 1988.

2 MacDonald, J. S., and Simon, G. M., "Development of a Particulate Trap System for a Heavy-Duty Diesel Engine," SAE Paper No. 880006 SP-735, 1988.

3 Pattas, K. N., Stamatellos, A. M., Patsatzis, N. A., Kikidis, P. S., Aidarinis, J. J., and Samaras, Z. C., "Forced Regeneration by Exhaust Gas Throttling of the Ceramic Diesel Particulate Trap," SAE Paper No. 860293 P-172, 1986.

4 Pattas, K. N., Samaras, Z. C., and Kikidis, P. S., "Operation Characteristics of the Ceramic Diesel Particulate Trap During Forced Regeneration," SAE Paper No. 870252 SP-702, 1987.

5 Hardenberg, H., "Urban Bus Application of a Ceramic Fiber Coil Particulate Trap," SAE Paper No. 870011 SP-702, 1987.

6 Hardenberg, H., Daudel, H., and Erdmannsdorfer, H., "Experience in the Development of Ceramic Fiber Coli Traps," SAE Paper No. 870015 SP-702, 1987.

7 Hardenberg, H., Daudel, H., and Erdmannsdorfer, H., "Particulate Trap Regeneration Induced by Means of Oxidizing Agents Injected Into the Exhaust Gas," SAE Paper No. 860016 SP-702, 1987.

8 Sachdev, R., Wong, V. W., and Shahed, S. M., "Analysis of Regeneration Data for a Cellular Ceramic Particulate Trap," SAE Paper No. 840076 P-140, 1984.

9 Frank, R., and Hardenberg, H., "Reduction of PM Emissions From the Break-In Facilities of an HD Engine Production Plant by Means of Ceramic Monolith Traps," *SAE Trans.*, Vol. 94, Paper No. 850268, 1985.

10 Pattas, K. N., Samaras, Z. C., Stamatellos, A.M., and Patsatzis, N. A., "Size Determination of the Ceramic Diesel Particulate Trap," SAE Paper No. 870253 SP-702, 1987.

11 Huthwohl, G., Pischinger, F., and Lepperhoff, G., "Self-Supported Regeneration of Diesel Particulate Traps," SAE Paper No. 870017 SP-702, 1987.

Control Considerations for an On-Line, Active Regeneration System for Diesel Particulate Traps

P. Stiglic

J. Hardy

B. Gabelman

Garrett Automotive Group,
Allied-Signal,
Torrance, CA 90505

Garrett Automotive Group is developing an exhaust aftertreatment system aimed at particulate emissions reduction from commercial diesel engines. The system uses a ceramic wall flow filter to trap the particulates, and regeneration is effected by raising gas temperature by throttling the exhaust downstream of the turbocharger. Lab testing at steady conditions demonstrated good performance with both catalyzed and uncatalyzed traps. Road testing shows the regeneration must be accomplished under severe transient conditions created by the normal vehicle operating modes. Primary efforts are to accommodate those transients using advanced control and digital computational techniques. Some of those techniques are described and are shown to yield improved control performance.

System Description

Implementation of legislated reductions in diesel particulate emissions seems likely to create a demand for exhaust aftertreatment systems. As reported [1, 2], engine manufacturers feel that the 1991 limit of 0.25 g/hp h will be achieved through basic engine improvements, but that the 1994 limits of 0.1 g/hp h will probably require some form of exhaust aftertreatment.

To be accepted, the aftertreatment systems must be proven to be:

(*a*) safe
(*b*) durable and reliable
(*c*) cost effective; both initially and throughout their life
(*d*) efficient; impose a minimum fuel penalty
(*e*) reasonably transparent; have a minimal and acceptable effect on the vehicle drivability
(*f*) small enough to package acceptably into the vehicle

If a system with the above characteristics were to become available, it would likely be used from that point on, just as automobile catalytic converters took hold starting in 1975.

Garrett Automotive's major products, turbochargers and intercoolers, have a strong influence on diesel exhaust emissions, particularly NO_x and particulates. Exhaust aftertreatment was therefore considered a logical extension to the present product line and a development program was started in 1985. After studying and experimentally evaluating candidate approaches, Garrett selected, and is concentrating on, a system using a wall flow monolith trap to filter particulates and the throttling of the exhaust flow to increase exhaust temperatures periodically enough to regenerate (burn the soot) the trap.

The configuration of the particulate control system is shown in Fig. 1. The particulate trap is installed downstream of the turbocharger and the back pressure valve is located between those components. The system operation involves closing the back pressure valve to throttle the engine exhaust and, thereby, raise the exhaust gas temperature sufficiently to burn the particulates collected in the trap.

The balance of the system shown in Fig. 1 includes various sensors: pressure, temperature, and speed; a digital controller; and an electro-pneumatic servo to position the back pressure valve. To date, butterfly-type valves have been used since they were available; they require little actuation torque and zero leakage is not required. Air at 70 to 120 psi, taken from the vehicle air brake system, is used for actuation.

The approach is similar to the systems developed by investigators at the University of Thessaloniki [3]. They have completed and reported on analytical and lab results as well as systems operated on buses and automobiles. The latter efforts are described in [4]. Differences in the approaches are that Garrett has primarily used turbocharged engines and is making wider use of electronics and closed-loop control.

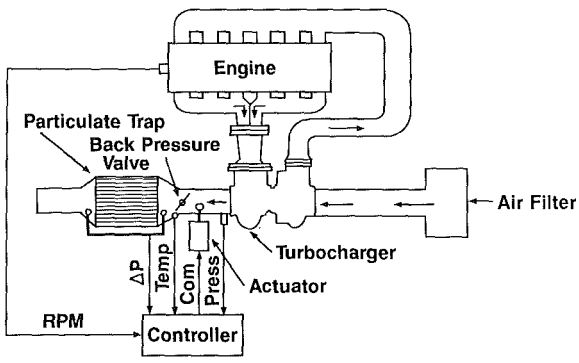

Fig. 1 Configuration of the particulate control system

Contributed by the Internal Combustion Engine Division and presented at the Internal Combustion Engine Division Technical Conference, San Antonio, Texas, October 2-5, 1988. Manuscript received by the Internal Combustion Engine Division June, 1988.

The configuration shown in Fig. 1 is for an engine with a mechanical fuel management system. If the engine were equipped with an electronic fuel control, some of the sensed parameters in the proper format should be available from that control and some or all of the particulate control system computations could be performed within the engine controller. That integration would further simplify the system.

This system is primarily aimed at heavy-duty and medium-duty trucks. The duty cycles of those vehicles show a good percentage of operation at moderate to heavy load, which enhances regeneration.

The exhaust throttling system was selected for study because it has potential for meeting the system requirements stated earlier. Its hardware is straightforward and should meet cost and reliability goals, especially if an uncatalyzed trap or a base metal catalyst can be used. Fuel penalties and the trap catalyst will likely be a tradeoff. A precious metal catalyst is expensive and forms sulfates in the engine exhaust [5], but it provides self-cleaning at temperatures above 800°F, which reduces trap pressure drop and, therefore, requires less frequent regeneration.

Packaging the system has not been a problem because the trap replaces the vehicle muffler and the remaining components are not large and can have considerable flexibility in their location. In addition, the back pressure valve can be used as an exhaust brake, if desired.

However, the effects of exhaust throttling on vehicle drivability must be carefully considered. Since improper throttling will affect drivability, the regeneration control systems must minimize those effects and also insure that any effects will be acceptable to the driver and not create a potential hazard. Drivability effects are mitigated to some degree by an all-speed governor and may further be reduced by advanced turbocharger technology such as variable nozzle and three-wheel turbochargers. Presently, advanced control techniques are being employed to reduce drivability effects.

System Operation

The prime objectives for the selected system are to provide acceptable performance, while keeping it simple, reliable, safe, and cost effective. Total systems integration and optimization will be critical to the system's functional and economic success in meeting the following objectives:

1 The system will be completely automatic; it will initiate, control, and when completed, terminate the regeneration.

2 There will be no bypass; the particulate trap will pass full exhaust flow at all times. This approach has the advantages of simplifying the system since bypass valving and the conventional muffler are not required and it also prevents defeat of the system by somehow making permanent use of the bypass. Also, the exhaust gas is filtered at all times.

3 Once a regeneration starts, the control must accommodate any operating conditions and changes to those conditions that may occur during the regeneration.

4 The system may affect vehicle drivability, but must only do so in a manner that is nonhazardous and acceptable to the driver.

5 If the vehicle is operated for a period under conditions where regeneration is not possible, such as idling in traffic for long periods, regeneration must be suspended until more favorable conditions are encountered.

6 If the trap pressure drop becomes excessive under the conditions of item 5, the driver must be informed to stop the vehicle, engage fast idle, and allow the regeneration to be completed.

The philosophy of setting up these difficult operational requirements is to keep the system hardware simple by taking advantage of an intelligent control and the memory, speed and computational capabilities of the digital computer.

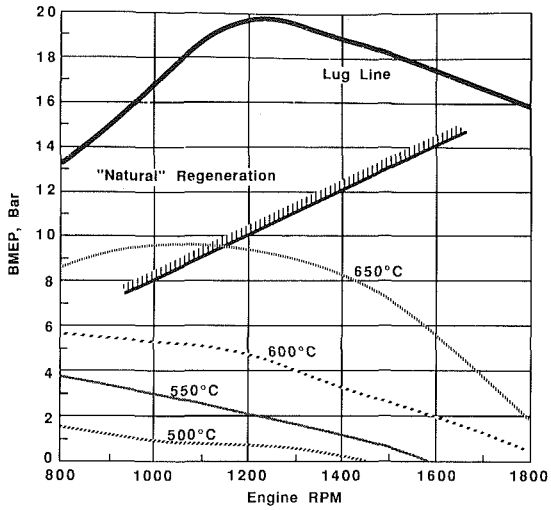

Fig. 2 Regeneration map for the Mack EC6-350-4VH engine

Operation in Lab

A test engine was installed in a cell in the Garrett Lomita, CA facility. An available Mack EC6-350-4VH turbocharged engine was used. A butterfly-type valve, pneumatically actuated, was installed downstream of the turbocharger. Control, data collection, and data reduction functions are performed by an IBM AT/PC computer. An 11.25-in.-dia by 12-in.-long wall flow type diesel filter, of the type described in [6], was purchased.

Initial tests were aimed at mapping the engine's regeneration region. Back pressure was increased, using the back pressure valve, at various speeds and torque settings, respecting the engine's back pressure limits and a minimum air fuel ratio of 17. The test engine back pressure limit is 40 psig due to lifting of the exhaust valves. The air fuel ratio of 17 represents the lowest practical excess oxygen level, about 2.4 percent, which can be considered for regeneration.

The regeneration map for the Mack engine is presented in Fig. 2. Trap inlet temperatures attainable at various engine operating conditions are shown. A temperature of 550°C (1022°F) seems to be the minimum for good, complete regeneration using a noncatalyzed trap. Figure 2 shows that that temperature can be attained at no load above 1600 rpm and at light loads at lower engine speeds. In general, complete regeneration appears possible over a large percentage of the engine operating envelope. With a catalyzed trap, self-cleaning or a slower regeneration can be accomplished at 500°C or even somewhat lower, which expands the regeneration map even further. Heavier valve springs, hence higher back pressure, would also increase the range.

Also shown in Fig. 2 is the "natural regeneration" line above which self-cleaning or regeneration will be attained with a catalyzed trap without exhaust throttling. Conditions above that line produce trap inlet temperatures of over 450°C (850°F) and sufficient excess oxygen.

Previously presented operational objectives 5 and 6 can be discussed in more detail with the aid of Fig. 2. Consider the case where a regeneration is in progress and the vehicle encounters stop-and-go traffic or is otherwise idled for an extended period. After a reasonable time at those conditions, say one to two minutes, the regeneration should be suspended until more favorable conditions (higher power, higher speed) are encountered. Continuing to attempt regeneration under operating conditions where required temperature cannot be attained would only waste fuel.

In the event particulate loading in the trap becomes excessive, the driver would be informed by an annunciator light. He would then pull off the road, secure the vehicle, and initiate

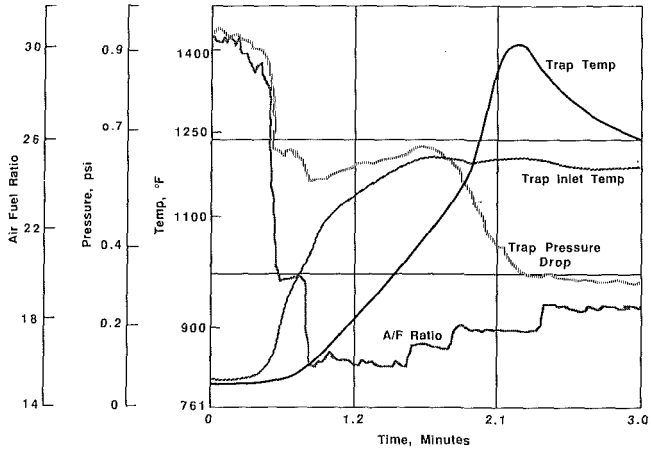

Fig. 3 Manual regeneration, uncatalyzed trap; 1600 rpm, 7.9 bar BMEP

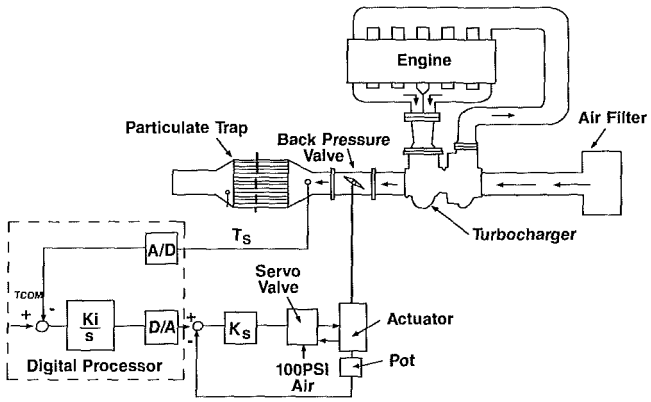

Fig. 4 Lab control system

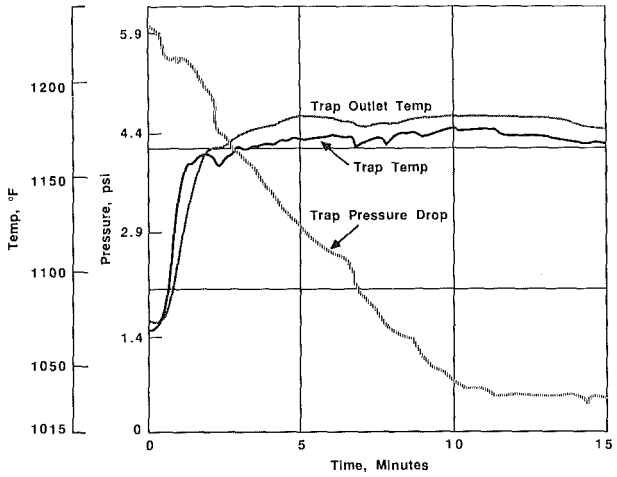

Fig. 5 Heavily loaded uncatalyzed trap; 1732 rpm, 8.9 bar BMEP

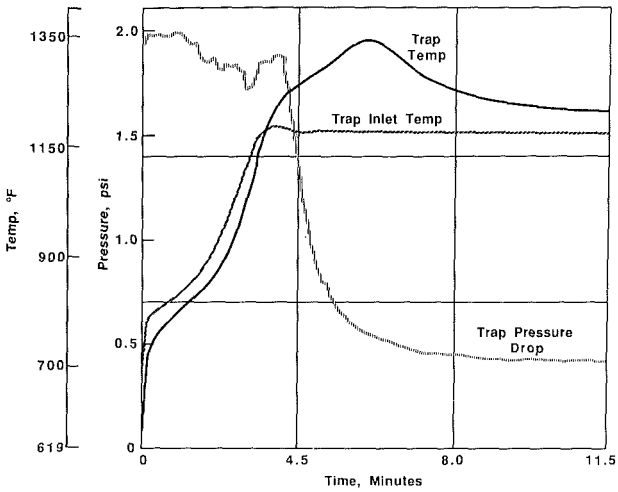

Fig. 6 Moderately loaded catalyzed trap; 1200 rpm midtorque

regeneration by setting engine speed to high idle, above 1600 rpm. When regeneration was complete the annunciator light would go out. *This must be an infrequent occurrence.*

Figure 3 shows an early attempt at regeneration with an uncatalyzed trap. Here the back pressure valve was positioned manually to produce the required trap inlet temperature. As can be seen on the regeneration map of Fig. 2, the operating conditions (1600 rpm and 7.9 bar BMEP) for this run are quite favorable.

A trap inlet temperature of 650°C (1200°F) is achieved 1.5 min into the run and an exotherm begins within the trap at about the 2 min point. The exotherm is detected when the trap temperature, the actual ceramic temperature, exceeds inlet gas temperature and indicates that particulates are burning within the trap. As a result of the burning, the trap pressure drop decreases quite rapidly and clean trap conditions are attained at the 2.5 min mark. The slight skew in indicated times is a result of data taking technique and the automatic plotting program.

Everything about this regeneration seems desirable; its time is short (less than 2.5 min), maximum ceramic temperature is a reasonable 762°C (1405°F), and the trap is returned to clean conditions. The trap pressure drop at the start of the regeneration was less than 1.0 psi, which is a light trap loading. The job looks easy.

Next an automatic control, as shown in Fig. 4, was added to the lab setup. Trap inlet gas temperature was sensed and fed back to the digital processor where the temperature loop was closed. The temperature error was integrated and commands were issued to the back pressure valve. The gain of the integrator was selected to provide slow and stable operation and it exhibited excellent steady-state accuracy.

An early run with the temperature control and an uncatalyzed trap is shown in Fig. 5. This trap had an initial pressure drop of 5.9 psi, which meant it was very heavily loaded. Inlet temperature was increased to 621°C (1150°F) and automatically controlled. Again, an exotherm occurs, here some 3 min into the run, but the trap temperature never exceeds 635°C (1175°F). The low trap temperature indicates that the particulates are burning quite slowly. As shown, the trap pressure drop steadily decreases, but the trap requires some 12 min to reach clean conditions. Considering the heavy particulate loading at the start, the 12 min regeneration is not unreasonable.

In an attempt to reduce regeneration times, a platinum catalyst was applied to the 11.25-in.-dia diesel filter. Results were immediate; times between regenerations increased and the regenerations were rapid and complete.

A typical regeneration with the catalyzed trap is shown in Fig. 6. An exotherm begins some 4 min after the start, and the trap achieves clean conditions in the following 4 or 5 min. Trap temperature profiles are low and within the limits defined in [7]. The regeneration range curve presented in Fig. 2 was tested by conducting regenerations over its entire envelope, including high idle. Results were generally very similar to those presented in Fig. 6.

To this point, results were encouraging. Effective regenerations could be accomplished, temperatures were reasonable, and the control problem did not appear that challenging. Some 100 regenerations were conducted without encountering a runaway regeneration or any other damage to the trap.

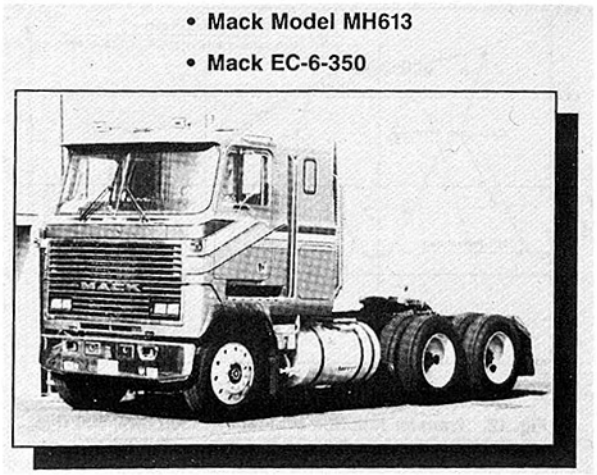

Fig. 7 Test vehicle

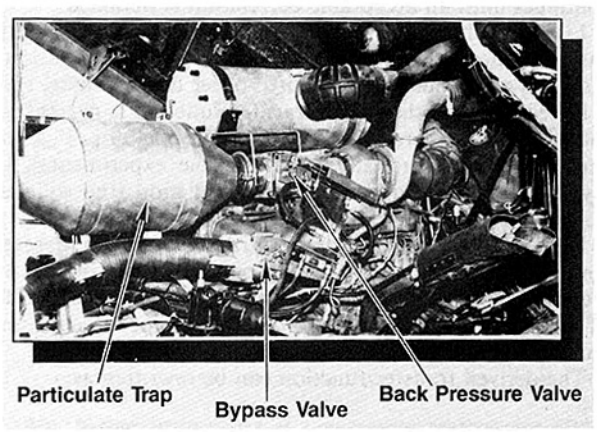

Fig. 8 Test vehicle installation

On-Highway Operation

The lab regenerations were run at steady conditions. An operating point was set up and the regeneration was conducted under those conditions. To obtain experience in a more realistic environment, a truck was equipped with the trap and regeneration system, and periodically placed in the company's normal hauling services. The vehicle selected was a Mack model MH613 class 8 tractor, shown in Fig. 7. It has the Mack EC6-350-4VH engine, which is the same as the test cell engine. The truck was also equipped with the same type digital processor and data acquisition system as used on the test cell. In this manner, control development can proceed in the test cell, then new control versions can be loaded into the truck's processor and road tested. A bypass was added to the truck, as shown in Fig. 8. The exhaust gas can either be directed through the particulate trap, or around it, and through the normal muffler. This arrangement is *only* for the prototype vehicle and was included to:

(*a*) Permit noise measurements of the particulate trap path and the normal muffler. The particulate trap will perform the muffler function on production systems.

(*b*) Allow visual comparison of filtered and unfiltered engine exhaust.

(*c*) Provide "limp home" capacity in the event of failure in the prototype system.

The test truck is used both in the company's intercity and on-highway operations, hauling a 48-ft trailer and loads of 20,000 to 40,000 lb.

Figure 9 is the history of a regeneration while the truck is on an open highway operating at 55 to 60 mph. There may

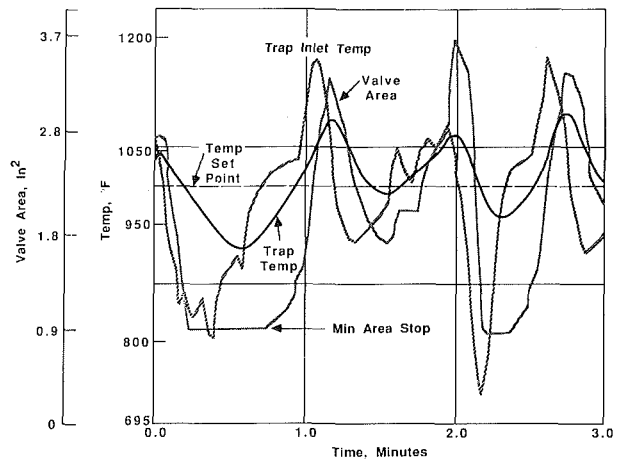

Fig. 9 On highway regeneration

have been one or two gear shifts during this run, down-shifting from 10th to 9th and back, but basically, the oscillations shown are caused by the driver manipulating the accelerator pedal. As can be seen, significant oscillations occur one or two times per minute and impose large disturbances on the regneration control.

The regeneration was started at zero minutes and the control was attempting to hold trap inlet gas temperature to 1000°F. The control was a low performance proportional plus integral arrangement using moderate gains. Examination of Fig. 9 reveals:

1 The system frequently encounters large, driver-induced disturbances.

2 The controlled parameter, trap inlet gas temperature, can be driven off its set point ±200°F or more by these disturbances.

3 The resulting oscillations in trap temperature are far less, usually ±50°F, due to the thermal inertial of the 20 lb ceramic trap. This is important because the particulate temperature should be near the trap temperature, which should lessen the effects of the gas temperature oscillations on the regeneration process.

4 When the trap inlet temperature drops below set point, the back pressure valve closes, sometimes into its stops, attempting to increase the temperature. This could occur downhill, where the driver eases off the accelerator. The action of the back pressure valve is useful here because the truck automatically receives exhaust braking.

5 As shown in Fig. 9 at the 2.2 min point, the back pressure valve closes to its minimum area stop in an attempt to increase temperature. The driver demands power at this point, but the valve remains in the stop until the control set point temperature is exceeded. Until the valve begins to open, the truck is sluggish due to the exhaust throttling. Hence some additional control features are required: a derivative term in the control or perhaps a kick-down switch under the accelerator, to give the driver power when he needs it.

The conditions shown on Fig. 9 are real world and something the proposed regeneration system must live with. Intracity operation involving frequent stops and gear shifting can produce even more frequent disturbances.

To this point, the exhaust throttling regeneration technique has been shown to be basically sound and attractive. However, it will require a control that is responsive and intelligent. Different control parameters and various control system configurations are being studied to obtain the most desirable solution. The system's final form has not yet been established.

Control System Design

The first step in designing a control system is to obtain a

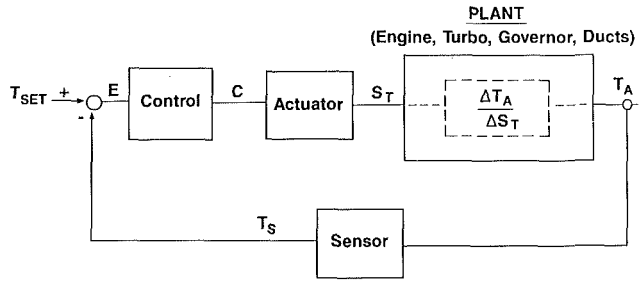

Fig. 10 Basic control system

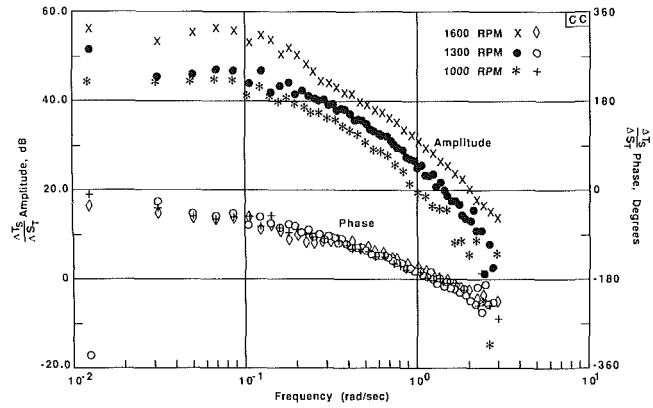

Fig. 11 Frequency response data

basic understanding of the static and dynamic characteristics of the plant, or item to be controlled, and to determine its transfer functions over its range of operation. Figure 10 shows the regeneration temperature control system. The plant in this case is the engine, turbo, governor, and duct volumes. The plant is disturbed by changes in back pressure valve stroke (S), which result in changes in trap inlet gas temperature (T_a). Required is the plant transfer function $\Delta T_a/\Delta S$. However, it is not possible to obtain actual gas temperature directly; it must be sensed. Therefore the transfer function will be obtained as T_s, where T_s is the sensed value from the thermocouple.

In the past, these transfer functions were evaluated by imposing sine or square wave inputs on the independent variable, S in this case, and analyzing their effect on the dependent variable T_s. For this effort, a frequency domain analysis computer program was used. The technique involves exciting the back pressure valve with inputs of shaped white noise, sum of sines functions, or a frequency sweep, then analyzing the output using Fourier and cross-spectral methods. Test data are gathered on digital files, which the computer program analyzes to provide graphic output. These techniques are described in [8, 9].

Typical frequency response data are shown in Fig. 11. Shown are the amplitude and phase characteristics of $\Delta T_s/\Delta S$ as a function of frequency. Data from three engine speeds at roughly 30 percent of rated torque are shown. The throttle was fixed for the 1000 and 1300 rpm runs, but a torque controller, which was part of the test cell equipment, was used for the 1600 rpm run, which probably distorted its lower frequency results. The quality of the data is excellent, falling into logical straight lines. This quality was obtained even though friction in the back pressure valve actuator seals at times distorted its waveform. Since the 1300 rpm data appear representative, they were selected for further analysis.

The next step is manual and iterative. The slopes, break points, and phase of the frequency response are analyzed to determine its components and the overall $\Delta T_s/\Delta S$ transfer function is estimated.

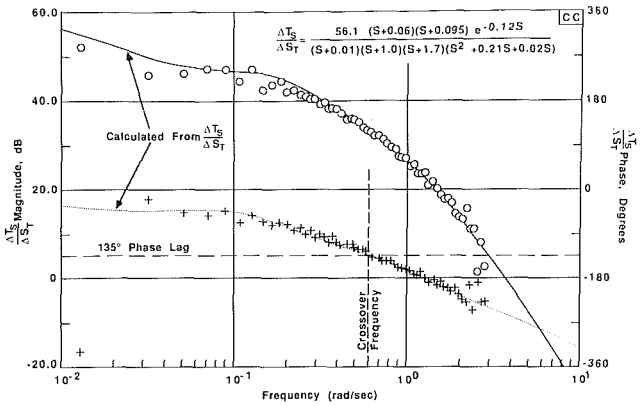

Fig. 12 Transfer function evaluation; 1300 rpm, 500 ft-lb

The frequency response of the estimated transfer function is then calculated and compared to test data. This process continues until an acceptable correlation is obtained.

Figure 12 shows the result of this process for the 1300 rpm case. The derived transfer function is shown and consists of a second-order numerator, a fifth-order denominator, and a 0.12 second dead time. The transfer function is presented in factored form where S is the Laplacian operator. Figure 12 shows excellent correlation between the experimental data (symbols) and the derived transfer function (the solid and dotted lines).

Each of the terms in the derived transfer function represents some physical phenomena of the plant that contribute to its frequency characteristics. To obtain a thorough understanding of the plant, it is important to identify each of these phenomena.

The derived transfer function can be rewritten as:

$$\frac{\Delta T_s}{\Delta S} = \frac{752.4(16.7S+1)(10.5S+1)}{(100S+1)(1.0S+1)(0.6S+1)((6.7)^2S^2+(2)(0.7)(6.7)S+1)}\, e^{-0.12S}$$

In this form it appears that the plant has three lags having time constants of 100, 1.0, and 0.6 seconds, one second-order term having an effective time constant of 6.7 seconds and a damping ratio of 0.7. At this time, there are insufficient data to positively identify those lags, but the second order could well be the thermocouple used to sense trap inlet temperature. The thermocouple bead is encased in ceramic, which is in turn enclosed in a 0.125-in.-diameter metal tube. The requirement to transfer heat from the ceramic to the bead could explain the second-order effect and the equivalent time constant of 6.7 s is about what might be expected from such a thermocouple. The 100 second lag probably involves the heating of the turbocharger and ducting while the 1.0 second and 0.6 second terms might be caused by the turbocharger rotor dynamics. The 0.12 second dead time, represented by the $e-0.12S$ term, is caused by the four per second data sampling rate of the digital computer.

If a system is to be optimized, it is important to understand the physical meaning of each term of the plant transfer function. In this manner it can be determined which parts of the plant might be changed to improve performance.

Examining the plant response shown in Fig. 12, its crossover frequency is at 0.6 rad/s. This means that unless the control adds some desirable compensation, the frequency band width that would be obtained from a closed loop temperature control would be the crossover, or 0.6 rad/s, which is comparatively slow. The crossover is the frequency where the open loop has a phase shift of 135 deg, which provides an acceptable 45 deg phase margin.

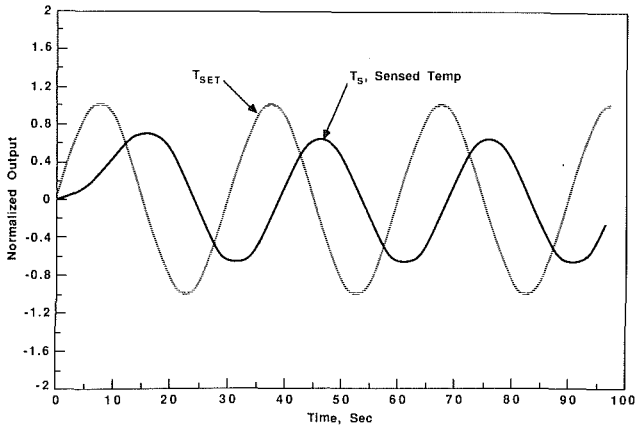

Fig. 13(*a*) System performance at 2 cycles/min; performance of original control

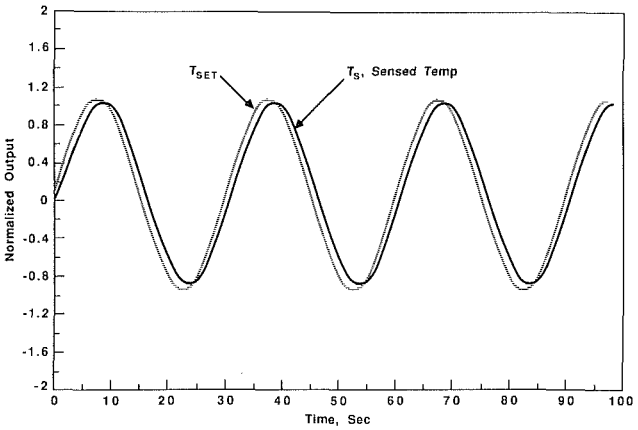

Fig. 13(*b*) System performance at 2 cycles/min; performance of improved control

Although a temperature control seems relatively slow, it can be improved to deal more effectively with the driver-induced oscillations shown in Fig. 9. Those disturbances occur about two per minute, which is about 0.2 rad/s, or well within the temperature controls band pass of 0.6 rad/s. Studies were performed to improve the temperature control response further. A control with proper phase compensation was added that extended the control crossover frequency to 1.5 rad/s. An indication of the performance of the improved control is shown by the analytical data presented in Fig. 13. These estimates show how the original control (Fig. 13(*a*)) and the improved control (Fig. 13(*b*)) might respond to command changes of two per minute. The T_{SET} is the temperature command as shown in Fig. 10, and T_s is the sensed trap inlet temperature. Since the improved control follows the two cycle/min frequency much better, it should also control the set trap inlet temperature much closer while the driver-induced disturbances are imposed.

However, all the performance improvements promised in Fig. 13 will not be realized. Performance improvements are obtained by overdriving the back pressure valve to force a more rapid temperature response. This technique is effective as long as the back pressure valve is not driven to its stops. When that happens, temperature response will not be improved. It is expected that the actual performance of the improved control will be somewhere between those shown in Fig. 13 because of various nonlinearities, such as valve range.

In addition, tradeoffs must be made between improved performance and drivability. As stated above, improved performance of the somewhat slow temperature control is obtained through overdriving the back pressure valve. If the movements of the valve become too large or too harsh, it could degrade drivability, which must be avoided.

Further Efforts

To date, our efforts and experience with the exhaust back pressure regeneration can be summarized as follows:

1 The basic concept is sound; required regeneration temperatures along with required air-to-fuel ratio can be attained over a large portion of the engine operating envelope.

2 The system is attractive from a hardware standpoint; production systems should be cost effective and durable. Integration of the regeneration system with the engine electronic fuel control will result in even further simplification.

3 Damaging runaway regenerations have not been encountered. The reasons for this are not completely clear, but are thought to be related to the high gas velocities of the full flow arrangement and the high airflow of a turbocharged engine.

4 Controlling engine parameters such as exhaust gas temperature can be readily accomplished. However, to control these parameters reasonably and safely when the engine is subjected to typical road disturbances presents a significant challenge.

5 Further work is being concentrated on improved control performance to provide reasonable regeneration performance without significantly degrading drivability in an objectionable manner.

In addition to improving performance of the temperature control, other forms of control are being investigated. Controls based on exhaust system pressures or engine air-to-fuel ratio could be made considerably faster than the temperature control and would not require as much overdriving of the back pressure valve. That should improve drivability. However, exhaust gas temperature would then not be directly controlled and would "float" to some degree. That effect on regeneration performance must be investigated.

It is likely that the most desirable control would employ two or more control variables, such as temperature and some pressure, for example. With proper blending of these parameters, a control with rapid response to accommodate normal driving disturbances while at the same time exercising reasonable control of the primary regeneration parameters should evolve.

Garrett will continue to concentrate its analytical and experimental resources toward the development of a practical and attractive particulate trap regeneration system.

References

1 Richards, R. R., and Sibley, J. E., "Diesel Engine Emissions Control for the 1990's," SAE Paper No. 880346, 1988.

2 Gill, A., "Design Choices for 1990's Low Emission Diesel Engines," SAE Paper No. 880350, 1988.

3 Pattas, K. N., Stamatellos, A. M., Patsatzis, N. A., Kikidis, P. S., Aidarinis, J. K., and Samaras, Z. C., "Forced Regeneration by Exhaust Gas Throttling of the Diesel Particulate Trap," SAE Paper No. 860293, 1986.

4 Pattas, K. N., Patsatzis, N. A., Michalopoulou, C. C., Stamatellos, A. M., Kikidis, P. S., Samaras, Z. C., and Sowul, H., "Ceramic Trap Regeneration Rate Control Through Bypass Technique," SAE Paper No. 880004, 1988.

5 Hunter, G., Scholl, J., Hibbler, F., Bagley, S., Leddy, D., Abata, D., and Johnson, J., "The Effect of an Oxidation Catalyst on the Physical, Chemical, and Biological Character of Diesel Particulate Emissions," SAE Paper No. 810263, 1981.

6 Howitt, J., and Montierth, M., "Cellular Ceramic Diesel Particulate Filter," SAE Paper No. 810114, 1981.

7 MacDonald, J. S., and Simon, G. M., "Development of a Particulate Trap System for a Heavy-Duty Diesel Engine," SAE Paper No. 880006, 1988.

8 Brigham, O. E., *The Fast Fourier Transform*, Prentice-Hall, New Jersey, 1974.

9 Bendat, J., and Piersol, A. G., *Random Data: Analysis and Measurement Procedures*, Wiley Interscience, New York, 1971.

J. Myers
University of Wisconsin,
Madison, WI 53706

M. Myers
IBM,
Rochester, MN

P. Myers
University of Wisconsin,
Madison, WI 53706

On the Computation of Emissions From Exhaust Gas Composition Measurements

This paper presents a calculation technique and related computer program to yield mass emission rates from measured exhaust gas composition and fuel flow rate or fuel plus air flow rate (if air flow rate is measured). The sensitivity of the computed emission rates to (1) the method of calculation and (2) experimental measurement errors is investigated. It is recommended that published emission rates be the average of the rates computed by several different methods, as discussed in this paper, to minimize the effect of experimental variations in measurement. This, plus use of the computer program presented, would standardize the assumptions used in computing emissions and minimize differences in reported emission rates from different laboratories.

Introduction

The use of exhaust gas measurements to judge and improve the performance of engines is almost as old as the internal combustion engine itself. As early as 1907, H_2 and CH_4 concentrations were found to be functions of the CO concentration. Fenning in 1916 prepared exhaust gas charts showing the relation of exhaust gas composition to air/fuel ratio from combustion bomb experiments. Until exhaust emissions became an important performance parameter for engines, the exhaust gas measurements were primarily used to determine overall engine air/fuel ratio (Spindt, 1965) or to estimate cylinder-to-cylinder air/fuel variation (Eltinge, 1969). Even after exhaust emissions were regulated, the composition of combustion products has been used to estimate local air/fuel ratios (Ingham et al., 1982; Logan et al., 1982; Rhee et al., 1978).

When exhaust emissions became an environmental concern, regulations were expressed in many different ways: concentration, concentration corrected for dilution, mass per unit time, mass per unit distance traveled by a vehicle, mass per unit of energy out, mass per unit of energy in, etc. Consequently, emphasis was shifted from computation of air/fuel ratio, as determined by exhaust composition measurements, to computation of mass of emissions per unit time. Computation of mass of pollutant per unit time is particularly useful since these values can be readily converted to other values such as mass per unit distance traveled by a vehicle, mass per unit of energy, etc.

Most computational procedures developed for mass emission rates have been for restricted cases. For example, in the moderately lean region, CO might be neglected from an atom balance standpoint but still be of importance from an emission standpoint. In the very lean or very rich region this assumption may not be valid. Similarly, H_2 is usually neglected and not measured; this is reasonably valid in the lean region but not in the rich region. Also, most computations have assumed only hydrocarbons (sometimes sulfur) in the fuel. However, fuels (landfill gases for example) increasingly contain additional compounds such as CO, CO_2, inerts, alcohols, etc., thus making the simplifying assumptions mentioned above less valid. At the same time, computers have become quite commonplace in the laboratory so that reasonably complex computations are routinely feasible. The purpose of this paper is to present a methodology and to make available a computer program for the generalized computation of mass pollutant rates as well as useful engine operating parameters such as air/fuel and equivalence ratio.

Basic Approach

Exhaust emissions are measured as a volume fraction of the exhaust gases. However, government regulations are most often expressed as mass per unit quantity such as time or energy. As will be shown later, mass per unit time can be readily converted to other quantities, and thus our initial task is to convert from a volume fraction measurement to a mass per unit time basis.

Given a volume fraction measurement of a pollutant, there are three possible procedures to convert this volume fraction measurement to a mass per unit time basis:

1 Measure the exhaust gas pressure, temperature, and volume flow rate; compute the volume flow rate of the pollutant from the measured volume fraction; and convert the pollutant volume flow rate to a mass flow rate.

2 Measure the pressure, temperature, and volume flow rate of the incoming air and fuel; convert the inlet volume flow rate to an exhaust volume flow rate. Then proceed as in 1.

3 Measure the fuel flow rate; compute exhaust volume

Contributed by the Internal Combustion Engine Division and presented at the Internal Combustion Engine Division Technical Conference, San Antonio, Texas, October 2–5, 1988. Manuscript received by the Internal Combustion Engine Division June 1988.

formed per unit of fuel in, and, using the fuel flow rate, compute the total exhaust volume flow rate. Then proceed as in 1.

Procedure 1, while computationally simple, is very seldom used because flow measurements in the hot, dirty exhaust are very difficult. Procedure 2 is often used in the laboratory but seldom in the field because of lack of equipment. Procedure 3 in commonly used in the field as well as in the laboratory. Thus, we shall only concern ourselves with Procedures 2 and 3.

With either Procedure 2 or 3, it is necessary to arbitrarily define a unit quantity of fuel. If the unit of fuel is chosen as CH_n, the sum of the carbons in the exhaust gases formed from the unit of fuel must equal unity and the required algebra becomes simpler; thus we shall use this definition. To illustrate the concept consider methane (CH_4) as the fuel; obviously $n=4$. The fuel, propane (C_3H_8), could be represented as $3CH_n$ where $n=8/3=2.667$. Note that n need not be an integer and that for methane there is one mol of CH_n per mol of fuel while for propane there are three mols of $CH_{2.667}$ per mol of fuel.

With the unit of fuel defined as CH_n, we can develop algebraic relationships for the mols of products per mol of CH_n fuel and then compute these quantities from measured exhaust gas concentrations. Development of these relationships is lengthy and will only be summarized in the main body of the paper (see Appendix D for details of the development).

General Equation for Mass of Pollutant per Unit Time

We can convert from a volume fraction to mass per unit time as follows. Define:

$$Mpolt = \frac{\text{mass pollutant}}{\text{unit time}}$$

Then

$$Mpolt = \frac{\text{mol pol}}{\text{mol exh}} * \frac{\text{mols exh}}{\text{mol CH}_n} * \frac{\text{mass pol}}{\text{mol pol}} * \frac{\text{mols CH}_n}{\text{mol fuel}} * \frac{\text{mols fuel}}{\text{unit time}}$$

$$\wp pol * \tilde{N} * MWpol * J * Nft \tag{1}$$

The mols of exhaust in the denominator of $\wp pol$ (the fraction of pollutant of interest in the exhaust) must cancel the mols of exhaust in the numerator of $\tilde{N}$ (mols of exhaust per mol of CH_n). As will be discussed in more detail later on, $\tilde{N}$ can have different values for the same exhaust sample depending, for example, on whether the water in the exhaust is completely, partially, or not at all condensed. J would also be different for different fuel molecules, e.g., 1 for CH_4 or 3 for C_3H_8.

Two procedures could now be followed. In the first, the conditions under which $\wp pol$ was measured could be considered fixed and the corresponding value of $\tilde{N}$ computed. In the second, one could consider the value of $\tilde{N}$ as being fixed for a particular condition (hot exhaust with no water condensed, for example) and adjust the value of the experimentally measured pollutant to this condition. We shall, arbitrarily, follow this second procedure considering the standard condition as hot, wet exhaust, i.e., none of the water condensed. In this case $\tilde{N}$ will be changed to $\tilde{N}W$, meaning all of the water is present. We will then need to add a moisture correction factor ($\mathfrak{C}$) to equation (1) to correct $\wp pol$ to this wet condition. $\mathfrak{C}$ can have two different values: $\mathfrak{C}dW$ will correct from the experimental pollutant concentration measured under completely dry conditions (no moisture in the products as indicated by d) to the wet condition: $\mathfrak{C}wW$ will correct the concentration measured under "dry" (water *partially* condensed as indicated by w) condition to the wet condition. If $\wp pol$ is measured wet, $\mathfrak{C}$ of course is unity.

Thus equation (1) becomes

$$Mpolt = \wp pol * \mathfrak{C} * \tilde{N}W * MWpol * J * Nft \tag{2}$$

Nomenclature

- a = mols of CO_2 in the exhaust per mol of CH_n fuel as in equation (3); when used as subscript, air
- act = actual
- b = mols of CO in the exhaust per mol of CH_n input fuel as in equation (3)
- °C = degrees Centrigrade
- d = mols of H_2 in the exhaust per mol of CH_n input fuel as in equation (3); when used as a subscript, dry (moisture-free) gas
- "dry" = condition of exhaust gas leaving the cooling bath, i.e., water *partially* condensed
- dry = completely moisture-free gas
- e = energy
- expt = experimental
- E = mols of oxygen in the incoming air per mol of CH_n fuel
- f = fuel
- fo = mol of O_2 in the fuel per mol of CH_n fuel as in equation (3)
- fi = mols of inert material in the fuel per mol of CH_n fuel as in equation (3). Any oxidizable atom coming in with the fuel (specifically C, H, or S) is not considered inert regardless of the compound it is in. For example, if CO_2 came in with the fuel it would not be considered inert because it has a C atom in it. The small amount of CO_2 coming in with the input air (approximately 300 ppm) is completely neglected and the H_2 coming in with the air or added H_2O is handled separately because of the wet, "dry," and dry situation
- F = degrees Fahrenheit
- g = particulates considered insignificant, i.e., "gas" only
- HCT = total hydrocarbons
- HR = humidity ratio of inlet air (mass H_2O/mass dry air)
- i = a row in Table 2 or 3 or a series of numbers
- j = mols of H_2O in the exhaust gas formed from the combustion of the hydrogen in the fuel per mol of CH_n fuel as in equation (3); when used as a subscript, a column in Table 2 or 3
- J = mols of CH_n per mol of fuel
- k = mols of NO in the exhaust gas per mol of CH_n fuel as in equation (3)
- K = degrees Kelvin—absolute temperature on the C scale
- L = mols of particulate (not in the gaseous phase) in the exhaust per mol of CH_n fuel as in equation (3). Note that n is assumed to be unity for particulates

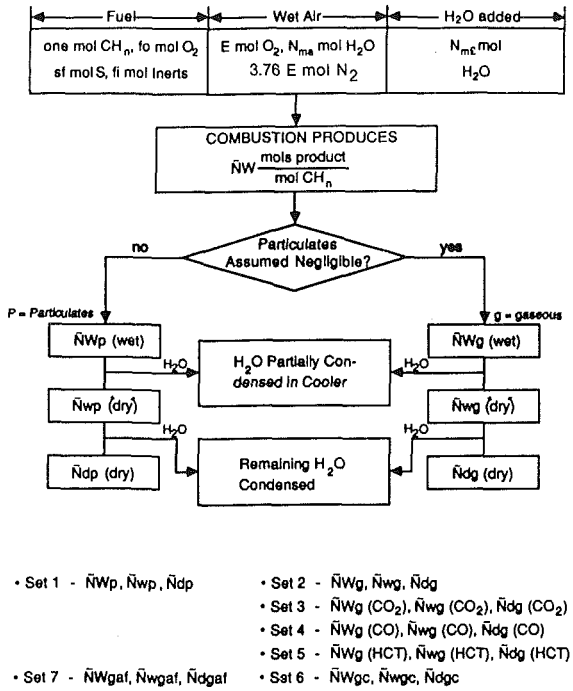

Fig. 1 Flow chart illustrating nomenclature used

$$= \frac{\text{mol pol}}{\text{mol exh (w or } d)} * \frac{\text{mol exh (}w\text{ or }d)}{\text{mol wet exh}} * \frac{\text{mol wet exh}}{\text{mol } CH_n}$$

$$* \frac{\text{mass pol}}{\text{mol pol}} * \frac{\text{mols } CH_n}{\text{mol fuel}} * \frac{\text{mols fuel}}{\text{unit time}}$$

where $\wp pol$ is measured experimentally; the numerical value of ¢ will depend on the condition of the exhaust sample when the pollutant concentration was measured; *MWpol* is known for any particular pollutant; *J* (as well as small *n*) can be determined from the known fuel composition as is shown in detail in Appendix A; and *Nft* is the experimentally measured fuel flow rate converted to a molar flow rate basis. Thus our primary problem is to compute ¢ and $\tilde{N}W$ from experimentally measured air-flow and/or exhaust concentration measurements.

General Procedure for Evaluation of $\tilde{N}W$

As will become evident later in the paper seven expressions for $\tilde{N}W$ can be derived. If all measurements were precise each of the seven expressions would give the same answer and we would only need to develop and use one of them. In the real world, however, the agreement between the different expressions is an indication of the integrity of the data and validity of the assumptions made.

Nomenclature

Because of the large number of variables and relationships presented in this paper, nomenclature is a problem. While some definitions have been presented and a complete list of nomenclature is given, a brief explanation of the logic of the nomenclature may be helpful in reading the rest of the paper and understanding the computer program.

Figure 1 illustrates the logic and sequence of the nomenclature. As indicated in this figure, one mole of CH_n and any associated O_2, S, and Inerts, plus wet air and any intentionally added water, are combusted to produce $\tilde{N}W$ mols of hot, wet exhaust products. See list of nomenclature for definitions of *fo*, *sf*, *fi*, *E*, *Nma*, *Nm£*. If particulates are assumed to be significant, the left-hand path in Fig. 1 is followed downward and the symbol *p* is added; if only gases are assumed to be formed (particulates not important) the right-hand side is followed and *g* is added instead. Regardless of which path is followed, if moisture is partially removed by cooling this gives either $\tilde{N}wp$ or $\tilde{N}wg$ and, if the moisture is entirely removed, $\tilde{N}dp$ and $\tilde{N}dg$. The fuel flow rate must always be measured. If any additional water is added, its flow

Nomenclature (cont.)

M = mass
MW = molecular weight
m = moisture
n = H/C ratio of the fuel
N = H/C ratio of the hydrocarbons in the exhaust or alternatively, mols
NFi = molar fraction of fuel component i
$Nmew$ = mols of moisture in the "dry" exhaust per mol of CH_n
$NmeW$ = mols of moisture in the wet exhaust per mol of CH_n
O2EQR = the ratio of the O_2 actually supplied (air plus fuel) per mole of CH_n fuel to the required stoichiometric O_2 (including O_2 in the fuel) per mol of CH_n fuel
p = mols of O_2 in the exhaust per mol of CH_n fuel as in equation (3); when used as a subscript, indicates particulates are significant
pol = pollutant
P = pressure
Pb = barometric pressure
Pw = vapor pressure of water
R = degrees Rankine—absolute on the F scale
Ro = molar gas constant = 1544 ft-lb/mol-R
s = stoichiometric
S = sulfur
sf = mols of sulfur in the fuel per mol of CH_n fuel as in equation (3)
t = time
TAF = total air fuel ratio, i.e., all of the input air (including all moisture) divided by all of the input fuel (including inerts), mass of air per mass of fuel
Vat = experimentally measured volumetric air flow rate
w = "dry" condition with some, but not all, of the moisture condensed
W = wet condition, none of the moisture condensed
z = mols of CH_N per mol of CH_n fuel as in equation (3)
ξ = quantity conceptually defined in equation (14D)
$\wp$ = decimal fraction of a constituent in the exhaust gas
$\wp(15\%)$ = decimal fraction in the exhaust gas adjusted to 15 percent O_2 to standardize concentrations
$\tilde{N}$ = mols of exhaust per mol of CH_n fuel
¢ = moisture correction factor
£ = moisture introduced into the inlet (other than with the atmospheric air) for control purposes
Γ = coefficients of individual terms in an expression
¥ = quantity conceptually defined by equation (15D)

Table 1 Required atom balances, flow rates, and concentrations

EXPRESSION	BALANCE USED C	H	O	FLOW RATE air	fuel	EXHAUST COMPOSITION MEASUREMENT CO_2	CO	HCT	O_2	H_2	NO
$\tilde{N}dp$	x	x	x		x	x	x	x	x	x	x
$\tilde{N}dg$		x	x		x	x	x	x	x	x	x
$\tilde{N}dg$ (CO_2)	x	x	x		x		x	x	x	x	x
$\tilde{N}dg$ (CO)	x	x	x		x	x		x	x	x	x
$\tilde{N}dg$(HCT)	x	x	x		x	x	x		x	x	x
$\tilde{N}dgc$	x				x	x	x	x			
$\tilde{N}dgaf$				x	x	x	x	x	x	x	x
$\tilde{N}dgO_2$	x	x	x		x				x		

rate must also be known. Measurement of the wet air flow rate is optional but, if measured, it provides an additional expression for calculating emission rates.

The expressions at the bottom of Fig. 1 are grouped into seven sets, each one containing an $\tilde{N}W$, $\tilde{N}w$, and $\tilde{N}d$ term. Within each set, the three terms differ only by moisture content. Between sets however, there are differences in the atom balances used and experimental measurements required. These differences are specified in Table 1. (Note that Table 1 only shows the $\tilde{N}d$ terms but the same requirements apply to the associated $\tilde{N}W$ and $\tilde{N}w$ expressions.)

Looking at line 1 of Table 1, if particulates are assumed significant then all of the possible atom balances are required as well as all of the exhaust concentration measurements. Consequently, only a single expression can be developed for each moisture condition and we obtain Set 1 shown on the bottom left-hand side of Fig. 1. If however, particulates are negligible, there is one less unknown and consequently, one extra equation is available (i.e., more equations than unknowns). As a result, five different expressions for $\tilde{N}$ can be derived for each moisture condition depending upon which atom balances and concentration measurements are used. The requirements for these five are listed in lines 2 through 6 of Table 1 and correspond to Sets 2 through 6 of Fig. 1. A term in parentheses in Table 1, e.g. (CO_2), means that the measurement indicated is not used.

Line 7 in Table 1 (corresponding to Set 7 in Fig. 1) is a special case that requires the air flow rate to be measured. No atom balances are required but all of the exhaust concentration measurements are needed. Note that we only use the subscript g in this case because the emission rates calculated with this expression are not affected by particulates, i.e., the experimental concentration readings automatically adjust for the presence or absence of particulates. Line 8 is presented only for reference. It is a special subset of Line 3 for the case where all exhaust concentrations except O_2 can be neglected; it is often referred to as an oxygen balance.

The rest of the paper is largely concerned with developing algebraic expressions for these seven sets of expressions for $\tilde{N}$. Once these algebraic expressions have been developed in terms of fuel properties and exhaust concentration measurements, equation (1) can be used to compute seven "different" mass emission rates (remember that ideally they would all agree). In addition, an error analysis is also presented as well as expressions for calculating air/fuel and oxygen equivalence ratios. Finally a brief description of an interactive computer program that calculates various emission rates from these seven expressions is presented. This program can be run on any PC that uses DOS.

At this point the reader, if so desired, can simply accept the derivations presented in the next sections and go directly to the description of the computer program. However, when using the program, a choice must be made as to which one, or which combination, of the seven expressions to use to compute emission rates. (This selection is not trivial; as can be seen on the program output sheet presented later there can be substantial differences between mass emission rates calculated using different expressions.) If the reader does not study the development of the expressions then he/she will have no choice but to accept the expressions recommended by the authors that are marked by an "R" in the portion of the program output sheet marked DATA INTEGRITY.

Equations for Atom Balances

Before computing ¢ and $\tilde{N}W$ some arbitrary decisions must be made regarding the atoms and molecules considered significant in the input fuel and air as well as in the exhaust gases. These decisions can be made on either of two different bases: the atom or molecule is negligible from a pollutant standpoint or negligible from an atom balance standpoint. We shall only be concerned here with whether or not they are negligible from an atom balance standpoint.

Most petroleum-derived fuels contain only H, C, and S. However, landfill and other gases contain inerts and O_2 in significant amounts as well as chlorinated, fluorinated, and other compounds. Also, there is a small amount of CO_2 (around 300 ppm) coming in with the input air. It was decided to consider six atoms (C, H, O, S, N, and inerts I) as input atoms for atom balance purposes. It was also decided to neglect the CO_2 coming in with the input air; this assumption is less valid for very lean mixtures.

The importance of exhaust compounds from an atom balance standpoint varies considerably with operating conditions. For example, H_2 and CO may be negligible from an atom balance standpoint during moderately lean operation but not during rich or very lean operation. Engine type may affect the assumptions, i.e., a stratified charge engine running slightly lean may have significant particulates in the exhaust while a premixed charge engine, under the same stoichiometry, may have negligible particulates. For present purposes, it was decided to consider CO_2, CO, H_2O, H_2, O_2, N_2, NO, SO_2, inerts, CH_N (unburned fuel), and CH (particulates) as potentially significant in the exhaust gas from an atom balance standpoint. Since there is an increasing tendency to measure the different HC compounds in the exhaust, the composition of the exhaust HC's was assumed to be CH_N where N could be computed in a manner similar to n (Appendix A). In the absence of measurements it is customary to assume that $N=n$; this assumption is currently used in the computer program.

Under the above assumptions, equation (3) presents the general form of the atom balance that will be used for emission computations

$$\mathrm{CH}_n + fo\mathrm{O}_2 + fi\mathrm{I} + sf\mathrm{S} + E\mathrm{O}_2 + 3.76E\mathrm{N}_2 + Nm\mathrm{H}_2\mathrm{O} = a\mathrm{CO}_2 + b\mathrm{CO} + (j+Nm)\mathrm{H}_2\mathrm{O} + d\mathrm{H}_2 + p\mathrm{O}_2 + (3.76E - 0.5k)\mathrm{N}_2 + k\mathrm{NO} + sf\mathrm{SO}_2 + fi\mathrm{I} + z\mathrm{CH}_N + L\mathrm{CH} \quad (3)$$

Several things should be noted about equation (3). First, in writing equation (3) we used a nitrogen balance to determine the coefficient for N_2 in the products. Secondly, we also used an inert atom balance to give the coefficient for inerts "I" in the products. Third, a sulfur balance was used and sulfur was assumed to be in the form of SO_2 in the products. Fourth, the nitrogen oxides were assumed to be in the form of NO even though some small percentage will be in the form of NO_2. Finally, note that the water coming in the inlet, Nm, could be either that associated with the atmospheric air, Nma, or that deliberately introduced Nm£. Thus $Nm = Nma + Nm$£.

The sum of the mols on the right-hand side of equation (3) (excluding the solid phase L) is by definition $\tilde{N}W$. It will be helpful in our thinking to divide the terms affecting $\tilde{N}W$ into two groups. The first group (a, b, Nma, d, p, k, and z) can be expressed in terms of measured mol fractions and $\tilde{N}$. These appear in the terms β and ξ in the general expression for $\tilde{N}W$ (equation (16D), Appendix D). Specifically,

$$\text{ℊCO}_2 = a/\tilde{N} \quad (4)$$

$$\text{ℊCO} = b/\tilde{N} \quad (5)$$

$$\text{ℊHCT} = z/\tilde{N} \quad (6)$$

$$\text{ℊH}_2 = d/\tilde{N} \quad (7)$$

$$\text{ℊO}_2 = p/\tilde{N} \quad (8)$$

$$\text{ℊNO} = k/\tilde{N} \quad (9)$$

Note that this group includes the atoms C, O, H, and N. The relationship between *Nma* and $\tilde{N}$ is shown later.

The second group (*j*, *Nm£*, *sf*, *fi*, *fo*) includes the atoms I, S, O, and H, enters into the terms Å and ¥ (equation 16D), and are specified input quantities. The quantity *fo* shows up in O_2 but needs to be treated differently from *E* (equation (3)), since no N_2 or water vapor accompanies *fo*. If the concentration of water vapor in the exhaust were measured both *j* and *Nma* could be determined; however, water vapor is not usually determined. Consequently *j* must normally be determined by atom balances.

Note that *E* is a measure of the N_2 coming in with the inlet air and, when corrected for NO and any nitrogen in the fuel, *the N_2 in the exhaust. E is unknown since we do not normally measure nitrogen concentration in the exhaust.* However, *E* can be evaluated using air flow rate and exhaust concentration measurements or from exhaust concentration measurements alone.

As indicated previously N, S, and I balances have already been used in deriving equation (3). The remaining three atom balances (C, H, and O) can be used to solve for *j*, *E*, and *L*.

Oxygen Atom Balance

$$2fo + 2E + Nm = 2a + b + j + Nm + 2p + k + 2sf \quad \text{or}$$

$$E = -fo + a + 0.5b + 0.5j + p + 0.5k + sf \quad (10)$$

Hydrogen Atom Balance

$$n + 2Nm = 2j + 2Nm + 2d + Nz + L \quad \text{or}$$

$$j = 0.5n - d - 0.5Nz - 0.5L \quad (11)$$

Carbon Atom Balance

$$1 = a + b + z + L \quad \text{or}$$

$$L = 1 - a - b - z \quad (12)$$

If *E* (equation (10)) is to be evaluated from exhaust concentrations, *j* must be known. But, as explained above, *j* is unevaluated. If *j* is evaluated using equation (11) and particulates are considered significant, then equation (12) must be used also since *L* appears in equation (11). If particulates are not significant, then we do not need to use equation (12) to evaluate *j* and the carbon balance can be used for other purposes. Thus, to evaluate *j* and *E*, we can either solve equations (11) and (12) together in the presence of particulates, or use equation (11) by itself in the absence of particulates. We will use the subscripts *p* or *g* to indicate which assumption we are using. Using equations (11) and (12)

$$jp = -0.5 + 0.5n - d + 0.5a + 0.5b + 0.5z - 0.5Nz \quad (13)$$

and

$$jg = 0.5n - d - 0.5Nz \quad (14)$$

Similarly we can have an *Ep* and an *Eg*

$$Ep = 1.25a + 0.75b - 0.5d + p + 0.5k - fo + 0.25n - 0.25 + sf + 0.25z - 0.25Nz \quad (15)$$

and

$$Eg = a + 0.5b - 0.5d - 0.25Nz + p + 0.5k - fo + 0.25n + sf \quad (16)$$

If all measurements were precise one would simply assume the possibility of particulates and use equations (13) and (15) for all cases since they should be generally applicable. In the real world, however, experimental readings have inaccuracies. The fact that *jp* and *jg* and *Ep* and *Eg* have different terms and coefficients means that different answers will be obtained depending upon experimental accuracy. It will be shown that various estimates of $\tilde{N}$ can thus be obtained and it will be a matter of judgment and experience as to which is the more correct estimate, although some guidelines for the best choice(s) will be presented later. While it may be confusing to have so many estimates, we will develop all of them for the sake of completeness.

Since it will be needed later, let us first develop an expression for the moisture coming in with the atmospheric inlet air, *Nma*.

$$Nma = \frac{\text{mols of } H_2O, \text{ inlet air}}{\text{mol } CH_n}$$

$$= \frac{\text{mols } H_2O, \text{ inlet air}}{\text{mols dry inlet air}} * \frac{\text{mols dry inlet air}}{\text{mol } CH_n}$$

$$= \frac{\text{mols } H_2O, \text{ inlet air}}{\text{mass dry air}} * \frac{\text{mass dry air}}{\text{mols dry inlet air}}$$

$$* \frac{\text{mols dry inlet air}}{\text{mol } CH_n} \quad (17)$$

By definition of *E* and the composition of air, the mols of dry air per mol of CH_n is 4.76*E*. Also, the humidity ratio (*HR*) is defined as mass H_2O/mass dry air and the molecular weight of H_2O is 18. Thus

$$Nma = \frac{\text{HR}}{18} * 28.95 * 4.76E = 7.656HR * E \quad (18)$$

We will also need an expression for $\tilde{N}d$. From equation (3), by definition

$$\tilde{N}d = a + b + d + p + 3.76 * E + 0.5k + sf + fi + z \quad (19)$$

Expressions for $\tilde{N}$

As shown in Appendix D, with but one exception, there is a general form for $\tilde{N}d$. The general expression is of the form

$$\tilde{N}d = \text{Å}/[1 - \beta] \qquad \text{(from Appendix D)} \quad (4D)$$

and the analogous expression for $\tilde{N}W$ is

$$\tilde{N}W = \tilde{N}d[1 + \xi] + ¥ = \frac{\text{Å}[1 + \xi]}{1 - \beta} + ¥ \quad (16D)$$

The one exception is $\tilde{N}dgc$, which has the form Å/β. The expression for $\tilde{N}dgc$ is valid for *d*, *w*, or *W* if the three constituents used (CO_2, CO, and HCT) are all measured on the same basis.

Both β and ξ contain the experimentally measured exhaust concentrations [ℊCO_2, ℊHCT, ℊO_2, ℊH_2, ℊNO] corrected to dry conditions. Å and ¥ simply contain constants or input quantities [*HR*, *N*, *n*, *fi*, *fo*, *sf*, *Nm£*]. Eight different expressions (or more correctly seven since $\tilde{N}dgO_2$ is special case of $\tilde{N}dg(CO_2)$) are developed in Appendix D for $\tilde{N}d$ and two different expressions for both ξ and ¥. Table 1 summarized these different expressions for $\tilde{N}d$, the atom balances used, the required flow rate measurements, and the exhaust concentration measurements that must be made.

The terms Å, β, ξ, and ¥ are shorthand for lengthy expressions having a number of terms. For example, look at equation (6D), Appendix D.

$$\beta dp = 5.7\text{ℊ}dpCO_2 + 3.82\text{ℊ}dpCO - 0.88\text{ℊ}dpH_2 + 4.76\text{ℊ}dpO_2 + 2.38\text{ℊ}dpNO + [1.94 - 0.94N]\text{ℊ}dpHCT \quad (20)$$

Note that each concentration value has a coefficient in front of it, e.g., 5.7 for CO_2, 3.82 for CO, etc. Since the terms comprising Å, ξ and ¥ have similar coefficients we can present expressions for Å, β, ξ, and ¥ in tabular form in terms of these

Table 2 Coefficients for concentration values, β and ξ

i	j	1 f_{CO_2}	2 f_{CO}	3 f_{HCT}	4 f_{O_2}	5 f_{H_2}	6 f_{NO}
1	βdp	5.7	3.82	1.94-.94N	4.76	-.88	2.38
2	βdg	4.76	2.88	1-.94N	4.76	-.88	2.38
3	βdg(CO2)	0	-1.88	-3.76-.94N	4.76	-.88	2.38
4	βdg(CO)	1.88	0	-1.88-.94N	4.76	-.88	2.38
5	βdg(HCT)	3.76+.94N	1.88+.94N	0	4.76	-.88	2.38
6	βdgc	1	1	1	0	0	0
7	βdgaf	1	1	1	1	1	.5
8	βdgO2	0	0	0	4.76	0	0
9	ξdp	.5+9.57HR	.5+5.742HR	[a]	7.656HR	-1-3.828HR	3.828HR
10	ξdg	7.656HR	3.828HR	[b]	7.656HR	-1-3.828HR	3.828HR

a = 0.5 − 0.5N + 1.914HR[1 − N]

b = -N[.5 + 1.914HR]

Table 3 Coefficients for input values, Å and ¥

	j	1	2	3	4	5	6	7	8
i		constant	HR	N	n	f1	fo	sf	Nmf
1	Adp	-.94	0	0	.94	1	-3.76	4.76	0
2	Adg	0	0	0	.94	1	-3.76	4.76	0
3	Adg(CO_2)	4.76	0	0	.94	1	-3.76	4.76	0
4	Adg(CO)	2.88	0	0	.94	1	-3.76	4.76	0
5	Adg(HCT)	1	0	-.94	.94	1	-3.76	4.76	0
6	Adgc	1	0	0	0	0	0	0	0
7	Adgaf	[a]	0	0	0	1	0	1	0
8	AdgO_2	4.76	0	0	.94	1	-3.76	4.76	0
9	¥Wp	-.5	-1.914	0	.5+1.914HR	0	-7.656HR	7.656HR	1
10	¥Wg	0	0	0	.5+1.914HR	0	-7.656HR	7.656HR	1

a = [.79 * Pda * Vat]/Ro * Ta * NFt*J]

coefficients as shown in Tables 2 and 3. All values are presented dry since $\tilde{N}W$ can be expressed in terms of $\tilde{N}d$, ξ, and ¥.

Note that the expression for βdp (equation (20)) can be read directly from Table 2; other values of Å, β, ξ, and ¥ can also be read from Tables 2 and 3. It is instructive to observe the different coefficients for the same compound but for different expressions. For example, for CO_2 the coefficients range from 0 to 5.7; for CO from -1.88 to 3.82; and for HCT from approximately -3.76 to unity. Since any error in concentration measurement is multiplied by these coefficients this means that, for different expressions for $\tilde{N}$, the same measurement error will result in different errors in $\tilde{N}$.

Error Analysis

To estimate the sensitivity of the different expressions for $\tilde{N}W$ to errors in concentration measurements we will differentiate equation (16D) using the chain rule and remembering that only β and ξ involve concentrations to give

$$\frac{d(\tilde{N}W)}{d(\text{ƒ})} = \frac{d}{d(\text{ƒ})}\left[\frac{\text{Å}[1+\xi]}{1-\beta} + ¥\right]$$

$$= \frac{[1-\beta]*\text{Å}*d(1+\xi)/d(\text{ƒ}) - \text{Å}(1+\xi)*d(1-\beta)/d(\text{ƒ})}{[1-\beta]**2}$$

$$= \text{Å}\left[\frac{d(\xi)/d(\text{ƒ})}{(1-\beta)} + \frac{(1+\xi)*d(\beta)/d(\text{ƒ})}{(1-\beta)**2}\right] \tag{21}$$

In order to understand the evaluation of $d(\xi)/d(\text{ƒ})$ and $d(\beta)/d(\text{ƒ})$ we need to establish more terminology. Let us characterize positions in Tables 2 and 3 by i (rows) and j (columns); i would vary from 1 to 10 in both Tables 2 and 3 while j would vary from 1 to 6 in Table 2 and 1 to 8 in Table 3.

If we define Γ as any entry in the table then Γij would identify a specific entry, i.e., $\Gamma 43$ would be $(-1.88-0.94\text{N})$. Using this terminology we could write equation (20) in the brief form:

$$\beta dp(i=1) = \sum_{6}^{j=1} [\Gamma ij*\text{ƒ}\,j] \tag{20a}$$

In developing our error analysis we will want to see the effect on *Mpolt* of a measurement error in any individual compound. In order to do this we can write the term $(1-\beta)$ in equation (21) as

$$1-\beta = 1-[\{\beta-\Gamma ij*\text{ƒ}\,j\}+\Gamma ij*\text{ƒ}\,j] \tag{22}$$

When we are taking the differential with respect to a specific compound, $\text{ƒ}\,j$, the term $[\beta-\Gamma ij*\text{ƒ}\,j]$ will be a constant. Similar arguments can be made for the quantity $[1+\xi]$ and give:

$$d(\xi i)/d(\text{ƒ}\,j) = \Gamma ij\xi \tag{23}$$

where the term ξ in $\Gamma ij\xi$ does not indicate multiplication but that $i=9$ and 10, i.e., we are speaking of ξ in rows 9 and 10 of Table 2.

Also

$$d(\beta i)/d(\text{ƒ}\,j) = \Gamma ij\beta \tag{24}$$

where again the term β in $\Gamma ij\beta$ indicates that $i=$ rows 1-6 and 8 in Table 2.

Since concentration measurements play a small role in $\beta dgaf$ in comparison to possible errors in flow measurements we will not consider $\beta dgaf$ for present purposes.

Using the above terminology equation (21) becomes

$$\frac{d(\tilde{N}W)i}{d(\text{ƒ}\,j)} = \text{Å}i\,\frac{\Gamma ij\xi}{1-\beta} + \frac{(1+\xi)\Gamma ij\beta}{(1-\beta)**2} \tag{25}$$

Let us examine the relative magnitude of the terms in equation (25). (In making these comparisons note that in Table 2 ξdp, which assumes particulates are present, must be associated with row 1, while ξdg is associated with all other rows.) The quantity $(1-\beta)$ will normally be unity or less; this will make the right-hand term larger than the left since it is in the denominator and squared. Also, the right-hand term is multiplied by the quantity $(1+\xi)$ and ξ is always positive. This will again tend to make the right-hand term larger. A term-by-term comparison of the values of $\Gamma ij\beta$ and $\Gamma ij\xi$ in Table 2, remembering that values of *HR* are on the order of magnitude of 0.01, will show that in the great majority of cases $\Gamma ij\beta$ is considerably smaller than $\Gamma ij\beta$. Consequently, for the sake of simplicity, we will neglect the term $\Gamma ij\xi/(1-\beta)$ in the following error analysis. The term $(1+\xi)$ has only two expressions (ξdp and ξdg). Consequently, it will be relatively constant and we will also neglect it for present purposes. Thus equation (25) becomes

$$\frac{d(\tilde{N}W)i}{d(\text{ƒ}\,j)} \approx \frac{\text{Å}i*\Gamma ij\beta}{(1-\beta)**2} = \frac{d(\tilde{N}d)i}{d(\text{ƒ}\,j)} \tag{26}$$

It can be seen by differentiation of the general expression for $\tilde{N}d$ (equation 4D) that the net effect of our assumptions has been to make the approximate expression $d(\tilde{N}W)i/d(\text{ƒ}\,j)$ equal to the exact expression for $d(\tilde{N}d)i/d(\text{ƒ}\,j)$. If we multiply and divide the center term of equation (26) by Åi and rearrange (remembering that $\tilde{N}d = \text{Å}/(1-\beta)$) equation (26) becomes

$$\frac{d(\tilde{N}d)i}{d(\text{ƒ}\,j)*\tilde{N}d} = \frac{\Gamma ij\beta*\tilde{N}d}{\text{Å}i} \tag{27}$$

Equation (27) indicates that the percent error in $\tilde{N}d$ due to an error in measuring the concentration of a specific compound varies with the ratio of $\Gamma ij\beta/\text{Å}i$ for that compound (and ex-

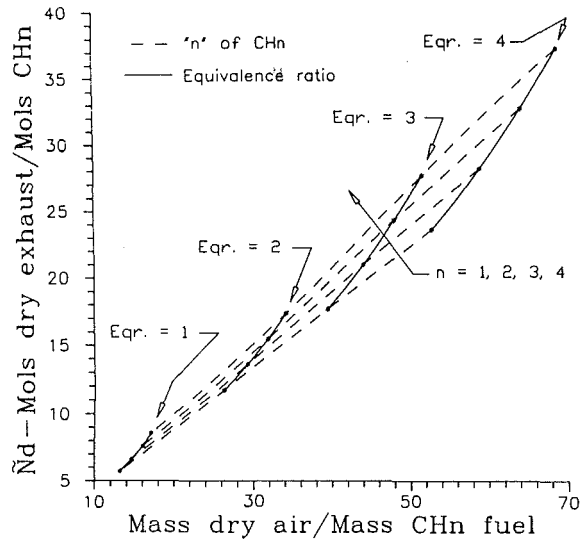

Fig. 2 Relationship between mols of dry exhaust per mol of CH_n fuel and air/fuel ratio

pression) as well as with $\tilde{N}d$. We shall call $\Gamma ij\beta/\text{Å}i$ an "error multiplier."

It can be shown that $\tilde{N}d$ is approximately proportional to air/fuel ratio; thus percent error is approximately proportional to air/fuel ratio. Assuming there was no change in mols during combustion (it is usually not large; for a complete reaction it will range from 0 to perhaps 5 percent) we could write, since mass is conserved during combustion

$$\tilde{N}d = \frac{\text{mols exhaust}}{\text{mol } CH_n \text{ fuel}} \approx \frac{\text{mols air}}{\text{mols } CH_n \text{ fuel}} = \frac{\text{mass air}}{\text{mass fuel}} * \frac{MWf}{MWa}$$

and $\tilde{N}d$ would be approximately proportional to air/fuel ratio. To illustrate the relationship and the effect of the change in mols during combustion Fig. 2 shows $\tilde{N}d$ as a function of exhaust air fuel/ratio for the case where the only fuel atoms were C and H, and all of the C went to CO_2, i.e., perfect combustion with a stoichiometric or leaner mixture. As is well known and is shown in Fig. 2, the same equivalence ratio requires different air/flow ratios for different values of n. Also note that for the same equivalence ratio, fuels having a higher value of n have a higher value of $\tilde{N}d$. This is not the result of additional H_2O in the exhaust but rather the additional N_2 accompanying the additional O_2 required to burn the additional H_2. In summary, for a given error in measuring concentration the percent error in mass emission rate is approximately proportional to the air/fuel ratio and the error multiplier $\Gamma ij\beta/\text{Å}i$.

In order to illustrate the relative errors for different expressions the error multiplier $\Gamma ij\beta/\text{Å}i$ was computed for different constituents and different values of n. When N (of CH_N) appeared in an equation it was assumed equal to n. It was also assumed that the fuel contained only C and H atoms. The results of the calculations are shown in Figs. 3 through 8 for the constituents CO_2, CO, HCT, O_2, H_2, and NO. In examining the plots it should be remembered that the larger (numerically) the value of error multiplier, the greater will be the percentage error in the mass emission rate for a given concentration measurement error. For example, Fig. 3 shows the relative sensitivity of $\tilde{N}dgc$, $\tilde{N}dg$ (CO), $\tilde{N}dg$, $\tilde{N}dp$, and $\tilde{N}dg$ (HCT) to experimental errors in the CO_2 measurement.

Figures 3 through 8 show that the sensitivity to error of some of the expressions for $\tilde{N}d$ is highly dependent on the value of n and that, in some cases, the measurement error is multiplied by very large factors. Note that the error multiplier can be either positive or negative, i.e., that the mass emission rate can be either over or underestimated. It is obvious that for most cases the expressions for $\tilde{N}dg$, $\tilde{N}dp$, and $\tilde{N}dg$ (HCT) have the greatest sensitivity to measurement errors.

It is unlikely that measurement error will occur in one constituent only. Thus it could be argued that the proper measure of sensitivity is the sum of the error multipliers for all of the components. Figure 9 presents the sum of the error multipliers for CO_2 and O_2 using the logic that they have the highest concentration values. Figure 10 presents the sum of the error multipliers for all constituents. Both figures show the same trend as the individual plots; the expressions for $\tilde{N}dg$, $\tilde{N}dp$, and $\tilde{N}dg$ (HCT) have the greatest sensitivity to concentration measurement errors and to changes in n.

To determine whether this inferred sensitivity to errors when using these three expressions was found in experimental data, computations were performed using data obtained for CO emission rates obtained from two different engines. The first set of data was selected randomly from published field measurements. The second set of data was from laboratory tests using very careful and repeated calibration of instruments and checking of data. The results are shown in Fig. 11. The data with a CO emission rate below 4 are the laboratory data; the rest are the data taken in the field. The agreement for all of the laboratory data is excellent. The $\tilde{N}dgc$ (carbon balance only) data are in excellent agreement with the air, fuel flow rate data, and the field data as well. The worst agreement is for the $\tilde{N}dg$ (HCT) expression. The next worse agreement is with $\tilde{N}dg$; this is in agreement with Figs. 9 and 10. Note that most of the values except those for $\tilde{N}dgc$ are lower than the measured flow rate data; this trend is also indicated by the negative values in Figs. 9 and 10.

In summary, it seems useful to compute $\tilde{N}W$ using all of the different expressions and to use agreement between the different expressions as a measure of the quality of the data. $\tilde{N}dg$, $\tilde{N}dp$, and $\tilde{N}dg$ (HCT) should be used only as a measure of the quality of the data and not to calculate the final results. If the quality of the data are high it makes little difference which of the remaining expressions are used, although it is recommended that the average of the values computed using $\tilde{N}dgc$, $\tilde{N}dg$ (CO_2), $\tilde{N}dg$ (CO), and $\tilde{N}dgaf$ be used, since they show both positive and negative sensitivities to the concentration measurement errors.

Moisture Correction Factor, ¢. In addition to expressions for $\tilde{N}W$ we need an expression for ¢ to correct the measured volume fraction of a constituent to the wet (no H_2O condensed) condition for use in equation (2). If the pollutant measurement is made wet, ¢ is obviously unity; if "dry" $¢w = \tilde{N}w/\tilde{N}W$. Using these definitions with equation (16D) gives

$$¢dp = 1/[1 + \xi dp + ¥p/\tilde{N}p] \tag{28}$$

and using equation (9D)

$$¢wp = 1/[1 + \xi dp + ¥p/\tilde{N}d) * (1 - Pw/Pb) = ¢dp/[1 - Pw/Pb] \tag{29}$$

There is, however, a complication in using these equations. Computation of ¢ requires a value of $\tilde{N}d$ and $\tilde{N}d$ requires that all of the concentration measurements be dry. In practice though, the measurements are usually a mixture of wet and "dry." Thus we need ¢ in order to correct the measurements and get $\tilde{N}d$ but we also need $\tilde{N}d$ in order to get ¢—a Catch 22 situation. The solution is to iterate until satisfactory results are obtained.

Expressions for Air/Fuel and Oxygen Equivalence Ratios. Air/fuel ratio can be defined in a number of ways:

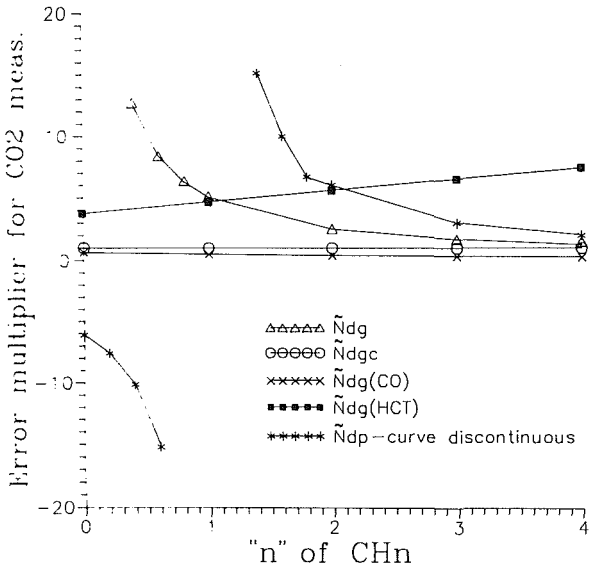

Fig. 3 Error multiplier for CO_2 versus *n* when using different expressions

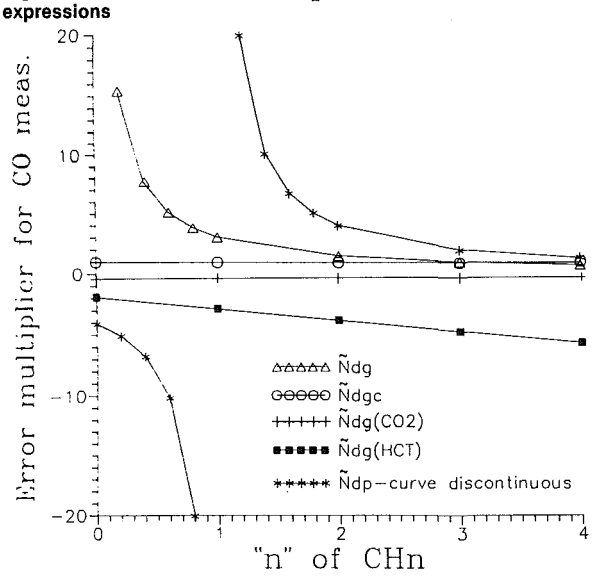

Fig. 4 Error multiplier for CO versus *n* when using different expressions

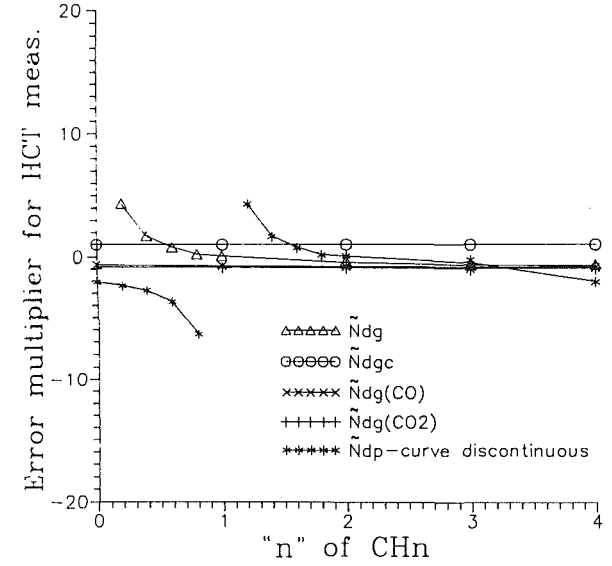

Fig. 5 Error multiplier for HCT versus *n* when using different expressions

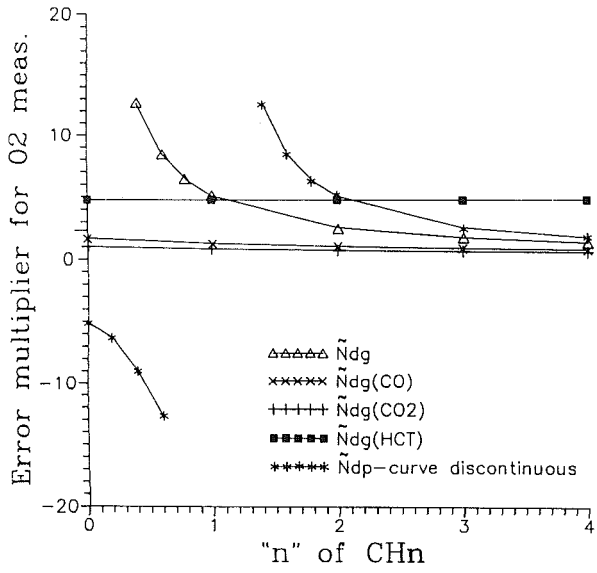

Fig. 6 Error multiplier for O_2 versus *n* when using different expressions

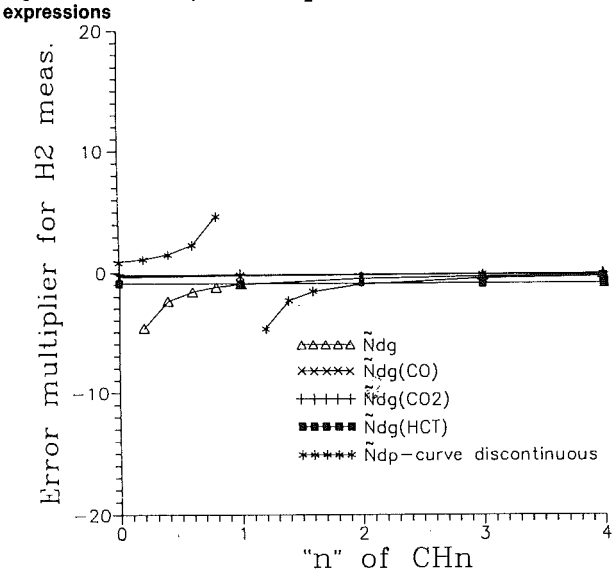

Fig. 7 Error multiplier for H_2 versus *n* when using different expressions

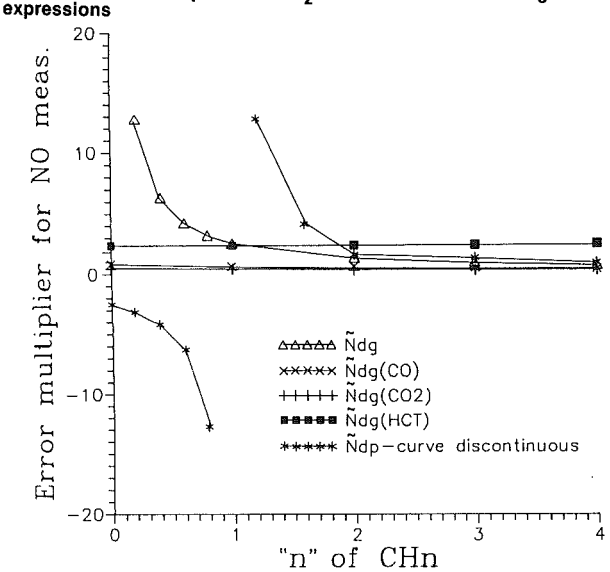

Fig. 8 Error multiplier for NO versus *n* when using different expressions

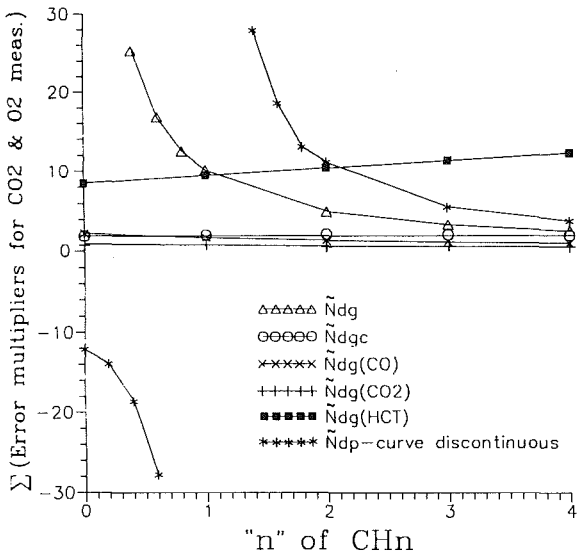

Fig. 9 Sum of error multipliers for CO_2 and O_2 versus n when using different expressions

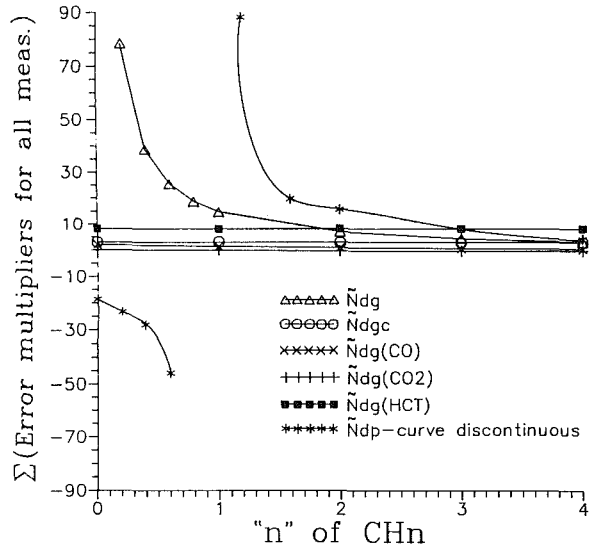

Fig. 10 Sum of error multipliers for all constituents versus n when using different expressions

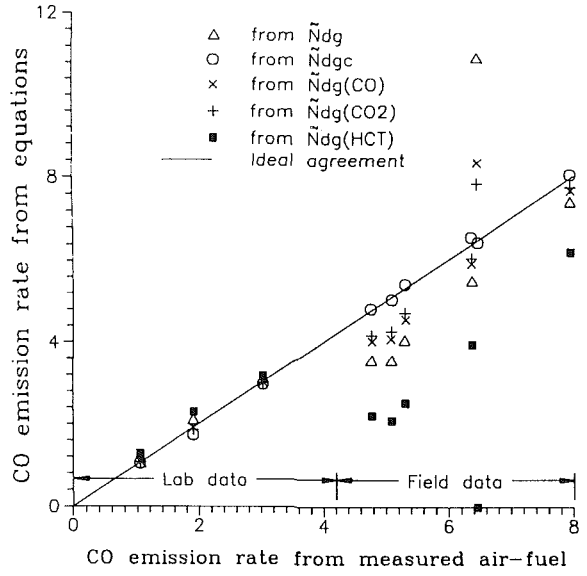

Fig. 11 Comparison of mass emission rate calculated from different expressions to the mass emission rate computed from measured air and fuel flow rates

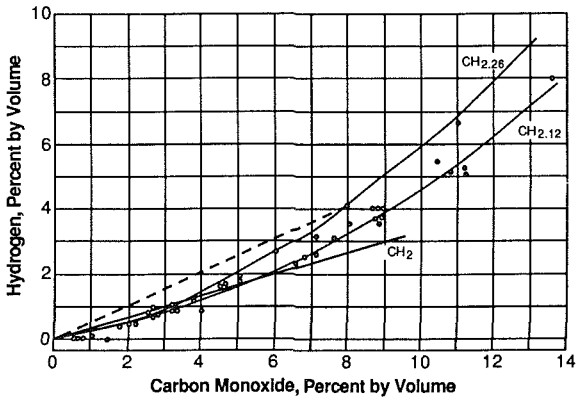

Fig. 12 Relationship between H_2 and CO as a function of n

total air divided by total fuel; dry air divided by total fuel; dry air divided by combustible portion of fuel, etc. We shall develop expressions for TAF (total air divided by total fuel) and for the oxygen equivalence ratio (O_2EQR) since TAF corresponds to the measured quantities and O_2EQR is measure of the O_2 necessary for complete combustion. $O_2$2EQR will include all of the O_2 in both the air and fuel.

It can be shown (Appendix E) that TAF can be expressed in terms of $\tilde{N}d$; consequently there are as many expressions for TAF as for $\tilde{N}d$.

Using exhaust concentration measurements the general form for TAF is

$$\mathrm{TAF} = \frac{36.65[1+HR][\tilde{N}d(1-\beta dga\text{ß})-fi-sf]+18*Nm\text{£}}{12+n+32*(fo+sf)+fi*MWI} \quad (7E)$$

Especially for unusual fuels, O_2EQR is a better measure of the potential combustion characteristics of the mixure. O_2EQR is defined as

$$O_2\mathrm{EQR} = \frac{(Eact+fo)}{(Es+fo)} = \frac{\tilde{N}d[(1-\beta dgaf)-fi-sf]+fo}{3.76(1+0.25n+sf]} \quad (11E)$$

Computation of Mass of Pollutant per Unit Energy In. If *Mpolt* is known, the mass of pollutant per unit of energy in (*Mpolei*) is easily calculated

$$Mpolei = \frac{\text{mass pol}}{\text{unit time}} * \frac{\text{unit time}}{\text{unit energy in}} \quad (29)$$

Computation of Mass of Pollutant per Unit Energy Out (Work). If the output of the engine is expressed in power (energy per unit time) the mass of pollutant per unit of work (energy) out (*Mpoleo*) would be

$$Mpoleo = \frac{\text{mass}}{\text{unit time}} * \frac{\text{unit time}}{\text{energy out}} \quad (30)$$

Computation of Concentration Corrected to 15 Percent Oxygen. Some regulations are written as the experimental concentration [(ßexpt)] corrected to 15 percent oxygen to standardize dilution. The expression used is

$$\text{ß}(15\%) = \frac{\text{ß}(\text{expt})*0.059}{[0.209-\text{ß}O_2(\text{expt})]} \quad (31)$$

Evaluating H_2. We have tacitly assumed throughout the paper that H_2 was either known or negligible; in practice it is

Table 4 Summary of emcomp setup

```
      PAGE 1                              PAGE 2
    (General)                        (Measurement Basis)
Monitor type = COLOR                 CO2         ===> 'DRY'
Input units  = English               CO          ===> 'DRY'
Output units = English               O2          ===> 'DRY'
Engine type  = 2 stroke              NOx         ===> 'DRY'
Engine Disp. = 7539.8 in**3          Total HC    ===>  WET .
Input PATH   = d:\emcomp\            Methane HC  ===>  DRY
Output PATH  = d:\emcomp\            Cooling bath temp: 34 Deg F

      PAGE 3
  (Equations Used)
      Ndgc
```

Table 5 Sample computer output sheet

EMCOMP: Page 1 , 06-21-1988

	RUN 1	RUN 2	RUN 3	RUN 4
FUEL DATA FILE	fuel.1	fuel.2	fuel.3	fuel.4
ENGINE/AIRFLOW DATA				
Power(Bhp)	1.1412E+03	1.7894E+03	1.6480E+03	1.8200E+03
Bmep(psi)	7.4922E+01	1.5818E+02	1.1654E+02	1.0135E+03
Speed(rpm)	8.0000E+02	7.2000E+02	9.0000E+02	3.3000E+02
Airflow(lbm/min)	0.0000E+00	0.0000E+00	3.9257E+02	5.7603E+02
Airflow(ft**3/min)	2.6380E+03	5.6000E+03	0.0000E+00	0.0000E+00
Temp(deg F)	8.6000E+01	6.0000E+01	0.0000E+00	0.0000E+00
Pressure(psia)	1.4250E+01	1.4700E+01	0.0000E+00	0.0000E+00
Wet bulb T(deg F)	7.6000E+01	3.9000E+01	4.0500E+01	3.2000E+01
Dry bulb T(deg F)	8.6000E+01	4.4000E+01	4.4000E+01	3.8000E+01
Barom. P(in. Hg)	2.9020E+01	2.9420E+01	2.9310E+01	2.8970E+01
Liq H20 (lbm/min)	0.0000E+00	0.0000E+00	0.0000E+00	0.0000E+00
EXHAUST GAS DATA				
CO2(%)	8.8459E+00	3.7000E+00	4.3590E+00	3.2000E+00
CO(ppm)	3.0000E+02	1.9000E+02	4.7000E+02	1.1000E+02
O2(%)	8.8384E+00	1.4500E+01	1.3119E+01	1.3900E+01
NOx(ppm)	1.2000E+03	3.6000E+02	3.5000E+02	5.3900E+02
Total HC (ppm)	2.2000E+02	4.1000E+02	1.3000E+03	2.5200E+02
Methane HC (ppm)	1.0000E+01	3.3000E+02	1.1030E+03	0.0000E+00
GASEOUS FUEL DATA				
Flow(ft**3/hr)	0.0000E+00	1.1896E+04	1.3007E+04	1.3671E+04
Temp(deg F)	0.0000E+00	6.0000E+01	6.0000E+01	6.0000E+01
Pressure(psia)	0.0000E+00	1.4700E+01	1.4700E+01	1.4700E+01
LIQUID FUEL DATA				
Flow(lbm/min)	7.4178E+00	5.8630E-01	0.0000E+00	0.0000E+00
DATA INTEGRITY(g/hr)	- agreement is a measure of data accuracy			
CO-from Ndgaf-R	1.3838E+03	2.0758E+03	4.6934E+03	1.6044E+03
*CO-from Ndgc-R	1.3725E+03	2.1646E+03	4.4785E+03	1.5857E+03
CO-from Ndg(CO2)-R	1.3807E+03	2.2059E+03	4.5268E+03	1.2968E+03
CO-from Ndg(CO)-R	1.3840E+03	2.2183E+03	4.5408E+03	1.2320E+03
CO - from Ndg(HCT)	1.4266E+03	2.5459E+03	4.9041E+03	5.7754E+02
CO - from Ndg	1.4041E+03	2.2641E+03	4.5908E+03	1.0472E+03
CO - from Ndp	1.4452E+03	2.3026E+03	4.6306E+03	9.3645E+02
POLLUTANT DATA(g/hr)				
CO	1.3725E+03	2.1646E+03	4.4785E+03	1.5857E+03
NOx	9.0190E+03	6.7379E+03	5.4791E+03	1.3505E+04
Total HC	4.9605E+02	2.8019E+03	7.6279E+03	2.1680E+03
Non Methane HC	4.7350E+02	5.4671E+02	1.1559E+03	2.1680E+03
POLLUTANT DATA(g/Bhp-hr)				
CO	1.2026E+00	1.2097E+00	2.7176E+00	8.7125E-01
NOx	7.9031E+00	3.7655E+00	3.3247E+00	7.4203E+00
Total HC	4.3467E-01	1.5658E+00	4.6286E+00	1.1912E+00
Non Methane HC	4.1491E-01	3.0553E-01	7.0141E-01	1.1912E+00
POLLUTANT DATA(g/million BTU)				
CO	1.6851E+02	6.4096E+03	3.7892E+02	1.3238E+02
NOx	1.1073E+03	1.9952E+04	4.6357E+02	1.1275E+03
Total HC	6.0904E+01	8.2967E+03	6.4538E+02	1.8100E+02
Non Methane HC	5.8136E+01	1.6189E+03	9.7799E+01	1.8100E+02
POLLUTANT DATA - fractions corrected to 15% Oxygen (ppm)				
CO	1.4675E+02	1.7516E+02	3.5638E+02	9.2714E+01
NOx	5.8699E+02	3.3187E+02	2.6539E+02	4.5430E+02
Total HC	1.0761E+02	3.7797E+02	9.8573E+02	2.1240E+02
Non Methane HC	1.0272E+02	7.3750E+01	1.4938E+02	2.1240E+02
POLLUTANT DATA(mg/Normal m**3)				
CO	3.7500E+02	2.3750E+02	5.8750E+02	1.3750E+02
NOx (NO2)	2.4643E+03	7.3929E+02	7.1875E+02	1.1069E+03
Non Meth HC (C2H6)	1.3393E+01	4.4196E+02	1.4772E+03	0.0000E+00
TOTAL AIR/FUEL(calc)	2.4626E+01	4.5631E+01	3.7395E+01	5.1678E+01
TOTAL AIR/FUEL(meas)	2.4801E+01	4.3673E+01	3.9121E+01	5.2196E+01
O2 EQUIV. RATIO	1.6735E+00	2.7804E+00	2.2583E+00	3.1416E+00

seldom measured. It has been observed, both in engines and in combustion bombs, that there is a relationship between H_2 and CO, probably resulting from the "freezing of the water gas reaction in $H_2 + CO_2 = CO + H_2O$." It will be noted in Table 2 that Γ for H_2 is -0.88. Consequently, the effect of errors in estimating the concentration of H_2 is small compared to some of the other constituents. One possibility is to assume that the water gas reaction always "freezes" at the same given temperature, compute the equilibrium constant for this temperature, and thus derive the relationship between CO and H_2. It has been observed experimentally that there is an approximately linear relationship between H_2 and CO (equation (1)) and that the slope of the curve is a function of n, Fig. 12 (equation (7)). This suggests the relationship

$$\wp H_2 = \text{const} * n * \wp CO \tag{32}$$

Reasonable results have been obtained using a constant of around 0.25. Equation (32) with a constant of 0.25 is used in the computer program.

Computer Program. An interactive computer program to calculate emission rates using the relationships developed in this paper has been written. It should run on any PC using the DOS operating system. The program basically consists of three parts: setup information, input data and output.

Table 4 shows a summary of the setup information requested by the program. Note that both the input and the output can be in either English or SI units and that the individual concentrations can be measured dry, "dry," or wet. The user must select one or more (if more than one, the values are averaged) of the seven expressions to be used for the final computation of emissions. The information shown in Table 4 is saved in a configuration file and automatically used for future runs unless the user chooses to reconfigure.

The data required to make a fuel file are the first of the required input data. If the fuel is gaseous, the molar (volume) fraction of the constituents must be known. If the heating values of the individual constituents are known, the heating value of the mixture is automatically calculated. If the heating value per standard unit volume is known it can be an alternative input item; heating value per unit volume can be updated without changing the fuel file. If the fuel is liquid, the mass fractions of C, H, and S are required as well as the heating value per unit mass. If a dual fuel is used the file must contain information about both fuels.

The rest of the required input data are shown in the upper half of the output sheet, Table 5 (with the exception of BMEP, which is of course a calculated item). The data are requested in units corresponding to the choice made in the setup procedure; the intent was to specify the actual measurement units used in the laboratory in order to facilitate the input process. The program will currently handle a maximum of 12 runs (three pages of output, each with four runs) before it becomes necessary to restart. Note that air flow may be given either in units of mass per unit time or volume per unit time at a measured pressure and temperature. The wet and dry bulb temperatures characterize the moisture coming in with the inlet air; the liquid H_2O represents moisture deliberately introduced into the inlet for operating or emission control reasons. The normal measuring units are used to express exhaust concentrations. The fuel flow rate must be specified; if it is a gaseous fuel it is expressed in volume per unit time at a measured pressure and temperature; if the fuel is liquid, the units are mass per unit time.

The input and output data are stored in a file specified by the user in the form shown in Table 5. For inspection purposes the output data can be viewed on the screen as well as printed. The section labeled DATA INTEGRITY presents a comparison of the mass emission rates of CO computed using the seven different expressions; the remaining sections present emission rates in different units. The expressions recommended for use when presenting data are marked by an R; the expression(s) actually used are marked with an *. If the data were perfect all of the values in the DATA INTEGRITY section would be identical.

The data shown in Table 5 were chosen to illustrate both "good" and "bad" agreement in the DATA INTEGRITY section. Run 1 shows very carefully taken laboratory data using a liquid fuel. Runs 2 and 3 are similar to each other except that 2 is for a dual fuel engine and 3 is for a gaseous fuel.[1] Run 4, which also is for a gaseous fuel, presents data taken in the field and shows the largest variation of the four runs. It should not be inferred that all field data contain large experimental error; data could have been selected that showed variations not much greater than runs 2 and 3. In practice, it would have been good to repeat run 4. While it is a matter of judgment and experience as to when the agreement is acceptable, the data from runs 1, 2, and 3 can be used as a rough guide.

[1] These runs represent typical laboratory data.

In summary, the program is highly flexible, user friendly, fast, and runs on commonly available PC's. It provides a direct indication of errors in concentration measurements and their effect on calculated emission rates; will handle a wide variety of fuels; and makes possible a direct comparison of emission rates since the assumptions used are constant and known. To facilitate general use of the program, a 5¼ in. floppy disk containing the compiled program and its documentation is available for a small duplicating fee from the last author of the paper; the disk is not copy protected.

Conclusions and Recommendations

In summary, several algebraic relationships applicable to complex fuels have been developed relating emission rates to measured exhaust gas concentrations and fuel flow rate. A sensitivity analysis shows that different expressions have different sensitivities to errors in experimental concentration measurements. Application to experimental data gives confidence in the validity of this sensitivity analysis. Since there should be agreement between emission rates computed from these different relationships the differences can be used as a measure of the integrity of the data. Final emission rates can be computed from a single expression or from the average of several expressions.

It is recommended that emission rates from these different expressions be routinely computed and used as a measure of the integrity of the data. It is further recommended that the final computed emission rate be the average of the rates computed from several expressions. Expressions using measured air and fuel flow rates, a carbon balance, a carbon–hydrogen–oxygen balance but not using the CO_2 measurement, and a carbon–hydrogen–oxygen balance but not using the CO measurement are preferred (in that order) for the final computation of emission rates. The interactive computer program briefly described above incorporates the above recommendations and can be used on any PC using DOS. If generally used it would be applicable to the great majority of both simple and complex fuels, standardize emission rate computations and format, provide a direct measure of the integrity of the data, and make possible general comparison of emission rates since the same assumptions would always be used.

Acknowledgments

The Diesel Engine Manufacturers Association provided the original stimulus for the work. The assistance of Fred Schaub and Harold Ballard by providing counsel, evaluation of programs, etc., is gratefully acknowledged. Professor Otto Uyehara helped initiate the approach used and supplied his usual wise counsel during development of the relationships. Professor E. F. Obert reviewed the paper and provided valuable suggestions. The DOD Center for Diesel Engines at the University of Wisconsin provided partial salary support during the development.

References

Eltinge, L., 1969, "Fuel-Air Ratio and Distribution From Exhaust Gas Composition," SAE Paper No. 690114.

Fenning, R. W., 1916, "The Composition of the Exhaust From Liquid Fuel Engines," *Proceedings of the Institution of Mechanical Engineers*, Mar. p. 185.

Ingham, M. C., Myers, P. S., and Uyehara, O. A., 1982, "In-Cylinder Sampling of Hydrocarbons in a Texaco L-141 TCP Engine," SAE Paper No. 820361.

Logan, M. R., Gudgeon, J., Uyehara, O. A., Myers, P. S., 1982, "Experimental Determination of Local HC Ratio and Hydrogen-Particulate," SAE Paper No. 820362.

Rhee, K. T., Myers, P. S., and Uyehara, O. A., 1978, "Time and Space-Resolved Species in Diesel Combustion Using Continuous Flow Sampling," SAE Paper No. 780226.

Spindt, R. S., 1965, "Air-Fuel Ratios From Exhaust Gas Analyzer," SAE Paper No. 650507.

APPENDIX A

Computation of Fuel Parameters for a Gaseous Fuel

We shall assume that the atoms in fuels of interest are carbon C, hydrogen H, oxygen O, inerts I (including N), and sulfur S. Thus we shall assume that the fuel or any one of its components can be represented by $C_vH_wO_xI_yS_z$ where the subscripts v, w, x, y, and z represent the number of atoms in the fuel or its component. Since we will be dealing with one mol of fuel, which will have i components, we can write for the mol of fuel:

$$\sum_i [NFi*(C_vH_wO_xI_yS_z)_i] = 1.0 \tag{A1}$$

and summing up for the components, by definition of terms

$$\sum_i (NFi*v_i) = J \tag{A2}$$

$$\sum_i (NFi*w_i/J) = n \tag{A3}$$

$$\sum_i (NFi*x_i/J) = fo \tag{A4}$$

$$\sum_i (NFi*y_i/J) = fi \tag{A5}$$

$$\sum_i (NFi*z_i/J) = sf \tag{A6}$$

$$\sum_i (NFi*HVi) = \text{heating value per mol of "as is" fuel} \tag{A7}$$

Table A-1 Computation of fuel parameters

1	2	3	4	5	6	7	8	9	10
atom		C	H	fo	fi	S			
molec weight		12	1.008	32	?	32.066			
component	mol frac	mols #	mols #	mols #	mols #	mols #	tot #	LHV,BTU per mol	(2)*(9) LHV,BTU
CH_n	.63	.63 7.56	2.52 2.52				10.08	345,117	217,424
C_2H_6	.05	.10 1.2	.30 .30				1.5	615,834	30,792
C_3H_8	.10	.30 3.6	.80 .80				4.4	879,640	87,964
CH_3OH	.05	.05 .60	.20 .20	.025 .8			1.6	292,762	14,638
CO	.05	.05 .60		.025 .8			1.4	121,716	6,086
CO_2	.04	.04 .48		.04 1.28			1.76		
H_2	.03		.06 .06				.06	103,246	3,097
N_2	.02				.02 .56		.56		
S	.01					.01 .32	.32	127,360	1,274
H_2S	.01		.02 .02			.01 .32	.34	223,289	2,233
NH_3	.01		.03 .03		.005 .14		.17	136,017	1,360
TOT	1.0	1.17 14.04	3.93 3.93	.09 2.88	.025 .700	.02 .64	22.19		364,868

n = TOT 4/TOT 3 = 3.359; H/C ratio

fo = TOT 5/TOT 3 = .09/1.17 = 0.0769; mols of O_2 in the fuel/mol CH_n

fi = TOT 6/TOT/3 = .025/1.17 = .0214; mols inerts/mol CH_n

af = TOT 7/TOT 3 = .02/1.17 = .0171; mols sulfur/mol CH_n

$MWCH_n$ = 12 + n × 12 + 3.359 = 15.359; molecular weight of CH_n

MWf = 22.19; molecular weight of the "as is" fuel

LHV = 364,868 BTU per mol of "as is" dry fuel

= 364,868/1.17 = 311,853 BTU per mol of CH_n

J = TOT 3 = 1.17; mols CH_n per mol "as is" fuel

$\sum_i (NFi*HVi)/J$ = heating value per mol of CH_n fuel (A8)

Note that, for a given component, several of the subscripts v, w, x, y, and z can be zero (for CH_4, $v=1$, $w=4$, x, y, and z are zero); and J can be greater or less than unity. The molecular weight of CH_n is $(12+n)$ but the molecular weight of fuel containing one mol of CH_n may be greater than $12+n$.

Table A-1 presents a numerical computation for a fictitious fuel containing a variety of components to illustrate the calculation technique.

The computations shown in Table A-1 proceed as follows. Consider the first component in Table A-1, CH_4. It is 63 volume percent of one mol of the dry fuel, consequently it contributes 0.63 mols of C having a mass of $0.63*12=7.56$ pounds mass (Column 3). Since it has 4 atoms of H it will contribute $0.63*4=2.52$ mols of H having a mass of $1.008*2.52=2.52$ pounds mass (Column 4). The total mass of the CH_4 per mol of fuel will be $7.56+2.52=10.08$ pounds mass (Column 8). The contribution of the CH_4 to the heating value will be the heating value per mol of CH_4 (on either the lower or higher heating value as arbitrarily decided) times the number of mols of CH_4 or $0.63*345{,}117=217{,}424$ (Column 10). The same procedure is followed for the rest of the constituents. The sum of Column 2 must equal unity since we have one mol of fuel. The sum of Column 3 equals the number of mols of C in one mol of fuel (1.17) and the corresponding number of pounds mass ($1.17*12=14.02$). The same logic applies to columns 4, 5, 6, and 7 for the atoms of H, O_2, I, and S. Column 8 is the mass of one mol of "as-is" fuel and is, therefore, the molecular weight of the composite fuel. Column 10 is the heating value of one mol of fuel on either a lower or higher heating values basis as chosen. Note that the heating value given above is on the dry basis; the gaseous fuel supplied to the engine may be accompanied by some water vapor. If so, the water may be negligible from an atom balance standpoint but not from a heating value standpoint.

To compute the molar fuel flow rate, Nft, assume that you have a gaseous fuel of composition shown in Table A-1 and that the measured gaseous volume fuel flow rate, Vft, is 75,000 cubic feet per hour at a pressure of 14.7 psia and 520 R. We can compute the molar flow rate of the gas from $P*Vft=Nft*Ro*T$ where Nft is the molar gaseous fuel flow rate in mols of fuel per hour and the gas constant, Ro, is independent of the gas composition and equals 1544 when the pressure is expressed in pounds per square foot and temperature in degrees Rankine. Thus

$$Nft=\frac{14.7*144*75{,}000}{1544*520}=197.74 \text{ mols of gaseous fuel per hour}$$

APPENDIX B

Computation of Fuel Parameters for a Liquid Fuel

Assume that you have a liquid fuel with a gravimetric (weight) analysis as shown below per pound of fuel:

C = 0.864315 H = 0.130685 S = 0.00500

The atomic analysis can be obtained by dividing the gravimetric analysis by the weight of each atom to give the number of atoms, adding up the number of atoms, and finding the atom percent. Thus

0.864315/12	= 0.072026—C
0.130685/1.008	= 0.129648—H
0.005000/32.066	= 0.000156—S
total	= 0.201830

as a check

C = 0.072026/0.201830 =	0.35687
H = 0.129648/0.201830 =	0.64236
S = 0.000156/0.201830 =	0.00077
total =	1.00000

Then n, the ratio of hydrogen to carbon atoms, is computed as

$$n=0.129648/0.072026=1.8$$

If the mass fuel flow rate is 7.41777 pounds of liquid fuel per minute there would be $7.41777*0.864315=6.411289$ pounds of carbon per minute

or $6.411289/12=0.53427$ mols of carbon per minute

It follows that the molar flow rate of $CH_{1.8}$ is also 0.53427 mols of $CH_{1.8}$ per minute since $CH_{1.8}$ contains one carbon.

The pounds of sulfur per minute would be

$7.41777*0.005=0.037089$ pounds of sulfur per minute

or

$0.037089/32.066=0.001157$ mols of sulfur per minute

or

$0.001157/0.53427=0.002165$ mols of sulfur per mol of $CH_{1.8}$

Since there is no oxygen or inerts in the liquid fuel fo and fi are both zero.

APPENDIX C

Computation of Fuel Parameters for a Combination of Liquid and Gaseous Fuels

Assume that the pilot fuel is liquid fuel and the main fuel is gaseous fuel. Assume that the liquid fuel flow rate is 100 pounds per hour using the liquid fuel described in Appendix B. Also, assume that the gaseous fuel has the composition shown in Table A-1, and the gaseous fuel flow rate is 75,000 cubic feet per hour as in Appendix A.

Calculation of n. The mols of carbon per hour from the liquid fuel would be

$100*0.864315/12=7.2026$ mols of carbon per hour from liquid fuel

Since there are 1.17 atoms of carbon per mol of gaseous fuel (Table A-1, Colulmn 3) the mols of carbon per hour from the gaseous fuel will be

$197.74*1.17=231.3558$ mols of carbon per hour from gaseous fuel

The total mols of carbon per hour then are

$7.2026+231.3558=238.5584$ mols carbon per hour in combined fuel

Since each mol of CH_n requires one mol of carbon it follows that there are 238.5584 mols of CH_n in the combined fuel.

The mols of H in the liquid fuel would be

$100*0.130685/1.008=12.9648$ mols of hydrogen per hour from the liquid fuel

The mols of H in the gaseous fuel would be (Table A-1, Column 4)

$3.93*197.74=777.1182$ mols of H per hour from gaseous fuel

The total mols of H per hour would be

$12.9648+777.1182=790.0830$ mols of H per hour in combined fuel

It follows then that for the combined fuel

$$n = 790.0830/238.5584 = 3.31$$

Calculation of Sulfur. The mols of sulfur in the liquid fuel would be

$0.005*100/32.066 = 0.0156$ mols sulfur per hour in liquid fuel

The mols of sulfur in gaseous fuel (Table A-1, Column 7) would be

$197.74*0.02 = 3.9548$ mols of sulfur per hour in gaseous fuel

The total mols of sulfur in the combined fuel would be

$0.0156 + 3.9548 = 3.9704$ mols of sulfur in combined fuel

The mols of sulfur, *sf*, per mol of CH_n would be

$3.97039/238.5584 = 0.01664$ mols sulfur per mol of CH_n combined fuel

Calculation of Oxygen. Since there is no oxygen in the liquid fuel the mols of O_2 per mol of CH_n (i.e., *fo*) in the combined fuel would be

$0.09*197.74/238.5584 = 0.0746$ mols oxygen per mol CH_n combined fuel

Calculation of Inerts. Since there are no inerts in the liquid fuel the mols of inerts per mol of CH_n (i.e., *fi*) in the combined fuel would be

$0.025*197.74/238.5584 = 0.0207$ mols inert per mol CH_n combined fuel.

APPENDIX D

Expressions for $\tilde{N}p$

Sample Development of Expression for $\tilde{N}$. We will illustrate the procedure followed in developing the coefficients in Tables 2 and 3 by developing the expressions for $\tilde{N}dp$ and $\tilde{N}Wp$. Assuming that particulates are significant we can substitute *Ep* (equation (15)) into equation (19). This gives

$$\tilde{N}dp = 5.7*a + 3.82*b - 0.88*d + 4.76*p + 2.38*k - 0.94 + 0.94*n + fi - 3.76*fo + 4.76*sf + 1.94*z - 0.94*N*z$$

Using equations (4) through (9) gives

$$\tilde{N}dp = \tilde{N}dp[5.7*\text{ℊ}dp\text{CO}_2 + 3.82*\text{ℊ}dp\text{CO} - 0.88*\text{ℊ}dp\text{H}_2 + 4.76*\text{ℊ}dp\text{O}_2 + 2.38*\text{ℊ}dp\text{NO} + (1.94 - 0.94\text{N})*\text{ℊ}dp\text{HCT}] - 0.94 + 0.94*n + fi - 3.76*fo + 4.76*sf \quad (2D)$$

Solving for $\tilde{N}dp$

$$\tilde{N}dp = \{-0.94 + 0.94*n + fi - 3.76*fo + 4.76*sf\}/[1 - \{5.7*\text{ℊ}dp\text{CO}_2 + 3.82*\text{ℊ}dp\text{CO} - 0.88*\text{ℊ}dp\text{H}_2 + 4.76*\text{ℊ}dp\text{O}_2 + 2.38*\text{ℊ}dp\text{NO} + 1.94 - 0.94*\text{N})*\text{ℊ}dp\text{HCT}\}] \quad (3D)$$

which can be expressed as

$$\tilde{N}dp = \frac{\text{Å}\,dp}{1 - \beta dp} \quad (4D)$$

where

$$\text{Å}\,dp = -0.94 + 0.94*n + fi - 3.76*fo + 4.76*sf \quad (5D)$$

and

$$\beta dp = 5.7*\text{ℊ}dp\text{CO}_2 + 3.82*\text{ℊ}dp\text{CO} - 0.88*\text{ℊ}dp\text{H}_2 + 4.76*\text{ℊ}dp\text{O}_2 + 2.38*\text{ℊ}dp\text{NO} + [1.94 - 0.94\text{N}]*\text{ℊ}dp\text{HCT} \quad (6D)$$

Sample Development of Expression for $\tilde{N}w$ and $\tilde{N}W$. By definition, the mols of wet exhaust equals the mols of water in the exhaust plus the mols of dry products in the exhaust, both per mol of CH_n. Thus

$$\tilde{N}w = \tilde{N}d + Nmew \quad (7D)$$

In the "dry" case the partial pressure of the water vapor (P_w) is the vapor pressure of water at the condensing temperature and since mol ratios are pressure ratios

$$Nmew = Pw*\tilde{N}w/Pb \quad (8D)$$

(where *Pb* is the barometric pressure)

Solving equations (7D) and (8D) together gives

$$\tilde{N}w = \tilde{N}d/[1 - Pw/Pb] \quad (9D)$$

By analogy with equation (7D)

$$\tilde{N}W = \tilde{N}d + NmeW \quad (10D)$$

By definitions and by comparison of equations (3) and (19)

$$NmeWp = jp + Nma + Nm£ \quad (11D)$$

where *Nm£* is a specified input quantity; *Nma* is given by equation (18), *jp* is given by equation (13); and *Ep* by equation (15). Combining gives

$$NmeWp = -0.5 + 0.5*n - d + 0.5*a + 0.5*b + 0.5*z - 0.5*N + 7.656*HR[1.25*a + 0.75*b - 0.5*d + p + 0.5*k - fo + 0.25*n - 0.25 + 0.25*z - 0.25*N*z + sf] + Nm£ \quad (12D)$$

Using equations (4)–(9) gives

$$NmeWp = \tilde{N}dp[(0.5 + 9.57*HR)*\text{ℊ}dp\text{CO}_2 + (0.5 + 5.742*HR)*\text{ℊ}dp\text{CO} - (1 + 3.828*HR)*\text{ℊ}dp\text{H}_2 + 7.656*HR\text{ℊ}dp\text{O}_2 + [0.5(1 - N) + 1.914*HR(1 - N)]\text{ℊ}dp\text{HCT} + 3.828*HR*\text{ℊ}[\text{NO}d] - 0.5 + (0.5 + 1.914*HR)N - 7.656*HR*fo - 1.914*HR + 7.656*HR*sf + Nm£ \quad (13D)$$

Let us define ξdp

$$\xi dp = [(0.5 + 9.57*HR)*\text{ℊ}dp\text{CO}_2 + (0.5 + 5.742*HR)*\text{ℊ}dp\text{CO} - (1 + 3.828*HR)*\text{ℊ}dp\text{H}_2 + 7.656*HR*\text{ℊ}d\text{O}_2 + [0.5(1 - N) + 1.914*HR(1 - N)]*\text{ℊ}dp\text{HCT} + 3.828*HR*\text{ℊ}dp\text{NO}_x] \quad (14D)$$

and

$$¥dp = 0.5 + (0.5 + 1.914*HR)*n - 7.656*HR*fo - 1.914*HR + 7.656*HR*sf + Nm£ \quad (15D)$$

Equation (10D) then becomes

$$\tilde{N}Wp = \tilde{N}dp + \tilde{N}dp*\xi dp + ¥dp$$

or

$$\tilde{N}Wp = \tilde{N}dp[1 + \xi dp] + ¥dp = \frac{\text{Å}\,dp[1 + \xi dp]}{1 - \beta dp} + ¥dp \quad (16D)$$

Development of Expression for $\tilde{N}dgaf$. If we measure the input air and fuel flow rates we will know the mass, but not the molar (volume), flow rate of the exhaust gases. This is because, for a given mass flow rate, the mols of exhaust will depend upon the distribution between gaseous exhaust compounds. Another subtle point is that the measured concentrations change with the presence or absence of particulates.

From equation (3) there are $4.76E$ mols of dry air per mol of CH_n. We can also express the mols of dry air per mol of CH_n as

$$Pda*Vat/(Ro*Ta*Nft*J) = 4.76*E \quad (17D)$$

Combining equations (19) and (17D) gives

$$\tilde{N}dgaf = a + b + d + p + [0.79*(Pa$$

Table D-1 Equations used to develop $\tilde{N}$ expressions

Eq. No.	4-9	10	12	13	15	16	18	19	11D
Characteristic		O	C	CH	OHC	OH	HR	$\tilde{N}d$	H_2O
$\tilde{N}dp$	x				x			x	
$\tilde{N}dg$	x					x		x	
$\tilde{N}dg(CO_2)$	x				x			x	
$\tilde{N}dg(CO)$	x				x			x	
$\tilde{N}dg(HC)$	x				x			x	
$\tilde{N}dgc$	x		x					x	
$\tilde{N}dgO2$	x	x						x	
ξdp	x				x		x		
ξdg	x			x		x	x		x
ξdp	x				x		x		x
ξdg	x			x		x	x		x

The letters O, H, and C indicate the atom balance(s) used in developing the equation listed in that column. (HR means humidity ratio.)

$$-Pw)*Vat]/[Ro*Ta*Nft*J] + 0.5k + sf + fi + z \quad (18D)$$

Again, using equations (4)–(9) and by analogy with equation (4D)

$$Å dgaf = [0.79*(Pa-Pw)*Vat]/[Ro*Ta*Nft*J] + fi + sf \quad (19D)$$

and

$$\beta dgaf = \text{ß}dg\text{CO}_2 + \text{ß}dg\text{CO} + \text{ß}dg\text{H}_2 + \text{ß}dg\text{O}_2 + 0.5*\text{ß}dg\text{NO} + \text{ß}dg\text{HCT} \quad (20D)$$

Development of Other Expressions. Development of other expressions for $\tilde{N}$ follow the same pattern as for $\tilde{N}dp$ and will not be shown. Table D-1 shows the equations used to develop the expressions.

APPENDIX E

Air Fuel and Oxygen Equivalence Ratios

By definition

$$\text{TAF} = \frac{(Nda*28.95) + (18*Nm)}{(12+n) + 32.066*(fo+sf) + (fi*MWi)} \quad (1E)$$

and

$$Nda = 4.76*E \quad (2E)$$

We can solve equation (19) for E to give

$$E = \frac{\tilde{N}d - a - b - d - p - 0.5k - sf - fi - z}{3.76} \quad (3E)$$

$$= [\tilde{N}d[1 - \text{ß}d\text{CO}_2 - \text{ß}d\text{CO} - \text{ß}d\text{H}_2 - \text{ß}d\text{O}_2 - 0.5\text{ß}d\text{NO} - \text{ß}d\text{HCT}] - fi - sf]/3.76$$

Now using the expression from Table 2 and $\beta dgaf$

$$E = [\tilde{N}d[1 - \beta dgaf] - fi - sf]/3.76 \quad (4E)$$

and by definition

$$Nm = Nma + Nm£ \quad (5E)$$

and using equation (18)

$$Nm = 7.656*HR*E + Nm£ \quad (6E)$$

Combining equations (1E), (2E), and (6E) gives

$$\text{TAF} = \frac{36.65[1+HR]*[\tilde{N}d(1-\beta dgaf) - fi - sf] + 18*Nm£}{[12+n] + 32[fo+sf] + [fi*MWI]} \quad (7E)$$

It is obvious from equation (7E) that there will be as many estimates of the total air fuel ratio as there are estimates of $\tilde{N}d$.

By definition, when both fuel and air flow rates are measured

$$\text{TAF} = \frac{Mdat + (Nmt*18)}{Mft} = \frac{\frac{Pda*Vat}{RaTa}*[1+HR] + Nm£*18}{Mft} \quad (8E)$$

Turning now to O_2EQR, by definition

$$O_2\text{EQR} = \frac{O_2act}{O_2s} = \frac{Eact+fo}{Es+fo} \quad (9E)$$

By an oxygen balance for the stoichiometric case

$$Es = 1 + 0.25*n + sf - fo \quad (10E)$$

Equation (4E) above gives the expression for $Eact$ so

$$O_2\text{EQR} = \frac{\tilde{N}d[(1-\beta dgaf) - fi - sf] + fo}{3.76[1 + 0.25*n + sf]} \quad (11E)$$

Emissions From IC Engines Fueled With Alcohol-Gasoline Blends: A Literature Review

Reda M. Bata

Alvon C. Elrod

Richard W. Rice

Clemson University,
College of Engineering,
Clemson, SC 29631

Since air pollution by automotive exhaust gases is of increasing concern around the world, an examination of the work that has been done with regard to evaluating and reducing it can help focus future efforts in dealing with it. Alcohol-containing fuels not only have been shown to have the potential to produce less of many of the polluting gases, but they also constitute a viable alternative to gasoline from the standpoint of efficiency and reducing dependence on the rapidly dwindling supply of petroleum fuel. This report provides a survey of the literature concerning research reported since 1975 on emissions from IC engines operating on alcohol-gasoline fuel blends. The effects of alcohol on the exhaust emissions (carbon monoxide (CO), hydrocarbons (HC), nitrogen oxides (NO_x), and the aldehydes (CHO)) are reviewed. A comparison is made of the emissions benefits achieved when methanol or ethanol is used either in neat form or as the blending agent with gasoline. The primary dependent variable considered is emission level (reported on various bases) with the main independent variables being fuel composition, equivalence ratio, and ignition timing. Brief mention is also made of the potential emissions reduction that may be achieved by using dissociated methanol.

Introduction

Although the currently depressed price of gasoline has, for the moment, lessened the public's interest in the topic of alternative automotive fuels, it is probable that within the next decade the combined incentives of economics and geopolitical independence will necessitate large-scale efforts to supplement the dwindling supply of gasoline with renewable fuels. Of the alternative fuels under consideration, alcohols, specifically, methanol and ethanol, appear to be the prime candidates; and, indeed, Brazil has already made a major commitment to ethanol [1]. The idea of using alcohol as an automotive fuel has been around since the development of the Otto engine nearly a century ago and, although interest in alcohol fuels has been sporadic over the years, an enormous volume of research literature has appeared on the topic [2–4] with much of the emphasis during the past decade being on the potential environmental impact of the use of such fuels. The main focus of this paper is a review of that subset of the literature primarily concerned with emissions from spark ignition internal combustion automobile engines operated on neat alcohol or alcohol/gasoline blends; but, as an aid to understanding, a brief discussion of several background items will be presented first. In the review, a short section concerning dissociated methanol is included.

Fuel-Related Properties. The differences in emission characteristics for alcohols relative to gasoline can be attributed to differences in physical and chemical properties, and most importantly to differences in combustion behavior arising from the latter. In view of this, it is instructive to note some of the ways in which the two main alcohols of interest, i.e., methanol and ethanol, differ from gasoline. The most obvious difference is that, while gasoline is a complex and widely variable mixture of true hydrocarbons, i.e., molecules comprised of only carbon and hydrogen atoms, methanol (CH_3OH) and ethanol (C_2H_5OH) are single species of what might be termed "partially oxidized hydrocarbons." Thus, in a sense, an alcohol might be thought of as the first product of oxidation in a sequence of oxidation reaction steps in which a given hydrocarbon (RH) is first converted to the corresponding alcohol (ROH), then sequentially to the corresponding aldehyde (RCHO) ketone, or carboxylic acid, then, ultimately, to carbon dioxide (CO_2) via carbon monoxide (CO).

The presence of the oxygen atom in molecules of methanol and ethanol coupled with the lower molecular weight (and more importantly the lower carbon number) of these species causes substantially different properties for the alcohols compared to gasoline. Table 1 [2] shows that in the realm of physical properties, the two alcohols are slightly denser than gasoline, they have a lower Reid vapor pressure (RVP), they have a much greater affinity for water, and they have a much higher heat of vaporization. In terms of combustion-related properties, relative to gasoline both alcohols have substantially smaller heating values (on either a mass or volume basis), they have better octane ratings, and they have much lower stoichiometric air/fuel mass ratio values. The last of these is understandable when one compares the stoichiometric equa-

Contributed by the Internal Combustion Engine Division and presented at the Internal Combustion Engine Division Technical Conference, San Antonio, Texas, October 2–5, 1988. Manuscript received by the Internal Combustion Engine Division June 1988.

Table 1 Selected liquid fuel characteristics*

	Gasoline	Methanol	Ethanol
Physical Properties			
Specific Gravity	0.70-0.78	0.796	0.794
Liquid Density (lb/ft³)	≈43.6	48.8	49.3
Vapor Pressure			
psi @ 100°F (Reid)	7-15	4.6	2.5
psi @ 77°F	≈ 0.3	2.31	0.85
Boiling Point (°F)	80-440	149	173
Freezing Point (°F)	≈-70	-144	-173
Water Solubility			
Fuel in H_2O	240 ppm	∞	∞
H_2O in Fuel	88 ppm	∞	∞
Dielectric Constant	1.8-2.6	32.6	24.3
Viscosity @ 100°F, (cst)	0.37	0.47	0.85
Specific Resistivity	2×10^{16}	0.14×10^{6}	0.3×10^{6}
Chemical Properties			
Formula	C_4-C_{12}	CH_3OH	C_2H_5OH
	Mixture		
Molecular Weight	Varies	32.0	46.1
% Carbon	85-88	37.5	52.1
% Hydrogen	12-15	12.6	13.1
% Oxygen	≈0	49.9	34.7
C/H Ratio	5.6-7.4	3.0	4.0
Fuel Vol. % of Vaporized Stoichiometric Mixture	2.1	12.3	6.5
Stoichiometric A/F Ratio	14.2-15.1	6.4	9.0
Thermal Properties			
Lower Heating Value			
Btu/lb	18,900 (Avg)	8,600	11,500
Btu/gal	115,400 (Avg)	56,560	75,670
Heat of Vaporization			
Btu/lb	≈150	506	396
Btu/gal	900	3,340	3,378
Octane Ratings			
Research	91-105	106-108	106-108
Pump	87-98	99-101	98-101
Flammability Limits			
(% by Vol. in Air)	1.4-7.6	6.7-36.0	4.3-19.0
Btu/ft³ @ Stoich. A/F; 60°F; one atm; Gaseous Reactants (Btu/ft³)	95	87.3	93.8
Specific Heat			
Btu/lb °F	0.48	0.60	0.60
Autoignition Temp. (°F)	450-900	878	685
Flash Point (°F)	-50	52	70

*Reproduced from reference no. 2.

tion for combustion of methanol with that for a representative gasoline component such as iso-octane (C_8H_{18}, MW = 114):

$$CH_3OH + 1.5\ O_2 \rightarrow CO_2 + 2\ H_2O$$
$$C_8H_{18} + 12.5\ O_2 \rightarrow 8\ CO_2 + 9\ H_2O$$

Although differences in alcohol and gasoline properties have important implications for fuel system and engine design/operation, e.g., the alcohol's high affinity for water has the potential to cause phase-separation-corrosion problems, only those properties that directly influence emissions will be examined further. The vapor pressure of pure methanol or ethanol is lower than that of gasoline in spite of the alcohol's lower molecular weight because of hydrogen bonding between hydroxyl groups. Thus for alcohols in pure form evaporative emissions from the fuel system would be expected to be lower than for gasoline. On the other hand, blending alcohol with gasoline, which is composed of nonpolar species, disperses the polar alcohol molecules, disrupting the stabilizing hydrogen bonding network and causing the alcohols then to behave as if their vapor pressure was much higher. This increases the apparent vapor pressure of the blend above that of gasoline [5], with a maximum value reached at an alcohol volume percent value of about 5 to 10 percent. Because of this increased volatility, evaporative emissions from such fuel blends would be expected to be higher than for gasoline. The much higher heat of vaporization for alcohols relative to gasoline has been observed to cause a fuel delivery (air-fuel mixture preparation) problem in conventional carburetion systems [6, 7] due to the fact that, on an equal fuel energy basis, more than eight times as much heat is required to vaporize methanol as gasoline [4]. For this reason the use of pure alcohols or high-alcohol-content blends would require fuel system modifications in order to achieve optimal engine performance [8] from both drivability and emissions points of view. The related issues of higher heat of vaporization and

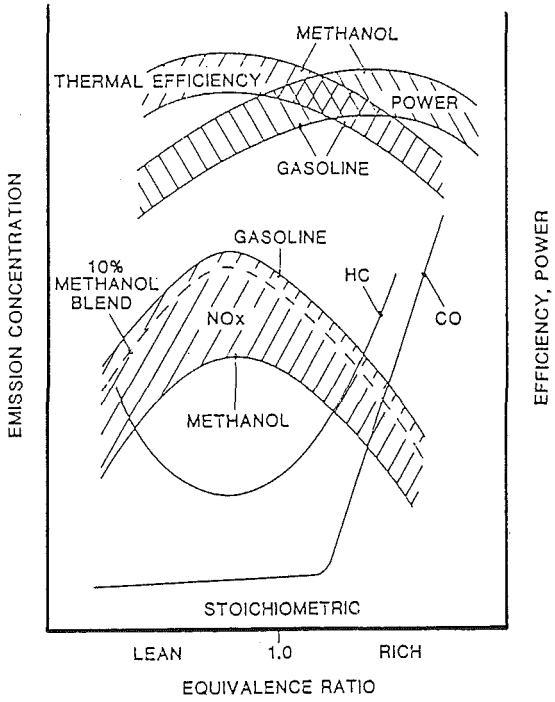

Fig. 1 Effects of alcohol fuels on engine emissions and performance [2]

fuel delivery system adjustments when alcohols are used are intertwined with the very important issues of air-fuel ratio and peak flame temperature, and these last two parameters have a major influence on an engine's exhaust emissions. The quantity "equivalence ratio" ϕ is defined as

$$\phi = \frac{\text{actual fuel/air ratio}}{\text{stoichiometric fuel/air ratio}}$$

The terms lean and rich are used to refer to operation when $\phi < 1$ and $\phi > 1$, respectively. It is clear from the stoichiometric equations for combustion of alcohol and gasoline that, for a given volumetric intake of a fuel vapor and air mixture, increasing the alcohol content of the fuel will have a "leaning" effect on the engine. One consequence of this effect, i.e., of providing more oxygen relative to fuel than would be the case for gasoline alone, is more complete combustion and thus a lowering of carbon monoxide (CO) emissions in the case of alcohol-gasoline blends relative to gasoline.

Hydrocarbon (HC) and nitrogen oxides (NO_x) emissions are also sensitive to equivalence ratio, but, as shown in Fig. 1 [2], the relationship is more complex, with maxima or minima occurring for near-stoichiometric mixtures. The nitrogen oxides, primarily NO and NO_2, are formed from reactions such as

$$N + O_2 \rightleftarrows NO + O$$
$$N_2 + O \rightleftarrows NO + N$$
$$NO + 1/2O_2 \rightleftarrows NO_2$$

in which small concentrations of nitrogen and oxygen atoms resulting from molecular dissociation at high temperature react with O_2 and N_2, respectively, to form nitric oxide (NO), which can later be further oxidized to nitrogen dioxide (NO_2). Because the formation reactions for NO are relatively slow, the reactions do not reach equilibrium during an engine cycle; thus the formation rate for NO, the major constituent of what is termed NO_x, is governed by kinetics rather than equilibrium and, consequently, is very strongly temperature dependent. The decrease in NO_x in the lean region as equivalence ratio is

decreased is a reflection of the lowering of peak combustion temperature due to dilution with air [9]. In the rich region an increase in equivalence ratio results in a decrease in NO_x because the reaction becomes progressively starved for oxygen. As shown in Table 1, the "energy density" in Btu/ft^3 of a stoichiometric alcohol–air fuel charge is somewhat less than that for gasoline and this results in lower flame temperatures, which, theoretically, should result in lower NO emissions, particularly in the fuel lean region, e.g., $\phi < 0.9$. Although the results depicted in Fig. 1 indicate a lowering of NO_x for alcohol at all equivalence ratios, experimental results from some studies have shown higher NO_x for methanol compared to gasoline in the rich region [9, 10]. Because most of the organic emissions from an engine operating on alcohols are oxygenated species, i.e., alcohol and aldehydes, which, as mentioned earlier, are technically not "true hydrocarbons," comparisons of organic emissions results for neat alcohol or alcohol–gasoline blend fueled engines with those for gasoline-fueled engines are not straightforward [10]. For this reason the term unburned fuel (UBF) has gained increasing use. A further complication in comparing organic emissions for oxygenated species versus true hydrocarbons is the often significant difference in flame ionization detector (FID) sensitivity for alcohols and aldehydes relative to hydrocarbons [7, 12–14]. Failure to recognize this and to determine relative response factors properly has presumably contributed to the wide variation in results reported for UBF and/or FID-determined aldehyde emissions from vehicles operated on alcohol-containing fuels [6, 15, 16]. Most investigations of emissions have dealt with the regulated pollutants, CO, NO_x, and total hydrocarbons (or unburned fuel), and many have measured aldehyde emissions. Only infrequently have data been reported on individual hydrocarbons, particulates, sulfur-containing species, ammonia, amines, etc. [11].

Emissions Measurement Methods. Over the years emissions testing has involved numerous procedures, and this has often made accurate quantitative comparison of data from different sources difficult, if not impossible. However, within the current decade progress toward standardization of test procedures has been made in the United States with the widespread adoption of the Sealed Housing for Evaporative Determination (SHED) procedure for evaporative emissions and the Federal Test Procedure (FTP) for tailpipe exhaust emissions [17].

In some instances, continuous exhaust monitoring [3] has been employed in addition to the standard practice of bag sampling. Typically, carbon monoxide and carbon dioxide are measured using nondispersive infrared analyzers, nitrogen oxides are monitored via a chemiluminescence analyzer, and total hydrocarbons are measured using a flame ionization detector. For determination of individual hydrocarbon concentrations or for distinguishing alcohol from hydrocarbons, one generally uses a gas chromatograph equipped with suitably chosen column(s) and a flame ionization detector. As mentioned earlier, FID response factors for oxygenated hydrocarbon species are significantly different from those for true hydrocarbons, thus calibration of the detector using pure components or a prepared standard mixture is necessary for accurate analysis.

Because aldehyde emissions from combustion of alcohol-containing fuels typically are appreciably higher than for gasoline, interest in measurement techniques for aldehydes has increased along with interest in alcohol utilization as an automotive fuel component. One reason that aldehyde analysis has required a special technique is that formaldehyde (CH_2O), the most abundant aldehyde in the exhaust from methanol or methanol-gasoline blends [8, 18] is essentially nondetectable by an FID [6]. One of the most commonly employed methods for total aldehyde determination involves passing a small stream of diluted exhaust gas through a heated sampling tube followed by a series of scrubbers or midget impingers [13, 19] containing an aqueous solution of 3-methyl-2-benzothiazalone hydrozone (MBTH) to trap aliphatic aldehydes. Aldehydes, computed as formaldehyde, are then determined by a colorimetric procedure [20, 21]. An alternative technique [12, 22] involves passing the gas sample through impingers containing an acetonitrile solution of 2, 4-dinitrophenylhydrazine (DNPH) and a catalyst, e.g., hydrochloric acid, then analysis via high-pressure liquid chromatography (HPLC).

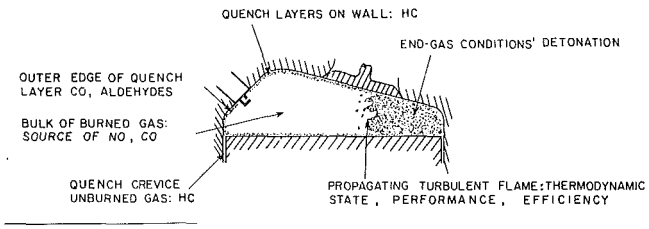

Fig. 2 Schematic of spark-ignition engine combustion process [24]

Review of Emissions Literature

The complete combustion process in an IC engine is very difficult to model. The combustion process is initiated with premixed air and fuel in a three-dimensional, time-varying, turbulent flow. The air–fuel mixture is composed of hundreds of different organic compounds and the combustion reactions occur in a variable volume combustion chamber; thus it is obvious that the process is exceedingly complicated [23–26]. Heywood [23, 24] has presented an excellent review about the formation and control of the exhaust pollutants. The engine combustion process also was modeled and discussed in terms of three major topics:

1 Engine efficiency;

2 Engine emissions, including unburned fuel hydrocarbons, carbon monoxide, nitrogen oxides, particulates, polycyclic aromatic hydrocarbons, aldehydes, odor, and noise;

3 Detonation.

Figure 2 [24] illustrates some of the interrelations among these features.

Combustion efficiency depends on the flame propagation process, which affects the rate of combustion. Hydrocarbons predominate in the low-temperature quench regions adjacent to the water jacket. Carbon monoxide originates in the bulk burned gas for fuel-rich mixtures. Nitrogen oxides also originate in the bulk burned-gas region behind the flame. Aldehydes originate in the outer edges of the quench regions. Detonation is controlled by the end-gas condition and the fuel characteristics.

The exhaust emissions (HC, CO, NO_x) were correlated to the fuel/air equivalence ratio, which is one of the most important variables. The correlation revealed that production of pollutants can be reduced [27–29] by operating at increasingly leaner mixtures until the combustion process starts to deteriorate and misfire occurs. The exhaust gas concentration for each species depends on engine design and operating conditions, but the following values are representative: hydrocarbons (HC), 3000 ppm as light HC or 25 g/kg of fuel; carbon monoxide (CO) 1 to 2 percent or 200 g/kg of fuel; and nitrogen oxides ($NO_x = NO +$ a small amount of NO_2) 500 to 1000 ppm or 20 g/kg of fuel [30].

The following review of the literature is structured such that all of the results for a given exhaust species, e.g., carbon monoxide, are presented together. In compiling the review the following reference databases were surveyed: Society of Automotive Engineers (SAE), U.S. Department of Energy (DOE), U.S. Environmental Protection Agency (EPA),

Table 2 Exhaust emission rates (g/mi) and fuel economy (mi/gal) for a 1981 Volkswagen Rabbit on neat methanol and 5.5 mass percent isopentane/methanol [35]†

TEST PHASE	METHANOL				
	CO	* UBF **		NO_x	MPG
COLD TRANSIENT	5	2.8	1.4	0.95	10.5
STABILIZED	0	0	0	0.4	11.6
HOT TRANSIENT	0	0.14	0.08	0.57	12.6
COMBINED FTP	1.1	0.7	0.4	0.54	11.6
FEDERAL STANDARD	9	.41		1.0	-

TEST PHASE	METHANOL-ISOPENTANE				
	CO	* UBF **		NO_x	MPG
COLD TRANSIENT	7	3.0	1.4	0.8	12
STABILIZED	1	0.04	0.03	0.4	11
HOT TRANSIENT	1	0.5	0.3	0.41	13
COMBINED FTP	2	0.7	0.4	0.5	12
FEDERAL STANDARD	9	.41		1.0	-

*Including oxygen.
**Not including oxygen.

†The number of significant figures in the table reflects the experimental uncertainty of the data.

American Society of Mechanical Engineers (ASME), National Technical Information Service (NTIS), and Cambridge Scientific Abstract.

Hydrocarbon (HC) Emissions. Over the years, the relationship between exhaust hydrocarbon (HC) or unburned fuel (UBF) levels in SI engine exhaust and both fuel properties and engine operating conditions have been studied for a variety of alcohol-gasoline blends. Allsup [31] used ten 1974/75 model cars following the Federal Test Procedure (FTP) [32, 33] to study the effect of ambient temperature on the exhaust emissions of the cars when fueled with methanol–gasoline blends. He examined both an indolene base fuel and a commercial base fuel blended with 5 and 10 percent methanol. Unburned fuel emissions generally increased with an increase in the ambient temperature and percent of methanol in the blend [34]. The increase in HC emissions was mainly due to the unburned fuel.

In another study two cars, a 1980 Ford Pinto and a 1981 Volkswagen Rabbit, each equipped with three-way catalysts and feedback-controlled carburetors, were tested [35]. Two fuels were used, neat methanol and a 94.5 mass percent methanol–5.5 mass percent isopentane blend. The study was designed to investigate the problems of cold starting and warm-up drivability associated with the high heat of vaporization and low vapor pressure of the alcohol fuels. The experimental work was conducted according to the FTP [17]. The results are cited in Table 2 [35]. In a continuation of this experimental work [36] it was observed that the production of UBF was higher than for gasoline and exceeded the current standard of 0.41 g total HC emitted per mile for both cars.

A Volvo car equipped with a three-way conversion (TWC) catalyst and a closed-loop feedback-controlled air/fuel metering system (to provide a near stoichiometric air/fuel ratio) was tested by Mooney [37]. The test fuels were ethanol–gasoline blends containing up to 30 percent ethanol. Hydrocarbon emissions were below the permissible concentrations. The effects of the oxygen sensor and catalyst on exhaust emissions were also studied [38]. Engines of a Volvo 244DL and a Chevrolet Monza were used for testing the effects of cold starting, sensitivity to water-induced phase separation in winter, and vehicle compatibility (F/A ratio and use of methanol). The emission control system successfully reduced the HC emissions for the 45 percent methanol/55 percent gasoline blend used, which demonstrated that the catalyst functioned well when this alternative fuel was used. Furey and King [5, 39] tested two alcohol–gasoline fuels (A-10, 6.7 percent by volume methanol + 3.3 percent butanol + 90 percent gasoline and A-18, 12 percent by volume methanol + 6 percent butanol + 82 percent gasoline) using 1981 and 1980 model GM cars. The hydrocarbon emissions for both A-10 and A-18 for the closed loop cars were the same as for the base gasoline. This contrasts only slightly with a 5 to 27 percent reduction with 10 percent methanol (M-10) reported by Stamper [40]. The evaporative emissions of A-10 fuel were 41–44 percent higher than for gasoline and for A-18 were 26–30 percent higher than for gasoline. In other studies [40, 41], involving a 10 volume percent methanol/90 percent gasoline blend, the evaporative emissions were 92 to 130 percent of the value for gasoline. In experimental work conducted by the Coordinating Research Council [19], fourteen 1980 model cars and three fuels were used: ET-1 (10 percent ethanol), ET-2 (10 percent ethanol with C_4 reduced to match the RVP of gasoline), and ET-3 (10 percent ethanol with C_4 and C_5 reduced to match both RVP and percent vaporization at 70°C). Fuel ET-1 produced 65 percent more evaporative emissions than the base gasoline. In another study [42] with methanol (M-15) UBF (HC) emissions were 10 percent lower than for gasoline.

Using 100 percent methanol (M-100) with two 1981 VW Rabbits and two 1981 Ford Escorts, following the FTP resulted in higher HC emissions than for gasoline [11, 43, 44]. Based on the highway fuel economy test (HFET), the HC emissions were less than those for the base gasoline. In West German tests on sixteen different engines from six different car manufacturers [45] the HC emissions were 6.7 percent lower without a catalyst using a 15 percent methanol–gasoline blend (M-15). A Mercedes car without a catalyst and fueled with 100 percent methanol produced 70 percent lower HC emissions, while for a Volkswagen vehicle HC was 85 percent lower. Running a fleet of eleven 1976–1981 model vehicles with 4.5 percent methanol, 4.5 percent tert-butyl alcohol, and 91 percent gasoline, HC emissions were lower than or equal to the base gasoline fuel [46]. In Brazil when eight vehicles were tested with pure ethanol (E-100) and six vehicles were tested with "pure" gasoline, HC emissions were 69 percent lower with E-100 fuel than with gasoline fuel [1].

Carbon Monoxide (CO) Emissions. The effect of alcohol

fuels on the production of the carbon monoxide was very clear in all of the articles reviewed. When alcohol was used as an automotive fuel, the emission level of CO was reduced dramatically [47–52] compared to that when pure gasoline fuel was used, due in major part to the aforementioned "leaning" effect related to the "partially pre-oxidized" nature of the alcohol fuel relative to gasoline hydrocarbons. From the experimental work of Espinola et al. [35] on a Ford Pinto and a VW Rabbit, with neat methanol and 5 percent (mass) isopentane–ethanol fuels, Table 2 shows that CO emissions from the Ford Pinto were within the current 9 g/mi requirement, despite the fact that car was running slightly rich and at a lower than optimal temperature. For the VW Rabbit, CO production was far below the standard production from base gasoline. Experimental work was conducted under the same low ambient temperature condition on four 1983 Ford Escorts by the Oakville Research Center (ORC) [53]. The fuels used were 15 percent super unleaded gasoline/85 percent methanol, 2 percent butane/8 percent lighting naphtha/90 percent methanol, and 10 percent super unleaded gasoline/5 percent dimethylether and 85 percent methanol. Over the ambient temperature range studied (−10°C to 25°C), the rate of CO emission decreased with increasing temperature, but the levels of CO at low temperatures were similar to levels with gasoline-powered vehicles in a previous work. The same trend was cited by several other authors [38, 54–56]. Other results [11] showed that, while one car with M-100 had 34 percent greater CO emissions, another car emitted 14 percent less CO than the base gasoline based on FTP. However, both cars showed lower CO emissions for methanol fuel based on the HFET. The FTP-based CO "engine-out" (before the catalyst) emissions reported by Publow and Grinberg [42] for a 15 percent methanol/85 percent gasoline blend fuel, i.e., M-15, were 15 to 33 percent lower. These results are similar to those reported by Wolff et al. [45] in which the reduction in tailpipe CO emissions for methanol/gasoline relative to gasoline was in the range of 26–50 percent. The production of CO from another fleet test [46] with a 4.5 percent methanol/4.5 percent gasoline grade tert-butyl alcohol/91 percent gasoline blend was lower than or equal to that of gasoline fuel. Using a 10 percent ethanol–gasoline blend, Miller et al. [46] observed that production of CO was 20–40 percent lower compared to gasoline fuel. In Brazil [1], tests with neat ethanol (E-100) showed that production of CO was 60 percent less than for gasoline under the same conditions.

Emissions of Nitrogen Oxides (NO_x). It is known that nitrogen oxides present in automobile exhaust gases are due to reaction of molecular oxygen and nitrogen with N or O atoms, respectively, resulting from dissociation of N_2 and O_2 [57–61]. The concentration of nitrogen dioxide (NO_2) in the exhaust gases is very small compared with that of nitric oxide (NO) for spark ignition engines, but in diesel engines NO_2 represents 10 to 30 percent of the total nitrogen oxides (NO_x) [62, 63]. The production of NO_x depends on many different parameters, e.g., air/fuel ratio, crank angle, temperature of the combustion chamber, and the residual gas in the combustion chamber. In experiments conducted by Espinola [35] using neat methanol and isopentane–methanol fuels, the NO_x emissions were below the standard value of 0.1 g/mi. The production of NO_2 is affected by the increase in UBF emissions [64], but this was not clear in the work. A continuation of this work was conducted by Stephen et al. [65] to measure the exhaust gases' photochemical reactivity, which was based on the rate of formation of NO_2. Three cars were used in this work: a 1980 Toyota Cressida, a 1980 Ford Escort, and a 1980 VW Rabbit, all equipped with a three-way-catalyst (TWC). The photochemical reactivities were reported as relative reactivity per gram of hydrocarbon [65]. Jackson [66] reported an average reactivity of FTP unburned gasoline fuel emissions of 0.0339/g for catalyst-equipped vehicles, while for methanol and ethanol the corresponding values were 0.0037/g and 0.0083/g, respectively. To put the comparison on a more suitable basis, the photochemical reactivities for the methanol and ethanol fuels were adjusted by excluding the oxygen atom in the alcohols from the calculation, i.e., going from a basis of 1 g of UBF to the revised basis of 1 g of HC only, and reactivities became 0.0075/g and 0.0127/g, which were still less than that for gasoline exhaust. When a 1982 Toyota Cressida equipped with multipoint electronic fuel injection (EFI) and a TWC was used in a study by Saito and Pefley [67], the results showed an increase in the production of the postcatalyst NO_x emissions with increasing percentage of methanol at both high and low compression ratios (CR) [53]. This finding was due to a mismatch between engine air–fuel ratio control parameters, oxygen sensor output, and the NO_x conversion efficiency of the catalyst. In another work by Mitchell [53], the NO_x emissions for different alcohol fuels tested at low ambient temperatures were comparable to those for gasoline. The production of NO_x for different vehicles fueled by methanol fuel synthesized from coal were less than that for gasoline fuel [68]. A study was conducted by Schrock and Clark [69] on a four-cylinder Renault engine running at 3500 rpm and wide open throttle (WOT). Two fuels were used: (1) gasoline and (2) a blend (called Blend 1) consisting of 51 weight percent *n*-butanol, 25 percent acetone, 18 percent water, and 6 percent ethanol. For the blend the NO_x emissions were substantially lower than those for gasoline fuel. The highest value of NO_x emissions from Blend 1 was 1610 ppm at an equivalence ratio ϕ of 0.92 compared to 2880 ppm for gasoline at $\phi = 0.99$. The concentration of NO_x was expected to peak at $\phi \approx 0.9$ [70].

Aldehyde Emissions. In the originally developed U.S. automobile emissions standards aldehydes, unlike hydrocarbons, were not designated as a regulated pollutant species, presumably because total aldehyde emissions levels in exhaust gases from gasoline-fueled IC engines are relatively small. Vehicles without exhaust control systems typically show 100 to 280 ppm aldehydes in the exhaust from gasoline-fueled vehicles based on the California standard test procedure [71]. However, aldehydes are one of the products of the photochemical reaction between hydrocarbons and nitrogen oxides and they are considered to be a cause of eye irritation associated with the phenomenon called "smog" [18, 64, 72, 73]. Because of their high photochemical reactivity, aldehydes are now viewed by many researchers as prime smog precursors [74, 75]. For this reason and because various studies [50, 76–79] have shown that aldehyde emissions are greater for alcohol fuels than for gasoline, research interest in this topic has paralleled interest in alcohol fuels. Aldehydes are mainly formed via partial oxidation of fuel remaining after flame extinction. The oxidation process of ethanol at low temperature (270–370°C) will produce acetaldehyde as an initial product [80] and the oxidation of methanol will produce formaldehyde as an intermediate product [81]. By way of contrast, the hydrocarbon fuel oxidation process is believed to occur through two paths, only one of which involves formation of aldehyde, thus the production of aldehyde should be greater with alcohol fuels than with gasoline [77, 78, 82].

Oberdorfer [18] found experimentally that the most influential factor affecting the production of aldehydes in automotive systems is the air/fuel ratio. Brinkman [82] conducted experimental work on a single-cylinder engine fueled with neat ethanol. Some of his results are illustrated in Fig. 3, showing that aldehyde emissions increased with increasing compression ratio, and were lowest at an A/F ratio near stoichiometric, i.e., increased as the mixtures were either enriched or leaned. Aldehyde emissions were 100–360 percent of those of gasoline fuel and this finding agrees with others [61, 83, 84]. Last et al. [38] used methanol–gasoline blends and found the same trend:

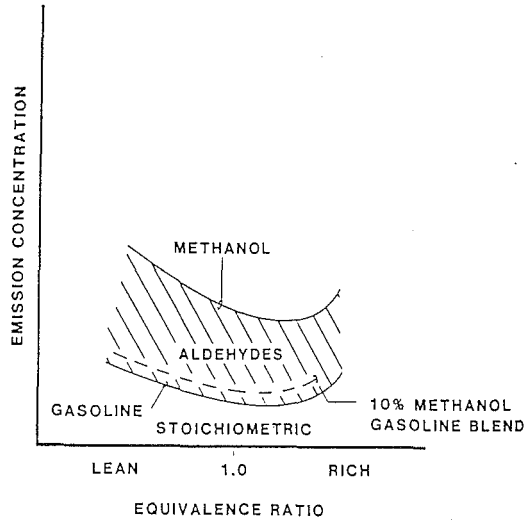

Fig. 3 Influence of fuel-air equivalence ratio on aldehyde emissions from spark ignition engines [82]

Aldehyde emissions increased with increased percentage of methanol in the blends. The same finding was also cited by others [85-87]. Alcohol fuel used in heavy-duty engines also produced high aldehyde levels [88, 89].

Emissions From Dissociated Methanol Powered IC Engines. While alcohol fuels have certain advantages over gasoline when used either as pure alcohol or in a blend with gasoline, these advantages are improved markedly when the alcohol is dissociated (decomposed) to provide a gaseous fuel that is almost entirely hydrogen and carbon monoxide [90-99]. Two processes are being investigated for the production of "energy enhanced" alcohol. The first involves evaporation of the alcohol using engine waste heat in the cooling water and then catalytically dissociating the alcohol while supplying energy from the exhaust gases for this endothermic reaction. The second involves evaporation and then steam reforming of the alcohol to produce hydrogen and carbon monoxide or hydrogen and carbon dioxide (this also is an endothermic reaction which makes use of the engine's waste heat). Special catalysts have been developed to facilitate the dissociation of methanol for producing this fuel. Both Yoon et al. [100] and Kikuchi et al. [101] have reported the development of catalysts that produce almost complete dissociation of methanol at temperatures compatible with the use of engine exhaust gas energy as the energy source for the endothermic reaction (temperatures up to about 380°C). The advantages of this energy-enhanced fuel include:

- the direct increase of the heating value of the fuel because the process is endothermic;
- the production of a hydrogen-rich fuel that allows a higher engine compression ratio with its attendant higher thermal efficiency;
- this hydrogen-enriched fuel is capable of good combustion characteristics when in a very lean fuel/air mixture (over 200 percent excess air);
- the use of large amounts of excess air results in reduced flame temperatures and consequently lesser amounts of polluting emissions, notably carbon monoxide and oxides of nitrogen, in the exhaust products.

In the context of this review, it is obvious that the last two of the advantages cited are the most relevant, but at present little specific information has been published concerning emissions from engines operating on dissociated methanol.

Summary and Conclusions

In reviewing the literature concerned with emissions from IC engines fueled with alcohol or alcohol-gasoline blends several general observations can be made. There appears to be widespread agreement that, relative to gasoline, alcohol-containing fuels have the positive feature of generating less carbon monoxide when combusted. This is primarily attributed to the "leaning effect" of the alcohol. On the other hand, there is a near consensus that alcohol fuels have the negative feature of causing higher aldehyde emissions. For hydrocarbon and nitrogen oxides emissions the picture is somewhat ambiguous, with some researchers reporting lower HC and/or NO_x emissions for alcohol-containing fuels, while others report higher emissions levels for these species. In most cases the percentage differences in NO_x and true HC releases for alcohol fuels and gasoline were relatively modest. Because alcohols are "oxygenated hydrocarbons," comparisons based on unburned fuel (UBF) are perhaps more relevant than those based on just FID-determined hydrocarbons and in the majority of the cases reported UBF was slightly higher for alcohols. Much of the apparent inconsistency or discrepancy in NO_x and HC (or UBF) emissions comparisons for alcohol versus gasoline among the various investigations may be attributed to differences in test procedures, emissions control equipment, and engine operating parameters, particularly the equivalence ratio. Finally, brief mention was made of articles concerned with the potential of dissociated methanol as a fuel that could achieve a substantial lowering of polluting emissions.

References

1 Szwarc, A., and Branco, G. M., "Automotive Use of Alcohol in Brazil and Air Pollution Related Aspects," SAE Paper No. 850390, 1985.

2 McCallum, P. W., Timbario, T. J., Bechtold, R. L., and Ecklund, E. E., "Alcohol Fuels for Highway Vehicles," *Chemical Engineering Progress*, Aug. 1982, pp. 52-59.

3 Pischinger, F. F., "International Outlook of Otto Versus Diesel Cycle Engine for Operation on Biomass Fuels," *Proceedings of the Fourth International Symposium on Alcohol Fuels Technology*, Sao Paolo, Brazil, Oct. 1980, pp. 935-944.

4 Hagen, D. L., "Methanol as a Fuel: A Review With Bibliography," SAE Paper No. 770792, 1977.

5 Furey, R. L., and King, J. B., "Emissions, Fuel Economy, and Driveability Effects of Methanol/Butanol/Gasoline Fuel Blends," SAE Paper No. 821188, 1982.

6 Hilden, D. L., and Parks, F. B., "A Single-Cylinder Engine Study of Methanol Fuel—Emphasis on Organic Emissions," SAE Paper No. 760378, 1976.

7 Wigg, E. E., and Lunt, R. S., "Methanol as a Gasoline Extender—Fuel Economy, Emissions and High Temperature Driveability," SAE Paper No. 741008, 1974.

8 Adelman, H. G., Andrews, D. G., and Devoto, R. S., "Exhaust Emissions From a Methanol-Fueled Automobile," SAE Paper No. 720693, 1972.

9 Most, W. J., and Longwell, J. P., "Single-Cylinder Engine Evaluation of Methanol-Improved Energy Economy and Reduced NO_x," SAE Paper No. 750119, 1975.

10 Lorusso, J. A., and Tabaczinski, R. J., "Combustion and Emissions Characteristics of Methanol, Methanol-Water, and Gasoline-Methanol Blends in a Spark Ignition Engine," *Proceedings of the Eleventh Intersociety Energy Conv. Eng. Conf.*, Vol. I, Sept. 1976, pp. 122-132.

11 Alson, J., and Baines, T. M., "Emissions and Energy Efficiency Characteristics of Methanol-Fueled Engines and Vehicles," *Proc. of Third Symposium on Non-Petroleum Vehicular Fuels*, Arlington, VA, 1982, pp. 399-431.

12 Waring, P., Kappatos, D. C., Galvin, M., Hamilton, B., and Joe, A., "The Application of Formaldehyde Emission Measurement to the Calibration of Engines Using Methanol as Fuel," *Proc. of the Sixth International Symposium on Alcohol Fuels Technology*, Ottawa, May 1984, Vol. II, pp. 53-60.

13 Edwards, C. F., and Baisley, W. H., "Emission Characteristics of Methanol Fueled Vehicles Using Feedback Carburation and Three Way Catalysts," SAE Paper No. 811221, 1981.

14 DeJovine, J. M., "Emission System Durability With Methanol Blended Gasoline," *Proc. of Seventh International Symposium on Alcohol Fuels*, Paris, Oct. 1986, Vol. 2, pp. 163-168.

15 Bernhardt, W. E., "Engine Performance and Exhaust Emissions Characteristics From a Methanol-Fueled Automobile," presented at 1975 GMR Symposium (Future Automotive Fuels—Prospects, Performance and Perspective), Warren, MI, Oct. 1975.

16 Cassady, P. E., "The Use of Methanol as a Motor Vehicle Fuel," *Proc. 169th Am. Chem. Soc. Nat'l Mtg.*, Philadelphia, PA, Apr. 1975.

17 Environmental Protection Agency, "Code of Federal Regulations," Title 40, Parts 60-99, 1978.

18 Oberdorfer, P. E., "The Determination of Aldehydes in Automobile Exhaust Gas," SAE Paper No. 670123, 1967.

19 Bernstein, L. S., Brinkman, N. D., and Carlson, R. R., "Performance Evaluation of 10 percent Ethanol-Gasoline Blends in 1980 Model Year U.S. Cars," SAE Paper No. 821185, 1982.

20 Cummins, R. L., and Hauser, T. R., "Determination of MBTH Colorimetric Aldehydes," *Anal. Chem.*, Vol. 36, 1964, p. 681.

21 Sawicki, E., Hauser, T. R., Stanley, T. W., and Elbert, W., "The Three-Methyl-Two-Benzothiazolone Test," *Anal. Chem.*, Vol. 33, 1961, p. 93.

22 Lipari, F., and Swarin, S. J., "An Improved 2, 4-Dinitrophenylhydrazine Method for the Determination of Formaldehyde and Other Aldehyde Species," General Motors Research Publication 3617, Apr. 1981.

23 Heywood, J. B., "Pollutant Formation and Control in Spark Ignition Engines," *Prog. Energy Combustion Sci.*, Vol. 1, 1976, p. 135.

24 Heywood, J. B., "Engine Combustion Modeling—An Overview," *Proc. Symposium on Combustion Modeling in Reciprocating Engines*, GM Research Laboratories, MIT, Cambridge, MA, 1978.

25 Mattavi, J. N., and Amann, C. A., *Combustion Modeling in Reciprocating Engines*, Plenum Press Inc., New York, 1980.

26 Newhall, H. K., "The Kinetics of Pollutant Formation in Spark-Ignition Engines," in: *Engine Emissions*, G. S. Springer and D. J. Patterson, eds., Plenum Press, New York, 1973, p. 167.

27 Wuebben, P., Smith, K. D., and Cackette, T., "Fuel Methanol: An Air Quality Strategy Based on Petroleum Displacement," *Seventh International Symposium on Alcohol Fuels*, Paris, Oct. 1986, Vol. 2, pp. 147-158.

28 Subrahmanyam, J. P., Mathur, H. B., and Gajendra Babu, M. K., "Studies on a Methanol Fueled Spark Ignition Engine With Exhaust Gas Recirculation," *Seventh International Symposium on Alcohol Fuels*, Paris, Oct. 1986, Vol. 1, pp. 130-135.

29 Ingamells, J. C., and Lindguist, R. H., "Methanol as a Motor Fuel or a Gasoline Blending Component," SAE Paper No. 750123, 1975.

30 Heywood, J. B., "Internal Combustion Engine Fundamentals," McGraw-Hill, New York, 1988.

31 Allsup, J. R., "Methanol Gasoline Blends as Automotive Fuel," SAE Paper No. 750763, 1975.

32 Environmental Protection Agency, "New Motor Vehicles and New Motor Vehicle Engines," Federal Register, Part II, Vol. 37, No. 221, Nov. 15, 1972.

33 Coordinating Research Council, "Research Technique for Determinations of Octane Number Requirements of Passenger Cars," CRC Designation E-15-73, Jan. 1973.

34 Johnson, R. T., and Riley, R. K., "Evaluation of Methyl Alcohol as a Vehicle Fuel Extender," Final Report DOT-TST-76-50, Aug. 1975.

35 Espinola, E. A., Tamura, A. T., Nebolon, J. F., and Pefley, R. K., "The Effect of Fuel Additives on Alcohol Exhaust and Evaporative Emissions," 75th Annual Meeting of the Air Pollution Control Division.

36 Espinola, E. A., and Pefley, R. K., "Alternative Fuels Influences on Emission Test Procedures," Symposium on Chemistry of Oxygenates in Fuels, Kansas City, Sept. 12-17, 1982.

37 Mooney, J. J., Hansel, J. G., and Burns, K. R., "Three-Way Conversion Catalysts on Vehicles Fueled With Ethanol-Gasoline Mixtures," SAE Paper No. 790428, 1979.

38 Last, A. J., et al., "Oxygen Sensor Equipped Engine Operation on Methanol-Gasoline Blends and Phase Separation Problems," Fourth International Symposium on Alcohol Fuels, Guaraji, Brazil, Oct. 5-8, 1980.

39 Furey, R. L., and King, J. B., "Evaporative and Exhaust Emission From Cars Fueled With Gasoline Containing Ethanol or Methyl tert-Butyl Ether," SAE Paper No. 800261, 1980.

40 Stamper, K. R., "Evaporative Emissions From Vehicles Operating on Methanol-Gasoline Blends," SAE Paper No. 801360, 1980.

41 Naman, T. M., and Allsup, J. R., "Exhaust and Evaporative Emissions From Alcohol and Ether Fuel Blends," SAE Paper No. 800858, 1980.

42 Publow, G., and Grinberg, L., "Performance of Late Model Cars With Gasoline-Methanol Fuel," SAE Paper No. 780948, 1978.

43 Menrad, H., Lee, W., and Bernhardt, W., "Development of a Pure Methanol Fuel Car," SAE Paper No. 770790, 1977.

44 Brinkman, N. D., "Vehicle Evaluation of Neat Methanol—Compromises Among Exhaust Emissions, Fuel Economy, and Driveability," *Energy Research*, Vol. 3, 1979.

45 Wolff, H. C., Bandel, J. P., and Seidel, G. H., "German Test Field Test Results on Methanol Fuels M-100 and M-15," *American Petroleum Institute, Refining Department, Proceedings*, Vol. 62, 1983, pp. 176-195.

46 Miller, D. J., Drake, D. A., DeJovine, J. M., and Yoges, G., "Material Compatability and Durability of Vehicles With Methanol-Gasoline Grade Tertiary Butyl Alcohol Gasoline Blends," SAE Paper No. 841383, 1984.

47 Baisley, W. H., and Edwards, C. F., "Emission and Wear Characteristics of an Alcohol Fueled Fleet Using Feedback Carburation and Three-Way Catalysts," Fourth International Symposium on Alcohol Fuels Technology, Brazil, Oct. 5-8, 1980.

48 Bata, R. M., and Roan, V. P., "Effects of Ethanol and/or Methanol in Alcohol-Gasoline Blends on SI Exhaust Emissions," ASME JOURNAL OF ENGINEERING FOR GAS TURBINES AND POWER, 1989, this issue.

49 El-Emam, S., and Desoky, A., "A Study on the Combustion of Alternative Fuels in Spark-Ignition Engines," *International Journal of Hydrogen Energy*, Vol. 10, No. 7/8, 1985, pp. 497-504.

50 Coordinating Research Council, Inc., "Performance Evaluation of Alcohol-Gasoline Blends in 1980 Model Automobiles, Phase I—Ethanol-Gasoline Blends," Final Report to the Department of Energy (DOE), Contract No. DE-AC03-79CS50003, 1982.

51 Coordinating Research Council, Inc., "Performance Evaluation of Alcohol-Gasoline Blends in 1980 Model Automobiles, Phase II—Methanol-Gasoline Blends," Final Report to the Department of Energy (DOE), Contract No. DE-AC03-79CS50003, 1984.

52 Price, R., and Stamets, L., "Automotive and Fuel Technologies: Current and Future Options," Technology Assessments Project Office, California Energy Commission, 1984.

53 Mitchell, D. K., "The Effects of Blending Agents on the Cold Weather Operation of Methanol Fueled Automobiles," International Symposium on Alcohol Fuels Technology, Ottawa, Ontario, Canada, May 21, 1984.

54 Gardner, D. P., and Bardon, M. F., "Cold Starting Tests on a Methanol Fuelled Spark Ignition Engine," SAE Paper No. 831175, 1983.

55 Menard, H., Decker, G., and Weidmunn, K., "Alcohol Fuel Vehicles of Volkswagen," SAE Paper No. 829468, 1982.

56 Bernstein, L. S., and Panzer, J., "Priming Agents for Methanol as an Automotive Fuel," 5th International Alcohol Fuel Technology Symposium, New Zealand, 1982.

57 Rajan, S., and Saniec, F., "Water-Ethanol-Gasoline Blends as Spark Ignition Engine Fuels," *Journal of Fuel Science*, Jan. 1983, pp. 117-121.

58 Newhall, H. K., and Starkman, E. S., "Direct Spectroscopic Determination of Nitric Oxide in Reciprocating Engine Cylinders," SAE Paper No. 670122, 1967.

59 Newhall, H. K., and Shahed, S. M., "Kinetics of Nitric Oxide Formation in High Pressure Flames," 13th International Symposium on Combustion, Salt Lake City, UT, 1971.

60 Lavoie, G. A., Heywood, J. B., and Keck, J. C., "Experimental and Theoretical Study of Nitric Oxide Formation in Internal Combustion Engines," *Combustion Science Technology*, Vol. 1, 1970, pp. 313-326.

61 Blumberg, P., and Kummer, J., "Prediction of Nitric Oxide Formation in Spark Ignited Engines—An Analysis of Methods of Control," *Combustion Science Technology*, Vol. 4, 1971, pp. 73-96.

62 Hilliard, J. C., and Wheeler, R. W., "Nitrogen Dioxide in Engine Exhaust," *SAE Trans.*, Paper No. 790691, Vol. 88, 1979.

63 Merryman, E. L., and Levy, A., "Nitrogen Oxide Formation in Flames: The Roles of NO_2 and Fuel Nitrogen," *Proceedings of 15th International Symposium on Combustion*, The Combustion Institute, 1975, p. 1073.

64 Bechtold, R., and Pullman, J. B., "Driving Cycle Economy, Emissions, and Photochemical Reactivity Using Alcohol Fuels and Gasoline," SAE Paper No. 800260, 1980.

65 Stephen, A., Espinola, E., and Pefley, R., "Alternate Fuel Influences on Emission Test Procedures," Symposium on Chemistry of Oxygenates in Fuels, American Chemical Society, Kansas City, MO, Sept. 12-17, 1982.

66 Jackson, M. W., "Effect of Catalytic Emission Control on Exhaust Hydrocarbon Composition and Reactivity," SAE Paper No. 780624, 1978.

67 Saito, N., and Pefley, R. K., "Comparative Study Between Low and High Compression EFI System for Alcohol Gasoline Blends," Technical Report Submitted to DOE/NASA, 1984.

68 Jackson, M. D., Powars, C. A., Smith, K. D., and Fong, D. W., "Methanol-Fueled Transit Bus Demonstration," ASME Paper No. 83-OGP-3, 1983.

69 Schrock, M. D., and Clark, S. J., "Butanol-Acetone Blends as S. I. Engine Fuels," *Transaction of American Society of Agricultural Engineer*, May-June 1983, pp. 723-728.

70 Myers, P. S., Vyehara, O. A., and Newhall, H. K., "The ABC's of Engine Exhaust Emissions," SAE Paper No. 710481, 1971.

71 Pollution Control Board, "California Procedure for Testing Motor Vehicle," Los Angeles, CA, Nov. 1965.

72 Caplon, J. D., "Smog Chemistry Points the Way to Rational Vehicle Emission Control," SAE Paper No. 650641, 1965.

73 Alshuller, A. P., "An Evaluation of Techniques for the Determination of the Photochemical Reactivity of Organic Emissions," *Journal of Air Pollution Control Association*, Vol. 16, No. 5, May 1966.

74 Lee, E. K., and Lewis, R. S., "Photochemistry of Simple Aldehydes and Ketones in the Gas Phase, *Advances in Photochemistry*, Vol. 12, No. 1, 1980.

75 Carter, W. P., et al., "Computer Modelling of Smog Chamber Data: Progress in Validation of a Detailed Mechanism for the Photooxidation of Propene and *n*-Butane in Photochemical Smog," *International Journal of Chemical Kinetics*, Vol. 11, 1979, p. 45.

76 Browning, L. H., Nebolon, J. F., and Pefley, R. K., "Research Investigation of Alcohol Usage in Spark Ignition Engines," *Proceedings of the Twentieth Automotive Technology Development Contractors Coordination Meeting*, Dearborn, MI, 1982.

77 Browning, L. H., and Pefley, R. K., "An Analytical Study of Aldehyde Formation During the Exhaust Stroke of a Methanol-Fueled SI Engine," *Proceedings of the Fourth International Symposium on Alcohol Fuels Technology*, Guaraji, Brazil, Oct. 1980.

78 Ito, K., and Yano, T., "Formaldehydes Emissions From a SI Engine Using Methanol," *Proceedings of the Third International Symposium on Alcohol Fuels Technology*, Asilomar, CA, May 1979.

79 Pischinger, F. F., and Kramer, K., "The Influence of Engine Parameters on the Aldehyde Emissions of a Methanol Operated Four-Stroke Otto Cycle

Engine." Paper No. II-25, Third International Symposium on Alcohol Fuels Technology, Asilomar, CA, May 29-31, 1979.

80 Bamford, C. H., and Dryer, F. L., "Chemical Kinetics," *Gas-Phase Combustion*, Vol. 17, Elsevier Scientific Publishing Company, New York, 1977.

81 Westbrook, C. K., and Dryer, F. L., "Chemical Kinetics and Modeling of Combustion Processes," *Proceedings of the 18th International Symposium on Combustion*, Waterloo, Ontario, Canada, Aug. 1980.

82 Brinkman, N., "Ethanol Fuel—A Single-Cylinder Engine Study of Efficiency and Exhaust Emissions," SAE Paper No. 810345, 1981.

83 University of Santa Clara, " Ethanol in Multicylinder Automotive SI Engines; A Study of Performance and Emission Characteristics Relative to Indolene and Methanol," Contract Report to U.S. Department of Energy, DOE Publication HCP/W1737-01, May 1978.

84 Bernhardt, W., "Future Fuel and Mixing Preparation Methods for Spark Ignition Automobile Engines," *Progress in Energy and Combustion Science*, Vol. 3, 1977, p. 139.

85 Harrenstein, M. S , Rhee, K. T., and Adt, R. R., "Determination of Individual Aldehyde Concentrations in the Exhaust of Spark Ignited Engine Fueled by Alcohol-Gasoline Blends," SAE Paper No. 790952, 1979.

86 Tomlin, J. A., and Kent, J. H., "Aldehyde Emissions From an Ethanol-Petrol Fueled Spark-Ignition Engine," Fifth International Alcohol Fuel Technology Symposium, Auckland, New Zealand, May 13, 1982.

87 Lipari, F., and Keski-Hynnila, D., "Aldehyde and Unburned Fuel Emissions From Methanol-Fueled Heavy-Duty Diesel Engines," SAE Paper No. 860301, 1986.

88 Seko, T., et al., "Combustion Exhaust Emissions of the Spark-Assisted Methanol Diesel Engine," SAE Paper No. 861165, 1986.

89 Ecklund, E. E., Timbario, T. J., and McCallum, P. W., "Environmental Implications of the Use of Alcohol-Fueled Highway Vehicles," 75th Annual Meeting of the Air Pollution Control Association, New Orleans, LA, June 20-25, 1982.

90 Pettersson, L., and Sjostrom, K., "Decomposed Methanol, an Excellent Cold Start Fuel for Spark Ignition Engines," *Seventh International Symposium on Alcohol Fuels*, Paris, Oct. 1986, Vol. 2, pp. 77-82.

91 Finegold, J. G., "Dissociated Methanol Vehicle Test Results," *Proceedings of the VI International Symposium on Alcohol Fuels Technology*, Ottawa, Canada, May 21-25, 1900.

92 Edo, T., and Foster, D., "A Computer Simulation of a Dissociated Methanol Engine," *Proceedings of the VI International Symposium on Alcohol Fuels Technology*, Ottawa, Canada, May 21-25, 1900.

93 Stocky, J. F., Dowdy, M. W., and Vanderburg, T. G., "An Examination of the Performance of Spark Ignition Engines Using Hydrogen-Supplemented Fuels," SAE Paper No. 750027, 1975.

94 Inagaki, T., Hirota, T., and Veno, Z., "Combustion and Emission of Gaseous Fuel From Reformed Methanol in Automotive Engine," *Proceedings of the 3rd International Symposium on Alcohol Fuels Technology*, Asilomar, CA, 1979.

95 Finegold, J., Karpuk, M., and McKinnon, T., "Demonstration of Dissociated Methanol as an Automotive Fuel: System Design," *Proceedings of the Fourth International Symposium on Alcohol Fuels Technology*, Guaraji, Brazil, 1980.

96 Finegold, J., McKinnon, J., and Karpuk, M., "Analysis of Dissociated Alcohol for Internal Combustion Engine for Transportation," *Proceedings of the Renewable Fuels and Advanced Sources for Transportation Workshop*, Boulder, CO, June 17-18, 1982.

97 Martin, M. D., "Gaseous Automotive Fuels Steam Reformed Liquid Hydrocarbons," SAE Paper No. 780465, 1978.

98 MacDonald, J. S., "Evaluation of the Hydrogen-Supplemented Fuel Concept With an Experimental Multicylinder Engine," SAE Paper No. 760601, 1976.

99 Van Egmond, C., et al., "Performance of a V-6 Engine Fueled With Vaporized Methanol," Energy-Sources Technology Conference and Exhibition, Dallas, TX, Feb. 15-20, 1987.

100 Yoon, H., and Burke, F., "Methanol Dissociation for Transportation Fuel Use," *Proceedings of the First Annual Pittsburgh Coal Conference*, Pittsburgh, PA, 1984.

101 Kikuchi, E., Kunitomo, Y., and Morita, Y., "Catalyst for On-Board Reforming of Methanol," *Journal of Japan Petroleum Institute*, Vol. 23, No. 5, 1980.

Effects of Ethanol and/or Methanol in Alcohol-Gasoline Blends on Exhaust Emissions

R. M. Bata
College of Engineering,
Clemson University,
Clemson, SC 29631

V. P. Roan
College of Engineering,
University of Florida,
Gainesville, FL

The effect on exhaust gas emissions (carbon monoxide, CO, hydrocarbons, HC, and aldehydes, CHO) resulting from mixing methanol and/or ethanol with gasoline for automotive fuels has been studied experimentally. Tests were conducted on an OEM four-cylinder engine running at different conditions of equivalence ratio and spark timing. Fuel blends with different percentages of alcohol content and different ratios of methanol to ethanol in the alcohol mixture were tested. Results of this investigation indicated that the presence of either or both of the alcohols in fuel blends significantly reduced the concentration of carbon monoxide in the exhaust emissions (up to 40–50 percent compared to pure gasoline only), with methanol slightly more effective than ethanol. Hydrocarbon emissions were also decreased by increasing the alcohol content of the fuel, with minimum hydrocarbon production occurring at percent alcohol-gasoline blends in conjunction with near-stoichiometric air-fuel ratios. However, aldehyde emissions were found to be markedly higher with alcohol-gasoline blends. The 10 percent alcohol-gasoline blends were found to produce about 50 percent more aldehyde emissions than pure gasoline.

Introduction

An advantage of using alcohol as a substitute for, or as a blend with, gasoline, other than decreasing the amount of gasoline used, is the reduction of the regulated emission products (unburned hydrocarbons [HC], carbon monoxide [CO], and oxides of nitrogen [NO_x]) in exhaust gases. However, this can be at the cost of increasing unregulated emissions (the aldehydes in particular). Questions of interest addressed in this study included:

1 How does the suppression of regulated emissions and the production of unregulated ones compare for blends of ethanol-gasoline versus methanol-gasoline?

2 Do combined blends of methanol-ethanol-gasoline produce emissions that can be predicted from consideration of the results of ethanol-gasoline and methanol-gasoline tests?

3 Are the unregulated emissions (aldehydes in particular) increases associated with ethanol blends or methanol blends sufficiently large that new emissions problems would be created through their use?

These questions have been answered to some extent by previous researchers (Smith et al., 1982; Most and Longwell, 1975; LoRusso and Tabaczynski, 1976; Bernhardt, 1975; Ayyasamy et al., 1981) where the use of alcohol-gasoline blends has shown an increase of aldehydes by a factor of two to four. This is not unexpected since the oxidation process for gasoline involves two parallel chemical reaction paths, only one of which involves the formation of alcohols (Bamford and Tipper, 1977; Westbrook and Dryer, 1980). On the other hand, the oxidation of alcohols always involves intermediate steps producing formaldehyde (HCHO) in the case of methanol or acetaldehyde (CH_3CHO) in the case of ethanol. (Ayyasamy, et al., 1981; Strehlon, 1984).

Furey and King (1980) tested two different eight-cylinder engines fueled with gasoline containing ethanol or methyl-tert-butyl-ether (MTBE) to study the effects of blended fuels on exhaust emissions. They found that evaporative emissions of hydrocarbons were as much as 51 percent higher with 10 percent ethanol fuel blends than with gasoline. This was related primarily to the higher fuel volatility and partly to an increase in hose permeability caused by the ethanol. The authors also recorded that tailpipe emissions of HC, CO, and NO_x from the engine with and without closed-loop fuel control were significantly lower with fuel blends than with pure gasoline, which they attribute to the leaning effect of ethanol and MTBE.

The effect of such engine parameters as compression ratio (CR), equivalence ratio (ϕ), spark timing(s), and exhaust temperature on hydrocarbon, carbon monoxide, and aldehyde emissions has been variously studied (Browning and Pefley, 1980; Ito and Yano, 1980; Dishart, 1979; Hosaka et al., 1978; Schuetzle et al., 1981; Dartnell, 1981; Andon et al., 1981; Wigg and Lunt, 1974; Bechtold and Pullman, 1980; Matsuno et al., 1979; Hagen, 1999; Pefley et al., 1971; Adelman et al., 1978; Royal Swedish Academy of Sciences and Swedish Methanol Development Co., 1976). Aldehyde emissions increased with increasing compression ratio and also with the change from stoichiometric to lean equivalence ratios. Other studies (Hagen, 1999) suggested that an increase in the compression ratio from 9.7 to 14 reduced aldehyde emissions by 50 percent to levels comparable with those for gasoline needed to

Contributed by the Internal Combustion Engine Division and presented at the Energy-Sources Technology Conference and Exhibition, New Orleans, Louisiana, January 11, 1988. Manuscript received by the Internal Combustion Engine Division October 13, 1987. Paper No. 88-ICE-7.

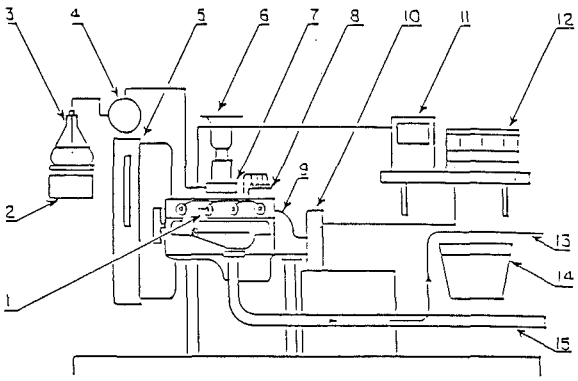

1 Pressure Transducer
2 Scale
3 Alcohol-Gasoline Blend
4 Fuel Pump
5 Radiator
6 Air Sensor
7 Carburetor
8 Distributor
9 4-Cylinder Engine
10 Absorption Unit
11 Oscilloscope
12 Console
13 Sample
14 Water Trap
15 Exhaust Pipe

Fig. 1 Schematic of engine dynamometer

be studied. Since exhaust temperatures with alcohol are lower than with gasoline fuel, reduced oxidation in the exhaust system may also contribute to the higher aldehyde emission. It has also been shown that the control of aldehydes in exhaust emissions can be achieved by suitable alteration of engine operating parameters, and by treatment of the mixture with additives like aniline and water (Ayyasamy et al., 1981), by heating the intake manifold with exhaust gases, and by improving fuel-air spray atomization (Bernhardt, 1975). Aldehyde emissions can also be reduced by using after-treatment devices such as catalytic converters.

Experimental Investigation

Engine Description. The test engine was a 1978 Ford 2.3 liter in-line four cylinder with an overhead camshaft, cogged belt drive, 9.0:1 compression ratio, and two-barrel carburetor. All emission controls and recirculation systems were disconnected and the engine was mounted on a Superflow SF-800 dynamometer (Fig. 1). All tests were made at predetermined loads (same engine output power) and speed (2500 rpm during the whole series of experiments).

Fuel Preparation. Blends of gasoline and anhydrous alcohol were prepared by volume measure. Specific gravities of the blends were determined by means of a sensitive balance measurement of the mass of 100 cc of each mixture. The fuel specific gravity calibration of the dynamometer was adjusted to the predetermined value.

Air Density. The air density calibration was set to the density of the air entering the air flow sensor (fixed on the top of the carburetor). The readings of the air flow were then indicated in standard cubic feet per minute (SCFM). Air density was determined by means of the perfect gas equation on the basis of measurements of the humidity ratio, temperature, and barometric pressure (test pressure). Dry and wet bulb thermometers were used to determine the humidity ratio.

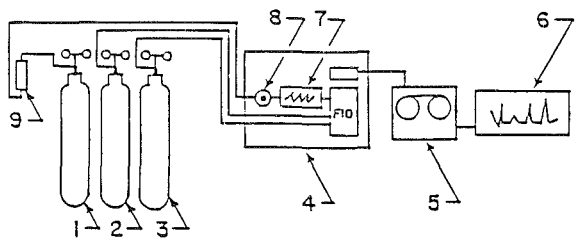

1 Nitrogen (carrier)
2 Air
3 Hydrogen
4 Gas Chromatograph
5 Data System
6 Gas Chromatogram
7 Column
8 Injection Port (sample)
9 Filter

Fig. 2 Schematic of exhaust gas analysis apparatus

Sample Preparation. Exhaust samples were taken using 50-cc syringes, with Luer-lock tips, from an auxiliary spiral tube inserted inside the main exhaust pipe, as shown in the schematic of the engine dynamometer (Fig. 1). Samples were injected into and analyzed by a gas chromatograph (Varian 3700) and the results were printed by the synchronized data system (Varian 401). A schematic diagram of the exhaust gas analysis equipment is shown in Fig. 2. The detector used was a thermal conductivity detector (TCD). A molecular sieve 5A column with the following specifications was fixed in the gas chromatograph:

Length ft.	OD, mm	ID, mm	Mesh	Maximum temperature, °C
12	6.35	2	80/100	400

The following steps were followed to determine the concentration of CO, HC, and CHO.

1 The flow rates of gases through the column were adjusted to achieve near-optimum sensitivity from the column.
- Carrier gas, nitrogen 25-30 ml/min
- Sample injected 40-200 μl

2 The column was reconditioned at 300°C overnight.

3 The injector (inlet) detector temperature was adjusted at 80°C.

4 Oven temperature was set between 40°C and 70°C to get high resolution output peaks from the exhuast gas species.

5 The system was allowed at least 30 minutes to stabilize before the start of recording of the base line with the programmed temperature.

6 The standard gas for each component was injected separately with a known concentration (ppm) to determine the standard retention time for each particular gas. For hydrocarbon, HC, because there are hundreds of hydrocarbon products, propane was selected to estimate the concentration of light hydrocarbon products. Gasoline, ethanol, and methanol were injected to estimate the concentration of the unburned

Nomenclature

A = relative ratio of ethanol to methanol in the blend
CHO = aldehyde group
CO = carbon monoxide
CR = compression ratio
HC = hydrocarbon group
M = volume percent of alcohol in the blend
MTBE = methyl-tert-butyl-ether
NO_x = nitrogen oxides
OEM = original equipment manufacturer
ϕ = equivalence ratio = (F/A) actual/(F/A) stoichiometric
ppm = parts per million
rpm = revolutions per minute
S = spark timing
TCD = thermal conductivity detector
UBF = unburned fuel

Table 1 Carbon monoxide in ppm in exhaust gases at constant load and 2500 rpm

Fuel Blend	S_1 (10°) Retard			S_3 (20°) Normal			S_5 (30°) Advance		
	ϕ_1	ϕ_3	ϕ_5	ϕ_1	ϕ_3	ϕ_5	ϕ_1	ϕ_3	ϕ_5
Pure Gasoline	3480	3610	3870	3510	3640	4020	3650	3720	4210
5% Ethanol	2140	2470	2540	2280	2430	2680	2330	2440	2610
10% Ethanol	NA	2050	2180	2000	2250	2420	2260	2370	2430
15% Ethanol	NA	1590	1770	1670	1830	1940	NA	2190	2060
20% Ethanol	NA	1380	1500	NA	1510	1490	NA	1630	1700
Pure Gasoline	3480	3610	3870	3510	3640	4020	3650	3720	4210
5% Eth.&Meth.	1980	2260	2390	2160	2360	2490	2200	2370	2530
10% Eth.&Meth.	NA	2030	2140	1970	2200	2350	2000	2110	2350
15% Eth.&Meth.	NA	1790	1860	1720	1850	1950	NA	1780	1940
20% Eth.&Meth.	NA	1450	1500	NA	1500	1610	NA	1450	1520
Pure Gasoline	3480	3610	3870	3510	3640	4020	3650	3720	4210
5% Methanol	1860	2300	2110	2200	2300	2400	2160	2370	2500
10% Methanol	NA	1900	2340	1810	1900	2030	1870	2000	2350
15% Methanol	NA	1500	1640	1410	1500	1650	NA	1690	1720
20% Methanol	NA	1420	1390	NA	1420	1500	NA	1330	1490

NA: Data was not available.

Table 2 Hydrocarbon (propane) in ppm in exhaust gases at constant load and 2500 rpm

Fuel Blend	S_1 (10°) Retard			S_3 (20°) Normal			S_5 (30°) Advance		
	ϕ_1	ϕ_3	ϕ_5	ϕ_1	ϕ_3	ϕ_5	ϕ_1	ϕ_3	ϕ_5
Pure Gasoline	1490	1470	1750	733	810	863	853	940	1030
5% Ethanol	1340	1413	1730	880	870	593	689	960	1100
10% Ethanol	NA	1440	1520	859	920	857	885	902	930
15% Ethanol	NA	1310	1380	642	940	842	NA	921	960
20% Ethanol	NA	1340	1420	NA	830	1200	NA	715	1010
Pure Gasoline	1490	1470	1750	733	810	863	893	940	1030
5% Eth.&Meth.	1270	1314	1490	770	870	763	720	900	990
10% Eth.&Meth.	NA	1290	1550	837	882	917	692	941	1060
15% Eth.&Meth.	NA	1340	1460	1116	910	894	NA	1056	1100
20% Eth.&Meth.	NA	1430	1540	NA	980	986	NA	966	920
Pure Gasoline	1490	1470	1750	733	810	863	893	940	1030
5% Methanol	1200	1410	1460	589	930	846	860	885	1070
10% Methanol	NA	1330	1510	866	931	896	723	974	1030
15% Methanol	NA	1410	1590	886	1040	1210	NA	1120	1090
20% Methanol	NA	1300	1430	NA	960	1084	NA	1060	1130

NA: Data was not available.

Table 3 Aldehyde (formaldehyde) in ppm in exhaust gases at constant load and 2500 rpm

Fuel Blend	S_1 (10°) Retard			S_3 (20°) Normal			S_5 (30°) Advance		
	ϕ_1	ϕ_3	ϕ_5	ϕ_1	ϕ_3	ϕ_5	ϕ_1	ϕ_3	ϕ_5
Pure Gasoline	280	260	250	320	280	250	370	330	280
5% Ethanol	500	440	410	530	460	440	560	520	490
10% Ethanol	NA	630	610	670	650	620	690	670	630
15% Ethanol	NA	740	720	810	770	740	NA	800	760
20% Ethanol	NA	890	870	NA	950	920	NA	980	950
Pure Gasoline	280	260	250	320	280	250	370	330	280
5% Eth.&Meth.	480	440	420	520	460	430	550	480	470
10% Eth.&Meth.	NA	640	630	690	670	640	710	690	660
15% Eth.&Meth.	NA	750	710	800	770	740	NA	810	760
20% Eth.&Meth.	NA	910	900	NA	960	940	NA	980	960
Pure Gasoline	280	260	250	320	280	250	370	330	280
5% Methanol	520	460	400	540	460	410	580	510	540
10% Methanol	NA	610	562	670	630	610	700	670	630
15% Methanol	NA	740	690	780	750	740	NA	780	750
20% Methanol	NA	800	780	NA	830	810	NA	870	860

NA: Data was not available.

fuel (UBF). For aldehyde, CHO, standard formaldehyde gas was used. A program of testing was conducted with variations in:

(*a*) Equivalence ratio ($\phi_1 = 0.85$, $\phi_3 = 1$, and $\phi_s = 1.15$)

(*b*) Spark timing ($S_1 = 10°$, $S_3 = 20°$ (normal), and $S_s = 30°$)

(*c*) Amount of total alcohol by volume in the blend (0, 5, 10, 15, and 20 percent)

(*d*) Relative amounts of ethanol and methanol in alcohol mixture (0–100, 50–50, and 100–0).

The variations of these parameters were controlled so that

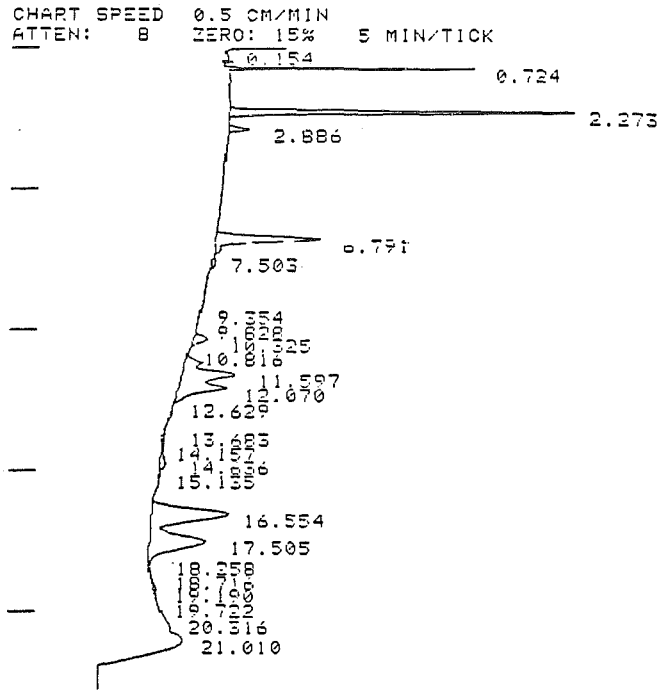

TITLE: EXHAUST GAS ANALYSIS 16:06 9 AUG 84

CHANNEL NO: 3 SAMPLE: 5%ETHANOL METHOD: REDA

PEAK NO	PEAK NAME	RESULT AREA%	TIME (MIN)	AREA COUNTS	SEP CODE
1		0.2108	0.507	230	VV
2		4.7281	0.724	5158	VB
3		21.4058	2.273	23352	BB
4		1.5475	2.886	1688	BB
5		12.5630	6.791	13487	BV
6		0.8195	7.158	894	VV
7		0.1732	7.561	189	VV
8		0.3181	7.654	347	VB
9		2.2091	10.325	2410	BV
10		2.1968	11.177	2396	VV
11		9.6315	11.597	10507	VV
12		8.3453	12.070	9104	VV
13		0.1137	14.519	124	VV
14		0.1989	14.636	217	VV
15		0.6802	14.737	742	VV
16		19.3286	16.554	21086	BV
17		15.3824	17.505	16781	VV
18		0.1027	18.918	112	VV
19		0.1522	19.088	166	VV
20		0.0990	19.165	108	VV
TOTALS:		100.0000		109092	

Fig. 3 Gas chromatograph analysis printout

the effect of each on the exhaust emissions could be measured. The results, which show the concentration of carbon monoxide (CO), hydrocarbons (HC), and aldehyde (CHO) in some of the samples, are tabulated in Tables 1, 2, and 3, and Fig. 3 shows a sample of gas chromatograph printout.

Results

Carbon Monoxide (CO) in Exhaust Gases. Figures 4, 5, and 6 (for retarded, normal, and advanced spark timing, respectively) show that carbon monoxide emission was primarily a function of the equivalence ratio (ϕ), with carbon monoxide production increasing on the rich side. The presence of methanol and ethanol reduced carbon monoxide production, probably because those molecules are rich in oxygen. It was found that as the mixture was leaned out either with methanol or ethanol, very low levels of carbon monoxide (2000 ppm) could be reached (Figs. 7, 8, and 9). This was due to the excess number of oxygen atoms available during the combustion process. From the above figures it is obvious that the controlling factor in the CO production is the atoms of oxygen, which are available in the alcohol and/or in case of lean mixture. The effect of spark timing on the production of CO is

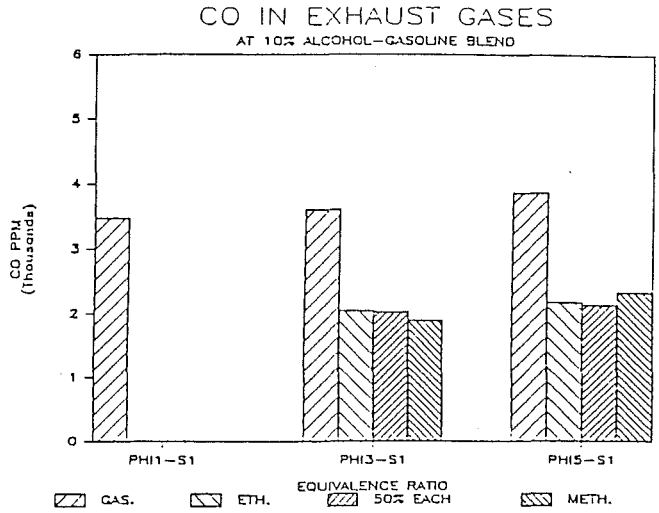

Fig. 4 Production of CO at different equivalence ratios and retard spark timing (S_1)

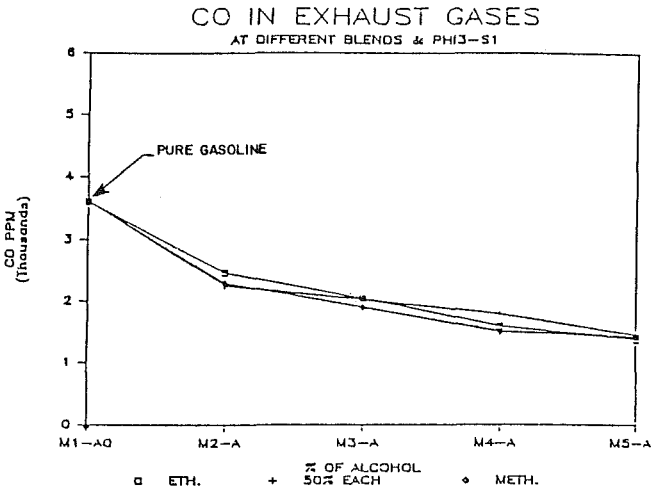

Fig. 7 Production of CO with different alcohol-gasoline blends at retard spark timing

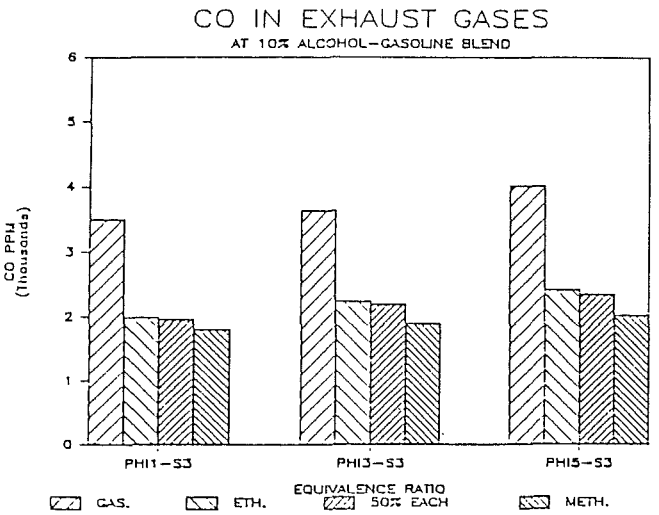

Fig. 5 Production of CO at different equivalence ratios and normal spark timing (S_3)

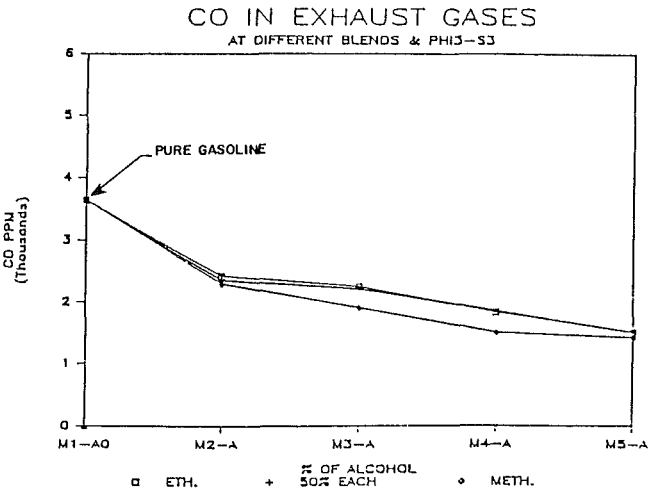

Fig. 8 Production of CO with different alcohol-gasoline blends at normal spark timing

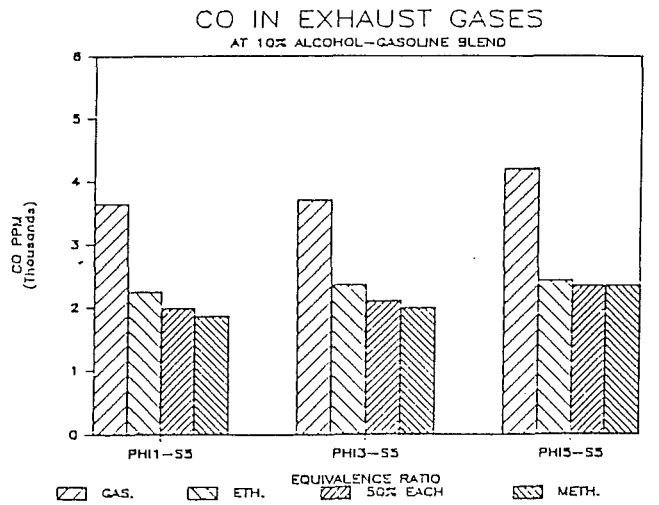

Fig. 6 Production of CO at different equivalence ratios and advance spark timing (S_5)

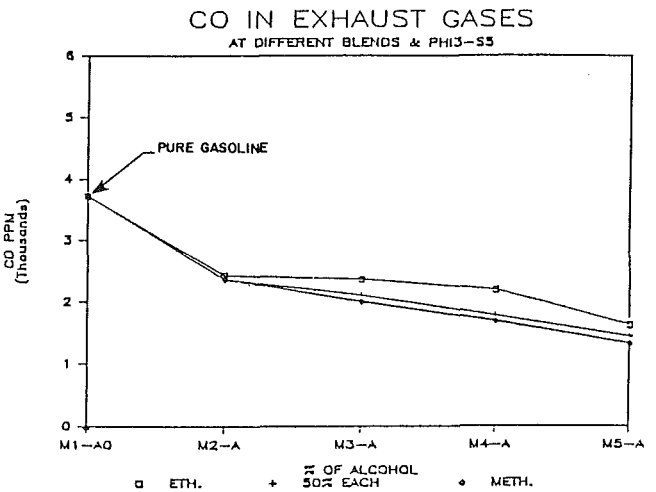

Fig. 9 Production of CO with different alcohol-gasoline blends at advance spark timing (S_5)

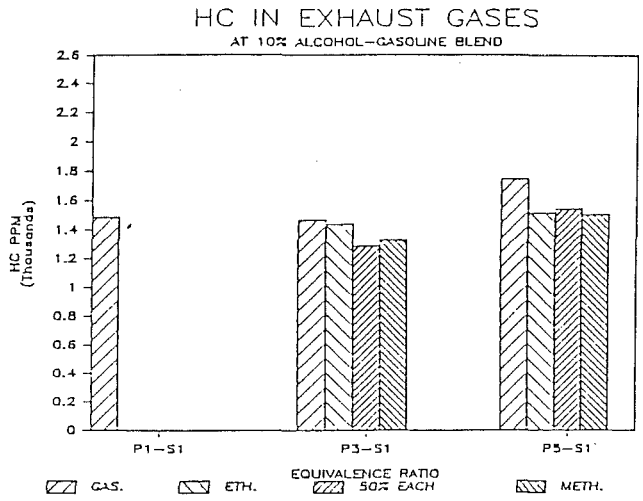

Fig. 10 Production of HC at different equivalence ratios and retard spark timing (S_1)

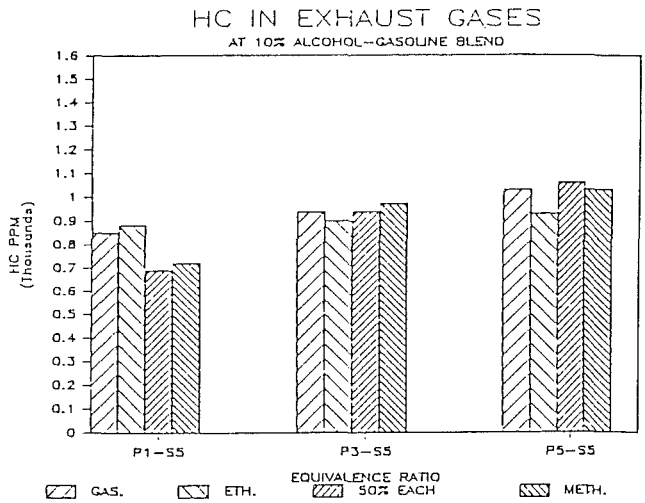

Fig. 12 Production of HC at different equivalence and advance spark timing (S_5)

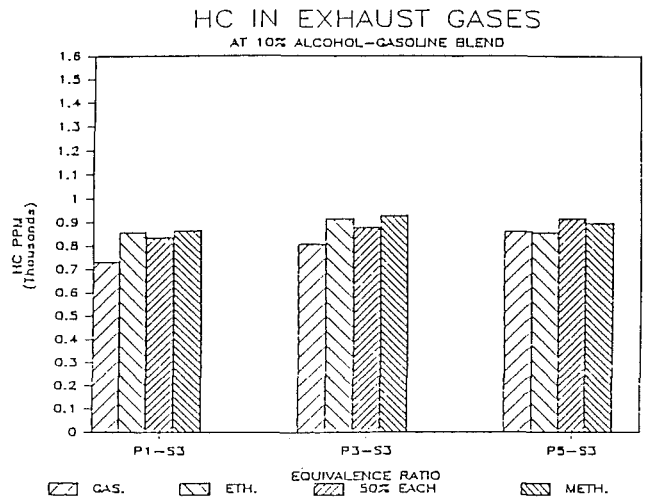

Fig. 11 Production of HC at different equivalence ratios and normal spark timing (S_3)

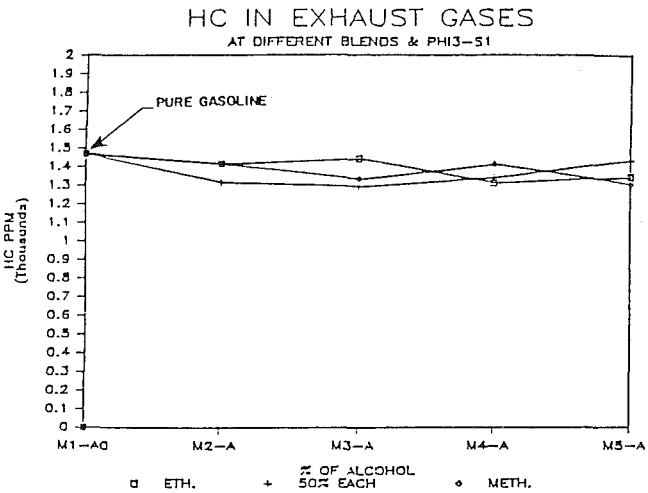

Fig. 13 Production of HC with different alcohol-gasoline blends at retard spark timing (S_1)

insignificant. The kind of alcohol has a minor effect on CO, and the figures show that methanol has a favorable effect on the reduction of CO due to its higher latent heat of vaporization, which decreases the intake manifold temperature and consequently increases the density of the air delivered to the combustion chamber. It is highly noteworthy that the alcohol–gasoline blends reduce the production of CO by about 40–50 percent compared to the pure gasoline.

Hydrocarbon (HC) in Exhaust Gases. From Figs. 10, 11, and 12 it is seen that hydrocarbon production increased as the equivalence ratios changed from lean to rich. The presence of alcohol in the blends did not cause large changes in the production of HC. In the case of retarded spark timing (Fig. 10), the production of HC in the exhaust gases was less with alcohol–gasoline blends than with gasoline fuel. In the case of normal and rich air–fuel ratios (Figs. 11 and 12), there was an increase in HC production as compared to gasoline. This increase may be due to the leaning effect of alcohol and/or of the alcohol's role in increasing the vapor pressure of the fuel which is being ingested into the engine.

The production of HC was slightly decreased with the increase of alcohol in the blend at retarded spark settings (Fig. 13) but was slightly increased with the increase of the alcohol percent in the blend at standard and advance spark timing (Figs. 14 and 15).

Aldehydes (CHO) in Exhaust Gases. Aldehyde emissions were markedly higher (60–100 percent) with the alcohol–gasoline blends than with gasoline (Figs. 16, 17, and 18). This was partly due to the lower maximum combustion temperature caused by the presence of the alcohol in the fuel. Aldehydes production is expected to be due to the partial oxidation of the remaining fuel at the end of the combustion process after the flame fades out (Bamford and Tipper, 1977). The lower temperature of the exhaust system probably affects the production of aldehydes, by lowering the aldehyde oxidation rate and consequently increasing the production of aldehydes. Aldehyde production is also increased with an increase of the percentage of alcohol in the alcohol–gasoline blend (Figs. 19, 20, and 21) and decreases as equivalence ratio passes from lean ($\phi_1 = 0.85$) to rich ($\phi_5 = 1.15$). The effect of spark timing and the kind of alcohol (ethanol and methanol) on the production of the aldehydes are significant. The aldehyde production decreased as the air/fuel mixture was made richer due to the increase in the combustion temperature.

Summary and Conclusions

The effects of using anhydrous ethanol and/or methanol with unleaded gasoline fuel on exhaust emissions (CO, HC, and CHO) have been experimentally investigated. The

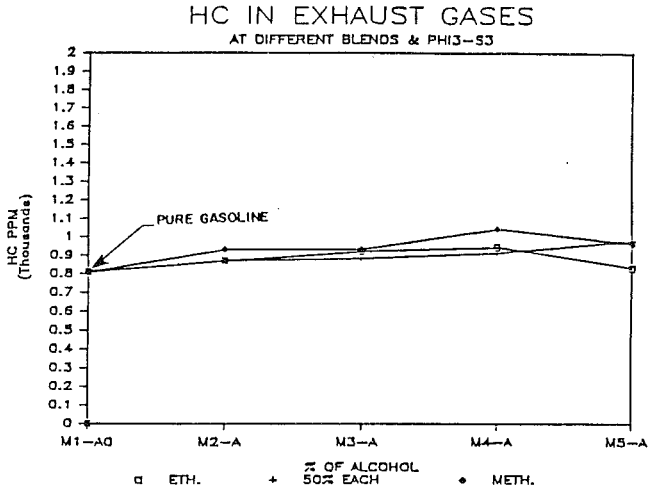

Fig. 14 Production of HC with different alcohol-gasoline blends at normal spark timing (S_3)

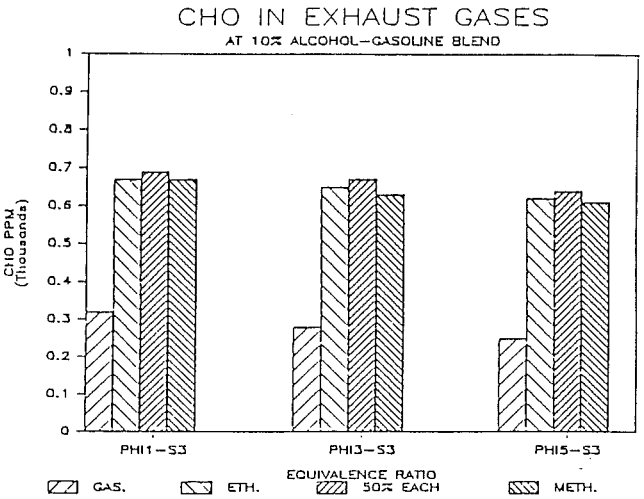

Fig. 17 Production of CO at different equivalence ratios and normal spark timing (S_3)

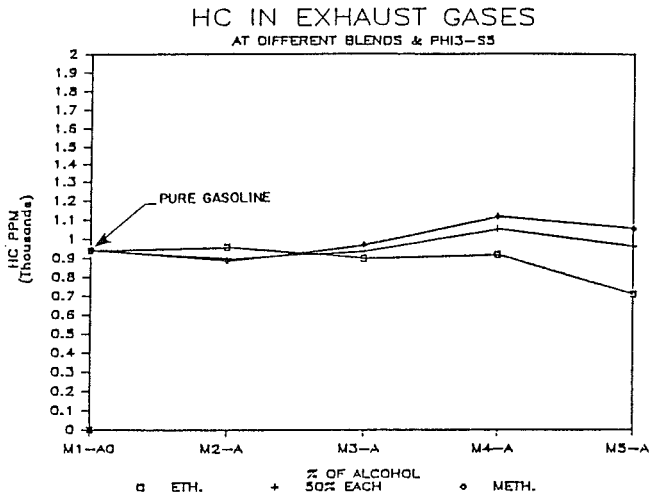

Fig. 15 Production of HC with different alcohol-gasoline blends at advance spark timing (S_5)

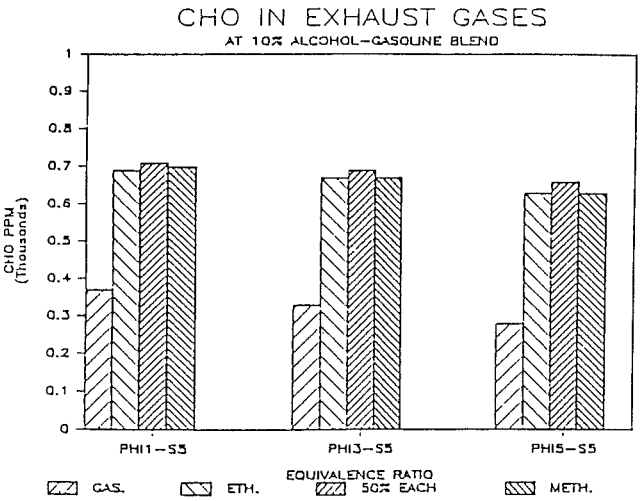

Fig. 18 Production of CHO at different alcohol ratios and advance spark timing (S_5)

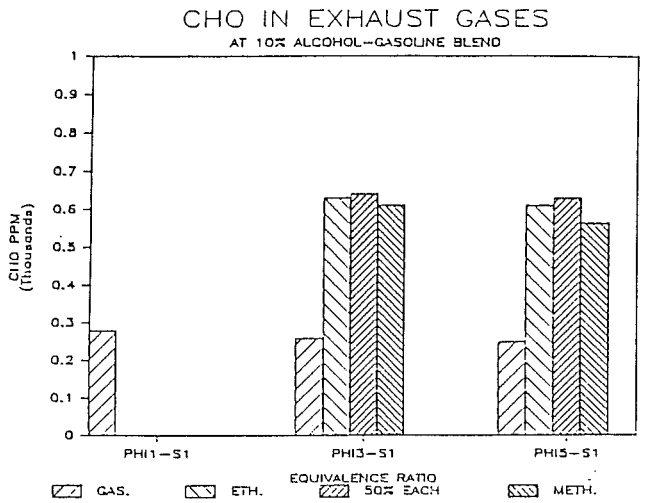

Fig. 16 Production of CHO at different equivalence ratios and retard spark timing (S_1)

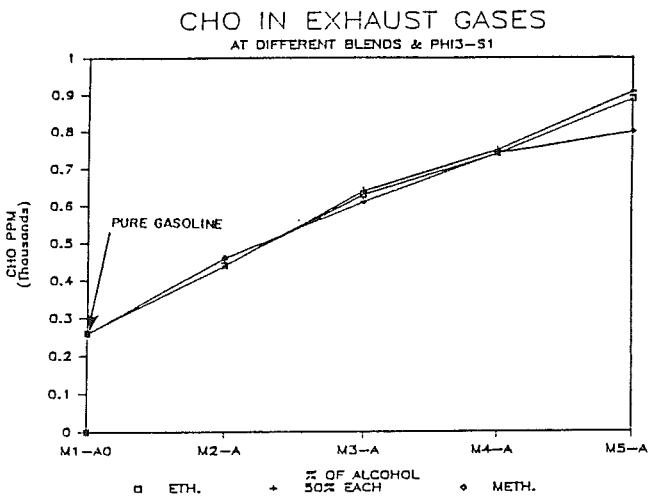

Fig. 19 Production of CHO with different alcohol-gasoline blends at retard spark timing (S_1)

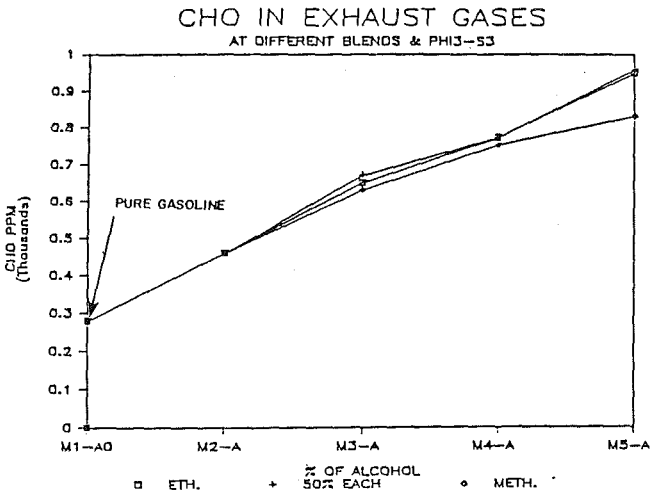

Fig. 20 Production of CHO with different alcohol-gasoline blends at normal spark timing (S_3)

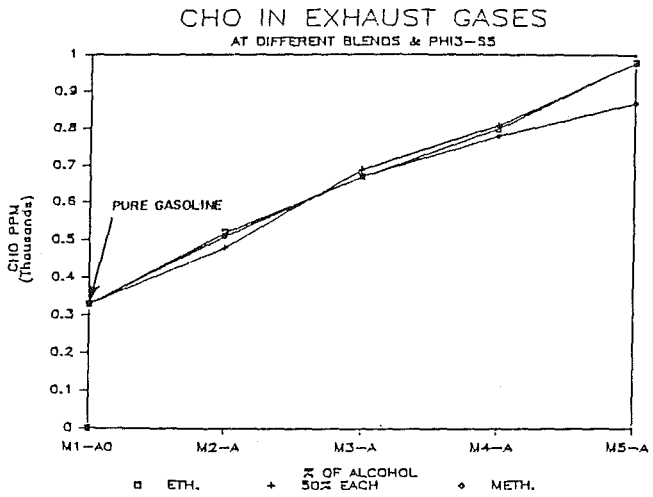

Fig. 21 Production of CHO with different alcohol-gasoline blends at advance spark timing (S_5)

variables studied were: equivalence ratio (ϕ), spark timing (S), percent of alcohol in the blend (M), and the relative ratio of ethanol to methanol in the blend (A). The production of CO was reduced by about 40–50 percent at an equivalence ratio on the lean side near stoichiometric. The effect of the type of alcohol (ethanol and/or methanol) on the production of CO was insignificant under the same conditions, but methanol generally produced less CO. Also the production of CO decreases as the percent of alcohol in the blend increases.

The effect of alcohol on HC was insignificant, but the unburned hydrocarbon (UBF) was slightly increased due to the increase in the vapor pressure. The minimum production of HC was at the lean side ($\phi_1 = 0.85$). For aldehyde, the emission was increased in the range of 60–100 percent due to the lower maximum combustion temperature and also with the increase of alcohol in the blend. Aldehyde is an eye irritant and unregulated. More research is required to control aldehyde production before alcohol can be used extensively.

In this work, it is shown that the difference in the production of CO, HC, and CHO under the same conditions, but with different alcohols used, was insignificant. This has not been shown before in any research work.

Acknowledgments

I would like to thank Dr. B. Vandermeer and his staff for their technical assistance and for allowing me to use the laboratory facilities at USDA in Gainesville, FL.

References

Adelman, H., Andrews, D., and Devoto, R., 1978, "Exhaust Emission From a Methanol-Fueled Automobile," SAE Paper No. 7820683.

Andoh, K., Yonemochi, X., Kawajiri, H., Sakuma, K., Tanabe, H., and Sato, G., 1981, "Combustion Characteristics of Various Alternative Fuel in SI Engines," SAE Paper No. 811384.

Ayyasamy, R., Nayalingam, B., Ganesan, V., Gopala Krishnan, V., and Murthy, B., 1981, "Formation and Control of Aldehydes in Alcohol Fueled Engines," SAE Paper No. 811220.

Bamford, C., and Tipper, C., 1977, *Chemical Kinetics*, Vol. 17, *Gas-Phase Combustion*, Elsevier Scientific Publishing Company, New York.

Bechtold, R., and Pullman, J. B., 1980, "Driving Cycle Economy, Emission and Photochemical Reactivity Using Alcohol Fuels and Gasoline," SAE Paper No. 800260.

Bernhardt, W., 1975, "Engine Performance and Exhaust Emission Characteristics From a Methanol-Fueled Automobile," presented at the 1975 GMR Symposium, Future Automotive Fuels – Prospects, Performance, and Perspective, General Motors Technical Center, Warren, MI, Oct. 6–7.

Browning, L., and Pefley, R., 1980, "An Analytical Study of Aldehyde Formation Driving and Exhaust Stroke of a Methanol-Fueled SI Engine," *Proceedings of the Fourth International Symposium on Alcohol Fuels Technology*, Vol. 2, Guaraji, Sao Paulo, Brazil, Oct.

Dartnell, P., 1981, "Future Engine Design for Minimum Fuel Consumption and Exhaust Emission," SAE Paper No. 811385.

Dishart, K., 1979, "Exhaust Hydrocarbon Composition, Its Relation to Gasoline Composition," 35th Midyear Meeting, American Petroleum Institute, Houston, TX, May 14.

Furey, R., and King, J., 1980, "Evaporative and Exhaust Emissions From Cars Fueled With Gasoline Containing Ethanol or Methyl Tert-Butyl Ether," SAE Paper No. 800261.

Hagen, D., 1999, "Methanol as a Fuel: A Review With Bibliography," in: *Alcohol as Motor Fuels*, Progress in Technology Series No. 19, pp. 189–221.

Hosaka, H., Onodera, T., and Wigg, E., 1978, "The Effect of Fuel Hydrocarbon Composition on Exhaust Emission From Japanese Vehicles," SAE Paper No. 780625.

Ito, K., and Yano, T., 1980, "Methanol and Formaldehyde Kinetics in the Exhaust System of a Methanol-Fueled Spark Ignition Engine," *Proceedings of the Fourth International Symposium on Alcohol Fuels Technology*, Vol. 2, Guaraji, Sao Paulo, Brazil, Oct.

LoRusso, J., and Tabaczynski, R., 1976, "Combustion and Emission Characteristics of Methanol, Methanol-Water, and Gasoline-Methanol Blends in a Spark Ignition Engine," SAE Paper No. 769019.

Matsuno, M., et al., 1979, "Alcohol Engine Emissions – Emphasis on Unregulated Compounds," Alcohol Fuels Technology Third International Symposium, Asilomar, CA, May 28–31.

Most, W., and Longwell, J., 1975, "Single-Cylinder Engine Evaluation of Methanol-Improved Energy Economy and Reduced NO_x," SAE Paper No. 750119.

Pefley, R., Saad, M., Sweeney, M., Kilgroe, J., and Fitch, R., 1971, "Study of Decomposed Methanol as a Low Emission Fuel – Final Report," Office of Air Programs, Environmental Protection Agency, NTIS No. PB-202732, Contract EHS-70-118.

Royal Swedish Academy of Sciences and Swedish Methanol Development Co., 1976, "Methanol as a Fuel," *Proc. Symp.*, Stockholm, March 23, Invameddelande No. 195.

Schuetzle, D., Prater, T., and Anderson, P., 1981, "Characterization of Emissions From Methanol and Methanol/Gasoline Blend Fuels," SAE Paper No. 810430.

Smith, L., Urban, C., and Baines, T., 1982, "Unregulated Exhaust Emissions From Methanol-Fueled Cars," SAE Paper No. 820467.

Strehlow, R. A., 1984, *Combustion Fundamentals*, McGraw-Hill, New York.

Westbrook, C., and Dryer, F., 1980, "Chemical Kinetics and Modeling of Combustion Processes," *Proceedings of the 18th International Symposium on Combustion*, Waterloo, Ontario, Aug.

Wigg, E., and Lunt, R., 1974, "Methanol as a Gasoline Extender – Fuel Economy, Emission, and High Temperature Drivability," SAE Paper No. 741008.

Combustion Phenomena of Alcohols in C. I. Engines

M. N. Saeed
Assistant Professor,
Mechanical Engineering,
Alexandria University,
Alexandria, Egypt

N. A. Henein
Professor and Director,
Center for Automotive Research,
Wayne State University,
Detroit, MI

A study was conducted on a direct-injection, single-cylinder, research-type diesel engine to determine the effect of adding ethanol or isopropanol to diesel fuel on the ignition delay period. The test parameters were alcohol content, intake-air properties, and fuel–air ratio. It was found that the ignition delay of alcohol–diesel blends is prolonged as the alcohol content is increased. Ethanol–diesel blends developed longer ignition delays than those developed by isopropanol–diesel blends. The results showed that ignition delay of alcohol–diesel blends can be effectively shortened using intake-air preheating and/or supercharging. The high activation energy of alcohols with respect to diesel fuel is believed to be responsible for the long ignition delays associated with the use of alcohols as alternate fuels in compression ignition engines.

Introduction

The energy crises of 1973 and 1979 dictated a growing demand for the use of alternate fuels, in general, and alcohols in particular. Many investigators consider alcohols as promising alternate fuels. Alcohols can be distilled from abundant renewable resources, namely woods, sugar cane, barley, and corn. They can be synthesized from gases like carbon dioxide and hydrogen. Combustion qualities of alcohols in spark ignition engines are superior compared to gasoline. As for their use in diesel engines, alcohols are still regarded as a considerable challenge because of their low cetane numbers, high latent heat of vaporization, and long ignition delays.

The ignition delay of alcohols has not received enough attention. Only a small number of workers have reported ignition delay measurements. Among those workers are Bro and Pedersen (1977), Moses et al. (1979, 1980), Stroment and Baker (1981), Shrivani et al. (1981), Borman and Foster (1981), Hashimoto and Henein (1982), and Saeed and Henein (1984, 1987). Discussions of chemical and physical phenomena associated with the combustion of alcohols in diesel engines have been very limited.

The present paper deals with ethanol–diesel and isopropanol–diesel blends. It reports investigations of their autoignition characteristics in a direct-injection, single-cylinder, research-type diesel engine.

Experimental Apparatus and Procedure

An IH – LABECO ATAC, single-cylinder, direct-injection diesel engine was used for conducting the study. The engine has a bore of 114.3 mm, a stroke of 114.3 mm, a displacement of 1172×10^{-6} m^3, and a compression ratio of 16:1. The engine was coupled to a General Electric DC cradle-type dynamometer. The dynamometer was equipped with a speed-and-load control and a tachometer. A schematic layout of the test setup is shown in Fig. 1. The flow rate of the pressure-regulated shop air was measured using a Meriam Laminar Flow Element. A surge tank and a flow straightener were used for reducing the pulsation of air flow. The air could be heated up to 810 K by using a 20 kW electric heater. The air then passed through a surge tank (coated with calcium silicate insulation) before being admitted to the engine. The pressure of exhaust gases was controlled by using a ball valve. Fuel consumption was measured per unit time and per cycle by using a weighing scale, a clock, and a revolution counter. A household gas meter was used for measuring the rate of flow of blowby gases (based on a reference temperature of 60°F). An electromagnetic transducer was used for generating the crank angle degrees. A Kistler piezoelectric pressure transducer (type 610 A/628c) was used for measuring the cylinder pressure. The signal from the transducer was amplified by a Kistler charge amplifier (type 504 E), and fed to a peak meter, in order to measure the peak cylinder pressure, and to a pressure differentiator, in order to measure the rate of change of cylinder pressure. The needle lift was measured by using an inductive Bently-Nevada probe-and-proximator system (3000 series).

The speed of the LABECO engine was kept constant at 900 ± 9 rpm. The coolant temperature was 315 ± 5 K. The lubricating oil temperature and pressure were 325 ± 5 K and 390 ± 30 kPa, respectively. Static injection timing was adjusted to 22 CAD BTDC, and the nozzle opening pressure was set at 20.8 ± 0.7 MPa as recommended by the manufacturer for straight diesel operation.

Lubricating oil (in both crankcase and fuel pump) was changed every 12 h of operation or before testing a new blend, whichever came first. The oil change was performed as a precautionary routine in order to avoid engine wear. The fuel system was filled with the test fuel. The engine was then motored for 15 min in order to warm it up. Motoring was followed by firing for at least 45 min in order to consume all

Contributed by the Internal Combustion Engine Division and presented at the Twelfth Annual Energy-Sources Technology Conference and Exhibition, Houston, Texas, January 22–25, 1989. Manuscript received by the Internal Combustion Engine Division August 1988. Paper No. 89-ICE-8.

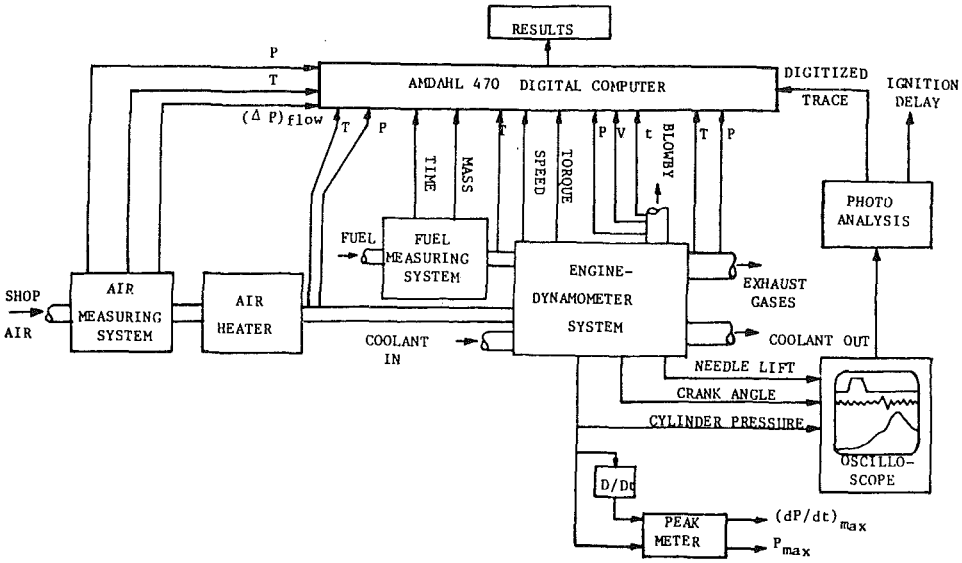

Fig. 1 Schematic diagram of test setup

the fuel left from the preceding set of tests, and allow the engine to reach steady-state operation prior to data recording. Seven fuels were tested:

1 100 percent DF2
2 25 percent 2-propanol + 75 percent DF2
3 25 percent ethanol + 75 percent DF2
4 50 percent 2-propanol + 50 percent DF2
5 50 percent ethanol + 50 percent DF2
6 75 percent 2-propanol + 25 percent DF2
7 75 percent ethanol + 25 percent DF2

When the effect of the fuel-air ratio was not being investigated, the fuel flow rate was kept constant at 1250 ± 50 cm^3/h.

Experimental Results and Discussion

Photographs were taken for the composite trace of cylinder pressure, needle lift, and crank angle degrees. These photos (Fig. 2) indicate that the time axis shifts by about 0.7 CAD during the exposure time of the camera (15 s). The variation in the ignition delay amounted to 3.3 CAD during the same period. It is clear that the shifting of the time axis is not the cause of the cycle-to-cycle variations in the ignition delay. Ignition delay and its cycle-to-cycle variations were determined from the photographs of 112 superimposed traces. The number 112 corresponds to the number of thermodynamic cycles at 900 rpm engine speed during the camera exposure time of 15 s. Ignition delay was measured from the start of needle lift to the occurrence of a detectable change in the slope of the pressure-time trace (and referred to as the pressure-rise delay, ID_p). The ignition delay was taken as the arithmetic mean of the longest and shortest periods.

Cycle-to-cycle variations in the ignition delay were quite observable for blends containing more than 30 percent alcohol (by volume). The variations increased as the alcohol content was increased and decreased as the intake-air pressure and temperature were increased. Figure 2 shows the cycle-to-cycle variation for a 50/50 ethanol–DF2 blend at equivalence ratio = 0.2, intake temperature = 300 K, and intake pressure = 140 kPa. The cyclic variations in ignition delay are shown in Fig. 2(*a*) for 112 superimposed cycles. The cyclic variations in peak cylinder pressure are shown in Fig. 2(*b*) for 118 consecutive cycles.

Figure 3 shows the composite traces for three different fuels: 100 percent diesel, 75/25 isopropanol–DF2 blend, and 75/25 ethanol–DF2 blend. Intake-air temperature and pressure were 360 K and 100 kPa, respectively. The fuel rate of flow was the same for all cases. The figure shows that straight-diesel operation produced the shortest ignition delay and the lowest rate of pressure rise. On the other hand, the 75/25 ethanol–DF2 blends produced the longest ignition delay and the highest rate of pressure rise, in addition to severe cycle-to-cycle variations.

Effect of Intake-Air Temperature

Figure 4 shows that ignition delay becomes shorter as the intake-air temperature is increased. This is due to the increase in temperature during ignition delay. When the fuel spray encounters hot air, both the physical and chemical processes will

Nomenclature

A = pre-exponential factor
BTDC = before top dead center
CAD = crank angle degrees
DF2 = No. 2 diesel fuel
E_a = activation energy
F/A = fuel–air ratio
ID = ignition delay
ID_p = pressure rise delay
k = rate constant of chemical reaction
P = pressure
P_i = intake-air pressure
P_m = integrated mean gas pressure during ignition delay
R = gas constant
T = temperature
T_a = air temperature
T_i = intake-air temperature
T_m = integrated mean gas temperature during ignition delay
TDC = top dead center
x = mole fraction
ϕ = equivalence ratio (based on fuel–air ratio)

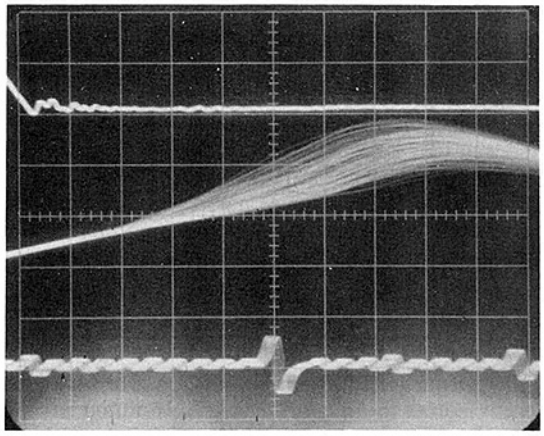

Fig. 2(a)

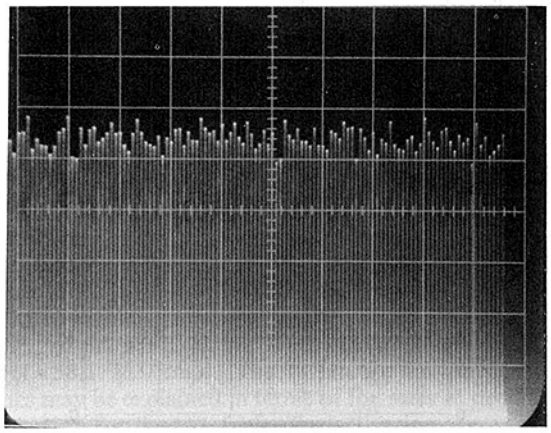

Fig. 2(b)

Fig. 2 Cycle-to-cycle variations for a 50/50 ethanol–DF2 blend, $\phi = 0.2$, $T_i = 300$ K, $P_i = 140$ kPa

be accelerated. A high gas temperature results in a faster rate of buildup of fuel vapor in the combustion chamber. Since the rates of chemical reactions increase by increasing both the temperature and the concentration of the reactants, the result will be a shorter delay period at higher intake-air temperatures. Addition of alcohols to DF2 increased the ignition delay. The increase with 2-propanol was less than that with ethanol at equal volumetric fractions.

Blends containing 75 percent alcohol did not autoignite at normal intake-air conditions ($P = 100$ kPa and $T = 300$ K). Isopropanol-containing blends required intake-air preheating to 350 K. Ethanol-containing blends did not autoignite reliably until the intake air was preheated to 430 K. The decrease in ignition delay with the increase in air temperature was more pronounced as the fraction of alcohol in the blends increased.

Effect of Intake-Air Pressure

The increase in intake-air pressure caused an increase in compression pressure and a reduction in ignition delay, as shown in Fig. 5. The increase in air pressure produced the following effects:

1 It decreases the mass diffusion of fuel vapor into the air (since the mass diffusivity is inversely proportional to the pressure), which leads to longer physical delays.

2 It increases the concentrations of the reactants, which

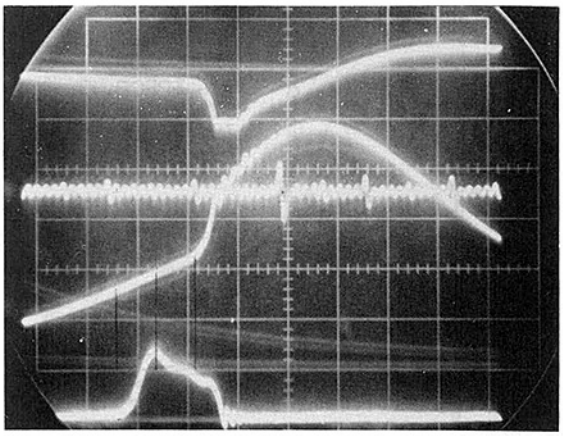

Fig. 3(a) DF2

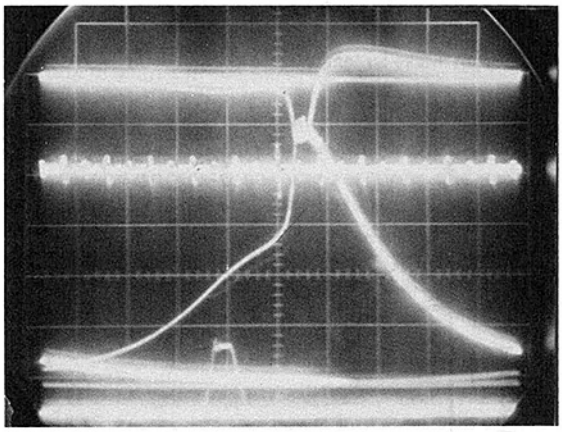

Fig. 3(b) 75 percent 2-propanol

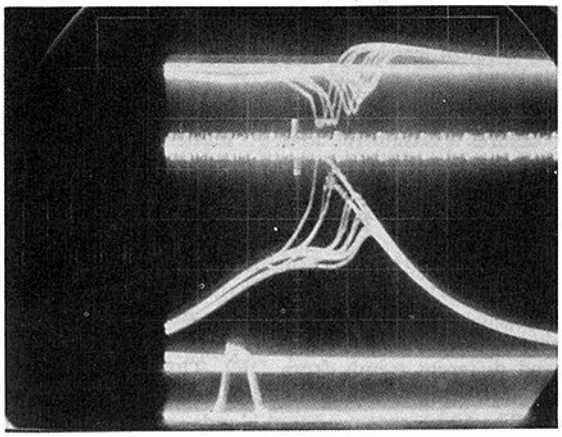

Fig. 3(c) 75 percent ethanol

Fig. 3 Combustion characteristics for various blends; $T_i = 300$ K, $P_i = 100$ kPa; fuel consumption = 1 kg/h

results in faster rates of chemical reactions and shorter chemical delays.

Since the experimental results showed that the net effect of increasing the chamber pressure is to shorten the ignition delay period, it may be concluded that the chemical effect (faster chemical reactions) is prevailing over the physical effect (slower mass diffusion). This is particularly the case at intake

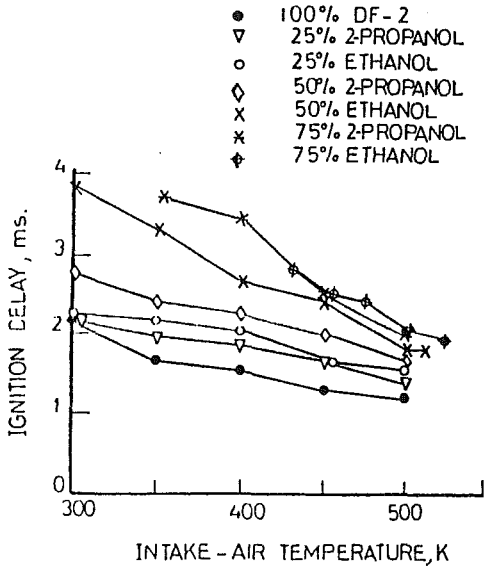

Fig. 4 Effect of intake-air temperature ignition delay for various blends

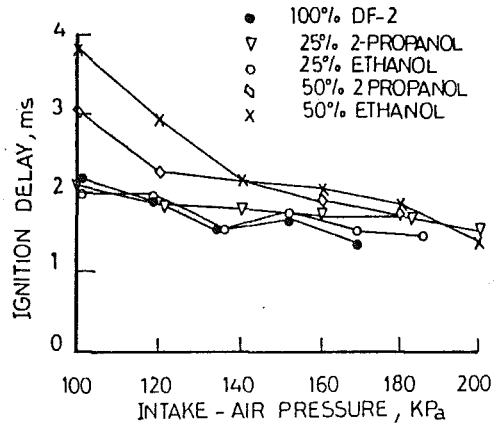

Fig. 5 Effect of increasing inlet air pressure on ignition delay for various blends

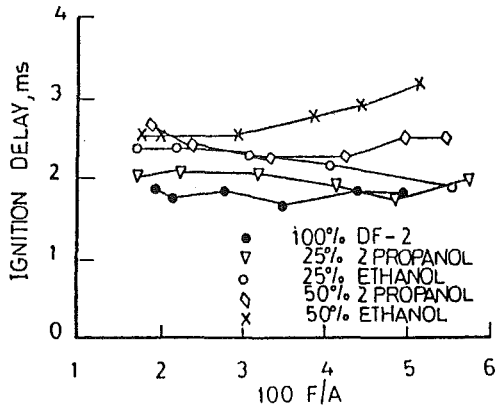

Fig. 6 Effect of fuel-air ratio on ignition delay for various blends

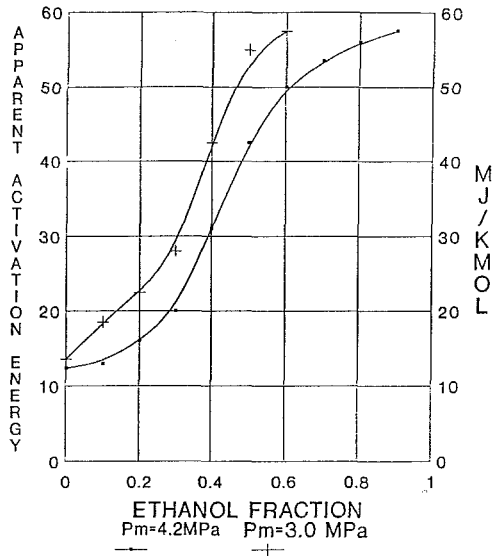

Fig. 7 Effect of ethanol contents on the apparent activation energy for ethanol-DF2 blends

air pressures less than 150 kPa. At higher air pressures the ignition delay is not very sensitive to air pressure.

Effect of Fuel-Air Ratio

Figure 6 shows the effect of fuel-air ratio on ignition delay for various blends. The ignition delay for DF2 remained almost constant over the whole range of fuel-air ratios. This agrees with previous findings (Henein, 1969). The blends showed different trends from DF2. The 25 percent alcohol blends showed reduction in ignition delay at the high fuel-air ratios. The 50 percent propanol blends showed a reduction in ignition delay as the fuel-air ratio increased from 0.015 to 0.03, after which it increased. The 50 percent ethanol showed a continuous increase in ignition delay as the fuel-air ratio increased.

Variations in fuel-air ratio affect the local air temperature in the vicinity of the fuel because of fuel evaporation. This effect may be significant with alcohols because of their high latent heats of evaporation. The latent heat of evaporation is 396 Btu/lbm for ethanol, as compared to 259 Btu/lbm for propanol and 95 Btu/lbm for DF2. Accordingly, the cooling effect due to the evaporation of propanol is less than that for ethanol.

The fuel-air ratio affects the ignition delay in two ways:

1 The increase in fuel-air ratio increases the concentration of the fuel vapor in the ignition zones. The higher the fuel concentration, the faster will be the rates of chemical reactions and shorter will be the ignition delay. This is confirmed by the work of Nicholas (1976), Westbrook (1979), Westbrook and Dryer (1980), and Miller and Matula (1980).

2 The increase in the fuel-air ratio reduces the air temperature and consequently reduces the rates of chemical reactions and increases the ignition delay period.

Depending on which effect (reactants concentration or temperature) is predominant, the ignition delay period may either increase or decrease as the fuel-air ratio is increased. Figure 7 shows that the ignition delay for ethanol is longer than for propanol, both having the same volumetric fraction. This may be attributed to the higher latent heat of evaporation of ethanol.

Effect of Ethanol on the Rate of Autoignition Reactions

The detailed elementary reactions that lead to the autoignition of fuels in diesel engines are not well defined. However, the global rate of all the autoignition reactions may be expressed in terms of the concentrations of the reactants and a reaction rate constant. The reaction rate constant may be expressed by an Arrhenius equation

$$k = A \cdot \exp\left(\frac{-E_a}{RT}\right) \quad (1)$$

where A is a pre-exponential factor, E_a is the global or apparent activation energy for the autoignition reactions, and R is the universal gas constant. If we consider that autoignition takes place when a critical concentration of radicals is reached, then the time taken to form these concentrations is equal to the ignition delay period. Accordingly the dependence of ignition delay on temperature can be expressed in the form

$$I.D. = C\exp\left(\frac{E_a}{RT}\right) \quad (2)$$

This argument is supported by the fact that most of the correlations for ignition delay as a function of temperature have the form of equation (2). These correlations are from Wolfer (1938), Elliott (1949), Sitkei (1963), Henein and Bolt (1967, 1969), Stringer (1970), Pedersen and Qvale (1974), Igura et al. (1977), Fujimoto et al. (1979), Birdi (1979), and Spadaccini and TeVelde (1982).

E_a was calculated from equation (2) by plotting log $I.D.$ versus $1/T_m$. The result showed a linear relationship. The slope of the line gives the value E_a/R. The mean pressure P_m during ignition delay was kept constant for all the runs. Figure 7 shows the effect of the volumetric fraction of ethanol, in ethanol–DF2 blends, on E_a, for two values of P_m. E_a for any blend increases with the drop in P_m. This indicates that for any blend the increase in the cylinder gas pressure would increase the rate of the autoignition reactions. E_a increases with the increase in the fraction of ethanol in the blend. The rate of increase of E_a is slow for ethanol fractions less than 20 percent, after which it increases sharply.

At P_m of 4.2 MPa, E_a for DF2 = 13 MJ/kmol and E_a for ethanol = 58.1 MJ/kmol. The difference in the activation energies may be explained in terms of the rates of decomposition reaction for the two fuels. The activation energy for the decomposition reactions for ethanol was estimated to be 337 kJ/mol (Saeed, 1984). Dodecane was considered to be representative of DF2 and the activation energy for its decomposition was estimated to be 308 kJ/mol (Saeed, 1984). The higher activation energy for the decomposition of ethanol may explain the difficulty in using it in diesel engines particularly at low temperatures. Figures 4 and 7 show that the increase in the rates of autoignition reactions with the increase in temperature is higher for ethanol than DF2.

The sharp increase in E_a for the blends with the increase in the fraction of ethanol may be explained in terms of the findings of Westbrook (1979). Westbrook conducted a shock-tube study on mixtures of two fuels, methane and ethane. Ethane has a lower activation energy than methane, or ethane is easier to autoignite than methane. The apparent activation energy for the mixture was found to increase sharply as the percentage of methanol increased from 80 to 95 percent. Westbrook attributed this behavior to the role the hydrogen atoms play in the autoignition reactions. Westbrook indicated that small fractions of ethane up to 20 percent provide H atoms rapidly and in large amounts, yielding a significantly higher rate of chain branching than in neat methane fuel. Once H atoms are produced, they react with the oxygen molecules to form O and OH radicals, which attack CH_4 and produce a methyl radical CH_3. The computational model developed by Westbrook et al. (1977) showed that ethane addition caused an increase in the branching ratio. This results in lowering the overall activation energy significantly as long as the mixture ratio is between 95 percent methane/5 percent ethane and 80 percent methane/20 percent ethane. However, increasing ethane over 20 percent did not change the branching ratio.

Westbrook's explanation (1979) means that for a mixture of two fuels of different ignition characteristics there is a critical mixing region where the addition of the higher ignition quality fuel is quite effective in reducing the activation energy. Figure 7 shows that, for the present study, the critical DF2 mole fraction is between 0.10 and 0.40. In this region, the addition of diesel fuels, which contain more methyl radical groups than ethanol, accelerates the branching reactions and reduces the activation energy needed for initiating the combustion processes. Figure 8 shows the rate of change of E_a with the change in the percentage of DF2 in the blend. E_a is reduced by adding DF2 to ethanol at a rate that peaks at mole fractions of DF2 equal to 0.30. Higher mole fractions of DF2 will reduce E_a, but at a lower rate.

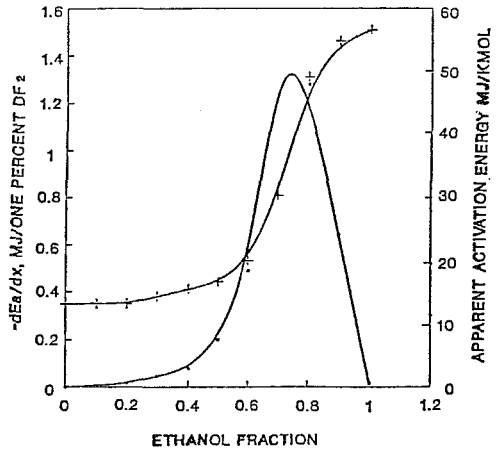

Fig. 8 Effect of adding DF2 to ethanol on apparent activation energy

Conclusions

1 The ignition delay of alcohol–diesel blends becomes longer as the alcohol content is increased.

2 Ethanol–diesel blends develop longer ignition delays than isopropanol–diesel blends.

3 The ignition delay of alcohol–diesel fuel blends is affected primarily by intake-air temperature preheating. Higher intake-air temperatures result in shorter delay.

4 The ignition delay of the blends containing 25 percent alcohol is slightly affected by the fuel–air ratio. With 50 percent ethanol, ignition delay increases with the fuel–air ratio due to the large portion of energy utilized in evaporating the fuel.

5 Increasing the charge pressure reduces the ignition delay of blends containing 50 percent alcohol. Blends with 25 percent alcohol are slightly affected by supercharging.

6 The global activation energy of the autoignition reactions, at a mean pressure of 4.2 MPa, for ethanol is 58.1 MJ/kmol as compared to 13.2 MJ/kmol for DF2. Adding DF2 to the blend reduces the activation energy by a rate that varies with the mole fraction of DF2. The highest rate is at a mole fraction of 0.30 DF2 in the blend.

References

Birdi, P. S., 1979, "General Correlation of Ignition Delay Period in Diesel Engines," Ph.D. Dissertation, Wayne State University.

Borman, G., and Foster, D., 1981, "Alcohol as a Fuel for Farm and Construction Equipment," Auto Technology Development Contractors' Meeting.

Bro, K., and Pedersen, P. S., 1977, "Alternative Diesel Engine Fuels: An Experimental Investigation of Methanol, Ethanol, Methane, and Ammonia in a D. I. Diesel Engine With Pilot Injection," SAE Paper No. 770794.

Elliott, M. A., 1949, "Combustion of Diesel Fuel," *SAE Quart. Trans.*, Vol. 3, pp. 490–515.

Fujimoto, H., Shimada, T., and Sato, G. T., 1979, "Investigation on Com-

bustion in Diesel Engines Using a Constant-Volume Combustion Chamber (Effect of Initial Temperature)," *Bull. JSME*, Vol. 22, pp. 1818–1825.

Hashimoto, I., and Henein, N. A., 1982, "A New System for Utilization of Neat Alcohol in Komatsu Diesel Engine," Final Report, prepared for Komatsu Ltd., Tokyo, Japan, by the Center for Automotive Research, Wayne State University.

Henein, N. A., and Bolt, J. A., 1967, "Ignition Delay in Diesel Engines," SAE Paper No. 670007.

Henein, N. A., and Bolt, J. A., 1969, "Correlation of Air Charge Temperature and Ignition Delay for Several Fuels in a Diesel Engine," SAE Paper No. 690252.

Igura, S., Kadota, T., and Hiroyasu, H., 1977, "Spontaneous Ignition Delay of Fuel Sprays in High Pressure Gaseous Environments," Department of Mechanical Engineering, Hiroshima University.

Miller, D. L., and Matula, R. A., 1980, "Ignition Delay Measurements of Ethanol Oxidation," Paper No. CSS/CI-80-08, Combustion Meeting (Central States Section), Louisiana State University, Mar. 24–25, Organized by the Combustion Institute.

Moses, C. A., 1979, "Engine Experiments With Alcohol/Diesel Fuel Blends," *3rd Intl. Symp. on Alcohol Fuel Technology*, Asilomar, CA, May 28–31.

Moses, C. A., Ryan, T. W., III, and Likos, W. E., 1980, "Experiments With Alcohol/Diesel Fuel Blends in Compression-Ignition Engines," 4th Intl. Symp. on Alcohol Fuels Technology, Sao Paulo, Brazil, Oct. 5–8.

Nicholas, J., 1976, *Chemical Kinetics—A Modern Survey of Gas Reactions*, Wiley, New York.

Pedersen, P. S., and Qvale, B., 1974, "A Model for the Physical Part of the Ignition Delay in a Diesel Engine," SAE Paper No. 740716.

Saeed, M. N., 1984, "Combustion Characteristics of Neat Ethanol and Blends of Ethanol and Diesel Fuel Number Two in a Direct-Injection Diesel Engine," Ph.D. Dissertation, Wayne State University.

Saeed, M. N., and Henein, N. A., 1984, "Ignition Delay Correlations for Neat Ethanol and Ethanol-DF2 Blends in a D.I. Diesel Engine," SAE Paper No. 841343.

Saeed, M. N., and Henein, N. A., 1987, "Physical Ignition Delay for Ethanol Droplets in Diesel Engines," ASME Paper No. 87-Pet-4, ASME Energy Sources Technology Conference & Exhibition, Dallas, TX, Feb. 15–20.

Shirvani, H., Goering, C. E., and Sorenson, S. C., 1981, "Performance of Alcohol Blends in Diesel Engines," SAE Paper No. 810681.

Sitkei, G., 1963, "Uber den Dieselmotoriseheh Zundverzug," *MTZ*, Year 24, Vol. 6, pp. 190–194.

Spadaccini, L. J., and TeVelde, J. A., 1982, "Autoignition Characteristics of Aircraft-Type Fuels," *Combustion and Flame*, Vol. 46, pp. 283–300.

Storment, J. O., et al., 1981, "Dual Fueling of a Two-Stroke Locomotive Engine With Alternate Fuels," SAE Paper No. 810252.

Stringer, Z. Z., et al., 1970, "Spontaneous Ignition of Hydrocarbon Fuels in a Flowing System," Symp. on Diesel Combustion, IMechE, London, Apr.

Westbrook, C. K., Creighton, J., Lund, C., and Dryer, F. L., 1977, "A Numerical Model of Chemical Kinetics of Combustion in a Turbulent Flow Reactor," *J. Physical Chemistry*, Vol. 81, p. 2542.

Westbrook, C. K., 1979, "An Analytical Study of the Shock Tube Ignition of Methane and Ethane," *Combustion Science and Technology*, Vol. 20, pp. 5–17.

Westbrook, C. K., and Dryer, F. L., 1980, "Prediction of Laminar Flame Properties of Methanol Air Mixture," *Combustion and Flame*, Vol. 37, pp. 171–192.

Wolfer, H. H., 1938, "Ignition Lag in the Diesel Engine," *VDI*, No. 392; translated by Royal Aircraft Establishment, Farnborough Library No. 358, Aug. 1959.

Preinjection—A Measure to Influence Exhaust Quality and Noise in Diesel Engines

H. Schulte

E. Scheid

FEV Motorentechnik Aachen,
Aachen, Federal Republic of Germany

F. Pischinger

U. Reuter

Aachen Technical University,
Aachen, Federal Republic of Germany

The combustion noise generated by DI diesel engines can be clearly reduced during both steady-state and transient operation in applying a pilot injection. After optimization, a slight increase in fuel consumption is found in the upper load range. The pilot injection also tends to reduce the NO_x emissions. An increase in black smoke emissions is considered to be the main drawback with pilot injection. High-speed Schlieren photographs of injection and combustion phenomena within a pressurized chamber show that the higher black smoke emissions may be due to the combustion of the main injection quantity that occurs in a mixture that is insufficiently prepared and with nearly no delay due to the pilot injection. On the basis of these findings, it is concluded that a high degree of atomization and rapid vaporization of the main injection quantity must be accomplished. To achieve these goals better, a separate injection nozzle for the pilot quantity is preferred to an injection system with a single injection nozzle, providing both the pilot and the main quantity. Therefore, rather simple injection systems with a separate pilot injector can be developed that provide a constant pilot quantity and controlled pilot injection time over the entire engine map.

Introduction

The desire for reductions in fuel consumption has led to worldwide development efforts in the field of high-speed DI diesel engines for passenger cars and light-duty applications. In addition to the anticipated gains in fuel consumption, the DI process, when compared to the IDI process, offers other distinct advantages such as lower component thermal stress and, consequently, greater potential for turbo/supercharging. These inherent advantages will provide the incentive for future developments of the DI concept. The advantages of the DI concept are especially apparent in engines equipped with a combustion chamber with central, direct injection [1]. In comparison with IDI diesel engines in light-duty applications, the higher NO_x emissions and combustion noise of the DI process are considered detrimental. Higher levels of combustion noise are particularly apparent under transient operational conditions where clear noise peaks occur that are not present during steady-state operation. This phenomenon does not appear in IDI or DI engines equipped with a peripheral fuel injection.

The injection of a small quantity of fuel at the start of injection will ensure a smooth initiation of combustion and, consequently, reduced excitation of the combustion noise. It will also result in lower component stresses resulting from the gas force. However, the principle of pilot injection is not a new concept. Several experimental investigations have been previously conducted to evaluate the effects of pilot injection on the combustion process [3, 7].

Contributed by the Internal Combustion Engine Division and presented at the Internal Combustion Engine Division Technical Conference, San Antonio, Texas, October 2-5, 1988. Manuscript received by the Internal Combustion Engine Division June 1988.

In principle, pilot injection can be achieved by using the main injection nozzle or by installing a separate injection nozzle with one or more spray holes. Systems using a single injection nozzle for each cylinder can be categorized into: (1) relatively simple mechanical systems incorporating a retraction volume that is introduced for a short time after start of injection, absorbing some of the fuel injected by the pump [5] and (2) somewhat more complex electronically controlled systems. Optimization of pilot quantity and pilot injection timing over the complete engine map cannot be obtained with a mechanical system. However, an entire electronic system can be adapted (in theory) over the whole engine map to consider the parameters identified above. In principle, all injection pumps and unit injectors that allow the control of start and duration of injection (injection quantity) by adequate magnetic spill valves [8, 9] can be used. In addition, an interruption of the injection can be obtained by all injection systems that incorporate pressure reservoirs and pressure amplifying techniques, e.g., in the injection nozzle [10].

This publication will present the results of an engine test program to evaluate the effect of pilot injection on the combustion behavior in a small, high-speed DI engine. In addition, high-speed Schlieren photographs, taken in a pressurized chamber, will be presented to explain injection and combustion phenomena with and without pilot injection.

Observation of Spray Development, Ignition, and Combustion

To analyze development, self-ignition, and combustion of pilot and main spray, high-speed Schlieren movies were taken.

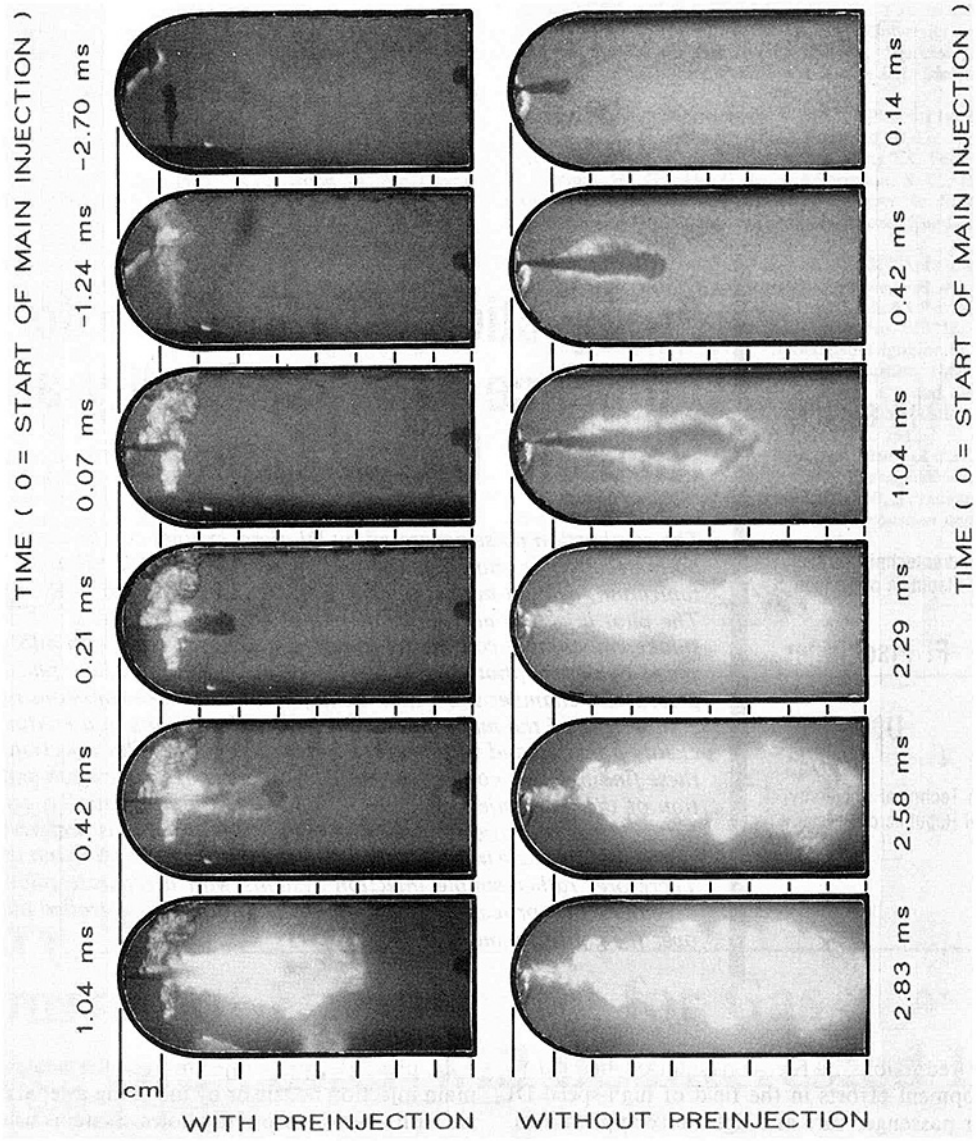

Fig. 1 High-speed Schlieren photographs without and with pilot spray injection

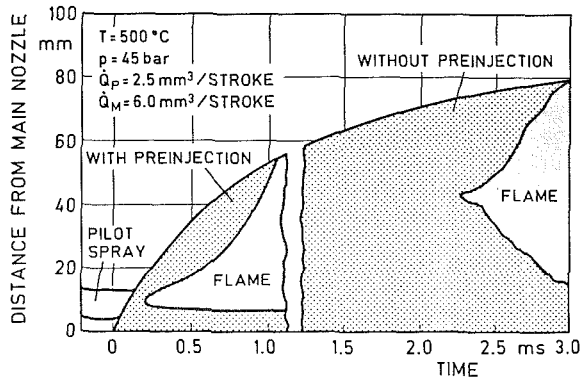

Fig. 2 Spray tip penetration and flame propagation in axis projection without and with pilot injection

The essential part of the test configuration used consists of a high-pressure chamber that allows air pressures up to 60 bar and air temperatures up to 900 K. These conditions are comparable to those of actual diesel engines as they occur during the period of ignition delay. The test configuration is described in [11, 12].

Figure 1 shows high-speed photographs with and without pilot spray injection. The chamber temperature was 773 K, and the pressure 45 bar. The volume injected by the pilot spray was 2.5 mm^3/stroke; the main spray volume was 6.0 mm^3/stroke.

The high-speed Schlieren photographs, which include pilot injection, show that the main spray starts burning with practically no delay, independent of the time between pilot and main injection. Thus, the issue whether the pilot quantity was still burning or not was considered to be unimportant. The ignition delay of the main injection is observed to be very short, whereas it is nearly 2 ms without pilot injection.

Figure 2 shows the spray tip penetration and the flame propagation of the main spray versus time. The region of pilot spray exhaust and flame can also be seen. The direction of main spray tip movement is perpendicular to the movement of the pilot spray. At 0.2 ms after start of main spray injection, ignition occurs. The combustion of the main spray starts before the fuel is sufficiently atomized and vaporized. The burning flame contains soot, which is indicated by the flame

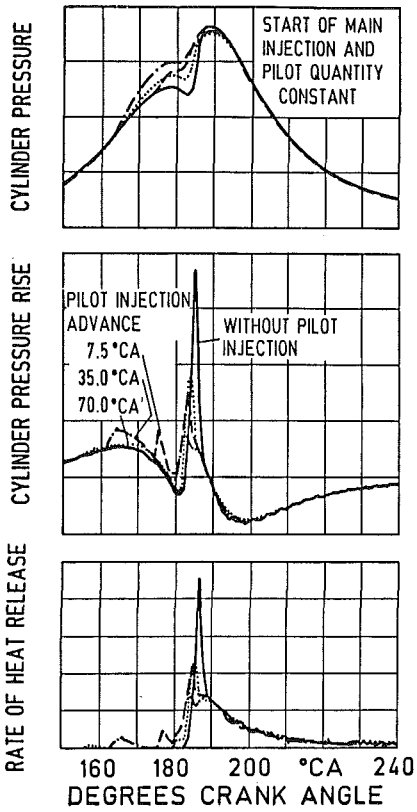

Fig. 3 Influence of a pilot injection on the combustion process

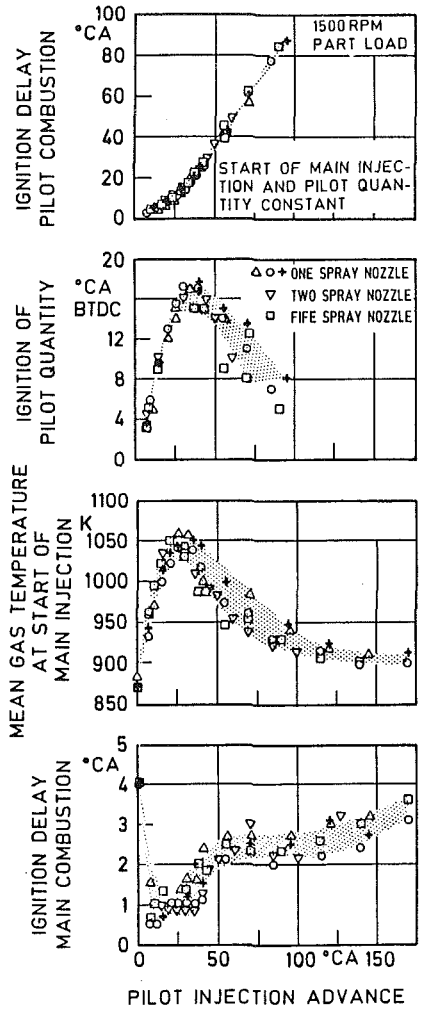

Fig. 4 Combustion process parameters for variations of the pilot injection advance and nozzle spray hole geometry

color. The soot is produced by the combustion of the very first droplets of the main injection, which are not sufficiently vaporized, and which start burning directly after leaving the spray holes.

Influence of the Pilot Injection on the Engine Combustion Behavior

Initially, the general influence of pilot injection on the combustion behavior is considered. Figure 3 gives examples of the cylinder pressure curve, the pressure rise, and the rate of heat release (ROHR) for a high-speed DI engine operated (1) without pilot injection and (2) with a constant pilot quantity and different pilot spray advances. The start of the main injection was kept constant.

It can be clearly seen that the large peak within the ROHR curve, which corresponds to the combustion noise excitation, can be significantly reduced.

Further analysis of the influence of the pilot injection (with varying advances) on the combustion behavior is shown in Fig. 4.

This figure displays the ignition delay of the pilot combustion, the ignition timing of the pilot quantity, the mean gas temperature in the combustion chamber at the start of main injection, and the ignition delay of the main combustion as functions of the pilot injection advance for one operational point under part-load conditions.

The ranges of variation represent the engine's operational behavior when using separate injection nozzles for the pilot quantity. The nozzles were located at the same position in the combustion chamber but they contained different spray hole geometries (number, direction, and diameter of the spray holes).

Remarkably, if the injected pilot quantity is kept constant, the engine exhibits similar behavior regardless of variations in nozzle orientation or configuration. For very large pilot injection advances, the situation is comparable to the introduction of a portion of the fuel into the intake manifold (fumigation).

As expected, the ignition delay of pilot combustion increases with greater pilot advance. The onset of ignition of the pilot quantity will advance only to approximately 35 deg CA with increasing pilot injection advances. A pilot injection advance exceeding this value, thereby injecting the pilot quantity into colder air, leads again to later ignition timing. With increasing advancement of pilot injection and, correspondingly, longer pilot ignition delays, an increasingly leaner mixture is obtained at the start of combustion. Despite the longer delay period, allowing more time for chemical prereaction to take place, this effect appears to dominate.

The mean gas temperature in the combustion chamber at the start of main injection increases with a pilot injection advance up to a maximum of 25 deg CA. At this point the temperature is almost 200 K greater than without pilot injection. When the advance of the pilot injection exceeds 25 deg CA, the dominant influence of the pilot injection is reduced, resulting in lower mean gas temperature at the start of main injection. The ignition delay of the main combustion, which strongly influences the combustion noise excitation, exhibits a behavior that is inverse to that of the mean gas temperature. This shows the great influence of the thermal conditions at the start of main injection on the ignition delay. In the range between 15 and 35 deg CA pilot injection advance, the ignition delay of the main injection can be reduced to less than 1 deg CA, basically indepenent of the nozzle configuration chosen.

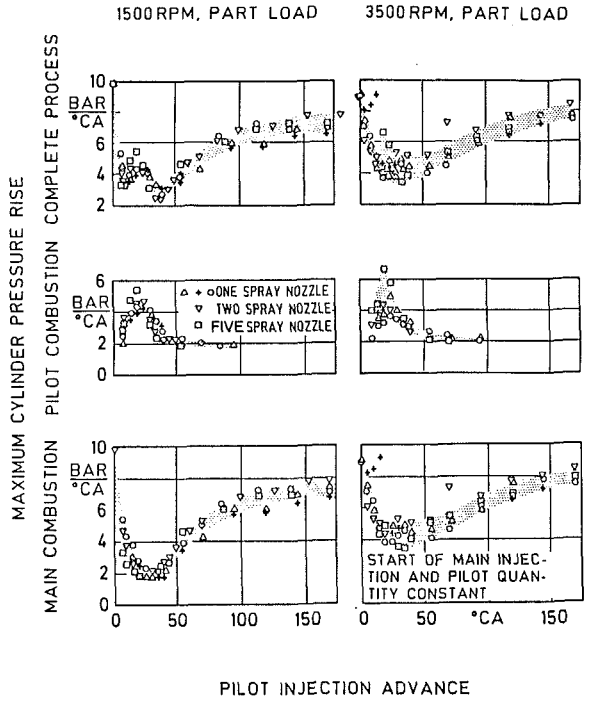

Fig. 5 Maximum values of the cylinder pressure rise for variations of pilot injection advance and pilot nozzle spray hole geometry

Reduction of Cylinder Pressure Rise by Pilot Injection Under Steady-State Conditions

Figure 5 depicts the effects of pilot injection on the maximum values of the cylinder pressure gradients as a function of the pilot injection advance for constant pilot quantity. Two partial load operating points at speeds of 1500 and 3500 rpm are shown. The use of pilot injection reduces the maximum value of the cylinder pressure rise of the overall process, which consists of both the main and the pilot injection combustion process. This is especially true for 1500 rpm where the cylinder pressure can be reduced to 7 bar/deg CA when the appropriate pilot injection advance is chosen.

Two striking minima are found among the cylinder pressure gradients of the overall process. They occur at low speeds with pilot injection advances of approximately 10 deg CA and 40 deg CA. The occurrence of these minima may be explained by evaluating the maximum values of the cylinder pressure rise for the pilot and the main combustion process. Depending on the particular pilot injection advance, the overall maximum cylinder pressure gradient is dominated by either the pilot combustion process or the main combustion.

When the start of the pilot injection is advanced to 100 deg CA or more, the combustion of the pilot quantity cannot be recognized when computing the burned mass fraction. However, in comparison to operations without pilot injection, reduced maximum values of the cylinder pressure rise for the overall process still exist, thus resulting from reduced ignition delay (cf. Fig. 4) of the main injection. The reduced ignition delay is, most probably, not due to higher gas temperatures in the combustion chamber, but to improved chemical preconditions leading to the formation of free radicals from premixed fuel fractions in the pilot quantity.

Figure 6 shows the influence of the pilot quantity on the maximum cylinder pressure rise for one partial-load condition and three variations of pilot injection advance. For these tests, the pilot quantity was supplied to the combustion chamber through a nozzle with two spray holes.

While increasing the pilot quantity, there is, regardless of the advance in pilot injection, a clear reduction in the maximum cylinder pressure rise of the overall process. The lowest

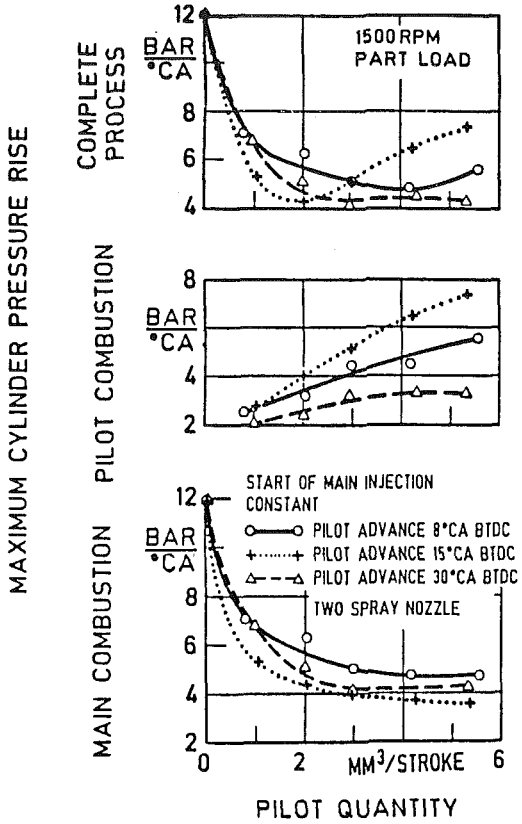

Fig. 6 Maximum values of the cylinder pressure rise for variations in the pilot injection quantity

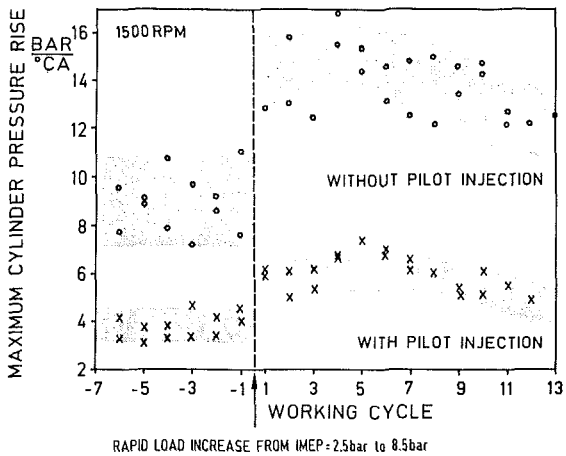

Fig. 7 Maximum values of the cylinder pressure rise under transient operation

values of the maximum cylinder pressure gradients for the overall process are obtained with pilot quantities between 2 and 4 mm^3/cycle. In the case of minor advances, the cylinder pressure rise of the pilot combustion does not exceed the pressure rise of the main combustion, which is due to the relatively short ignition delay of the pilot quantity.

As the pilot quantity is increased above 4 mm^3/cycle, the cylinder pressure rise of the overall process even tends to increase. This is due to the logical increase in the cylinder pressure rise, associated with pilot combustion, together with an increase in pilot quantity.

Reduction of Cylinder Pressure Rise During Transient Conditions

In addition to the steady-state combustion noise, the com-

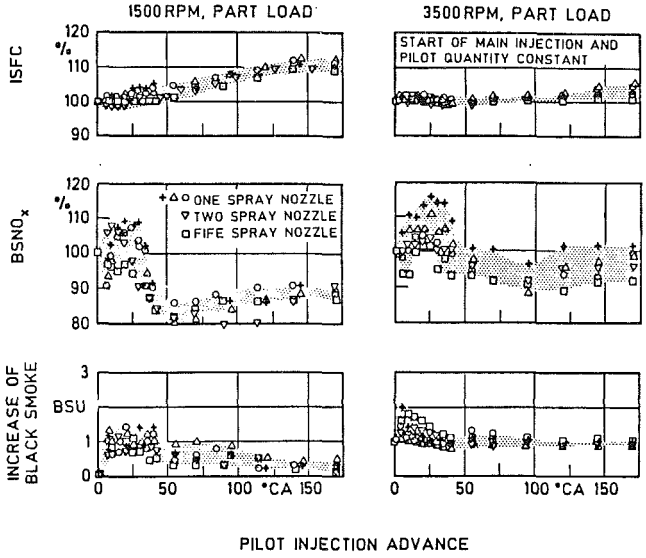

Fig. 8 Fuel consumption and exhaust emissions for variation of the pilot injection advance and the nozzle spray hole geometry

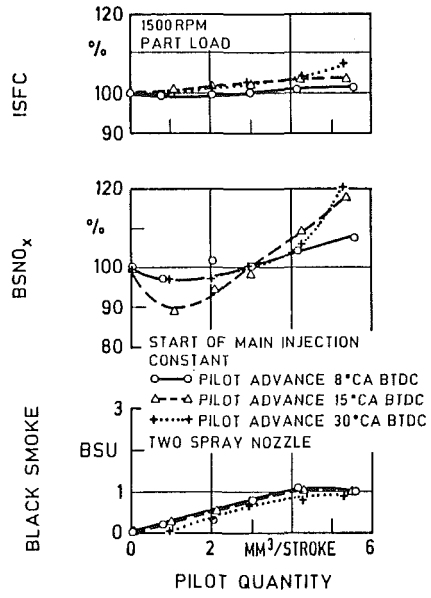

Fig. 9 Fuel consumption and exhaust emissions for different pilot quantities

bustion noise peaks that occur during the acceleration of DI diesel engines with central injection are undesirable, especially in passenger cars and light-duty applications.

As shown in Fig. 7, the use of pilot injection may also improve the transient situation. The figure shows the maximum values of the cylinder pressure gradient for 7 working cycles before and 13 cycles after a rapid load increase (IMEP = 2.5 to 8.5 bar) with and without pilot injection. It can be seen that the pilot injection reduces the absolute values of the cylinder pressure rise before and after the load increase. In addition, the relative increase in the cylinder pressure rise immediately following the load increase is lower with pilot injection (about 3 bar/deg CA) than without pilot injection (about 6 bar/deg CA).

Effect of the Pilot Injection on Fuel Consumption and Exhaust Emissions

The information provided above demonstrates the significant potential of the pilot injection for a lower combustion noise. However, the acoustic advantages must not, at the same time, produce significant disadvantages with respect to fuel consumption or exhaust emissions. In this context, Fig. 8 presents data at two partial-load conditions, which show the impact of pilot injection advance on the indicated specific fuel consumption (ISFC) as well as on the NO_x and black smoke emissions at constant pilot quantity. The results are displayed for the same test cycles as those shown in Figs. 4 and 5. In comparison to the combustion process parameters, indicated in these figures, ranges of variations are shown exhibiting similar tendencies for all injection nozzles used.

At a speed of 1500 rpm the indicated specific fuel consumption increases only slightly with a pilot injection advance of approximately 50 deg CA. Concerning higher speed, the fuel consumption is not affected or even slightly reduced for all nozzles if the pilot injection advance does not exceed 50 deg CA. However, the fuel consumption increases distinctly, especially in the case of low speed, if the pilot injection is advanced further.

The NO_x emissions, as a function of the pilot injection advance, have similar behavior concerning the mean gas temperature in the combustion chamber at the start of main injection. This is shown in Fig. 4 for pilot advances up to 50 deg CA approximately. The highest values for the NO_x emissions as well as for the mean gas temperatures at the start of main injection occur at a pilot injection advance of approximately 25 deg CA. These levels represent 110 to 115 percent of the emissions measured without pilot injection. If the pilot injection is continuously advanced, the NO_x emissions can be clearly reduced, especially in the case of 1500 rpm, below the level obtained without pilot injection.

Although the fuel consumption and the NO_x emissions are only slightly affected by the pilot injection, the black smoke emissions tend to increase. In particular, at low speeds, a strong increase in black smoke is observed at pilot injection advances up to 50 deg CA.

To demonstrate this factor, Fig. 9 shows, independent of the degree of advance, that black smoke emission increases with an increase in the pilot quantity.

Black smoke is generated when the hydrocarbons of the injected fuel are dehydrated and the remaining hydrocarbon structures agglomerate to particulates, thereby increasing in size. The prerequisites for this process are high temperature and limited air concentration. These conditions are prevalent in regions where fuel that has not yet vaporized comes in contact with the progressing flame of the burning cylinder charge. However, this condition does not occur if the pilot quantity is sufficiently burned.

Since there is only a very small pilot fuel quantity injected and the pilot ignition delays are long, it can be assumed that the pilot fuel is already completely vaporized upon ignition. Therefore, the contribution to the black smoke emissions by the pilot quantity is minor. The soot emissions are strongly dependent on the main combustion conditions.

Under low-load conditions, a large portion of the soot produced at the start of main injection can be oxidized during the following diffusion combustion. Therefore, a relatively small increase in black smoke can be observed, compared to the operation without pilot injection (cf. Fig. 10). With increasing load, the boundary conditions for oxidation of the soot deteriorate, which is due to the locally lower air/fuel ratios. At full-load operation, especially with a large pilot quantity, smoke increases drastically.

Operational Behavior With a Constant Pilot Quantity Over the Entire Operational Range

Figure 11 depicts the potential benefits of using pilot injection over the speed range. These results were obtained with a

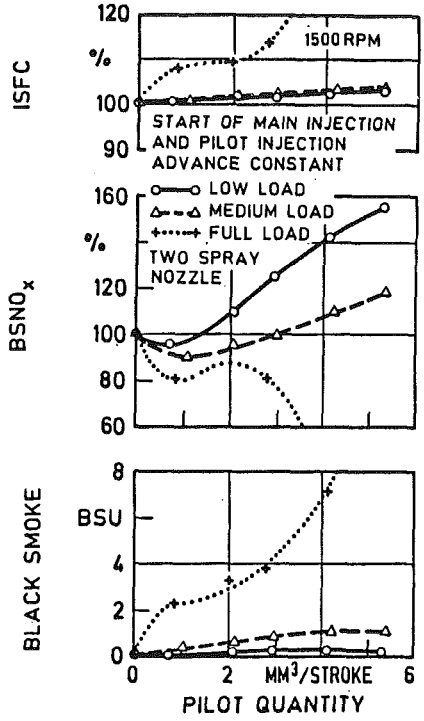

Fig. 10 Fuel consumption and exhaust emissions at different loads for different pilot quantities

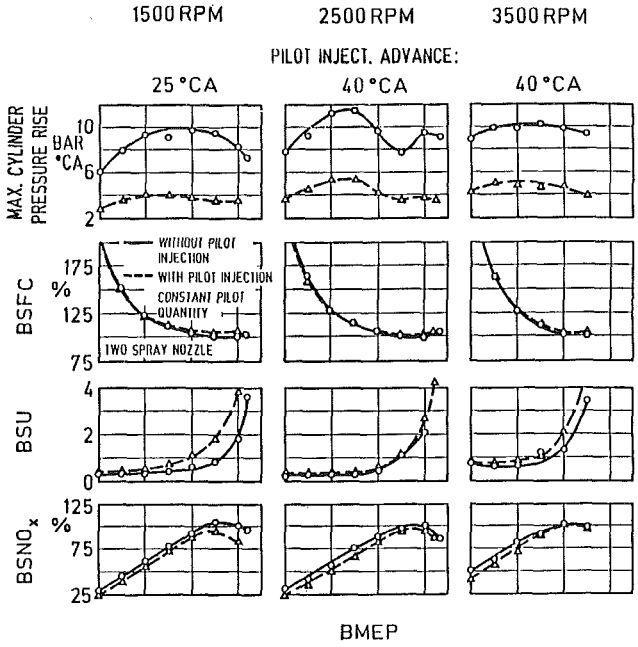

Fig. 11 Operational behavior without and with pilot injection

constant pilot quantity, which, regardless of load and speed, was injected through a separate nozzle. Both the start of pilot injection and the start of the main injection were controlled as functions of speed and not controlled by the load.

The use of pilot injection leads to clearly reduced rises in cylinder pressure for all speeds. The fuel consumption is only slightly affected by the pilot injection and the NO_x emissions have even been reduced. The pilot injection, however, produces a somewhat detrimental effect on the smoke emission, especially in the upper load range. However, at 2500 rpm, the black smoke emissions are practically unchanged.

When a separate injection nozzle is used for the pilot quantity, the high-pressure hydraulic characteristics of the main injection supply are unaffected by the pilot injection. This allows an optimization of the main injection system without constraint of the pilot injection.

As shown above, the atomization and vaporization of the pilot injection fuel have a much less significant influence on the overall operation than the quality of the main injection. Based upon this fact it seems to be possible to develop a somewhat simple injection system for pilot injection through a separate nozzle that would not require quantity control over the engine map.

Acknowledgments

The authors wish to thank the Volkswagen AG for providing a test engine, and the Deutsche Forschungsgemeinschaft for financial contributions to the optical spray investigations.

References

1 Kirsten, K., Pouille, J. P., Mercier, C., Schulte, H., and Pischinger, F., "Combustion Process Analysis of Different Combustion Systems for Passenger Car Diesel Engines," Congres International Moteurs Diesel Pour Vehicules Automobiles et Utilitaires, Lyon, France, May 13-14, 1987.

2 Rust, A., and Thien, E., "Verbrennungsgeräusch direkteinspritzender Dieselmotoren im instationären Betrieb, Parts 1 and 2," *MTZ*, Vol. 48, 1987.

3 Terado, K., "Beeinflussung der Dieselverbrennung bei Kraftstoffeinspritzung," *MTZ*, Vol. 20, 1959, p. 8.

4 Rönitz, R., "Chancen der Direkteinspritzung bei schnellaufenden PKW-Dieselmotoren für die Großserie," FISITA Paper No. 845090, 1984.

5 Mayer, K. P., "Fuel Economy, Emissions and Noise of Multispray Light Duty DI Diesels—Current Status and Development Trends," SAE Paper No. 841288, 1984.

6 Athenstaedt, G., Herzog, P., and Noraberg, J., "Combustion Improvement Potential Through the Use of Split Injection," CIMAC 1987, Warschau, Poland.

7 Mercier, C., and Filiot, G., "Interet de la preinjection pour la reduction du bruit des petits moteurs diesel a injection directe," Congres International Moteurs Diesel Pour Vehicules Automobiles et Utilitaires, Lyon, France, May 13-14, 1987.

8 Scott, D., "Electric Unit Injector Cuts DI Diesel Noise," *Automotive Engineering*, Dec. 1983.

9 Yamada, K., "The Second Generation of Electronic Diesel Fuel Injection Systems—Investigation With Rotary Pumps," SAE Paper No. 860145, 1986.

10 Ganser, M., "Akkumuliereinspritzung: theoretische und experimentelle Untersuchung eines elektronisch gesteuerten Dieseleinspritz-systems für Personenwagenmotoren," Dissertation ETH, Zurich, Switzerland, 1984.

11 Scheid, E., Pischinger, F., Knoche, K. F., Daams, H.-J., Hassel, E. P., and Reuter, U., "Spray Combustion Chamber With Optical Access Ignition Zone Vizualization and First Raman Measurements of Local Air-Fuel Ratio," SAE Paper No. 861121, 1986.

12 Pischinger, F., Reuter, U., and Scheid, E., "Self Ignition of Diesel Sprays and Its Dependence on Fuel Properties and Injection Parameters," ASME Paper No. 88-ICE-14.

Spray and Flame Structure in Diesel Combustion

E. N. Balles
Arthur D. Little, Inc.,
Cambridge, MA 02140

J. B. Heywood
Sloan Automotive Laboratory,
Massachusetts Institute of Technology,
Cambridge, MA 02139

The diesel combustion process in direct-injection diesel engines consists of four distinct stages: an ignition delay, a premixed phase, a mixing-controlled phase, and a late combustion phase. This paper uses geometric information from high-speed direct and shadowgraph movies and corresponding combustion chamber pressure histories, taken in a rapid compression machine study of direct-injection diesel combustion, for a coupled analysis of the diesel flame geometry and energy or heat release to develop our understanding of the diesel spray and flame structure during the ignition delay period and premixed combustion phase. It is shown that each fuel spray from a multihole fuel-injector nozzle consists of a narrow liquid-containing core centered within a much larger fuel-vapor air region, which has a distinct boundary. The liquid core does not penetrate to the chamber periphery, while the vapor containing spray interacts strongly with the boundary. Ignition occurs part way along each growing spray. Once combustion starts, the outer boundary of the fuel-vapor-containing region expands more rapidly due to the combustion energy release. Very high initial spreading rates of the luminous region boundary are observed. A comparison of enflamed areas and volumes, and burned gas volumes, indicates that the luminous region during the early stages of combustion (assumed stoichiometric) is around 1 cm thick and does not fill the full height of the chamber. During the premixed combustion phase, the burned gas volume is one-half the enflamed volume, indicating the presence of a substantial unburned (rich) fuel-vapor/air core within the luminous region of each fuel spray. A close correspondence of flame geometry to spray geometry is evident throughout the combustion process.

Introduction

In direct-injection diesel engines, the fuel enters the combustion chamber through a multihole nozzle on or close to the chamber axis to form four or more sprays that penetrate rapidly outward toward the chamber periphery. Fuel injection starts toward the end of the compression stroke (some 20 crank angle deg before the top center crank position), the fuel vaporizes and mixes rapidly with the high-temperature high-pressure air in the chamber (which often is swirling to increase the rate of mixing), the mixture spontaneously ignites, and then burns over a period of about 50 crank angle deg [1].

A descriptive model of this combustion process developed by Lyn [2] is now well accepted. The overall diesel combustion process is divided into four stages. An *ignition delay* (of order 1 ms or 10 crank angle deg) separates start of injection from start of combustion. During this period, physical processes (atomization, vaporization, mixing) and chemical processes (pre-ignition reactions) prepare the fuel–air mixture for spontaneous ignition. Once ignition occurs, fuel and air, which have mixed to within combustible limits, burn rapidly in the *premixed* stage. The rate of fuel energy release during the stage is extremely high. Once the fuel and air that mixed during the delay period and premixed stage have been consumed, the *mixing-controlled* stage commences. In this stage, the burning rate is governed by the rate at which mixture becomes available for combustion, which is controlled primarily by the fuel vapor/air mixing rate. Finally, in a *late-combustion* stage, combustion goes to completion at a much lower rate as regions containing richer-than-average combustion products and soot burn up.

There have been extensive photographic studies of the diesel combustion process in engines, bombs, and rapid compression machines (RCM) (see for example references [3–8]). Much insight has been obtained from detailed descriptions developed from high-speed movies of combustion. There have been efforts to date to extract quantitative geometric information from these diesel combustion movies. For example, Kobayashi et al. [6] calculated the air entrainment rates for diesel sprays and flames in a rapid compression machine based on focused shadowgraph images. By assuming an axisymmetric spray or flame, they calculated a volume for the zone defined by the outer boundary seen in the shadowgraph image (no distinction was made between unburned fuel–air mixture and the burning zone or combustion products). By comparing noncombusting sprays (N_2 environment) with burning fuel sprays, Kobayashi concluded that the rapid expansion during the initial heat release period increases the air entrainment rate.

There has been little effort to couple flame geometry data

Contributed by the Internal Combustion Engine Division and presented at the Twelfth Annual Energy-Sources Technology Conference and Exhibition, Houston, Texas, January 22–25, 1989. Manuscript received by the Internal Combustion Engine Division August 1988.

Table 1 Rapid compression machine details [12]

Geometry:	
bore	10.16 cm
stroke	44.7 cm
clearance height	3.07 cm
compression ratio	15.5
Operating Conditions:	
initial air temperature	-20 to 150 C
inlet air velocity	10 to 150 m/s
initial swirl level	0 to 6000 rev/min
initial cylinder pressure	1 to 2 bar abs.
fuel injection pressure	60,000 to 120,000 kPa
compression time	50 to 35 ms
mean piston speed	9 to 13 m/s
These experiments:	
air pressure at injection	39 bar
air temperature at injection	900 K
mass of fuel injected	0.1245 g (constant)
overall equivalence ratio	0.5

obtained from photographs with the progress of the diesel combustion process as defined by an energy release or first law analysis of the cylinder or chamber pressure. Such coupled flame geometry and pressure data analysis have proved especially useful in developing our understanding of spark-ignition engine flame structure (see for example references [9, 10]).

In one especially noteworthy photographic study of diesel combustion, Kamimoto et al. [7] have developed a phenomenological model that uses empirical data from combustion movies to predict the heat release rate of the flame. The model consisted of air entrainment, mixing, and combustion submodels. They used a rapid compression machine in which the spray was free from wall interactions to develop and validate the predictive model over a range of ignition delay times, injection rates, and injection durations.

This paper uses an extensive data base of high-speed movies and combustion chamber pressure records of diesel combustion taken in a rapid compression machine to quantify enflamed and burned gas volumes and develop our understanding of the direct-injection diesel engine's flame structure. In our study, the injector was sized to match the dimensions of the RCM combustion chamber. With this setup, the interaction between each fuel spray and the chamber walls is significant. The focus is on processes occurring during the earlier stages of combustion, the ignition delay and premixed combustion phases. The flame essentially fills the combustion chamber early in the mixing-controlled phase, and our ability to extract flame geometry information is then much more limited.

Apparatus and Diagnostics

The M.I.T. rapid compression machine simulates the diesel engine combustion environment, provides easy visual access to the combustion chamber for photography, and allows precise control over the initial conditions [11, 12]. The machine consists of three coaxial piston-cylinder sections with the pistons connected by a common shaft as shown in Fig. 1. The pneumatic driving chamber provides the force required to drive the shaft through the compression stroke. The snubbing chamber controls the piston velocity profile to simulate reciprocating engine piston motion during the compression stroke. The compression cylinder has a radially mounted shrouded inlet air valve at the combustion chamber end in the clearance volume, and three radial exhaust ports at the opposite end. Air flows steadily through the cylinder, generating swirl or not depending on the inlet valve shroud orientation, until just before the shaft is released. Following the compression stroke, the piston is locked in place and fuel is injected through an American Bosch EFIS fuel injector mounted in the center of the cylinder head. The fuel used was a standard diesel fuel (cetane number 47) commonly used in engine testing. Injection and combustion take place under conditions typical of direct-injection diesel engines. The cylinder head is fitted with a visualization window for high-speed photography as shown. A summary of the major component dimensions and operating conditions is given in Table 1.

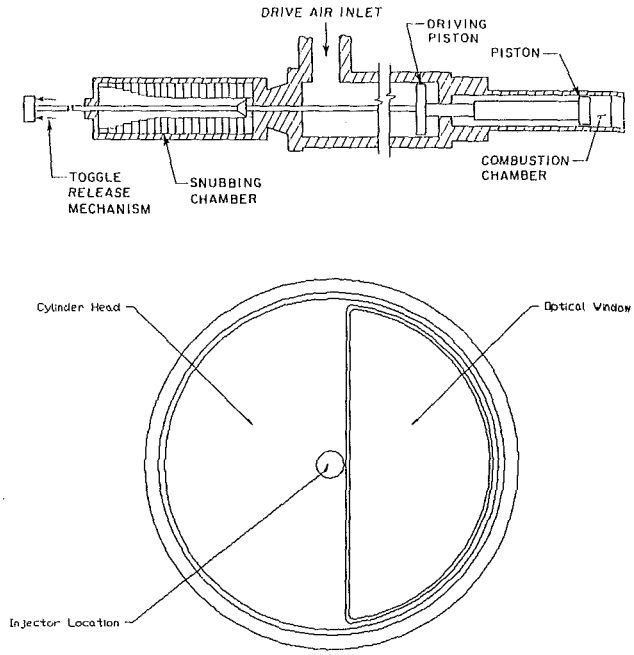

Fig. 1 Schematic diagram of the M.I.T. rapid compression machine and the geometry of its combustion chamber and cylinder head

The primary diagnostics during compression, injection, and combustion are the following. Cylinder pressure, used for heat release analysis, was measured using a quartz piezoelectric transducer mounted in the cylinder head. Injector needle lift was measured by a fiber optic device mounted in the body of the EFIS injector, which provides an analog signal proportional to needle lift. Operating experience indicated the injector exhibits an exceptionally square needle lift profile. Fuel injection pressure was estimated by multiplying the measured fuel rail pressure by six, the value of the area ratio of the hydraulic amplifier piston.

Nomenclature

A = area
m = mass
p = pressure
Q = heat release
T = temperature
t = time
V = volume
x = mass fraction

Subscripts

a = air
b = burned
f = flame or fuel
u = unburned

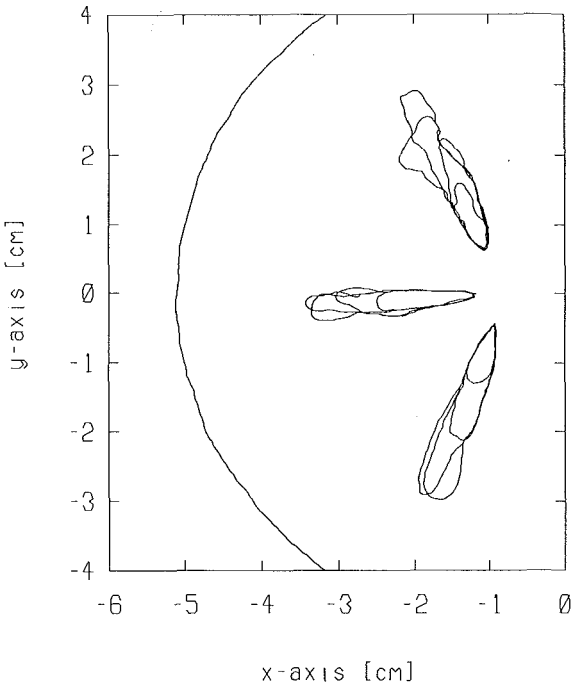

Fig. 2 Tracings of the outer boundary of the dense core region of the fuel spray seen with direct photography; 60,000 kPa injection pressure, 39 bar air pressure, and 900 K air temperature at injection, 7200 frames/second

High-speed movies of injection and combustion were filmed using direct and shadowgraph photography. For direct photography, a Hycam camera with a 75 mm f/1.9 Macro Switer lens and a rotating shutter with a shutter constant of 1/2.5 was used yielding an effective exposure time of 50 μs per frame at a framing rate of 7200 frames/second. A system of three flash bulbs was synchronized to illuminate the fuel spray. A laser shadowgraph system was used to study the fuel spray development and combustion in more detail. A double pass refocused laser shadowgraph technique similar to one described by Witze and Vilchis [13] was developed. The Hycam camera with a Canon 50 mm f/3.5 macro lens was used. The shutter constant was 1/20 giving an exposure time of approximately 7 μs per frame at a framing rate of 7200 frames/second. Eastman Ektachrome High-Speed 7250 color film was used throughout.

Synchronization of pressure data with film was established in two independent ways. All experiments used the start of the injection event and the appearance of the jet on the film to synchronize the data. Synchronization accuracy was estimated to be ± 70 μs. In some experiments, a timing wheel and a shaft encoder driven by a synchronous motor were used. The shaft encoder output was recorded with the pressure and needle lift data while the timing wheel position was recorded on film. This system provided direct synchronization of the film and pressure data, and measurement of film speed for each movie run. The resulting film-to-pressure synchronization was estimated to be ± 60 μs. Although this second method did not substantially improve data synchronization, it provided an important and independent check on film speed and synchronization.

Direct Photography Results

The direct photography movies provided information on the liquid core of the fuel spray and location of ignition sites. The flash bulbs illuminate the combustion chamber periphery and the injector nozzle, and the developing fuel sprays are clearly seen at the start of the injection event. Tracings of the outer boundary of this core region from one experiment are shown in Fig. 2. The boundary of the visible spray is fuzzy rather than a sharp demarcation. This boundary penetrates only 2.5 to 4 cm from the nozzle tip (1/2 to 4/5 of the distance from the on-the-cylinder-axis injector location to the cylinder wall). Under the conditions tested with air temperature and pressure after compression of 900 K and 40 bar (typical of normal diesel operation), the visible spray does not contact the cylinder wall, and the projected image of each spray is quite long and thin. The results obtained by Kamimoto et al. [5] were similar. Our interpretation of these visible regions is that they represent the core of the fuel spray where there is a high density of liquid droplets that reflect light from the flash illumination. The jet velocity at nozzle exit was estimated to be 220 m/s by assuming incompressible fluid flow through an orifice with a discharge coefficient of 0.6. Data from such movies show that the leading edge of the liquid-containing spray core slows to 50 to 100 m/s within the first 200 μs after the start of injection.

The projected area of the dense core region is small compared to the combustion chamber area. When fully developed, this region for all five sprays occupies less than 10 percent of the cylinder cross-sectional area. The core region is also small compared to the fuel vapor region seen in shadowgraph movies (discussed in the next section). The initial swirl level did not have a measurable impact on the development of the dense core region.

The onset of luminous combustion seen in these direct movies occurred in a range of locations. Our observations indicate that the luminous ignition sites tended to be closer to the combustion chamber periphery with increasing injection pressure and with increasing ignition delay time. This would be expected since the regions that are most favorable for autoignition (regions that have a fuel–air mixture within combustible limits and have sufficient residence time at elevated temperature) move away from the injector as injection pressure or time increases. The initial flame spreading rates, calculated immediately after the first luminous zone is visible, can be as high as 260 m/s. These flame spreading rates are more than an order of magnitude higher than turbulent flame front speeds seen in spark-ignition engines [9]. It is unlikely the initial flame growth is a flame propagation process. It is believed that this very fast apparent flame spreading results from spontaneous ignition of premixed fuel vapor and air initiated by pressure waves propagating outward from previously ignited regions [14].

A general observation that has been made from all high-speed films is that the onset of visible luminous combustion occurs after the start of combustion (defined by the change in sign of dp/dt where p is the chamber pressure). The work done to synchronize the cylinder pressure data with the high-speed movies confirms that there is a detectable pressure rise before any luminosity is seen in the film. The time lag between pressure rise and luminous combustion is 0.1 to 0.3 ms.

Shadowgraph Photography Results

Shadowgraph photography provides information on the development of the vapor region of the fuel spray that cannot be seen with direct photography. A set of four shadowgraph photos is shown in Fig. 3. The chamber periphery and the window holder edge appear as dark outlines. The highly polished piston face appears bright because it reflects the collimated laser light directly into the camera lens. The shadowgraph image of the combustion chamber contains light and dark regions, which correspond to density gradients in the chamber. During and after the compression process, one can see a considerable amount of wrinkling throughout the field of view due to small-scale irregular density gradients in the chamber most likely due to turbulence in the thermal bound-

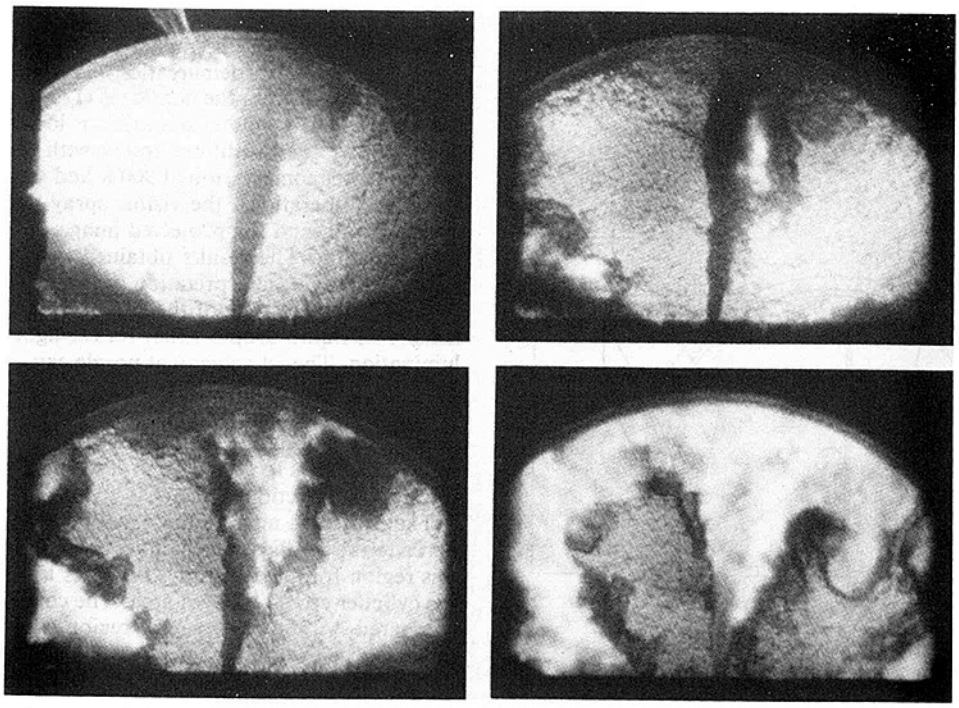

Fig. 3 Four shadowgraph photos of fuel spray with luminous flame superposed; times after start of injection: 0.97, 1.11, 1.25, 1.81 ms

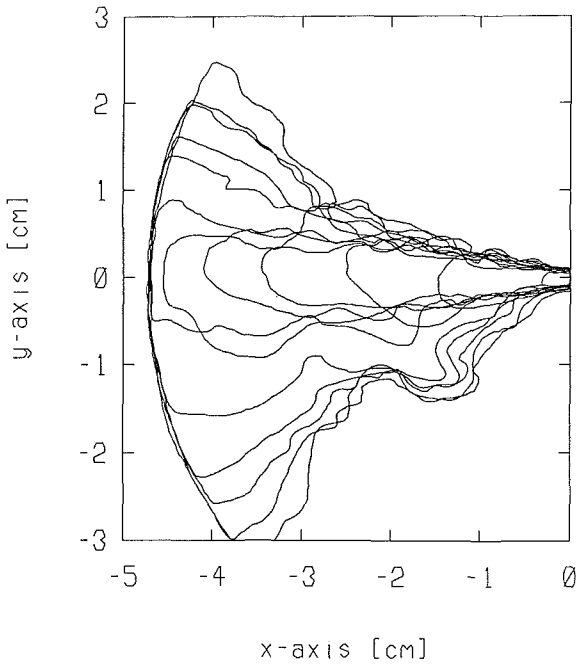

Fig. 4 Composite picture of tracings from the first 12 sequential frames of the outer contour of the fuel-air mixture region visible with high-speed shadowgraph photography: 100°C initial temperature, 100 m/s inlet velocity, 4000 rpm swirl, 60,000 kPa injection pressure, 39 bar air pressure, and 900 K air temperature at injection, 7200 frames/s

ary layer near the window and the piston face. When fuel injection begins, a dark region is seen developing from the nozzle tip. This region has a sharp but irregularly contoured boundary and is much larger than the region that reflects light from the flash bulbs during direct photography. This fuel spray image continues to penetrate to the periphery and extends rapidly along the wall. The projected shadowgraph image of the spray grows to be quite large (occupying up to 70 percent of the cylinder cross-sectional area). Our interpretation of this dark region is that the outer boundary corresponds to the boundary between fuel-air mixture and pure air. Figure 4 illustrates the position of the fuel-air mixture boundary from a single fuel spray for the first 12 sequential frames after the start of injection.

By suitable arrangement of the shadowgraph system optics, it is also possible to capture the flame illumination on the same film as shown in Fig. 3. As with direct photography, luminous ignition sites were observed in a range of locations. The combined shadowgraph and flame luminosity movies show how the flame spreads through the fuel-air mixture and how flame development affects the size and shape of the fuel-air mixture region. Figure 5 shows a series of contour tracings made from high-speed shadowgraph movie frames of the type shown in Fig. 3. The outer contour shown in each frame is the outer edge of the fuel-air mixture region and the inner contours show the boundary of the luminous combustion region. In quiescent cases, the expansion of the luminous combustion region boundary is uniform with respect to the fuel-air mixture region boundary. In high swirl cases, the luminous combustion region boundary expands to the upstream edge of the fuel-air mixture region boundary faster than to the downstream edge (upstream and downstream refer to the swirling air flow), confirming that swirl does affect fuel-air mixture preparation and flame development [1].

The rate of development of this fuel-air mixture region has been quantified from the high-speed movies. Figure 6 shows the projected fuel-air mixture area as a function of time. Development of the projected area of this region is nearly linear with time up to the point where luminous combustion begins. At the onset of luminous combustion, there is a rapid expansion of the outer boundary of the fuel-air region. This phenomenon was observed in every shadowgraph movie that has been analyzed to date. The luminous combustion region grows rapidly immediately after luminosity is first detected. The projected luminous combustion area, defined by the outer boundary of the luminous region seen in the high-speed movies, is expanding faster than the fuel-air mixture region boundary.

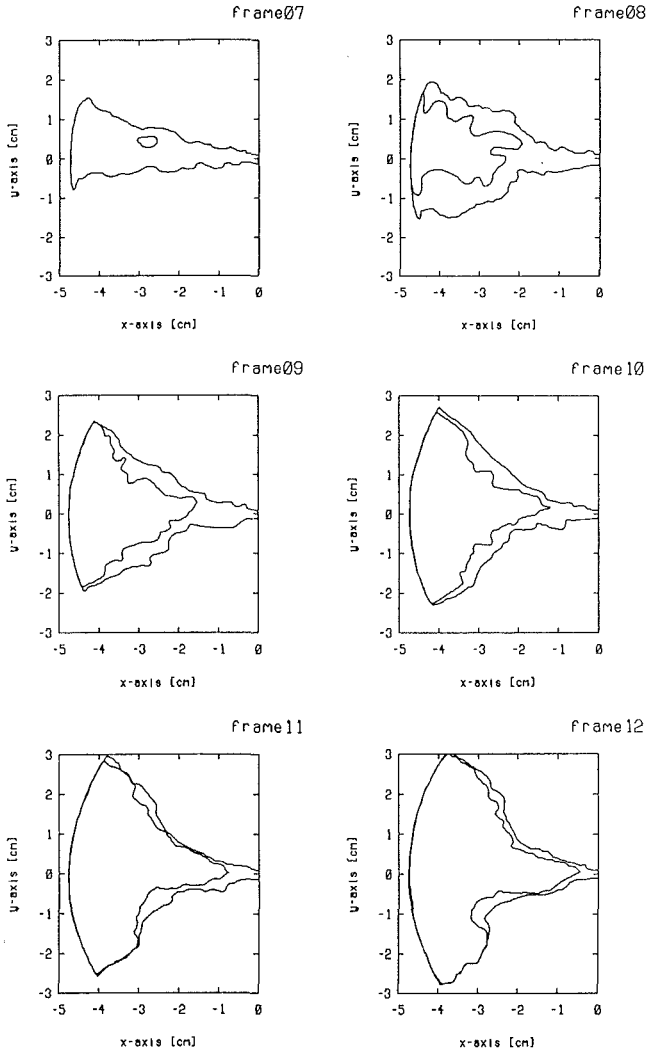

Fig. 5 Tracing from frames #7-12 of the outer contour of the fuel-air mixture region and the luminous combustion region visible with high-speed shadowgraph photography. 100°C initial temperature, 10 m/s inlet velocity, negligible swirl, 60,000 kPa injection pressure, 39 bar air pressure and 900 K air temperature at injection. 7200 frames/sec; fuel injection was first visible in frame #1, luminous combustion was first visible in frame #7; 0.14 ms between frames.

Coupled Photographic and Heat Release Analysis

Analysis that combines information from combustion photographs with information from a heat release analysis of the cylinder pressure data provides additional insight into the structure of the diesel engine flame. Geometric data on the size of the luminous combustion region obtained from the high-speed movies were compared with burned gas volume estimates developed from heat release analysis based on the chamber pressure data.

Table 2 lists the projected luminous combustion region area, A_f, for the first five frames of flame development from one experiment. Other experiments were analyzed in identical fashion and gave similar results. Data are given up to the time that the luminous regions from adjacent fuel sprays begin to merge and are no longer distinct. This corresponds approximately to the end of the premixed rapid burning phase of the total diesel combustion process. At this point, the luminous region occupies approximately 50 percent of the cylinder cross-sectional area. Table 2 also gives values of x_b and V_b obtained from the heat release analysis that correspond to each frame, where x_b is the fraction of the fuel energy released and

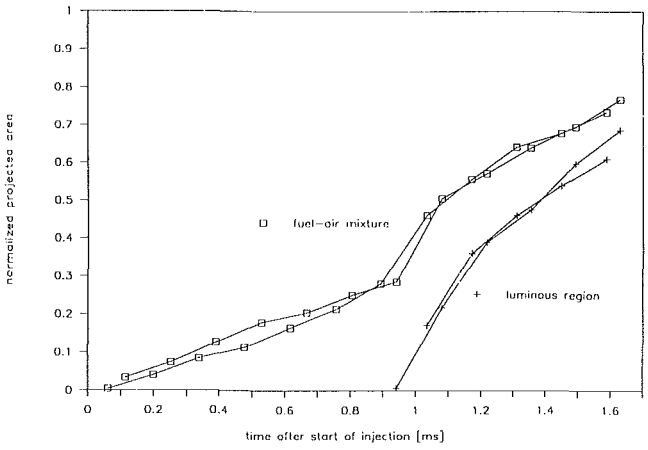

Fig. 6 Fuel-air mixture region projected area and luminous region projected area as a function of time after start of injection: 100°C initial temperature, 10 m/s inlet velocity, negligible swirl, 60,000 kPa injection pressure, 39 bar air pressure, and 900 K air temperature at injection

Table 2 Enflamed areas and burned gas volumes from coupled heat release and photographic analysis

Frame #	$\frac{m_f(t)}{m_f(\text{total})}$	x_b	V_b [cm^3]	A_f [cm^2]	V_b/A_f [cm]
8	0.34	0.048	15.3 (0.06)	14.0 (0.17)	1.09 (0.35)
9	0.39	0.096	28.2 (0.11)	28.8 (0.36)	0.98 (0.32)
10	0.44	0.145	40.1 (0.16)	37.4 (0.46)	1.07 (0.35)
11	0.48	0.177	48.6 (0.19)	43.6 (0.53)	1.11 (0.36)
12	0.53	0.209	54.8 (0.22)	49.7 (0.61)	1.10 (0.36)

100 C inlet air, 100 m/s inlet velocity, 4000 rev/min swirl, 60,000 kPa injection pressure.

( ) indicates normalized values: volumes are normalized by the combustion chamber volume; areas are normalized by the piston area; lengths are normalized by the clearance height.

Frame # refers to the number of frames after start of fuel injection. Film speed was 7200 frames/second: 0.14 ms between frames.

V_b is the burned gas volume associated with x_b. The fraction of the fuel energy released was estimated directly from the net heat release analysis from the relation

$$x_b = Q(t)/Q_{\max} \tag{1}$$

where $Q(t)$ is the net heat release at the time of each frame, and $Q_{\max}$ is the total cumulative net heat release at the end of combustion. The burned gas volume is calculated using the ideal gas relationship

$$V_b = m_b R T_b / p \tag{2}$$

where m_b is the total burned mass, R is the gas constant, T_b is the burned gas temperature, and p is the instantaneous chamber pressure. The chamber pressure is assumed to be spatially uniform and comes directly from measurements during each experiment. The burned mass m_b is the sum of the burned fuel mass m_{bf} and the corresponding burned air mass m_{ba}:

$$m_b = m_{bf} + m_{ba} \tag{3}$$

where

$$m_{bf} = Q(t)/Q_{HV} \tag{4}$$

and

$$m_{ba} = m_{bf}(A/F)_s \tag{5}$$

Q_{HV} is the fuel lower heating value and $(A/F)_s$ is the stoichiometric air/fuel ratio. The calculation of the burned air mass assumed that, on average, combustion during this

Table 3 Burned gas and luminous region volumes from coupled heat release and photographic analysis

Frame #	$\frac{m_f(t)}{m_f(\text{total})}$	x_b	V_b [cm^3]	V_f [cm^3]	V_b/V_f
8	0.34	0.048	15.3 (0.06)	13.2 (0.05)	--
9	0.39	0.096	28.2 (0.11)	60.8 (0.24)	0.46
10	0.44	0.145	40.1 (0.16)	75.5 (0.30)	0.53
11	0.48	0.177	48.6 (0.19)	95.4 (0.38)	0.51
12	0.53	0.209	54.8 (0.22)	122.9 (0.49)	0.45

100 C inlet air, 100 m/s inlet velocity, 4000 rev/min swirl, 60,000 kPa injection pressure.

( ) indicate normalized values: volumes are normalized by the combustion chamber volume.

Frame # refers to the number of frames after start of fuel injection. Film speed was 7200 frames/second: 0.14 ms between frames.

premixed phase takes place at an equivalence ratio of unity. The burned gas temperature is approximated by the equation

$$T_b = [1 + 0.0002317(T_a - 950)] \times (2726.3 + 0.9306p - 0.003233p^2) \quad (6)$$

where T_a is the instantaneous air temperature in deg Kelvin and p is the cylinder pressure in atmospheres. This correlation was obtained by applying a least-squares curve fit to results of the NASA equilibrium program [15] for the adiabatic combustion of a typical diesel fuel with air at temperatures in the range of 800 K to 1200 K. Equation (6) is evaluated using the cylinder pressure and air temperature at the time of injection.

The last column of Table 2 is the ratio of burned gas volume calculated from the heat release analysis as described above and the projected luminous combustion area obtained directly from the high-speed film. This ratio, V_b/A_f, corresponds to a characteristic thickness of the burned gas region. During the premixed phase (when in our experiments the first 20 percent of the fuel is burned), this length remains nearly constant with a value of approximately 1 cm. Since the combustion chamber height is 3.08 cm, this indicates that, on average, the luminous combustion region occupies much less than the full height of the chamber during this stage of the burning process.

This coupled analysis of photographic and heat release data was taken an additional step. The geometric film data for the luminous combustion region area presented in Table 2 can be used to estimate a volume of the luminous region by assuming an appropriate geometric shape for this region. A simple axisymmetric cone shape and a characteristic length was used to convert the area data to volume data. The extent of the luminous region seen in the film measured radially outward from the nozzle tip was used as the characteristic length. This length represents the height of this cone shaped volume. A cone base diameter was then determined so that the two-dimensional projected area of the cone was equal to the projected luminous-combustion-region area.

This calculated luminous combustion volume (the volume within the boundary of the luminous region, the enflamed volume) is presented in Table 3 along with the burned gas volume calculated earlier (see above) up to the point where the luminous zones from adjacent fuel sprays begin to merge with each other. At this point, the volume associated with the luminous combustion region is approximately 50 percent of the combustion chamber volume, and the cone base dimension becomes larger than the clearance height of the chamber.

The last column of Table 3 is the ratio of burned gas volume to luminous combustion region volume. This ratio, V_b/V_f, is an estimate of the fraction of the "enflamed" volume, which is actually combustion products. It has a value of approximately 0.5 and remains nearly constant during this premixed stage of the diesel combustion process in these experiments (up to 20 percent of the fuel burned). Based on a density ratio, unburned to burned gas, of 4 this gives the mass fraction of unburned mixture within the enflamed region of the spray as 0.8. That the ratio V_b/V_f remains constant implies that the enflamed luminous region is entraining fresh mixture about five times more rapidly than mixture is burning. Thus during this period the fluid within the outer boundary of the visible luminous region is largely unburned mixture. This observation is consistent with the existence of a substantial central unburned core in the spray consisting of rich fuel-vapor air mixture.

Conclusions

The following observations and conclusions can be made from the above analysis of high-speed movies of fuel injection and combustion under typical direct-injection diesel conditions:

1 Each individual fuel spray consists of a narrow liquid-containing core centered within a much larger distinctly bounded fuel-vapor air mixture region. The liquid-containing core does not penetrate to the outer wall of the combustion while the boundary of the fuel vapor containing region impinges strongly on the outer wall.

2 The onset of visible luminous combustion occurs after the start of detectable combustion-produced pressure rise. The time lag is 0.1 to 0.3 ms.

3 The site where luminous combustion is first visible appears to be a function of ignition delay time and injection pressure. The trend observed is that the ignition sites are further from the injector as delay time or injection pressure increases.

4 A rapid expansion of the boundary of the fuel-vapor/air mixture containing region seen in high-speed shadowgraph movies occurs immediately after luminous combustion first becomes visible, due to the combustion energy release.

5 The spreading of the luminous combustion region into this fuel–air mixture region is affected by bulk gas motion. The flame spreads less quickly into the downstream region of the fuel spray when there is swirl.

6 Initial spreading rates of the luminous combustion region as fast as 260 m/s were observed. It is unlikely that initial flame development in diesel combustion is a flame propagation process; a pressure-wave-induced autoignition process is more plausible.

7 The ratio of the burned gas volume (assumed stoichiometric on the average for the premixed phase) to the projected luminous combustion region area is approximately 1 cm and remains constant during the premixed stage of the total diesel combustion process. On average, this luminous region only fills a fraction of the full height of the combustion chamber.

8 The ratio of the burned gas volume to the luminous combustion region volume is approximately 0.5 and is nearly constant during the premixed combustion stage. This implies that the amount of unburned mixture within the outer boundary of the enflamed luminous region is substantial (of order 80 percent of the total enflamed mass). It also implies that this enflamed region is entraining fresh unburned mixture much more rapidly than mixture is burning.

Acknowledgments

This work was sponsored by the Consortium for Engine Research in the Sloan Automotive Laboratory at M.I.T. The members supporting this research were: Caterpillar Tractor Company, Cummins Engine Company, Deere & Company, Ford Motor Company, Gulf Research & Development Company, Peugeot Societe Anonyme, and Regie Nationale des Usines Renault.

References

1 Heywood, J. B., *Internal Combustion Engine Fundamentals*, McGraw-Hill, New York, 1988, Chap. 10.

2 Lyn, W. T., "Study of Burning Rate and Nature of Combustion in Diesel Engines," *Ninth Symposium (International) on Combustion*, The Combustion Institute, 1962, pp. 1069–1082.

3 Alcock, J. F., and Scott, W. M., "Some More Light on Diesel Combustion," *Proc. Auto. Div. Instn. Mech. Engrs.*, No. 5, 1962–63, pp. 179–191.

4 Lyn, W. T., and Valdmanis, E., "The Application of High Speed Schlieren Photography to Diesel Combustion Research," *J. of Photographic Science*, Vol. 10, 1962, pp. 74–82.

5 Kamimoto, T., Kobayaski, H., and Matsuoka, S., "A Big Size Rapid Compression Machine for Fundamental Studies of Diesel Combustion," *SAE Trans.*, Vol. 90, SAE Paper No. 81104, 1981.

6 Kobayashi, H., Kamimoto, T., and Matsuoka, S., "A Photographic and Thermodynamic Study of Diesel Combustion in a R.C.M.," *SAE Trans.*, Vol. 90, SAE Paper No. 810259, 1981.

7 Kamimoto, T., Chang, Y. J., and Kobayashi, H., "Rate of Heat Release and Its Prediction of a Diesel Flame in a Rapid Compression Machine," *SAE Trans.*, Vol. 93, SAE Paper No. 841076, 1984.

8 Kamimoto, T., Yokota, H., and Kabavashi, H., "Effect of High Pressure Injection on Soot Formation Processes in a Rapid Compression Machine to Simulate Diesel Flames," SAE Paper No. 871610, 1987.

9 Beretta, G. P., Rashidi, M., and Keck, J. C., "Turbulent Flame Propagation and Combustion in Spark Ignition Engines," *Comb. Flame*, Vol. 52, 1983, pp. 217–245.

10 Groff, E. G., and Matekunas, F. A., "The Nature of Turbulent Flame Propagation in a Homogeneous Spark-Ignited Engine," *SAE Trans.*, Vol. 89, SAE Paper No. 800133, 1983.

11 Rogowski, A. R., "A New Machine for Studying Combustion of Fuel Sprays With Controlled Air Motion," SAE Paper No. 436, 1961.

12 Colella, K. J., Balles, E. N., Ekchian, J. A., Cheng, W. K., and Heywood, J. B., "A Rapid Compression Machine Study of the Influence of Charge Temperature on Diesel Combustion," SAE Paper No. 870587, 1987.

13 Witze, P. O., and Vilches, F. R., "Stroboscopic Laser Shadowgraph Study of the Effect of Swirl on Homogeneous Combustion in a Spark-Ignition Engine," *SAE Trans.*, Vol. 90, SAE Paper No. 810226, 1981.

14 Theobald, M. A., and Cheng, W. K., "A Numerical Study of Diesel Ignition," ASME Paper No. 87-FE-2, 1987.

15 Svehla, R. A., and McBride, B. J., "Fortran IV Computer Program for Calculation of Thermodynamics and Transport Properties of Complex Chemical System," NASA Technical Note TN D-7056, 1973.

On Heat Transfer Measurements in Diesel Engines Using Fast-Response Coaxial Thermocouples

D. N. Assanis

E. Badillo

Department of Mechanical and Industrial Engineering,
University of Illinois at Urbana-Champaign,
Champaign, IL 61801

Finite element models of fast-response CO-AX thermocouples typically used for heat transfer measurements in diesel engines have been developed. Due to the small differences in thermal properties between the thermoelements and the iron engine components, CO-AX thermocouples are capable of measuring transient temperatures of iron components within an accuracy of 98 percent. However, these relatively small errors in temperature measurement result in as high as 25 percent errors in peak surface heat flux calculations. This implies that heat flux results depend not only on the temperature of the surface thermocouple junction, but are also sensitive to its time rate of change. Increasing the thin film thickness can significantly alter the heat flux profile deduced from surface junction temperatures.

Introduction

Measuring the surface and subsurface temperature profiles of combustion chamber components is crucial for analyzing the transient thermal shock and fatigue characteristics of these components. Transient temperature measurements are also needed to determine the heat flow paths during operation of an engine. This information can be used to determine the distribution of energy released during the engine cycle and also to assess component cooling and tribological requirements.

Combustion chamber components are exposed to rapidly changing combustion gas temperatures and convective heat coefficients due to the rapid succession of thermodynamic events and fluid motion during the engine cycle. As a result, the combustion chamber surface temperatures may change by about 15 to 20 K in 20 crank-angle deg [1]. These rates of change of temperature can be substantially higher for ceramic-coated combustion chamber surfaces. In order to measure such fast surface temperature transients, every crank-angle degree, at engine speeds up to 3000 rpm, transducer with a response time of a few microseconds are required. Thus, suitable transducers need to be very small (less than 1 mm in diameter) [2].

Another important requirement is that a transducer actually indicate the true surface temperature of a component. The latter is defined as the temperature that the component would obtain if the temperature transducer were not present. In most cases, the introduction of a transducer perturbs the temperature distribution of the component at the point of attachment. Thus, to measure true component temperatures, transducers that have thermal properties identical to those of the measured media are required.

Given these considerations, the coaxial (CO-AX) type thermocouple, originally described by Bendersky [3], has been the most commonly used transducer for engine heat transfer measurements [4, 5]. This CO-AX thermocouple is made up of a small wire consisting of one thermoelement, which is coated with a very thin (12 μm) insulation (aluminum oxide) of high dielectric strength, and embedded securely in a tube consisting of the second thermoelement [6]. The thermocouple junction(s) is formed by vacuum depositing an electrically conductive coating of 1–10 μm over the sensing end of the probe. A subsurface junction is also added on the outside of the tube for measuring a second temperature needed for heat flux calculations.

The output voltage of a CO-AX thermocouple, and thus the measured temperature, directly corresponds to the temperature of its junction(s). Therefore, it is crucial that the thermocouple junction attain the true surface temperature. However, the thermal properties of standard thermoelements often differ from the properties of typical I. C. engine materials, like steel or aluminum alloys. Therefore, the focus of this study is to analyze whether these property differences could result in significant errors in the measurement of transient surface temperatures and heat flux rates in diesel engines.

Coaxial Thermocouple Operating Principles

Figure 1 illustrates the cross section of a fast response coaxial thermocouple and its major dimensions. The thermoelectric principles that apply to conventional thermocouples [2] apply to coaxial thermocouples as well. The net electromotive force of the coaxial thermocouple circuit can be calculated by adding the thermoelectric voltage due to the temperature gradient across each wire, including thermoelements, thin film, and lead wires. Thus, the net voltage output for this coaxial thermocouple is given by

Contributed by the Internal Combustion Engine Division and presented at the Twelfth Annual Energy-Sources Technology Conference and Exhibition, Houston, Texas, January 22–25, 1989. Manuscript received by the Internal Combusion Engine Division August 1988.

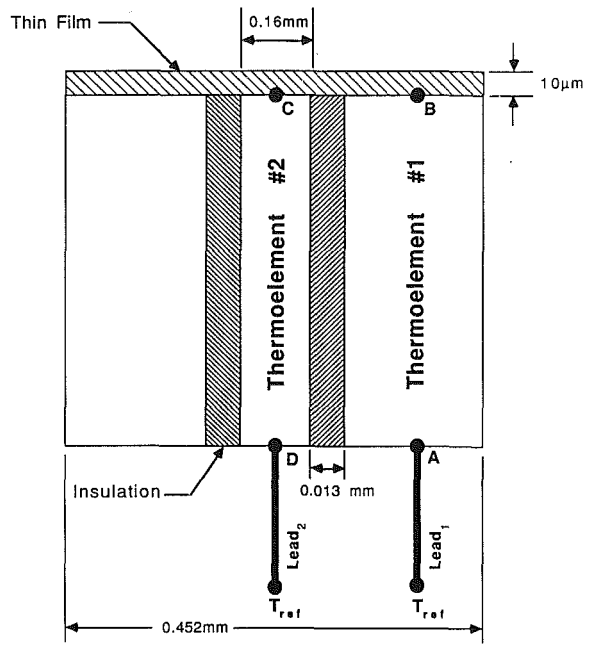

Fig. 1 Cross section of a fast response coaxial thermocouple showing major dimensions

$$E_{\text{net}} = \text{EMF}_{\text{L1}}(T_A) - \text{EMF}_{\text{L1}}(T_{\text{ref}}) + \text{EMF}_{\text{TE1}}(T_B)$$

$$- \text{EMF}_{\text{TE1}}(T_A) + \text{EMF}_{\text{TF}}(T_C) - \text{EMF}_{\text{TF}}(T_B) + \text{EMF}_{\text{TE2}}(T_D)$$

$$- \text{EMF}_{\text{TE2}}(T_C) + \text{EMF}_{\text{L2}}(T_{\text{ref}}) - \text{EMF}_{\text{L2}}(T_D) \quad (1)$$

where

$$\text{EMF}(T) = a_1 T + a_2 T^2 + a_3 T^3 + \ldots + a_n T^n \quad (2)$$

is the thermoelectric voltage of a wire with respect to platinum at a given junction temperature; the coefficients a_n are given by the National Bureau of Standards (NBS) curve fits. The subscripts L1 and L2 represent the lead wires attached to thermoelements TE1 and TE2, respectively; the subscript TF refers to the thin film; T_{ref} is the temperature of the reference junction; and T_B and T_C are the average temperatures over the thermocouple measuring junction areas B and C, respectively. Obviously, if there is no temperature gradient along the surface of the thermocouple, T_B equals T_C, resulting in no voltage contribution from the thin film.

Furthermore, assuming that the lead wires are identical to the thermoelements they are attached to, equation (1) reduces to

$$E_{\text{net}} = \text{EMF}_{\text{TE1}}(T_B) - \text{EMF}_{\text{TE1}}(T_{\text{ref}}) + \text{EMF}_{\text{TF}}(T_C)$$

$$- \text{EMF}_{\text{TF}}(T_B) + \text{EMF}_{\text{TE2}}(T_{\text{ref}}) - \text{EMF}_{\text{TE2}}(T_C) \quad (3)$$

The net thermocouple voltage outputs can be converted to indicated temperature data using the NBS polynomial curve fits [7], which are of the form

$$T\,(^\circ\text{C}) = b_0 + b_1 E + b_2 E^2 + b_3 E^3 + b_4 E^4 \quad (4)$$

It should be noted that all thermocouple voltage and temperature functions used in this study were based on a reference junction temperature of 0°C.

Modeling Assumptions

The finite element method was used to model the coaxial thermocouple and predict its transient temperature distribution when installed in the center of a diesel flat-top piston. In order to model the 10-μm-thick conductive thermocouple thin film, elements with very fine spacings were used near the thermocouple surface. Away from the surface, increasing element spacings were used to reduce the computational effort. In constructing the variable spacing mesh, well-proportioned aspect ratios were maintained, following the methodology that we reported in [8]. The temperature distribution of the piston without the thermocouple was also obtained in order to compare the thermocouple-predicted temperatures against the true component temperatures. Thus, the magnitude of the temperature disturbance introduced due to the presence of the thermocouple could be assessed.

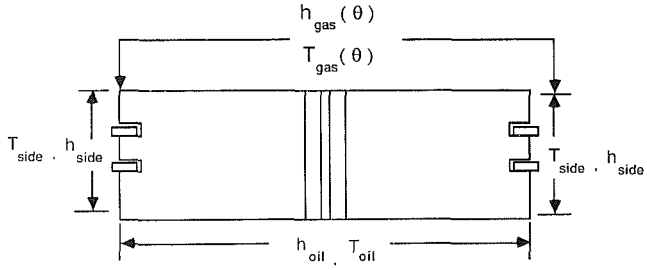

Fig. 2 Boundary conditions applied to the model

Figure 2 illustrates the boundary conditions applied to the model. Forced convection and radiation from the combustion gas to the piston top surfaces were modeled by applying an instantaneous mean gas temperature and an enhanced convective heat transfer coefficient, which includes the effects of radiation [8]. The underside of the piston was assumed to be exposed to the cooling oil with $h_{\text{oil}} = 2000$ W/m^2-K and $T_{\text{oil}} = 350$ K. Further, assuming that each of the two piston rings accounted for 5 percent of the piston side area, the convective coefficient h_{side} for the liner side was obtained by

$$h_{\text{side}} = 0.90 * h_{\text{skirt}} + 2 * 0.05 * h_{\text{rings}} \quad (5)$$

where $h_{\text{skirt}} = 150$ W/m^2-K and $h_{\text{rings}} = 1000$ W/m^2-K [9]. Thus, the side of the piston facing the liner was exposed to $h_{\text{side}} = 245$ W/m^2-K and $T_{\text{side}} = 380$ K. Finally, a zero net heat flux was imposed along the line of symmetry passing through the center of the fast response CO-AX thermocouple.

The combustion gas boundary conditions were obtained from an engine simulation of a typical, six-cylinder direct injected diesel engine [1]. The engine has a bore of 110 mm and a stroke of 140 mm. Since the study focuses on cyclic transient phenomena, the engine was assumed to be warmed up and operating at a steady-speed of 1900 rpm. At this speed operating at an equivalence ratio of 0.5, intercooled, and 3.5 atm boost, the engine delivers approximately 250 bhp.

Heat Flux Calculations From Fast Response Thermocouple Data

Once the fast response thermocouple junction temperatures were predicted, the net thermocouple voltage outputs were calculated using equations (2) and (3). In turn, the net thermocouple voltage outputs were converted to transient temperature data using equation (4). The resulting temperatures were treated as digitized transient temperature data that would be obtained from an actual engine experiment, and thus, were used for heat-flux predictions.

The heat-flux calculations were conducted in a manner that is common to engine heat-flux analysis. Assuming that heat flow through the component is one-dimensional, and that material properties are constant, the unsteady heat conduction equation can be written as

$$\frac{1}{\alpha}\frac{\partial T}{\partial t} = \frac{\partial^2 T}{\partial x^2} \quad (6)$$

It should be noted that one-dimensionality for the unsteady component of heat flux can be readily justified since the

Table 1 Coaxial thermocouple configurations studied

Thermocouple	Center Wire	Outer Tube
J-Type	Constantan	Iron
E-Type	Constantan	Chromel
K-Type	Alumel	Chromel
S-Type	Platinum	Platinum +10 % Rhodium

Table 2 Thermoelement heat transfer properties

Material Type	Conductivity (W/m-K)	Diffusivity $(m^2/s) \times 10^{-6}$
Iron	57	16.2
Platinum	73	25.3
Alumel	29	6.7
Constantan	23	5.9
Chromel P	19	4.9

temperature transients penetrate only within a very small distance from the surface [8]. However, this assumption is seldom true for the steady-state component of heat flux, except when the probe is specially constructed to ensure one-dimensional heat flow.

The Fourier series method can be used to solve the unsteady heat conduction equation for surface heat flux [10], i.e.,

$$q_{FFT} = \frac{k}{L}(T_{surf} - T_{sub}) + k \sum_{n=1}^{N} \sqrt{\frac{n\omega}{2a}} * ((A_n + B_n) \cos n\omega t - (A_n - B_n) \sin n\omega t) \quad (7)$$

where k is thermal conductivity of the measured object, L is distance between the surface and subsurface thermocouples, T_{surf} is average surface thermocouple temperature, T_{sub} is average subsurface thermocouple temperature, n is harmonic number, ω is one-half of angular speed of the engine if sampling period is for two crankshaft revolutions (four-stroke), α is thermal diffusivity, A_n and B_n are Fourier coefficients, and t is time.

Results

Four different types of fast response, CO-AX thermocouples that are commonly used for transient heat transfer measurements in diesel engines were studied in order to assess the errors involved in such measurements. Details of the thermocouple configurations are given in Table 1 [6]. All CO-AX thermocouples studied used a vacuum deposited iron conductive thin film. The thermal properties of the elements of the various CO-AX thermocouples studied are summarized in Table 2.

Accuracy of Fast Response Temperature Measurements. Figure 3 illustrates the transient response of a J-type CO-AX thermocouple with a 10-μm vacuum-deposited iron thin-film when installed in an iron piston top. The "outer tube" temperature in Fig. 3(*a*) represents the area-averaged temperature of the surface thermocouple junction directly above the outer cylindrical thermoelement of the CO-AX fast response thermocouple. The "center wire" temperature represents the area-averaged temperature of the surface thermocouple junction directly above the center wire that makes up the outer thermoelement of the CO-AX fast response thermocouple. The "true" temperature refers to the temperature response of the steel component if no thermocouple were installed.

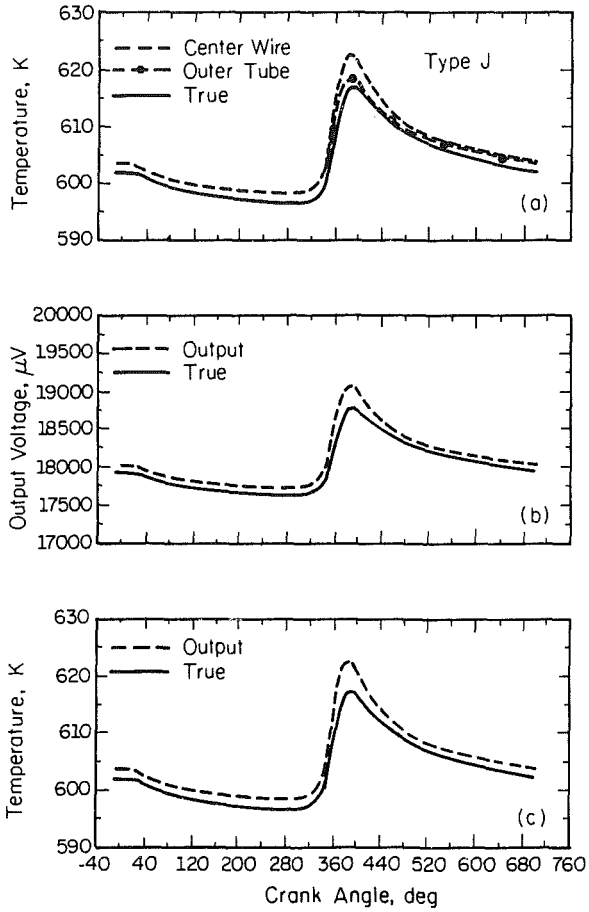

Fig. 3 Transient response of a J-type, iron thin-film, CO-AX thermocouple when installed in a cast-iron piston: (a) junction temperatures, (b) net voltage outputs, (c) indicated temperatures against respective true values

The predicted voltage output for the J-type thermocouple is shown in Fig. 3(*b*). Assuming that the iron thin film is metallurgically identical to the iron outer tube thermoelement, only one junction, directly above the center wire, is formed at the surface. Since the temperature of the center wire junction is higher than the true temperature throughout the cycle, the thermocouple output voltage exceeds the true voltage by as much as 0.5 percent (or 80 μV), 1.7 percent (330 μV), and 0.5 percent (85 μV), during intake, combustion, and exhaust, respectively. These voltage errors result in temperature errors during intake, combustion, and exhaust of +0.3 percent (or +2 K), +1.0 percent (5 K), and +0.3 percent (2 K), respectively.

The resultant transient temperature profile indicated by the J-type thermocouple is compared to the true temperature in Fig. 3(*c*). The measured temperature is higher than the true temperature throughout the engine cycle, and especially so during combustion due to the insulating effect of the constantan center wire. Heat transfer during combustion occurs so rapidly that the large heat sink surrounding the constantan center wire cannot cool it fast enough to control the transient response of the thermocouple junction. Therefore, although the large solid body surrounding the thermocouple controls the average temperature of the thermocouple junction, the thermocouple elements tend to influence the transient response of the junction.

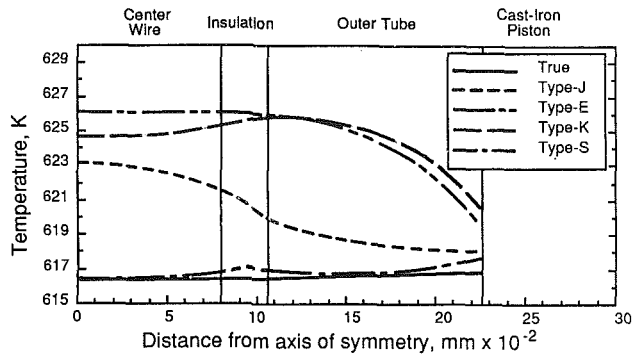

Fig. 4 Radial profile of peak temperatures along the thermocouple surface from the centerline of the center wire to the outer edge of the thermocouple

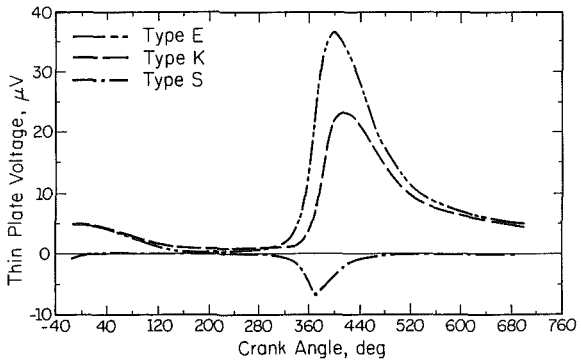

Fig. 5 Voltage contributions due to the thermal gradient between the two thermocouple junctions of E-type, K-type, and S-type thermocouples

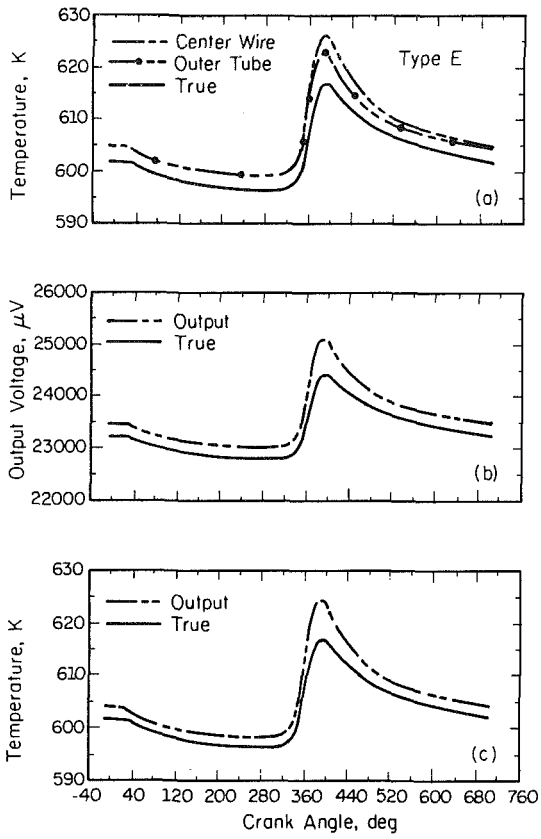

Fig. 6 Transient response of E-type, iron thin-film, CO-AX thermocouple when installed in a cast-iron piston: (a) junction temperatures, (b) net voltage outputs, (c) indicated temperatures against respective true values

Figure 4 illustrates the radial profile of peak temperatures along the thermocouple surface starting from the centerline of the center wire and ending at the outer edge of the thermocouple. The J-type constantan center wire affects most of the thermocouple surface even though the outer tube thermoelement is made of iron. This means that during peak temperatures the thermocouple disturbance caused by the presence of the 0.16-mm-diameter constantan center wire penetrates across most of the 0.452 mm diameter thermocouple.

The transient response of E-type, K-type, and S-type iron thin-film thermocouples is somewhat more complicated because two surface junctions are formed, one above the center wire and one above the outer tube. Thus, the net thermocouple voltage output will also depend on the thermoelectric potential between the two junctions. The voltage contributions due to the thermal gradient between the two thermocouple junctions of E-type, K-type, and S-type thermocouples are shown in Fig. 5. Obviously, the larger the temperature gradient between the two measuring junctions, the larger the voltage contribution. A positive voltage contribution signifies that the center wire is hotter than the outer tube, while a negative voltage contribution means just the opposite.

Figure 6(a) shows the area-averaged temperatures of the center wire and outer tube junctions of the E-type thermocouple. The thermocouple junction temperatures are always higher than the true temperatures. Also, during the combustion and exhaust phases of the engine cycle, a thermal gradient exists between the center wire and outer tube thermoelectric junctions. Because both thermoelements of the E-type fast response CO-AX thermocouple have properties significantly different from those of iron, the temperature disturbance for this thermocouple configuration is greater than for the J-type thermocouple. The net voltage output for both junctions of the E-type thermocouple can be seen in Fig. 6(*b*). The voltage output errors for this thermocouple within an iron piston during intake, peak combustion, and exhaust were +0.9 percent (210 μV), +2.8 percent (700 μV), and +1.0 percent (250 μV), respectively. This corresponded to temperature errors during intake, combustion, and exhaust of +0.3 percent (2 K), +1.3 percent (8 K), and +0.4 percent (2 K), respectively.

Figure 6(*c*) compares the transient temperature profile of the E-type thermocouple to the true temperature response. It is interesting to note that the net output voltage of a CO-AX thermocouple with two measuring junctions at different temperatures yields a final temperature between the two junction temperatures, but biased toward the temperature of the hotter junction.

Figure 7 illustrates the transient response of the K-type thermocouple. Overall, the K-type behaved much like the E-type. The only exception is that the temperature of the E-type constantan center wire overshoots slightly more than that of the K-type alumel center wire, since constantan has lower thermal conductivity and diffusivity than alumel [8]. Figure 4 also shows this fact, as the K-type alumel center temperature falls slightly below that of the E-type. Net voltage errors for the K-type thermocouple during intake, combustion, and exhaust were +1.2 percent (160 μV), +2.3 percent (330 μV), and +1.1 percent (150 μV), respectively. These voltage errors resulted in temperature errors during intake, combustion, and exhaust of +0.7 percent (4 K), +1.3 percent (8 K), and +0.7 percent (4 K), respectively.

Figure 8(*a*) shows the transient temperature response for the S-type CO-AX thermoelement junctions for one complete engine cycle. During combustion, the junction temperatures are about the same as the true temperature. In fact, the temperature disturbance at peak temperatures is minimal as shown in Fig. 4. During intake, compression, and exhaust, the

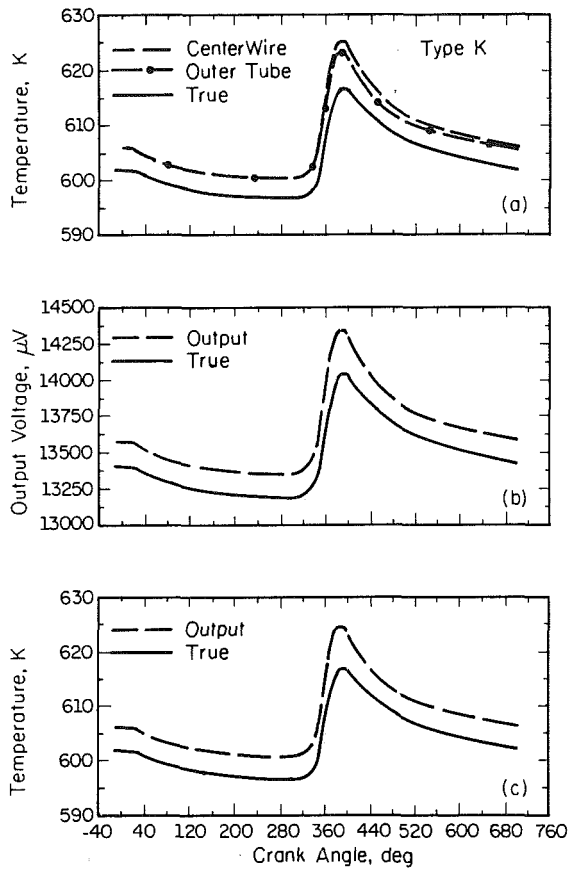

Fig. 7 Transient response of K-type, iron thin-film, CO-AX thermocouple when installed in a cast-iron piston: (*a*) junction temperatures, (*b*) net voltage outputs, (*c*) indicated temperatures against respective true values

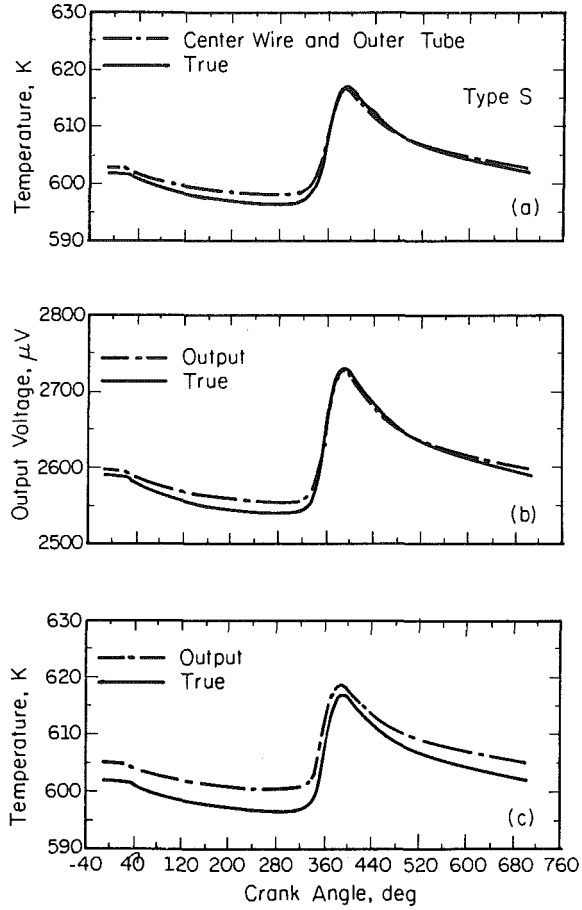

Fig. 8 Transient response of S-type, iron thin-film, CO-AX thermocouple when installed in a cast-iron piston: (*a*) junction temperatures, (*b*) net voltage outputs, (*c*) indicated temperatures against respective true values

thermoelement junction temperatures are slightly higher than the true temperature. Overall, the S-type thermocouple indicates slightly lower temperature swings than what the actual piston experiences. This is expected since the S-type thermoelements have greater thermal diffusivity than iron.

Figure 8(*b*) illustrates the transient voltage output corresponding to the junction temperatures of Fig. 8(*a*). Output voltage errors during intake, combustion, and exhaust were +0.5 percent (13 μV), −0.2 percent (−6 μV), and +0.3 percent (7 μV), respectively. It should be noted that the voltage contribution for the outer tube is zero since this thermoelement is platinum, and all voltages are referenced with respect to platinum. Thus, the net output voltage for the S-type thermocouple is a function of the center wire junction temperature and the temperature gradient existing across the iron thin film, if any. The voltage contribution due to a thermal gradient between the two junctions is very small and occurs only during peak temperatures as shown in Fig. 5.

Figure 8(*c*) shows that converted temperatures from voltage outputs are higher than true temperatures throughout the engine cycle. However, junction temperatures and net voltage outputs are slightly higher than the true values only during intake and compression. This rather surprising result is attributed to the limited accuracy of the S-type thermocouple polynomial used to convert net voltages to temperatures. Actual junction temperatures obtained from finite element results were consistently 2°C below the voltage-converted thermocouple temperatures, which falls within the −11 to +3°C accuracy of the polynomial (7). Discrepancies like this only occurred for the S-type thermocouple, which suggests that a higher degree polynomial should be used for voltage-to-temperature conversions for this thermocouple. Indicated temperature errors during intake, combustion, and exhaust were +0.6 percent, +0.4 percent, and +0.5 percent, respectively.

Figures 9(*a*) and 9(*b*) show the output voltage and indicated temperature errors of the different CO-AX thermocouples installed in a cast-iron piston top. The errors have been normalized with respect to the true absolute temperature and the true absolute voltage for each thermocouple type in order to provide a consistent basis for comparison. In particular, it should be noted that absolute voltage errors (quoted in parentheses above) can be very misleading due to the large variation in the output voltage level of the various thermocouples. For instance, for a temperature of 615 K, a J-type thermocouple should read 18.7 mV, while an S-type should read only 2.72 mV. Table 3 summarizes the indicated transient response of the various thermocouples with a 10 μm iron thin film.

It can be concluded that the S-type thermocouple indicates the most accurate temperatures at peak cylinder conditions. On the other hand, the J-type thermocouple indicates the best results during the intake, compression, and exhaust portions of the engine cycle. However, Fig. 9(*a*) suggests that the S-type thermocouple should give the best results throughout the cycle if a more accurate scheme is used to convert resultant voltages to temperatures. The ultimate selection of a thermocouple will involve other tradeoffs, such as the absolute level of the signal of the thermocouple, which are beyond the scope of our paper. Overall, commonly used high-speed CO-AX thermocouples are capable of measuring transient temperatures in iron components within an accuracy of 98 percent. It should be noted that these errors are strictly related to thermocouple

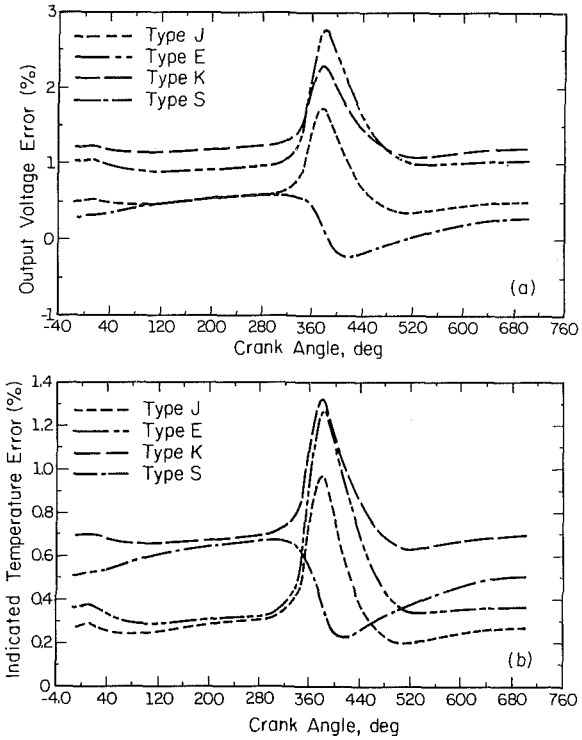

Fig. 9 Output voltage and indicated temperature errors relative to respective absolute values for various CO-AX thermocouples installed in a cast-iron piston top

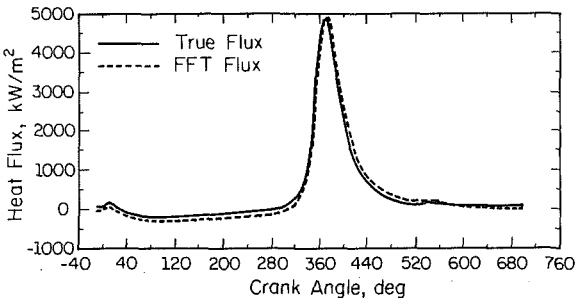

Fig. 10 Comparison of FFT calculated heat flux against true heat flux from the combustion gas to the surface

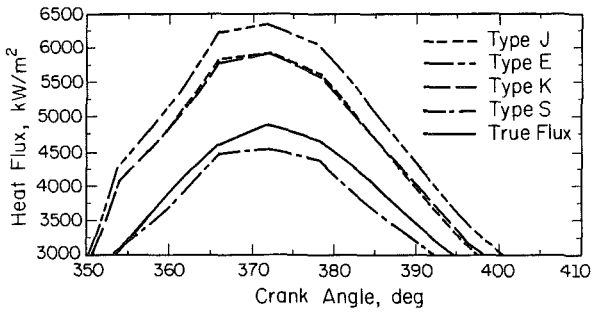

Fig. 11 Comparison of peak heat flux rates measured using various CO-AX thermocouple types against true heat flux rates

temperature disturbances and do not account for any digitizing errors.

Accuracy of Transient Heat Flux Measurements. Calculation of instantaneous heat flux rates was based on processing transient temperature measurements using the Fast Fourier Transform (FFT) technique. First, the FFT scheme was optimized and its accuracy was assessed. The finite element

Table 3 Summary of transient response indicated by CO-AX thermocouples in cast-iron piston; iron thin-film thickness = 10 μm

Thermocouple Type	Temperature (K) Min	Max	Temperature (K) Swing	Peak Temp. Error (%)
True	597	617	20	0
J-Type	598	622	24	+1.0
E-Type	598	625	27	+1.3
K-Type	601	625	24	+1.3
S-Type	601	619	18	+0.8

model was used to predict the transient temperature distribution of a flat top, cast-iron piston, without the presence of any thermocouples. Then, the transient nodal temperatures corresponding to the thermocouple measuring junction positions were used as the surface and subsurface temperatures for the FFT heat flux calculations. The FFT heat flux results were compared to the true heat flux, which was calculated by

$$q_{\text{true}}(\theta) = h(\theta)*(T_{\text{gas}}(\theta) - T_{\text{node}}(\theta)) \quad (8)$$

where $q_{\text{true}}(\theta)$ is true instantaneous heat flux from the combustion gas to the surface node in question, $h(\theta)$ is instantaneous effective convection coefficient, $T_{\text{gas}}(\theta)$ is instantaneous mean combustion temperature, and $T_{\text{node}}(\theta)$ is instantaneous nodal temperature.

Figure 10 indicates that the FFT heat flux calculations can indeed provide an accurate heat flux profile throughout the engine cycle. The small discrepancies between the true and FFT heat fluxes resulted from the assumption that heat flow is one-dimensional. Since the boundary conditions imposed on the piston were actually two-dimensional (see Fig. 2), the subsurface temperatures used to calculate the steady-state component of the FFT heat flux were slightly off. It should be noted that 60 FFT terms were used for all the heat flux predictions. Initially, up to 360 FFT terms were used to calculate heat flux. However, it was found that results were not significantly different compared to using only 60 terms to justify the addition of terms.

Having validated the FFT scheme, the next step is to calculate heat flux rates using the thermocouple-measured temperatures and to compare these rates against true heat flux rates based on undisturbed component temperatures. For both cases, FFT heat flux calculations were based on the conductivity of the piston, while the distance between the surface and subsurface nodes was exactly the same. Hence, the only source of error would be due to calculating heat flux from transient surface temperatures that are accurate to within 98 percent (due to the differences in thermal properties between the thermoelements and the piston).

Figure 11 shows that small errors (based on absolute temperatures) associated with CO-AX thermocouple surface temperature measurements can result in significant heat flux errors during the combustion period. In fact, peak heat flux measured by the J-type, E-type, and K-type thermocouples at crank angle 372 is 18 percent, 23 percent, and 18 percent higher than the true flux, respectively. The large percentage error implies that heat flux results depend not only on the temperature of the surface thermocouple junction, but are also sensitive to its time rate of change dT/dt. At top center of combustion, dT/dt for the true, J-type, E-type, K-type, and S-type thermocouples was 6600, 8000, 8600, 8000, and 6000 K/s, respectively. As shown in Fig. 11, higher than true dT/dt rates resulted in higher than true heat flux rates, and vice versa.

It is interesting to note that peak heat flux values for the

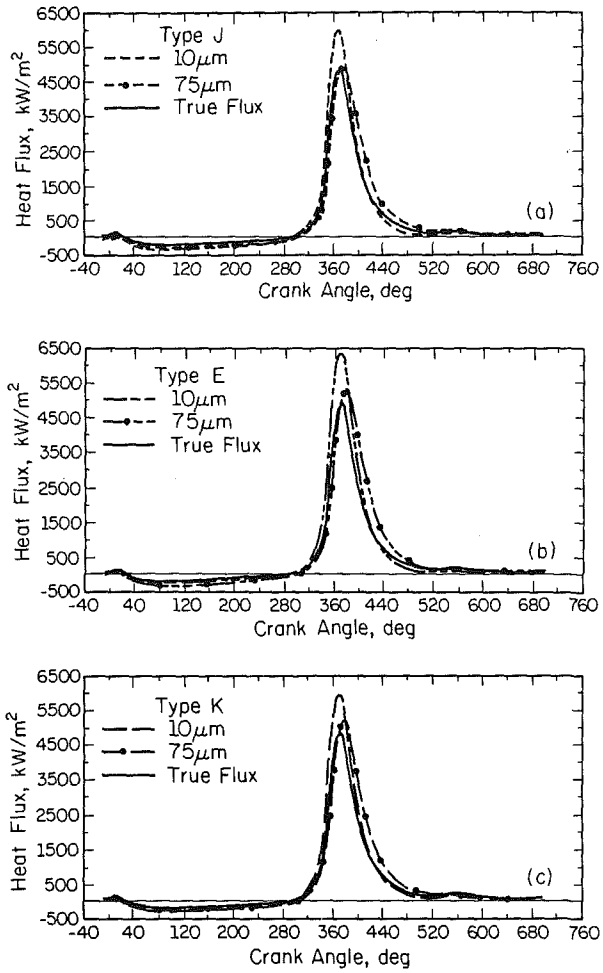

Fig. 12 Effects of increasing thin film thickness of heat flux measured by: (*a*) J-type, (*b*) E-type, and (*c*) K-type thermocouples

S-type thermocouple were lower than the true heat flux. However, the temperature indicated by the S-type thermocouple was approximately 2 K higher than the true temperature during combustion, and 4 K higher during the other processes (Fig. 8). Apparently, in this case, indicated temperatures by the S-type thermocouple were close enough to the true temperatures, so that the smaller rate of change of temperature dominated, resulting in lower peak heat flux values. The heat flux values obtained for the S-type thermocouple should be of no surprise, since this thermocouple was the only one of the four types studied that had a thermal diffusivity and thermal conductivity greater than iron.

Effect of Thin Film Thickness on Measurement Accuracy. The above results showed that, with the exception of the S-type thermocouple, all other types would overpredict heat flux. A possible solution to improve measurement accuracy of J, K, and E-type thermocouples is to force their junctions to approach the magnitude and time rate of change of the true temperature. This can be accomplished by increasing the conductive thin-film thickness so as to bury the measuring junctions beneath a critical depth that would sufficiently dampen (and thus correct) their response.

Indeed, Fig. 12(*a*) shows that, for a J-type thermocouple, an increase in thin-film thickness from 10 μm to 75 μm decreased the indicated peak heat flux values from 5910 kW/m^2 to 4870 kW/m^2 and shifted the peak 6 crank-angle deg later. With the original iron thin-film thickness of 10 μm, there was virtually no thermal gradient through the thickness of the thin film, except for a 3/4 deg temperature gradient at the midpoint of the center wire at peak combustion temperatures. Therefore, the effect of increasing the thin-film thickness to 75 μm was to create an insulation barrier between the combustion gases and the thermocouple measuring junction, which decreased the magnitude and swing of the junction temperature. Thus, the J-type thermocouple junction was forced to behave much like the true response, but with a 6 deg phase lag.

Table 4 Summary of transient response indicated by CO-AX thermocouples in cast-iron piston; iron thin-film thickness = 75 μm

Thermocouple Type	Temperature (K) Min	Max	Temperature (K) Swing	Peak Temp. Error (%)
True	597	617	20	0
J-Type	598	619	21	+0.4
E-Type	600	623	23	+1.0
K-Type	601	623	22	+1.0

The above analysis is not meant to imply that a 75 μm iron thin film possesses the optimum thickness to correct for the difference in thermal properties between a J-type thermocouple and an iron piston. Instead, the results should be interpreted as optimal under full load engine conditions for this particular piston-thermocouple combination. Under part-load conditions, the thermocouple error may not be as dramatic. Therefore a 75-μm-thick iron thin film may overcompensate the errors due to property differences, thus causing an underprediction of heat transfer.

Figures 12(*b*) and 12(*c*) illustrate similar trends for the heat flux behavior of E-type and K-type thermocouples with increasing thin-film thickness. For the E-type, peak heat flux dropped from 6330 to 5290 kW/m^2 when thin-film thickness was increased from 10 μm to 75 μm. Likewise, for the K-type thermocouple, peak heat flux dropped from 5910 to 5180 kW/m^2. From Figs. 12(*b*) and 12(*c*), it appears that higher accuracy in the magnitude of peak heat flux measurements obtained with E and K-type thermocouples could be achieved for further increases in thin-film thickness. However, thicker thin films would introduce an even more pronounced phase lag between the true and the indicated heat flux profiles.

A summary of the indicated thermocouple transient response with a 75-μm-thick iron thin film is shown in Table 4. The maximum temperature drop created by the 75-μm-thick iron thin film for the J-type, E-type, and the K-type thermocouples was approximately 3 K during peak junction temperatures. As a result, all thermocouples indicated a decreased peak heat flux that was accompanied by a 6 crank-angle deg phase lag.

Conclusions

Finite element modeling of fast-response CO-AX thermocouples typically used for heat transfer measurements of combustion chamber components has shown that:

1 CO-AX thermocouples are capable of measuring transient temperatures in iron components within an accuracy of 98 percent. The errors analyzed here are due to the differences in thermal properties between typically used thermoelements and a cast-iron piston.

2 These relatively small errors (based on absolute temperatures) in temperature measurement result in errors as high as 25 percent in peak surface heat flux calculations. This implies that heat flux results not only depend on the temperature of the surface thermocouple junction, but are also sensitive to its time rate of change dT/dt.

3 Increasing the thin-film thickness from 10 μm to 75 μm can decrease the magnitude and swing of the junction temperature, and thus decrease the magnitude of measured peak heat flux. However, the measured heat flux profile tends to follow the true heat flux profile with a 6 deg phase lag.

Acknowledgments

This material is based upon work supported by the National Science Foundation under Grant CBT-8707853.

References

1 Assanis, D. N., and Heywood, J. B., "Development and Use of a Computer Simulation of the Turbocompound Diesel System for Engine Performance and Component Heat Transfer Studies," *SAE Trans.*, SAE Paper No. 860329, 1986.

2 Eckert, E. R. G., and Goldstein, R. J., *Measurements in Heat Transfer*, Hemisphere Publishing Corporation, New York, 1976.

3 Bendersky, D. A., *Mechanical Engineering*, Vol. 75, 1953, p. 117.

4 LeFebvre, T., Myers, P. S., and Uyehara, O. A., "Experimental Instantaneous Heat Fluxes in a Diesel Engine and Their Correlation," SAE Paper No. 690464, 1969.

5 Alkidas, A. C., and Myers, J. P., "Transient Heat-Flux Measurements in the Combustion Chamber of a Spark-Ignition Engine," ASME *Journal of Heat Transfer*, Vol. 104, 1982, pp. 62–67.

6 Medtherm Corporation, Bulletin 500, Huntsville, AL, May 1982.

7 Powell, R. L., and Burns, G. W., "Thermocouple Reference Tables Based on the IPTS-68," National Bureau of Standards, Department of Commerce, Washington, DC, Mar. 1974.

8 Assanis, D. N., and Badillo, E., "Transient Heat Conduction in Low-Heat-Rejection Engine Combustion Chambers," *SAE Trans.*, SAE Paper No. 870156, 1987.

9 Li, C.-H., "Piston Thermal Deformation and Friction Considerations," SAE Paper No. 820086, 1982.

10 Overbye, V. D., Bennethum, J. E., Myers, P. S., and Uyehara, O. A., "Unsteady Heat Transfer in Engines," *SAE Trans.*, Vol. 69, 1961, pp. 461–493.

Extraction Techniques and Analysis of Turbulence Quantities From In-Cylinder Velocity Data

A. E. Catania
Mem. ASME

A. Mittica

Dipartimento di Energetica,
Politecnico di Torino,
Turin, Italy

In addition to the frequently used statistical ensemble-average, non-Reynolds filtering operators have long been proposed for nonstationary turbulent quantities. Several techniques for the reduction of velocity data acquired in the cylinder of internal combustion reciprocating engines have been developed by various researchers in order to separate the "mean flow" from the "fluctuating motion," cycle by cycle, and to analyze small-scale engine turbulence by statistical methods. Therefore a thorough examination of these techniques and a detailed comparison between them would seem to be a preliminary step in attempting a general study of unconventional averaging procedures for reciprocating engine flow application. To that end, in the present work, five different cycle-resolved data reduction methods and the conventional ensemble-average were applied to the same in-cylinder velocity data, so as to review and compare them. One of the methods was developed by the authors. The data were acquired in the cylinder of a direct-injection automotive diesel engine, during induction and compression strokes, using an advanced hot-wire anemometry technique. Correlation and spectral analysis of the engine turbulence, as determined from the data with the different procedures, were also performed.

Introduction

An improved understanding of in-cylinder flow processes, with particular reference to turbulence, is a key requirement for further improvements in the fuel economy and emissions of internal combustion (IC) reciprocating engines. More specifically, the degree of success achieved with new engine concepts, such as high-speed direct-injection diesel engines, lean-mixture, and stratified-charge engines, depends in part on the knowledge of the effects of the geometric engine features and operating conditions on the in-cylinder turbulent flow field during induction and the part of the compression stroke prior to injection or ignition (Lancaster et al., 1976; Nagayama et al., 1977; Brandl et al., 1979; Inoue et al., 1980; Monaghan and Pettifer, 1981; Belaire et al., 1983; Davis et al., 1984; Shimoda et al., 1985; Matsushita et al., 1985; Hashimoto et al., 1986; Kato and Onishi, 1987; Evans and Dohring, 1987; Balles and Heywood, 1988; Chau et al., 1988).

Owing to the difficulties of making turbulence measurements in combusting flows, most of the investigations on the relationship between in-cylinder turbulent flow parameters and the engine combustion process have been performed by correlating the flow data acquired under motored conditions to combustion data acquired in the firing engine. Although an interaction between engine turbulence and combustion may exist (Martin et al., 1985; Hall and Bracco, 1987), the validity of this approach is confirmed, at least in some circumstances, by two facts. Firstly, similar turbulent flow patterns before combustion under motored and firing conditions, respectively, have been shown (Ohigashi et al., 1971; Rask, 1979; Hall and Bracco, 1987) and, more recently, insignificant differences between scavenged and unscavenged engine cycles were found in swirling-flow turbulence and mean velocity during the latter part of the compression stroke, prior to ignition, in a skip-fired engine (Witze et al., 1988). Secondly, cycle-resolved analysis of in-cylinder velocity data under firing conditions (Witze and Mendes-Lopes, 1986; Hall and Bracco, 1987) led to the conclusion that combustion virtually did not increase the turbulence intensity ahead of the flame, and conditionally sampled measurements (Witze et al., 1984) showed that turbulence intensity trends in the unburned gas correlate with flame arrival time, with the faster burns having the higher turbulence level. This is in agreement with the general finding that the burn rate increases with turbulence intensity.

Many experimental investigations on reciprocating engine flows have been performed using both hot-wire anemometry (HWA) (Semenov, 1958; Huebner and McDonald, 1970; Ohigashi et al., 1971; Dent and Salama, 1975; Lancaster, 1976; Witze, 1977; Catania, 1980, 1985; Wakisaka et al., 1982; Tindal et al., 1982; Catania and Mittica, 1985b, 1987; Khalighi et al., 1986; Dinsdale et al., 1988) and laser Doppler velocimetry (LDV) (Rask, 1979; Ball et al., 1983; Witze et al., 1984; Liou et al., 1984; Coghe et al., 1985; Bopp et al., 1986; Saxena and Rask, 1987; Hall and Bracco, 1987; Arcoumanis et al., 1987; Ikegami et al., 1987; Fansler and French, 1988; Fraser and Bracco, 1988; Glover et al., 1988).

Most of these are Eulerian single-point studies of turbulent flow at different locations in engine cylinders. Of course, in order to explore the spatial features of the flow field,

Contributed by the Internal Combustion Engine Division and presented at the Twelfth Annual Energy-Sources Technology Conference and Exhibition, Houston, Texas, January 22-25, 1989. Manuscript received by the Internal Combustion Engine Division August 1988.

simultaneous multiple-point measurements would be desirable and, in particular, these are required for a direct evaluation of turbulence spatial scales. Attempts have recently been made to measure instantaneous spatial-velocity distributions in engines. However, only rough approximations of spatially resolved results were obtained with the laser homodine technique (Ikegami et al., 1987), due to the relatively long measuring volume required, over which constant bulk velocity and lateral integral length scale of turbulence are assumed. On the other hand, only approximately simultaneous velocities were measured either by the flying HWA technique (Dinsdale et al., 1988) or by the scanning LDV technique (Glover et al., 1988), due to the flight or scan duration, respectively, over which no significant time variations are assumed, not to mention the additional uncertainty sources that these sophisticated techniques involve and, moreover, the crude assumptions made in the data reduction methods used.

A thorough literature review of main achievements, with particular reference to the effects of the intake system on the in-cylinder turbulent flow parameters, was recently reported by the authors (1987). We pointed out that the results obtained by different researchers were consistent with the respective measurement techniques and definitions of turbulence adopted.

It should be recalled that the fluid-dynamics of IC reciprocating engines is a very challenging field of research as far as the way of defining turbulence is concerned. To give an example, it was shown by Liou et al. (1984), with reference to a specific ported engine, that the question of whether the in-cylinder turbulence intensity without swirl is smaller or larger than with swirl could have different answers depending on the procedure used to extract turbulence intensity from the same velocity data, particularly for the no-swirl case. Another important question was addressed by Fansler and French (1988), that of whether the squish-generated velocity fluctuations observed in a re-entrant-bowl-in-piston engine near TDC of compression could influence turbulent mixing and combustion within individual engine cycles, or should be correlated with cyclic variations in combustion performances.

The in-cylinder turbulent flow field is highly three-dimensional and nonstationary, due to the intake system configuration and the time-dependent boundary conditions imposed by the piston motion and valve transients. Changes in the mean (or bulk) flow occur on a time scale of milliseconds, that is, the same order of magnitude as typical time scales of turbulence. Furthermore, the task of determining which part of the velocity is turbulence and which part is mean velocity is made more difficult by the recognized presence of cycle-to-cycle variations in the mean flow.

The conventional statistical approach for stationary turbulent flows is to decompose the instantaneous flow properties into a time-averaged component and a fluctuating component. For nonstationary flows, an equivalent definition is based on ensemble averaging over a statistically acceptable number of data records (or cycles, in an engine). These are the so-called Reynolds operators (Monin and Yaglom, 1971). Non-Reynolds filtering operators have also been proposed for nonstationary turbulent quantities (Kampé de Fériet, 1957; Monin and Yaglom, 1971). Even though these require the definition of a characteristic integration time or cutoff frequency to obtain a certain degree of filtering, while ensemble averaging is unambiguous, as for reciprocating engine flow application, they have the advantage of giving information about the flow in a particular engine cycle.

The combustion process in a reciprocating engine, in fact, occurs within each individual cycle and so it is directly influenced by the in-cycle turbulent flow parameters. This suggests that the analysis of engine turbulence should be performed on a single-cycle basis first. To that end, several reduction techniques of in-cylinder velocity data have been developed to characterize the mean velocity and turbulence in each cycle and to perform a statistical analysis of turbulent flow parameters, as obtained from the cycle resolved results (Lancaster, 1976; Rask, 1981; Liou and Santavicca, 1985; Catania and Mittica, 1985a; Daneshyar and Fuller, 1986). HWA measurements were used for data reduction by Lancaster, Catania and Mittica, and Daneshyar and Fuller, while LDV data were used by Rask, and by Liou and Santavicca.

A thorough examination of these techniques and a detailed comparison between them would seem to be a preliminary step in attempting a general study of non-Reynolds averaging procedures for reciprocating engine flow application.

To that end, in the present work, all of the five cycle-resolved data reduction procedures, as well as the conventional ensemble-average, were applied to the same in-cylinder velocity data, so as to review and compare them.

The data were acquired in the cylinder of a direct-injection automotive diesel engine on the induction and compression strokes, using an advanced HWA technique (Catania, 1980, 1982).

Correlation and spectral analysis of the engine turbulence, as determined from the data with the different procedures, was also performed.

Cycle-to-Cycle Variations in the Mean Flow

The following considerations can support the consistency of the notion of cycle-to-cycle fluctuations in the mean flow inside an engine cylinder and physical explanations of their origin.

Cyclic variations have long been observed in engine combustion process from pressure development histories (Patterson, 1966) and, more recently, also from flame photography experiments (Matekunas, 1983; Witze et al., 1984). The differences in the trajectory of the initial flame kernel in different cycles were determined to be the major cause of cyclic variation in spark-ignition engine combustion (Matekunas, 1983). These were ascribed to the larger scale motion and correlated to drastic changes in the flow pattern from cycle to cycle or, more specifically, to the relatively high cycle-to-cycle fluctuations observed in the mean velocity inside the same engine under motored conditions (Saxena and Rask, 1987).

Evidence of drastic differences in the flow pattern from cycle to cycle and of the instantaneous velocity pattern in one cycle with respect to the ensemble-averaged velocity was given by Rask (1981) and by Catania and Mittica (1985a); examples of these are shown in Fig. 2 and in Figs. 3(f) and 4(f), respectively.

The small-scale turbulence intensity determined with the authors' procedure of cycle-resolved data reduction was verified effectively to affect the engine combustion rate (Evans and Dohring, 1987), as expected, and was found to be more sensitive to the intake system configuration than the rms fluctuation of mean velocity. Instead, the latter was more sensitive to the engine speed (Catania and Mittica, 1987). This is consistent with results obtained by other researchers for rms velocity fluctuation (Bopp et al., 1986) and for cycle-resolved turbulence (Saxena and Rask, 1987), according to the finding that the mean-flow cyclic fluctuation could play a major role in rms velocity fluctuations (Lancaster, 1976; Catania and Mittica, 1985a; Liou et al., 1984; Hall and Bracco, 1987; Fansler and French, 1988).

On the other hand, the swirl center precession in an engine cylinder was characterized as a quasi-periodic motion superimposed on the unsteady, turbulent in-cylinder flow (Arcoumanis et al., 1987). The variations in phase and amplitude exhibited by this motion may give rise to cycle-to-cycle variations in the flow around the cylinder axis. It could have a wide range of characteristic frequencies (up to more than 300 Hz).

The physical description proposed by Reynolds (1980) for the origin of cyclic variations in the mean flow is that both the location and size of recirculating regions formed during the intake process are very sensitive to minor variations in the induction flow field.

In an engine, the swirl center precession may originate from the interaction of the swirling flow with the valve wake formed behind the valve early on the induction stroke (Arcoumanis et al., 1987).

The in-cylinder flow field may be subject to other instabilities, such as, for example, flapping of the squish jet (Fansler and French, 1988) or of the secondary intake jet, and, in multivalve engine geometries, intake jet interference (Catania, 1982, 1985). Such instabilities could be considered to give rise to bulk flow cyclic fluctuations, owing to the interaction of these jet flows with the main flow.

Ensemble-Averaging and Related Data-Reduction Schemes

The periodic nature of the engine cycle suggests that ensemble-averaging (or phase-averaging) may be used, where the instantaneous velocity, or more simply the velocity, at a specific crank-angle position is averaged over many cycles, so as to obtain the mean velocity; the turbulence intensity is taken to be equal to the rms fluctuation of the velocity about the ensemble-averaged velocity.

According to this approach, the instantaneous velocity in the engine cycle i is decomposed into two components:

$$U_i(t) = U_E(t) + u_{i,E}(t) \tag{1}$$

where $U_E(t)$ is the ensemble-averaged velocity at time t (or crank angle ϑ) over N records (or cycles), that is, using the brackets $\langle\ \rangle$ to indicate an ensemble-averaged quantity:

$$U_E(t) = \langle U_i(t) \rangle = \frac{1}{N} \sum_{i=1}^{N} U_i(t) \tag{2}$$

and $u_{i,E}(t)$ is the turbulent fluctuation about the mean velocity. The turbulence intensity, or the rms velocity fluctuation, is given by

$$u'_E(t) = \sqrt{\langle u^2_{i,E}(t) \rangle} = \sqrt{\frac{1}{N} \sum_{i=1}^{N} u^2_{i,E}(t)} \tag{3}$$

The mean velocity defined in this way is identical from cycle to cycle, while there is evidence that the bulk flow does change from cycle to cycle; therefore, the turbulence intensity may be overestimated, owing to these variations (Reynolds, 1980).

To remove cyclic variations from phase-averaged data, conditionally sampled velocity measurements were chosen for investigation inside firing engines (Cole and Swords, 1980; Swords et al., 1982; Witze et al., 1984; Martin et al., 1984). Based on a correlation, to be established, between the flow at a particular time and place in the engine and an index of the combustion process, such as peak pressure, flame speed, or the time of flame arrival at the LDV probe volume, velocity measurements were sorted and ensemble averaged according to similar combustion events. However, apart from the difficulty in selecting relevant conditioning parameters, those which are easily measurable are generally time and/or space-averaged quantities, so multiparameter conditionally sampling was also required to reduce integration effects. It was not specified how cyclic variations in turbulence intensity should be quantified (only trends for these were presented) and what the resolution of each segment forming a conditionally sample data set should be. Furthermore, no indication was given of the way to remove the apparent turbulence in the phase average due to other cyclic variations in the selected conditioning process (e.g., variation of the flame surface geometry).

An alternative approach to the problem of discriminating between turbulence and mean-flow cyclic variation in the rms velocity fluctuation was to identify cyclic variations as processes that exhibit phase stability relative to either crank-angle or spatial position (Glover et al., 1988); nonstationary velocity autocorrelation functions were used to assess the temporal or phase coherence of the fluctuations about the ensemble-mean velocity. However, besides the care that should be taken in handling nonstationary velocity autocorrelation functions to extract information from them, as will be seen later on, this procedure is limited by the underlying drastic simplifications and the assumptions made, such as turbulence isotropy and homogeneity, the analytical form of the turbulence contribution to the autocorrelation function, the noise assumed as the dominant effect on the less than unit autocorrelation peak, where inadequate spatial resolution could be the major effect, as well.

Cycle-Resolved Data Reduction Procedures

The instantaneous velocity is split into a mean nonstationary component and a turbulent fluctuation about this, so that, with reference to the engine cycle i

$$U_i(t) = \tilde{U}_i(t) + u_i(t) \tag{4}$$

where $\tilde{U}_i(t)$ is the mean velocity at time t (corresponding to the crank angle ϑ) and $u_i(t)$ is the velocity fluctuation about the mean.

Basically, the way of determining the in-cycle mean velocity $\tilde{U}_i(t)$ differs from author to author, while the procedures followed to evaluate the turbulence intensity from the velocity fluctuation $u_i(t)$ can be grouped into two main classes: ensemble-averaging; time- and ensemble-averaging.

In the first approach, the turbulence intensity is obtained as pure rms fluctuation of the velocity about its in-cycle mean, that is

$$u'(t) = \sqrt{\langle u_i^2(t) \rangle} = \sqrt{\langle [U_i(t) - \tilde{U}_i(t)]^2 \rangle} \tag{5}$$

This implies that the ensemble-average of $u_i(t)$, as will be indicated by $\Sigma(t)$, should be zero. By ensemble averaging all terms in equation (4), and setting

$$U(t) = \langle \tilde{U}_i(t) \rangle \tag{6}$$

it follows, taking into account equation (2)

$$\Sigma(t) = \langle u_i(t) \rangle = U_E(t) - U(t) \tag{7}$$

Consequently, the ensemble-averaged mean velocity $U(t)$ should equal the ensemble-averaged velocity $U_E(t)$.

It is worth noting that, within the framework of this procedure, the turbulence intensity definition in one specific engine cycle cannot easily find any traditionally consolidated collocation, though an attempt to consider the absolute value of the fluctuation velocity $u_i(t)$ as in-cycle turbulence intensity has been made (Liou and Santavicca, 1985).

In the other approach, a time-averaged in-cycle turbulence intensity is evaluated from the velocity fluctuation $u_i(t)$ within specific time (or crank-angle) intervals into which the engine cycle is divided, so that, using the symbol $\bar{f}$ to represent the average of any variable $f(t)$ (or $f(\vartheta)$) in the time interval T (or in the crank-angle interval Θ)

$$\bar{f} = \frac{1}{T} \int_0^T f(t+\tau)\, d\tau = \frac{1}{\Theta} \int_0^{\Theta} f(\vartheta + \varphi)\, d\varphi \tag{8}$$

the turbulence intensity u_i' in the interval T and in the engine cycle i, is given by

$$u_i' = \sqrt{\bar{u}_i^2} = \sqrt{(U_i - \tilde{U}_i)^2} \tag{9}$$

An ensemble-averaged turbulence intensity in T can be defined as

$$u' = \sqrt{\langle \tilde{u}_i^2 \rangle} \tag{10}$$

In agreement with the conventional definition of turbulence for stationary flows, this approach requires that, in each interval

$$\tilde{u}_i = 0 \tag{11}$$

or, from equation (7)

$$\tilde{U}_i = \bar{\tilde{U}}_i \tag{12}$$

The in-cycle mean velocity can be expressed as the sum of the ensemble-averaged mean velocity and a fluctuating component about this

$$\tilde{U}_i(t) = U(t) + \tilde{u}_i(t) \tag{13}$$

where $U(t)$ is the ensemble-averaged mean velocity , obtained from the ensemble of the individual cycle mean velocity over all the cycles, and $\tilde{u}_i(t)$ is the low-frequency cyclic fluctuation of the mean velocity, so that: $\langle \tilde{u}_i(t) \rangle = 0$. $U(t)$ is given by equation (6) and should be equal to $U_E(t)$; therefore, some researchers write equation (13) with $U_E(t)$ instead of $U(t)$ (Rask, 1984; Fansler and French, 1988).

In terms of time-averaged values equation (13) becomes

$$\bar{\tilde{U}}_i = U + \bar{\tilde{u}}_i \tag{14}$$

where $U = \langle \bar{\tilde{U}}_i \rangle$ and $\langle \bar{\tilde{u}}_i \rangle = 0$.

In the ensemble-averaging approach the rms fluctuation of the in-cycle mean velocity about the ensemble-mean velocity is

$$U_{\text{rms}}(t) = \sqrt{\langle \tilde{u}_i^2(t) \rangle} = \sqrt{\langle [\tilde{U}_i(t) - U(t)]^2 \rangle} \tag{15}$$

In the time- and ensemble-averaging approach the rms fluctuation of the in-cycle mean velocity and turbulence intensity values about the respective ensembles in the interval T are

$$U_{\text{rms}} = \sqrt{\langle \bar{\tilde{u}}_i^2 \rangle} = \sqrt{\langle (\bar{\tilde{U}}_i - U)^2 \rangle} \tag{16}$$

$$u'_{\text{rms}} = \sqrt{\langle (u_i' - u')^2 \rangle} \tag{17}$$

From equations (1), (3), (4), (7), and (13) it follows that

$$u_E'^2(t) = \langle [u_i(t) + \tilde{u}_i(t) - O(\Sigma)]^2 \rangle \tag{18}$$

where $O(\Sigma)$ indicates a term with the same order of magnitude as $\Sigma(t)$.

Hence, through equations (5), (6), and (16), the rms velocity fluctuation $u'_E(t)$ is related to the cycle-resolved turbulence intensity $u'(t)$ by

$$u_E'^2(t) - u'^2(t) = U_{\text{rms}}^2(t) + 2\langle u_i(t)\tilde{u}_i(t) \rangle - O(\Sigma^2) \tag{19}$$

and also, for the equations (7) and (13), by

$$u_E'^2(t) - u'^2(t) = U_{\text{rms}}^2(t) + 2\langle u_i(t)\tilde{U}_i(t) \rangle - 2U_E(t)O(\Sigma) + O(\Sigma^2) \tag{20}$$

The cross terms $\langle u_i(t)\tilde{u}_i(t) \rangle$ and $\langle u_i(t)\tilde{U}_i(t) \rangle$ are usually neglected since the high-frequency turbulent fluctuations are assumed to be statistically independent of the mean velocity and its low-frequency fluctuations (Witze and Mendes-Lopes, 1986; Fansler and French, 1988).

The analysis of these terms is important because they contribute to non-Reynolds stresses yielded by nonconventional averaging of the dynamical flow equations.

In what follows, the procedures to determine the in-cycle mean velocity $\tilde{U}_i(t)$ are reviewed.

A low-pass/high-pass filter was used to acquire HWA data by Dent and Salama (1975).

The conventional procedure of time-averaging the velocity to obtain a steady mean velocity for specific intervals within each engine cycle (Wakisaka et al., 1982) includes as turbulence the time-varying component of the bulk motion.

Nonstationary Time-Averaging (NTA) (Lancaster, 1976). Eight successive 45-deg crank-angle intervals were considered throughout intake and compression. The ensemble-averaged velocity was first calculated from the measured velocities at each crank-angle degree and then the in-cycle unsteady mean velocity was evaluated, in each interval, as the sum of the ensemble-averaged velocity and a constant quantity (but not the same for each interval) given by the time average of the difference between the instantaneous velocity and the ensemble-averaged one in the specific interval, that is

$$\tilde{U}_i(t) = U_E(t) + \bar{U}_i - \bar{U}_E \tag{21}$$

Cycle-resolved time-averaged turbulence intensity in each interval was then obtained from the turbulent velocity component, considered as a stationary random fluctuation superimposed on the unsteady bulk motion. In fact, by time averaging each member of equation (21), equation (12) and consequently the condition (11) are satisfied. Furthermore, by ensemble averaging each term in equation (21), taking into account the interchangeability of the order of this operation with time averaging in the term $\bar{U}_i$, that is

$$\langle \bar{U}_i \rangle = \overline{\langle U_i \rangle} = \bar{U}_E \tag{22}$$

if follows that

$$U(t) = \langle \tilde{U}_i(t) \rangle = U_E(t) \tag{23}$$

and consequently, from equation (7), the ensemble average of $u_i(t)$ is zero.

No indication was given about the criteria for the selection of the averaging time (or crank-angle) interval length.

Cubic Spline Fitting (CSF) (Rask, 1981); Inverse Fast Fourier Transform (IFT) (Liou and Santavicca, 1985). The first step taken in both procedures was to calculate a velocity for each 1-deg crank-angle window by arithmetically averaging the data in those windows with multiple measurements and by assigning linearly interpolated values to those windows with no measurement. Of course this sort of filtering reduces the frequency content of the original data. This limitation however was inherent to the LDV measurements used and is removed in the present application to HWA measurements. As for the next step, while in the CSF procedure a mean velocity curve was fitted to the average window values using a cubic spline smoothing routine, in the IFT procedure the frequency spectrum of the average window data was obtained using the fast Fourier transform, then all frequency components above a selected cutoff frequency were set to zero and the inverse transform was taken yielding the in-cycle mean velocity curve. An ensemble-averaged turbulence intensity was evaluated from the velocity fluctuation about the in-cycle mean velocity at each window.

The smoothing parameter in the CSF procedure was set to its statistically expected value (depending on the number of windows with data) and the standard deviations of the window mean velocity estimates were used as weighting functions in its expression, according to Reinsch (1967).

Regarding the choice of the cutoff frequency in IFT filtering, Liou and Santavicca (1985) stated that it should be related to a characteristic time of the engine combustion process. However, since the structure of engine flames was, and still is, poorly understood, the highest frequency present in the ensemble-averaged velocity was assumed as cutoff frequency. This value depends on the ensemble-averaged velocity pattern, which, in turn, is related not only to the engine variables and measurement locations, but also to the part of the engine cycle considered.

Time-Average Filtering (TAF) (Catania and Mittica, 1985). The authors' procedure was referred to as a novel nonstationary time-averaging procedure in previous works

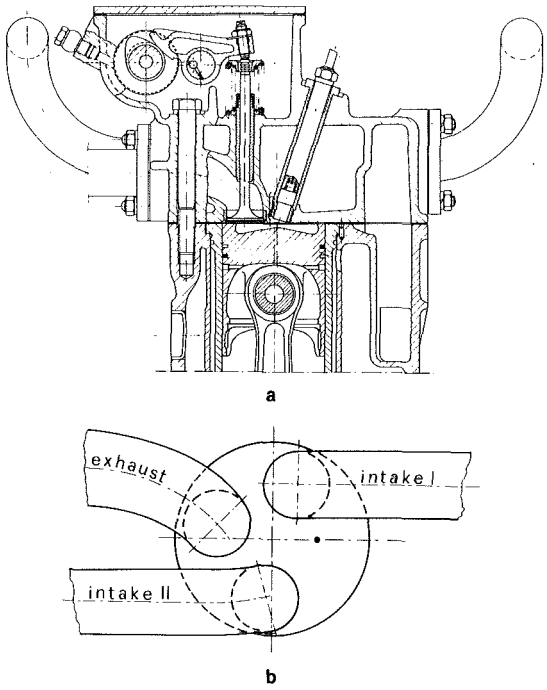

Fig. 1 Test engine and schematic of the intake system

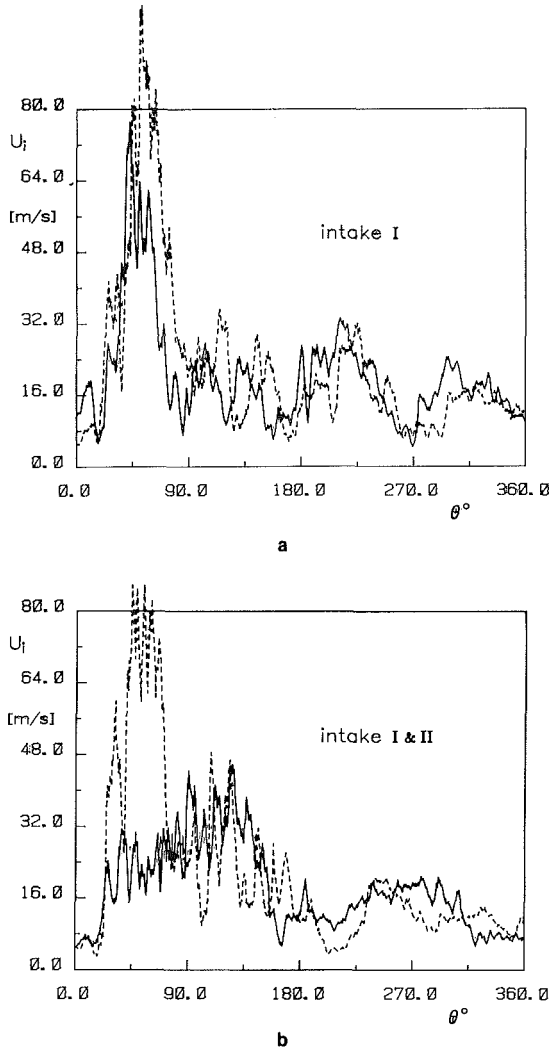

Fig. 2 Individual-cycle velocity patterns

(Catania and Mittica, 1985a, 1985b, 1987) where the differences with the Lancaster definition of in-cycle mean velocity were detailed. Here it seems convenient to rename it as curve fitting of time-averaged velocity in discrete crank-angle intervals, or, more simply, time-average filtering. Evaluation of the in-cycle nonstationary mean velocity is accomplished through the following steps. First the time average of the instantaneous velocity is evaluated in discrete crank-angle intervals into which the engine cycle is divided and the resulting averaged velocity values, taken in the middle of the respective intervals, are interpolated to obtain the initial in-cycle mean velocity curve, from which, through an iterative process, the final mean velocity curve is obtained so that equation (12), and condition (11), are satisfied everywhere in the engine cycle (Catania and Mittica, 1987). The ensemble-averaged mean velocity $U(t)$ is obtained by interpolating the ensemble-averaged mean velocity values given, for each interval, by equation (22). This is, in effect, equivalent to the result of equation (6) and should only correspond to a slight smoothing of the ensemble-averaged velocity $U_E(t)$ (Catania and Mittica, 1985a). The in-cycle time-averaged turbulence intensity in each interval is given by equation (9) and the ensemble-averaged turbulence intensity by equation (10). Turbulence intensity curves, $u_i'(t)$ and $u'(t)$, are obtained from the cycle-resolved results by interpolation.

The basic requirements to fit the averaging interval length for selection were: The interval had to be relatively long with respect to the micro time scales of turbulence determined, but sufficiently short to avoid such a high degree of filtering as to include in the turbulence a significant time-varying component of the bulk flow. A relatively narrow range (between 8 and 18 deg) was estimated where the crank-angle averaging interval could reasonably fall, and in which, furthermore, the upper frequency limit of the spectrum of the ensemble-averaged mean velocity, obtained using the fast Fourier transform, showed a broad minimum.

Linear Trend Removal (LTR) (Daneshyar and Fuller, 1986). This procedure basically consists in taking the time-averaged value of the instantaneous velocity as the mean velocity value for a given period in the engine cycle, and in evaluating the turbulent fluctuation with respect to a linear function of the time (or crank angle) obtained from the instantaneous velocity in the same period using a linear trend removal procedure (Bendat and Piersol, 1986). A time-averaged turbulence intensity is then evaluated and ensemble averaged over the number of cycles sampled.

A period of 30 crank-angle deg was chosen for investigation by Daneshyar and Fuller.

Velocity Data Measurements

Experimental System and Procedure. The in-cylinder velocity data, for reduction and analysis with the different procedures, were taken in the direct-injection automotive diesel engine previously described (Catania, 1985). The engine (Fig. 1*a*), derived from a production engine at Fiat Research Center, had a 75.5 mm bore, an 83.5 mm stroke, and a compression ratio of 16. The induction system was made up of two equiverse swirl tangential ducts, and valves of the same size and lifts. The measurements were taken for the different swirl flow conditions produced by two intake system configurations (Fig. 1(*b*): with only one duct operating (intake I) and with both ducts operating (intake I and II), at an engine speed of 1600 rpm (167.6 rad/s). These conditions, in fact, were of particular interest for analysis, at the measurement location evidenced by the dot in Fig. 1(*b*). This was ≈ 3.5 mm underneath the flat cylinder head and at a radial distance of 17.5 mm from the cylinder axis, approximately in the middle of the right-hand section of the shallow combustion bowl at

TDC. It was, for intake I, upstream of the valve, and for intakes I and II, downstream of the other valve, so, in the first case, only a secondary jet flow could be sensed on induction, while, in the other case, the main swirling flow was sensed on induction too.

The measurements were carried out in the crank-angle interval $\vartheta = 0$–360 deg, that is from the start of the induction stroke to the end of the compression stroke.

Sixty sample data records were acquired using an advanced HWA technique (Catania, 1982), with the sensing wire parallel to the cylinder axis, at a rate of one measurement per 0.2 crank-angle deg, that is, high enough to give a virtually continuous velocity trace in every cycle.

Experimental Uncertainties. The method used to compute gas velocity from the anemometer output is different from all the semiempirical corrections considered by Witze (1980) and was validated in nonstationary as well as stationary conditions, at different gas pressures and temperatures (Catania, 1985; Catania and Mittica, 1987). The main sources of uncertainty in the gaseous engine environment are of different types and give rise to very complex effects, which are difficult to evaluate; many of them were reduced as far as possible (Catania, 1982).

Based on the previous findings and on the average deviations of repeated measurement sets, a maximum uncertainty of ± 10 percent could be ascribed to the computed velocities. However, it can be expected that the implications of the results and the related conclusions are not influenced by the overall experimental uncertainty.

Data Reduction Results and Discussion

Figure 2 shows instantaneous velocity patterns in distinct cycles, as obtained from the anemometer output. These give evidence of drastic variations from cycle to cycle and of instabilities in the secondary intake jet, which is sensed by the wire at the early stage of induction ($\vartheta = 0$–70 deg). Flapping of the incoming secondary jet may be a consequence of the sudden expansion it undergoes in the cylinder and of its interaction with the strong recirculating region formed as a result of flow separation from either side of the valve orifice. In the configuration with both intake ducts operating, the interference between the secondary jet flows issuing from the two valves could give rise to instabilities evidenced by the presence or the absence of a secondary jet on early induction in Fig. 2(*b*). It could be considered that such instabilities give rise to bulk flow cyclic fluctuations, owing to the interaction of the secondary jets with the main flow. The interference of these flows is an additional source of turbulence in engine swirling flows.

In order to give illustrative examples of the results obtained using the different procedures to separate in-cycle mean velocity from turbulence, Figs. 3 and 4 report the measured instantaneous velocity U_i[1] in one cycle (ragged line), the corresponding mean velocity and turbulent fluctuations obtained by applying the filtering procedures described, and, for comparison, the conventional statistical method.

An averaging interval of 12 deg was used in the authors' procedure, to obtain $\tilde{U}_{i,\mathrm{TAF}}$ in Figs. 3(*d*) and 4(*d*). It corresponds to a period of 1.25 ms at the engine speed of 1600 rpm.

Consecutive crank-angle intervals of 45 deg and 30 deg were considered throughout intake and compression in the NTA and LTR procedures, respectively. These procedures lead to in-cycle mean velocity and fluctuating velocity curves with discontinuities at the boundaries of each interval, as evident in Figs. 3(*a*), 3(*e*), 4(*a*), 4(*e*).

$\tilde{U}_{i,\mathrm{CSF}}$ in Figs. 3(*b*) and 4(*b*) was obtained using the normal or expected value for the smoothing parameter and the standard deviations of one-deg-window mean velocity estimates as weighting functions. While on the compression stroke this curve fits the instantaneous velocity pattern, on induction it tends to bear a degree of smoothing so high as to include a significant bulk velocity component in turbulence. This is particularly evident in Fig. 3(*b*) on early induction where a secondary jet peak was detected; an underlying trend in the fluctuating velocity component $u_{i,\mathrm{CSF}}$ was found there. If a lower smoothing parameter was used to allow a more effective influence of the highest weighting function values occurring in the narrow crank-angle interval where the secondary jet is present (Fig. 7*a*), too small turbulent fluctuations would result on the compression stroke. This could be an effect of the ICSSCU cubic spline smoothing routine itself, which treats turbulence as an uncertainty in the velocity measurements.

$\tilde{U}_{i,\mathrm{IFT}}$ in Figs. 3(*c*) and 4(*c*) was obtained using a cutoff frequency of about 500 Hz, that is, virtually the maximum frequency in the spectrum of the ensemble-averaged mean velocity U_{TAF} obtained with the authors' procedure. It should be pointed out that this frequency is considerably lower than the cutoff frequency suggested by Liou and Santavicca, that is, the maximum frequency in the spectrum of the ensemble-averaged velocity U_E. If this value was assumed, a very low degree of filtering would be attained yielding too small or insignificant turbulence intensities. This could be explained mainly by the fact that Liou and Santavicca limited their analysis to a crank-angle interval of 64 deg across TDC of compression, with the result of a lower upper frequency limit in the ensemble-averaged velocity.

Figures 3(*f*) and 4(*f*) compare the instantaneous velocity pattern in one cycle to the ensemble-averaged velocity, giving further evidence of cyclic fluctuations in the mean flow. These are particularly significant during the early part of induction where secondary intake jets occur.

Examples of low-frequency fluctuation patterns $\tilde{u}_i$ in one cycle, as determined by the different procedures, are reported in Fig. 5 for intake I. The instantaneous velocity data record, from which the in-cycle mean velocity curves were obtained in this figure, was the same as in Fig. 3. In spite of the considerable differences that $\tilde{U}_{i,\mathrm{CSF}}$ exhibits with respect to $\tilde{U}_{i,\mathrm{IFT}}$ and $\tilde{U}_{i,\mathrm{TAF}}$ at the early stage of induction, the trend of the mean velocity fluctuations is the same throughout induction and compression for all the procedures considered in Fig. 5. The highest frequency content is readily seen in $\tilde{u}_{i,\mathrm{IFT}}$, which suggests that the IFT procedure tends to give a lower degree of filtering, so that an inexplicably low cutoff frequency may be required. Mean velocity fluctuations are evaluated as constant values in the 45-deg or 30-deg crank-angle intervals, with the NTA and LTR procedures, respectively; therefore these are not reported in Fig. 5.

In order to make the following data reduction results comparable, besides using a cutoff frequency of about 500 Hz in the IFT procedure, 30 successive crank-angle intervals of 12 deg were considered throughout intake and compression in the NTA and LTR procedures. Time-averaged quantities in the intervals were interpolated to obtain a continuous distribution of these, as a function of the crank angle, on induction and compression. The specified values of the smoothing parameter and weighting functions were used in the CSF procedure, except that a lower degree of smoothing was chosen in the cubic spline fitting of the turbulence intensity values.

Figure 6 compares the ensemble-mean velocity distributions, obtained with the cycle-resolved data reduction procedures, to the conventional ensemble-averaged velocity distribution. The velocities are normalized by the mean piston

[1] For simplicity, we will only give the symbol of the velocity, omitting that of its dependence on time.

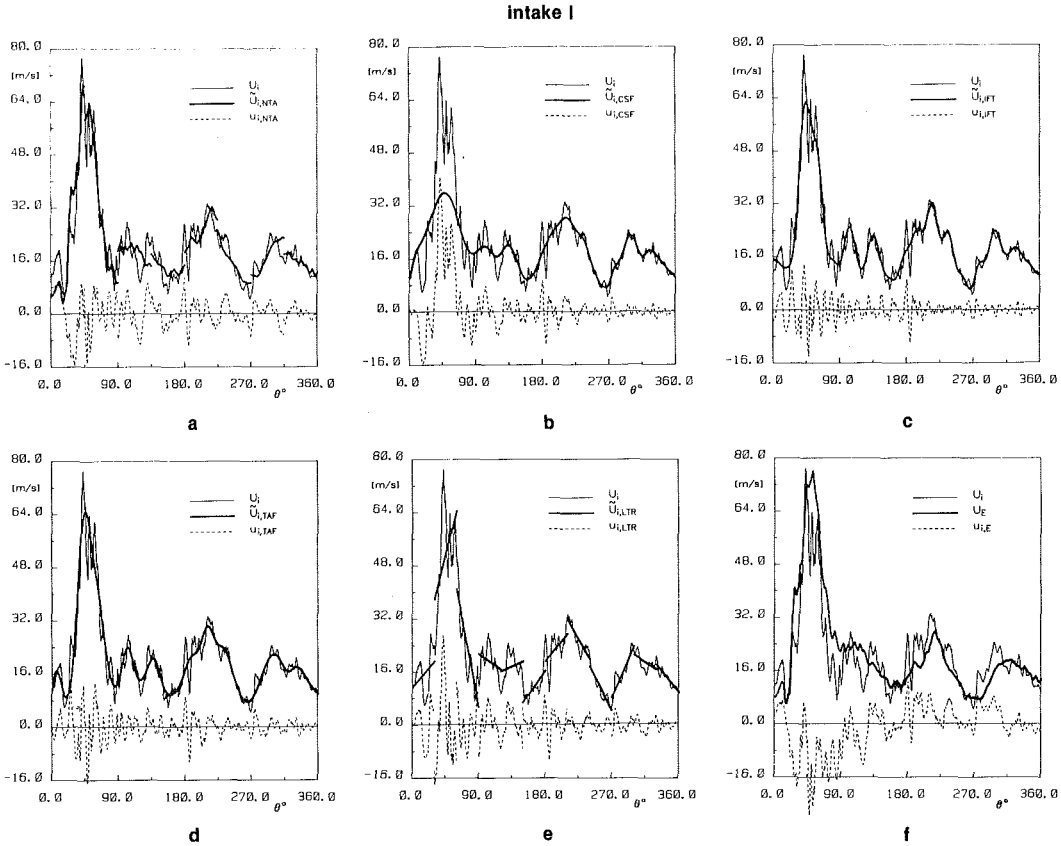

Fig. 3 Instantaneous velocity, mean velocity, and turbulent fluctuation in one cycle

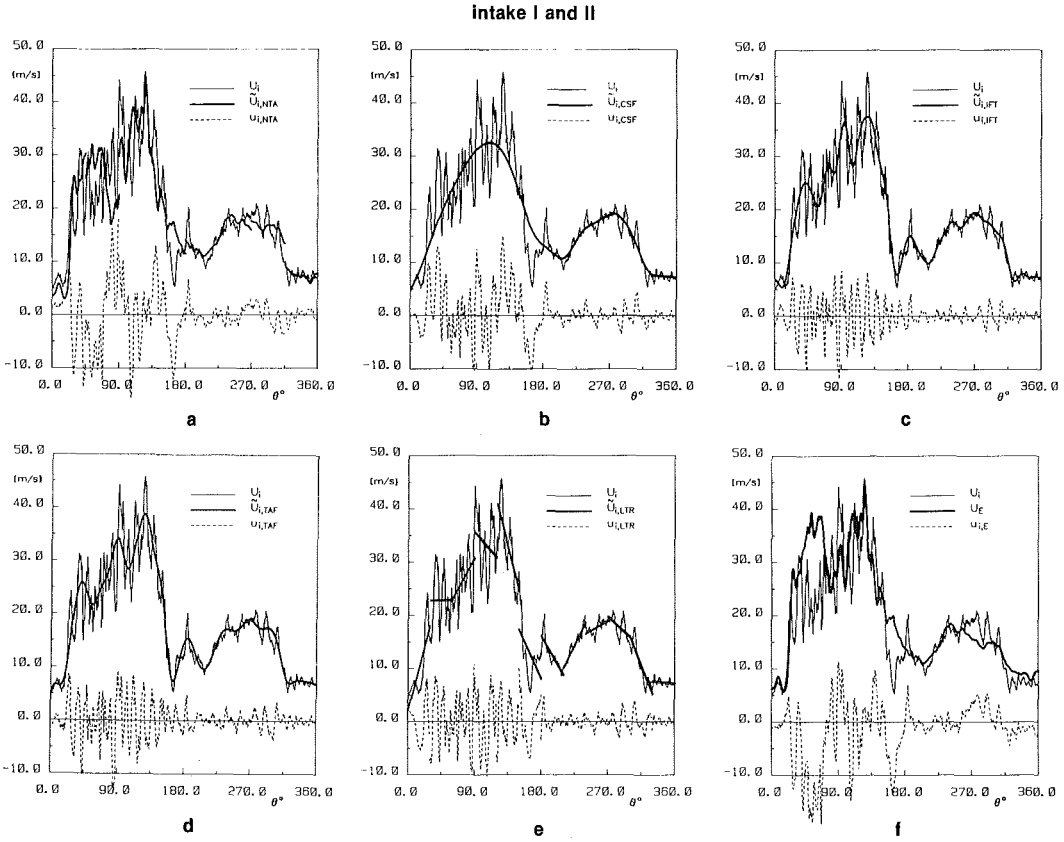

Fig. 4 Instantaneous velocity, mean velocity, and turbulent fluctuation in one cycle

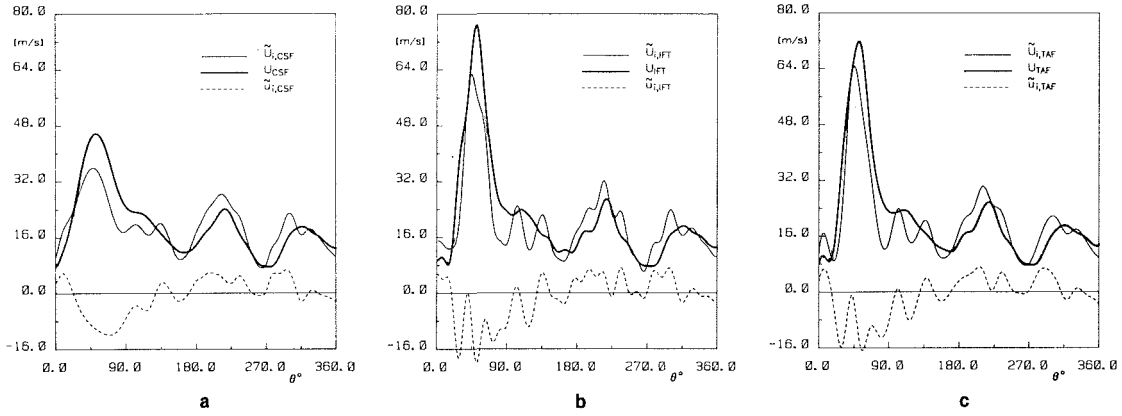

Fig. 5 In-cycle mean velocity, its ensemble and cyclic fluctuation

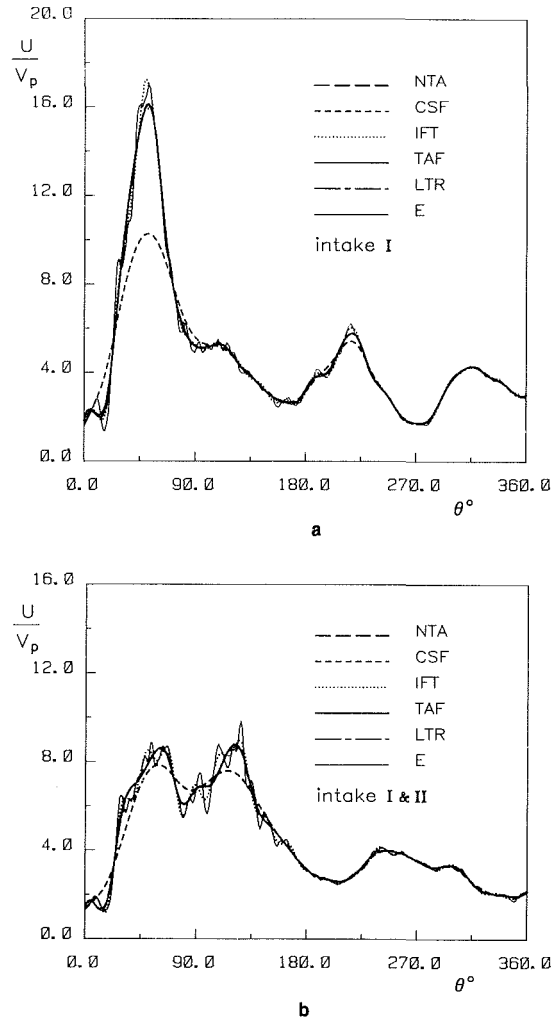

Fig. 6 Normalized ensemble-averaged mean velocity

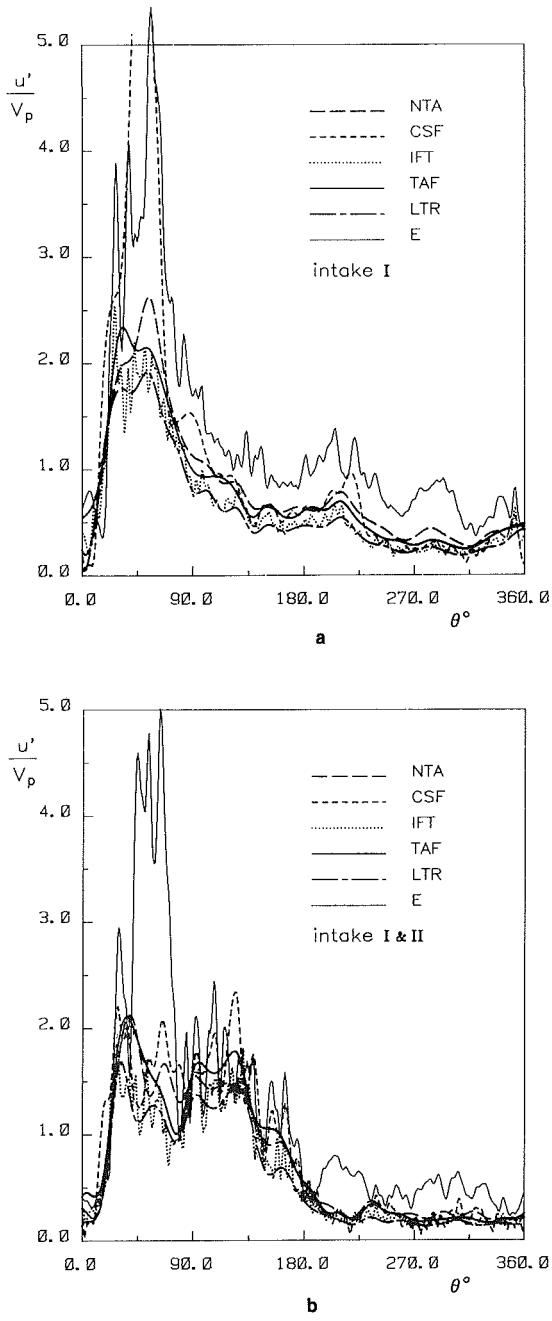

Fig. 7 Normalized turbulence intensity distributions

speed, which is $V_p = 4.45$ m/s at the angular speed of 1600 rpm. All the curves virtually coincide with that of U_E during the last part of the induction stroke and the whole of compression. However, during the early part of induction for intake I (Fig. 6*a*) and almost the whole of this stroke for intakes I and II (Fig. 6*b*), U_{CSF} deviates more or less considerably from the other distributions, which are quite a good approximation of U_E. Only U_{NTA} corresponds exactly to U_E. The oscillatory pattern of U_E showing a wide range of frequencies, with relatively high amplitudes, on induction in Fig. 6(*b*) may be

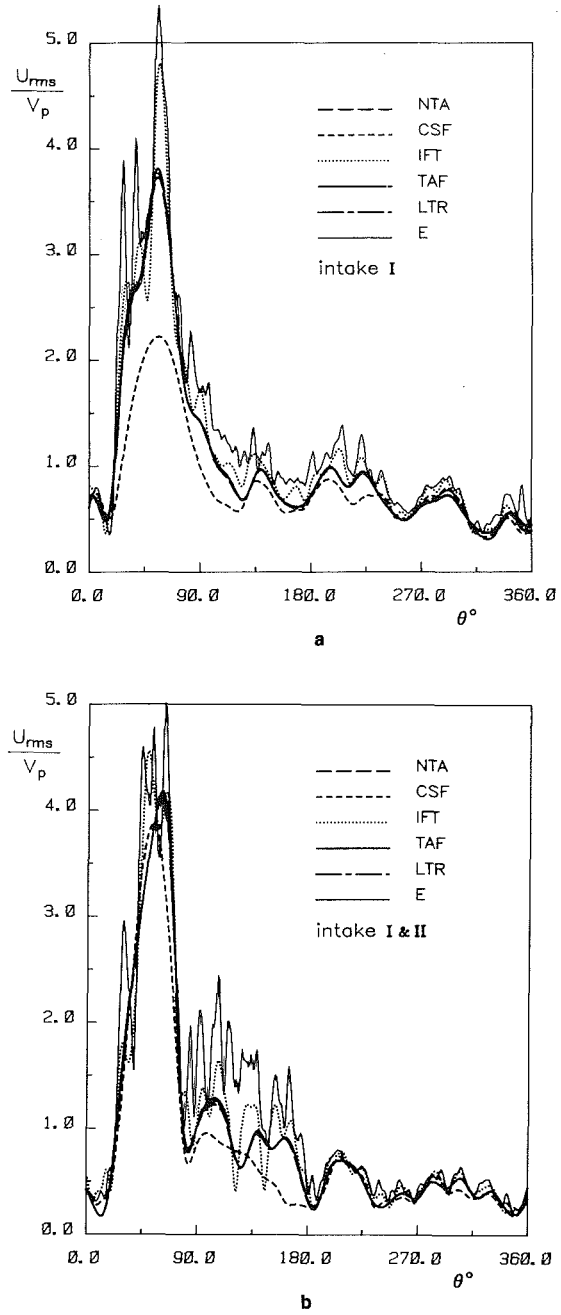

Fig. 8 Normalized rms fluctuation of the mean velocity

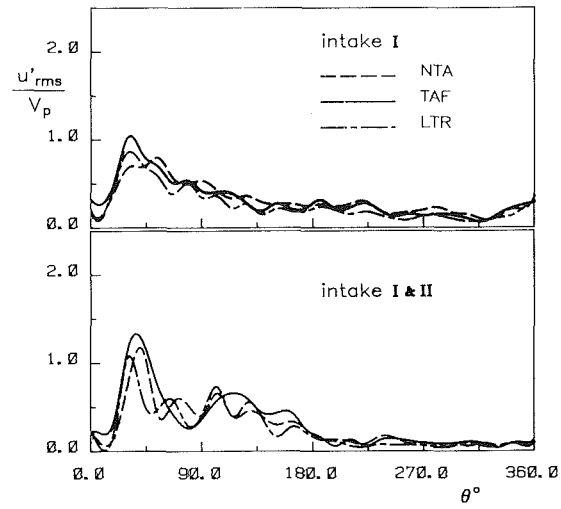

Fig. 9 Normalized rms fluctuation of the turbulence intensity

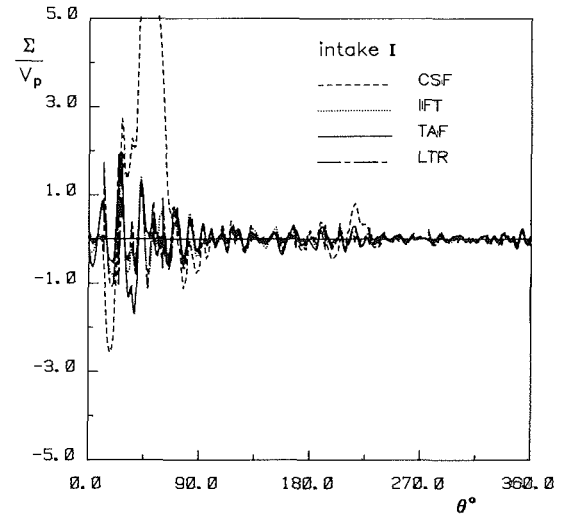

Fig. 10 Normalized ensemble average of the velocity turbulent fluctuation

partly due to the number of cycles considered, which, though not small, seems to be limited for a pure statistical analysis in that phase of the engine cycle where strong instabilities occur.

Figure 7 compares the ensemble-averaged turbulence intensities as derived from the cycle-resolved results and the rms velocity fluctuation u'_E, all normalized by the mean piston speed. At the early stage of induction in Fig. 7(*a*) u'_{CSF} has excessively high values, as expected, since it includes a significant component of the mean flow, and, to a lesser extent, the same occurs on induction in Fig. 7(*b*). u'_{IFT} and u'_{LTR} show the lowest values owing to the smaller filtering capability of the IFT and LTR procedures. During the last part of induction and at the early stage of compression u'_{CSF} is closer to u'_{TAF}, while during the last part of compression it is closer to u'_{IFT} and u'_{LTR}. u'_{NTA} exhibits higher values than u'_{TAF} on most of the induction and compression strokes. This can be explained as follows: The procedure of Lancaster includes in the in-cycle turbulence a spurious contribution due to the fact that the mean velocity pattern may be considerably different from cycle to cycle and therefore dissimilar to the ensemble-averaged velocity pattern. Anyway, apart from the highest values of u'_{CSF} on induction and at some stages of compression, it can be deduced from Fig. 7 that the distributions of the ensemble-averaged turbulence intensity given by all the cycle-resolved procedures considered have a similar trend.

Figure 8 shows the results obtained for the cyclic fluctuation of the mean flow. From comparison with Fig. 7 it is evident that the peak in u'_E on early induction is mainly due to cycle-to-cycle variations in the bulk motion; these may play a major role in the rms velocity fluctuation. An additional result that can be drawn from Figs. 7 and 8 is that the low-frequency cyclic fluctuations are less sensitive to the intake system configuration than the turbulence intensity.

Figure 9 reports the rms fluctuation of the turbulence intensity obtained in the time- and ensemble-averaging approach, showing a good agreement between the results of the different procedures. Cyclic variations in the turbulence intensity were evaluated by Liou and Santavicca (1985) as cyclic fluctuation of the "time-averaged" turbulence intensity over the whole part of the engine cycle considered (that is 64 deg across TDC of compression).

The requirement expressed by equation (11) or (12) is fulfilled by all the time- and ensemble-averaging methods. The approximation, within which the requirement $\Sigma(t) = 0$ is satis-

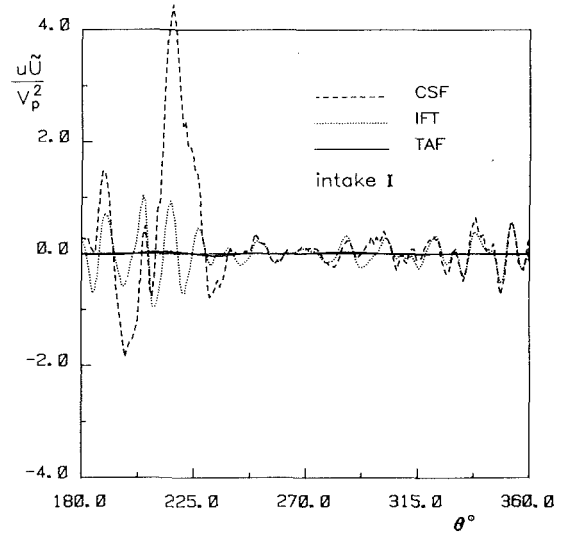

Fig. 11 Normalized cross-product between fluctuation and mean velocity

fied by those procedures based on ensemble-averaging, is evidenced, for example, in Fig. 10. Anomalous high positive values are assumed by Σ_{CSF} at the early stage of induction, showing the limits of the CSF procedure. During the last part of compression relatively small values of both Σ_{IFT} and Σ_{CSF} occur, fluctuating about zero. The same figure also reports, for comparison, the distribution of Σ_{TAF} and Σ_{LTR}. These are comparable to Σ_{IFT}, demonstrating that the turbulent velocity component in both definitions, of the authors and of Daneshyar and Fuller, fulfills requisites to be considered a stationary random function, as it is in the definition of Lancaster.

Figure 11 shows, for intake I, the degree of statistical dependence of the turbulent fluctuation on the mean velocity during the compression stroke. It plots the cross term $\langle u_i(t)\tilde{U}_i(t)\rangle$, evaluated with the CSF and IFT procedures, and the interpolated values of $\langle u_i\tilde{U}_i\rangle$ obtained with the authors' procedure, all normalized by the squared mean piston speed. In the NTA and LTR approaches it can be easily verified that $\langle u_i\tilde{U}_i\rangle = 0$ in each time-averaging interval. For simplicity, the notation of the figure will be used to indicate cross terms. $u\tilde{U}_{CSF}$ becomes considerably large, showing a strong correlation between mean velocity and turbulent fluctuation, in those parts of the cycle where the latter includes a significant component of the former; in the rest of the cycle it has a fluctuating pattern similar to that of $u\tilde{U}_{IFT}$. The normalized values of $u\tilde{U}_{TAF}$ are negligibly small. Similar results, but with more intense oscillations, were observed on induction. The same was found for intakes I and II. The cross terms $\langle u_i(t)\tilde{u}_i(t)\rangle$ and $\langle u_i\tilde{u}_i\rangle$ had very small values on compression.

Correlation and Spectral Analysis

Autocorrelation and Autospectra Estimation Procedures. As suggested by the authors (1985b), the Eulerian time autocorrelation coefficient in the period T (or crank angle Φ), starting at time t_0 (corresponding to the crank angle ϑ_0), can be defined by

$$\mathbf{R}(T, t_0, \tau) = \frac{1}{u'^2}\left\langle \frac{1}{T-\tau}\int_{t_0}^{t_0+T-\tau} u_i(t)u_i(t+\tau)dt \right\rangle \quad (24)$$

where the time variable τ in T ranges from 0 to $\tau_{max} = T/2$. For a collection of sample records $u_i(t)$ from a stationary random process the right-hand side of equation (24) is an unbiased and consistent estimate of the autocorrelation coefficient $R(\tau)$ independent of T and t_0 (Bendat and Piersol, 1986). For a nonstationary random process $R(T, t_0, \tau)$ should be averaged with respect to t_0 and T in order to be only a function of τ and, furthermore, on the analogy of stationary processes, an even function of τ will result by substituting $u_i(t-\tau/2)u_i(t+\tau/2)$ for the integrand in equation (24).

To obtain information about the structure of turbulence during the engine cycle, discrete intervals T should be considered, long enough to reduce the variance of the estimate, but, at the same time, short enough to have a negligible effect on the turbulence time-dependence. It was shown by the authors (1985b) that no significant differences were obtained with correlation intervals ranging from 15 to 60 crank-angle deg and so a 30-deg interval was taken as a good compromise.

In the ensemble-averaging procedures, both conventional (Witze, 1977) and unconventional (Liou and Santavicca, 1985), the autocorrelation coefficient is given by

$$R(t_0, \tau) = \frac{\langle u_i(t_0)u_i(t_0+\tau)\rangle}{u'(t_0)u'(t_0+\tau)} \quad (25)$$

which expresses a different type of time correlation with respect to equation (24).

The normalized energy spectral density function in T can be defined by

$$E(T, t_0, f) = 4\int_0^{\tau_{max}} R(T, t_0, \tau)w(\tau)\cos(2\pi f\tau)d\tau \quad (26)$$

where f is the frequency; $w(\tau)$ is a window function of rectangular or Hamming type. The approximation of an even function of τ was made for R; that is, a virtually stationary random function was anticipated for the turbulent fluctuation in T. A similar expression was used for $E(t_0, f)$ by Witze and by Liou and Santavicca, but with the autocorrelation coefficient given by equation (25). The micro time scale of turbulence is given by

$$\lambda_\tau(T, t_0) = 1/\sqrt{2\pi^2\int_0^{f_{max}} f^2E(T, t_0, f)df} \quad (27)$$

where f_{max} is the maximum frequency for which $E(T, t_0, f)$ is still finite and significant.

For completeness, it should be mentioned that another characteristic turbulence time scale can be evaluated on the analogy of the integral time scale defined in stationary turbulent flows (Hinze, 1975), by taking the integral of R over τ from 0 to τ_{max}, when R has positive values and decays over a sufficiently long period. However, if the autocorrelation function has a negative region and then decays over a characteristic period, the time delay τ over which the fluctuations about the mean velocity remain correlated is that at which R is a minimum (Tritton, 1977). Since this still seems to be a controversial point, no results about this time scale are presented.

Results. Figure 12 gives examples of the autocorrelation coefficient as a function of $\vartheta - \vartheta_0$ for the crank-angle correlation intervals indicated by Φ, starting from ϑ_0 (all crank angles are in deg unit). For comparison, R_{CSF} was also reported, since its patterns were, alternatively, closer to R_E (Figs. 12*a* and 12*e*), to R_{IFT} (Fig. 12*f*), or to R_{TAF} (Fig. 12*c*). In this latter case all the patterns, except R_E, were similar to each other, although R_{IFT} showed more pronounced fluctuations with respect to R_{TAF}, in general. From comparison of Figs. 12(*a*) and 12(*b*) it is evident that the influence of the correlation interval length on R_{TAF} can be relatively small. Figure 12(*b*) also shows a decaying pattern of R_{TAF} with rapidly damped oscillations. Drastic differences between R_{IFT} and R_{TAF} can be seen from Fig. 12 in some cases.

Figure 13 reports the normalized energy spectral density functions corresponding to the corrrelation coefficients of Fig. 12. Fluctuating and negative values are present in E_E,

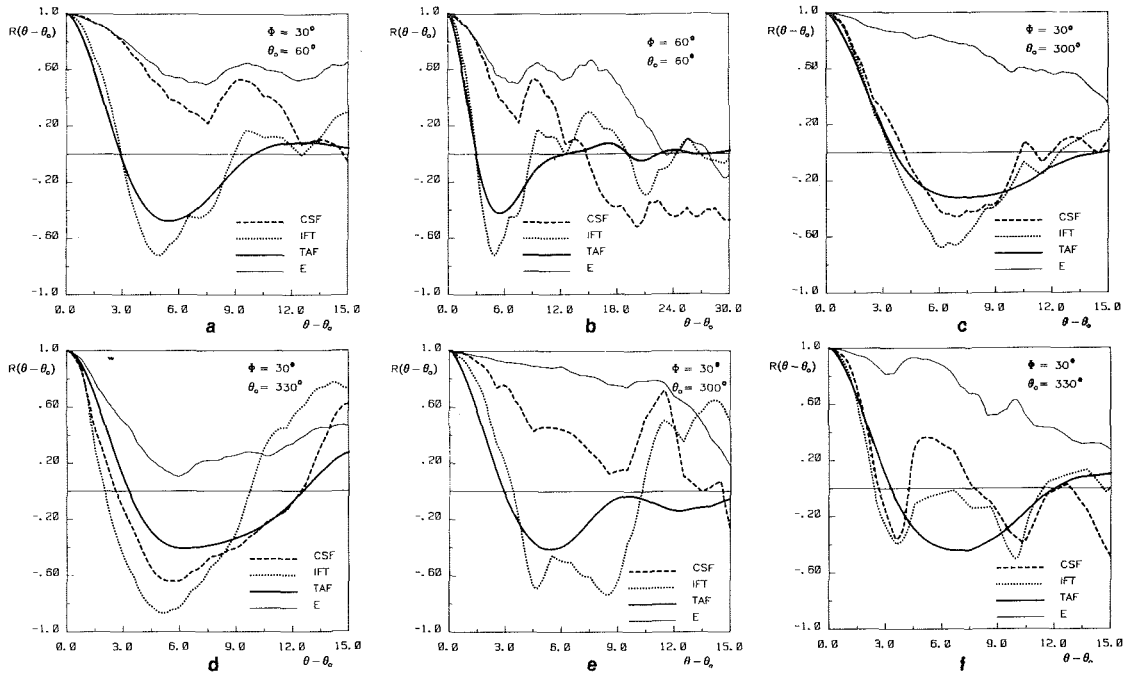

Fig. 12 Autocorrelation coefficients (*a*, *b*, *c*, *d*: intake I; *e*, *f*: intakes I and II)

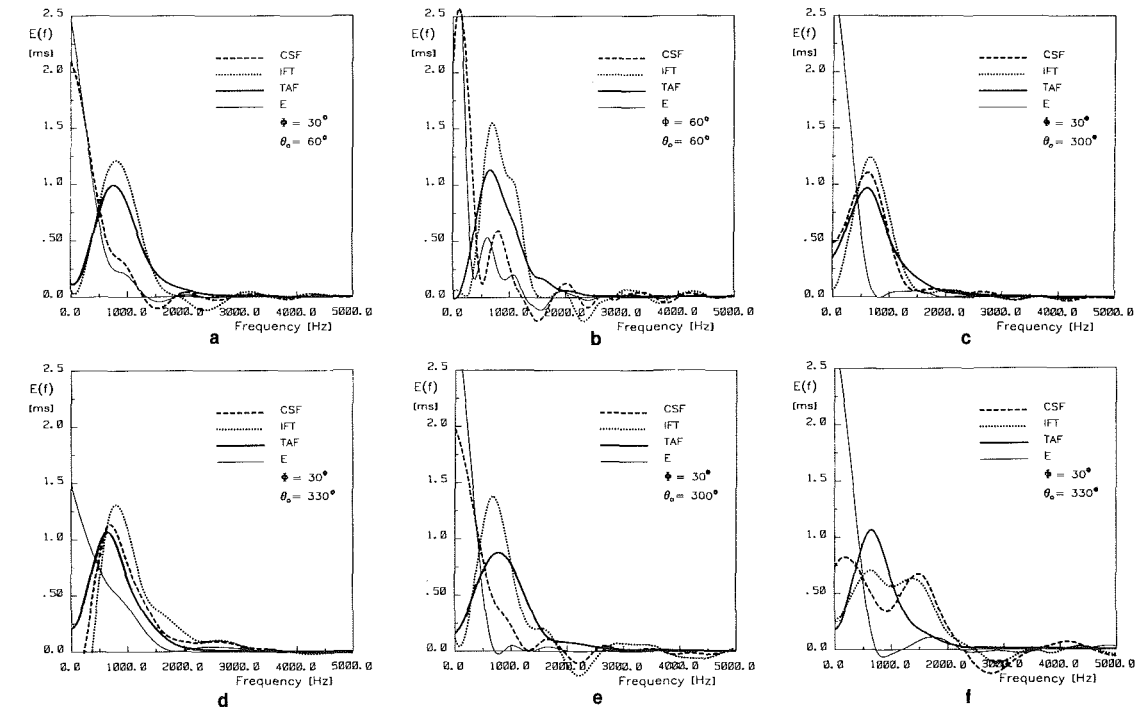

Fig. 13 Normalized energy spectral density functions (*a*, *b*, *c*, *d*: intake I; *e*, *f*: intakes I and II)

E_{CSF} and E_{IFT}, while always positive and more regular patterns are shown by E_{TAF}. In some cases E_{CSF} indicates the presence of a low-frequency component and a higher frequency peak like E_E, while E_{IFT} and E_{TAF} show generally similar frequency distributions. However, some situations can occur where the distributions of E_{IFT} and E_{CSF} show the presence of two distinct components in the frequency spectrum, while in E_{TAF} the higher frequency component is in the tail of the spectrum (Fig. 13*f*). This has to be ascribed to the different type of time correlation involved by ensemble averaging with respect to time averaging in the autocorrelation estimate (Fig. 12*f*). In fact, a result in agreement with E_{IFT} and E_{CSF} was obtained by using the turbulent fluctuation $u_{i,TAF}$ in equation (25) and using this latter in equation (26).

Figure 14 plots, for intake I, the distributions of the micro time scale of turbulence, versus crank angle, during the cycle, for the two correlation intervals indicated. $\lambda_{\tau TAF}$ is almost uniform on induction and compression indicating that the small-scale turbulence structure before combustion was practically the same as on induction. $\lambda_{\tau TAF}$ was shown to be vir-

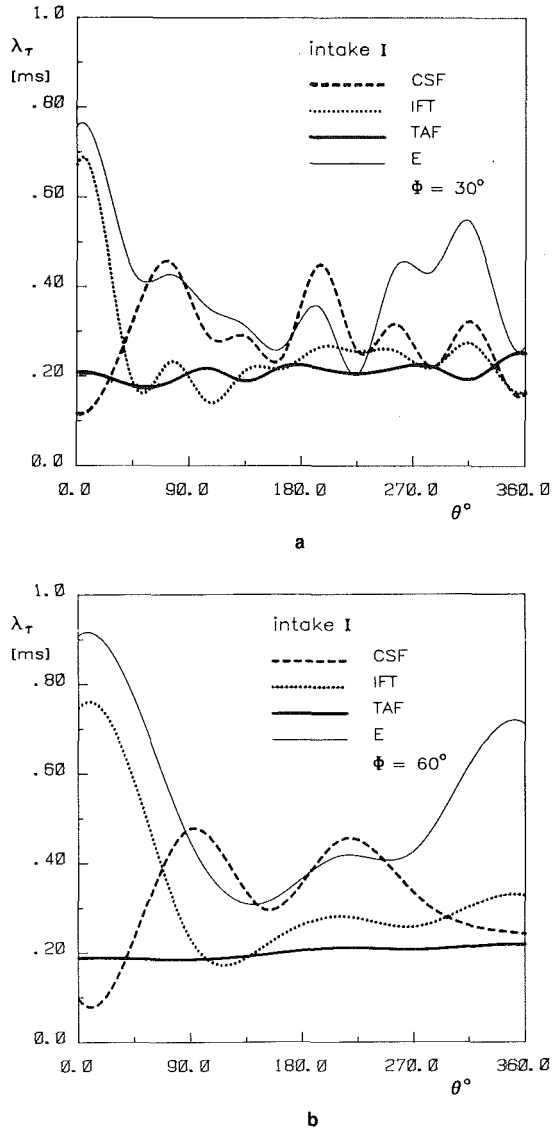

Fig. 14 Distributions of the micro time scale of turbulence

tually independent of Φ. On the other hand, the patterns of $\lambda_{\tau IFT}$, $\lambda_{\tau CSF}$, and $\lambda_{\tau E}$ show a respectively increasing deviation from that of $\lambda_{\tau TAF}$ (Fig. 14*a*) and an increasing dependence on the correlation period (Fig. 14*b*).

Concluding Remarks

Turbulent velocity data, acquired in the cylinder of a direct-injection automotive diesel engine, using an advanced HWA technique, were analyzed with five different cycle-resolved data reduction procedures, and the conventional statistical ensemble average, as a preliminary endeavor toward a general study of non-Reynolds averaging operators for engine flow application. Even though these require the definition of a characteristic integration time or cutoff frequency or other parameters to obtain a specific degree of filtering, while ensemble averaging is univocal, they have the advantage of giving information about the flow in a particular engine cycle.

In the two main approaches, ensemble-averaging and time-ensemble-averaging, the turbulent fluctuating component about the in-cycle mean velocity should have a zero mean value, either as ensemble-averaged value over many cycles or as time-averaged value in each cycle. The first requirement was practically satisfied by the IFT procedure, where an inexplicably low cutoff frequency may be required. A significant bulk velocity component may be included in the turbulent fluctuation obtained with the CSF procedure, in those narrow crank-angle intervals where high turbulent velocity peaks occur. Both requirements are fulfilled by the NTA and, virtually, also by the TAF and LTR procedures. However, the NTA and LTR procedures lead to in-cycle mean velocity and fluctuating velocity curves with discontinuities at the boundaries of the consecutive crank-angle intervals considered throughout the cycle; furthermore, no indication was given about the way to select these intervals, as well as for spectral analysis of cycle-resolved turbulence. All the procedures, when fitted for the same data reduction, so as to be comparable, give consistent results for turbulence intensity and cyclic fluctuations in the mean flow.

The authors' procedure was shown to be suitable for correlation and spectral analysis of cycle-resolved turbulence on the analogy of stationary turbulent flows, since the turbulent velocity component could be treated as a stationary random function in characteristic time intervals, over which the autocorrelation coefficient decays.

Caution should be taken in discriminating between high-frequency turbulence fluctuations and low-frequency mean-flow cyclic fluctuations from nonstationary velocity autocorrelation functions, owing to the possible presence of a low-frequency component in the filtered-velocity nonstationary autocorrelation function when the ensemble-averaging approach is used.

Acknowledgments

Financial support for this work was provided by M.P.I. (Ministero Pubblica Istruzione) under 40 percent funding and partially by C.N.R.-P.S.T. (Consiglio Nazionale delle Ricerche—Progetto Strategico Termomeccanica).

References

Arcoumanis, C., Hadjiapostolou, A., and Whitelaw, J. H., 1987, "Swirl Center Precession in Engine Flows," SAE Paper No. 870370.

Ball, W. F., Pettifer, H. F., and Waterhouse, C. N. F., 1983, "Laser Doppler Velocimeter Measurements of Turbulence in a Direct-Injection Diesel Combustion Chamber," IMechE, Paper No. C52/83.

Balles, E. N., and Heywood, J. B., 1988, "Fuel-Air Mixing and Diesel Combustion in a Rapid Compression Machine," SAE Paper No. 880206.

Belaire, R. C., Davis, G. C., Kent, J. C., and Tabaczynski, R. J., 1983, "Combustion Chamber Effects on Burn Rates in a High Swirl Spark Ignition Engine," *Trans. SAE*, Paper No. 830335.

Bendat, J. S., and Piersol, A. G., 1986, *Random Data: Analysis and Measurement Procedures*, 2nd ed., Wiley, New York.

Bopp, S., Vafidis, C., and Whitelaw, J. H., 1986, "The Effect of Engine Speed on the TDC Flowfield in a Motored Reciprocating Engine," SAE Paper No. 860023.

Brandl, F., Reverencic, I., Cartellieri, W., and Dent, J. C., 1979, "Turbulent Air Flow in the Combustion Bowl of a D.I. Diesel Engine and Its Effect on Engine Performance," *Trans. SAE*, Paper No. 790040.

Catania, A. E., 1980, "Air Flow Investigation in the Open Combustion Chamber of a High-Speed, Four-Stroke Diesel Engine," ASME, Paper No. 80-FE-5.

Catania, A. E., 1982, "3-D Swirling Flows in an Open-Chamber Automotive Diesel Engine With Different Induction Systems," in: *Flows in I.C. Engines*, T. Uzkan, ed., ASME, New York.

Catania, A. E., 1985, "Induction System Effects on the Fluid-Dynamics of a D.I. Automotive Diesel Engine," ASME, Paper No. 85-DGP-11.

Catania, A. E., and Mittica, A., 1985a, "A Contribution to the Definition and Measurement of Turbulence in a Reciprocating I.C. Engine," ASME, Paper No. 85-DGP-12.

Catania, A. E., and Mittica, A., 1985b, "Cycle-by-Cycle, Correlation and Spectral Analysis of I.C. Engine Turbulence," in: *Flows in Internal Combustion Engines—III*, FED-Vol. 28, T. Uzkan, W. G. Tiederman, and J. M. Novak, eds., ASME, New York.

Catania, A. E., and Mittica, A., 1987, "Induction System Effects on Small-Scale Turbulence in a High-Speed Diesel Engine," ASME JOURNAL OF ENGINEERING FOR GAS TURBINES AND POWER, Vol. 109, pp. 491–502.

Chau, E. L., Iiyama, A., Schipperijn, F. W., Nagasaka, R., and Sawyer, R. F., 1988, "Effect of Intake Valve Configuration on Lean Combustion," SAE Paper No. 880202.

Coghe, A., Gamma, F., Mauri, M., Brunello, G., Calderini, F., and Ferri

Degli Antoni, L., 1985, "In-Cylinder Air Motion Measurements by Laser Velocimetry Under Steady-State Flow Conditons," SAE Paper No. 850123.

Cole, J. B., and Sword, M. D., 1980, "An Investigation of the Ignition Process in a Lean-Burning Engine Using Conditionally Sampled Laser-Doppler Anemometry," *Trans. SAE*, Paper No. 800043.

Daneshyar, H., and Fuller, D. E., 1986, "Definition and Measurement of Turbulence Parameters in Reciprocating I.C. Engines," SAE Paper No. 861529.

Davis, G. C., Tabaczynski, R. J., and Belaire, R. C., 1984, "The Effect of Intake Valve Lift on Turbulence Intensity and Burnrate in S.I. Engines—Model Versus Experiment," *Trans. SAE*, Paper No. 840030.

Dent, J. C., and Salama, N. S., 1975, "The Measurement of Turbulence Characteristics in an Internal Combustion Engine Cylinder," SAE Paper No. 750886.

Dinsdale, S., Roughton, A., and Collings, N., 1988, "Length Scale and Turbulence Intensity Measurements in a Motored Internal Combustion Engine," SAE Paper No. 880380.

Evans, R. L., and Dohring, K. W., 1987, "A Rapid Intake and Compression Machine for Fundamental Combustion Research," ASME, Paper No. 87-FE-9.

Fansler, T. D., and French, D. T., 1988, "Cycle-Resolved Laser-Velocimetry Measurements in a Reentrant Bowl-in-Piston Engine," SAE Paper No. 880377.

Fraser, R. A., and Bracco, F. V., 1988, "Cycle-Resolved LDV Integral Length Scale Measurements in an I.C. Engine," SAE Paper No. 880381.

Glover, A. R., Hundleby, G. E., and Hadded, O., 1988, "An Investigation Into Turbulence in Engines Using Scanning LDA," SAE Paper No. 880378.

Hall, M. J., and Bracco, F. V., 1987, "A Study of Velocities and Turbulence Intensities Measured in Firing and Motored Engines," SAE Paper No. 870453.

Hashimoto, T., Okada, K., and Oikawa, T., 1986, "ISUZU New 9.8L Diesel Engine With Variable Geometry Turbocharger," SAE Paper No. 860460.

Hinze, J. O., 1975, *Turbulence*, McGraw-Hill, New York.

Huebner, K. H., and McDonald, A. T., 1970, "A Dynamic Model and Measurement Technique for Studying Induction Air Swirl in an Engine Cylinder," ASME JOURNAL OF ENGINEERING FOR POWER, Vol. 92, pp. 189–197.

Ikegami, M., Shioji, M., and Nishimoto, K., 1987, "Turbulence Intensity and Spatial Integral Scale During Compression and Expansion Strokes in a Four-Cycle Reciprocating Engine," SAE Paper No. 870372.

Inoue, T., Nakanishi, K., Noguchi, H., and Iguchi, S., 1980, "The Role of Swirl and Squish in Combustion of the S.I. Engine," *FISITA 80*, Paper No. 80.4.4.4.

Kampé de Férie, J., 1957, "La Motion de Moyenne dans La Théorie de la Turbulence," *Rend. Sem. Mat.e Fis.*, No. 27, Milano.

Kato, S., and Onishi, S., 1987, "New Mixture Formation Technology of Direct Fuel Injection Stratified Combustion," SAE Paper No. 871689.

Khalighi, B., El Tahry, S. H., and Kuziak, W. R., Jr. 1986, "Measured Steady Flow Velocity Distributions Around a Valve/Seat Annulus," SAE Paper No. 860462.

Lancaster, D. R., 1976, "Effects of Engine Variables on Turbulence in a Spark-Ignition Engine," *Trans. SAE*, Paper No. 760159.

Lancaster, D. R., Krieger, R. B., Sorenson, S. C., and Hull, W. L., 1976, "Effects of Turbulence on Spark-Ignition Engine Combustion," *Trans. SAE*, Paper No. 760160.

Liou, T.-M., Santavicca, D. A., and Bracco, F. V., 1984, "Laser Doppler Velocimetry Measurements in Valved and Ported Engines," *Trans. SAE*, Paper No. 840375.

Liou, T.-M., and Santavicca, D. A., 1985, "Cycle Resolved LDV Measurements in a Motored IC Engine," ASME *Journal of Fluids Engineering*, Vol. 107, pp. 232–240.

Martin, J. K., Witze, P. O., and Borgnakke, C., 1984, "Multiparameter Conditionally Sampled Laser Velocimetry Measurements During Flame Propagation in a Spark Ignition Engine," *Twentieth International Symposium on Combustion*, Sandia Report No. SAND84-8224.

Martin, J. K., Witze, P. O., and Borgnakke, C., 1985, "Combustion Effects on the Preflame Flow Field in a Research Engine," *Trans. SAE*, Paper No. 850122.

Matekunas, F. A., 1983, "Modes and Measures of Cyclic Combustion Variability," General Motors Internal Report, GMR-4239, SAE Paper No. 830337.

Matsushita, S., Inoue, T., Nakanishi, K., Okumura, T., and Isogai, K., 1985, "Effects of Helical Port With Swirl Control Valve on the Combustion and Performance of S.I. Engine," SAE Paper No. 850046.

Monaghan, M. L., and Pettifer, H. F., 1981, "Air Motion and Its Effect on Diesel Performance and Emissions," *Trans. SAE*, Paper No. 810255.

Monin, A. S., and Yaglom, A. M., 1971, *Statistical Fluid Mechanics*, MIT Press, Cambridge, MA.

Nagayama, I., Araki, Y., and Iioka, Y., 1977, "Effects of Swirl and Squish on S.I. Engine Combustion and Emissions," *Trans. SAE*, Paper No. 770217.

Ohigashi, S., Hamamoto, Y., and Tanabe, S., 1971, "Swirl—Its Measurement and Effect on Combustion in a Diesel Engine, *IMechE J.*, Vol. 134.

Patterson, D. J., 1966, "Cylinder Pressure Variations, a Fundamental Combustion Problem," *Trans. SAE*, Paper No. 660129.

Rabiner, L. R., Schafer, R. W., and Dlugos, D., 1979, "Correlation Method for Power Spectrum Estimation," *IEEE Programs for Digital Signal Processing*.

Rader, C. M., 1970, "An Improved Algorithm for High Speed Autocorrelation With Applications to Spectral Estimation," *IEEE Trans., Audio Electroacoustic*, Vol. AU-18, No. 4, pp. 439–441.

Rask, R. B., 1979, "Laser Doppler Anemometer Measurements in an Internal Combustion Engine," *Trans. SAE*, Paper No. 790094.

Rask, R. B., 1981, "Comparison of Window, Smoothed-Ensemble, and Cycle-by-Cycle Data Reduction Techniques for Laser Doppler Anemometer Measurements of In-Cylinder Velocity," in: *Fluid Mechanics of Combustion Systems*, T. Morel, R. P. Lohmann, and J. M. Rackley, eds., ASME, New York.

Rask, R. B., 1984, "Laser Doppler Anemometer Measurements of Mean Velocity and Turbulence in Internal Combustion Engines," General Motors Internal Report, GMR-4839.

Reinsch, C. H., 1967, "Smoothing by Spline Functions," *Numerische Mathematik*, Vol. 10. pp. 177–183; see also: Subroutine ICSSCU, International Mathematical and Statistical Libraries, 1976, IMSL Subroutine Package.

Reynolds, W. C., 1980, "Modeling of Fluid Motions in Engines—An Introductory Overview," *Combustion Modeling in Reciprocating Engines*, J. N. Mattavi and C. A. Amann, eds., Plenum Press, New York.

Saxena, V., and Rask, R. B., 1987, "Influence of Inlet Flows on the Flow Field in an Engine," SAE Paper No. 870369.

Semenov, E. S., 1958, "Studies of Turbulent Gas Flow in Piston Engines," *Otedelinie Technicheskikh Nauk*, No. 8 (NASA Technical Translation F97).

Shimoda, M., Shigemori, M., and Tsuruoka, S., 1985, "Effect of Combustion Chamber Configuration on In-Cylinder Air Motion and Combustion Characteristics of D.I. Diesel Engine," *Trans. SAE*, Paper No. 850070.

Swords, M. D., Kalghatgi, G. T., and Watts, A. J., 1982, "An Experimental Study of Ignition and Flame Development in a Spark Ignited Engine," *Trans. SAE*, Paper No. 821220.

Tindal, M. J., Williams, T. J., and Aldoory, M., 1982, "The Effect of Inlet Port Design on Cylinder Gas Motion in Direct Injection Diesel Engines," in: *Flows in I.C. Engines*, T. Uzkan, ed., ASME, New York.

Tritton, D. J., 1977, *Physical Fluid Dynamics*, Van Nostrand Reinhold.

Wakisaka, T., Hamamoto, Y., and Shimamoto, Y., 1982, "Turbulence Structure of Air Swirl in Reciprocating Engine Cylinders," in: *Flows in I.C. Engines*, T. Uzkan, ed., ASME, New York.

Witze, P. O., 1977, "Measurements of the Spatial Distribution and Engine Speed Dependence of Turbulent Air Motion in an I.C. Engine," *Trans. SAE*, Paper No. 770220.

Witze, P. O., 1980, "A Critical Comparison of Hot-Wire Anemometry and Laser Doppler Velocimetry for I.C. Engine Applications," *Trans. SAE*, Paper No. 800132.

Witze, P. O., Martin, J. K., and Borgnakke, C., 1984, "Conditionally-Sampled Velocity and Turbulence Measurements in a Spark Ignition Engine," *Combustion Science and Technology*, Vol. 36, pp. 301–317.

Witze, P. O., and Mendes-Lopes, J. M. C., 1986, "Direct Measurement of the Turbulent Burning Velocity in a Homogeneous-Charge Engine," *SAE*, Paper No. 861531.

Witze, P. O., Hall, M. J., and Bennett, M. J., 1988, "Are Gas Velocities in a Motored Piston Engine Representative of the Pre-Ignition Fluid Motion in a Fired Engine?" Sandia Report No. SAND88-8878.

Investigation of the Effect of Inlet Port on the Flow in a Combustion Chamber Using Multidimensional Modeling

R. Taghavi
Research Scientist.
Mem. ASME

A. Dupont
Research Scientist.

Direction des Etudes,
Regie Nationale des Usines Renault,
92508 Rueil Malmaison Cedex, France

The computational fluid dynamics simulation program KIVA is augmented with a k–ϵ turbulence model and enhanced geometric capabilities. It is applied to the case of flow in an inlet port and a combustion chamber with a moving valve in order to investigate the effect of inlet flow on the prevailing aerodynamic conditions in the cylinder. The needed initial and time-varying boundary conditions at the upstream section of the intake port are obtained from a one-dimensional acoustic model of the complete single cylinder engine. The three-dimensional flow domain includes an intake port, a combustion chamber, and a moving valve. An internal dynamic rezoning procedure is presented and incorporated in the flow code, which ensures an adequate I, J, K-structured hexahedral mesh when the boundaries of the computation domain are severely distorted, as is the case with a moving valve. Flow computation is carried out from induction TDC to BDC. The resulting velocity and residual burned gas mass fraction fields are then examined and effects due to the geometry of the port and chamber are discussed.

Introduction

The purpose of this study is to show, using a complex engine flow problem as an example, the possibilities and limitations of a present-day computational fluid dynamics code as an engine design tool. The particular example of flow in a port and chamber under motoring conditions is chosen because of its significance in the determination of prevailing aerodynamic conditions at ignition.

It is well known that the intake process and the resulting flow phenomena inside the combustion chamber of an internal combustion engine can have a significant influence on the combustion process and consequently on the pollutant emission and performance of spark ignition and diesel engines.

In direct-injecton diesel engines, large-scale turbulent structures enhance fuel-to-air mixing, thereby reducing ignition delay [1]. In spark ignition engines, these structures reduce cycle-to-cycle variation [2] and lower the misfire fuel-to-air ratio lower limit, thus allowing lean burn and high exhaust gas recirculation ratios and reducing HC production in lean burn mixtures [3].

There are few published examples of simultaneous flow computation in inlet ports and combustion chambers. Works by Menne et al. [4] and Errera [5] are those known to the present authors. On the other hand, steady flow computations of inlet ports have drawn more interest and have been reported by several investigators. The resulting velocity distributions in the valve passage have been compared with experiments [6, 7] and satisfactory agreement has been obtained.

Advantages of Simultaneous Modeling in Port and Combustion Chamber

Multidimensional flow simulations in complex combustion chambers under motoring conditions have been carried out to a much larger extent [8–10].

A major subject of investigation has been the computation of flow inside combustion chambers using experimentally determined boundary conditions at the valve. Studies have been carried out in order to investigate the effect of swirl [11, 12], inlet ports in general [13, 14] and multivalve intakes on [15, 16] the development of in-cylinder flow.

The rationale for discoupling port and chamber flows is twofold:

- the presumed weak downstream effect on flow at the valve, if velocities are high and the valve is far from the cylinder wall;
- the inability to predict accurate velocity profiles, viewed in planes containing the valve axis, at the valve outlet passage.

The latter inaccuracy is due, in part, to the shortcomings of turbulence models in predicting flow separation at higher valve lifts [17]. While the valve annular jet angle may be erroneous, satisfactory bulk swirls or horizontal plane velocity profiles have been obtained in the case of helical ports [6, 7].

In production internal combustion engines, valves are usually located very close to the cylinder wall. This is even

Contributed by the Internal Combustion Engine Division and presented at the Twelfth Annual Energy-Sources Technology Conference and Exhibition, Houston, Texas, January 22–25, 1989. Manuscript received by the Internal Combustion Engine Division August 1988.

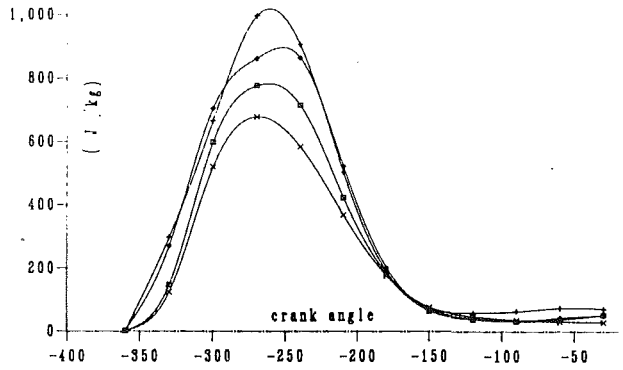

Fig. 1 Evolution of average TKE in four versions of the present combustion chamber computed with an SGS turbulence model (from [10])

more true in multivalve engines where, even in the case of a pentroof combustion chamber, little room is available for the valves. Furthermore, one-dimensional gas dynamics engine models indicate that, in the valve passage area, flow velocity varies greatly with time and that even backflow can occur during the initial as well as the later stages of intake.

It becomes clear then that for such real-world engine situations, the conditions for the transposition of steady-state results to transient flow are not met in practice. By applying multidimensional modeling to flow within an inlet port and a combustion chamber separated by a moving valve, we wish to circumvent the above problems and identify new problem areas that are not addressed when simple engine geometries or experimentally obtained valve velocity profiles are used.

Computer Code

The KIVA computer program, developed at the Los Alamos National Laboratory [18, 19], is used to perform the computations. This code solves the equations of transient multicomponent chemically reactive fluid dynamics together with those for the dynamics of an evaporating liquid spray, and was developed specifically for applications in internal combustion engines. It is a time-marching finite-difference program that uses an acoustic subcycling method in order to overcome time-step size limitation due to the CFL criterion.

In its initial version this code had, among others, the following features:

- the capability of taking into account a piston bowl;
- a subgrid scale turbulence model based on grid size and a transport equation for the turbulent kinetic energy (hereafter referred to as TKE);
- an internal mesh generator for simple engine geometries.

First, the capability of handling recesses both in the cylinder head and piston was added to KIVA in order to make the code more suitable for a wide range of engine applications. This addition made it possible to model pentroof combustion chambers, indirect-injection diesel engine chambers and prechambers, and helical inlet ports [7].

Later, the following features were added by the present authors [20] in order to accommodate a wider range of engine flow situations:

- prescribed inlet and outlet boundary conditions;
- annular inlet and exhaust valves;
- inlet and exhaust ports and moving valves;
- $k-\epsilon$ turbulence model;
- interface with industrial mesh generators;
- post-processing, including arbitrary cut-through surfaces and animations of flow visualization.

Shortcomings of the SGS Turbulence Model

Computations of average TKE carried out by Dupont [10] in four variants of the production spark ignition engine used in this work indicate that the initial turbulence model of KIVA does not correctly account for the evolution and level of TKE, with most of the inaccuracies occurring during the compression stroke (Fig. 1). TKE dies off too fast and no contribution of compression to the creation of TKE is observed. This is in contradiction to trends observed by Hall and Bracco [21] for a pancake-shaped combustion chamber, for which a much slower decrease in TKE is reported.

Furthermore, the analysis of Morel and Mansour [22] suggests that at least a k–ϵ turbulence model, containing appropriate compression-induced turbulence generation terms, is needed in order to describe TKE evolution correctly in an internal combustion engine.

In addition, computations of wall heat flux in a pentroof-shaped combustion chamber carried out by Argueyrolles et al. [7], using KIVA's original subgrid scale turbulence model, unveiled a second shorting. A corrective factor of 8 had to be applied to the local heat fluxes so that the globally computed heat loss could be made consistent with that obtained using a thermodynamic analysis of the recorded pressure trace.

These inconsistencies led us to replace KIVA's initial turbulence model by a k–ϵ turbulence model based on that proposed by El Tahry [23]. This turbulence model was shown by Ahmadi-Befrui [24] to be suitable for engine applications.

The transport equation for the turbulent kinetic energy k is

$$\frac{\partial}{\partial t}(\rho k)+\frac{\partial}{\partial x_j}(\rho\, U_j\, k)=$$

$$\frac{\partial}{\partial x_j}\left(\frac{\mu_T}{\sigma_k}\frac{\partial}{\partial x_j}k\right)+\mu_T\left(\frac{\partial}{\partial x_j}U_i+\frac{\partial}{\partial x_i}U_j\right)\frac{\partial}{\partial x_i}U_j$$

$$-2/3\,(\mu_T\frac{\partial}{\partial x_l}U_l+\rho\, k)\frac{\partial}{\partial x_l}U_l-\rho\epsilon \tag{1}$$

where ρ is the density, U_l is the l-direction component of mean velocity, σ_k is the turbulent Prandtl number for the transport of TKE, μ_T is the turbulent dynamic viscosity, and ϵ is the TKE rate of dissipation

The transport equation for the rate of TKE dissipation ϵ is

$$\frac{\partial}{\partial t}(\rho\epsilon)+\frac{\partial}{\partial x_j}(\rho\, U_j\,\epsilon)=\frac{\partial}{\partial x_j}\left(\frac{\mu}{\sigma_\epsilon}\frac{\partial\epsilon}{\partial x_j}\right)$$

$$+\frac{\epsilon}{k}\left(c_{\epsilon 1}\,\mu_T\left(\frac{\partial}{\partial x_j}U_i+\frac{\partial}{\partial x_i}U_j\right)\frac{\partial}{\partial x_j}U_i\right.$$

$$\left.-2/3\,\frac{\partial}{\partial x_l}U_l\,(c'_{\epsilon 1}\,\mu_T\frac{\partial}{\partial x_l}U_l+c''_{\epsilon 1}\,\rho\, k)\right)$$

$$+c_{\epsilon 3}\rho\epsilon\frac{\partial}{\partial x_l}U_l+c_{\epsilon 4}\,\frac{\rho\epsilon}{\mu}\,\frac{\partial\mu}{\partial t}-c_{\epsilon 2}\,\frac{\rho\epsilon^2}{k} \tag{2}$$

where σ_ϵ is the turbulent Prandtl number for the transport of dissipation rate and the coefficients $c_{\epsilon 1}$, $c'_{\epsilon 1}$, $c''_{\epsilon 1}$, $c_{\epsilon 2}$, $c_{\epsilon 3}$, and $c_{\epsilon 4}$ are obtained on the basis of experimental results and analytical considerations.

The wall boundary condition is based on the wall function method, which is a representation of the region near the wall by a quasi-steady and one-dimensional couette flow [25].

In this approach the usual three-layer model of turbulent boundary layer is replaced by a two-layer formulation, with a cutoff nondimensional distance from the wall of $y^+ = 11.63$, where the distance to the wall has been nondimensionalized using the kinematic viscosity and friction velocity at the wall.

In the wall layer constant shear stress and heat flux are assumed. This leads to the following expressions for the nondimensional velocity and temperature:

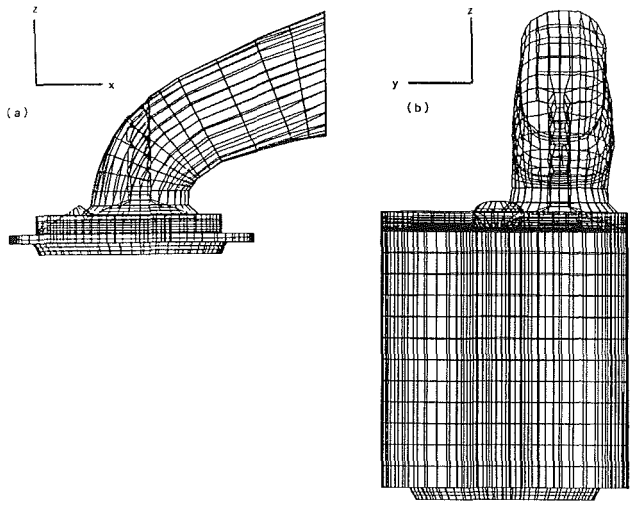

Fig. 2 Port/cylinder assembly showing the minimum (*a*) and maximum (*b*) valve lift

$$U^+ = y^+ \quad \text{for } y^+ \leq 11.63 \tag{3}$$

$$T^+ = \sigma_h U^+ \tag{4}$$

In the inertial sublayer a mixing length turbulent viscosity based on the distance from the wall is assumed. For the wall heat flux an expression from Jayatillaka [26] is used. The following expressions result:

$$U^+ = \frac{1}{\kappa} \ln (Ey^+) \quad \text{for } y^+ > 11.63 \tag{5}$$

$$T^+ = \sigma_{h,t}(U^+ + P) \tag{6}$$

with

$$P = 9\left(\frac{\sigma_h}{\sigma_{h,t}} - 1\right)\left(\frac{\sigma_h}{\sigma_{h,t}}\right)^{-1/4} \tag{7}$$

where

$$y^+ = \rho U_\tau y/\mu \tag{8}$$

$$U^+ = U_R/U_\tau \tag{9}$$

$$T^+ = (h_W - h)/(q_W/\rho U_\tau) \tag{10}$$

$$U = \sqrt{\tau_W/\rho} \tag{11}$$

and

τ_W = wall shear stress

U_R = tangential velocity at a distance y from the wall

h_W = fluid enthalpy at the wall

q_W = wall heat flux

Further details on the adopted turbulence formulation can be found in [27].

Finite-Difference Mesh Generation for the Combustion Chamber/Port Assembly

Finite-difference grid generation for industrial applications is a tedious task. Most of today's preprocessors are designed for finite element computations. Once the designer has defined the outer boundaries of an object, the automatic mesh generator proceeds with the task of filling the computational volume with the required elements and their numbering. In finite difference, however, each cell layer has to be carefully built and particular attention should be paid to the numbering of cells and vertices.

The various parts of the computational grid used in this study were built using the preprocessors GIBI and SUPERTAB. The final grid was assembled according to the requirements of KIVA with an in-house renumbering procedure. This procedure transforms any mesh structure made of arbitrary hexahedrons (if the input mesh is not homeomorphic to a cube, inactive cells are automatically added so that the final mesh is homeomorphic to a cube) into a mesh acceptable by KIVA as long as no cell face is shared by more than two cells at a time.

A wire frame representation of the final mesh is depicted in Fig. 2 showing the position of the valve at its minimum and maximum lifts.

The grid at TDC is provided to the computer program. Then, as the piston moves, cell layers are either added to or deleted from the space between the piston bowl and the cylinder head in order to ensure a constant mesh density.

In the present example, at TDC, there are 13,520 cells, about half of which are inactive. Active cells are added layer by layer so that at BDC, there are 19,760 cells.

Grid Handling and Code Modification

The moving valve is simulated by translating all cell vertices pertaining to the valve as prescribed by the lift function. The mesh topology is not altered during valve movement and consequently the connectivity of each computational cell is maintained during this operation. With no grid preconditioning such a practice would quickly lead to distorted and/or negative volume cells.

Commonly, an iterative method, based on the solution of a Poisson equation (solved in the transformed coordinate space for the physical coordinates) with pointwise Dirichlet boundary conditions, has been used in order to change distorted meshes into adequately distributed ones. However, as soon as the boundary contours become complex, this method runs into trouble; constant coordinate lines cross and extensive regions of negative volume cells may appear.

The difficulties associated with the Poisson equation mesh relaxation method are circumvented using a rezoning procedure [20] in the flow simulation code, which greatly decreases the likelihood of generating negative volume cells when the boundary of the computational domain is severely distorted. As the piston and the valve move, the mesh is treated at the beginning of each time step.

Model Boundary and Initial Conditions

A one-dimensional gas dynamics model of the complete single-cylinder engine based on the method of characteristics is used to determine boundary and initial conditions. The model uses the geometric characteristics of the intake and exhaust sides of the engine as well as a prescribed valve lift function and a simplified combustion model and solves for pressure, mass flow rate, temperature, and various species mass fractions at different points of the engine. Figure 3 shows the variation of port inlet velocity in the course of intake and compression.

A flat velocity profile is assumed at the upstream section of the inlet port and the initial velocity field at TDC is assumed to be quiescent. It is further assumed that initially the entire combustion chamber and intake port are filled with residual burned gases resulting from previous cycles. The port is assumed to be filled with burned gas in order to simulate burned gas backflow in the intake due to an intake valve opening 20 deg. C.A. prior to the induction TDC. Finally, it is assumed that the initial gas content of the combustion chamber is equal to 17 percent of the mass of gas that would be contained in the cylinder at BDC under atmospheric pressure.

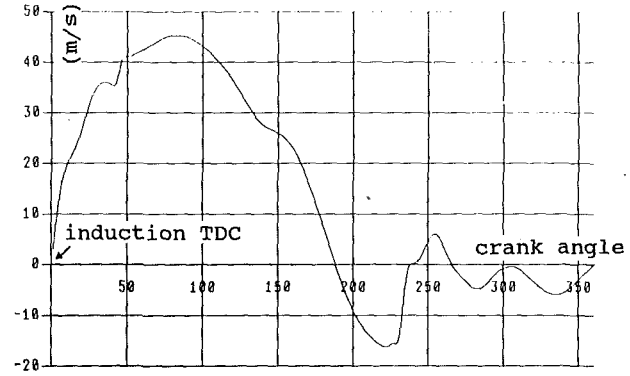

Fig. 3 Port upstream section velocity, calculated with a one-dimensional gas dynamic model of the engine

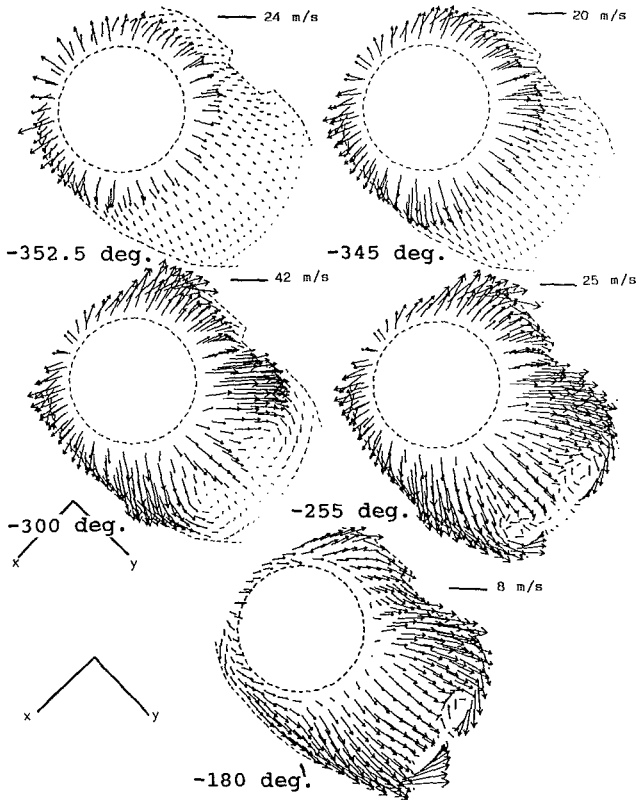

Fig. 4 Velocities in the lower plane of the valve

Engine Operating Conditions and Flow Simulation

Due to a limitation in the minimum allowable cell size, valve movement cannot be carried out all the way to closure. The minimum valve lift for this particular simulation is 2.3 mm. Valve closure is made possible by assigning solid cell flags to all the cells in the valve clearance area. The maximum valve opening is limited to 5.6 mm due to a limitation whereby the valve cannot descend below the piston's maximum vertical position.

With these conditions the design valve lift function is truncated. The original valve opening occurs at 20 deg. C.A. BTDC and closure at 240 deg. C.A. ATDC and, due to truncation, actual opening occurs at 0 deg. C.A. ATDC and closure at 220 deg. C.A. ATDC.

The combustion chamber is made of two parts: a piston bowl 4 mm deep and an ellipsoidal cavity in the cylinder head 6 mm deep. The spark plug is located on the edge of the cavity.

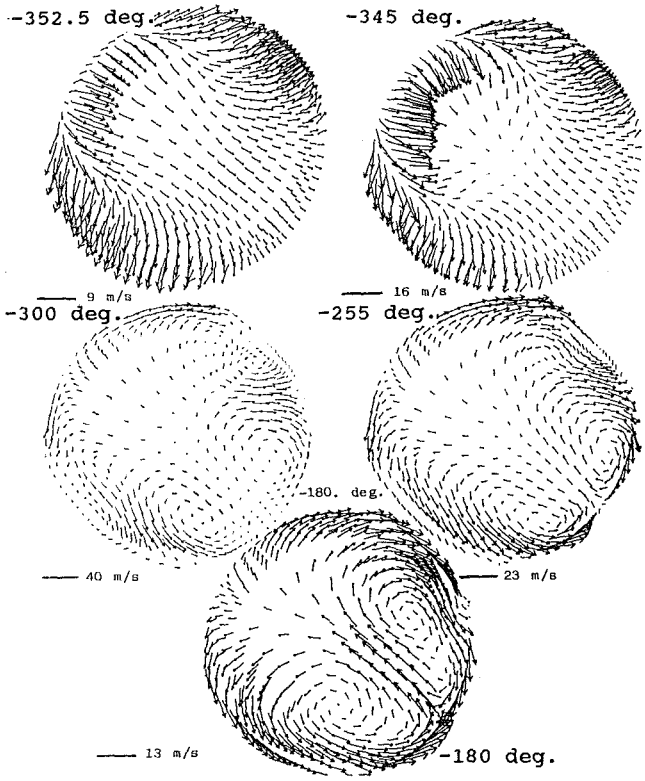

Fig. 5 Velocities 1 mm below the head gasket plane

The intake port is of a nonswirling conventional type. The inlet valve is 40 mm in diameter with a seat angle of 45 deg. The valve stem in the inlet port is also modeled. The compression ratio is equal to 9.5. Simulation starts at induction TDC and proceeds down to BDC. The engine is run at 2000 rpm and the computation is carried out on a CRAY X-MP 14 Computer System.

Discussion of Results

Figure 4 depicts the velocity field on a horizontal plane coinciding with the lower surface of the valve. It can be seen that at lower valve lifts (e.g., −352.5 deg. C.A. with 0 deg. C.A. taken at compression TDC in all velocity and concentration plots) the velocity profile is less affected by the presence of the wall than at higher lifts. Soon after, as the valve lowers, wall effects become predominant and the flow is diverted to regions of the valve circumference that are further away from the wall.

The effect of wall proximity is to create an axis of symmetry for the flow, which tends to supercede the effects of the inlet port direction. Two factors contribute to the establishment of this axis. First, the line that joins the closest and the farthest points from the cylinder wall on the valve periphery imposes a preferential direction because valve flow is diverted in this direction. Secondly, this direction is approximately that of the major axis of the cylinder head recess.

Figure 5 shows the flow field on a plane located 1 mm below the cylinder head gasket plane. The wall proximity effect is obvious at −345 deg C.A. The jet issuing from the valve bounces back into the cylinder over at least the first 15 deg. C.A. of intake. Later, two counterrotating eddies are established, which, at BDC, occupy more than half the view plane. It should be noted that the axis of symmetry persists at least up to BDC and seems to erase other effectts such as the presence of the spark plug well or other geometric features of the cylinder head cavity.

Figures 6 and 7 represent the flow field on two vertical

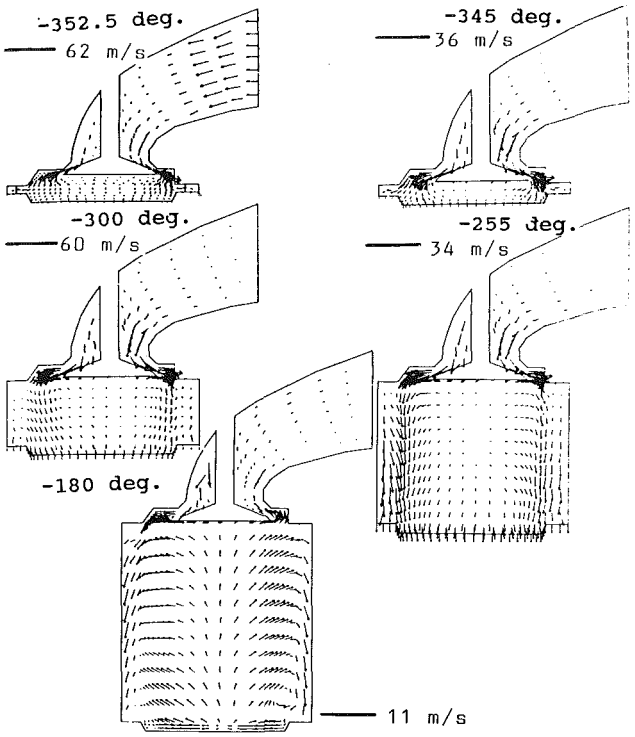

Fig. 6 Velocity fields in a y = const plane containing the valve axis

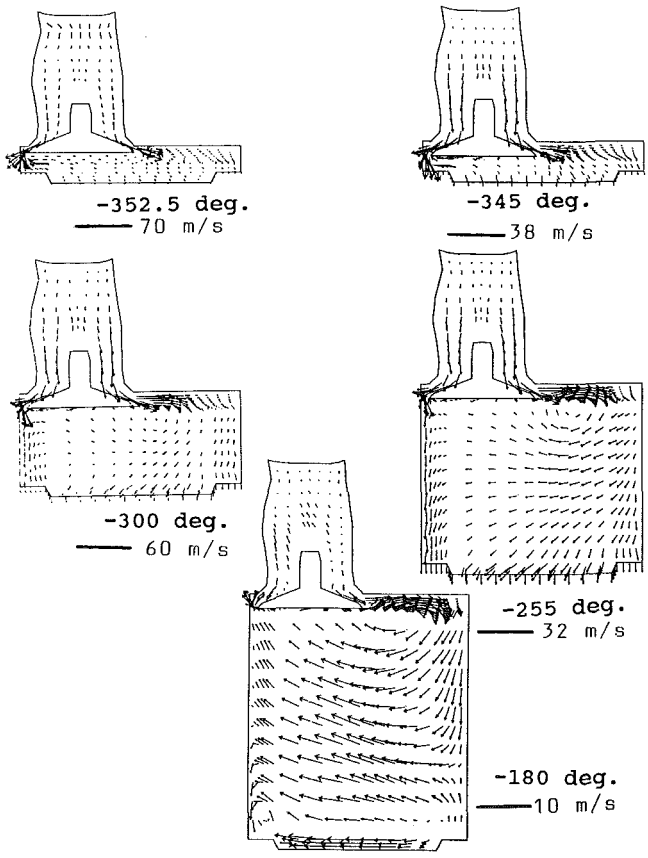

Fig. 7 Velocity fields in an x = const plane containing the valve axis

planes containing the valve axis. The projection plane used in Fig. 7 actually passes through the center of the chamber (along the aforementioned axis of symmetry).

Figure 6 indicates that the incoming flow is distributed even-

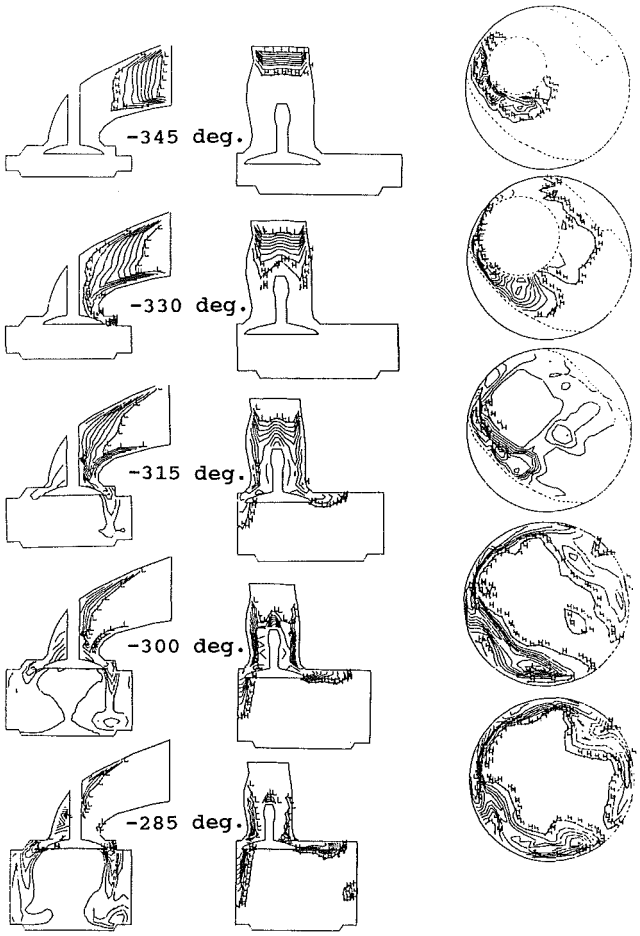

Fig. 8 Residual burned gas concentration fields during intake

ly with respect to the z axis and that a downdraft is established near the walls. At BDC the flow field is reversed and some gas returns into the inlet port.

Figure 7 shows clearly that, due to wall proximity, the flow field is essentially from left to right in the cylinder head cavity. The return flow takes place in the entire cylinder with the establishment of a single large eddy rotating clockwise. At BDC, the eddy persists but sends the flow upwards towards the valve.

Figure 8 illustrates the early stages of the intake process. The fresh charge front advances through the inlet port, through the valve passage outlet, and along the walls of the combustion chamber. It can be noted the port velocity profile is skewed. The fresh charge front is accelerated at the wall that is closer to the center of curvature of the port and decelerated close to the opposite wall. Consequently, the fresh charge penetrates the combustion chamber first from the point of the valve clearance area that is the closest to the center of curvature of the port. Wall blockage causes the front to descend while on the opposite side the front moves horizontally. Finally, it can be seen that the region immediately below the valve is reached the latest by the fresh air front.

Summary and Conclusion

The computational fluid dynamics simulation program KIVA was augmented with a k-ϵ turbulence model and enhanced geometric capabilities. With the addition of an industrial mesh generator interface, its field of application was extended to a wider range of engine geometries and flow situations.

A methodology for grid generation and handling for C.F.D.

codes is applied to the case of flow in an inlet port and a combustion chamber separated by a moving valve under motoring conditions.

Velocity and residual burned gas mass fraction fields were examined and related to the geometric features of the port and the cylinder head.

Effects due to the particular shape and direction of the inlet port could not be observed in this preliminary analysis. The effect of wall proximity, especially at higher valve lifts, on the development of large-scale structures inside the combustion chamber was observed. It was noted that this effect tends to erase other effects such as the incoming inlet flow direction and the geometric features of the chamber.

An important consequence of these observations is that the relative position of the intake valve with respect to the rest of the cylinder head determines the prevailing flow field in the combustion chamber. Other geometric features of the cylinder head, such as the position and shape of the spark plug well and the direction of the inlet port, seem to be secondary.

Limitations of turbulence models and their inability to predict flow separation correctly may lead to inaccurate valve annular jet angles and discharge rate coefficients. The prescription of the location and timing of flow separation could bring a partial solution to this problem.

Problems regarding mesh density and distortion are difficult to quantify and choices are mostly dictated by available memory and computation cost and the researcher's judgment.

Finally it should be borne in mind that the results of such numerical simulations must be summarized in the form of bulk quantities, such as bulk turbulent kinetic energy, bulk swirl, or bulk residual burned gas homogenization rate, for these simulations to be of any relevance in comparisons between different chamber or inlet port designs.

Acknowledgments

GIBI was developed by the C.E.A., the French Atomic Energy Authority. SUPERTAB is a product of SDRC CAE International. CRAY X-MP is a trademark of Cray Research, Inc.

References

1 Brandl, F., Reverencic, I., Cartellieri, W., and Dent, J. C., "Turbulent Air Flow in the Combustion Bowl of a D.I. Diesel Engine and Its Effect on Engine Performance," SAE, Paper No. 790040, 1979.

2 Witze, P. O., and Vilchis, F. R., "Stroboscopic Laser Shadowgraph Study of the Effect of Swirl on Homogeneous Combustion in a Spark-Ignition Engine," SAE Paper No. 810226, 1981.

3 Nagayama, I., Araki, Y., and Ioka, Y., "Effects of Swirl and Squish on S. I. Engine Combustion and Emission," SAE paper No. 770217, 1977.

4 Menne, R. J., Mennicken, A., and Adams, W., "A Method for the Efficient Development of SI Combustion Chambers," *Proceedings of the European Automobile Engineers Cooperation Conference on New Developments in Power Train and Chassis Engineering*, Vol. 1, Strasbourg, France, 1987.

5 Errera, M. P., "Numerical Prediction of Fluid Motion in the Induction System and the Cylinder in Reciprocating Engines," SAE paper No. 870594, 1987.

6 Isshiki, Y., Shimamoto, Y., and Wakiska, T., "Numerical Prediction of Effect of Intake Port Configuration on the Induction Swirl Intensity by Three-Dimensional Gas Flow Analysis," *Proceedings of the COMODIA Symposium*, JSME, 1985.

7 Argueyrolles, B., Taghavi, R., and Zellat, M., "Potentials of Today's CFD Codes for Modeling Real Engine Geometries," *Proceedings of the Second International Conference on Supercomputing in the Automotive Industry*, Sevilla, Spain, Oct. 1988.

8 Brandstaetter, W., and Kratochwill, H., "Three-Dimensional Calculation of the Flow in a Square Shaped Piston Bowl of a DI Diesel Engine," Presented at the SIA conference, Lyons, France, May 1987.

9 Wakisaka, T., Shimamoto, Y., and Isshiki, Y., "Three-Dimensional Numerical Analysis of In-Cylinder Flows in Reciprocating Engines," SAE Paper No. 860464, 1986.

10 Dupont, A., "Using a Three Dimensional Aerodynamic Code as a Guide for Choosing Between Various S. I. Engine Chamber Designs," *Proceedings of the Second International Conference on Supercomputing in the Automotive Industry*, Sevilla, Spain, Oct. 1988.

11 Uzkan, T., and Hazelton, J. R., "The Influence of Swirl on the Fresh Charge Stratification in an IC Engine Combustion Chamber," SAE Paper No. 860466, 1986.

12 Schaepertoens, H., and Thiele, F., "Three-Dimensional Computations for Flowfield in DI Piston Bowls," SAE Paper No. 860463, 1986.

13 Brandstaetter, W., Johns, R.J.R., and Wigley, G., "The Effect of Inlet Port Geometry on In-Cylinder Flow Structure," SAE Paper No. 850499, 1985.

14 Brandstaetter, W., Johns, R.J.R. and Wigley, G., "Calculation of the Flow Produced by a Tangential Inlet Port," *Proceedings of the International Symposium on Flows in Internal Combustion Engines*, Vol. 3, ASME FED-Vol. 28, 1986.

15 Yamada, T., Inoue, T., Yoshimatsu, A., Hiramatsu, T., and Konishi, M., "In-Cylinder Gas Motion of Multivalve Engine Three Dimensional Numerical Simulation," SAE Paper No. 860465, 1986.

16 Wakisaka, T., Shimamoto, Y., and Isshiki, Y., "Induction Swirl in a Multiple Intake Valve Engine Three-Dimensional Numerical Analysis," IMechE Paper No. C40/88, 1988.

17 Gosman, A. D., and Ahmed, A. M. Y., "Measurement and Multidimensional Prediction of Flow in an Axisymmetric Port/Valve Assembly," SAE Paper No. 870592, 1987.

18 Amsden, A. A., Ramshaw, J. D., O'Rourke, P. J., and Dukowicz, J. K., "KIVA, a Computer Program for Two and Three-Dimensional Fluid Flows With Chemical Reactions and Fuel Sprays," Los Alamos National Laboratory Report No. LA-10245-MS, 1985.

19 Amsden, A. A., Ramshaw, J. D., Cloutman, L. D., and O'Rourke, P. J., "Improvements and Extensions to the KIVA Computer Program," Los Alamos National Laboratory Report No. LA-10534-MS, 1985.

20 Taghavi, R., and Dupont, A., "Multidimensional Flow Simulation in an Inlet Port/Combustion Chamber Assembly Featuring a Moving Valve," *Proceedings of the ASME Energy-Sources Technology Conference and Exhibit*, Houston, TX, 1989.

21 Hall, M. J., and Bracco, F. V., "A Study of Velocities and Turbulence Intensities Measured in Firing and Motored Engines," SAE Paper No. 870453, 1987.

22 Morel, T., and Mansour, N. N., "Modeling of Turbulence in Internal Combustion Engines," SAE Paper No. 820040, 1982.

23 El Tahry, S. H., "k-. . . Equation for Compressible Reciprocating Engine Flows," *AIAA Journal of Energy*, Vol. 7, No. 4, 1983.

24 Ahmadi-Befrui, B., "Assessment of Variants of the *k-*. . Model for Engine Flow Applications," *Proceedings of the ASME Energy Sources Technology Conference and Exhibit*, Dallas, TX, 1987.

25 Launder, B. E., and Spalding, D. B., *Mathematical Models of Turbulence*, Academic Press, London, 1972.

26 Jayatillaka, C.V.L., "The Influence of Prandtl Number and Surface Roughness on the Resistance of the Laminar Sub-Layer to Momentum and Heat Transfer," in: *Progress in Heat and Mass Transfer*, Vol. 1, Pergamon Press, London, 1969.

27 Ahmadi-Befrui, B., "Analysis of Flow Evolution in the Cylinders of Motored Reciprocating Engines," Ph.D. Thesis, Imperial College of Science and Technology, University of London, 1985.

Coal-Fueled Diesels: Systems Development

M. H. McMillian

H. A. Webb

U.S. Department of Energy,
Morgantown Energy Technology Center,
Morgantown, WV 26505

The U.S. Department of Energy (DOE) Office of Fossil Energy has sponsored research in the area of coal-fueled diesel engines since the late 1970s. The program began as an exploratory effort and has grown into a proof-of-concept program that includes several major medium-speed diesel engine manufacturers. Those manufacturers have identified the utility, industrial cogeneration, and transportation markets as areas in which expensive clean distillate fuel may be displaced by low-cost, domestically abundant coal. The development of a coal-fueled diesel engine system will require the parallel development of coal fuels, engine components, wear and emission control system, and a support infrastructure. Because of notable success in earlier projects of the coal-fueled diesel program, the DOE's Morgantown Energy Technology Center (METC) recently expanded the program with the award of contracts for two 5-year, proof-of-concept project. These major projects will build on the results of past work to complete development of technology for the commercialization of coal-fueled diesel engines. This paper summarizes progress in the DOE program and planned research to overcome technical and economic barriers to that commercialization.

Background

This paper is an update of previous papers describing the METC coal-fueled diesel program. As described in one of those references (Carpenter/Crouse, 1985a), Rudolf Diesel conceived the compression ignition cycle prior to 1900 as a method for combustion of both solid and liquid fuels. Although coal was discussed in his original patent, it was several years after hardware tests were initiated before Diesel experimented with coal fuels. Fuels handling, safety, and ash deposition problems discouraged Diesel from any further pursuit of coal as an engine fuel.

Coal fuel testing in compression ignition engines continued through the early 1900s with the work of Pawlikowski and others (Pawlikowsi, 1928; Morrison, 1928). There was extensive German development of the use of pulverized coal in diesel during the period of 1920 to 1944, but this development ended with the end of World War II. The need for industrial products in Germany far exceeded any need to develop an engine for using expensive domestive coal instead of amply available low-cost imported oil.

In spite of this early work, coal-fueled diesel engines are not yet commercially available. Although there are no basic thermodynamic reasons that diesels cannot run on coal, there are significant differences in the mechanical operation of oil-fueled and coal-fueled engines. These differences lead to a number of problems in the areas of (*a*) fuel properties and cost, (*b*) combustion efficiency and carbon burnout, (*c*) engine component durability, and (*d*) emissions. The most critical technical problem is engine component durability. Nozzle lifetimes operating on coal–water slurry (CWS) are on the order of 5 hours, but preliminary tests with specially hardened materials are promising (Flynn, 1988; Rao et al., 1988). Overall, there has been significant technical progress in recent projects, and the promise for viable coal-fueled diesel engines now appears attainable.

DOE has recently enhanced their program to address the technical and ecomonic barriers to commericalization of coal-fueled diesel engines. Two 5-year duration, proof-of-concept projects were initiated in 1988 and will culminate in engine tests that will pave the way for commercialization of coal-fueled diesel systems. Each project includes a major engine manufacturer providing up to 20 percent cost share. In addition to the two proof-of-concept projects, one proof-of-principle project was started that will develop a higher risk approach to combustion of coal-based fuel in diesels. Several smaller research contracts were also awarded in 1988 to look at specific coal-fueled engine technology issues.

Over 100 engine test hours have been accumulated using CWS as the primary fuel source. These slurries typically have approximately 1 percent of ash and sulfur and a mean particle size from 5 to 20 μm. This paper provides a review of progress to date and future work required to provide the scientific and engineering foundation for commercialization of coal-fueled diesel engines.

Economics

Significant progress has been made in understanding the economic requirements of diesel engine systems. Recent studies have shown that both coal-fueled diesel locomotives and stationary coal-fueled diesel systems in the 2- to 20-megawatt (MW) size range will be economically attractive

Contributed by the Internal Combustion Engine Division and presented at the Twelfth Annual Energy-Sources Technology Conference and Exhibition, Houston, Texas, January 22–25, 1989. Manuscript received by the Internal Combustion Engine Division August 1988.

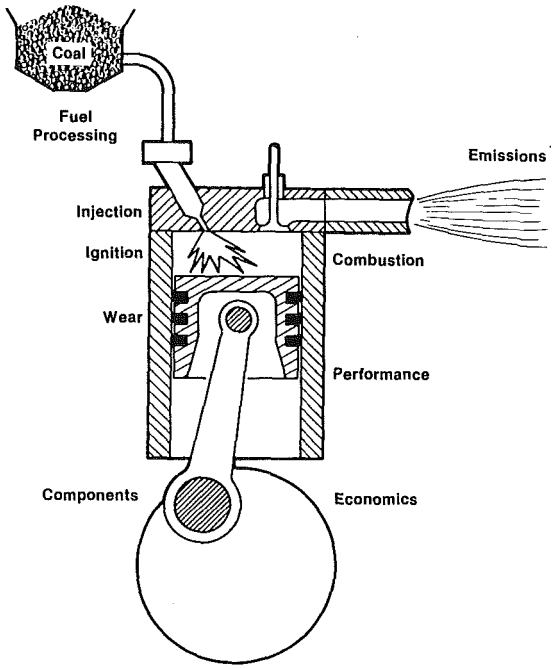

Fig. 1 Coal-fueled diesel issues

by the mid-1990s provided that engine grade slurry costs can be brought down to less than $2 million Btu above the cost of the source coal (Arthur D. Little, 1986, 1988). This assumes an increase in oil prices to approximately $25 to $30/barrel. These prices would provide enough economic incentive for investors to build both coal-fueled engines and fuel manufacturing plants with an attractive return on investment.

While oil is the fuel of choice in transportation applications, natural gas is also a competitive fuel source for stationary power applications. Recent predictions show a large amount of natural gas recoverable at modest prices (Argonne National Laboratory, 1988), and a slow rate of natural gas price increase should be expected during at least the next decade.

Changing an engine system from oil or natural gas to CWS changes not only the cost of fuel but the engine capital costs, maintenance costs, and emissions control costs. Recent estimates by Arthur D. Little (ADL) and Cooper-Bessemer include a cost premium of 0.33 cents per kilowatt-hour (kWh) for maintenance and overhaul of a 6-MW coal-fueled engine. Engine wear due to the use of coal fuel causes the increased maintenance and overhaul costs.

An increase in the capital cost of the installed engine system is expected because of the increased cost of numerous durable engine components designed to withstand the increased wear from the coal fuel. An engine cost premium of $1.67 million over the base cost of $3.5 million for the 6-MW engine is predicted. Emission control costs are expected to be 1.03 cents/kWh, including both capital and operating costs. ADL projects a total cost of 6.85 cents/kWh, including CWS, capital charges, overhead and maintenance, and emission control.

The primary factor influencing the economic viability of coal-fueled diesel engines is the cost of fuel. It is estimated that a break-even point will be reached when oil and gas prices increase above $5.00 per million Btu, perhaps in the mid- to late-1990s, at which time the coal-fueled engine will be economically attractive (Arthur D. Little, 1986).

Critical Issues

The primary technical concerns for coal-fueled diesel power systems are their ability (*a*) to ignite and burn the coal fuels successfully, (*b*) subsequently to survive the hot gas stream contaminants (ash, unburned coal particles, and sulfur compounds), and (*c*) to emit pollutants at an acceptable level. The critical issues for a coal-fueled diesel engine are shown schematically in Fig. 1.

From Fig. 1, the areas of concern can be logically grouped into five categories: fuels technology, combustion phenomena, fuel engine interaction, contaminant control, and systems integration and performance. The areas of concern have been discussed previously (Carpenter and Crouse, 1985a), but are repeated for clarity below.

Fuels Technology. Understanding the impact of fuel composition and fuel processing economics while developing fuel specification guidelines is of key technical importance for coal-fueled diesel engines. Currently, CWS, coal powders, and coal gasifier fuel streams are of primary interest in the DOE diesels program. For future applications, advanced coal-derived fuel forms are being developed that have promise to be easy to handle and cost competitive.

There are several processes for cleaning coal that include physical beneficiation and chemical cleaning to remove unwanted ash and sulfur constituents (Keller, 1983; Bhasin, 1985; Im and Wolfe, 1985). The evolution of a viable coal fuel specification will depend on fuel cost considerations as well as the performance and economics of the engine system and the effect of coal fuels on the engine and the environment. Fuel specifications will change continually as the program progresses.

A broad range of fuels-related issues is under investigation in the DOE coal-fueled diesels program. Specific issues of critical importance include fuel rheology and the atomization and wear resulting from fuel injection.

Combustion Phenomena. The diesel engine must achieve complete combustion of the coal fuel within a limited residence time in order to achieve high system efficiency and to reduce degradation of the engine and environment. The ability intermittently to ignite and burn coal fuels in a diesel engine is considered a critical issue that has received major attention. Over 100 hours of operating time have been accumulated using micronized coal or CWS as the primary fuel in diesel engines.

The combustion of coal fuels in a diesel engine is primarily a function of fuel properties and chamber residence time. The relative influences of chamber geometry, fuel characteristics, and changes in engine load on coal particle burnout need to be fully understood in order to optimize process performance.

Fuel Engine Interaction. Minimizing the effects of coal contaminants on the performance of the diesel engine is the most critical technical issue. Problems stem from the unburned coal and ash particles, which cause accelerated wear of the injector systems, cylinder walls, rings, valves, pumps, and downstream components. Research in this area is aimed at (*a*) reduction of harmful coal constituents through cleaning and (*b*) innovative applications of durable materials.

The chemical and physical processes that affect the ash constituents, like those that affect coal combustion, are not totally understood. Trace amounts of some coal elements can change the phase of an ash particle affecting how the ash will interact with the diesel engine (Carpenter, 1985). Research is ongoing to develop an understanding of the interaction of the ash and the engine operation.

Contaminant Control. Coal-based fuels currently under consideration contain ash particles, fuel-bound nitrogen, and sulfur compounds. These elements are of environmental concern. System studies and experimental research programs are underway to develop a scientific, engineering, and economic understanding of the environmental aspects of a coal-fueled

Table 1 Coal-fired diesel engine development

Company	Application	Fuel
ADL/Cooper-Bessemer	Modular Utility/ Cogeneration	Coal-Water Slurry/Dry Powder
General Electric	Locomotive Stationary Power	Coal-Water Slurry
Caterpillar	Locomotive/ Stationary Power	Coal Processor Gas

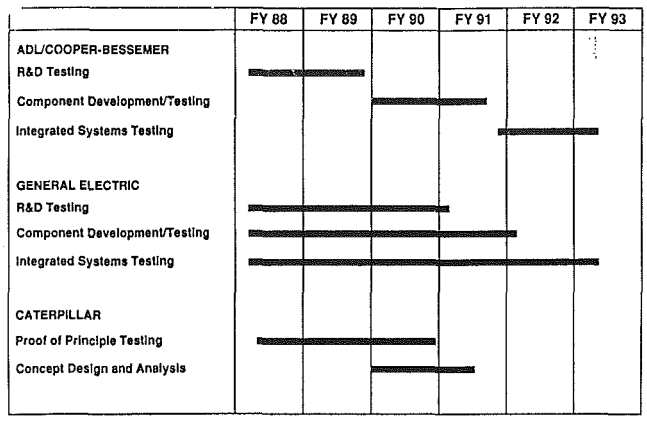

Fig. 2 Coal-fuel diesel engine program schedule

diesel engine. At minimum, the engines to be developed must not increase the emission levels of those power systems that they will displace.

There are some encouraging results in this area. Diesel engines burning petroleum-based fuels typically produce relatively high levels of nitrogen oxide (NO_x) emissions, but recent CWS tests indicate that NO_x levels are in some cases reduced by half (Arthur D. Little, 1988). This brought about by a reduction in thermal NO_x from the flame caused by the cooling effects of the water in the slurry. Carbon monoxide (CO) and hydro-carbons were also found to be reduced during slow-speed engine tests (Stieger, 1985).

Although these test results are encouraging, additional research is needed and is underway to characterize and control emission levels further, especially those from medium speed diesels used in locomotive (Flynn, 1988) and cogeneration applications.

Systems Integration and Performance. Understanding the economic benefits and technical merits of using coal in a diesel engine is critical to a successful program. This includes an understanding of the relationships between fuel quality, system components, and overall system performance. Systems assessments have been completed (Arthur D. Little, 1986; Hapeman and Savkar, 1985) that are very positive about the future economic viability of coal-fueled systems. These assessments are frequently updated to provide guidance for the program.

The discussion above shows that there are technological obstacles to be overcome before a reliable and economic coal-fueled diesel engine can be commercialized. However, as summarized in several references (Soehagen, 1976; Robben, 1984; Carpenter and Crouse, 1985), programs to date have greatly advanced the initial technology base, and these successes point the way to early commercialization.

DOE Program

Within the past decade, the majority of work on coal-fueled diesels has been sponsored by the DOE. Up to 1987, DOE programs were conducted by both the Office of Fossil Energy and the Office of Conservation but are now supported only by the Office of Fossil Energy. In the past, the Office of Conservation conducted activities to develop a slow speed (120 revolutions per minute [rpm]), two-stroke industrial engine. Since 1979, the Office of Fossil Energy has supported research to develop U.S.-manufactured, heavy-duty, medium-speed diesel engines (engine speeds greater than 250 rpm) for transportation, industrial, cogeneration, and utility applications.

The results of the DOE Conservation slow speed diesel tests were encouraging (Nydick and Wang, 1986; Anson et al., 1987). A Swiss-manufactured Sulzer diesel engine test rig was fueled by a 50/50 CWS with mean coal particle sizes up to 16 μm in diameter. The engine was operated at various power levels with fuel efficiency equal to No. 2 petroleum diesel, and emissions were greatly reduced. Wear and rheological problems did exist, and it was concluded that additional research was needed in these areas. Detailed results of the activities are not discussed in this paper but are available in other references (Nydick and Wang, 1984; Stieger, 1985; Nydick, 1986; Anson, 1987).

The METC is responsible for implementation of the ongoing Office of Fossil Energy program. The program began with the establishment of engineering feasibility and is currently moving toward proof-of-concept testing. The program is being implemented through multiple projects with industry and private laboratories, as well as internal DOE research and development. The program is now progressing into more advanced engineering work, which includes development of components and proof-of-concept testing.

Building on the technology base established in earlier projects, the current DOE program includes two major proof-of-concept and one proof-of-principle projects (shown in Table 1 and Fig. 2) and a number of support projects. The two contracts for proof-of-concept testing were awarded in Mar. 1988 to General Electric (GE) and ADL/Cooper-Bessemer to demonstrate the use of coal-fueled diesels for locomotive and industrial cogeneration applications. GE is a major manufacturer of locomotive engines from 2000 to 4000 hp (1 to 3 MW), and their project will include use of a CWS-fueled locomotive in commercial service for a 50-hour test period. Cooper-Bessemer, the primary subcontractor to ADL, is a major manufacturer of stationary power engines in the 3- to 20-MW range and will conduct coal-fueld tests on a six-cylinder industrial engine. The fuels being tested are CWS and coal powder. A third major contract was awarded in 1988 to Caterpillar, Inc., to explore a higher risk aproach to coal-fueled diesel operation. Caterpillar will develop a high-pressure coal fuel processor to gasify coal in exchangeable cartridges to produce a low-Btu gas for combustion in a locomotive diesel engine. Caterpillar will separately test the fuel processor and the burning of simulated product gas in a diesel engine.

Table 2 summarizes selected projects from the current Fossil Energy program. The information provided includes those organizations that were under contract with METC as of Oct. 1988. The table lists the major contractors and their key subcontractors, and indicates each organization's effort to resolve critical issues in fuels technology, combustion phenomena, fuel engine interactions, environmental research, and systems integration.

In the METC program, CWS, powdered coal, and coal gas are being used as diesel engine fuels. Combustion tests have succeeded in identifying basic fuel/design conditions necessary to sustain combustion under laboratory- and bench-scale engine tests. Performance data have also been obtained on the effect of fuel injector design and fuel variables on com-

Table 2 Fossil energy activities

AREAS OF ACTIVITY		FUELS TECHNOLOGY					COMBUSTION PHENOMENA				FUEL-ENGINE INTERACTION			ENVIRONMENTAL ASSESSMENT			SYSTEMS INTEGRATION	
CONTRACT ORGANIZATION	FORM	SUPPLIER	SPECIFICATION DEVELOPMENT	RHEOLOGY STUDIES	HANDLING/INJECTION/ATOMIZATION	MODEL/THEORY	LAB STUDIES	SMALL ENGINE TESTS	FULL SCALE TESTS	PISTON/RING/LINER WEAR STUDIES	ENGINE DURABILITY TESTS	NOZZLE WEAR STUDIES	STUDIES	LAB TESTS	ENGINE TESTS	ECONOMIC STUDY	COMPONENTS DEVELOPMENT	PROOF-OF-CONCEPT TESTING
A.D. LITTLE	S/P		X	X	X	X	X	X	X	X	X	X	X			X	X	
- COOPER BESSEMAR			X				X	X	X		X	X				X	X	X
- AMAX		X	X	X	X											X	X	
- BATTELLE																	X	
- AMBAC					X					X	X					X	X	
- PSI										X	X	X				X	X	
GENERAL ELECTRIC	S		X	X	X	X	X	X	X	X	X	X	X	X	X	X	X	
- CORPORATE RESEACH				X	X	X	X	X	X	X				X			X	
- TSBO									X	X						X		X
- OTISCA																	X	
- GEESI		X	X	X	X								X	X	X		X	
CATERPILLAR	G		X		X		X	X			X	X	X	X	X	X	X	
- SOLAR					X							X	X	X				
- UCC					X							X	X	X				
GENERAL MOTORS	S		X	X	X		X	X		X	X		X			X	X	
- ALLISON																		
- EMD					X		X			X	X							
- SOUTHWEST RESEARCH					X	X	X	X		X	X			X	X			
- AMAX		X	X	X	X													
ADIABATICS	S/P		X		X		X	X		X		X	X		X		X	
- DEFENSE RESEARCH					X													
- TEKNOCRAFT																		
DOE/MORGANTOWN	A		X		X		X	X								X		
- CUSSONS/RICARDO																		
TECOGEN	S/P									X	X						X	
MECHANICAL TECHNOLOGIES, INC.	S/P									X	X						X	
SOUTHWEST RESEARCH	S/P			X						X	X						X	

COAL FUEL FORMS: S=SLURRY, P=POWDER, G=GAS, A=ADVANCED COAL DERIVED FUEL

ponent wear. In addition, relevant data have been generated on the wear characteristics of candidate materials in the presence of simulated ash particles and on emissions from coal-fueled diesels. Currently, the main objective of the Fossil Energy program is to proceed through component development to proof-of-concept testing with major U.S. engine manufacturers.

Program Status

In an ongoing activity, ADL has been under contract since 1985 to investigate the use of coal-fueled diesel engines in the industrial and modular power markets. From 1985 to 1988, the project team included ADL, Cooper-Bessemer, the Massachusetts Institute of Technology (MIT), and AMBAC International (American Bosch). The group conducted system assessments (Wilson, 1986), laboratory research using the MIT rapid compression machine, and engine diesel studies aimed at a 1987 coal-fueled, full-scale (13-in. bore), single-cylinder engine test at Cooper-Bessemer (Rao et al., 1988). The application for the Cooper medium speed 6-MW diesel engine being developed is the industrial cogeneration and small modular utility market.

ADL and Cooper-Bessemer are making good progress in their full-scale, 400 rpm, 13-in. bore, single-cylinder engine tests (Rao et al., 1988; Arthur D. Little, 1988). AMAX produced CWS with up to 55 percent solids loading, which was burned with a specific fuel consumption and combustion efficiency comparable to a No. 2 petroleum fuel. These results were verified through heat release and pressure analysis, exhaust particulate measurements, and CO/CO_2 ratios. Ignition delays were acceptable and reproducible, and the engine was operated on 100 percent CWS on several occasions. Recent testing has emphasized component development.

ADL was awarded a 5-year, proof-of-concept contract in early 1988. The team for this new project includes Cooper-Bessemer, AMBAC International, Battelle Columbus Laboratories, Physical Sciences, Inc., and AMAX Extractive Research and Development Center. The group will continue development of a stationary diesel engine for cogeneration or modular utility applications. The product of the development effort will be a four-cycle, 400 rpm, 3000 to 8000 hp engine fueled by a CWS. Work during the first year of the contract will concentrate on critical design issues such as nozzle erosion, deposition, ash removal, component wear, and emission control. The second two years will focus on developing and testing individual components. The final two years will culminate in a 400-hour, full-scale "proof-of-concept" test of a six-cylinder Cooper-Bessemer engine that will integrate all of the advanced components developed in earlier work.

GE has also been under contract to DOE since 1985. The locomotive development team includes three divisions of GE: the Corporate Research and Development Center, the Transportation Systems Business Operations (TSBO), and General Electric Environmental Services (GEESI). The program has included systems assessments of several different coal-fueled locomotive systems (Hapeman and Savkar, 1986, 1987), and ongoing research includes both small-scale engine

tests and short-term, full-scale (9.5-inch bore), single-cylinder engine tests.

GE has had significant success in burning coal–water fuels in their full-scale, single-cylinder engine. The tests are being conducted at full power (270 hp at 1050 rpm) (Hsu, 1988), and combustion efficiency has been improved to over 98 percent. To achieve this, manifold air temperatures and pressures were varied from their normal values to improve combustion performance. In these tests, GE took the first full-scale emission measurements to be made in this country with coal fuels. The NO_x levels confirmed the previous finding of Sulzer that NO_x levels were less than half the normal values typically measured for petroleum-fueled diesel engines. Further performance improvements are expected with a new modified accumulator injector that GE will use in future engine tests (Hsu, 1989).

GE was awarded a 5-year proof-of-concept contract in 1988 and will develop a four-cycle, 1050 rpm, 3900 hp coal-fueled diesel power systems for locomotives. The goal is to have a CWS-fueled GE 7FDL locomotive engine tested within 2 years after the start of the program.

The GE technology will be used first in a test cell, where long-term durability tests will be conducted on an eight-cylinder 7FDL engine with two cylinders operating on coal–water mixtures. Subsequent tests in the test cell and on a GE test track will use a 12-cylinder engine, running CWS in all cylinders. Based on those results, Ge will then run a second locomotive test to expose the coal-fueled diesel to an actual railroad operating environment. These tests will begin within 3 years after the project starts. The final series of tests, beginning 4 years after contract award, will integrate as many of the new systems and components as possible into a locomotive operating in commercial service for a short period.

Caterpillar, Inc., signed a 3-year, proof-of-principle contract with METC in mid-1988 to demonstrate feasibility of a high-pressure coal fuel processor, which will directly feed a locomotive diesel engine. The technology involves the conversion of run-of-mine coal to low-Btu gas in a batch-loaded fuel processor, hot gas cleanup, and combustion of the coal gas in a high-compression-ratio diesel engine. Under contract to Caterpillar, the United Coal Company will develop the unique coal fuel processor, which will be tested separately from the diesel engine. Combustion tests of a diesel engine running on simulated low-Btu product gas will be conducted by Caterpillar.

General Motors (GM) is also developing coal-fueled diesel engines for locomotive applications. The project team includes the GM Electromotive Division, Southwest Research Institute (SWRI), and Adiabatics, Inc. The program has included an up-front systems assessment (Koch, 1986), combustion bomb studies, and small engine tests. A full-scle (9.5 in. bore), single-cylinder engine test series was completed in early 1989.

In support of the GM locomotive development efforts, SWRI completed a full series of diesel tests in their half-scale, three-cylinder engine (Urban, 1988) with only one of the cylinders fueled with coal. The screening tests included a variety of coal fuels (e.g., coal water, coal methanol, and coal oil) and have provided GM/SWRI with information on coal fuels, engine configurations, and operational characteristics.

Results of these projects involving major diesel engine manufacturers are confirming the merit of fueling U.S.-manufactured diesel engines with coal. The contractors are defining coal-fueled engine requirements for successful operation, including fuel specifications, combustion limits, performance constraints, requirements for environmental compliance, physical size limitations, and infrastructure constraints. The conduct of major portions of the program by diesel manufacturers will lessen the difficulties of technology transfer from developer to manufacturer.

Support projects complement the work done in the major projects involving engine manufacturers by addressing critical technology issues. Although these projects are too numerous to discuss in any detail in this paper, recent progress is covered in the most recent proceedings of the annual contractors review meeting, which covers the METC heat engines program (Dellefield and Webb, 1988). Progress in a few of these projects will be briefly discussed. Of particular note is the work carried out by Adiabatics, Inc., to evaluate the combustion enhancement of coal fuels when using adiabatic (low heat rejection) diesel engine technology. The increased gas and surface temperatures in this kind of engine decrease the burning time required for a given coal particle, resulting in an improvement in combustion efficiency and an increase in permissible engine operating speed. Adiabatics has conducted tests in which dry powder was fumigated into the air intake manifold of a single-cylinder diesel engine (Kamo, 1986; Kakwani, 1989). Good combustion efficiency was obtained with ignition timing controlled using an exhaust gas recirculation system.

The Adiabatics tests were conducted using bituminous coal in a single-cylinder, 5.125-in. bore engine at speeds from 800 to 1800 rpm. At first, the coal powder fumigated into the engine was less than 10 μm in diameter, but more recent tests used 21μm sized coal particles at engine engine speeds up to 1800 prm. The engine started and sustained operation on 100 percent coal powder, and data analysis showed that engine efficiency with the coal fuel equaled engine efficiency with petroleum fuels. Problem areas included fuel throttling and increased piston blowby. In the future, Adiabatics will continue their work in the DOE program in projects that address fuel injection system development, combustion, and wear.

In support work being performed in-house at METC, advanced fuels such as mild gasification liquids are being tested in an advanced diesel research engine (Ayers, 1988). The engine is a Ricardo Proteous, 5-in. bore, single-cylinder engine; and fuel combustion characteristics are predicted from combustion bomb results before engine tests are conducted. The engine experiments explore the combustion and emission characteristics of fuels and their effects on engine performance. In many cases the tests represent the first time that fuels are tested in an engine.

Modeling studies at METC support the engine testing as well as studies to assess engine performance, emissions, and economic incentives of diesel systems fired with coal-derived fuels. The primary diesel engine modeling tool is a model developed at the Texas A&M University for METC (Caton, 1987). Because diesels are part of total systems, the diesel engine modeling work is frequently integrated with modeling of other system units (gasification, sulfur removal, heat recovery, etc.).

Also of particular note are three recent support contract awards made to Tecogen, Mechanical Technologies, Inc., (MTI), and SWRI. These projects will look at techniques to overcome problems with ring and liner wear. Tecogen will evaluate a liquid flush system, while MTI will determine the feasibility of using dry powders as lubricants. SWRI will conduct a broad evaluation of potential wear reduction systems before focusing on the most promising candidates.

Summary

The DOE office of Fossil Energy is supporting a continuing program to develop coal-fueled diesel engines. The program is being implemented through the METC to demonstrate the economic and technical feasibility of coal-fueled diesel systems and to provide the technology base necessary for commercialization. Numerous projects are being supported to resolve critical issues and to develop the technical basis for engine manufacturers to commercialize coal-fueled diesel engines. The core of the program consists of three proof-of-concept and proof-of-principle projects being carried out by

teams including major diesel engine manufacturers. A number of support projects address specific technology issues. All of this work builds on the base of results of earlier projects sponsored by the Department of Energy and others.

The discussion above has briefly described the history of the development of coal-fueled diesels, critical issues, and the current research program. The prospect of an efficient engine for operation with coal fuels has become increasingly realistic. Test results have frequently shown that CWS can be burned in diesels with good combustion and environmental performance, and much progress has been made in the critical areas of fuel injection and component durability. Economic assessments show that coal-fueled diesels can be economically attractive with believable fuel price scenarios. Technical results are encouraging, and the program is progressing with increasing confidence from engineering feasibility through component development to systems integration.

References

Anson, D., Barber, S. A., Feldmann, H. F., and Gurney, M. D., 1987, "Development Plan for a Coal/Water Slurry Fired Diesel Engine for Cogeneration Applications," DOE Contract No. AC02-86CE40747, July.

Argonne National Laboratory, 1988, "An Assessment of the Natural Gas Base in the United States," prepared for U.S. DOE Office of Policy and Planning, May.

Arthur D. Little, Inc., 1986, "Coal Fueled Diesel Systems for Stationary Power Applications," Topical Report for DOE Contract No. DE-AC21-85MC22182, Sept.

Arthur D. Little, Inc., 1988, "Coal-Fired Diesel Systems Research," Final Report for DOE Contract No. DE-AC21-85MC22182, Sept.

Ayers, W. J., Strickland, L. D., Leep., J. R., and Wojewodka, R. A., 1988, "Diesel Engines Liquid Fossil Fuels, a Scoping Study," presented at the Annual Coal Fuel Heat Engines and Gas Stream Cleanup Systems Contractors Review Meeting, June.

Bell, S. R., and Caton, J. A., 1985, "Cycle Simulation of Reciprocating, Internal-Combustion Engines Using Coal-Slurry Fuels," presented at the Spring States Section/Combustion Institute Meeting, Paper No. 2-1A, Apr.

Bhasin, A. K., et al., 1984, "Manufacture and Testing of Ultra-Clean Coal–Water Slurry Fuels for Direct-Fired Gas Turbines," Final Report prepared for DOE/METC, Report No. DOE/MC/20700-16365, Aug.

Carpenter, L. K., and Crouse, F. W., Jr., 1985, "Coal-Fueled Diesels, Fossil Energy Activities," ASME Paper No. 85-DGP-18.

Carpenter, L. K., Crouse, F. W., Jr., and Halow, J. S., 1985, "Coal-Fueled Turbines: Deposition Research," ASME Paper No. 85-GT-213.

Carpenter, L. K., and Crouse, F. W., Jr., 1986, "Coal-Fueled Diesels: Progress and Challenges," ASME Paper No. 86-ICE-6.

Caton, J. A., 1986, "Coal-Fueled Diesel: Cycle Simulation," Technical Report prepared for DOE/METC, Report No. DOE/METC/21175, Oct.

Crouse, F. W., Jr., 1984, "Proceedings of the 1st Annual Heat Engines Contractors Review Meeting," Topical Report prepared by DOE/METC, Report No. DOE/METC/84-31, Nov.

Crouse, F. W., Jr., 1985, "Proceedings of the 2nd Annual Heat Engines Contractors Review Meeting," Topical Report prepared by DOE/METC, Report No. DOE/METC/86-6023, May.

Crouse, F. W., Jr., 1986, "Proceedings of the 3rd Annual Heat Engines Contractors Review Meeting," Topical Report prepared by DOE/METC, Report No. DOE/METC/86-6041, May.

Cummins, L., 1985, "Birth of the Diesel Dynasty," *Diesel Progress*, 50th Anniversary Supplement, pp. 12–30.

Dellefield, R. J., and Webb, H. A., 1988, "Proceedings of the Annual Coal-Fueled Heat Engines and Gas Stream Cleanup Systems Contractors Review Meeting," Topical Report prepared by DOE/METC, Report No. DOE/METC/88-6094, June.

Flynn, P. L., and Hsu, B. D., 1988, "Coal-Fueled Diesel Developments," presented at the SAE Future Transportation Technology Conference and Exhibition, Aug.

Gentry, R. A., 1986, "Numerical Analysis of Coal-Fired Diesel Engines," presented at 3rd Annual Heat Engines Contractors Meetings, DOE/METC, Report No. DOE/METC/86-6041, May.

Gurney, M. D., 1984, "Combustion of Coal Slurry Fuels in a Diesel Engine," Final Report prepared for DOE/METC, 2 Vols., Nov.

Hapeman, M. J., and Savkar, S. D., 1986, "Economic Assessment of Coal Burning Diesel Locomotives," ASME Paper No. 86-ICE-14.

Hapeman, M. J., and Savkar, S. D., 1987, "Economic Assessment of Coal Burning Locomotives," presented at the 1987 ASME Joint Railroad Conference, Apr.

Hsu, B. D., 1988, "Progress on the Investigation of Coal–Water Slurry Fuel Combustion in a Medium Speed Diesel Engine: Part 1—Ignition Studies," ASME Journal of Engineering for Gas Turbines and Power, Vol. 110, pp. 415–422.

Hsu, B. D., 1988, "Progress on the Investigation of Coal–Water Slurry Fuel Combustion in a Medium Speed Diesel Engine: Part 2—Preliminary Full Load Test," ASME Journal of Engineering for Gas Turbines and Power, Vol. 110, pp. 423–430.

Hsu, B. D., Leonard, G. L., and Johnson, R. N., 1989, "Progress on the Investigation of Coal-Water-Slurry Fuel Combustion in a Medium-Speed Diesel Engine: Part 3—Accumulator Injector Performance," ASME Journal of Engineering for Gas Turbines and Power, this issue.

Im, C., and Wolfe, R. A., 1985, "Conceptual Design and Economic Analysis for the Manufacture of an Ultra-Clean Coal/Water Mixture," Topical Report Prepared by United Coal for DOE/METC, Report No. DOE/MC/20122-11722, Feb.

Kakwani, R. M., Kamo, R., Smith, W. C., and Cutlip, R. G., 1989, "Combustion Characteristics of Dry-Coal Powder Fueled Adiabatic Diesel Engine," paper accepted at the ASME-ETCE Conference, January 1989.

Kamo, R., Kakwani, R. M., Woods, M. E., and Carpenter, L. K., 1986, "Introduction of Micronized Coal in the Intake Air of a Medium-Speed Adiabatic Diesel Engine," ASME Paper No. 86-ICE-19.

Keller, D. M., Jr., 1983, "Coal Refining by Physical Methods for the Preparation of Coal Slurries With Less than One Weight Percent Ash," presented at the 5th International Symposium on Coal Slurry Combustion and *Technology, Tampa, FL*, Apr.

Koch, R. L., Curry, C. E., Mason, D. L., and Slezinger, J. D., III, 1986, "Commercialization Considerations for a Coal-Fueled Diesel Locomotive," ASME Paper No. 86-ICE-5.

Leonard, G. L., and Fiske, G. H., 1986, "Combustion Characteristics of Coal/Water Mixtures in a Simulated Medium-Speed Diesel Engine Environment," ASME Paper No. 86-ICE-15.

Likos, W. E., and Ryan, T. W., 1988, "Experiments With Coal Fuels in a High-Temperature Diesel Engine," ASME Journal of Engineering for Gas Turbines and Power, Vol. 110, pp. 444–452.

Morrison, L. H., 1928, "The Coal Dust Engine—Details of the Design," *Power*, Vol. 68, pp. 746–748.

Nelson, P., 1986, "Combustion of Coal–Water Mixtures in Conventional Diesel Engines," presented at the 3rd Annual Heat Engines Contractors Meeting, DOE/METC, Report No. DOE/METC/86-6041, May.

Nydick, S., and Wang, C. C., Wang, 1984, "Development of Coal/Water Slurry-Fueled Diesel Engine for Industrial Cogeneration," Topical Reports prepared by Thermal Electron for DOE Office of Conservation, Contract No. DE-AC02-82CE40539, Task 1, Report No. DOE/CE/40539-01 (Fuel Preparation) and Task 2, Report No. DOE/CE/40539-02 (Thermodynamic Analysis), May.

Nydick, S., 1986, "The Development of Coal/Water Slurry-Fueled Diesel Engine for Industrial Cogeneration," Topical Report prepared for the DOE Office of Conservation/Industrial Programs," Report No. DE-AC02-82CE40539-04, Apr.

Pawlikowski, R., 1928, "The Coal Dust Engine Upsets Tradition," *Power*, Vol. 68, pp. 136–139.

Prater, J. T., and Courtwright, E. L., 1985, "Combustion Zone Durability Program," Final Report prepared for DOE/METC, Report No. PNL-5259, Jan.

Rao, A. K., Melcher, C. H., Wilson, R. P., Balles, E. N., Schaub, F. S., and Kimberly, J. A., 1988, "Operations Results of the Cooper-Bessemer JS-1 Engine on Coal–Water Slurry," presented at the ASME 1988 Energy Sources and Technology Conference, Jan.

Robben, F., 1983, "Coal-Fueled Diesel Engines," SAE Paper No. 831747.

Robben, F., et al., 1984, "Coal-Fueled Diesel Engines," presented at the 6th International Coal Slurry Combustion Conference, prepared under Contract with DOE/METC, June.

Ryan, T. W., 1986, "Combustion Characteristics of Coal Fuels in Adiabatic Diesel Engines," presented at the 3rd Annual Heat Engines Contractors Meetings, DOE/METC, Report No. DOE/METC/86-6041, May.

Siebers, D. L., and Dyer, T. M., 1985, "The Auto-Ignition and Combustion of Coal–Water Slurry Under Simulated Diesel Engine Conditions," presented at the ASME 1985 Energy Sources Technology Conference, prepared under Contract with DOE/METC, Feb.

Shadbolt, C. F., 1986, "Advanced Diesel Research Engine Test Facility," presented at the 3rd Annual Heat Engines Contractors Meetings, DOE/METC, Report No. DOE/METC/86-6041, May.

Soehngen, E. E., 1976, "Development of Coal-Burning Diesel Engines in Germany," Final Report prepared for the Energy Research and Development Administration/Office of Fossil Energy, Report No. FE/WAPO/3387-1, Aug.

Steiger, H. A., 1985, "Sulzer, Single Cylinder Test Results With Various Coal–Water Slurries," Seminar Presentation, Coal-Fueled Diesel for Cogeneration, DOE Office of Conservation, Chicago, July.

Urban, C. M., McCredy, H. E., Ryan, T. W., Ingalls, M. N., and Jett, B. T., 1988, "Coal–Water Slurry Operation in an EMD Diesel Engine," presented at the ASME 1988 Energy Sources and Technology Conference, Jan.

U.S. DOE Morgantown Energy Technology Center, 1985, "Coal Fueled Heat Engines: Technology Status Report," Oct.

Wilson, R. P., 1986, "Coal-Fueled Diesel Engines for Stationary Power," presented at the 3rd Annual Heat Engines Contractors Meetings, DOE/METC, Report No. DOE/METC/86-6041, May.

Environmental Aspects of Coal-Fueled Diesel Engines

M. C. Williams

N. T. Holcombe

M. McMillian

U.S. Department of Energy,
Morgantown Energy Technology Center,
Morgantown, WV 26507

Conventional diesel engines are considered by some to be contributors to environmental problems since they emit NO_x, a suspected acid rain precursor. Initial testing has shown that CWS-fueled diesels emit substantially reduced NO_x emissions. While emissions of particulates and SO_x may be potentially higher with coal fuels, assessment of the control technology indicates excellent potential for meeting existing and future standards for these emissions. As a result of activities managed by the Morgantown Energy Technology Center, the economic and technical feasibility of CWS-fueled diesel engines has been determined. Recently, both General Electric and A. D. Little/Cooper Bessemer were selected for 5-year contracts aimed at developing by 1993 the components and subsystems necessary for subsequent private sector demonstration and commercialization of coal-fueled diesel power systems. The development of these CWS-fueled systems will necessitate the application of hot gas cleanup contaminant control technology to ensure that the systems burn coal in an environmentally sound manner. The objective of this paper is to discuss the environmental concerns, emission goals, and the control methodologies, devices, and strategies that will be used to ensure CWS-fueled diesel engines will meet current and potential environmental standards.

Introduction

Since the late 1970s/early 1980s, the Department of Energy (DOE) has sponsored efforts to reassess the use of coal fuels in diesel engines (Carpenter and Crouse, 1986). Prior advancements in coal fuel processing and in engine materials of construction had led DOE to a point where it appeared technically feasible to burn clean, micronized coal in diesel engines. The incentive for the program continues to be a perceived need for modular, low-cost heat engines system for the 1990s for power generation, cogeneration (both process heat and electricity production), and transportation applications. Advanced coal-fueled systems are being developed with the objective of lowering the emission levels as compared to current diesel systems. Although technological hurdles still remain, researchers are obtaining encouraging results from diesel coal-fueled injection, combustion, emissions, and component wear tests.

The recent DOE awards of major contracts (Carpenter and Byam, 1987) to diesel engine manufacturers are structured to conduct the necessary additional research to develop coal-compatible components and emission controls and integrate the components into a full-scale, proof-of-concept engine test. General Electric Transportation Systems was selected to develop a locomotive diesel engine and Arthur D. Little with support from Cooper Bessemer was selected to develop a large, stationary engine for industrial/cogeneration applications. This development should be sufficient to allow subsequent private sector demonstration and commercialization of environmentally acceptable coal-fueled diesel power systems.

General Electric plans to lead a team of subcontractors in the development of a multicylinder (8 to 16-cylinder), coal-water, slurry- (CWS) fueled locomotive diesel engine. Building on technology developed in previous contracts, General Electric plans initially to test a CWS-fueled locomotive within 2 years. Tests will evolve from an engine test cell to actual track tests within the General Electric complex. A 1000-revolutions per minute (rpm), four-cycle, 3900-hp engine will ultimately be tested in an actual railroad operational environment.

The A. D. Little/Cooper Bessemer team will concentrate on a stationary diesel engine that could be used for cogeneration or small, modular utility applications in the 5- to 50-megawatt (MW) range. The product of the development effort will be a four-cycle, 400-rpm, 8000-hp, CWS-fueled engine. Beginning in 1991, a six-cylinder Cooper Bessemer engine will be tested for several hundred hours on CWS.

Included within these two contracts are key activities to characterize emissions from CWS-fueled diesel engines and develop control technology, that is, strategies or devices to minimize emission levels. The goal is to develop CWS-fueled systems that are environmentally superior to those systems that will be displaced.

Current emissions data from coal-fueled diesel engines are very limited. But in development tests to date, nitrogen oxide (NO_x) emissions from CWS combustion were shown to be 50 percent less than emissions from a diesel engine fueled with No. 2 diesel fuel (DF2).

With respect to sulfur oxide (SO_x) emissions, measurements

Contributed by the Internal Combustion Engine Division and presented at the Twelfth Annual Energy-Sources Technology Conference and Exhibition, Houston, Texas, January 22–25, 1989. Manuscript received by the Internal Combustion Engine Division October 1988.

have not been made, but, because of initially higher sulfur content in the fuel, untreated SO_x emissions should be higher for the CWS-fueled engine. In comparison, it should be recognized that specifications for DF2 permit sulfur contents as high as 1 weight percent (wt %); however, the value is usually on the order of 0.25 wt %. Typically, cleaned CWS fuel contains 0.5 wt % sulfur. In addition, because of higher inherent ash in the coal fuel, particulate emissions should also be higher. Although data are limited, it is generally recognized that emission controls will be required.

Environmental Concerns

Based on data to date, emissions of greatest concern for CWS-fueled diesel applications will be SO_x and particulates. NO_x is of additional concern, but initial data suggest that it will not be a major problem. Carbon monoxide (CO) and some hydrocarbons (HC) are troublesome during startup or system malfunction situations, but the combustion process is expected to be refined to minimize and possibly reduce these pollutants to levels below conventional DF2-fueled systems.

SO_x

The quantity of residual sulfur in CWS fuels reflects the amount of organic sulfur in the parent coal. Advanced physical and chemical coal cleaning processes effectively remove most pyritic sulfur in coals. But because coal seams vary in their characteristics, the level of sulfur may also be expected to vary. With the coal fuels tested to date, sulfur in the dry processed coal has typically been less than 1 wt %. During combustion the sulfur will appear as SO_x. The choices for SO_x control, which are discussed later in this paper, include both precombustion fuel processing and postcombustion cleanup.

Particulates

Particulate emissions, like SO_x emissions, directly correlate with the amount of ash in the fuel. Particulate matter emissions consist of the mineral content of the coal, plus the unburned carbon passing through the engine. Assuming that the coal fuel contained 1 wt % ash, the ash alone would contribute about 0.7 pound per million British thermal units (lb/MMBtu) to the exhaust. This number assumes 100 percent combustion efficiency. If combustion is 96 percent, the fly ash would contain about 80 wt % carbon and 20 wt % mineral ash. Therefore, the carbon portion of the fly ash would be about 2.8 lb/MMBtu and the total, 3.5 lb/MMBtu. Clearly, control techniques, as well as complete combustion, are needed. These are being addressed under current programs.

NO_x

NO_x is produced during combustion by thermal fixation of nitrogen in the combustion air and/or through oxidation of fuel-bound nitrogen. For conventional diesel engines, thermal NO_x is the primary source. In addition to thermal NO_x, it could be expected that for coal fuels additional NO_x would be generated due to fuel-bound nitrogen. However, in tests to date the fuel water content appears to suppress NO_x formation. In these tests (to be discussed later in this paper), the reduction is upward of 50 percent.

Review of Experimental and Analytical Data

Emissions measurements for all large (locomotive/industrial type) diesel engines are limited. Measurements with engines operating on coal fuels are generally unavailable. To date, four manufacturers have published limited full-scale engine test data with CWS fuel. The manufacturers who have tested the coal fuels include Sulzer, General Motors ElectroMotive Division with support from Southwest Research Institute, A. D. Little/Cooper Bessemer, and General Electric.

Sulzer. Table 1 is a summary of reported emissions data by Sulzer (Nydick et al., 1987). Tests were conducted on a large, low-speed, 120-rpm diesel engine. The 2000-hp, single-cylinder engine had a 30-in. bore and a 61-in. stroke. The 120-rpm engine had an 80-millisecond (ms) combustion residence time (CRT), which can be compared to an 18 ms CRT for 600 rpm engines or a 10 ms CRT for 1000-rpm engines.

Sulzer conducted tests with four types of coal fuel, all of which utilized a 50 wt % CWS. The coal ash and sulfur contents were all less than 1 wt %. Coal particle sizes differed for each fuel, varying from 5 to 15 μm mean particle size. The coal tests were conducted using a 3 wt % DF2 pilot.

Gas compositions were measured in parts per million (ppm). NO_x values were approximately 50 percent less than those obtained with DF2. Considering that the fuel-bound nitrogen content of the coal fuels was nearly 2 percent compared to nearly zero for DF2, the reduction was a significant finding. It was concluded that the reduction was largely attributed to the water content of the slurry. The water reduces the local combustion flame temperature, an effect that apparently suppresses thermal NO_x generation.

Particulates emissions were measured, but the amount was less than the coal ash being digested, which suggests that not all of the ash was accounted for. At 90 percent load, the particulate rate was approximately one-half the ash generation rate. Although the particulate was reported in units of mg/

Table 1 Sulzer test data

Fuel	AMAX Fine Slurry				Resource Slurry				AMAX Course Slurry				DF2			
Test Number	M55	M56	M57	M58	M65	M66	M67	M68	M77	M78	M79	M80	M81	M82	M83	M84
Load (Percent)	90	75	50	25	90	75	50	25	90	75	50	25	90	75	50	25
Speed, rpm	120	120	120	120	120	120	120	120	120	120	120	120	120	120	120	120
NO_x, ppm	610	760	740	370	430	640	600	380	408	590	590	315	1,565	1,780	1,695	1,520
CO, ppm	82	63	40	60	90	50	53	68	94	70	77	147	110	58	84	90
HC, ppm	60	60	85	80	70	60	74	80	55	50	53	70	76	80	100	100
Total Particulates, mg/nm^3	99	NM	NM	NM	135	116	168	102	82	69	69	78	NM	NM	NM	NM

NM = Not measured.

Table 2 General Motors ElectroMotive-Southwest Research coal-slurry emission test results

	Test Number						
	17-3	22-1	Average	17-5	22-2	23-1	23-2
Fuel Type	DF2			DF2 and CWS			
rpm	806	801	804	806	806	794	805
Power	144	147	146	140	152	136	140
Diesel Fuel Rate, lb/hr[1]	70	70	70	44	45.1	45.2	45.2
Pilot Diesel, lb/hr	--	--	--	10.2	10.3	10.1	9.4
Pilot Timing, Deg BTC	--	--	--	35	35	45	55
Coal-Slurry Rate, lb/hr	--	--	--	78.6	93.0	80.3	79.5
HC Measured, ppm	140	198	169	190	260	218	240
HC Coal Only, ppm[2]	--	--	--	240	322	267	311
CO Measured, ppm	817	992	904	ND	ND	779	ND
CO Coal Only, ppm[2]	--	--	--	ND	ND	858	ND
NO_x Measured, ppm	947	786	866	676	601	601	671
NO_x Coal Only, ppm[2]	--	--	--	486	336	336	476
Particulate Measured, mg/scf	1.62	2.91	2.26	13.0	32.4	31.9	27.0
Particulate Coal Only[2], mg/scf of Exhaust	--	--	--	23.7	62.5	61.5	51.8

[1] Includes pilot injection.

[2] Based on average of 17-3 and 22-1.

Deg BTC = Degrees before top center.

Fanick, E. R., and Ingalls, M. N., "Coal-Fueled Diesel Engine Exhaust Emissions Assessment," Southwest Research Institute Topical Report for DOE/METC, October 1987.

Table 3 Estimated diesel locomotive emission factors

	Emission Factors/No Environmental Controls, lb/MMBtu	
	CWS-Fueled Diesel	DF2-Fueled Diesel
HC	0.317	0.317
CO	1.43	1.43
NO_x	2.04	4.08
SO_x	0.86 - 1.54	0.25
Particulate	0.43 - 0.77	0.15

nm^3, it is believed that the values are in milligrams per cubic meter.

For the Sulzer data, the HC emissions for coal-slurry fuels were always less than those for the DF2 baseline. These data are not consistent with other published data, but the lower Sulzer trends suggest that their engine was operating at very desirable combustion efficiencies. Further substantiation of the good Sulzer operating characteristics are the low CO measurements, which were equivalent to well-tuned DF2 tests. No SO_x measurements were made.

General Motors/Southwest Research Institute. In support of General Motors ElectroMotive, Southwest Research Institute (Fanick and Ingalls, 1987) conducted a limited test program on a two-cylinder ElectroMotive-567 engine. The 1000-rpm, 9.5-in. bore engine was operated with one cylinder fueled with DF2 and one cylinder fueled with CWS. The coal-fueled cylinder was assisted with a DF2 pilot.

Table 2 is a summary of the Southwest Research Institute test results. Exhaust from the DF2- and CWS-fueled cylinders were not separated; thus the coal emissions data shown are a combination of both cylinders. The combined gaseous emissions of HC, CO, and NO_x were taken from the engine exhaust, passed through an ice trap, and pumped into a Tedlar bag. Particulate was determined from a diluted sample of the combined engine exhaust. Particulate was reported in milligram/standard cubic foot (mg/scf).

Since the engine speed and load conditions were essentially the same for all six test points, an attempt was made to calculate the coal-burning cylinder emission concentrations. It was assumed that with DF2, each cylinder produced equal concentrations of emissions and that when burning CWS in one cylinder, the diesel cylinder still produced the same emissions it did when both cylinders were run on DF2. Thus, DF2 emissions were subtracted from the CWS-fueled tests.

Except for HC emissions, which were higher, the Southwest Research Institute data provided trends similar to those from the Sulzer data. NO_x tended to be half of that generated by DF2-fueled engines, while CO emissions appear to be comparable.

The particulate emissions from the CWS-fueled cylinder were approximately 10 to 30 times the particulate emissions obtained when both cylinders were burning DF2. These numbers are higher than the Sulzer values but still are less than what would be expected considering that the coal ash content is approximately two orders of magnitude greater than that of DF2.

It is of interest that Southwest Research Institute used their test data to develop an estimate for potential locomotive emission factors. The SO_x factor was calculated under the reasonable assumption that fuel sulfur is directly converted to exhaust SO_x. Table 3 contains a summary of the Southwest Research Institute estimate for locomotive-type, CWS-fueled diesel systems as they compare to DF2-fueled systems. The values are for systems that are not equipped with environmental controls. The CWS-fueled differences include:

- a 50 percent reduction in NO_x;
- an increase in SO_x emissions, shown as a variable to account for coal sulfur content (varying between 0.6 and 1.0 wt %) and heating value (varying between 13,000 and 14,000 Btu/lb); and

- particulate emissions, which may be up to five times that of DF2-fueled systems.

From the experimental and analytical data, it is obvious that SO_x and particulates are the major pollutants of concern. Programs ongoing are further characterizing engine exhaust streams and developing control methodologies to address SO_x, particulate, and other emissions from CWS-fueled diesel engines.

A. D. Little/Cooper Bessemer. Cooper Bessemer with the help of A. D. Little conducted a series of CWS-fueled engine tests in late 1987 (Rao and Melcher, 1988). The tests were a part of a 3-year DOE program to advance coal-fueled diesel engine technology. That effort will continue via a separate contract through fiscal year 1992. The new contract is designed to bring current technology to commercialization.

Emissions measurements were performed in 1987 on a single-cylinder, JS-1 research engine. The JS-1 engine is a 13-in. bore, 16-in. stroke, four-cycle engine with a nominal output of 160 brake horsepower (bhp) at 400 rpm. Both CWS and DF2 were tested and their performances compared using DF2 as a baseline. Two types of CWS were used during the test series, the specifications of which are given in Table 4. Table 5 is a partial summary of the test results.

Table 4 A. D. Little/Cooper Bessemer fuel specifications

CWS Specifications	AMAX Coarse	AMAX Fine
Coal Content (Wt %)	53	53
Ash Content (Wt %)	0.20	0.25
Lower Heating Value (Btu/lb)	7,280	7,280
Viscosity (cp) at 100°F to 1,000 sec^{-1}	180	180
Particle Size (Wt % Less Than)	Microns	Microns
98 Percent	65	45
90 Percent	38	27
50 Percent	11	8
13 Percent	2	1
Proximate Analysis (Dry Wt %)		
Ash	0.4	0.5
Volatiles	41.5	40.9
Fixed Carbon	58.1	58.6
Sulfur	1.1	1.1
Coal Type	High Volatile A Bituminous Kentucky Splint	

The effects of variations in manifold air temperature (MAT), pilot fuel quantity, pilot fuel timing, size of injector nozzle holes, and the fuel type on engine performance and emissions were investigated. During testing the engine was always started on DF2 and switched over to CWS. For all the runs discussed in this section, the pilot fuel was diesel and the nominal engine speed and break mean effective pressure (BMEP) were 400 rpm and 150 lb/in.^{2} (psi), respectively.

The results show equivalent exhaust air levels for both DF2 and CWS (about 90 to 110 percent). In theory, clean coal requires 3 to 5 percent more air than DF2 to release the same amount of energy in combustion because of its higher carbon-hydrogen ratio.

Tests at 100 to 200°F MAT showed NO_x reductions of 32 to 68 percent compared to DF2 under the same conditions. This reduction is similar to other results and stems from the reduction of local peak flame temperatures due to fuel water content. Interestingly, in the tests that were run at elevated MAT (330 to 440°F), the NO_x levels for CWS and DF2 did not differ significantly (see Table 5). Of additional interest, a larger fuel nozzle size (0.30 millimeter [mm] versus 0.25 mm) produced a 30 percent reduction in NO_x (compare runs 2 and 7 in Table 5). This latter effect was also observed with DF2.

NO_x, CO, and carbon dioxide (CO_2) levels were very similar for runs 5 and 6, 15 percent DF2 pilot versus no pilot. A slight increase in CO might indicate poorer combustion in the case of no pilot. The exhaust gas analysis revealed no significant difference in CO, NO_x, or CO_2 (compare runs 4 and 9 in Table 5).

Although SO_x measurements were not performed during this test series, the high level of combustion performance would indicate that nearly all of the fuel-bound sulfur will end up as SO_x in the exhaust.

For the given test conditions, the CO/CO_2 ratio was less than 0.5 percent, indicating excellent carbon burnout.

General Electric Transportation Systems. General Electric conducted a series of coal-fueled engine tests in late 1987 (Hsu, 1987). The tests were a part of a 3-year DOE program to advance coal-fueled diesel engine technology. These efforts will continue via a new contract designed to bring current technology to commercialization.

General Electric has made significant progress on the investigation of CWS fuel combustion in a medium speed diesel

Table 5 A. D. Little/Cooper Bessemer measured exhaust gas composition

Run No.	Fuel	Feature	Air Temperature, °F	CO_2, %	O_2, %	CO, ppm	NO_x, ppm As Measured	NO_x, ppm At 15% O_2	Excess Air, %	CO/CO_2 Ratio
1	Baseline DF2	Larger Hole	337	9.0	8.75	800	850	403	68	.009
2	CWS/DF2 Pilot	Larger Hole	344	8.7	10.6	360	750	426	100	.004
3	Baseline DF2	High Air Temperature	440	7.8	10.4	NA	1,250	697	92	NA
4	CWS/DF2 Pilot	High Air Temperature	439	8.5	11.2	210	1,200	725	108	.002
5	CWS/DF2 Pilot	Repeat Run 4	433	8.4	11.5	95	1,650	1,029	116	.001
6	CWS	No Pilot/High Air Temperature	434	8.3	11.6	150	1,440	907	120	.002
7	CWS/DF2 Pilot	Moderate Air Temperature	349	8.9	10.8	200	1,080	626	100	.002
8	Baseline DF2	High Air Temperature	425	7.6	10.7	510	1,325	864	98	.007
9	CWS/DF2 Pilot	Fine Coal	427	8.8	10.8	108	1,200	696	100	.001

All runs at 400 rpm, 150 psi BMEP; excess air variations were due to breathing effects (the excess air of trapped cylinder mixture was approximately constant for all runs); DF2 pilot, 14 percent of total fuel energy (when used).

Table 6 General Electric fuel specifications

	Kentucky	New Zealand
Proximate Analysis (Dry Wt %)		
Ash	1.01	0.36
Volatiles	41.5	40.9
Fixed Carbon	58.1	58.6
Ultimate Analysis		
Carbon	82.59	86.15
Hydrogen	5.34	5.15
Nitrogen	2.08	1.26
Chlorine	0.18	0.11
Sulfur	1.01	0.36
Oxygen	7.58	6.39
Mean Particle Size D_{50} Microns	4.63	2.88
High Heating Value (kJ/kg) (1 Btu/lb = 2.33 kJ/kg)	34,630	35,580

under full load conditions. Both CWS and diesel fuel were tested and their performances compared using diesel fuel as a baseline. Predominantly Kentucky Blue Gem coal CWS provided by OTISCA was used during the testing, but a New Zealand coal was also used. The coal compositions are shown in Table 6.

Full-load (186-kW/cycle) operation using coal–water slurry at 1050 rpm has been achieved on a single-cylinder General Electric-7FDL test engine of 229 mm bore and 267 mm stroke (25.4 mm/in.). The externally controlled inlet air pressure was raised to 722 kPa (105 psi) and the MAT heated to 401°F. No major changes in engine parameters were made. With normal inlet air conditions, 3 to 5 percent pilot, separately injected or stratified into the main coal charge, was used.

The coal burnout was about 95 percent and the cycle efficiency was comparable to that using DF2. The NO_x and CO emissions were about half those obtained normally with diesel fuel. SO_x and particulate emissions were not measured.

Contaminant Control Methodologies

A review of the contaminant control technologies most applicable to coal-fueled diesel systems has been conducted. The review provides insight and understanding of the technical issues that must be addressed in developing viable emission control strategies for diesel engine systems.

Diesel systems differ significantly from the systems for which these control techniques were developed. Consideration has been given as to whether the control strategy fits the application (mobile or stationary). The following are the most prominent methodologies being considered in ongoing programs aimed at developing coal-fueled diesel cleanup systems.

SO_x Control. The most likely place for sulfur removal is upstream of the turbocharger. Of several sulfur control strategies that have been investigated for other uses, the one most applicable to diesel systems is sorbent injection of a calcium-based material. Calcium hydroxide has been shown to be an effective sulfur sorbent in conventional power plant operation when injected into the inlet of the economizer, a device that operates in the 1000°F temperature range similar to that of gases exiting a diesel cylinder.

While much of the basic chemistry of hot gas stream sulfur removal is reasonably well understood, adapting it to diesel engine systems will pose many questions. These include determining:

- whether reaction times will be sufficient for sulfur absorption within the size limitations imposed on the diesel engine systems;
- what effect the water will have on the chemistry involved at these evaluated temperatures; and
- how the calcium-based sorbents will interact with particulate filters.

Particulate Control. As indicated in the previous section, particulates will result from the combustion of coal in diesel engine systems. In addition to being a pollutant, the particulate can cause damage to the turbocharger and heat exchange equipment. Therefore, it is desirable to remove the particulate upstream of the turbocharger in the engine exhaust manifold. The temperature in this region is approximately 1000°F; thus advanced hot gas cleanup technologies will be required.

Considerable research has been conducted for hot gas stream particulate removal. Technologies that have been investigated include barrier filters, granular-bed filters, cyclones, and electrostatic precipitators. However, few large-scale, hot-gas particulate cleanup tests have been conducted and none on diesel engine systems. Perhaps the most applicable technology for coal-fueled systems is high-temperature, compact barrier filters composed of ceramics or other nonmetallic materials arranged in a crossflow or pleated configuration. Research areas specific to diesel engines which are being addressed include both pre- and postcombustor considerations. The postcombustor considerations include:

- postcleanup coal ash handling;
- vibrational effects on particle reentrainment (for locomotive systems);
- strength of filter material;
- re-entrainment of particulates due to pulsing of the gas stream; and
- pressure drop through the filter system.

NO_x Control. As previously indicated, the use of CWS results in a significant reduction of NO_x from conventional systems. It is hoped that this reduction will be maintained as CWS-fueled systems are further developed. If not, however, there are several technologies that may be employed for further NO_x reduction. These include reburning selective catalytic reduction (SCR), the Raprenox process, and NO_xOUT. These processes are briefly discussed below.

Reburning. In this process additional fuel is added to the exhaust, which will create local fuel-rich pockets. These oxygen-starved pockets are known to destroy NO_x. Oxygen is stripped from the nitrogen oxides. This technique has been successfully applied to applications similar to diesel engine systems.

SCR. In this process ammonia is injected into the gas stream over a catalyst, whereby the NO_x is reduced to form nitrogen and water. This process has been successfully applied to utility boilers, but there are several potential problems for coal-fueled diesel application. The SCR only works in a narrow temperature range. In addition, at low temperatures the SCR reaction is slow or nonexistent, and at high temperatures the noble metal catalyst is destroyed.

Raprenox Process. This process is a relatively new process, which employs cyanuric acid to remove NO_x. This is an immature process that would require significant research to employ for the removal of NO_x from actual diesel exhaust gases.

NO_xOUT Process. The method involves injecting an aqueous solution of urea into the combustion system at various locations. This process may be effective in the temperature range of 750 to 2000°F.

Emission Level Goals

Currently, there are no emission standards applicable to large diesel engine systems. However, this will probably not be the case in the future. Thus, it is reasonable to anticipate emission standards and have these as goals for the development program. In anticipation of future emission standards, it is necessary to consider not only the size of the engine, but also the application. The two applications under consideration in-

Table 7 Environmental standards for diesels

Pollutant/ Effect	Emission Standards for Fossil-Fueled Systems: Current Locomotives	1985 Heavy-Duty Diesel Engines	1991 Heavy-Duty Diesel Engines	Federal NSPS* for Fossil-Fueled Fired Steam Generators (Heat Input Rate** Greater than 250 MMBtu/hr)	Federal NSPS for Fossil-Fueled Fired Steam Generators (> 29 MW or 100 MMBtu/hr)	Emissions from Distillate Fuel Oil-Fired Locomotives: Average Emissions from Distillate Fuel Oil-Fired Locomotives	Range of Emissions from Distillate Fuel Oil-Fired Locomotives (Road and Switch Service)	Expected Emissions from Coal-Water Slurry Diesel Engine****
Particulate Matter (PM)	No Standard	No Standard	0.1 gm/BHP-hr	.03 lb/MMBtu	.05 lb/MMBtu	0.18 lb/MMBtu (0.59 gm/hp-hr)***	No Range, Use Average	0.7-2 gm/hp-hr***
Sulfur Dioxide (SO_2)	No Standard	No Standard	No Standard	1.2 lb/MMBtu	1.2 lb/MMBtu	0.41 lb/MMBtu (1.35 gm/hp-hr)***	No Range, Use Average	3.0 gm/hp-hr***
Nitrogen Dioxide (NO_2)	No Standard	10.7 gm/BHP-hr	5.0 gm/BHP-hr	0.7 lb/MMBtu	0.70 lb/MMBtu	2.67 lb/MMBtu (8.81 gm/hp-hr)***	1.80 lb/MMBtu*** 3.53 lb/MMBtu***	5-6 gm/hp-hr***

* NSPS = New Source Performance Standards.
** Designed coal-fueled locomotives will likely have a heat input rate at full power of about 56 x 10 Btu/hr.
*** Heat input.
**** Assume thermal efficiency of diesel locomotive is 35 percent and fuel sulfur content is 0.4 percent.

(1) Sulfur Dioxide

Solid or Solid-Derived	Liquid or Gaseous
≤ 520 ng/J (1.20 lb/MMBtu).	≤ 340 ng/J (0.80 lb/MMBtu).
≥ 90 percent reduction in potential concentration or when emissions are less than 0.60 lb/MMBtu.	≥ 90 percent reduction in potential concentration.
≤ 260 ng/J (0.60 lb/MMBtu).	≤ 86 ng/J (0.20 lb/MMBtu).
≥ 70 percent reduction in potential concentration.	

Note: BHP-hr = Brake horsepower-hour = lph; where l = load factor (average power produced during an operation divided by available power), p = available horsepower, and h = hours of usage at load factor l.

Note: 1 hp-hr = 2,545.0 Btu (mean).

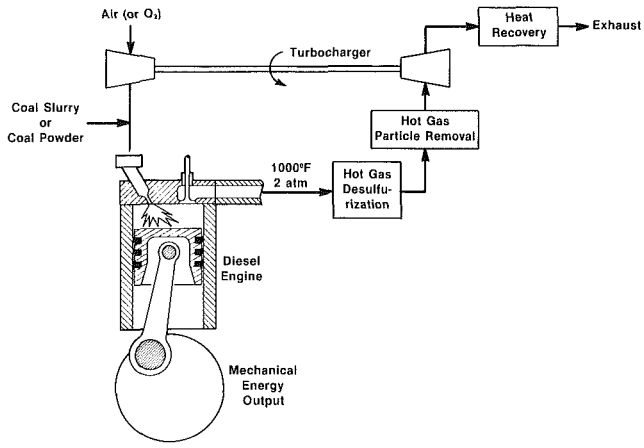

Fig. 1 Conceptual coal-fueled diesel system

clude mobile (locomotive) and stationary power source applications. Table 7 lists the emission goals that are being considered in development of coal-fueled diesel engine systems.

Locomotive Systems

Because of their dispersed operations and relatively low numbers, there are no current emission standards for locomotives. However, there are emission standards (1985) for heavy-duty diesel engines (trucks) for NO_x, which are listed in Table 7. Standards for particulates and revised standards for NO_x are anticipated in 1991. These are also listed in Table 7 and are addressed below.

SO_x Emissions. Currently, there are no SO_x emission standards for heavy-duty diesel engines. However, should the NSPS be applied, it can be met for a large number of coals from different regions of the country by first physically cleaning the coal and then performing 50 percent postcombustion sulfur capture. This postcombustion sulfur capture will be attainable by employing hot gas stream cleanup technology.

Particulate Emissions. Currently, there are no particulate emission standards that apply to diesel engine systems. However, there will be emission standards in 1991 for heavy-duty (truck) diesel engines of 0.03 lb/MMBtu. This is approximately the same as the NSPS requirement for plants greater than 73 MW.

The average particulate emissions from distillate fuel petroleum-fueled locomotives is 0.18 lb/MMBtu (0.59 gm/hp-h). It is reasonable to have the same emission requirements as competing technology. Thus, a value of 0.03 lb/MMBtu is a reasonable goal and one that can be met with advanced control technologies.

NO_x Emissions. The 1985 emission standards for NO_x for heavy-duty diesel (truck) engines is 10.7 gm/BHP-h (Table 7). In 1991 this level will be reduced to 5.0 gm/BHP-h. For comparison, the current average emission for distillate-fueled locomotives is 2.7 lb/MMBtu (8.8 gm/hp-h). This represents a 34 percent reduction by 1991 if these standards are to be applied to locomotives. For comparison, the NSPS for fossil-fueled steam generators is 0.7 lb/MMBtu. If the NSPS were to be applied to distillate-fueled stationary diesel engines, it would mean almost a 73 percent reduction in NO_x. The NSPS for steam generation seems to be excessive for locomotive systems and the most likely target for locomotive sources is considered to be the 1991 truck standard.

From the limited testing of CWS-fueled diesel engine systems, the NO_x should be less than 50 percent of the DF2-fueled diesel engine. Thus, the CWS-fueled engine should not have any difficulty meeting the proposed truck standards. In fact, if more stringent standards were to be applied to diesel locomotives, the CWS-fueled engine might form the basis for this standard.

Stationary Power Systems

While there are no current emission requirements applicable to stationary power systems, there are two sets of emission standards that may be applicable in the future. These are the NSPS for fossil fuel-fired steam generators greater than 29 MW and for fossil fuel-fired steam generators greater than 73 MW. These emission requirements are summarized in Table 7.

SO_x Emissions. The SO_x emission standard for stationary sources is 1.2 lb/MMBtu. However, it can be met for a large number of coals from different regions of the country by first physically cleaning the coal and then performing postcom-

bustion sulfur capture. This postcombustion sulfur capture will be attainable by employing advanced cleanup technology.

Particulate Emissions. Particulate emission standards that most likely will apply to stationary diesel engine systems will be from 0.03 to 0.05 lb/MMBtu. This is a reasonable goal and one that can be met with advanced control technologies.

NO_x Emissions. The current emission standard for NO_x for stationary sources is 0.7 lb/MMBtu. To meet this standard, the NO_x emissions would have to be reduced to 73 percent of those of conventional diesels. Since the NO_x is already less than 50 percent of the conventional-fueled diesel engine, the CWS-fueled engine may be able to meet this proposed standard through performance optimization.

The NSPS requirements (for SO_x, NO_x, and particulate) for systems larger than 73 MW seem to be reasonable as emission goals for stationary source applications since they apply to the currently competing technology.

Summary

In the United States today, it is not enough that a prime mover be an efficient producer of power; the engine must also be environmentally acceptable. If a new engine type is to replace a current engine successfully, the engine should produce no more and preferably less emissions than the current engine type.

Coal-fueled diesel engines are being developed with the goal of being environmentally superior to current technology. The major emission contaminant from conventional diesel engines has been NO_x, although data to date suggest that a comparable CWS-fueled diesel engine will produce less than one-half the amount of NO_x. SO_x and particulates appear to be the major concern for CWS-fueled diesel engines.

Emission controls will be required and are being developed. These may include the injection of a sorbent into the hot gas stream to capture sulfur compounds. In addition, filters or cyclones may be needed to remove particles and sorbent material. Catalytic techniques may be used to remove NO_x and/or SO_x. These and other techniques are currently being studied and integrally developed for CWS-fueled diesel engines.

The application of coal to diesels can be accomplished without a negative effect on the environment. In fact, with the development of reasonable hot gas cleanup technologies, the CWS-fueled engine systems should be less polluting than current diesel-fueled engines. The Department of Energy program in CWS-fueled diesel development constitutes a major step forward in developing coal-based power systems while mitigating the potential for acid rain production. Systems that will be operating within the next 5 years will demonstrate this ability to burn coal while reducing the emissions of suspected acid rain precursors from diesel engine systems.

References

Carpenter, L. K., and Byam, J. W., Jr., 1987, "Coal-Fueled Diesels: Technology Developments," presented at the Energy Conference and Exhibition, Washington, DC.

Carpenter, L. K., and Crouse, F. W., 1986, "Coal-Fueled Diesels: Progress and Challenges," presented at the Energy Sources Technology Conference, New Orleans, LA.

Fanick, E. R., and Ingalls, M. N., 1987, "Coal-Fueled Diesel Engine Exhaust Emissions Assessment," Southwest Research Institute Topical Report for DOE/METC.

Hsu, B., 1987, "Progress on the Investigation of Coal–Water Slurry Fuel Combustion in a Medium-Speed Diesel Engine. Part 2. Preliminary Full Load Test," Topical Report for DOE/METC.

Nydick, S. E., Porchet, F., and Steiger, H. A., 1987, "Continued Development of a Coal-Water, Slurry-Fired, Slow-Speed Diesel Engine. A Review of Recent Test Results," ASME Paper No. 87-ICE-10.

A. K. Rao
Cooper-Bessemer Reciprocating,
Grove City, PA

R. P. Wilson, Jr.

E. N. Balles

R. A. Mayville
Arthur D. Little, Inc.,
Cambridge, MA 02140

M. H. McMillian
Morgantown Energy Technology Center,
Morgantown, WV 26505

J. A. Kimberley
Ambac International, Inc.,
Springfield, MA

Cooper-Bessemer Coal-Fueled Engine System—Progress Report

Single-cylinder engine tests were conducted as part of a long-range effort to develop a technology base for coal-fueled stationary modular power plants based on the Cooper-Bessemer LS Series four-stroke diesel engine. These engine test results established the new state of development for this technology as well as setting priorities for the remaining R&D effort on specific components. The current outlook on the overall economics of coal diesel power is presented, indicating that CWS processing cost dominates the question of economic feasibility. A description of the coal-tolerant fuel injection system development is also given. Wear results indicate that nozzle erosion is the critical element in extending the duration of continuous engine operation. Substantial nozzle wear was observed in just two hours of CWS operation. The ash content of the coal was found to affect the wear rate of the ring set as well as the nozzle tip. Combustion results indicate that the natural gas jet cell is a viable ignition aid and that the variable area poppet nozzle, which lends itself to the use of durable coatings, provides satisfactory engine performance.

Introduction and Background

The JS engine tests described below were conducted as part of a long-range effort to develop a technology base for coal-fueled stationary modular power plants with low emissions, based on the Cooper-Bessemer LS Series four-stroke diesel engine. This effort is one of several parallel projects that make up the DOE/METC Heat Engines Program (McMillian and Webb, 1989).

In earlier papers (Balles et al., 1987; Rao et al., 1988; Benedek et al., 1988), operating results of the first tests of the Cooper-Bessemer JS-1 engine on coal-water slurry were reported. The focus of these papers was on ignition, combustion, cycle efficiency, and emissions. Successful engine operation was achieved at both part load and full load, and this is the first important step for the coal diesel technology to become viable for stationary power plants. However, additional development challenges include:

- Durability and wear rate of critical engine components
- Development of reliable coal-tolerant fuel injection system, including metering, timed injection, and atomization
- Overall economics of coal diesel power, considering the efficiency, cost of clean coal slurry fuel, and cost of emission control

The results reported below constitute a progress report on the first two technology areas (durability and injection system). As described below, these test results not only establish the new state of development for this technology, but also help us set priorities for the remaining R&D effort on specific components.

Contributed by the Internal Combustion Engine Division and presented at the Twelfth Annual Energy-Sources Technology Conference and Exhibition, Houston, Texas, January 22–25, 1989. Manuscript received by the Internal Combustion Engine Division August 1988.

However, before turning to this progress report, we will summarize the current outlook on the overall economics of coal diesel power, in light of the exploratory JS engine test results that have become available since the earlier system study (Wilson, 1986). The economic viability of coal diesel power has been analyzed in detail based on assumptions regarding:

- Maintenance and overhaul estimates for coal engine operation
- Specific emission control costs
- Engine efficiency for coal versus DF2
- Coal processing cost estimates and raw coal costs

The economic analysis gives perspective on the conditions under which the coal diesel could be cost competitive with oil or gas-fueled stationary engines. Our conclusions, as discussed below, are that (1) the current best-estimate projected cost of coal diesel power is 6.54 ¢/kWh, with an uncertainty of about ± 20 percent; (2) economic viability hinges on the cost of CWS production more than any other single factor (specifically, slurry price must be kept below about $2/million Btu above the source coal price); and (3) emission control costs have emerged as the second most important parameter.

Engine-Related Cost Premiums Associated With Coal. The use of beneficiated coal slurry will necessitate certain modifications to the standard large diesel engine, both in terms of special components and special maintenance practices. The engine components expected to be affected by coal fuel are generally "moving parts," which are exposed to either the fuel or the products of combustion. Although the precise nature of these modifications cannot be determined until the research and development is complete, it is still useful to project ap-

Table 1 Impact of coal fuel on maintenance and overhaul practices

Item	Standard Diesel	Coal Diesel
Injectors	2,000 hr.	500 hr.
Minor Maintenance Checks	8,000 hr.	4,000 hr.
Top-End Overhaul	25,000 hr.	12,000 hr.
Major Overhaul	70,000-100,000 hr.	25,000 hr.

proximate cost premiums. The estimated cost premium associated with the modification of these components is $1.67 million. That is, the standard 6-MW engine costs $3.5 million, whereas the future coal-fueled version is projected to cost $5.2 million, on an installed basis.

On a per-kWh basis, this capital cost translates to 1.21 cents per kWh versus 0.81 cents per kWh for the standard oil or gas engine, based on 20-year life and 80 percent load factor. This premium of 1.21 − 0.81 = 0.40 cents per kWh is exclusive of emission control equipment costs, which are accounted for separately below.

The present maintenance practices for a 6-MW Cooper engine are compared to the expected coal diesel practices (as revised in view of JS test results) in Table 1.

The cost premium associated with this increased level of maintenance and overhaul is projected to be 0.33 ¢/kWh.

In summary, the total cost premium for a 6-MW Cooper-Bessemer coal diesel compared to an oil-fired diesel of comparable size is projected to be about 0.73 ¢/kWh, including both capital cost and maintenance. Although this premium is significant, it is still by no means prohibitive, since the standard cost of diesel fuel alone can range from about 3 to 5 ¢/kWh, depending on prevailing fuel prices.

Cost to Produce Engine-Grade Coal Fuels. An essential ingredient in the future of coal-fueled diesels is the eventual emergence of a price advantage of the engine-grade coal fuel. Recognizing that (*a*) fuel oil prices will almost certainly rise, and (*b*) the extent and timing of the oil price increase is virtually unpredictable, we focused our attention on the coal slurry fuel cost and how it might be reduced as much as possible. Our findings are based on detailed inputs from AMAX and other leading manufacturers of coal slurries, followed by an independent analysis of production costs. Key assumptions were as follows:

- Dedicated engine-grade slurry facility; plant incorporates cogeneration using the high ash coal by-products from physical cleaning.
- Plant capacity: 1.8 million tons per year (supports 100 engines at 5 MW).
- Coal price: $1.50 per million Btu, delivered to slurry plant (includes $0.46/MMBtu for transportation cost ($12/ton for 400 miles) plus $27/ton for mine-mouth coal).
- Electricity: 175 kWh/ton.
- Capital recovery costs: 10 percent interest/12 year payback.

The results of this analysis indicate that engine grade slurry will cost about $2.50 per million Btu more than the source coal. This coal cleaning cost will add $0.022/kWh to the cost of power. "Low" and "high" estimates of this coal cleaning cost premimum are $1.66 and $3.00 per million Btu.

Table 2 Estimated cost of coal diesel power

Cost Element	Contribution to Cost of Power
Installed Engine Capital Cost	$ .0121/kWh
Cost of O & M	.0052/kWh
Raw Coal incl./Transp. ($1.50/MMBtu)	.0131/kWh
CWS Fuel Process Cost ($2.52/MMBtu)	.0220/kWh
Emission Control Cost ($1.18/MMBtu)	.0103/kWh
Slurry Transportation Cost	.0027/kWh
Total Cost of Power Using Coal Diesel	$ .0654/kWh
Sensitivity Analysis:	
o 50% Higher emission cost ($1.78/MMBtu)	$ .0706/kWh
o 25% Lower CWS Process Cost ($1.84/MMBtu)	.0595/kWh
o Both of above	.0647/kWh

There is one area where further process developments could reduce the cost of engine-grade slurries. The additives and reagents that currently account for about 30 percent of the slurry cost have not been optimized. These additives and reagents are needed to keep the coal particles in suspension and to tailor viscosity. Further effort is needed to identify lower cost formulations that perform these functions.

Factors Most Important to Viability. Based on the individual cost premiums for installing and operating a diesel engine designed for coal fuel, it is possible to determine the relative importance of each economic parameter. Our key findings from this analysis can be presented in the form of Table 2, which lists various estimates for key economic parameters. Note that both the capital cost and O&M premiums are in the acceptable range, no matter which estimate is taken. This suggests that the coal engine designer can afford to consider more expensive components if that results in an engine that tolerates lower cost coal fuel.

The most important parameter is the cost to clean the coal fuel, which essentially dominates the question of economic feasibility. If engine-grade slurry costs can be brought below $2/million Btu above the source coal, then the coal diesel can probably be competitive with diesel fuel by 1995, given long-range oil price trends.

Another important parameter is the engine efficiency associated with coal fuel. Based on the JS test results, our best estimate is that the coal engine efficiency will be 39 percent, identical to the standard Cooper engine. The penalty derived from slurry water evaporation (2–3 percent) appears to be compensated by faster heat release and other thermodynamic processes.

The final economic parameter is emission control cost, which must include control of sulfur oxides, particulates, and NO_x. As shown in Table 2, emission control costs in the range of $0.78 to $1.78/MMBtu are projected. This reflects both the JS test results on particulate emission level and further cost analysis of SO_x, NO_x, and particulate control equipment.

Nomenclature

ATC = After Top Center
bmep = brake mean effective pressure
bsfc = brake specific fuel consumption
BTC = Before Top Center
CWS = Coal-Water Slurry
DF2 = Number 2 Diesel Fuel
l/d = length-to-diameter ratio
NG = Natural Gas
O&M = Operation and Maintenance

Conversion Factors

1 Btu = 1.055 kJ
1 hp = 745.5 W
1 in. = 2.54 cm
1 MMBtu = 1055 MJ
1 psi = 6.895 kPa

Table 3 Model JS-1 test engine specifications

Configuration	Single-Cylinder, Four Stroke
Bore	13 in
Stroke	16 in
Connecting rod length	32 in
Compression ratio	10.5
Number of valves	4 (2 intake, 2 exhaust)
Valve diameter	4.125 in
Valve lift	1.250 in
Intake valve timing	1VO 59 BTC IVC23 ABC
Exhaust valve timing	EVO 50 BBC EVC13 ATC
Speed range	300-450 rev/min
Load range	100-200 psi bmep
Intake air temperature range	80 to 450°F
Intake air pressure range	0 to 50 in. Hg (gage)
Turbocharger	Simulated by exhaust orifice

Apparatus and Instrumentation

The Cooper-Bessemer Model JS-1 single-cylinder research engine was used for the exploratory tests with CWS that are described in this paper. This four-stroke diesel engine is designed to operate on natural gas, diesel fuel, or a combination of these fuels. As shown below, it will also operate for short periods on clean coal slurry, subject mainly to injector wear limitations. The intake air for this research engine is supplied from an external source and the air temperature and pressure can be independently adjusted to simulate a wide range of intake manifold conditions. An orifice plate in the exhaust manifolds simulates the pressure drop of a turbocharger. Engine specifications can be found in Table 3.

A special research cylinder head was designed and fabricated for CWS engine experiments. The cylinder head has four valves (2 intake, 2 exhaust) and can accept shrouded or unshrouded intake valves. A cross section of the cylinder head is shown in Fig. 1. The main injector is located centrally, and was used to inject CWS or DF2. There are two additional openings in the cylinder head, each of which may be fitted with a diesel pilot injector (shown in the right port), a "Jet Cell" natural gas torch ignitor (shown in the left port), or a cylinder pressure transducer. The Cooper-Bessemer JS-1 research engine is capable of using a diesel fuel pilot injector or a natural gas jet cell ignitor as an ignition aid. The pilot injector is a standard multihole diesel fuel nozzle (three to six holes) with a hole pattern specifically designed for the JS combustion chamber. Much of the CWS combustion study to date has used a pilot injector as the ignition aid. A diagram of the jet cell ignitor is shown in the left cylinder head port of Fig. 1. Natural gas is admitted to the jet cell through a check valve during the time when the NG header pressure is greater than the cylinder pressure. During the compression stroke, combustion air from the main chamber is forced into the cell forming a combustible mixture. The jet cell mixture is ignited by a spark plug and hot combustion gases enter the main chamber as a jet which serves as a positive ignition source. The natural gas jet cell ignitor was originally developed by Cooper-Bessemer for their gas engines as a method for achieving lean burn operation (to reduce NO_x), reducing cycle-to-cycle variations, and stabilizing operation at part load. Because of its success as an ignition aid in other applications, there has been interest in evaluating the performance of the jet cell ignitor as a CWS ignition aid, as an alternative to diesel fuel pilot ignition.

The piston is a standard Cooper-Bessemer design for dual fuel engines. It has a shallow bowl with cutouts for the valves. The ring pack consists of five compression rings and three oil control rings. The top compression ring is a filled groove tapered ring made of hardened ductile iron. All other rings are made of cast gray iron. The cylinder liner is a porous chrome-coated cast iron sleeve.

Cylinder pressure and injection pressure were measured using strain gage transducers and were recorded by a multichannel FM data tape recorder and digitized at crank-angle

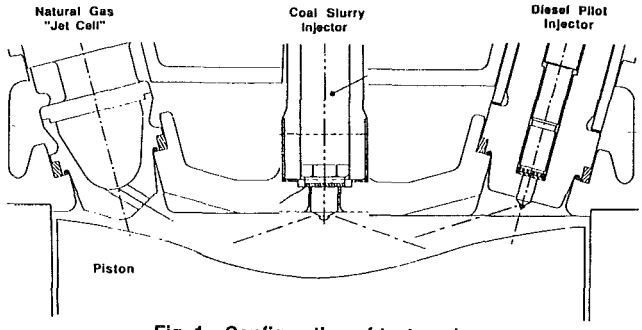

Fig. 1 Configuration of test engine

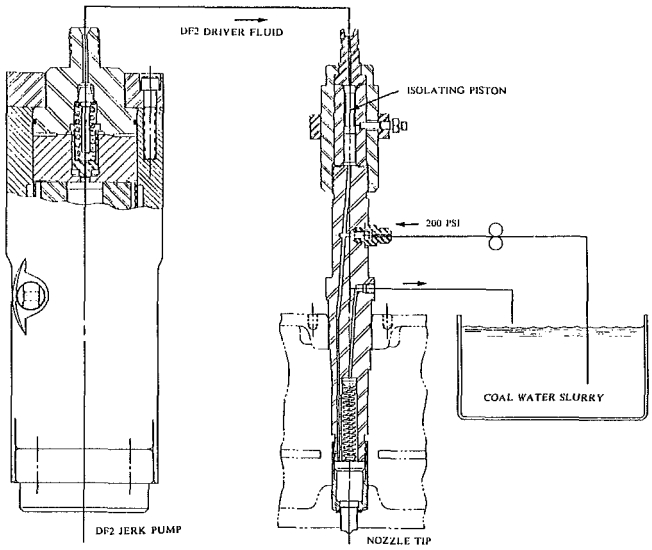

Fig. 2 Injection system for CWS

degree intervals using a 12 bit analog-to-digital converter. Exhaust emissions were sampled through a heated sample line (375°F) and were analyzed for total hydrocarbons, carbon monoxide, carbon dioxide, oxides of nitrogen, and oxygen. Hydrocarbon measurement was by flame ionization detection; CO and CO_2 measurements were made by nondispersive infrared analyzers; NO_x measurement was made by a chemiluminescence analyzer. Particulate samples were collected on a submicron filter from a port in the exhaust manifold during engine operation.

Fuel Injection System

Principle of Operation. The fuel injection system used in the JS tests injects CWS under high pressure (5000 to 15,000 psi) through a multihole nozzle both to atomize the fuel and to distribute it throughout the combustion chamber. The nozzle tip is designed to function much like a conventional injector except that the number of holes is more than doubled and the hole diameter is decreased. The hole size range (0.25 to 0.40 mm) was selected based on high pressure atomization tests at MIT (Benedek, 1987; Lai et al. 1987).

To meter the CWS fuel and pressurize it with minimum exposure of moving parts to the slurry, we developed the injection system shown in Fig. 2. The pump shown is a standard diesel injection pump, which meters the desired quantity of injected fuel by rotationally positioning the plunger helix with respect to a fuel passage in the side of the plunger bore. Fuel can pass in or out of this hole whenever it is not covered over by the helix-shaped land. A cam in the engine strokes the plunger as the engine shaft rotates. As the plunger strokes upward, the port is covered over, thus forcing the displaced fuel to flow toward the injector (Fig. 2). The flow restriction,

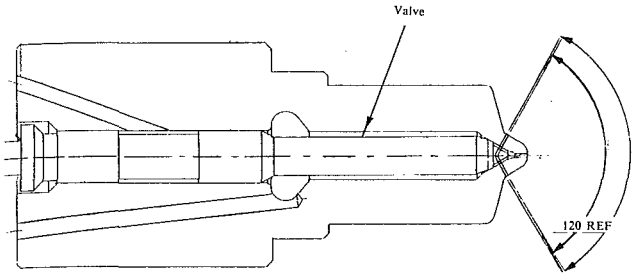

Fig. 3 CWS nozzle tip (multihole design)

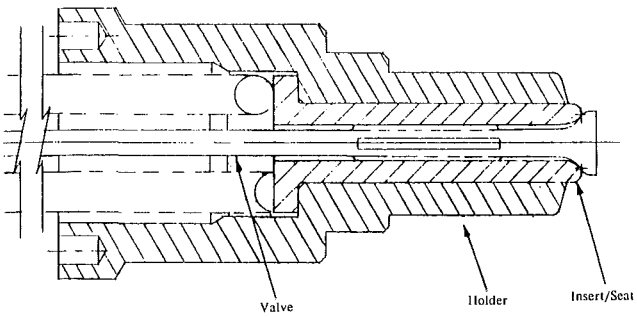

Fig. 4 CWS nozzle tip (poppet design)

caused first by the closed nozzle and then by the nozzle spray holes, causes the pressure of the fuel to rise quickly to the several thousand psi range. The increase in pressure forces the plunger to move and opens the nozzle, allowing fuel injection to begin.

When the continuing stroke of the plunger causes the helix land to uncover the hole in the side of the bore, the pressurized fuel above the plunger spills into the sump. The pressure falls and the nozzle is closed by spring action. A check valve above the plunger closes to prevent back flow from the line.

The check valve was modified for CWS injection as described below. The injector has a shuttle piston, which keeps the DF2 fuel separated from the CWS, as shown at the top of the injector body in Fig. 2. Displacement of DF2 fuel from the pump moves the shuttle piston downward and displaces an equal volume of CWS out of the nozzle at the pressure generated by the pump.

After injection is complete and the pressure drops in the CWS passages, the CWS supply at approximately 200 psi pushes the check valve open and replaces the injected quantity of CWS by pushing the shuttle piston back to its most upward position. This displaces DF2 fuel back to the pump. A small hole is drilled through the length of the outlet check valve (called a delivery valve) to let the DF2 fuel escape into the pump sump.

With a system of this type, pressure is only generated when it is needed. In between injections, there is only a nominal 200 psi pressure in the injector—not enough to open the nozzle, which is set to open at 5000 psi.

Critical Problem Areas and Solutions. The critical problems with this system are: shuttle piston sticking, check valve sticking and leaking, nozzle sticking, CWS packing under the nozzle valve, and nozzle tip hole wear. The only critical problem that has not been resolved is the nozzle tip hole wear.

The problem of shuttle sticking has been solved by using a combination of (*a*) titanium nitride coating on the piston running against a nitralloy barrel, (*b*) introducing engine oil into an annulus at the edge of the piston, and (*c*) reduced clearance dimension. The oil pressure is maintained at 1000–2000 psi higher than the maximum injection pressure. In this way, coal cannot enter the clearance between the plunger and the barrel. The clearance between the plunger and the barrel is held at approximately 100 millionths of an inch. With this range of

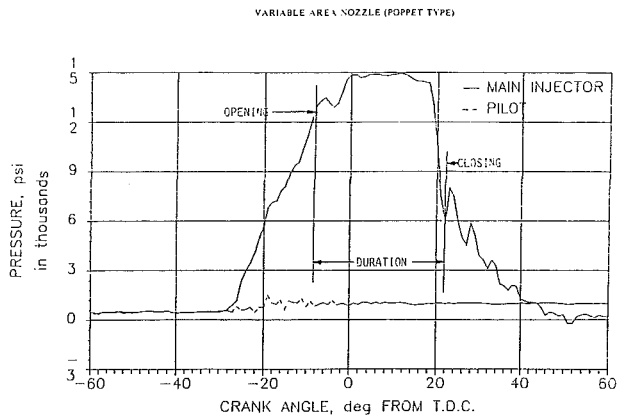

Fig. 5 Injection pressure trace of the variable area poppet area

clearance (2-1/2 microns) there is only a limited amount of the coal that can get into the close clearance in the first place, and such a close clearance restricts the loss of 40 weight engine oil into the coal.

The problem of check valve sticking and leakage has been solved by making the valve an unguided poppet type valve with the spring located on the low-pressure side of the valve. Two valves in series were used to provide absolute sealing against high injection pressure during injection and high cylinder pressure at the end of injection. The problem of nozzle valve sticking has been solved by introducing 40 weight engine oil to an annulus on the guide portion of the valve. The problem of packing of the coal under the valve between the valve seat and the orifice holes has been solved by maintaining a high flow velocity in this area during injection and using a very narrow valve seat width (25 thousandths of an inch).

Nozzle Tip Designs for CWS. The multihole type nozzle (Fig. 3) has been used extensively for testing to date. This is a multihole nozzle with 18 holes in two rows that inject into the combustion chamber at an included angle of 120 (see Fig. 3). There is a 19th hole at the end of the nozzle to prevent packing of coal under the end of the valve tip. The hole sizes that have been tested have ranged from 0.25 mm to 0.40 mm.

A second experimental nozzle type is a poppet-type nozzle (Fig. 4). This nozzle design lends itself to the use of various hard coatings. Combustion performance (atomization, ignition, burn rate, and burnout) has been good using multihole nozzles. However, the severe wear experienced by multihole nozzles when operating on CWS has lead to research in the area of durable materials and alternate nozzle geometries. The poppet type nozzle is the first alternate nozzle design tested on the JS engine.

Injection System Performance. The injection pressures shown in Fig. 5 are those typically obtained with the poppet type. In this case, the valve opening pressure is considerably higher than with the multihole, but once the nozzle starts to open, it quickly opens to the point that holds a constant injection pressure. The opening point of this type of nozzle is difficult to determine, but is approximately as shown in Fig. 5. On the other hand, the closing point of this nozzle is easy to distinguish because once the valve reaches the seat only oscillations from reflected waves are seen in the trace. The duration shown in this case is somewhat shorter than usually seen with a multihole type nozzle because the poppet valve is free to open relatively widely and the average injection pressure is higher.

Nozzle Wear Results

Nozzle erosion remains the critical element in extending the maximum time of continuous engine operation on coal slurry.

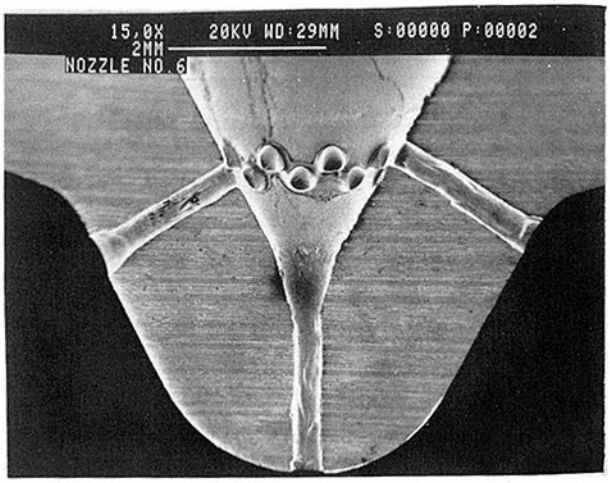

Fig. 6 Cross section of multihole nozzle (8620 carbo-nitrided steel) after 40 min of operation on low-ash CWS (0.6 percent ash in dry coal)

Fig. 7 High magnification photo of orifice surface after operation on low-ash CWS

Substantial wear is observed with just two hours of operation for the conventional steel diesel engine nozzles tested. The wear mechanism appears to be a combination of cavitation and solid particle erosion and requires that extremely hard materials be employed to extend life into practical ranges.

Most tests have been performed with low ash coal fuel—less than 1 percent ash—with the multihole nozzle design described earlier. Orifices with original diameter 0.40 mm enlarge *at the exit end by 50 percent after less than one hour of operation*. Figure 6 shows a cross section of a nozzle that operated on 0.6 percent ash content coal for 40 min. The "trumpeting" geometry can be explained by the sudden drop in fluid pressure and the resulting cavitation damage. The wear first progresses diametrically and then longitudinally back toward the inlet side of the orifice. A high magnification scanning electron micrograph (Fig. 7), taken at the advancing material loss front, shows fatigue features indicative of cavitation damage. Considerably less wear occurs at the inlet side of the orifice, where there is evidence of grazing solid particle impacts.

An engine test run with a 3.8 percent ash content coal fuel resulted in substantially more wear than with the low-ash (0.6 percent) fuel. Figure 8 shows a cross section of the nozzle after 40 min of operation. The wear pattern is also different in that the enlarged orifice diameter progresses from the inlet side toward the exit side. Material loss in this case is now controlled by solid particle erosion, as seen by the high magnification photo of the orifice exit region shown in Fig. 9. There is obviously a severe penalty to be paid in nozzle erosion through use of high ash coal fuel.

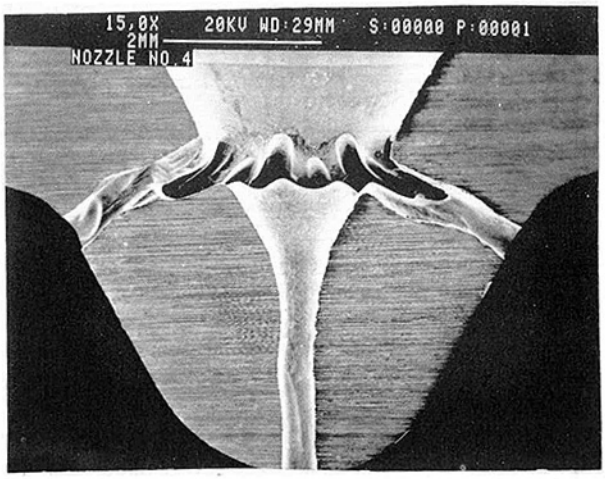

Fig. 8 Cross section of multihole nozzle (8620 carbo-nitrided steel) after 40 min of operation on high-ash coal slurry (3.8 percent ash in dry coal)

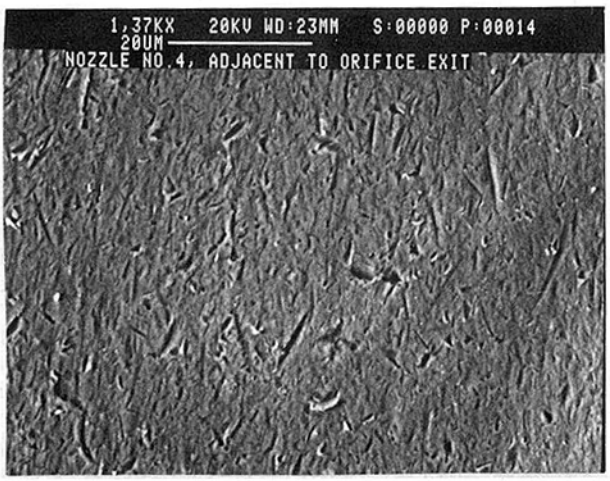

Fig. 9 High magnification photo of orifice surface after operation on high-ash coal slurry

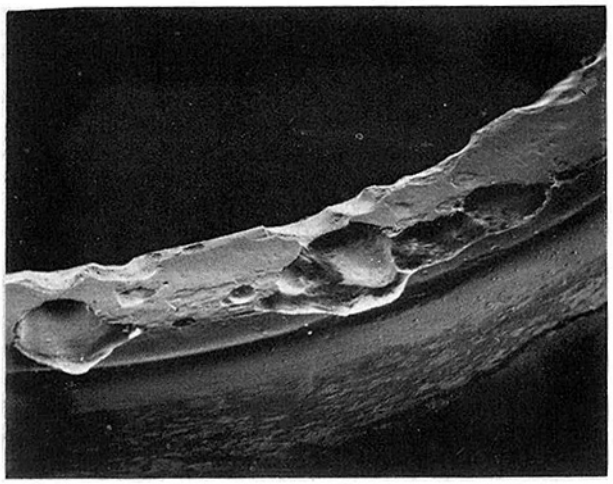

Fig. 10 Variable area poppet nozzle seat (titanium nitride coated) after 40 min of operation on low-ash coal slurry (0.6 percent ash in dry coal)

Engine tests with the variable-area poppet nozzle show wear results similar to those of the multihole design. Figure 10 shows the wear pattern of the valve seat after approximately one hour of operation on 0.6 percent ash content coal. This particular nozzle had been coated with a thin layer of titanium nitride, the remainder of which is visible in some locations on the valve seat. It is unclear whether the coating was removed by cavitation damage, solid particle erosion, or impact wear during

Table 4 JS engine compression ring wear rates after 24 hours of operation on 0.4–0.6 percent ash coal fuel

Ring		End Gap Change (mm)	Wear Rate* (mm/hr)
1	(top)	1.88	0.078
2		0.36	0.015
3		0.48	0.020
4		0.30	0.012

* End gap change/hr.

Table 5 Top compression ring wear rates for the gas-fired engine wear apparatus

Liner Material	Ring Material	Total Time (hr)	End Gap Change (mm)	Wear Rate* (mm/hr)
Chrome	Cast Iron	40	0.89	0.022
Cast Iron	WC-Co	98	0.13	0.001

*End gap change/hr

repeated opening and closing of the valve. Comparable wear is anticipated because fluid flow conditions in this design, in terms of pressure drop and velocity, are very similar to the multihole design. The benefit of the variable area nozzle is the ease with which wear surfaces can be coated.

Ring Wear Results

The top compression ring of the coal-fueled diesel engine also experiences severe wear, and with conventional materials lasts approximately 30 hours before it must be removed. Solutions to this problem are being investigated with three apparatus: the coal-fueled JS engine, a smaller gas-fired engine, and a laboratory bench-top apparatus. Hard, plasma-sprayed coatings look promising for the required reduction in wear.

Figure 11 shows the JS top compression ring end gap change with operating time on coal slurry. These data correspond to a ductile iron ring, hardness 400 kg/mm^2, run on a chrome-plated cylinder liner. Wear rate is not constant because of break-in and the different operating conditions under which the engine was run during the 25 hours of testing.

One of the primary differences in operating conditions during various test phases was the ash content of the exhaust particulate. It is increased by both a higher ash content coal fuel and a higher degree of carbon burnout. Our hypothesis is that the combusted coal particulate deposits in the oil film on the cylinder wall, resulting in wear on the passage of the ring set. A significant demonstration of the effect of ash content on wear is given by the last hour of JS engine operation, which was on a 3.8 percent ash content coal fuel, in contrast to the 0.4–0.6 percent ash coal used prior to this. The slope of the ring end gap change versus time is observed to increase dramatically during this period.

Total end gap changes after 24 hours of operation for the four combustion rings are listed in Table 4. Data have not been collected on the oil control rings and there has been no measurable wear on the chrome-plated liner.

A 7.25 in. bore gas-fired diesel engine was chosen as the apparatus to investigate wear-resistant ring/liner materials. The abrasive conditions of the coal-fueled engine are simulated by injecting a 20 percent ash coal-SAE 20W oil slurry into the side of the power cylinder during operation. To date, experiments have been conducted with cast iron rings on a chrome-lined power cylinder, the same materials as used in the conventional JS engine, and plasma-sprayed tungsten carbide/cobalt rings on a cast iron power cylinder. The top compression ring wear rates for these two cases are listed in Table 5.

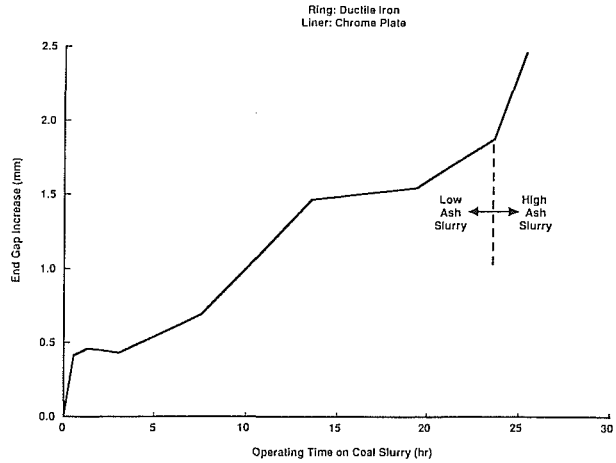

Fig. 11 Top compression ring wear versus time

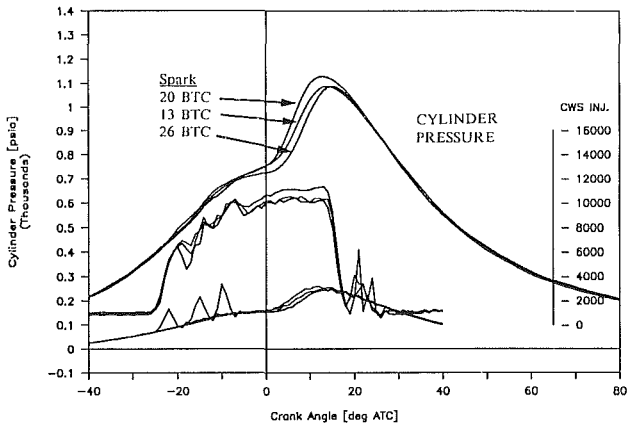

Fig. 12 Effect of jet cell spark timing on cylinder pressure trace

The gas-fired engine apparatus is seen to induce about one-third as much wear as the JS engine. In addition, the tungsten carbide rings are observed to exhibit a 20-fold increase in wear resistance over the cast iron rings. No detectable wear has occurred in the power cylinder surfaces.

Laboratory bench-top experiments have been conducted primarily to study the wear mechanism under reciprocating conditions. The apparatus used in these studies has a stroke of 125 mm with speeds up to 1000 rpm. A detailed description of the apparatus and of experiments conducted to study the effects of coal properties on wear are reported by Mayville (1989). Tests with the apparatus show a linear dependence of wear on ash content in the unburned coal particulate, and of the abrasive concentration in oil. These results were utilized to select the abrasive used in the gas-fired engine tests. Experiments are underway to determine whether this apparatus can be used to rank wear resistance properly in the coal-fueled diesel engine.

Engine Combustion Results

Jet Cell Ignition. Previous work (Rao et al., 1988; Hsu, 1988; Likos and Ryan, 1988) has shown that CWS will ignite without the use of auxiliary fuel or ignition aids when atomization of the fuel spray is sufficient and the surrounding air temperature is relatively high (compression air temperature greater than ~ 1000 K). At compressed air temperatures below 1000 K, ignition aids are required for timely ignition of the

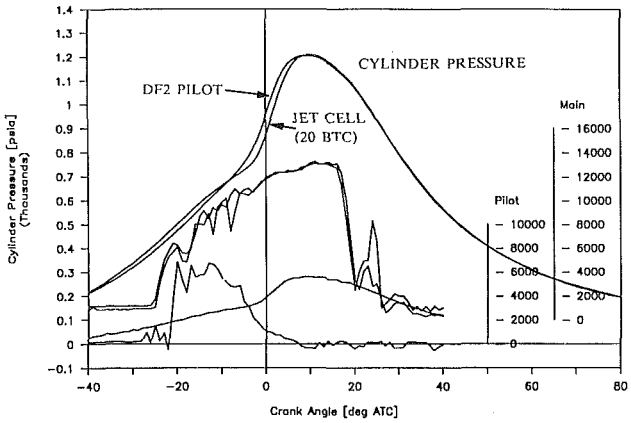

Fig. 13 Cylinder pressure comparison of DF2 pilot and jet cell ignitor

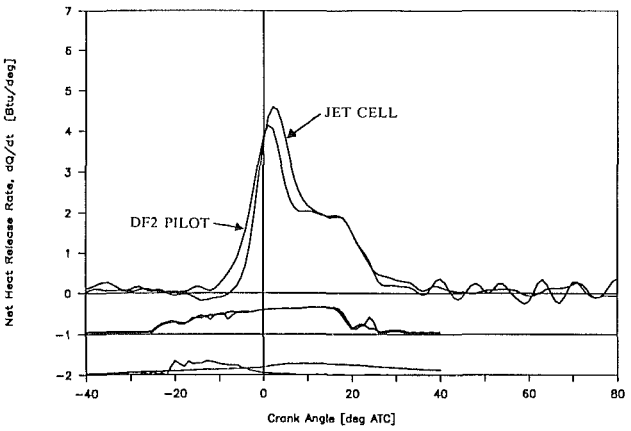

Fig. 14 Heat release rate comparison between DF2 pilot and jet cell ignitor

coal particles and engine performance has been shown to be sensitive to the details of the ignition aid. One engine design goal is to lower the amount of auxiliary ignition fuel required for a given manifold air temperature and compression ratio. Another goal is to have the flexibility to use either natural gas or diesel fuel as the ignition aid.

There are several major variables that influence the efficiency of natural gas jet cell ignition and the subsequent combustion process. For example, geometry of the jet cell (cell volume, throat diameter, orifice *l/d*), amount of natural gas introduced per cycle, and the spark timing will affect CWS ignition and combustion behavior. An unmodified production version of the jet cell was used for NG ignition studies and jet cell geometry was not changed. The effects of spark timing and natural gas quantity admitted to the jet cell were studied. Preliminary results are described below.

Jet cell spark timing (relative to CWS injection timing) affects the relationship between the issuing jet of hot combustion gases and the developing CWS fuel spray. Start of CWS injection was set to the baseline timing of 20 deg BTC and engine speed and load were set to 400 rpm and 150 psi bmep, respectively. Spark timing was varied from 26 deg BTC (6 deg before start of CWS injection) to 13 deg BTC (7 deg after start of injection). Figure 12 shows the cylinder pressure, main injection pressure (CWS), and the jet cell pressure for three spark timings (26, 20, and 13 deg BTC). The jet cell pressure trace illustrates the time delay between spark and appreciable pressure rise in the jet cell. This delay is of order 2 crank deg (~1 ms) for a detectable pressure rise and 5 crank deg (~2 ms) for development of the maximum pressure during jet cell combustion. Previous visualization studies have indicated a 3 to 5

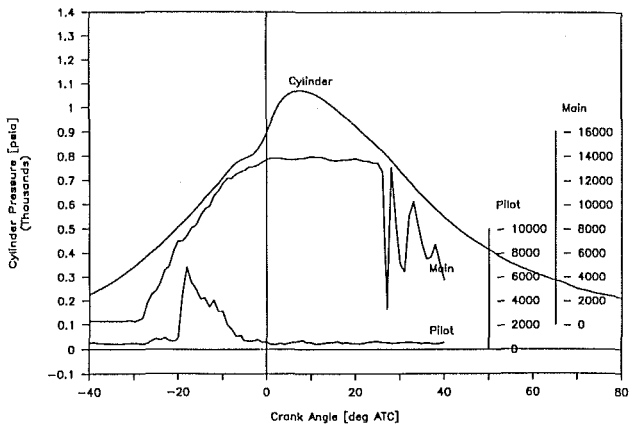

Fig. 15 Cylinder pressure, CWS injection pressure, and DF2 pilot injection pressure for JS engine operation using a variable area poppet nozzle

Table 6 Cylinder pressure data as a function of jet cell spark timing

Spark Timing (deg BTC)	CWS Ignition Delay (deg)	Peak Cylinder Pressure (psia)	Peak Pressure Location (deg ATC)
13	16	1090	14
20	13	1130	12.5
26	16	1090	15

crank deg delay between time of spark and the time the jet penetrates into the main combustion chamber.

Figure 12 demonstrates that a jet cell spark timing of 20 deg BTC produced the shortest ignition delay, highest peak cylinder pressure, and best timing of peak pressure, indicating that near optimum timing was obtained for the conditions studied. Table 6 summarizes the ignition delay and cylinder pressure data as a function of spark timing. The spark timing variations were run with a natural gas header pressure of 40 psig, which corresponds to approximately 5 percent natural gas contribution to the total fuel energy. Lower quantities of natural gas (down to 3 percent) were still effective as an ignition aid; however the best performance (i.e., reliable ignition) was achieved at the 5 percent setting.

Figures 13 and 14 illustrate that the jet cell ignitor provided ignition and combustion performance similar to that of the three-hole pilot injector. In this comparison, 4 to 5 percent of the total fuel energy was supplied by the ignition aid. For both cases, peak cylinder pressure was approximately 1200 psia at 9 deg after top center. The pilot test exhibited a slightly shorter ignition delay and corresponding lower peak heat release rate. Brake specific fuel consumption and exhaust temperatures were also nearly identical for the two runs.

Variable-Area Poppet Nozzle: Combustion Performance. The initial poppet nozzle test was short in duration but showed promising results. The poppet valve and seat were then coated with titanium nitride (to reduce wear) and re-evaluated. Subsequent tests were geared toward assessing nozzle wear rate as a function of injection velocity. This was accomplished by varying the nozzle opening pressure, spring rate, and pump plunger diameter. These tests yielded valuable combustion performance data, which are described below.

Figure 15 illustrates the typical cylinder pressure and injection pressure traces of the JS engine operating with a poppet nozzle and Fig. 16 shows the corresponding heat release profile. The heat release rate shows the usual premixed burning stage followed by a mixing controlled stage with a net heat release rate of approximately 1.7 Btu/deg. The poppet nozzle exhibits a longer than usual burnout phase (compared to a multihole

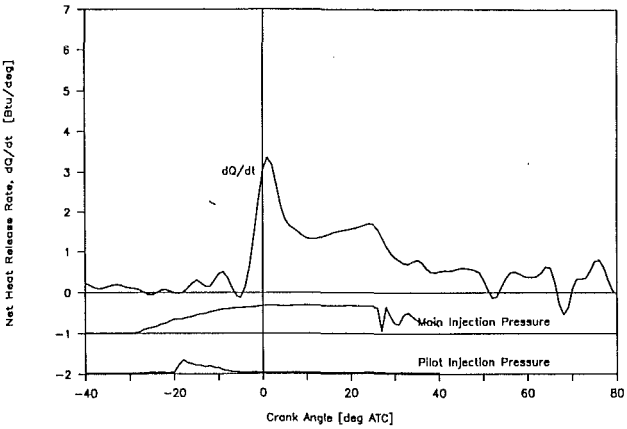

Fig. 16 Heat release rate profile of the variable area poppet nozzle

Table 7 Engine results with poppet nozzle

	Run	A	B	C	D	E	F
Set Up	Opening Pressure (psi)	12,500	12,000	6,000	7,000	5,500	Conventional Multihole
	Plunger Diameter (mm)	26	26	26	26	22	26
	Spring Rate (lb/in)	5,300	5,300	5,300	5,300	2,750	-
Results	Max. Inj. Pressure (psi)	14,500	13,800	8,500	9,500	7,500	12,000
	Start of Injection (degrees BTC)	8	6	16	17	20	20
	Inj. Duration (degrees)	30	31	26	28	32	37
	BMEP (psi)	125	140	135	130	135	150
	BSFC (Btu/bhp-hr)	7,900	8,000	7,300	7,200	7,150	6,900
	T_{ex} (°F)	840	855	880	830	860	880
	NO_x (ppm)	-	470	530	550	500	1,200

nozzle) with a net heat release rate of approximately 0.5 Btu/deg at 40 deg after top center.

A number of tests were conducted with the poppet nozzle in which nozzle opening pressure, spring rate, and pump plunger diameter were changed. Reducing the opening pressure reduces the nozzle stem preload, which reduces the injection pressure. It also allows injection to begin sooner, lowering the initial slurry velocity. Reducing the nozzle spring rate also should lower the average injection pressure. Reducing the injection pump plunger diameter lowers the fuel delivery rate to the nozzle tip and lengthens the injection duration. The results of these changes are summarized in Table 7 and a comparison with results from a multihole nozzle is also shown. These preliminary tests indicate that high injection pressures are not absolutely required with the poppet nozzle for successful engine operation. The data even suggest that poppet nozzle performance is better (i.e., lower bsfc) at lower injection pressures (7000 versus 12000 psig).

Engine performance using the poppet nozzle was satisfactory, as indicated by Figs. 15 and 16 and Table 7. The brake specific fuel consumption approached 7000 Btu/bhp-h, which is essentially equivalent (within experimental error) to the bsfc achieved with the standard multihole nozzle at the same operating conditions (6900 Btu/bhp-h). Exhaust temperatures (approximately 850°F) were comparable to those under multihole operation and indicate good combustion without significant late burning. Preliminary results indicate NO_x levels of approximately 500 ppm compared to 1200 ppm for multihole operation at the same manifold air temperature (330°F).

Summary and Conclusions

1 A novel injection system has been developed that enables abrasive coal–water slurry to be pumped, metered, and injected at high pressure using a conventional diesel fuel pump.

2 An experimental poppet nozzle with a variable-area annular orifice has been designed and tested on CWS using the Cooper JS engine. This nozzle gave comparable peak injection pressure but a more advantageous "top-hat" pressure profile than the multihole nozzle. Atomization was apparently satisfactory as evidenced by the cylinder pressure profiles, inferred heat release versus crank angle traces, and observed bsfc and gaseous emissions.

3 Spark-ignited natural gas torch ignition using the Cooper Bessemer jet cell is a viable alternative for CWS engine operation, according to the test results. The quantity of natural gas can be as low as 3 percent of the total fuel energy, although 5 percent gives improved engine performance.

4 Nozzle wear is severe when conventional steel components are used in high-pressure injection (10,000 to 15,000 psi and 200 to 300 m/s slurry velocity). Useful nozzle life under these conditions is only a few hours with 0.4–0.6 percent ash coal. The mechanism of wear appears to be a combination of erosion and cavitation.

5 Piston ring wear rate is also significantly increased by engine operation on CWS, with useful top ring life of approximately 30 hours when conventional steel components are used.

6 The ash content of the coal used in the CWS greatly affects wear of both nozzles and piston rings. For example, tests with 3.8 percent ash coal gave 3 to 5 times the wear rate of both types of component compared to 0.6 percent ash coal.

7 Although improved durability of injection system, piston rings, and other components represent technical challenges, the cost of coal-tolerant engine components will not be critical compared to the cost of processing raw coal to an engine-grade clean coal slurry. It is this CWS processing cost that dominates the question of economic feasibility, along with the cost of emission control.

Acknowledgments

This work was performed with the support of the DOE Morgantown Energy Technology Center under Contract DE-AC21-88MC-25124. We acknowledge the guidance and suggestions offered by Nelson F. Rekos, Jr. and Larry K. Carpenter, particularly duing the earlier stages of the program. The authors wish to acknowledge AMAX extractive R&D for providing test fuels; Battelle Columbus Laboratories for assistance with nozzle photographs; Fred Schaub, Jesse Smith, Bob Brannon, Charles Melcher, and Terry Baker of Cooper's Mt. Vernon Research Laboratory for setting up and conducting engine tests; Karen Benedek and Todd Burger of Arthur D. Little for technical assistance on the coal fuels and economic modeling aspects of this effort.

References

Balles, E. N., Benedek, K. R., Wilson, R. P., and Rao, A. K., 1987, "Analysis of Cylinder Pressure and Combustion Products From an Experimental Coal-Fueled Diesel Engine," *New Technology for Cogeneration*, ICE Vol. 2, ASME, New York, pp. 75–81.

Benedek, K. R., 1987, "Coal-Fueled Diesel Systems for Stationary Power Applications: Coal Water Slurry Injection and Combustion Experiments," Task 2—Topical Report prepared by ADL and MIT under DOE Contract No. DE-AC21-85-MC22181, Sept.

Benedek, K. R., Menzies, K. T., Johnson, S. A., Wilson, R. P., Rao, K. A., and Schaub, F. S., 1988, "Emission Characteristics and Control Technology for Stationary Coal-Fueled Diesel Engines," *Engine Emissions Technology for the 1990's*, ICE Vol. 4, pp. 169–176, Oct.; ASME JOURNAL OF ENGINEERING FOR GAS TURBINES AND POWER, this issue.

Hsu, B. D., 1988, "Progress on the Investigation of Coal-Water Slurry Fuel Combustion in a Medium Speed Diesel Engine: Part 1—Ignition Studies," ASME

JOURNAL OF ENGINEERING FOR GAS TURBINES AND POWER, Vol. 110, pp. 415–422.

Lai, M. C., Zhou, B., Cheng, W. K., Wong, V. W., and Benedek, K. R., 1986, "Parametric Studies of Coal-Water Slurry Combustion in a Rapid Compression Machine," ASME Paper No. 87-ICE-9.

Likos, W. E., and Ryan, T. W., 1988, "Experiments With Coal Fuels in a High-Temperature Diesel Engine," ASME JOURNAL OF ENGINEERING FOR GAS TURBINES AND POWER, Vol. 110, pp. 444–452.

Mayville, R. A., 1981, "Abrasive Concentration Effects on Wear Under Reciprocating Conditions," to be presented at the International Conference on Wear of Materials—1989, Denver, CO, Apr.

McMillian, M. H., and Webb, H. A., 1989, "Coal-Fueled Diesels: Systems Development," ASME JOURNAL OF ENGINEERING FOR GAS TURBINES AND POWER, this issue.

Rao, A. K., Melcher, C. H., Wilson, R. P., Balles, E. N., Schaub, F. S., and Kimberley, J. A., 1980, "Operating Results of the Cooper-Bessemer JS-1 Engine on Coal-Water Slurry," ASME JOURNAL OF ENGINEERING FOR GAS TURBINES AND POWER, Vol. 110, No. 3, pp. 431–436.

Wilson, R. P., 1986, "Coal-Fueled Diesel Systems for Stationary Power Applications: Assessment of Merit," Topical Report prepared by Arthur D. Little, Inc., under contract to the Department of Energy/Morgantown Energy Technology Center, Sept.

K. R. Benedek

K. T. Menzies
Arthur D. Little, Inc.,
Cambridge, MA 02140-2390

S. A. Johnson
PSI Technology Company,
Andover, MA 01810

R. P. Wilson, Jr.
Arthur D. Little, Inc.,
Cambridge, MA 02140-2390

A. K. Rao
Cooper-Bessemer,
Grove City, PA 16127

F. S. Schaub
Cooper-Bessemer,
Mt. Vernon, OH 43050

Emission Characteristics and Control Technology for Stationary Coal-Fueled Diesel Engines

Emissions of primary concern for coal-fueled diesel cogeneration and electric power plants are nitrogen oxides, sulfur dioxide, particulate matter, and aromatic hydrocarbons. In addition, the exhaust particulate size distribution and ash content are relevant to durability of the exhaust valves, turbocharger, and other engine components. This paper summarizes preliminary measurements of "uncontrolled" emissions in the exhaust of a Cooper-Bessemer 33-cm (13-in.) bore, 400 rpm, single-cylinder research engine, operated on "engine-grade" coal-water fuel (0.5 percent ash, 1 percent sulfur, 8 μm mean size coal). Based on these results, we present a preliminary evaluation of emission control options for satisfying hypothetical future emission standards for 2–50 MW power plants. The paper describes coal-diesel component subsystems such as (a) "reburning" for reducing NO_x and hydrocarbon emissions, (b) high- and low-temperature injection of calcium sorbents for SO_2 capture, and (c) high-temperature bag filters for control of fine particles. The expected performance of a conceptual, integrated control system is presented.

1 Introduction

The feasibility of using coal-water slurry (CWS) as a fuel for large stationary diesel engines is being investigated using a single-cylinder research engine. This study is part of an ongoing research program funded by the US Department of Energy to establish a knowledge base for the development of coal-fueled diesel systems. Several critical aspects of this program (application, fuel, injection system, combustion, wear, and emissions) have been discussed in previous papers [1–4]. The focus of this paper is emission control for the coal-fueled diesel engine. This paper summarizes preliminary measurements of uncontrolled emissions in the exhaust of the research engine, and presents a preliminary evaluation of emission control options to satisfy hypothetical future emission standards for 2–50 MW power plants.

Exhaust emission measurements provide valuable information for the development of three characteristics of the coal-fueled engine: emissions control, durability, and atomization/combustion processes. The control of nitrogen oxides, sulfur oxides, particulates, and aromatic hydrocarbons is of primary concern for cogeneration and electric power applications. The characteristics of the exhaust particulate (size distribution, shape, ash content, and abrasiveness) affect the durability of rings, liner, exhaust valves, and turbocharger. The analysis of these same particulate characteristics can shed light on the atomization/combustion phenomena that occur in the cylinder.

Contributed by the Internal Combustion Engine Division and presented at the Internal Combustion Engine Division Technical Conference, San Antonio, Texas, October 2–5, 1988. Manuscript received by the Internal Combustion Engine Division June 1988.

2 Background

Attempts to develop a coal-fueled diesel engine have been motivated by cost premiums of petroleum fuel. In 1884 Rudolf Diesel attempted to operate an experimental engine with coal dust inducted into the air intake manifold. Between 1916 and 1945 Pawlikowski and others in Germany experimented with the direct-cylinder injection and combustion of bituminous coal dust [5]. Recent (1979–present) and onging DOE sponsored efforts by Sulzer, GE, Adiabatics, SwRI, ADL/Cooper Bessemer, and others have had considerable success using "engine-grade," ultraclean coal-water slurry, generally with high-pressure, direct cylinder injection (40–140 MPa, 6000–20,000 psi) [6, 7].

The ongoing research being conducted by ADL/Cooper Bessemer has established that coal combustion efficiency in the medium-speed, single-cylinder research engine is high (>90 percent) [4] and that durability and emissions control issues now need to be addressed.

Since stationary coal-fueled diesel engines are still in the development stages, the US Environmental Protection Agency has not promulgated New Source Performance Standards (NSPS) covering this technology in the 2–50 MWe size range. The emission control system currently being designed is based on hypothetical, future emission standards for the coal-fueled diesel engine. The conservative assumption is that these targets will be similar to the NSPS for coal-fired stationary sources.

3 Research Engine and Fuels

The Cooper-Bessemer JS-1 single-cylinder research engine

Table 1 JS-1 engine specifications

Bore	33 cm (13 in.)
Stroke	40.6 cm (16 in.)
Compression ratio	10.5
Speed range	300 to 450 rpm
Load range	0.7–1.2 MPa (100 to 175 psi) bmep
Intake air temperature	80 to 430°F
Intake air pressure	0 to 50 in. Hg (gage)

was used for CWS combustion experiments in the present program. This four-stroke diesel engine can operate on natural gas, diesel fuel, coal-water slurry, or a combination of these fuels. The intake air is supplied from an external source and the air temperature and pressure can be independently adjusted to simulate a wide range of intake manifold conditions. An orifice plate in the exhaust manifold simulates the pressure drop of a turbocharger. A high-pressure, multihole, single injector was used for both CWS and DF2 operation. A smaller diesel fuel injector was located offset from the cylinder axis and used as a "pilot" injector during CWS operation (the DF2 pilot served as an ignition aid for the CWS). Additional engine details are presented in Table 1.

The ultraclean coal-water slurries used for these engine tests were formulated by AMAX R&D, Inc. from a high-volatile bituminous (Kentucky Splint) coal. Table 2 gives the fuel specifications of the base case slurry. The coal was cleaned to 0.4 percent ash and 0.7 percent sulfur. The solids content of the CWS was 53 percent by weight. The base case slurry used in these tests had a top size of 45 μm and a mass mean of 8 μm. A second batch of slurry tested was an ultrafine grind, with a top size of 15 μm and a mean size of 3 μm. The ultrafine CWS was made from the same coal feedstock as the base case CWS. We experienced no handling problems associated with drying or clogging, but the slurries did settle and had to be resuspended by mixing.

The shape of the coal particles is more cubic than spherical; the sharp edges and flat sides of the raw coal are marks that can be identified to distinguish raw coal from heated or burned coal. There is no outward appearance of mineral matter clusters or crystals on the surface of the coal.

Table 2 Coal-water slurry specifications

CWS Properties	
Coal content (wt. %)	52
Ash content (wt. %)	0.22
Higher heating value (Btu/lb)	7555
Viscosity (cp) @ 100-1000 s	207
Particle size (wt. % less than)	(microns)
98%	45
90%	30
50%	8
10%	2
Coal Properties	
Coal type	High Vol. A. Bituminous
Proximate analysis (dry)	(wt %)
Ash	0.42
Volatiles	38.13
Fixed carbon	61.46
Ultimate analysis (dry)	(wt %)
Carbon	82.03
Oxygen	10.34
Hydrogen	5.35
Nitrogen	1.59
Sulfur	0.68
Ash Composition	(wt %)
SiO_2	26.8
Al_2O_3	16.4
Fe_2O_3	31.2
CaO	4.4
Na_2O	5.3
TiO_2	8.6

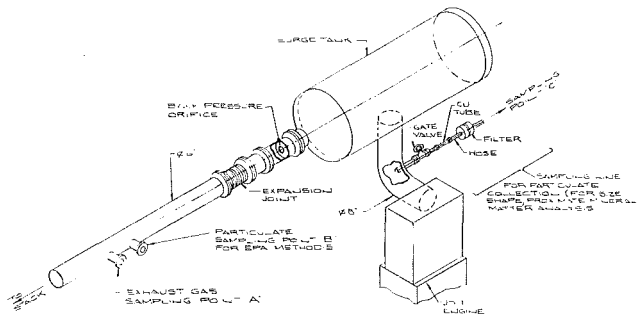

Fig. 1 Exhaust gas sampling locations, C-B, JS-1 single-cylinder research engine

4 Exhaust Sampling and Analysis Methods

A schematic of the engine exhaust duct work and the sampling locations is shown in Fig. 1. Three sampling locations were utilized. Exhaust gases were collected 5 m downstream of the engine (Location A in Fig. 1). Particulates were collected 3 m (20 pipe diameters) downstream of the engine in a 15-cm (6-in.) diameter duct (Location B in Fig. 1). At this location, the pulsations from the engine were damped and isokinetic particulate sampling was possible. Particulates were also sampled immediately downstream of the engine exhaust manifold in a 20-cm (8-in.)-dia duct (Location C in Fig. 1).

Exhaust gases (i.e., NO_x, CO, O_2, and CO_2) were sampled through a common heat-traced (190°C) manifold. The exhaust gas analyzed for CO, CO_2, and O_2 was additionally conditioned by drying (condenser) and cooling (heat exchanger) prior to instrumental analysis. The gases were continuously analyzed using the methods shown in Table 3. Certified gas standards were used for daily calibration of the analyzers.

Particulate mass loading was determined by the EPA Method 5 stack sampling procedure (Fig. 2) with the addition of a glass cyclone to the sample train. Methods 1–3 were used to define th isokinetic sampling rate in the 15-cm-dia duct. Particle size distribution was determined by isokinetic sampling with an Anderson Stack Cascade Impactor (Fig. 3). Individual impactor filters were analyzed gravimetrically to define mass median aerodynamic diameter.

In order to estimate the concentration of polycyclic aromatic hydrocarbons (PAH) in the exhaust, the Method 5 filters were dried at 30°C and soxhlet extracted with dichloromethane (16 h). The Method 5 impinger solutions were also liquid–liquid extracted with dichloromethane and the extract combined with the filter extract. The extracts were analyzed by High Performance Liquid Chromatograph/UV/Fluorescence Detection (EPA Method 610).

In addition to the EPA Method 5 stack sampling procedure, exhaust particulates were collected through a sampling line located immediately downstream of the engine exhaust manifold. Particulates were collected close to the engine in order to shed some light on atomization and combustion phenomena occurring in the engine. Sampling at Location C reduced the amount of char combustion or particulate loss that might have occurred in the exhaust duct between the engine and the sample filter. It was understood that isokinetic sampling was not feasible this close to the engine. Improved sampling methods at this location are currently being developed.

Monolayer particulate catches (on Nuclepore 0.1 μm hole size filters) were collected using the sampling line shown in Fig. 1 at Location C. These samples were analyzed directly in a Scanning Electron Microscope fitted with an energy dispersive X-ray spectrometer to examine particulate size, shape, and mineral matter composition. Larger amounts of particulate (50–100 mg) were collected on 0.8 μm AA cellulose filters for proximate analysis.

A proximate analysis of stack particulates was conducted by Thermal Gravimetric Analysis (TGA) to assess the percents of moisture, volatiles, fixed carbon, and ash. The particulates

Table 3 Exhaust gas analysis methods

Parameter	Method
NO_x	Chemiluminescent NO/NO_x analyzer (Teco Model 10/700)
CO	Nondispersive infrared analyzer (Beckman Model 864)
CO_2	Nondispersive infrared analyzer (Beckman Model 864)
O_2	Amperometric analyzer (Teledyne Model 320P4)

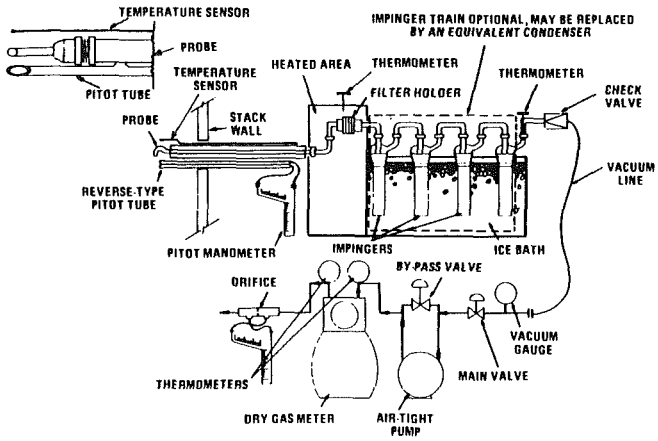

Fig. 2 EPA Method 5 train

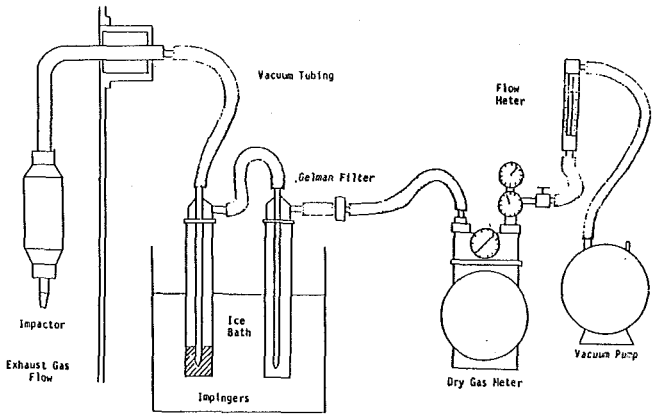

Fig. 3 Cascade impactor train

Table 4 Engine test conditions (for exhaust sampling)

Run No.	Fuel	Nozzle (mm)	Analytes
1	Diesel fuel #2	0.30	Gases Particulate PAH
2	Coal-water slurry (CWS)	0.30	Gases Particulate PAH Particle size
3	CWS	0.25	Gases Particulate PAH Particle size
4	CWS	0.25 (worn)	Gases Particulate PAH
5	Ultrafine CWS	0.25	Gases Particulate PAH

were heated in a Dupont 951 TGA under nitrogen at 200°C and 900°C followed by oxidation under air at 900°C (Dupont Application Method TA-54).

Over a three-day period, exhaust samples for the analytes of interest were collected under several conditions of fuel type and nozzle diameter. Table 4 indicates the test plan conditions.

5 Emission Characteristics—Particulates

The residue collected on the Method 5 sampling train yielded data from which particulate concentration, mass distribution, and PAH concentrations were assessed. The material collected on filters from Location C provided information about particulate shape, mineral matter, and proximate analysis. The results of the particulate sampling analyses are presented below. All the data shown are preliminary; the numbers have not yet been confirmed by either a carbon or a mineral matter balance.

5.1 Mass Loading. An initial baseline run was conducted with #2 diesel fuel to confirm that the diesel engine generates exhaust particulate concentrations of about 10^1–10^2 μg/L with negligible particulates greater than 10 μm (Table 5).

Subsequent engine operation with coal-water slurry (CWS) produced an exhaust mass concentration about ten times higher than with diesel fuel (10^2–10^3 μg/L). Approximately 20–40 percent of the mass is found in a large particle size fraction (> 10 μm) collected in the cyclone. The material larger than 10 μm may have been formed from a variety of physical and chemical processes. Much of this material may be agglomerates of coal particles that burned as fused droplets, not as individual coal particles [8]. Given that 45 percent of the raw coal was larger than 10 μm, some of the large particulate fraction may be partially combusted coal particles that only decreased slightly in diameter during char combustion. Additionally, it is possible that a small number of sticky flyash particles agglomerated in the exhaust duct and were subsequently caught in the cyclone.

A trend that was apparent was that the smaller nozzle (0.25 mm versus 0.30 mm) is correlated with a higher mass concentration. Following this trend, the worn 0.25 mm nozzle used in Run 4 yielded a mass concentration between those of the 0.25 mm and 0.30 mm nozzles. The reason for this trend is unclear and is currently being investigated further. Injection parameters that varied during these tests included a slightly higher injection pressure and longer injection duration for the smaller hole size.

Engine operation with the ultrafine CWS and the 0.25-mm nozzle produced a similar mass loading (10^3 μg/L) but a smaller cyclone fraction than observed with the standard CWS and 0.25-mm nozzle.

5.2 Particle Size Distribution. The cascade impactor samples for Runs 2 and 3 indicate a particle size distribution that is not log-normal. A log-probability curve (Fig. 4) indicates that the mass median aerodynamic diameter is approximately 4 μm. However, it is clear from the Method 5 cyclone catch that a significant fraction of the exhaust particulate is larger than 10 μm. Note that the cascade impactor discriminates against this size fraction. Thus, it is likely that a bimodal size distribution exists for the CWS and consists of relatively large coal aggregates (>10 μm) and much smaller coal fragments (<10 μm). The Method 5 data indicate that the large coal fraction may account for 20–40 percent of the total mass of exhaust particulate.

As slurry droplets or individual coal particles burn, they may swell, fragment, or gradually decrease in diameter during char combustion [9]. Mineral matter that is released during combustion may condense in the exhaust in the shape of small glassy spheres. Conceptually, it is reasonable that this mix of physical and chemical phenomena results in a particle size distribution that is bimodal, with partially combusted coal and agglomerates in the large fraction and condensed mineral mat-

Table 5 Particulate concentration

Run	Fuel	Mass fraction			Total mass concentration, μg/L	lb/mm Btu input
		Nozzle	Cyclone	Filter/impinger		
1	DF2	0.30	0	1.00	65	---
2	CWS	0.30	0.24	0.76	580	0.7
3	CWS	0.25	0.40	0.60	1000	1.3
4	CWS	0.25 (worn)	0.26	0.74	720	0.9
5	Ultrafine CWS	0.25	0.21	0.79	1000	1.2

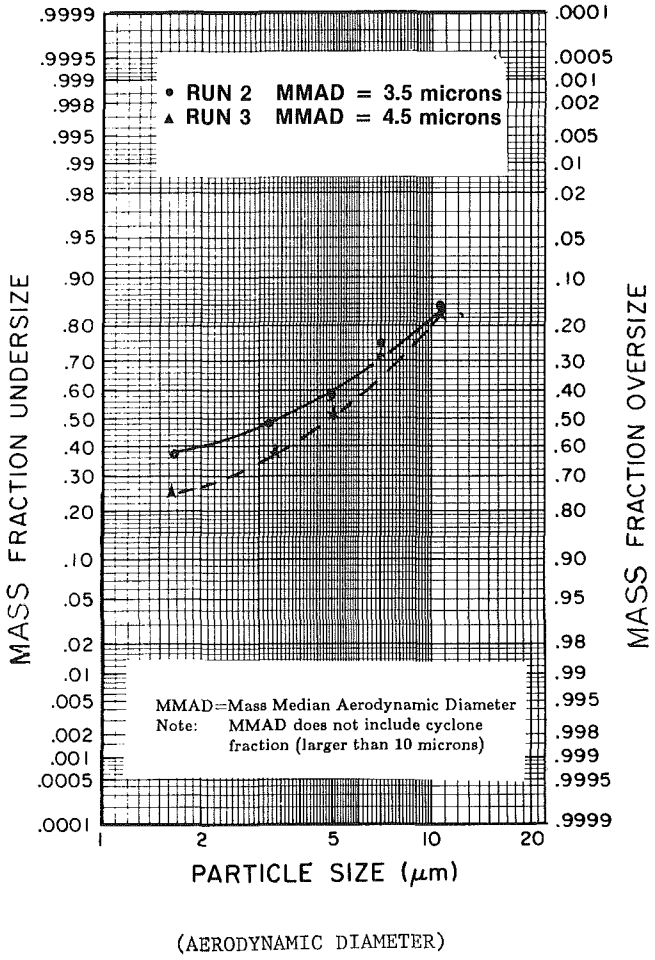

Fig. 4 Particulate size distribution

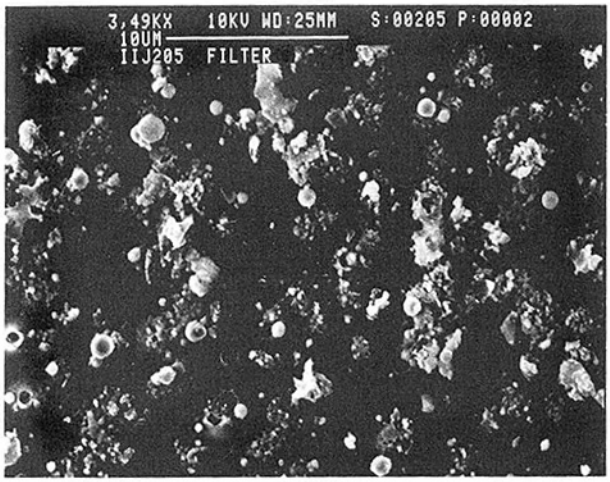

Fig. 5 Coal-fired engine exhaust particulate

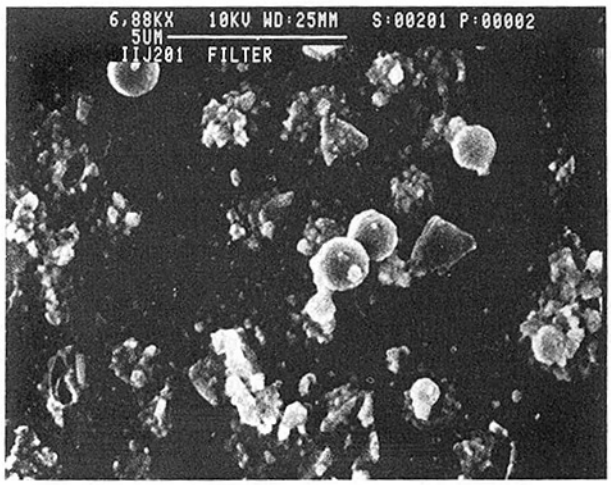

Fig. 6 Coal-fired engine exhaust particulate: close-up

ter and combusted coal fragments in the small size fraction. Photomicrographs of the exhaust particulates (shown in the next section) confirm the existence of this variety of exhaust material.

5.3 Particulate Shape. Figure 5 shows a SEM micrograph of the coal-fired engine exhaust particulate (on the filter on which it was collected). There is a variety of particle shapes present. Small, spherical, mineral matter particles are present in sizes roughly 2 μm and below. Energy dispersive X-ray analysis indicated that these spheres contain aluminum, silicon, iron, calcium, sulfur, and titanium. Agglomerates of combusted coal particles range in size from 5 to 10 μm. There are also some angular particles that appear to be raw coal. Figure 6 shows a close-up of the agglomerates. One can see that the particles are comprised of many submicron particles.

A photomicrograph of diesel exhaust collected in the same sampling line is shown in Fig. 7 for comparison. The particulates are chains or agglomerates of smaller soot particles, as

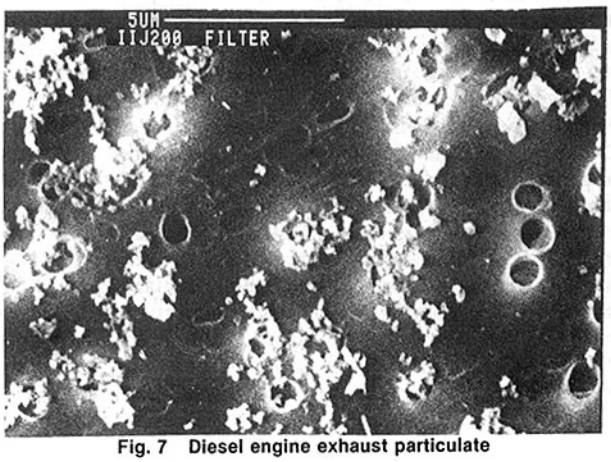

Fig. 7 Diesel engine exhaust particulate

expected. X-ray analysis of these particulates indicated no detectable mineral matter present.

5.4 Polycyclic Aromatic Hydrocarbons (PAH). PAH's are of interest due to their presence in coal and middle-distillate fuel combustion sources and their potential carcinogenicity. The particulate matter collected in the Method 5 train was extracted with an organic solvent and analyzed by HPLC to quantify the PAH's.

PAH's of approximately 2–4 ring size were detected in the exhaust at levels ranging from 1–70 ng/L (Table 6). Higher ringed PAH's (5–6 rings) were not observed at a detection limit of 0.1–0.5 ng/L. Such a distribution is not unusual for similar combustion sources.

The comparison of diesel fuel and CWS results indicates similar or slightly higher levels of PAH's in CWS exhaust streams on a volume basis. However, since the total exhaust mass loading of CWS is ten times higher than for diesel fuel, the individual PAH mass concentration (gram PAH per gram of particulate) is about ten times lower for CWS ($\sim 10^1$ ppm) than for diesel fuel ($\sim 10^2$ ppm).

5.5 Proximate Analysis. Table 7 presents the proximate analyses and calculated burnout of the particulate matter collected from Location C for the four coal runs of this test program.

Proximate analysis indicates the amount of volatiles, fixed carbon (combustible solids), and ash in the particulates. On average, the particulates contain between 88–94 percent carbon. Not all the volatiles are consumed in the combustion process; volatile matter in the particulate ranged from 11–20 percent. The existence of volatiles in the exhaust particulates could come from some of the coal that escapes unburned from the engine. Alternatively, this volatile matter could indicate that volatile evolution was inhibited by the high pressure or by the short residence time of the coal in the cylinder. At the high temperatures and pressures in the cylinder, the coal is likely on the surface; char combustion does not necessarily follow volatile evolution and combustion.

As was indicated by the mass loading analysis, the coal had slightly better burnout when injected through the 0.3 nozzle than the 0.25 nozzle. Significant difference between the burnout of ultrafine grind coal and the standard grind coal was not discernible from the proximate analysis, as was found in the mass loading analysis.

6 Gaseous Emission Characteristics

SO_x. The particulate samples collected were analyzed for sulfur content to estimate the amount of sulfur released in the exhaust in a gaseous form. Sulfur in the particulate was about 1 percent, indicating that 97 percent of the sulfur was released from the coal. In general, sulfur burnout is expected to be comparable to carbon burnout (as is the case here) because the sulfur in the chemically cleaned coal is predominantly organic sulfur. The organic sulfur is bound in the coal matrix and is released as the carbon burns away, making the burnout of the sulfur comparable to the burnout of the carbon. Instrumentation and methods to measure sulfur oxides in the exhaust gas are currently being developed in order to confirm these sulfur oxide emission estimates.

NO_x, CO, CO_2. The gaseous emissions measured during these runs is presented in Table 8. The air intake temperature for all the runs was 120°C. At this condition the NO_x level in diesel fuel run was 1400 ppm. In comparison, the NO_x concentrations in the CWS runs were slightly lower (1125 to 800 ppm). The lowest NO_x levels were associated with the 0.25-mm worn nozzle. There was no difference in NO_x emissions between the standard grind and ultrafine grind CWS. The NO_x emissions reported here are higher than those reported in previous papers [4] for this engine. The difference may be attributed to the higher air intake temperatures of the engine runs reported here. We are currently investigating the effects of air intake temperature and injection conditions on NO_x emissions.

Carbon monoxide (CO) concentrations during the CWS runs were consistently low (100–180 ppm); the ratios of CO to CO_2 concentrations were 0.1 to 0.2 percent indicating adequate air mixing and good conversion of CO to CO_2. CO concentration in the diesel run (345 ppm) was slightly higher than in the CWS runs.

Table 6 PAH concentration (ng/L)

Compound	Aromatic ring size	RUN # 1	2	3	4	5	Blank
Naphthalene	2	40	30	10	30	40	<2
Acenaphthalene	2-1/2	<1	<1	<1	<1	<1	<1
Acenaphthene	2-1/2	<6	100	40	70	90	<6
Fluorene	2-1/2	<1	2	<1	<1	2	<1
Phenanthrene	3	<4	10	4	6	<4	<4
Anthracene	3	<1	2	<1	<1	<1	<1
Fluoranthene	3-1/2	7	6	10	4	6	<1
Pyrene	4	<5	70	<5	20	9	<5
Benz(a)anthracene	4	6	2	2	10	30	<0.3
Chrysene	4	20	20	10	20	7	<0.3
Benzo(b)fluoranthene	4-1/2	<0.2	<0.2	0.6	<0.2	0.5	<0.2
Benzo(k)fluoranthene	4-1/2	<0.1	<0.1	<0.1	<0.1	<0.1	<0.1
Benzo(a)pyrene	5	<0.4	<0.4	<0.4	0.5	<0.4	<0.4
Dibenz(a,h)anthracene	5	<0.4	<0.4	<0.4	<0.4	<0.4	<0.4
Benzo(g,h,i)perylene	6	<0.5	<0.5	<0.5	<0.5	<0.5	<0.5
Indeno(1,2,3-c,d)pyrene	6	<1	<1	<1	<1	<1	<1

Table 7 Proximate analysis of particulate samples

Run #	Nozzle size	Fuel type	Proximate analysis (dry basis, % by weight) Volatiles	Fixed carbon	Ash	Burnout (percent)
2	0.3	CWS	19.3	71.7	9.0	96
3	0.25	CWS	11.4	81.8	6.8	94
4	0.25 (worn)	CWS	15.5	73.0	11.5	97
5	0.25	Ultrafine CWS	20.0	74.1	5.9	94

Table 8 Gaseous emission measurements

Run #	Description	Percent excess air	NO_x (ppm as measured)	CO (ppm dry)	CO_2 % dry	O_2 % dry
1	DF-2 0.3 mm nozzle	80	1400	345	8.4	9.75
2	Standard CWS 0.3 mm nozzle	85–90%	1125	100	9.4	10.25
3	Standard CWS 0.25 nozzle	85–90%	1090	135	9.6	10.3
4	Standard CWS 0.25 nozzle (worn)	85–90%	800	130	9.4	10.0
5	Ultrafine CWS 0.25 nozzle	80–85%	1100	180	9.9	9.75

7 Emission Control Options and Strategies

7.1 Emission Reduction Goals. Since stationary coal-fueled diesel engines in the 2–50 MWe size range are still in the developmental stages, the U.S. Environmental Protection Agency has not promulgated New Source Performance Standards (NSPS) covering this technology. However, the following benchmarks can be used for setting emission reduction goals for coal-fueled diesel power plants:

- NSPS for conventional large stationary reciprocating engines firing natural gas or diesel fuel (standards were proposed by EPA in 1982 but not implemented).
- NSPS for coal-fired stationary sources (industrial boilers larger than 100 million Btu/h heat input).
- Emission levels achievable by other technologies expected to compete with coal-fueled diesels in the near future.

Current/suggested standards for transportation diesels are 2.4 lb NO_2/mm Btu for NO_x, with no standard for SO_2 (premium engine fuels contain negligible sulfur) or for particulate matter. These standards will probably not be applied to coal-fired heat engines since coal will produce significant amounts of SO_2 and particulate matter. NO_x emissions may increase or decrease relative to conventional diesel engine fuels.

The conservative assumption, which we will adopt for the purposes of discussion in this paper, is that current NSPS for coal-fired stationary sources will be extended to cover coal-fueled stationary diesel power generators. These standards are listed in Table 9.

These standards are currently being applied to new coal-fired stationary sources larger than 300 million Btu/h heat input (which corresponds to about 30 MWe based on a 34 percent efficiency power plants), and have been recommended for smaller stationary sources down to 100 million Btu/h. In addition, emerging coal power technologies such as fluidized bed boilers (atmospheric or pressurized), gasification/combined cycle units, and slagging combustors can meet or exceed these levels of emission control.

Based on this reasoning, the emission control system for coal-fueled diesels will be designed to meet current EPA New Source Performance Standards for coal-fired stationary sources. These emission goals are shown in Table 10. Based on the preliminary single-cylinder engine test results described above, the emission control system will be designed to achieve a 75 percent reduction in NO_x and a 70 percent reduction in SO_2. The design must include provisions for particulate emissions to be reduced by 98–99.5 percent.

7.2 Particulate Control Options. In addition to the emission control requirements, particulate matter must be controlled to minimize wear on the engine turbocharger. Therefore, partial hot-gas-particle removal may be required upstream of the turbocharger where the engine exhaust gas temperature is about 450–500°C (840–1020°F). The simplest and lowest-cost hot particulate matter collector is a cyclone, which can be designed to remove 90 percent of the particulates larger than 10 μm. This could be placed upstream of the turbocharger, subject to pressure-drop limitations. However, since the particles contained in the coal-fueled diesel exhaust include a substantial fraction smaller than 10 μm, a secondary particulate control device capable of 98 percent collection efficiency would still be required. This device could be a conventional collector such as a bag filter located downstream of the heat recovery sytem or an emerging technology such as a crossflow filter, ceramic baghouse, or ceramic barrier filter located at the engine exhaust manifold.

Table 9 Hypothetical emission standards for coal-fueled diesel engines

Pollutant	lb/mm Btu
NO_x	0.6
SO_2	1.2
Particulate matter	0.03

Another primary consideration in the selection of the secondary particulate control device will be the feasibility of combining particulate removal with NO_x and/or SO_2 control. For example, bag filters operating at 100–150°C could be used to contact SO_2 with hydrated lime sorbents, or at 150–250°C to contact NH_3 with NO over a carbon catalyst. We will explore the use of carbonaceous engine particulate as a catalyst for the NH_3–NO reaction.

7.3 NO_x Control Options. Table 11 lists six options for NO_x control in order of priority. The preferred approach will be reburning. In this process NO is reduced to N_2 by hydrocarbon radicals created in locally reducing pockets of a "low-temperature" flame. NO_x reductions of 50–90 percent have been achieved in the laboratory using natural gas as the reburning fuel under conditions representative of boiler furnaces and process heaters [10]. Although reburning has not yet been applied to diesel engines, reductions of up to 50 percent have been demonstrated with gas turbine combined-cycle systems equipped with either duct burners or exhaust-fired heat recovery boilers under nonoptimized mixing conditions [11–13]. (In the gas-turbine system, the duct burner is only designed to raise the temperature of the turbine-exhaust gas which improves the economy of the heat recovery equipment.)

The low capital cost of reburning combined with the potential for more efficient waste heat recovery and more complete burnout of coal char make the process attractive. The reburning process must be optimized for the coal-fueled diesel engine. In particular, the effects of mixing, exhaust gas composition, and temperature on NO_x reduction will be explored.

Two processes for reducing NO_x by ammonia injection over a particulate carbon catalyst will be considered next. Both options use the carbon-containing particles from the engine as a catalyst for NO_x reduction. In option 2, a baghouse filter at 200°C traps the particulate carbon and provides residence time

Table 10 Emission goals

Pollutant	Anticipated standards, lb/mmBtu	Expected emission	Required reduction to meet NSPS
NO_x	0.6	800–1650 ppm* (2–4 lb/mm Btu)	70–86%
SO_2	1.2 or 70%	200 ppm (0.8 lb/mm Btu)**	~70%
Particulate			99.1%
Carbon		1.2 lb/mm Btu*	(worst case)
Mineral	0.03	0.3 lb/mm Btu***	
Sorbent		2.0 lb/mm Btu	
Total		3.5 lb/mm Btu	

*Based on preliminary emission measurements reported in this paper.
**Based on 1–2 percent sulfur in the raw coal.
***Based on 0.5 percent ash in the raw coal.

Table 11 NO_x control options

	Process	Percent removal	Advantage	R&D needs
1	Reburning	50–75	• Very inexpensive compared to SCR • Can recover heat • May be able to burn excess carbon	• Effect of exhaust conditions on NO_x reduction • Effect of mixing rate, fuel rate on NO_x reduction • Can carbon be burned?
2	NH_2 injection with baghouse	40–60	• Relatively inexpensive to run • Capital cost shared with particle removal	• Effectiveness of engine particles as catalyst • Catalyst poisoning by SO_2 • Effect of residence time, temperature
3	NH_3 injection in reactor	50–70	• Better NO_x removal than No. 2 • Inexpensive to run	• Same as No. 2 • Configuration of catalyst
4	NH_3 injection over CuO (UOP)	70	• Removes NO_x and SO_2 and particles, in principle	• Effect of engine particulate on catalyst lifetime and regeneration • Effect of temperature, NH_3 • Reactor design parameters
5	SCR at 400°C (750°F)	60–90	• Commercially available SCR	• Effect of engine particulate on catalyst lifetime and regeneration
6	RAPRENOX process	TBD	• No catalyst	• Temperature window • Process chemistry • Reactor design

Table 12 SO_2 control options

	Process	Percent removal	Advantages	R&D needs
1	$Ca(OH)_2$ injection at 540°C (1000°F)	40–60	• Inexpensive • Disposal of waste is relatively easy	• Effect of temperature, sorbent particle size, sorbent type, mixing
2	$Ca(OH)_2$ injection at 150°C (300°F)	50–80		• Effect of temperature, sorbent type, water content • Residence time in baghouse
3	Granular bed of CuO (UOP)	80	• Removes NO_x and SO_2 and particles	• Effectiveness of engine particulate on catalyst lifetime and regeneration • Reactor design parameters
4	Ca acetate in fuel	TBD	• No capital equipment required	• Determine required residence time in engine • Feasibility of adding Ca acetate to slurry
5	Adsorption on engine particulate	TBD	• Inexpensive	• Effect of residence time, temperature • Regeneration of sorbent • Simultaneous NO_x removal
6	Wet or dry scrubber at 66°C (150°F)	70–90	• Commercially available	

for the reduction of NO_x. If this is not sufficient residence time, a reactor can be built to provide better gas–solid contact (option 3). Option 3 is more expensive than option 2 because of the need to built a reactor. The operating costs of both 2 and 3 are relatively low, being determined by the cost of ammonia. These processes may not remove enough NO_x. Options 4 and 5 are more certain to achieve the desired reduction in NO_x because of previous work in research and experience with applications. However, these options, which involve a reduction of NO_x using ammonia in the presence of a metal catalyst, are more expensive.

The Shell/UOP process (option 4) has been used successfully to control both NO_x and SO_2 from boiler flue gases [14]. The capital cost is high, but since the process removes both NO_x and SO_2, and possibly particulate matter, the cost of an emission control system using this process might be comparable to other systems under consideration. Operating costs are high, mainly because the catalyst must be regenerated. In the past, regeneration has been accomplished by using hydrogen, which is expensive. If this process is used to control NO_x and particulate matter only, the expensive regeneration step can be avoided. However, we must ascertain whether particulate matter poisons the catalyst activity for NO reduction at this temperature. The effect of the engine particulate on catalyst lifetime is unknown at this point and must be studied if this option is to succeed.

Selective Catalytic Reduction or SCR (option 5) is used commercially to control NO_x from large stationary sources. Recently, SCR has been tried on oil-fired diesel engines with mixed results [15, 16]. As with option 4, understanding the effect of the engine particulate on the catalyst lifetime is crucial to making this process work.

Another option is the RAPRENOX process, using cyanuric acid to reduce NO_x [17]. At this time, this option should be considered very high risk. Only laboratory testing has been accomplished to date, and the temperature requirement of the process may not be compatible with coal-fueled diesel engines.

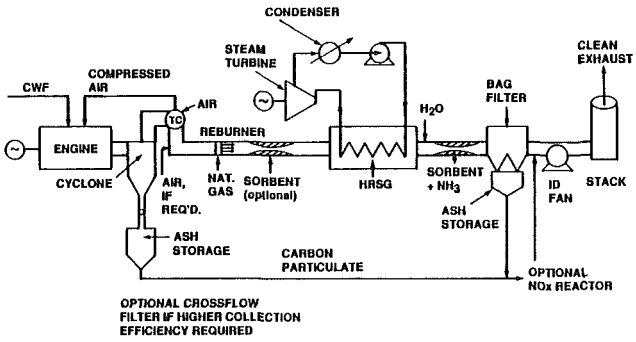

Fig. 8 Coal-fueled diesel, combined-cycle mode for power generation

7.4 SO_2 Control. Table 12 lists options for SO_2 control in the order of priority. Several options involve contacting the exhaust gas with calcium oxide or hydroxide to remove sulfur. Options 1 and 2 use direct injection of $Ca(OH)_2$ at 540°C and 150°C, respectively. The cost of direct injection is significantly lower than the cost of a scrubber (option 6). In order to optimize the processes in options 1 and 2, the effect of temperature, sorbent type and size, and residence time on sulfur capture will be studied. Option 1 might not remove enough SO_2 in the residence time that is available. Option 2 uses a baghouse to collect sorbent and provide long contact times between gas and sorbent.

Option 3, the Shell/UOP process, has been discussed above. The process is expensive when used to remove SO_2, but could potentially remove NO_x, SO_2, and particulate matter.

Options 4 and 5 are considerably more speculative than the ones discussed thus far. Injecting a calcium compound (calcium acetate) into the engine produces a fine aerosol of CaO that can capture sulfur at 1000–2000°C. This has not been tried in coal-fueled diesel engines. No equipment is required for this option, but the feasibility and cost of adding calcium acetate to the slurry needs study. Option 5 utilizes the carbon particulate from the engine as a sorbent for SO_2. This option appears inexpensive, but the amount of sulfur capture has not yet been defined and questions remain concerning the disposal of the acid-laden carbonaceous residue.

7.5 System Integration. A schematic diagram of a preliminary conceptual coal-fueled diesel emission control system is shown in Fig. 8. Here we have included a high-temperature cyclone collector to protect the turbocharger, a reburning system downstream of the turbocharger, a heat recovery steam generator, sorbent injection (hydrated lime for SO_2, ammonia for NO_x) at 150°C, a bag filter for final particle cleanup and contacting of sorbent with NO_x and SO_2, and an induced draft fan to assure exhaust gas flow to the stack. The expected performance of these devices is shown in Table 13. Another possible configuration would place the reburn system upstream of the turbocharger.

Note that reburning is effective in reducing both NO_x and particulates. Using natural gas as the reburning fuel, the pollutant concentrations are diluted by 20 percent on a heat-input basis. In addition, we expect further burnout of carbonaceous particles and destruction of 50 percent of the NO_x in the reburning flame giving overall reductions of 36 percent for particulate matter and 60 percent for NO_x.

Also note that the SO_2 reduction due to hydrated lime injection is enhanced by using a bag filter to collect the particles. The bag filter also provides contact area for reaction with NO with ammonia over carbon surfaces that may be catalytically active for this reaction.

References

1 Carpenter, L. K., and Crouse, F. W., Jr., "Coal-Fueled Diesels: Progress and Challenges," ASME Paper No. 86-ICE-6, Feb. 1986.

Table 13 Preliminary performance of a 5 MWE coal-fueled diesel cogeneration emission control system

	Particulate matter, lb/mm Btu			SO_2, lb/mm Btu			NO_x, lb/mm Btu		
Emission control component	In	Out	Percent reduction	In	Out	Percent reduction	In	Out	Percent reduction
Cyclone (including ash handling)	1.5	0.69	54	1.60	1.60	0	2.4	2.4	0
Reburning	0.69	0.44	36	1.60	1.28	20	2.4	0.96	60
Low temperature lime injection	0.44	2.54	--	1.28	1.00	22	0.96	0.96	0
Bag filter w/NH_3 injection (including ash handling)	2.54	0.03	98.8	1.00	0.50	50	0.96	0.6	38

2 Wilson, R. P., "Coal-Fueled Diesel Systems for Stationary Power Applications: Assessment of Merit," Topical Report prepared by Arthur D. Little, Inc., under contract to the Department of Energy/Morgantown Energy Technology Center, Sept. 1986.

3 Lai, M. C., Zhou, B., Cheng, W. K., Wong, V. W., and Benedek, K. R., "Parametric Studies of Coal-Water Slurry Combustion in a Rapid Compression Machine," ASME Paper No. 87-ICE-9, Feb. 1987.

4 Balles, E. N., Benedek, K. R., Wilson, R. P., and Rao, A. K., "Analysis of Cylinder Pressure and Combustion Products from an Experimental Coal-Fueled Diesel Engine," presented at the Internal Combustion Engine Division Technical Conference, Kansas City, MO, Oct. 4–7, 1987.

5 Soehngen, E. E., "The Development of Coal-Burning Diesel Engines in Germany: A State-of-the-Art Review," Report prepared for the United States Energy Research and Development Administration, Report No. FE/WAPO/3387-1, Aug. 1976.

6 *Proceedings of the Fourth Annual Heat Engine Contractors Meeting*, United States Department of Energy, Office of Fossil Energy, Morgantown Energy Technology Center, Apr. 1987.

7 Caton, J. A., and Rosegay, K. H., "A Review and Comparison of Reciprocating Engine Operation Using Solid Fuels," SAE Paper No. 831362, 1983.

8 Walsh, P., Zhang, M., Farmayan, W., and Beer, J., "Ignition and Combustion of a Coal-Water Slurry in a Confined Turbulent Diffusion Flame," presented at the Twentieth Symposium (International) on Combustion, Ann Arbor, MI, Aug. 12–17, 1984.

9 Dunn-Rankin, D., and Kerstein, A., "Numerical Simulation of Particle Size Distribution Evolution During Pulverized Coal Combustion," *Combustion and Flame*, Vol. 69, pp. 193–209.

10 Yang, R. J., Arand, J. K., and Garcia, F. J., "Laboratory Evaluation of In-Furnace-NO_x-Reduction for Industrial Combustion Application," ASME Paper No. 84-JPGC-FU-12, Oct. 1984.

11 Arand, J. K., and Muzio, L. J., "Oklahoma Gas and Electric Combined Cycle NO_x Reduction Laboratory Tests," KVB, Irvine, CA, 1977.

12 Johnson, S. A., and Rawdon, A. H., "Control of NO_x Emissions From Power Boilers," *The Institute of Fuel*, Adelaide, Australia, Nov. 1974.

13 McElroy, M. W., "Oklahoma Gas and Electric Full-Scale Demonstration of NO_x Destruction in Fuel-Rich Burners," EPRI Program RP-782, Palo Alto, CA, 1977.

14 Faucett, M. L., Maxwell, J. D., and Burnett, T. A., "Technical Assessment of NO_x Removal Processes for Utility Application," U.S. EPA Report EPA-600/7-77-127, Nov. 1977.

15 Wasser, J. H., and Perry, R. B., "Diesel Engine NO_x Control With SCR," presented at the 1985 Joint Symposium on Stationary Combustion NO_x Control, sponsored by the U.S. EPA and the Electric Power Research Institute, Boston, MA, 1985.

16 Wasser, J. H., and Perry, R. B., "Diesel Engine NO_x Control: Selective Catalytic Reduction and Methanol Emulsion," presented at the 1987 Joint Symposium on Stationary Combustion NO_x Control, sponsored by the U.S. EPA and the Electric Power Research Institute, New Orleans, LA, 1987.

17 Siebers, D. L., and Perry, R. A., "NO_x Removal From Diesel Exhaust Using RAPRENOX," DOE Diesel Working Group Meeting, Cummins Engine Company, Columbus, IN, Feb. 1987.

APPENDIX

Metric Conversions

inch	=	2.54 cm
psi	=	6.895 kPa
inch Hg	=	3.386 kPa
Btu	=	1.055 kJ
lb	=	0.454 kg
lb/mmBtu	=	0.645 g/kWh

B. D. Hsu
GE Transportation Systems,
Erie, PA

G. L. Leonard

R. N. Johnson

GE Research and Development Center,
Schenectady, NY

Progress on the Investigation of Coal-Water-Slurry Fuel Combustion in a Medium-Speed Diesel Engine: Part 3—Accumulator Injector Performance

Coal-water-slurry (CWS) engine tests designed to evaluate a new accumulator-based injection system are described in this paper. The new injection system was found to improve CWS burnout considerably at both full and part engine loads. The peak cylinder firing pressure when operating with CWS was no higher than when operating with diesel oil. These data demonstrate the improved engine performance that can be achieved with the accumulator-based injection system.

Introduction

GE has been conducting research directed toward demonstrating the feasibility of burning coal-water slurries in medium-speed diesel engines. Early engine tests were run with conventional positive-displacement fuel injection systems. These tests, described by Hsu (1988a, 1988b), demonstrated that conventional injection systems were not suitable for buring CWS in medium-speed diesel engines. Only 95 percent coal burnout at full load was achievable, with the burnout fraction falling rapidly with decreasing engine load. Because of long ignition delays, peak firing pressures when operating with CWS were 10 percent higher than with oil-fired engine operation. A decision was made to build a new injection system with improved atomization characteristics at the start of the injection cycle. A system design goal was to also maintain good atomization characteristics over the load cycle of the engine. An accumulator-based system, with the injection pressure high at the start of the injection cycle and whose operation was independent of engine speed and load, appeared to meet the requirements. A prototype system was built and combustion bomb experiments, described by Leonard and Fiske (1987, 1988), demonstrated that improved CWS combustion resulted. The system was then further developed and tested on the GE 7 FDL medium-speed diesel engine. These engine test results along with a review of the new injection system are described in this paper.

Accumulator Injection System Design and Operation

A block diagram of the CWS accumulator injection system is shown in Fig. 1. A conventional jerk pump was used to pump diesel oil onto the backside of a thin metal diaphragm located between thick metal heads. The CWS on the opposite side of the diaphragm was thus pressurized and pushed into the accumulator injector. A check valve was included in the injector inlet line to trap the high-pressure CWS in the injector on the refill cycle of the diaphragm. A check valve was also included in the CWS fill line to keep the CWS from reverse-flowing on the pressurization cycle of the diaphragm pump. A normal pump plunger with a standard relief helix was used in the jerk pump. It was therefore possible to use the jerk pump for metering the fuel as well as for pressurization.

A cross-sectional sketch of the accumulator volume of this injector is shown in Fig. 2. The accumulator volume of this injector was approximately 235 cm^3. The system was sized to inject 3 g of

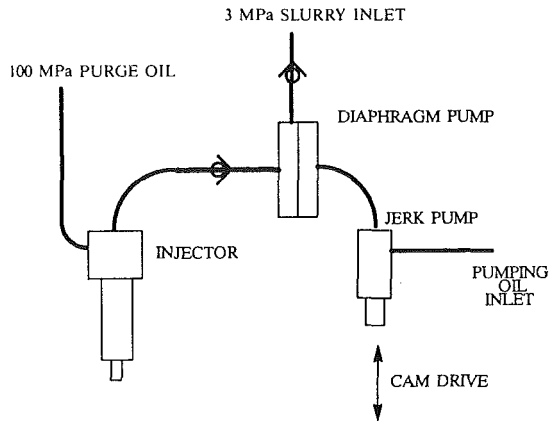

Fig. 1 Coal-slurry injection system

Contributed by the Internal Combustion Engine Division and presented at the Twelfth Annual Energy-Sources Technology Conference and Exhibition, Houston, Texas, January 22–25, 1989. Manuscript received by the Internal Combustion Engine Division August 1988.

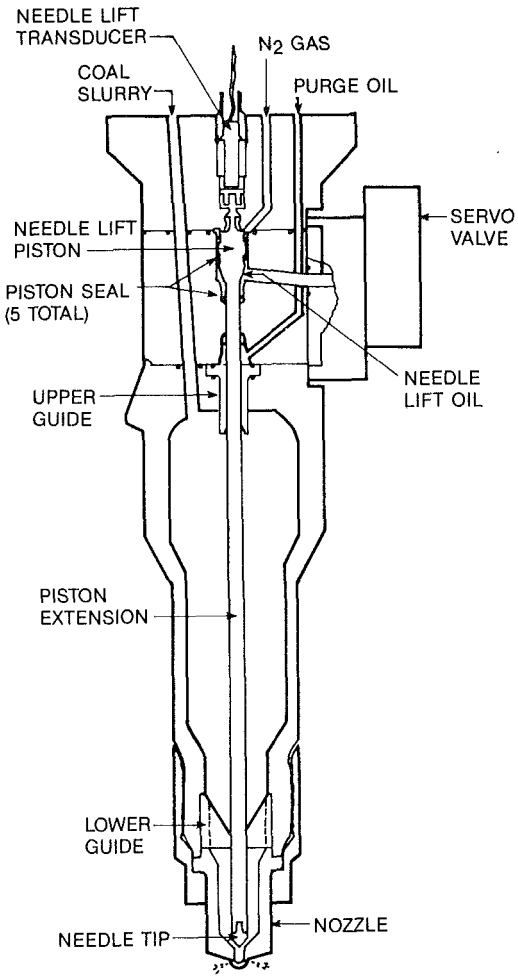

Fig. 2 Coal-slurry injector

CWS per injection, with the pressure in the injector falling from approximately 83 MPa to 48 MPa as injection occurred. The lower injection pressure limit of 48 MPa was found to yield good combustion efficiency and allowed the peak injection pressure to be kept at 83 MPa.

The injection cycle proceeded as follows: The jerk pump was stroked, pushing CWS into the injector and raising the pressure. The injector shutoff needle was kept from opening by high-pressure gas on top of the needle assembly. At the appropriate injection time, the Moog Series 31 valve, which was mounted on the injector, was opened and 27.5 MPa servo oil flowed under the needle lift piston. This oil lifted the needle, allowing the high-pressure CWS to flow into the nozzle sack region and into the engine. At the injection shutoff time specified by the electronic control, the servo valve was toggled, and the oil pressure under the needle lift piston was relieved. The needle was then shut by the high-pressure gas spring on top of the needle piston. The injection event was timed using the engine crank shaft encoder as the clock.

Before engine testing, the injector was run on a test stand. Figure 3 shows the needle lift profile along with the oil pressure in the diaphragm pump and the CWS pressure in the injector. The injector needle opened fully in about 0.5 ms and closed in 0.75 ms, meeting initial design goals. However, the goal of achieving stable and continuous operation at 83 MPa full-flow operation was not attained. This failure resulted from higher than expected leakage rates in the oil side of the diaphragm pump. Nevertheless, stable and continuous operation at an injection pressure of about 70 MPa was attained and engine test proceeded at this reduced injection pressure.

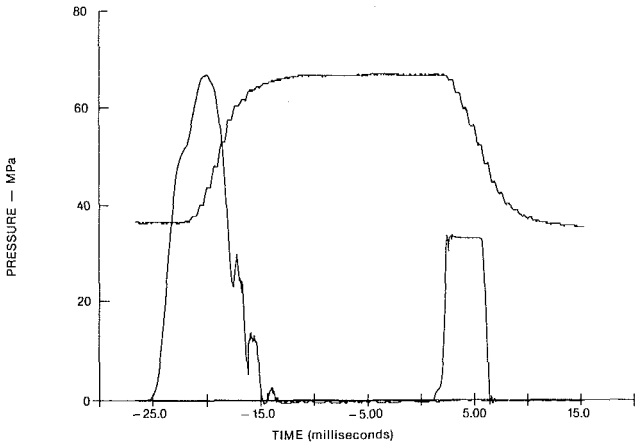

Fig. 3 Injector needle lift, accumulator pressure, and diaphragm pump-pressure

Table 1 Coal nominal lot analysis

Proximate Analysis		Ultimate Analysis	
% Ash	0.8	% Carbon	82.59
% Volatile	39.4	% Hydrogen	5.34
% Fixed carbon	59.8	% Nitrogen	2.08
		% Chlorine	0.18
Particle size (mass mean)		% Sulfur	0.85
Diameter (μm)	5.47	% Ash	0.81
		% Oxygen (diff.)	8.15
High heating value	34630 kJ/kg		

Engine Test Conditions and Fuel

The test engine, instrumentation, and data reduction procedures are identical to those described by Hsu (1988a, 1988b) and will not be repeated here. Tests were conducted at full engine speed (1050 rpm) and one mid-engine speed (785 rpm). Three to five percent of the fuel energy was derived from use of a diesel pilot. With the improved ignition characteristics associated with the pilot, the inlet air conditions (temperature and pressure) could be set at standard diesel-fuel operation levels. As stated earlier, the pumping system driving the accumulator injector leaked excessively, and consequently the full engine load of 196 kW was not reached. The test loads shown in the following results are the maximum loads attainable.

The CWS fuel was prepared by Otisca Industries using Kentucky Blue Gem coal. It was cleaned to 0.8 percent ash as shown in the Table 1 analysis. The as-delivered percentage of solids in the slurry was about 49 percent and the viscosity was from 147 to 254 cP at 112 s^{-1}.

The present investigation includes the effects on combustion of nozzle flow restriction and nozzle hole shape as well as their relationship to the accumulator injection pressure. A comparison of the combustion of CWS fuel using the new accumulator injection system and the positive-displacement injection system is also presented.

Engine Test Results

Injector Flow Area Effect. A number of different nozzle geometires were evaluated. Figure 4 shows heat-release profiles obtained with the best of the two classes of nozzles tested. All nozzles in the "high-flow" class had a flow area of approximately 2 mm^2. In the "low-flow" class, all nozzles had an area of about 1.2 mm^2. The best high-flow nozzle tested had 12 holes, each 0.51 mm in diameter. The best low-flow nozzle had 10 holes, each 0.39 mm in diameter. Figure 4 shows that

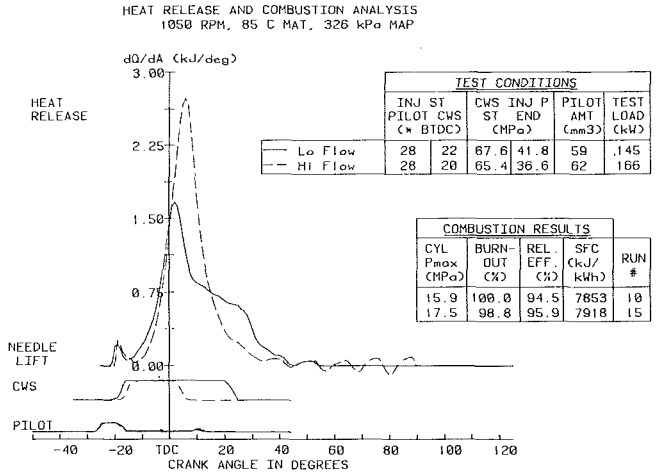

Fig. 4 High and low-flow injectors

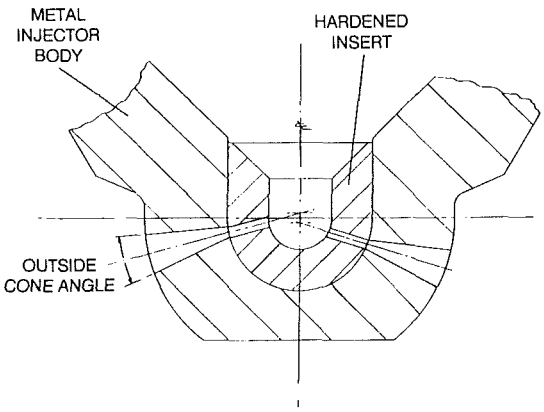

Fig. 5 Injector with hardened insert

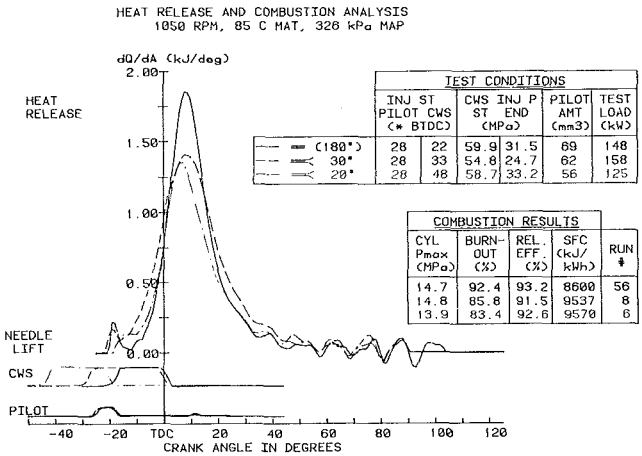

Fig. 6 Injector hole shape effect

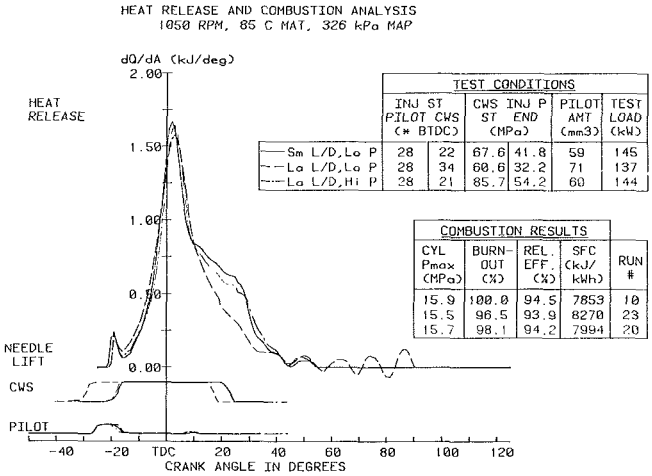

Fig. 7 Injector hole *L/D* effect

the heat-release profiles produced with the two different nozzle classes are quite different. While the heat-release trace of the high-flow nozzle retained the predominantly "premixed" combustion of CWS fuel reported previously (Hsu, 1988b), that of the low-flow nozzle distinctly showed a diffusion burning stage characterized by the hump or "knee" between 10 and 30 deg crank angle ATDC. The initial CWS premixed burning peak (those after TDC) is also much smaller in the latter case (the first small heat-release peak is credited to the premixed burning of the pilot diesel fuel). The resultant effect of this heat release, as analyzed by the method in (Hsu, 1984), is lower cylinder firing pressure, which is very desirable for coal-fuel engine combustion. The high-flow nozzle has a maximum cylinder firing pressure of 17.5 MPa; the low-flow nozzle developed only 15.9 MPa, which is not much different from the 15.5 MPa value obtained with standard diesel fuel operation.

The lower CWS premixed peak is probably the result of less fuel being in the cylinder at the time of maximum heat release. The CWS needle lift traces indicate that at the time of peak heat release, all the fuel had been injected into the cylinder for the high-flow nozzle, but for the low-flow nozzle the needle lift was only halfway into the total duration. The fuel that was injected after the premixed stage evidently was burned in the diffusive stage characterized by the later heat-release hump. Some diesel combustion experts consider this heat-release pattern a result of wall-wetting combustion caused by fuel jet impingement on piston top (Martin and Ahmed, 1986). However, from its timing relationship with CWS fuel injection needle lift in the present case, airborne diffusive burning seems more likely. Considering the uncertainties in calculating burnout (3 to 5 percent) it is interesting to note that the burnout rates in the two cases are not much different. The specific fuel consumptions are also essentially the same. Using the low-flow-rate nozzle together with high-pressure injection seems to have solved the previously raised question (Hsu, 1988b) of limiting firing pressure while obtaining high burnout rate for coal fuel diesel engine combustion.

The Effect of Injector Hole Shape. Tests at GE have shown that CWS nozzle tips must be built of superhard materials, such as diamond compact or BCN (cubic boron nitrite). Figure 5 is a sketch of a nozzle tip in which a hard insert was held in a metal housing. The metal housing outlet was flared 20 to 30 deg in an attempt not to disrupt the atomization process. This nozzle was tested and the results compared with a thin-wall injector without an insert (equivalent to 180 deg flare) having the same number of holes (12) and diameter (0.51 mm). The test conditions and combustion results are shown in Fig. 6. The maximum heat-release rate and coal burnout were much higher for the thin-walled nozzle with the 180 deg flare. As a result, the SFC for the thin-wall case was much lower than for the flared nozzle case.

The Effect of Injector Hole L/D Ratio. Since externally flared nozzle holes led to poor combustion, other approaches for using hard materials were needed. One approach would be to build the entire nozzle tip out of hard materials. Because of the low tensile strengths of hard materials the nozzle body would have to be significantly thickened. A metal nozzle with a large L/D (15.6) was built to determine whether good combustion could be achieved with thick-walled nozzles. The com-

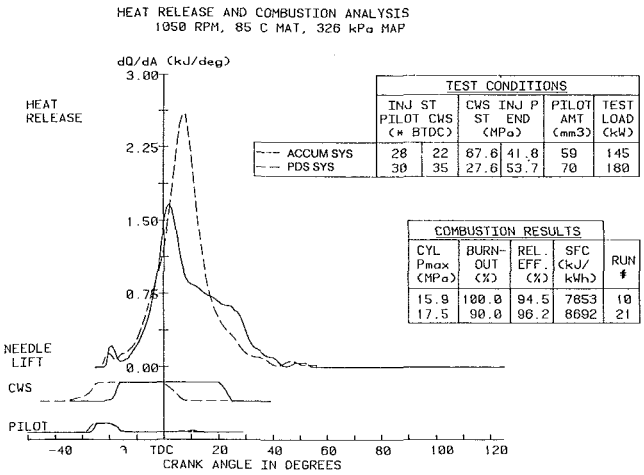

Fig. 8 Accumulator versus positive displacement injection systems (full engine speed)

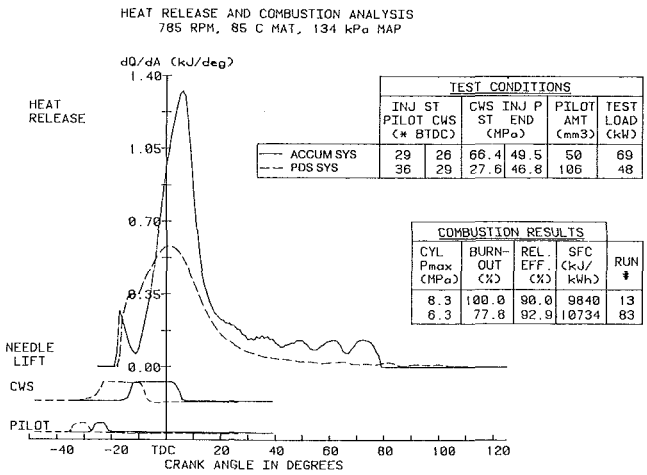

Fig. 9 Accumulator versus positive displacement injection systems (part-load speed)

bustion performance of this nozzle was compared with a small L/D ratio (5.6) nozzle having the same number of holes with slightly smaller diameter (0.39 mm versus 0.41 mm). The results are shown in Fig. 7. The solid and dashed lines are heat-release profiles of the small and the large L/D injectors, respectively. They were run with relatively low injection starting pressure (60 to 65 MPa). The peak heat-release values are almost the same and the crank angle positions of CWS ignition (the first valleys of the heat-release trace) are also the same. However, for the large L/D tip, the CWS fuel injection timing had to be advanced,as seen from the CWS needle lift traces. The heat-release knee that followed the peak also did not exist with the large L/D injector. The result is lower burnout (96.5 versus 100 percent) and higher specific fuel consumption (8270 versus 7853 kJ/kWh). Because the maximum cylinder firing pressure is determined primarily by the early portion of heat-release pattern, the P_{max} values for the two runs were not much different.

By increasing the starting injection pressure from 67.6 to 85.7 MPa it was possible to improve the combustion performance of the large L/D nozzle (Fig. 7). The heat-release profile of the high-pressure, large L/D case is almost identical to the low-pressure, small L/D case. Evidently higher injection pressure can compensate for the degradation in combustion with increasing L/D.

Injection System Comparison

Full Engine Speed. The combustion of CWS fuel using the accumulator injection system and the previously reported positive displacement system (Hsu, 1988b) at full engine speed is compared in Fig. 8. The accumulator injector had a high injection pressure at the start of injection (67.6 MPa), with the pressure falling to 41.8 MPa at the end of injection. The positive-displacement system had low injection pressure at the start of injection (27.6 MPa) and higher value (53.7 MPa) at the end. The heat release diagrams together with the needle lift traces graphically depict the combustion difference associated with these different injection profiles. The injection timing associated with the accumulator system could be delayed significantly relative to the timing of the positive-displacement system. This was possible because of the reduced ignition delay achieved with the accumulator system. Apparently the high injection pressure at the start of injection led to smaller slurry droplets and a reduced physical ignition delay. This reduction in ignition delay resulted in less fuel in the cylinder at the time of ignition and a lowering of the peak heat-release rate and peak firing pressure. Interestingly, at the recent DOE coal fuel heat engines conference, another researcher (Balles, 1988) showed the same kind of heat-release shape difference burning CWS in a diesel engine as a result of large inlet air temperature difference. In this case, the ignition delay was shortened as a consequence of inlet air temperature increase and not because of injection pressure modifications. However, the net effect on the heat release was the same. Finally, note that the coal burnout improved from 90 to near 100 percent when changing from the positive-displacement injection system to the accumulator injection system.

Part Engine Load. In Fig. 9, for the part-load case at 785 rpm engine speed, in-cylinder combustion is compared between the accumulator injector and the positive displacement injector. As discussed in previous literature (Leonard and Fiske, 1987), as the engine speed and load are reduced, the injection pressure developed with the positive-displacement system drops. The CWS INJ PRESSURE column in Fig. 9 shows that the highest injection pressure developed by the positive displacement system was only 46.8 MPa, which happened at the end of injection period. The injection pressure of the accumulator injector is independent of engine speed. In this test, it was at the same level as the previous full-speed case. It started at the high value of 66.4 MPa and ended at the low value of 49.5 MPa, which is still higher than the highest injection pressure of the positive-displacement system. As a result, complete burnout was achieved with accumulator system and less than 80 percent burnout was obtained with the positive-displacement system. Note that the pilot fuel injection timing for the positive-displacement system had to be very much advanced to compensate for the long CWS ignition delay.

Conclusions

- An accumulator-based CWS fuel injector has been developed for medium-speed diesel engine applications.
- CWS ignition delay can be significantly reduced by increasing the injection pressure early in the injection cycle. The accumulator injection system has this characteristic.
- As a consequence of reduced ignition delay, the accumulator injector can provide the kind of engine heat-release pattern that develops low cylinder firing pressure and high combustion efficiency.
- The accumulator injection system can provide complete CWS fuel burnout under part engine load condition.
- Flared injector holes led to poor combustion performance.
- An improved pumping system is required before full-load engine operation can be achieved with the accumulator injection system. A new pumping system is currently being built.

Acknowledgments

The support, and permission to publish this study, from the General Electric Company and Morgantown Energy Technology Center, DOE (Contract No. DE-AC21-85MC22181) are gratefully acknowledged. The authors would like to thank Dr. S. D. Savkar and Messrs. R. H. Jones and D. Mckinney of GE-CRD, Dr. P. L. Flynn, Messrs, J. F. Beal, E. G. Bricker, K. J. Giacomuzzi, D. J. Lecker, and R. C. McCall of GE-TS for their many valuable contributions. The guidance and support of this project by Messrs. L. K. Carpenter and N. F. Rekos of DOE METC are also greatly appreciated.

References

Balles, E. N., 1988, "Coal-Fuel Diesel Combustion: Cooper Bessemer Test Results," presented at the Annual Coal Fuel Heat Engines and Gas Stream Cleanup Systems Contractors Review Meeting, Morgantown, WV, June 14–16.

Hsu, B. D., 1984, "Heat Release, Cycle Efficiency and Maximum Cylinder Pressure in Diesel Engine—The Use of an Extended Air Cycle Analysis," *SAE Transactions*, 1984, pp. 4.766–4.778.

Hsu, B. D., 1988a, "Progress on the Investigation of Coal-Water Slurry Fuel Combustion in a Medium Speed Diesel Engine: Pt. 1—Ignition Studies," ASME JOURNAL OF ENGINEERING FOR GAS TURBINES AND POWER, Vol. 110, No. 3, pp. 415–422.

Hsu, B. D., 1988b, "Progress on the Investigation of Coal-Water Slurry Fuel Combustion in a Medium Speed Diesel Engine: Pt. 2—Preliminary Full Load Tests," ASME JOURNAL OF ENGINEERING FOR GAS TURBINES AND POWER, Vol. 110, No. 3, pp. 423–430.

Leonard, G. L., and Fiske, G. H., 1986, "Combustion Characteristics of Coal/Water Mixture in a Simulated Medium-Speed Diesel Engine Environment," ASME Paper No. 86-ICE-15.

Leonard, G. L., and Fiske, G. H., 1987, "A Comparison of a Positive Displacement Fuel Injection System With an Accumulator Based System for Coal Fueled Diesel Applications," ASME Paper No. 87-ICE-32.

Martin, J. K., and Ahmad, T., 1986, "Heat Release Characteristics of an Open-Chamber Diesel Engine Employing a Wall-Wetting Combustion System," SAE Paper No. 860420.

P. L. Flynn
GE Transportation Systems,
Erie, PA

G. L. Leonard

R. L. Mehan

GE Corporate Research,
Schenectady, NY

Component Wear in Coal-Fueled Diesel Engines

Practical use of coal-fueled diesel engines depends on the improvement of component durability. The wear characteristics of standard materials in the coal-fueled engine were studied first. Candidate wear-resistant materials were sorted by bench-scale tests. The best material combinations were applied to small-scale engine tests for operation on seeded diesel fuel. Components with hard materials and coatings were scaled up for coal–water mixture testing on the locomotive engine. Results indicate practical solutions for ring and liner wear and positive progress toward defining the material requirements for the fuel injection nozzle.

Introduction

This paper discusses the progress made in the durability development of a coal–water mixture (CWM) fueled, medium-speed diesel engine. The impact of engine durability and component cost on overall economics is discussed. The abrasive properties of the CWM fuel and its combustion products are characterized. The development of wear-resistant materials through bench-scale and small-engine testing is presented. Baseline oil-fueled diesel engine wear conditions are compared to the wear of standard materials and ceramic materials on CWM fuel.

The durability developments described in this paper are part of a larger overall program sponsored by the US Department of Energy to burn coal directly in heat engines. The diesel engine is a reasonable choice for coal fuel because it is moderately priced, already highly developed, and has a wide range of uses. The desire to burn coal in a diesel engine dates back to Rudolf Diesel's original experiments in the 1890s. Extensive work was done by Pawlikowski and others in Germany from 1930 to 1945. All of these studies recognized the wear of engine components as one of the serious hurdles to commercial success [1].

While the earlier workers attempted to burn uncleaned, raw coal in engines made of conventional metal components, the present program has the advantage of clean coal–water mixture fuels and today's engineering ceramics and superhard materials. The proper combination of fuel quality, analytic design, and material technology should make the coal-fueled diesel both technically and economically feasible.

Economic Potential

The economic potential for a coal-fired diesel engine is created by the cost difference between the coal-based fuel and the presently used petroleum-based fuel. The price of raw coal varies from 5 to 10 times cheaper than diesel fuel, depending on the price of oil. The price and the supply of coal are also much more stable than the price of oil since coal is obtained domestically and insulated from world politics.

The price differences between coal and oil-based fuels are strongly affected by the amount of processing that is necessary to prepare the coal for use as a heat engine fuel. While there are no full-scale production costs to calculate accurately the price of coal–water slurry, detailed studies of its production costs predict a much lower cost than fully refined coal-based synthetic liquids. Any coal-fueled heat engine must be able to use minimally beneficiated coal if it is to be justified on an economic basis. Coal-based synthetic liquids will only be viable at very high oil prices or when oil is unavailable [2].

The objective of the durability development phase of the coal-fueled diesel engine program is to provide engine life comparable to today's oil-fueled diesel. The level of material and design development necessary to achieve this goal is a function of the fuel quality, as shown in Fig. 1, and its price in comparison to diesel fuel. Increases in new engine component and repair parts costs counteract the benefit of burning a cheaper fuel. The durability aspects of the coal-fueled diesel will be properly developed when the minimum point in Fig. 1 is determined.

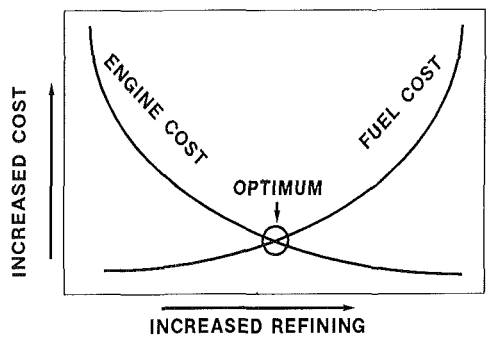

Fig. 1 Relationship between refining level of fuel and system cost

Contributed by the Internal Combustion Engine Division and presented at the Twelfth Annual Energy-Sources Technology Conference and Exhibition, Houston, Texas, January 22–25, 1989. Manuscript received by the Internal Combustion Engine Division August 1988. Paper No. 89-ICE-15.

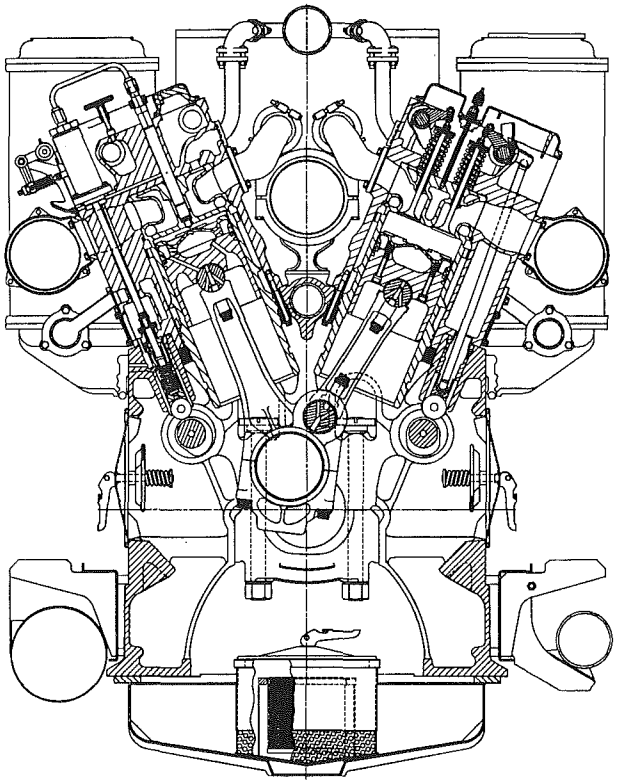

Fig. 2 Typical cross-sectional view of General Electric 7FD16 diesel engine

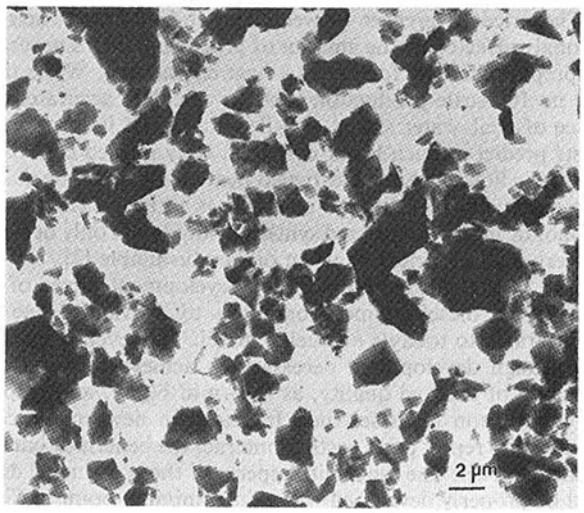

Fig. 3 Magnified appearance of particles in coal-water mixture before combustion; mass mean particle size is 3.0 μm

Scope of Problem

The durability of modern oil-fueled diesel engines has been developed over a period of many years. Today, lifetimes of several thousand full load hours are common. These life improvements have been accomplished through careful design and experimentation together with improvements in materials, filtration, and lubricating oil.

Coal–water mixture fuel is a mixture of finely ground coal and water with a small portion of additives to control settling and stabilize the viscosity. The coal in the slurry can be cleaned to less than 1 percent ash and sulfur by any of several methods. It has a specific gravity of approximately 1.12 and a heating value of about 14 MJ/kg. As a liquid–solid slurry, it cannot be easily filtered and does not make a good lubricant.

Even before combustion, the solid coal and mineral particles in the slurry would cause problems for conventional fuel injection systems. The particles in the slurry are about the same size as the close sliding fits in the fuel injection equipment. The particles can cause rapid wear and jamming of the pump plunger and barrel and needle valve. The solid particles (both organic and mineral) can cause rapid erosion on metal injector nozzle holes.

During combustion, the mineral particles fuse into spherical ash particles. The fine atomization needed for good combustion results in ash particles with about the same size distribution as the original slurry. Since the gas is immediately cooled by expansion, the ash resolidifies before it can impact on any solid surfaces. There is also the possibility of incomplete combustion of the coal that would leave some char particles. Some of these particles will be deposited on the bore of the cylinder liner and be trapped in the oil film. Particles will also be carried into the crankcase with the gas that leaks through the piston rings. Most of the ash will be carried out with the exhaust gas, where it can affect the operation of the exhaust valve and the turbocharger.

GE 7FDL Diesel Engine. The durability developments described in this paper are directed toward coal–water mixture fuel operation of the GE 7FDL diesel engine. This four-stroke, medium-speed diesel engine has been highly developed to provide the high power, reliability, durability, and efficiency needed for modern locomotive operation. It has a 229 mm bore and a 267 mm stroke. Full speed is between 900 and 1200 rpm, and full load ranges from 186 to 205 kW per cylinder depending on the application [3].

The engine is ruggedly built with a solid cast frame and separate cylinders for easy maintenance. A cross section of the engine is shown in Fig. 2. Its underslung crankshaft, large bearings, articulated connecting rods, and steel crown pistons are all designed to take the high loads concomitant with its high rating. The cast steel cylinder head is welded to a nitrided steel cylinder to withstand the rapid thermal cycling experienced in locomotive operation. The top piston ring is chromium plated for long life and the lower two rings are designed for good oil control.

In average locomotive applications, the engine has a useful life of about 25,000 hours between overhauls. This constitutes about four years of operation in which the locomotive may cover 1,000,000 km and accumulate over 4000 hours at full load. The fuel injection nozzles are usually changed at one or two year intervals depending on the severity of service.

Abrasives in the System

Fuel Characteristics. The fuel is a micronized coal–water mixture containing 50 percent coal and 50 percent water by weight. The fuel is beneficiated by a process known as selective agglomeration [4], in which mineral matter is reduced to 0.8 percent in the coal on a dry basis. Figure 3 shows a scanning transmission micrograph of the fuel. The fuel is generally sharp and angular, but with few obvious exposed grains of mineral matter.

Table 1 presents a typical ash analysis of the fuel. The fuel is rich in metals associated with softer minerals including iron and calcium. X-ray powder diffraction patterns of the low-temperature ash of this fuel reveals the presence of quartz, kaolinite, illite, calcite, dolomite, anhydrite, and pyrite. The most abrasive of these minerals (quartz) was present in low amounts, while the softer clays constitute the bulk of the mineral matter.

Products of Combustion. The second major source of wear concerns combustion products and their interaction with ring and liner surfaces. Particles captured in the exhaust duct are shown in Fig. 4. Here there are four types of combustion

Table 1 Properties of Otisca coal-water mixture

PROXIMATE ANALYSIS (Dry Basis)	
Ash Content	0.90%
Total Sulfur	0.80%
Volatile	37.92%
Fixed Carbon	61.18%
Solids	49.87%
Viscosity (112/s)	270 cp
Top Particle Size	12 micron
Mass Mean Particle Size	3.5 micron
ASH COMPOSITION	
SiO_2	22.4%
$A1_2O_3$	29.15
TiO	1.80
Fe_2O_3	28.54
CaO	9.86
MgO	3.00
K_2O	0.17
Na_2O	0.54
SO_3	0.62
P_2O_5	0.33
SrO	1.09
BaO	0.67
MnO	0.04

product including fused ash, unburned char, metal fume, and soot. The latter two species consist of 5–50 nm particles that most likely condensed from the vapor during the expansion stroke of the engine.

Ash particles consist of glass spheroids that had been fused in the flame, and then frozen before devitrification could occur. The fact that they are rounded and glassy should serve to reduce their contribution to wear as compared to their angular, crystalline mineral precursors. They average 1.1 μm in diameter. Each spheroid has unique composition associated with its local mineral environment during the combustion process.

The final component of the combustion products is char. For combustion efficiencies less than 99 percent, char will actually constitute the majority of combustion products by weight. Considering the high degree of porosity and the hollow-shell habit of the carbon, the char particles contributed the vast majority of abradant surfaces presented to the ring/liner region in these experiments.

Figure 5 shows a transmission electron micrograph of sludge taken from the centrifuge in the lubricant circuit. Noteworthy is the presence of both char fragments and ash spheres in concentrations comparable to those obtained from exhaust. Both forms of particulate, char and ash, reveal evidence of wear; the char edges are rounded, while the ash spheres are somewhat distorted. The significance and generality of these observations is not fully understood at this time.

Wear-Resistant Component Development

Fuel Nozzle Erosion. The fuel injection nozzle has to withstand high pressures and flow rates in order to atomize the fuel into fine droplets that can be ignited and burned within the time allowed by the diesel engine. It is one of the highest loaded and shortest lived parts in an oil-fueled diesel engine. The operating pressure of the nozzle is between 70 and 140 MPa. CWM-fueled diesel will operate in the upper part of this range to achieve better fuel atomization. Direct injection engines use nozzles with several spray holes to atomize the fuel. The liquid velocity through the holes is about 250 m/s for the CWM-fueled engine, compared to about 200 m/s for oil fueled applications.

Wear of Standard Steel Nozzle. During an early combustion test the same fuel injection nozzle was operated for 4.5 hours

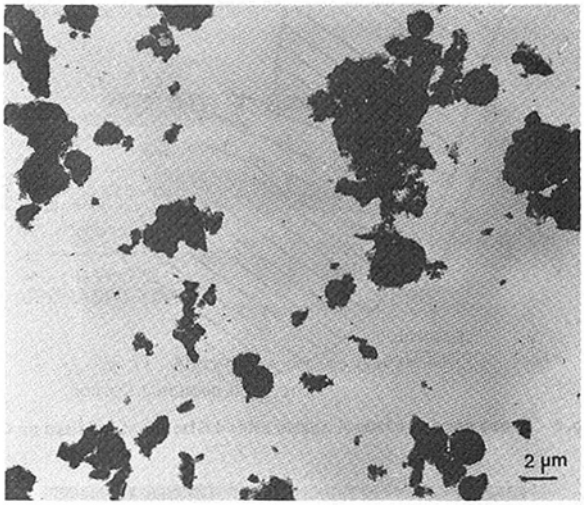

Fig. 4 Magnified appearance of particles from the exhaust of the diesel engine operated on the fuel shown in Fig. 3

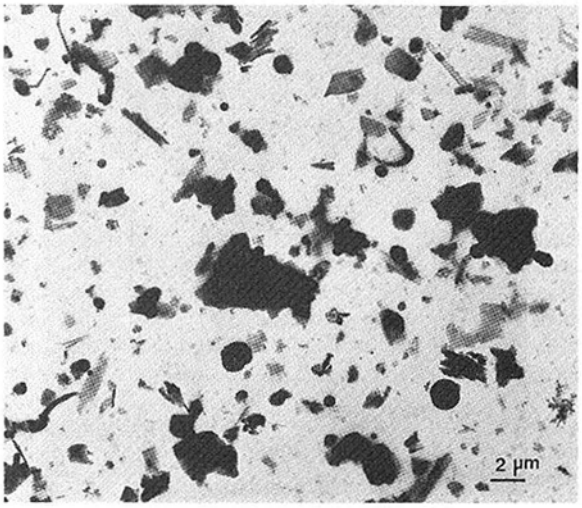

Fig. 5 Magnified appearance of particles collected from the lubricating oil of the coal-fueled diesel engine

at full load on CWM fuel. The nozzle was removed because injection pressure had dropped 15 percent during this period and the combustion quality had become unacceptable. The nozzle was a commercially available Lucas Bryce design with 12, 0.55-mm-dia spray holes. The part was made from carburized and hardened steel.

The nozzle was sectioned to examine the condition of the hole entry and to measure the wear along the length of the hole. The wear of the spray hole was not uniform in dimensional change or in wear mechanism. The exit of the hole was worn more than the entry, as is shown in the cross section in Fig. 6. The entry of the hole was rounded by an erosive mechanism, as shown in the electron micrograph in Fig. 7.

The middle and exit of the hole did not appear to be worn by the same erosive mechanism. Its surface showed hard phases standing up in relief over the martensitic matrix with some etching of the matrix. There were no erosion furrows as seen at the entry. This suggests a different and more complex wear mechanism than previously suspected. In addition to simple erosion from the solid particles in the liquid stream, cavitation and corrosion may also be involved in fuel nozzle wear.

Orifice Erosion Tests. Candidate nozzle materials were sorted by pumping 28 MPa CWM through small orifices. The change in effective orifice flow area (defined as the product of the

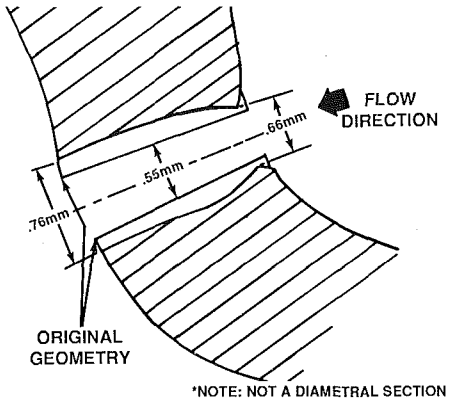

Fig. 6 Cross section of steel nozzle after 4.5 hours at full load on CWM

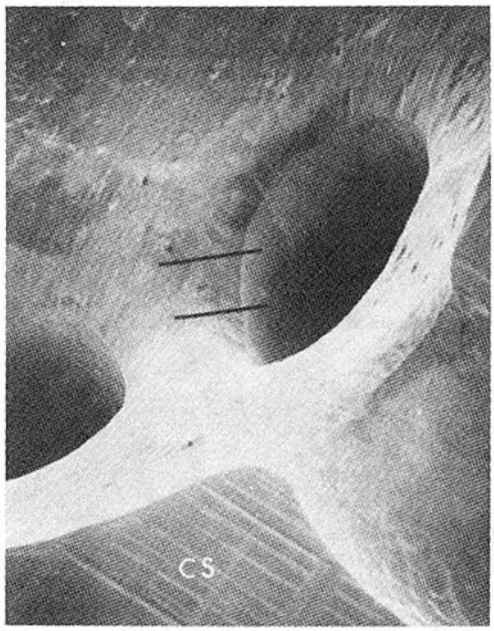

Fig. 7 The interior of the fuel nozzle shown in Fig. 6. The entry of the hole was eroded by the CWM fuel. The distinct change in surface appearance after the entry indicates a change in wear mechanism.

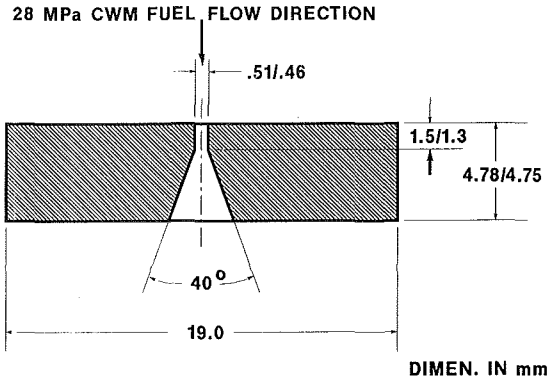

Fig. 8 Orifice erosion test specimen

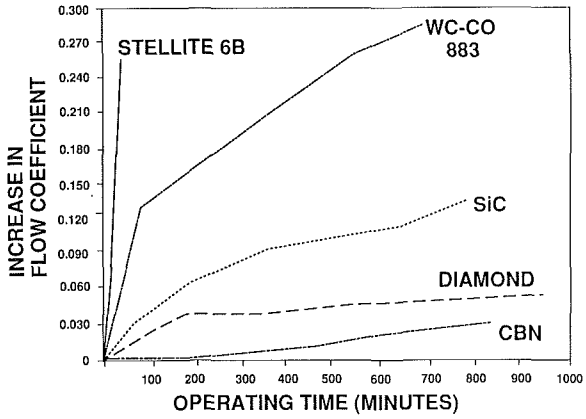

Fig. 9 Results of orifice erosion test. Superhard diamond and CBN materials are able to resist CWM fuel erosion.

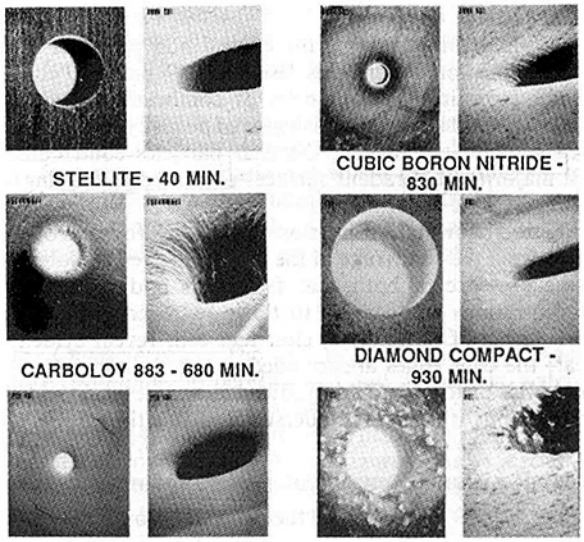

Fig. 10 Erosive wear of orifices by continuous 4000 psi CWM flow

flow discharge coefficient and geometric cross-sectional area) was measured and used as the criterion for assessing wear. A sketch of the orifice geometry is given in Fig. 8. Slurry entered the sharp-edged side of the nozzle and exited via the flared cone portion. The cone section provided structural support to the orifice.

The fractional change in effective flow area is plotted against slurry flow time in Fig. 9. The change in effective area was determined by collecting for 5 min and then weighting the water passed through the orifices at 0.7 MPa. The erosion experiments were conducted on a continuous basis, versus the pulsed flow of a diesel engine injector. Therefore the test duration does not reflect the expected life of a nozzle in an engine, but rather provides a means to compare material performance in an erosive environment.

When interpreting the results given in Fig. 9 it should be noted that the change in effective flow area is not linearly related to the volumetric loss of material from the nozzle tip. This results from the large change in the flow discharge coefficient of an initially sharp-edged orifice as the edge is rounded. Photographs of the orifices after the testing period are given in Fig. 10. The material that wore the most rapidly, Stellite 6B, had a completely rounded inlet and the diameter had changed from 0.46 to 0.61 mm during the 40 min test duration. Clearly, Stellite 6B would not be a suitable nozzle tip material.

The diamond compact and CBN (cubic boron nitride) demonstrated high resistance to erosive wear. The diamond compact, a product of GE Specialty Materials and commonly used in wire drawing die applications, wore very little after an initially short period of time during which a few of the more loosely held diamond grains were pulled away. The wear of the CBN orifice differed somewhat from the diamond case. The sharp edge of the CBN was being uniformly worn away,

Table 2 Ranking of materials using the orifice air erosion tests

MATERIAL	ORIFICE EROSION RATE	90° AIR EROSION RATE cm3 gm-1 x 10-6
Diamond Compact		0
Cubic Boron Nitride		0
Si3N4	–	0.5
WC + 6Co (K313)	–	3.5
TiB2	–	4.3
Sapphire	–	9.8
A1203/SiC Composite	–	14.4
SiC		15.9
WC + 6Co (Carboloy 883)		18.3
Stellite 6B		34.5
440C Steel	–	39.1

but at an extremely slow rate. Similar rates of wear are common in diesel nozzle tips operating on clean oil. After the initially aggressive wear associated with the highly accelerating flow around the sharp edge, it is likely that the rate of wear of the CBN would decrease significantly. Both the diamond compact and CBN look like excellent candidates for CWM nozzle tip applications.

The silicon carbide orifice was made from Hexalloy SA, a Carborundum Corp. grade of alpha sintered silicon carbide. The sharp edge of this orifice was wearing at a significantly higher rate than the CBN. But like the CBN, there was no measurable change in the diameter of the silicon carbide orifice. From the test durations employed, it is difficult to determine whether the silicon carbide material can yield the minimum of 2000 hours of nozzle life.

The final material tested was a cemented tungsten carbide, Carboloy 883. This grade of carbide is not particularly fine grained and has a binder content of 6 percent cobalt. From the figures it can be seen that this grade of carbide, although an order of magnitude more erosion resistant than the Stellite 6B, wore rapidly. Carbide grades optimized for erosive resistance where introduced by the Kennametal Corp. after the erosion testing described in this section were completed. Results obtained with the new carbides are described in the next section of this paper.

Air Erosion Tests. The orifice erosion tests described in the previous section provide accurate erosion information under actual CWM operation, but are difficult and time consuming. In order to evaluate a large number of materials of arbitrary shape, an air erosion test was developed. A large number of materials can be screened using this device, and as will be shown below, materials are ranked in the same order using both erosion techniques.

The apparatus is shown in schematic form in Fig. 11. It consists of an S. S. White Model 6500 Airbrasive unit with the abrasive flow controlled by a Plasmadyne powder feeder. The particle velocity was measured by the two-disk method, and was approximately 160 m/s [5]. The tests were conducted for 120 s at a particle flux of 83 mg/s. Impingement angles of 90 and 30 deg were tested. In most cases, the unused portion of the circular orifice specimen was used for the air erosion tests so the same material was evaluated.

The comparison between the orifice and air erosion test is shown in Table 2. Because of the different ways the two tests were conducted, it is not possible to compare quantitative erosion rates. However, the relative ranking of the evaluated materials is identical, which makes it feasible to evaluate candidate nozzle materials using the simpler and less expensive air erosion technique.

Wear of Tungsten Carbide Nozzle. During the first part of the engine test with hardened materials, a fuel injection nozzle

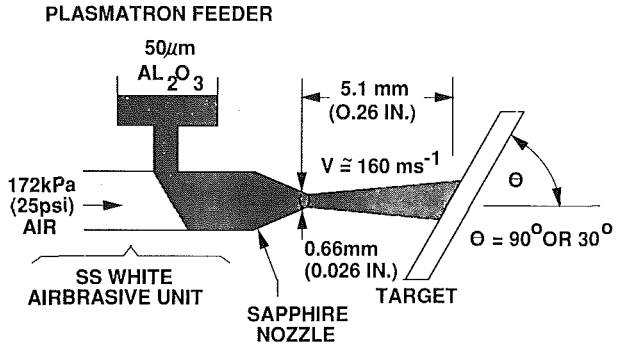

Fig. 11 Alumina air erosion test schematic

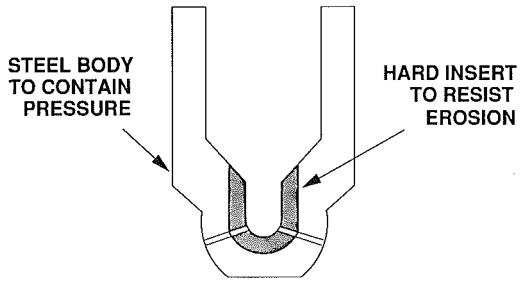

Fig. 12 Proposed design of CWM fuel injection nozzle with erosion-resistant ceramic insert

with a Kennametal K-313 tungsten carbide insert was tested. The nozzle ran 4.5 hours before a crack in the insert was detected. The nozzle was constructed with the hard insert on the inside surrounded by steel, as shown in Fig. 12. The insert was to protect the hole entry and the steel body was to carry the tensile load. This configuration resulted in a long aspect ratio hole.

When sectioned after 4.5 hours of operation, the tungsten carbide insert showed a wear pattern similar to the steel nozzle, but the wear rate was considerably lower. The hole inlet was slightly rounded and the body of the hole was slightly enlarged. Different wear mechanisms appeared to be acting on the entry and the body of the hole, similar to the steel hole. The steel outer portion of the hole was not surface hardened and was greatly eroded during the test.

The wear of the tungsten carbide insert indicates that this material is not hard enough to resist the erosive action of CWM. It will be necessary to go to superhard materials to combat erosion in the fuel nozzle. The rapid erosion of the steel housing indicates that this design is not acceptable. The entire length of the hole must be protected from the CWM. This means that designs with the hard material in tension will have to be developed.

Effect of Injector Wear on Performance. An injector with a Kennametal K313 insert and 12 straight 0.36-mm-dia holes was run on the engine for 12 hours. During this period, the injection timing and duration were periodically adjusted to yield optimum performance to compensate for injector hole wear. A comparison between the engine combustion with the new injector and after 12 hours is shown in Fig. 13. When new, the heat release shape has the characteristic "knee" with about 98 percent burnout. At the end of the 12 hours, the CWM fuel injection had to be advanced by 5 crank angle degrees, as shown with the needle lift traces, to maintain efficient combustion. The "knee" on the heat release shape disappeared and the total burnout rate dropped down to about 90 percent.

When tested under 690 kPa water pressure, the flow rate of

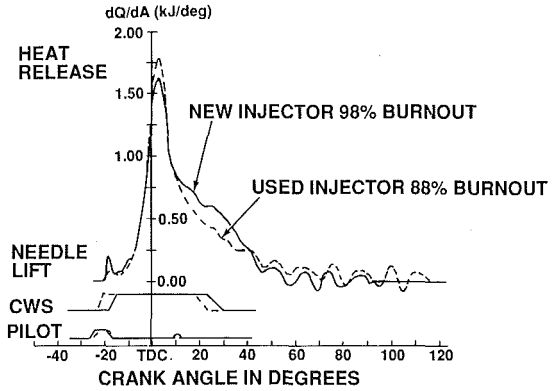

Fig. 13 Effect of fuel nozzle wear on CWM combustion performance

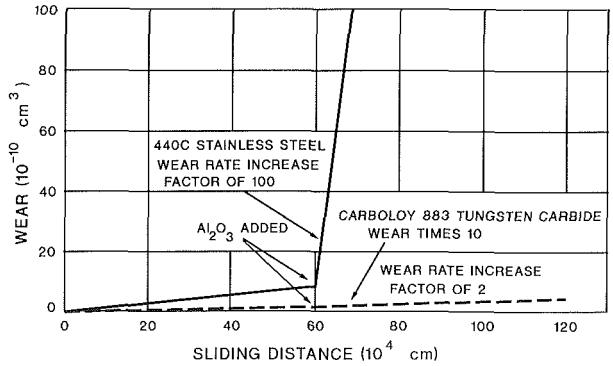

Fig. 14 Results of pin-on-disk test of 440C stainless steel and sintered tungsten carbide

the used injector had increased 15 percent over the test period. While the hole sizes in the hardened insert measured with wire gages did not increase much, those in the soft body material increased to over 0.50 mm. A cone shape evidently developed as a result of hole wear. The cone shape probably deteriorated the combustion more than the absolute flow rate increase.

Ring and Cylinder Liner Wear. The piston ring and cylinder liner form the main tribological couple in the engine. It is the interface between the fixed and moving parts of the engine and is responsible for a major part of the frictional losses. It also must seal the combustion gas during compression and combustion and contain the lubricating oil in the crankcase.

The worst wear condition occurs when the piston reverses at the top of the stroke. This is the hottest part of the liner and the farthest from the lubricating oil supply. Gas pressures are highest at this point and the ring velocity goes through zero as the piston reverses. The combination of these severe tribological conditions lead to a wear step in the liner at the top reversal position. The majority of the ring wear also occurs during this part of the cycle. Both the top compression ring and the cylinder liner can wear 0.2 percent on a diametral basis before the operation of the engine is compromised.

Bench Scale Wear Tests. Material couples for ring and liner application were sorted with pin-on-disk wear tests [6]. The pins were 1.27 cm long and 4.75 mm in diameter with a polished 4.75 mm hemispherical end. The pin was rotated at 18.8 cm/s against the stationary disk. All tests were conducted with a lubricant present, either with or without added contaminant. The lubricating fluid was white mineral oil with a viscosity of 75 cs held in a container surrounding the stationary disk and rotating test pin. The contaminant added to the mineral oil was 2.0 μm alumina (Al_2O_3), in a concentration of 2 g/L.

Materials in the form of wear pins and/or disks were fabricated either as coatings or in monolithic form. Monolithic materials were tested to establish baseline data for comparison with data on coatings of the same or similar composition. Coatings were applied by a variety of methods, including plasma deposition, chemical vapor deposition, and electroplating.

The addition of Al_2O_3 to a lubricant resulted in a dramatic increase in the wear rate of metals. The wear rate of 440C stainless steel increased by a factor of about 100 with the addition of Al_2O_3, as shown in Fig. 14. The effect of alumina addition depended on the hardness of the sliding members. The wear of tungsten carbide sliding against itself only increased by a factor of two after alumina addition.

Approximately 100 material pairs were surveyed for potential use as sliding members in a lubricant containing an abrasive, including: SiC, Al_2O_3, WC + Co, Cr_2O_3, Cr_3C_2, TiC, and Si_3N_4. Of these materials, the tungsten carbide family of materials consistently showed the best performance. Furthermore, this is a mature family of materials with several proven methods available for monolithic production and coating applications.

Table 3 Yanmar engine results

Run Number	Ring Material	Liner Material	Ring Wear Rate cc/hr
Uncontaminated Runs:			
50	Chrome	Cast Iron	1.8E-5
51	WC+Co (ST)	WC+Co (LPPD)	1.4E-5
2%-D4 Contamination:			
52	Chrome	Cast Iron	41.5E-5
53	WC+Co (ST)	WC+Co (LPPD)	55.0E-5
54	WC+Co (PT)	WC+Co (LPPD)	64.0E-5
56	WC+Co (K96)	WC+Co (K703)	0.8E-5
57	WC+Co (ST)	WC+Co (K703)	3.5E-5
58	Chrome	WC+Co (K703)	7.1E-5
59	Chrome	Cast Iron	28.8E-5
60	Cr3C2+Mo (K1008)	WC+Co (703)	24.5E-5
Otisca Ash Contaminated			
61	WC+Co (K96)	WC+Co (K703)	1.43E-5
62	WC+Co (ST)	WC+CO (K703)	7.00E-5
63	Chrome	Cast Iron	250.00E-5

ST - SermaTech Plasma Sprayed
PT - Plasma Technics Plasma Sprayed
LPPD - CRD Low Pressure Plasma Deposited
K96 - Kennametal Monolithic Carbide
K703 - Kennametal Monolithic Carbide

Small Engine Tests. In an effort to identify ring and liner materials for use in CWM-fueled engines, piston rings and cylinder liners were fabricated from various materials and run in an engine to which abrasives had been added to the fuel. Tests were conducted on a single cylinder Yanmar prechambered diesel engine at 9 kW and 2100 rpm. The engine's fuel, standard diesel oil, was doped with either coal ash or octamethyl/cyclotetra siloxane (D4). When burned, this additive formed fumed silica, which, like the coal ash, deposited on the liner and wore the rings and liner as the engine ran.

The first series of tests was conducted with uncontaminated fuel. A new engine was used for these baseline tests. In the second series of tests, 2.0 percent by weight D4 was added to the diesel fuel. In the final test series 0.2 percent by weight coal ash was added to the diesel fuel. This ash was removed from the parent bituminous coal via the Otisca T process and had not been exposed to a hot oxidizing environment prior to being added to the diesel fuel.

Results of the engine tests are given in Table 3. In each case new rings were installed in the engine prior to testing. In the baseline tests the engine was run for 16 hours after which it was dismantled and the ring wear was determined. The same rings were then reinstalled and run for another 8 hours. The rings were removed and the wear that occurred in the last 8

test hours was measured. The rings were run for 8 hours and the wear was measured when run on contaminated fuel.

In test 50 standard commercial grade engine materials were operated on clean diesel fuel. The rate of piston ring material loss (1.8×10^{-5} cc/h) is typical of ring wear and corresponds to several thousand hours of useful ring life. When these materials were run on D4 contaminated fuel in run 52, the wear rate increased by a factor of approximately 20.

A new liner and piston rings were built of monolithic tungsten carbide/cobalt and installed in the engine. These components were then run with the D4 doped fuel. As shown in Table 3 (test 56) the monolithic materials performed extremely well. The rate of wear of these parts when running with abrasives was less than the wear of standard engine components running with clean fuel. A plasma-sprayed ring run against the monolithic carbide liner (test 57) also showed low wear rates. It is interesting to note that the chromium-plated ring wore much less when run against the monolithic liner (test 58) when abrasives were present as compared to the case iron liner (test 52). In test 60 a commercially available chromium carbide/moly piston ring did not perform very well. The plasma-coated liner performed well on diesel fuel but caused high ring wear when operated on the abrasive. The cause of this behavior is not clearly understood at this time.

Coal ash was added to the fuel in tests 61 and 63. The coal ash proved to be more aggressive toward the engine than the fumed silica. Standard engine materials wore approximately 100 times their normal rate when the ash was added (test 63). In contrast, the monolithic tungsten carbide ring, when run against the monolithic carbide liner, performed very well, test 61.

The testing described in this section demonstrated that tungsten carbide has a high potential for use as piston ring and cylinder liner material in CWM-fueled engines. These results are consistent with the bench scale pin-on-disk test described in the previous section. The testing also demonstrated, as did the pin-on-disk tests, that chromium carbide/moly rings will not run well against tungsten carbide in CWM-fueled engines. Finally, the plasma-sprayed liner did not perform well in the engine tests, although the pin-on-disk tests suggested it would. The discrepancy can probably be traced to the differences in manufacturing necessitated by the vast difference in size between the pin and liner specimens.

Full-Scale Ring and Liner Tests. Piston ring and cylinder wear was investigated in three steps on the full-size GE 7FDL engine. Standard metal components were operated first on diesel fuel, and then were run on CWM to determine the most important components for improvement. Third, improved materials were chosen through the bench-scale tests and ceramic-coated components were prepared for full-scale testing on CWM. All of the comparative tests were run for 25 full load hours with one intermediate examination.

Cylinder Liner Wear. The nitrided layer on the cast iron cylinder linear has a soft porous surface layer that wears away during the break-in period. When a new cylinder liner was run on diesel fuel, rapid wear was detected at the top and bottom ring reversal areas after the 8.5 hour break-in, as shown in Figs. 15 and 16. Wear was considerably less during the period between 8.5 and 25 hours. Further operation would show decreasing wear rates until a stable wear rate of about 20 μm per 1000 full load hours is attained.

The wear response of the nitrided cast iron liner to CWM fuel operation was similar to the operation on diesel fuel, except that the wear rate was about six times higher. Rapid break-in was seen, followed by lower wear rates. The wear surface of the liner had a polished appearance that was typical of a liner that had operated on diesel fuel for a longer period of time.

The first attempt at a harder cylinder bore used a commercially available, plasma-sprayed tungsten carbide coating, Union Carbide LW11B. The first 13 hours of operation on CWM fuel used a chromium carbide coated top ring, a chromium-plated middle ring, and an iron oil ring. Between 13 and 26 hours a tungsten carbide top ring and chromium plated lower rings were used. During both periods, the liner wear was much lower than with the cast iron liner operated on CWM. The wear rate at the top ring reversal was only two times higher than the cast iron liner operated on diesel fuel. The wear rate at the bottom ring reversal was very low, within the experimental error of the replication system used to make the measurements.

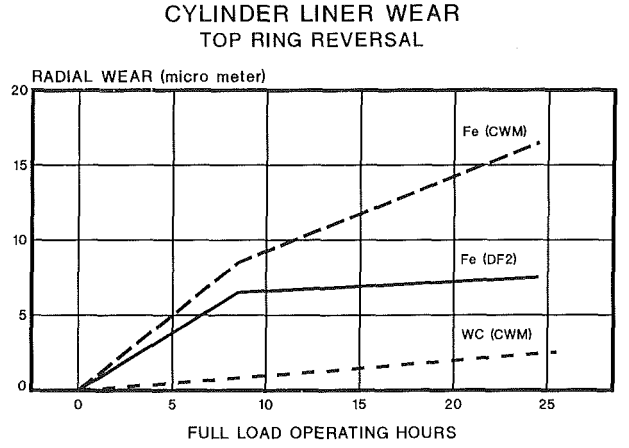

Fig. 15 Cylinder liner wear at the upper ring reversal position. Cast iron liner run on diesel fuel and CWM. Plasma-sprayed tungsten carbide liner run on CWM fuel.

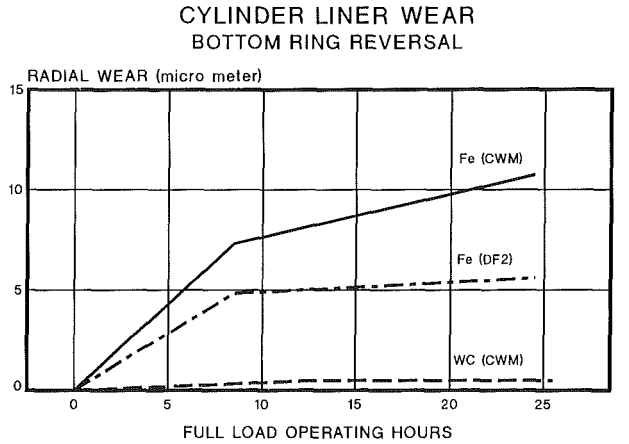

Fig. 16 Cylinder liner wear at the lower ring reversal position. Cast iron liner run on diesel fuel and CWM. Plasma-sprayed tungsten carbide liner run on CWM.

The surface of the tungsten carbide coated liner appeared to be wearing in normally during the first 13 hours when the chromium carbide top ring was used. During the 13 to 26 hour period, when tungsten carbide top ring and chromium-plated middle and oil rings were used, scuffing occurred between the chromium plated middle ring and the liner. The liner developed a metallic appearance over about one half of its circumference. The scuffing did not seem to affect the liner wear rate, but higher middle ring wear was seen.

The fact that the wear rate of the first attempt at a harder cylinder restored the wear rate to within a factor of two of the diesel fuel situation is a strong indication the cylinder liner wear can be solved within existing material technology.

Piston Ring Wear. Ring wear was studied with the same strategy used on cylinder liners. The standard materials were run first with diesel fuel and CWM fuel to understand the

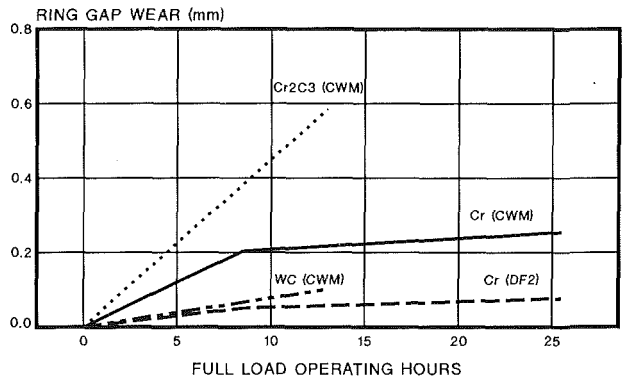

Fig. 17 Top ring wear. Chrome-plated ring run on diesel fuel and CWM. Plasma-sprayed chrome carbide and tungsten carbide run on CWM.

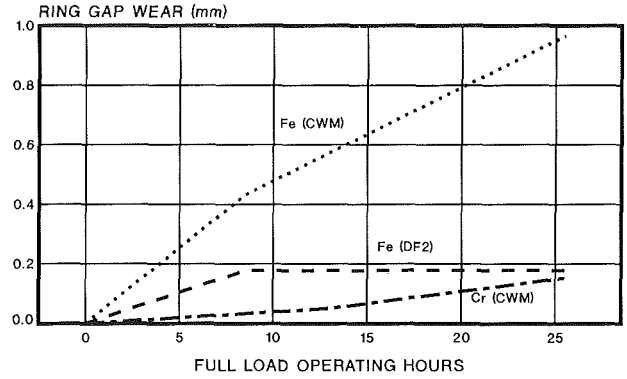

Fig. 18 Middle ring wear. Ductile iron ring run on diesel fuel and CWM. Chrome-plated ring run on CWM.

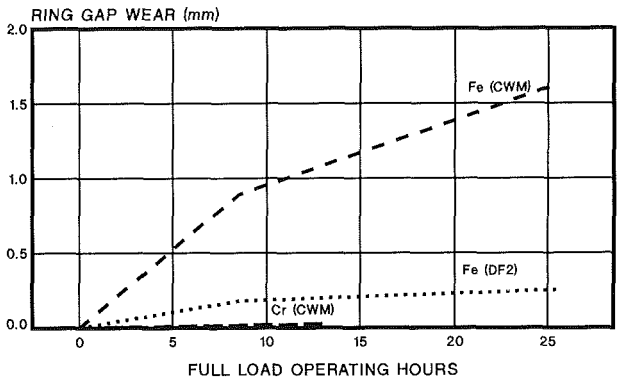

Fig. 19 Oil ring wear. Cast iron ring run on diesel fuel and CWM. Chrome-plated ring run on CWM.

wear problems. Materials selected in the bench tests were then scaled up to the GE 7FDL engine. However, the situation is more complicated with piston rings because each ring performs a different function and has a different design and a different material.

When operated on diesel fuel, all three rings showed the typical break-in behavior. The chromium-plated top ring wore less than the iron middle and oil rings, as seen in Figs. 17, 18, and 19.

When the same materials were operated on CWM fuel, accelerated wear rates were seen. The top ring showed a break-in behavior, but the wear rates were about five times higher than with diesel fuel. The iron middle and oil rings continued very high wear rates after the break-in period.

The first attempt at a more durable top ring used a commercially available chromium carbide-molybdenum, plasma spray coating. It ran well against the tungsten carbide liner on a preliminary diesel fuel run. It did not perform well in the bench tests, but was used because the tungsten carbide rings were not yet available. It did not perform well in the full-scale CWM test. Its wear rate was about twice that of the standard chromium-plated ring on CWM as shown in Fig. 17.

A plasma-sprayed, tungsten carbide coated top ring was run between 13 and 26 hours. The coating was the GG-WC-105 material that performed well in the bench tests. It was applied by the Gator-Gard high-energy plasma process. This coating performed very well on CWM fuel. Its wear rate was only about two times the rate of the standard chromium ring on diesel fuel.

The wear rates of the middle and oil ring were greatly improved by the application of chromium plate, as shown in Figs. 18 and 19. A standard chromium-plated top ring was run in the middle position for the full 26 hours with the tungsten carbide coated liner. The chromium-plated middle ring wore very little during the first 13 hours. Its wear rate was about one fourth that of the iron middle ring on diesel fuel. The scuffing that occurred in the second half of the test increased the wear rate of the middle ring. A chromium-plated oil ring was used during the last 13 hours only. The chromium-plated oil ring showed no measurable wear during this period.

The ring wear results appear to be very encouraging. As with the cylinder liner, wear rates similar to the diesel-fueled engine are attainable with reasonable advancements in material technology.

Other Potential Wear Problems. When this program was started, many potential wear problems were anticipated. To this point in time, over 50 hours of full-load CWM operation have been accumulated on the GE 7FDL research engine. Beyond the ring, liner, and nozzle problems already discussed, other serious wear problems have not developed.

Ash deposition and erosion was anticipated in the combustion chamber and the exhaust system, but these parts of the engine have remained very clean throughout the CWM tests. The diesel engine expands and cools the combustion gas immediately and the fused ash is resolidified in place before it can contact a solid surface.

Exhaust valve seat and stem wear was originally anticipated, but no evidence of abnormal wear has yet been seen. When the exhaust valve closes, the seat experiences a nearly normal impact. Some ash and unburned coal is trapped in the interface, but it does not accumulate or cause abnormal wear. The valve stem is chromium plated, which has proven to help resist coal ash wear.

Bearing wear was a great concern at the start on the test program. The main and connecting rod bearings of the CWM-fueled research engine have been examined at about 10 hour intervals and no abnormal wear has been seen. The bearings are fed with pressurized lubricating oil that is cleaned with a full-flow filtration system and a bypass centrifuge.

The durability of these areas of concern and additional components will continue to be monitored during further engine tests. Undoubtedly, longer periods of endurance testing and the scale up to multicylinder engines will uncover additional wear and durability problems, but we are confident that we have identified the highest priority problems. The secondary areas can be treated with similar design and material improvements.

Conclusions

Although the durability development of the coal-fueled diesel engine is just beginning, some conclusions regarding the measures necessary for commercially acceptable engine life can already be made.

1 The shortest life component is the fuel injection nozzle. Superhard materials, such as cubic boron nitride or diamond compact, will be necessary to restore the durability of the nozzle. The nozzle hole erosion mechanism is more complex than originally thought and may require design modifications to improve flow conditions.

2 Piston ring wear is high with standard materials, but tungsten carbide coatings can nearly restore the top ring wear rate to diesel fuel levels. Chromium plate is effective in reducing the wear rate of the lower rings, but design and material compatibility need to be addressed further.

3 Cylinder wear is not as rapid as earlier expected. Tungsten carbide coatings should provide adequate wear resistance for the cylinder liner. Further work remains to develop reliable and cost effective coating and finishing processes.

4 Exhaust valve, bearings, and other lubricated moving parts have not been seriously affected by operation on CWM fuel. These components will be monitored during future engine operation and scaled up to multicylinder configurations.

5 The overall wear conditions in the engine appear to be strongly related to the quality of the coal combustion. Finely ground CWM produced small wear particles. Ash particles are fused and resolidified in situ to form glassy spheres. Unburned carbon can contribute to the wear process and should be minimized in the combustion process.

Acknowledgments

The support and permission to publish the results of this study from GE Transportation Systems and DOE Morgantown Energy Technology Center are gratefully acknowledged. The work on which this paper is based was conducted under DOE Contract No. DE-AC21-85MC22181. The authors would like to thank Dr. Cliff Spiro, GE Corporate R&D; Mr. Anthony Giammarise and Dr. Bertrand Hsu of GE Transportation Systems; Mr. Nelson Rekos, Mr. Larry Carpenter, and Mr. Leland Paulson, Contracting Officer Technical Representatives DOE/METC, for their contributions, comments, and encouragements in the course of this study.

References

1 Soehngen, E. E., "Development of Coal-Burning Diesel Engines in Germany," Energy Research and Development Administration, Report No. FE/WAPO/3387-1, Aug. 1976.

2 Hapeman, M. J., and Savkar, S. D., "Economic Assessment of Coal-Burning Diesel Locomotives," ASME Paper No. 86-ICE-14, Feb. 1986.

3 Dean, J. W., and Johnson, B. L., "Reliability and High Specific Output—an American Manufacturers View," IMechE Conference 1982-7, Sept. 1982.

4 Keller, D. V., Jr., "Coal Refining by Physical Methods for the Preparation of Coal Slurries With Less Than One Per Cent Ash," 5th International Symposium on Coal Slurry Combustion & Technology, Apr. 1983.

5 Ruff, A. W., and Ives, L. K., "Measurement of Solid Particle Velocity in Erosive Wear," *Wear*, Vol. 35, 1975, pp. 195–199.

6 Mehan, R. L., "The Wear of Selected Materials in Mineral Oil Containing a Solid Contaminant," *Wear*, Vol. 124, 1988, pp. 65–85.

S. Doughty
Professor of Mechanical Engineering,
University of Wisconsin—Platteville,
Platteville, WI 53818

A. J. Smalley
Institute Engineer.

B. F. Evans
Senior Research Engineer.

Southwest Research Institute,
San Antonio, TX 78284

Internal Dynamic Force Analysis for V-Type Engine/Compressor With Articulated Power Cylinder Connecting Rod Mechanism

This paper presents a systematic analysis of the internal dynamic forces within a **V***-engine/compressor with articulated power cylinders. All inertial terms are included in the formulation, which is solvable for the crankshaft torque and all reactions. After formulating the necessary description, the results are applied to two case studies involving pipeline compressor units.*

Introduction

This paper will describe a systematic approach to the analysis of internal forces and external reactions for a **V**-type engine/compressor with articulated power cylinders. The number of moving parts and the complexity of the motion associated with the articulated connecting rod give rise to a more involved analysis than that usually given for a slider-crank machine. The application of this method of analysis is demonstrated in two examples following the development.

Early work in the internal force analysis of articulated engines was done in Germany, notably by Rickert (1929, 1930), who presented first and second-order harmonic analyses for radial engines. Higher order harmonic analysis was developed by Kimmel (1940). In contrast to these earlier efforts, digital computational capability makes a more direct approach feasible today, avoiding the need for the harmonic order analysis. The methods to be presented here are adaptable to a variety of machine configurations, and are especially suited to computer implementation. These methods are further described by Doughty (1988a, 1988b).

The kinematic analysis is based on the use of scalar loop equations representing the closure of the position, velocity, and acceleration polygons. An individual crank throw with attached pistons involves only a single degree of freedom, and that degree of freedom may be associated with the crank rotation, here denoted q. All other kinematic position variables (angles, distances, etc.) are ultimately expressible in terms of q. In general, let S denote any position variable other than q

$$S = S(q) \tag{1}$$

When this expression is differentiated with respect to time, the velocity of S is

$$\dot{S} = \frac{dS}{dq}\frac{dq}{dt} = \dot{q}\frac{dS}{dq} = \dot{q}K_s(q) \tag{2}$$

where the derivative dS/dq is denoted $K_s(q)$ and called the velocity coefficient for S. This shows that all velocities throughout the mechanism are proportional to $\dot{q}$, through position-dependent velocity coefficients. To go a step further, the acceleration of S is

$$\begin{aligned}\ddot{S} &= \frac{d}{dt}[\dot{q}K_s(q)] \\ &= \ddot{q}K_s(q) + \dot{q}\frac{dK_s}{dq}\frac{dq}{dt} \\ &= \ddot{q}K_s(q) + \dot{q}^2L_s(q)\end{aligned} \tag{3}$$

where $L_s(q) = dK_s(q)/dq$ is called the velocity coefficient derivative for S. Thus the focus for the initial part of the kinematic analysis is to obtain the positions, velocity coefficients, and velocity coefficient derivatives for various items of interest.

There are three possible approaches to the force analysis: (1) static analysis in which the inertial reaction terms are ignored (assumed to be zero), (2) kinetostatic analysis assuming constant crankshaft rotation rate and thus neglecting only the $\ddot{q}$ terms in the acceleration expressions, or (3) true dynamic analysis reflecting the variations in crankshaft speed from position to position through a crank revolution. The second approach is adopted here as a realistic engineering approach without requiring the solution for the equation of rotational motion for the crankshaft. Thus in implementing the analysis given below, only the $\dot{q}^2$ terms in the accelerations will be evaluated, although the $\ddot{q}$ terms have been retained in the analysis.

Kinematic Analysis

A kinematic skeleton for the crank throw and connected mechanism is shown in Fig. 1. Piston motion is assumed to be pure translation in all cases; piston tipping is not considered. Note that all variables identified in Fig. 1 are positive as shown, except for the slave cylinder connecting rod obliquity A_2; the angle A_2 is negative in this position.

Compression Cylinder Kinematics. Referring to Fig. 1, it

Contributed by the Internal Combustion Engine Division and presented at the Energy-Sources Technology Conference and Exhibition, New Orleans, Louisiana, January 11, 1988. Manuscript received by the Internal Combustion Energy Division September 1987. Paper No. 88-ICE-12.

is evident that the compression cylinder involves only a simple slider-crank mechanism with the cylinder axis inclined to the reference line at an angle B_o and with the bore offset an amount E_o from a radial line through the crankshaft center line. The subscript "o" is used to denote quantities associated with the compression cylinder. The crosshead guide pin position is S_o, and the connecting rod obliquity is A_o. The configuration of this assembly is described by the following two position equations:

$$R\cos(q-B_o)+L_o\cos A_o-S_o=0 \tag{4}$$

$$R\sin(q-B_o)-L_o\sin A_o-E_o=0 \tag{5}$$

For any assigned value of the generalized coordinate q, the values of A_o and S_o are determined by solving equations (4) and (5) with the results

$$A_o=\text{Arcsin}\{[R\sin(q-B_o)-E_o]/L_o\} \tag{6}$$

$$S_o=R\cos(q-B_o)+L_o\cos A_o \tag{7}$$

The velocity coefficients for A_o and S_o are obtained by differentiation

$$K_{ao}=dA_o/dq=R\cos(q-B_o)/(L_o\cos A_o) \tag{8}$$

$$K_{so}=dS_o/dq=-[R\sin(q-B_o)+L_oK_{ao}\sin A_o] \tag{9}$$

With these expressions known, the velocities $\dot{A}_o$ and $\dot{S}_o$ are readily expressed in terms of the crank rotation rate q

$$\dot{A}_o=\dot{q}K_{ao} \tag{10}$$

$$\dot{S}_o=\dot{q}K_{so} \tag{11}$$

Further differentiation gives velocity coefficient derivatives for A_o and S_o

$$L_{ao}=dK_{ao}/dq=\frac{R[-\cos A_o\sin(q-B_o)+K_{ao}\sin A_o\cos(q-B_o)]}{L_o\cos^2 A_o} \tag{12}$$

$$L_{so}=dK_{so}/dq=-[R\cos(q-B_o)+L_oL_{ao}\sin A_o+L_oK_{ao}^2\cos A_o] \tag{13}$$

These results enable the accelerations $\ddot{A}_o$ and $\ddot{S}_o$ to be expressed as

$$\ddot{A}_o=\ddot{q}K_{ao}+\dot{q}^2L_{ao} \tag{14}$$

$$\ddot{S}_o=\ddot{q}K_{so}+\dot{q}^2L_{so} \tag{15}$$

The center of mass for the connecting rod is assumed to have body coordinates (U_{co}, V_{co}), referred to the body coordinate system fixed on the compressor connecting rod. In the dynamic analysis to follow, it becomes necessary to describe the motion of the connecting rod center of mass. The first step in that direction is to express the base coordinates for the connecting rod center of mass

$$S_{co}=R\cos(q-B_o)+U_{co}\cos A_o+V_{co}\sin A_o \tag{16}$$

$$T_{co}=R\sin(q-B_o)-U_{co}\sin A_o+V_{co}\cos A_o \tag{17}$$

The velocity coefficients for the components of velocity for the center of mass are obtained by differentiation

$$K_{sco}=dS_{co}/dq=-R\sin(q-B_o)+K_{ao}(-U_{co}\sin A_o+V_{co}\cos A_o) \tag{18}$$

$$K_{tco}=dT_{co}/dq=R\cos(q-B_o)-K_{ao}(U_{co}\cos A_o+V_{co}\sin A_o) \tag{19}$$

The components of the velocity for the compressor rod center of mass are then given by

$$\dot{S}_{co}=\dot{q}K_{sco} \tag{20}$$

$$\dot{T}_{co}=\dot{q}K_{tco} \tag{21}$$

Further differentiation produces the velocity coefficient derivatives for the center of mass motion

$$L_{sco}=dK_{sco}/dq=-R\cos(q-B_o)+L_{ao}(-U_{co}\sin A_o+V_{co}\cos A_o)-K_{ao}^2(U_{co}\cos A_o+V_{co}\sin A_o) \tag{22}$$

$$L_{tco}=dK_{tco}/dq=-R\sin(q-B_o)-L_{ao}(U_{co}\cos A_o+V_{co}\sin A_o)+K_{ao}^2(U_{co}\sin A_o-V_{co}\cos A_o) \tag{23}$$

With these expressions determined, the components of acceleration for the compressor rod center of mass are easily expressed as

$$\ddot{S}_{co}=\ddot{q}K_{sco}+\dot{q}^2L_{sco} \tag{24}$$

$$\ddot{T}_{co}=\ddot{q}K_{tco}+\dot{q}^2L_{tco} \tag{25}$$

Nomenclature

A_x = oblique angle for connecting rod X
B_x = inclination of cylinder X
E_x = centerline offset for cylinder X
F_{ab} = internal force number a on body b
I_{cmi} = mass moment of inertia with respect to point CM for body i
I_{cr} = mass moment of inertia for crank throw with respect to axis of rotation
K_{yx} = velocity coefficient, dY/dq, for cylinder X
L_{yx} = velocity coefficient derivative, d^2Y/d^2q, for cylinder X
L_i = connecting rod length, $i=$ o, 1, 2
M_{ci} = connecting rod mass, $i=$ o, 1, 2
M_{pi} = piston mass, $i=$ o, 1, 2
q = crank rotation angle
R = crank radius
R_x = cylinder reaction force on piston X
S = typical secondary position variable
S_x = piston pin or crosshead position measured parallel to cylinder X
S_{p2}, T_{p2} = inclined coordinates for the articulation pin joining the slave rod and master rod
T_o = crank torque from adjacent throws
t = time
U_{cr} = crank throw CM position, positive from centerline toward crank pin
U_{yx} = body coordinate measured along the connecting rod for point Y on cylinder X
V_{yx} = body coordinate perpendicular to the connecting rod for point Y on cylinder X
X_{p2}, Y_{p2} = global coordinates for articulation pin joining slave rod to master rod

Subscripts

a = refers to oblique angle A
c = refers to a connecting rod
cr = refers to crankshaft
o = refers to compression cylinder
p = refers to a piston
s = refers to position S
1 = refers to master power cylinder
2 = refers to slave power cylinder

Master Power Cylinder Kinematics. Referring again to Fig. 1, the subscript "1" denotes quantities associated with the master power cylinder. Convenient coordinates for describing this part of the machine are the axes S_1 and T_1, parallel and perpendicular to the bore of the cylinder. In this particular system, the piston wrist pin location is the point (S_1, E_1), where E_1 is the cylinder centerline offset. The S_1 axis is inclined at angle B_1 with respect to the reference line.

The master power cylinder mechanism is a second, simple slider-crank mechanism, and hence is described in a manner exactly like the compression cylinder. The results have exactly the same forms, except that the subscript "1" replaces the subscript "o" used for the compression cylinder.

Slave Cylinder Kinematics. In Fig. 1, the subscript "2" denotes the slave power cylinder. The lower end of the slave power cylinder connecting rod is shown attached to the master connecting rod at the articulation pin. The location of the articulation pin *in the master rod body coordinates* is the point (U_2, V_2). The position of the articulation pin in the global X-Y coordinate system is given by the base coordinates

$$X_{p2} = R\cos q + U_2\cos(A_1 - B_1) + V_2\sin(A_1 - B_1) \tag{26}$$

$$Y_{p2} = R\sin q - U_2\sin(A_1 - B_1) + V_2\cos(A_1 - B_1) \tag{27}$$

In describing the motion of the slave cylinder mechanism, it is convenient to use the S_2-T_2 coordinate system, inclined to the reference line by the angle B_2, so that the S_2 axis is parallel to the slave cylinder bore. In this coordinate system, the location of the articulation pin is given by (S_{p2}, T_{p2})

$$S_{p2} = X_{p2}\cos B_2 + Y_{p2}\sin B_2 \tag{28}$$

$$T_{p2} = -X_{p2}\sin B_2 + Y_{p2}\cos B_2 \tag{29}$$

Successive differentiations of these expressions give the velocity coefficients K_{sp2} and K_{tp2} and the velocity coefficient derivatives L_{sp2} and L_{tp2} for the articulation pin.

The slave piston wrist pin location is (S_2, E_2) in the S_2-T_2 coordinate system, and the connecting rod obliquity is A_2. In terms of the position of the articulation pin, the wrist pin location and the obliquity are

$$A_2 = \text{Arcsin}[(T_{p2} - E_2)/L_2] \tag{30}$$

$$S_2 = S_{p2} + L_2\cos A_2 \tag{31}$$

These expressions are in turn differentiated, once for the velocity coefficients K_{a2} and K_{s2}, and again for the velocity coefficient derivatives L_{a2} and L_{s2}.

The center of mass of the slave connecting rod is located by body coordinates (U_{c2}, V_{c2}) in the slave connecting rod body coordinate system. In the stationary S_2-T_2 coordinate system, this point is given by

$$S_{c2} = S_{p2} + U_{c2}\cos A_2 + V_{c2}\sin A_2 \tag{32}$$

$$T_{c2} = T_{p2} - U_{c2}\sin A_2 + V_{c2}\cos A_2 \tag{33}$$

Repeated differentiations again give the velocity coefficients K_{sc2} and K_{tc2} and velocity coefficient derivatives L_{sc2} and L_{tc2} for the slave connecting rod center of mass motion.

Free Body Force Analysis

The free body diagrams on which the internal force analysis is based are shown in Fig. 2. Piston friction is neglected in the present development. For each cylinder, the components of force are determined in the S-T coordinate system for that cylinder. The force components for the power cylinder connecting rods must be appropriately combined, and the results eventually transferred to the crank throw.

The system of equations developed below can, in principle, be used to determine both the internal forces and the motion. If the motion is to be determined, this will require the numerical solution of the equation of motion using a method such as Runge-Kutta or a scheme based on finite difference

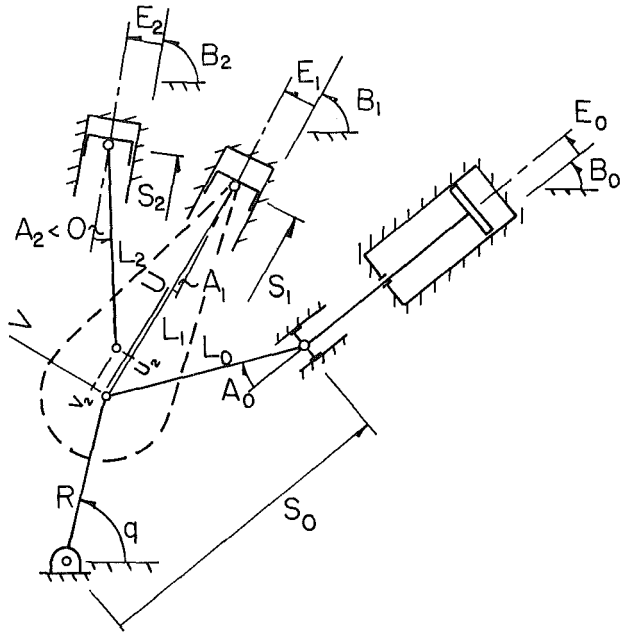

Fig. 1 Schematic diagram of individual crank throw and attached pistons

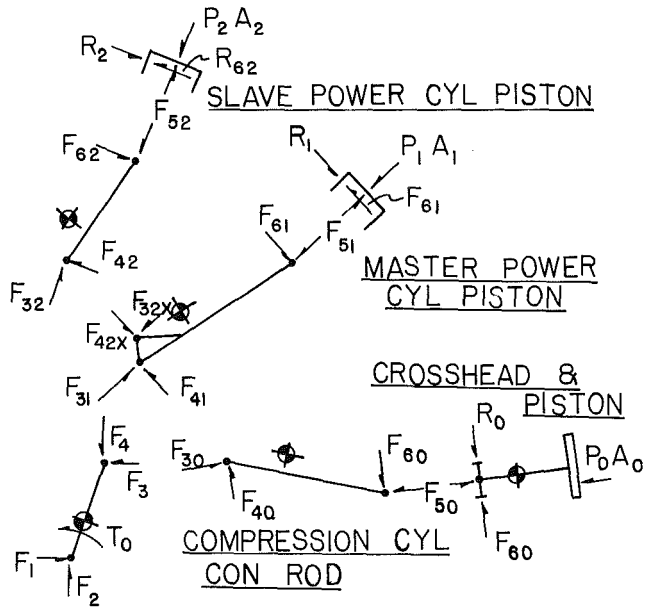

Fig. 2 Free body diagrams for analysis of internal forces

replacement of the derivatives. With the present formulation, either of these will be a difficult procedure. An alternative approach is simply to compute the forces based on an assumed motion. In the computer implementation described later for the expressions developed below, it is assumed that the crankshaft rotation rate is a known constant and that the angular acceleration is zero. Other angular velocity and acceleration rates could be used if they are known.

Compression Cylinder Force Analysis. There are two free bodies associated with the compression cylinder, one for the piston and one for the connecting rod. The sums of forces and moments on these bodies are:

Connecting Rod

$$F_{30} - F_{50} = M_{co}(\ddot{q}K_{sco} + \dot{q}^2 L_{sco}) \tag{34}$$

$$F_{40} - F_{60} = M_{co}(\ddot{q}K_{tco} + \dot{q}^2 L_{tco}) \tag{35}$$

$$F_{30}(U_{co}\sin A_o - V_{co}\cos A_o)$$
$$+F_{40}(U_{co}\cos A_o + V_{co}\sin A_o)$$
$$+F_{50}[(L_o - U_{co})\sin A_o + V_{co}\cos A_o] \quad (36)$$
$$+F_{60}[(L_o - U_{co})\cos A_o - V_{co}\sin A_o]$$
$$= I_{cmo}(\ddot{q}K_{ao} + \dot{q}^2 L_{ao})$$

Crosshead and Piston

$$F_{50} - P_o A_o = M_{po}(\ddot{q}K_{so} + \dot{q}^2 L_{so}) \quad (37)$$
$$F_{60} - R_o = 0 \quad (38)$$

These equations are linear in the unknown forces and are easily solved for F_{30}, F_{40}, F_{50}, F_{60}, and R_o after values for $\dot{q}$ and $\ddot{q}$ are available. The horizontal and vertical components of the resultant of F_{30} and F_{40} will be required later:

$$F_{30x} = F_{30}\cos B_o - F_{40}\sin B_o \quad \text{(horizontal)} \quad (39)$$
$$F_{40x} = F_{30}\sin B_o + F_{40}\cos B_o \quad \text{(vertical)} \quad (40)$$

Slave Power Cylinder Force Analysis. There are two free bodies in the slave cylinder force analysis. The force and moment sums for these bodies are:

Slave Connecting Rod

$$F_{32} - F_{52} = M_{c2}(\ddot{q}K_{sc2} + \dot{q}^2 L_{sc2}) \quad (41)$$
$$F_{42} - F_{62} = M_{c2}(\ddot{q}K_{tc2} + \dot{q}^2 L_{tc2}) \quad (42)$$
$$F_{32}(U_{c2}\sin A_2 - V_{c2}\cos A_2)$$
$$+F_{42}(U_{c2}\cos A_2 + V_{c2}\sin A_2)$$
$$+F_{52}[(L_2 - U_{c2})\sin A_2 + V_{c2}\cos A_2] \quad (43)$$
$$+F_{62}[(L_2 - U_{c2})\cos A_2 - V_{c2}\sin A_2]$$
$$= I_{cm2}(\ddot{q}K_{a2} + \dot{q}^2 L_{a2})$$

Slave Piston

$$F_{52} - P_2 A_2 = M_{p2}(\ddot{q}K_{s2} + \dot{q}^2 L_{s2}) \quad (44)$$
$$F_{62} - R_2 = 0 \quad (45)$$

This system of equations in linear in the forces F_{32}, F_{42}, F_{52}, F_{62}, and R_2 and is readily solved for them. In order to transfer the connecting rod forces onto the master connecting rod, the components of the connecting rod force are needed in the S_1-T_1 system (parallel and perpendicular to the master power cylinder centerline)

$$F_{32x} = F_{32}\cos(B_2 - B_1) - F_{42}\sin(B_2 - B_1) \quad \text{(parallel)} \quad (46)$$
$$F_{42x} = F_{32}\sin(B_2 - B_1) + F_{42}\cos(B_2 - B_1) \quad \text{(perpendicular)} \quad (47)$$

Master Power Cylinder Force Analysis. The two free bodies involved in the master power cylinder force analysis are subject to the force transferred from the slave cylinder connecting rod, as well as the gas pressure forces from combustion. The force and moment sums for these two bodies are

Master Connecting Rod

$$F_{32} - F_{32x} - F_{51} = M_{c1}(\ddot{q}K_{sc1} + \dot{q}^2 L_{sc1}) \quad (48)$$
$$F_{41} - F_{42x} - F_{61} = M_{c1}(\ddot{q}K_{tc1} + \dot{q}^2 L_{tc1}) \quad (49)$$
$$F_{31}(U_{c1}\sin A_1 - V_{c1}\cos A_1)$$
$$+F_{41}(U_{c1}\cos A_1 + V_{c1}\sin A_1)$$
$$+F_{51}[(L_1 - U_{c1})\sin A_1 + V_{c1}\cos A_1]$$
$$+F_{61}[(L_1 - U_{c1})\cos A_1 - V_{c1}\sin A_1] \quad (50)$$
$$-F_{32x}[(U_{c1} - U_2)\sin A_1 - (V_{c1} - V_2)\cos A_1]$$
$$-F_{42x}[(U_{c1} - U_2)\cos A_1 + (V_{c1} - V_2)\sin A_1]$$
$$= I_{cm1}(\ddot{q}K_{a1} + \dot{q}^2 L_{a1})$$

Master Piston

$$F_{51} - P_1 A_1 = M_{p1}(\ddot{q}K_{s1} + \dot{q}^2 L_{s1}) \quad (51)$$
$$F_{61} - R_1 = 0 \quad (52)$$

Once again, the force and moment sums are linear in the unknown forces and may be solved for the values of F_{31}, F_{41}, F_{51}, F_{61}, and R_1. For transfer to the crankshaft, the components of the crank pin force are needed in the global X-Y coordinate system

$$F_{31x} = F_{31}\cos B_1 - F_{41}\sin B_1 \quad \text{(horizontal)} \quad (53)$$
$$F_{41x} = F_{31}\sin B_1 + F_{41}\cos B_1 \quad \text{(vertical)} \quad (54)$$

Crank Throw Force Analysis. The crank throw is shown as a single free body, subject to the crank pin forces $F_3(=F_{30x}+F_{31x})$ and $F_4(=F_{40x}+F_{41x})$, the bearing reaction forces F_1 and F_2, and the external driving torque T_o. The force and moment sums for this body are

$$F_1 - F_{30x} - F_{31x}$$
$$= M_{cr}(-\ddot{q}U_{cr}\sin q - \dot{q}^2 U_{cr}\cos q) \quad (55)$$
$$F_2 - F_{40x} - F_{41x}$$
$$= M_{cr}(\ddot{q}U_{cr}\cos q - \dot{q}^2 U_{cr}\sin q) \quad (56)$$
$$T_o + R(F_{30x} + F_{31x})\sin q$$
$$- R(F_{40x} + F_{41x})\cos q = I_{cr}\ddot{q} \quad (57)$$

From these the bearing reactions F_1 and F_2 are readily determined, as well as the external torque T_0.

Analysis Implementation

The foregoing kinematic and free body force analyses have been implemented in a computer code for investigation of reciprocating machinery dynamics. The resulting analysis tool can be used to investigate internal combustion engines and reciprocating compressors of various configurations, including in-line and **V**-engines, single or double acting compressors, as well as other various cylinder axis arrangements. The implementation accounts for proper phasing of multiple crank throws, two or four stroke cycles, single or tandem compressor cylinders, or scavenging cylinders.

The calculation procedure involves determining the internal forces at each increment of crank rotation for each cylinder on a crank throw. Calculations then proceed to the next crank throw and each increment of rotation is again calculated for that throw. After accounting for proper crankshaft phasing and cylinder orientation, the resulting bearing forces are then calculated. The general input data include:

- machine geometry, which includes crankshaft and cylinder dimensions, spacing, orientation, etc.;
- machine inertia data, including the piston masses and connecting rod mass, mass moment of inertia, and center of mass locations;
- crank rotational increment, number of strokes per cycle, speed, etc.;
- complex pressure wave amplitude in each cylinder at each increment of rotation. This information can also be calculated based on thermodynamic state points if necessary.

The typical output of interest from the analysis includes:

- Rod loading
- Piston side force
- Pressure force
- Cylinder torque
- Inertia forces
- Summation of shaking forces and moments
- Bearing loading
- Produced or consumed horsepower

Each of the above is calculated as a function of rotation. Harmonic analyses of some of the above items are calculated,

such as torque harmonics, bearing load harmonics, etc. The torque harmonics are useful especially when calculated at each crank throw, for use as input excitations in a torsional analysis of the system. Harmonic analyses of the bearing forces are sometimes useful in comparing to field data since they should yield a frequency spectrum similar to that measured.

The shaking force values given below are the first and second-order amplitudes from the harmonic analysis of the external support forces acting on the frame. Similarly, the shaking moments are the first and second-order harmonic amplitudes for the external moments acting on the frame. The Vertical Moment is a pitching moment, tending to cause one end to rise and the other to fall; the Horizontal Moment is a moment tending to cause the frame to rotate in a horizontal plane.

Examples

In the past, typical calculations for reciprocating machinery did not take into account the articulation mechanism present in some machines. The following two examples illustrate the application of the foregoing analysis to two types of articulated machinery.

The first example is a reciprocating compressor driven by an integral two-cycle engine. The typical arrangement is shown in Fig. 3. Both power cylinders are articulated from separate points on the master compressor cylinder connecting rod. This geometry requires an analysis similar to, but slightly different from that presented in the eariler part of this paper. This unit is a five-throw, ten-cylinder engine driving three double-acting reciprocating compressor cylinders. One item of interest is the net power torque produced by all ten cylinders as a function of crank angle. For this particular machine, it was also of interest to calculate the net power torque with the deactivation of one power cylinder (Smalley, et al., 1987). Figure 4 illustrates the comparison at 300 rpm. For the reference case, a fairly uniform curve is predicted with a strong fifth-order component. By deactivating one cylinder, the distortion in the net power torque curve is seen in the lower part of Fig. 4. Also of interest were the net mechanical shaking forces for this engine, with the cylinder pressure forces set to zero. This provides an evaluation of the mechanical unbalanced forces and moments transmitted to the machine foundation. These are reviewed in Table 1.

The second example also concerns a reciprocating compressor driven by an integral engine. In this case, the 20-cylinder, ten-throw engine was driving five compressor cylinders and five reciprocating counterweights, which were included in the system for balancing purposes. The articulation mechanism for this machine was similar to that shown in Fig. 1 in which one power cylinder is articulated from another on the same crank throw. The actual machine arrangement provided for the articulated cylinder to alternate from the left to the right bank along each throw of the crankshaft. As a comparison of the articulated versus nonarticulated calculations, the second part of Table 1 illustrates the unbalanced shaking forces and moments. Due to the alternating arrangement, it is seen that the forces sum to zero, but that the moments do not. The primary and secondary shaking moments in vertical and horizontal directions are actually a net result from all of the crank throws being phased together. It is seen that the primary horizontal and vertical shaking moments increased by over a factor of two when the articulated mechanism was considered. The secondary vertical shaking moments actually decreased and the secondary horizontal moments remained approximately the same.

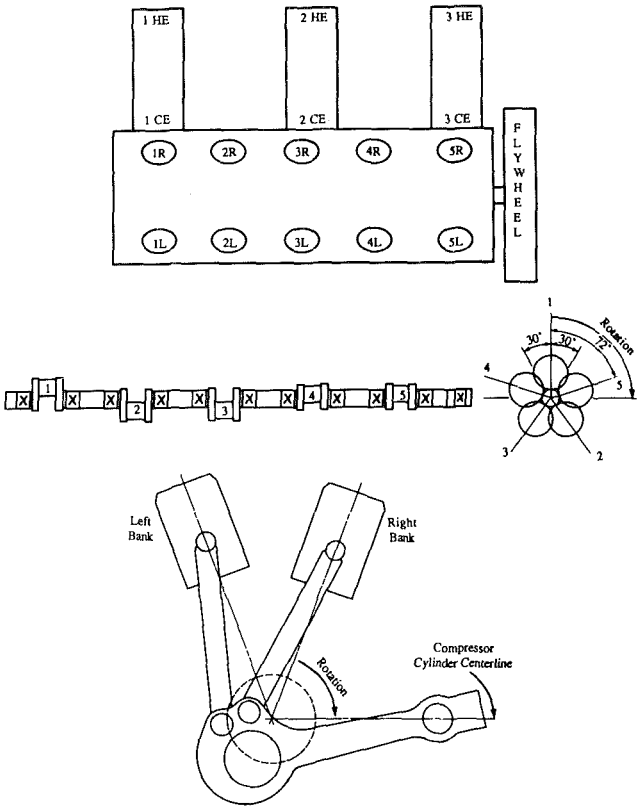

Fig. 3 Case 1—engine/compressor physical arrangement

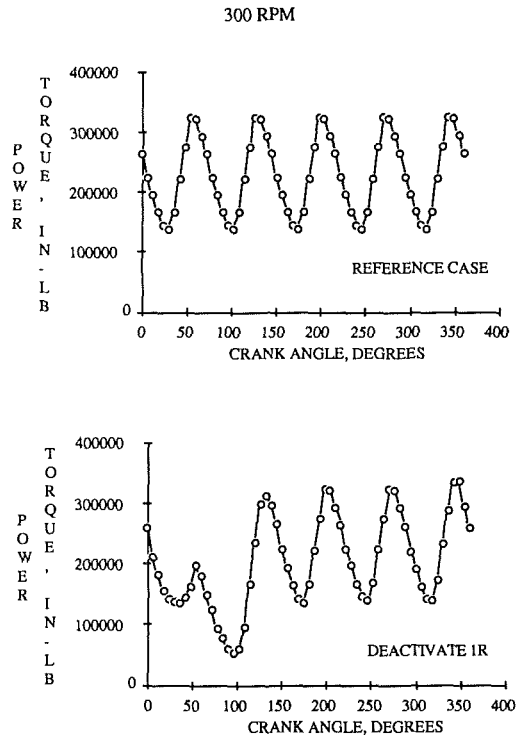

Fig. 4 Case 1—net power torque versus crank angle

Summary

An approach to the internal dynamic force analysis of articulated reciprocating mechanisms has been presented. The implementation of the method has been achieved and results presented for two different articulation schemes. Consideration of articulation in the analysis solutions has been shown to predict significant differences in the unbalanced forces and moments as compared to the nonarticulated solutions.

Table 1 Unbalanced mechanical shaking forces and moments

	Forces, lb			
	Primary		Secondary	
	Vertical	Horizontal	Vertical	Horizontal
Case 1	4470	800	0	2840
Case 2 articulated	0	0	0	0
Case 2 nonarticulated	0	0	0	0

	Moments, ft-lb			
	Primary		Secondary	
	Vertical	Horizontal	Vertical	Horizontal
Case 1	132,170	12,260	28,710	102,040
Case 2 articulated	108,040	108,040	74,670	9470
Case 2 nonarticulated	46,820	46,820	122,290	9040

References

Doughty, S., 1988a, "Fundamentals of IC Engine Torsional Vibration," ASME Paper No. 88-ICE-6.

Doughty, S., 1988b, *Mechanics of Machines*, Wiley, New York, pp. 23–31, 338–350.

Hartman, J. B., 1956, *Dynamics of Machinery*, McGraw-Hill, New York, pp. 171–210.

Kimmel, A., 1940, "Die freien Massenkrafte des Sternmotors," *Ingenieur-Archiv*, Springer, Berlin, pp. 424–431.

Mabie, H. H., and Reinholz, C. F., 1987, *Mechanisms and Dynamics of Machinery*, Wiley, New York, pp. 434–450, 513–533.

Riekert, P., 1929, "Bietrag zur Theorie des Massenausgleiches von Sternmotoren," *Ingenieur-Archiv*, Springer, Berlin, pp. 16–21.

Riekert, P., 1930, "Beitrag zur Theorie des Massenausgleiches von Sternformmotoren mit nicht-zyklischsymmetrischen Gleitbahnen," *Ingenieur-Archiv*, Springer, Berlin, pp. 245–254.

Shigley, J. E., 1961, *Theory of Machines*, McGraw-Hill, New York, pp. 526–563.

Shigley, J. E., and Uicker, J. J., 1980, *Theory of Machines and Mechanisms*, McGraw-Hill, New York, pp. 451–476, 500–509.

Smalley, A. J., Vinyard, S., and Evans, B. F., 1987, "Power Cylinder Deactivation for Reduced Fuel Consumption Under Part Load," *Operating Section Proceedings, American Gas Association Distribution/Transmission Conference*, Las Vegas, NV, pp. 69–80.

Table 1 Unbalanced mechanical shaking forces and moments

	Forces, lb			
	Primary		Secondary	
	Vertical	Horizontal	Vertical	Horizontal
Case 1	4470	800	0	2840
Case 2 articulated	0	0	0	0
Case 2 nonarticulated	0	0	0	0
	Moments, ft-lb			
	Primary		Secondary	
	Vertical	Horizontal	Vertical	Horizontal
Case 1	132,170	12,260	28,710	102,040
Case 2 articulated	108,040	108,040	74,670	9470
Case 2 nonarticulated	46,820	46,820	122,290	9040

References

Doughty, S., 1988a, "Fundamentals of IC Engine Torsional Vibration," ASME Paper No. 88-ICE-6.

Doughty, S., 1988b, *Mechanics of Machines*, Wiley, New York, pp. 23–31, 338–350.

Hartman, J. B., 1956, *Dynamics of Machinery*, McGraw-Hill, New York, pp. 171–210.

Kimmel, A., 1940, "Die freien Massenkrafte des Sternmotors," *Ingenieur-Archiv*, Springer, Berlin, pp. 424–431.

Mabie, H. H., and Reinholz, C. F., 1987, *Mechanisms and Dynamics of Machinery*, Wiley, New York, pp. 434–450, 513–533.

Riekert, P., 1929, "Bietrag zur Theorie des Massenausgleiches von Sternmotoren," *Ingenieur-Archiv*, Springer, Berlin, pp. 16–21.

Riekert, P., 1930, "Beitrag zur Theorie des Massenausgleiches von Sternformmotoren mit nicht-zyklischsymmetrischen Gleitbahnen," *Ingenieur-Archiv*, Springer, Berlin, pp. 245–254.

Shigley, J. E., 1961, *Theory of Machines*, McGraw-Hill, New York, pp. 526–563.

Shigley, J. E., and Uicker, J. J., 1980, *Theory of Machines and Mechanisms*, McGraw-Hill, New York, pp. 451–476, 500–509.

Smalley, A. J., Vinyard, S., and Evans, B. F., 1987, "Power Cylinder Deactivation for Reduced Fuel Consumption Under Part Load," *Operating Section Proceedings, American Gas Association Distribution/Transmission Conference*, Las Vegas, NV, pp. 69–80.

DISCUSSION

J. W. Holmes[1]

The authors are to be complimented on an analysis that treats the articulated rod mechanism with complete generality. The paper represents an original contribution, inasmuch as work done in this area in the early days of the multibanked internal combustion engine usually involved one or more of these simplifying assumptions:

1 Cylinder centerlines were not offset.

2 The articulating pin angle to the master rod centerline was equal to the bank angle (common in aircraft radial engines).

3 The articulating pin was so located that it lay on the line through the crankpin and wristpin at outer dead center of the slave cylinder.

The paper is very well organized; however, one wonders if it would not have been somewhat less forbidding in Figs. 1 and 2 and in the analysis if two deletions had been made. As the authors state, the compression rod is merely a special case of the master power rod and therefore does not merit separate analysis. Since angular acceleration of the crankthrow is neglected, the main bearing reactions arrived at are simply the combination of the crankpin applied forces and the centrifugal force of the crankthrow. It is felt that omitting the analysis of both the compressor rod and the crankthrow would have focused attention more sharply on the analysis of the rod mechanism, where the paper makes its most significant contribution.

The paper points out that the harmonics of the torque at the individual crank throws are useful for determining the excitation of torsional vibration. The harmonics of bearing reactions at each throw are also valuable for evaluating the internal bending moments in the engine frame. In a unit whose mounting gives a stiff coupling to earth and whose frame has a typical degree of flexibility, these moments are apt to be of greater concern than are the overall shaking forces and couples.

It is hoped that in further extensions of this effort the authors will consider the development of a direct formulation of the harmonics of force and torque at the individual crankthrow as has been done for the more restricted analyses mentioned earlier. Not only are such expressions convenient for many computations, but they also give better insight into the significance of the many parameters involved.

Again, the authors are to be praised for an ambitious and stimulating treatment, which encompasses the total scope of variation in the articulated rod mechanism.

[1]Mount Vernon, Ohio.

Authors' Closure

The authors wish to thank Mr. Holmes for his interesting discussion. He has brought additional historical insight into this problem, particularly in regard to the assumptions made in previous analyses. He has also pointed out the further application of this type of analysis to the engine frame forces.

In regard to the bearing force analysis, the angular acceleration of the crank throw has been neglected in the present computer implementation. The angular acceleration is clearly included in the analysis (equation (57)), and can be readily included if desired.

In the matter of a direct harmonic order analysis, the authors believe that the present approach is preferable. As given in the paper, the instantaneous forces are calculated. From this it is a relatively simple process to search out the maxima, and these are often quite important. If the anaylsis is approached in terms of individual harmonic orders, the entire series must be summed to obtain maxima. If harmonic components are required from the instantaneous force calculation, only those components that are required need to be computed.

Piston Motion and Thermal Loading Analyses of Two-Stroke and Four-Stroke Cycle Engines for Locomotives

S. D. Haddad
Professor,
Dept. of Mechanical and Aerospace Engineering,
University of Missouri,
Columbia, MO 65211

Two-stroke cycle and four-stroke cycle diesel engines are in use in rail traction, with the four-stroke cycle design dominating the field. Cycle simulations using computer programs have shown that the conventional two-stroke cycle is somewhat inferior to its four-stroke cycle counterpart in combustion efficiency and thermal loading. Research at Sulzer concluded that the conventional two-stroke cycle engine is not very suitable for locomotive application. A survey by Ricardos, based on an investigation of engines in current production for traction application, suggested that there are potentials in two-stroke cycle design. This paper presents a summary of the results of a research project concerned with comparison of two well-proven typical locomotive diesel engines, one with a two-stroke cycle and the other with a four-stroke cycle. Performance, mechanical loading, thermal loading, and vibration were chosen as parameters to be investigated to provide information on the status of the two cycles in relation to power range, fuel consumption, reliability, and durability, with a view to assisting the users of locomotive engines to make the correct choice.

1 Introduction

Four-stroke cycle diesel engines are widely used in railway traction; two-stroke cycle diesel and gas turbine engines are also used, but not extensively.

This paper presents the case for the diesel engine, comparing its two main types, since there has been a certain amount of conflicting argument promoting either type, especially in relation to diesel engines of the medium power range. Diesel engines used in rail traction lie in the disputed medium power range, so the designer requires some guidance toward effective choice of two-stroke or four-stroke for specific applications. This cycle choice concerns both engine manufacturer and the end user in view of heavy commitments and subsequent implications in railway applications.

A number of researchers have found it normally more demanding to design a good two-stroke cycle diesel engine than an equivalent four-stroke type. This is because when designing a two-stroke engine, extra care must be exercised toward effective scavenging, proper air swirl, exhaust timing, injection tip and piston bowl configuration, and careful design of ports and rings, as the piston rings must traverse the inlet ports in addition to the requirement of higher specific air flow. Otherwise, the two engine types are basically similar for the provision of crankshaft, bearings, etc.

In the final analysis, the rail traction user requires the engine to provide appropriate power range, speed/load specification, specific weight and volume, reliability and maintainability criteria, acceptable fuel consumption, and at the right cost in relation to usage. This paper presents results of two important aspects of engine design to compare the two-stroke and four-stroke cycles; using piston motion and thermal loading analyses.

2 Background Investigation

An extensive investigation was conducted of available published and some unpublished literature and data on the two types of diesel engine in common railway use [1]. Most of this literature originated from General Motors, Sulzers, Ricardos, and others [2–8] reporting on predictive studies, test results, and comparison of performance and design of engines in current production. The following general observations were obtained from this initial literature study:

2.1 Cycle simulation predictions show that the two-stroke cycle is somewhat inferior to the four-stroke cycle in the gas exchange process. This results in lower combustion efficiency and higher thermal loading.

2.2 Test results from experimental engines confirmed the relative inferiority of the two-stroke engine performance and its higher thermal loading.

2.3 Analyses of two- and four-stroke diesel engines in current production have led to the conclusion that the two-stroke engines have not realized their theoretical advantages.

In an effort to provide further guidance for the engine designer and user with regard to choice and merits of two-stroke and four-stroke, it was decided to study two typical,

Contributed by the Internal Combustion Engine Division and presented at the Twelfth Annual Energy-Sources Technology Conference and Exhibition, Houston, Texas, January 22–25, 1989. Manuscript received by the Internal Combustion Engine Division August 1988. Paper No. 89-ICE-4.

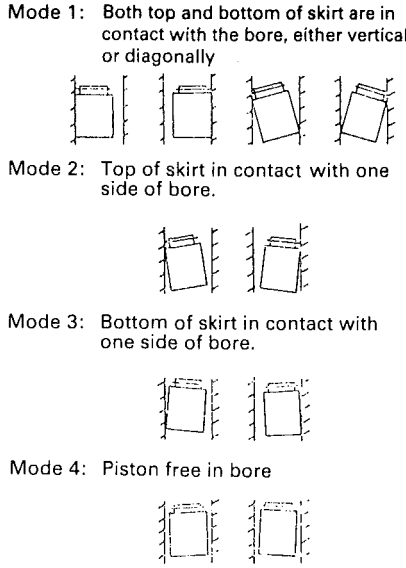

Fig. 1 Basic modes of motion of the piston in the bore

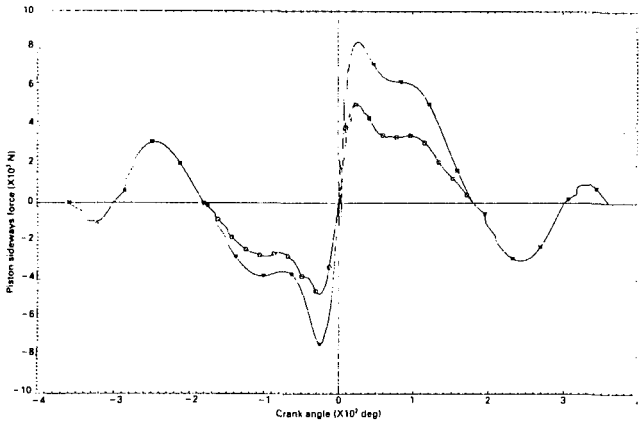

Fig. 2 Piston sideways force versus crank angle: ◯, 645E3B; ★, RKC; at full load/speed

well-established rail traction engines: the General Motors/EMD two-stroke 645-12E3B and the Ruston four-stroke 8RKC. Both of these engine types are successfully used in Sudan Railways and other parts of the railway world. Preliminary investigation confirmed that meaningful comparison should be based on performance, mechanical loading, vibration and thermal loading parameters. Visits to LaGrange (USA) and Newton-le-Willows (UK) provided sufficient test data for the two engines. Subsequently, two well-developed computer programs were used to predict engine characteristics; a GEC computer program to predict the thermal loading and a Haddad-LUT piston motion computer program to predict the vibration and mechanical loading. Before discussing the results of this research, it is appropriate to outline some general pointers in relation to the development of these two engines [9–12].

(*i*) Historically, General Motors has pioneered the medium speed, two-stroke cycle diesel engine, although they are not irrevocably committed to any specific type of design. In the early 1930s, research at EMD/GMC had led to an eight-cylinder, two-stroke cycle diesel engine design, which could be built with a rating of 600 hp. The best four-cycle, eight-cylinder of the same bore and stroke as EMD's two-cycle design was then rated 400 hp, so it appeared that their two-cycle engine had a fair edge over the four-cycle, and then they produced the eight-cylinder, two-stroke cycle.

(*ii*) My perceived notions of the general philosophy of

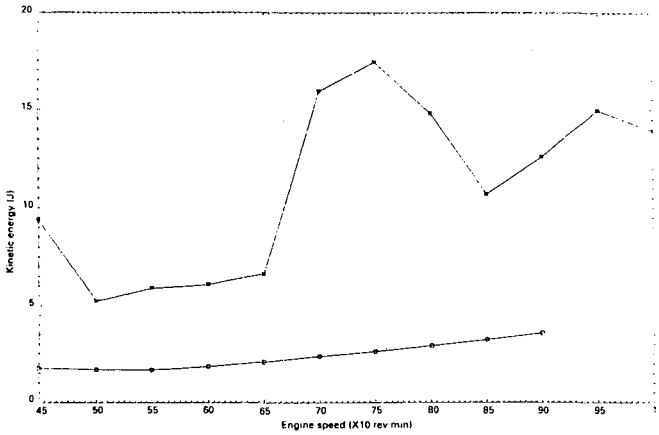

Fig. 3 TKE of cycle impacts versus engine speed: ◯, 645E3B; ★, RKC; at full load/speed

EMD/GMC is to solve the problems related to two-stroke cycle design. The development work is for the enhancement of reliability, durability and engine performance. A conservative attempt to uprate Series 645 engines was made (645FB).

(*iii*) My perceived notion of the Ruston philosophy is that of uprating. Development work is for solving the problems related to higher thermal and mechanical loading due to uprating and to enhance reliability and durability. Redesigning for ease of maintenance was also considered. The horsepower that had been available from a 16-cylinder version (RK3) was extracted from a 12-cylinder version with the same bore and stroke (RKC). It is now possible to see an eight-cylinder version replacing the 12-cylinder with the same horsepower. In addition, it was possible to glean a great deal of essential information and data to illustrate the user's experience in relation to the philosophy of engine development and manufacture [13–16].

3 Mechanical Loading, Vibration, and Frictional Forces of the Two Engines Under Investigation

Two versions of a piston motion computer program (for two-stroke and four-stroke, respectively), developed by Haddad in collaboration with Wellworthy, Ltd. [17, 18], were used to predict mechanical loading, vibration, and frictional forces of the two engines. Figure 1 shows the basic modes of piston motion computer program. The piston motion programs needed to be further developed and extended to suit conditions of the two railway engines of the EMD and Ruston size and type.

A computer plotting routine was developed to present the piston motion program results in appropriate formats. A complete set of computer results is presented by Nabag [1] and Haddad [23], but only typical ones are discussed here.

Figure 2 compares the piston sideways force of the two engines showing higher values for th RKC engine. There are some fluctuations in the plots around TDC for both engines. These are due to some gas pressure oscillations in turbocharged engines. Figure 3 shows the total kinetic energy of cycle (TKE of cycle) versus engine speed. In the case of the 645E3B engine, there is a clear tendency for increased cycle kinetic energy (hence increased vibration) with speed. In the case of the RKC engine, there is greater tendency of increasing cycle kinetic energy with some fluctuations at intermediate speeds. These fluctuations are mainly due to varying piston modes during a cycle. Modes are related to engine geometry as well as to gas pressures, inertias, friction, and speeds. It is clear, therefore, that the 645E3B engine produces greater surface vibration than the RKC engine. Figure 4 shows Friction Mean Effective Pressure (FMEP) for both engines. FMEP is

directly proportional to engine speed. The RKC has higher values with a maximum of 11,325 N/M^2 at its maximum speed of 1000 rpm. The 645E3B engine has lower values with a maximum of 653.6 N/M^2 at its maximum speed of 900 rpm. The reader should bear in mind that, for the two-cycle operation, we allowed approximate values for the friction due to rings passing through the port openings.

From the basic piston motion theory, piston sidways force, kinetic energy of impacts, and friction mean effective pressure are directly related to frictional, inertial and gas pressures [18]. The gas pressures and inertias of 645E3B engine are smaller than those of the RKC engine. Also, friction is a function of piston speed and gas pressures, resulting in smaller FMEP for the 645E3B engine when compared with the RKC engine.

It can be concluded that for the range of parameters investigated and within the approximations noted before, the results are in favor of the 645E3B engine. The smaller sideways force, piston slap, total cycle kinetic energy, and FMEP are signs of lower vibrational excitation, smaller mechancial stresses, and smaller mechanical wear with higher mechanical efficiency.

The higher the magnitude and the number of piston slaps, the higher the vibration excitation and consequently, the higher the rate of pitting attack on the coolant side of the thrust of the liner, the side on which the piston bears during the power stroke.

Since inertia is an area of which designers look to control mechanical loading and vibration of engines, it was decided to investigate its effect in isolation from the effect of gas pressures. This has been done by putting the digitized pressure diagrams with zero values to eliminate the effect of gas pressures.

Figures 5–7 combine results of the 645E3B and RKC engines for inertia effect only. Higher values of piston sideways force, total KE of cycle, and FMEP for the RKC engine are evident. The resultant forces and torques in two- and four-stroke cycles vary. The outward forces near TDC are opposing the gas pressures during the expansion stroke. They are also acting outward during the exhaust stroke. Inertia, therefore, reduces the maximum gas load on the connecting rod.

In some cases, pistons and connecting rods are made heavier than necessary in order to reduce crank pin bearing maximum loading. In four-stroke engines, the outward inertia load during the exhaust stroke is not offset by gas pressure and may be large at high piston speeds. The two-stroke engines in this respect are favored for two reasons. First, due to the low piston speed of the two-stroke cycle engines, they permit the use of heavier pistons, and this will offset the gas pressures during expansion stroke and reduce mechanical loading. Secondly, there is no exhaust stroke cycle design, which eliminates high outward inertia during this stroke.

The 645E3B engine has a heavier piston when compared with the RKC piston. The fork connecting rod of 645E3B engine is lighter than the RKC connecting rod, but it is heavier than the blade rod, which is also used in the 645E3B engine in the fork and blade construction.

Part-load and other engine conditions have been investigated [1]. Table 1 shows typical results extracted from the

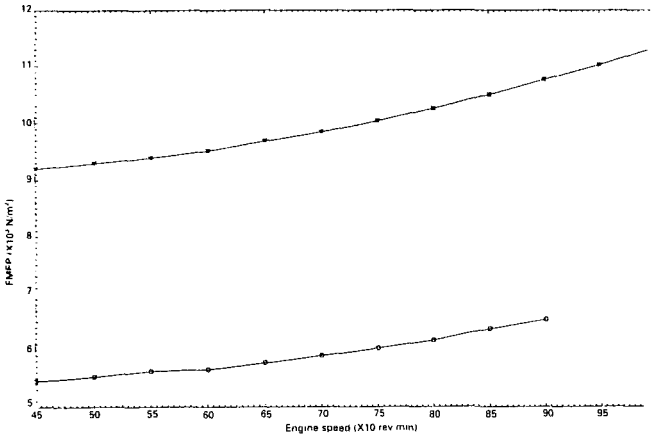

Fig. 4 FMEP versus engine speed: ◯, 645E3B; ★, RKC; at full load/speed

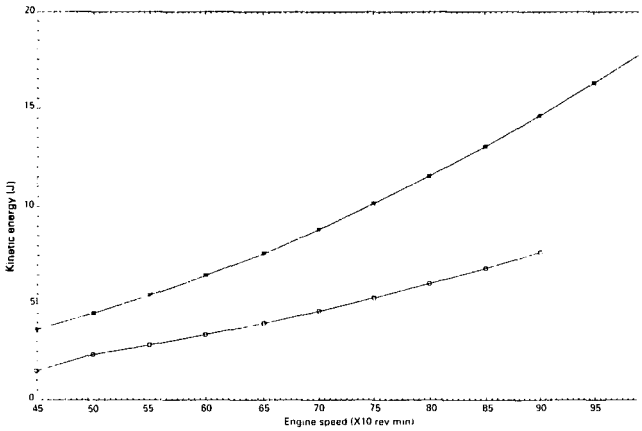

Fig. 6 TKE of cycle impacts due to inertia only versus engine speed at full load and speed: ◯, 645E3B; ★, RKC

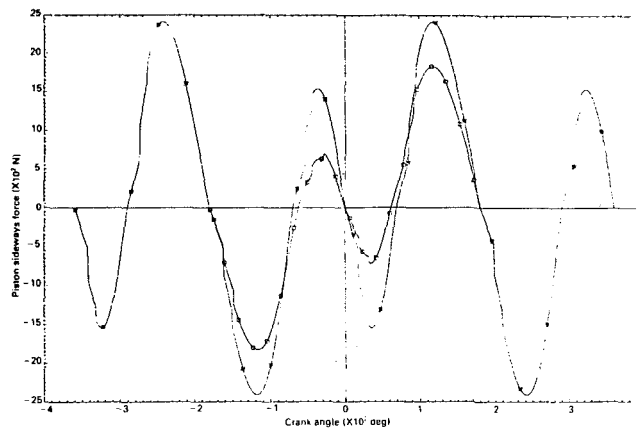

Fig. 5 Piston sideways force due to inertia only versus crank angle at full load and speed: ◯, 645E3B; ★, RKC

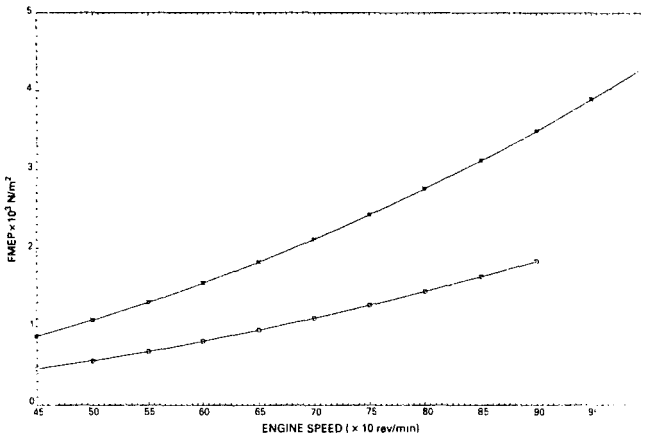

Fig. 7 FMEP due to inertia only versus engine speed at full load: ◯, 645E3B; ★; RKC

Table 1 Results extracted from the computer output for the two engines under investigation

Engine condition, full-load and speed						Engine condition, full-load speed, inertia only					
Results of computer analysis			Results versus engine speed			Results of computer analysis			Results versus engine speed		
Maximum *side* force (N)	Number *of* impacts	Impact *magnitude* (J)	Engine *speed* (rev/min)	TKE *of* cycle (J)	FMEP (N/m^2)	Maximum *side* force (N)	Impact *magnitude* (J)	Number *of* impacts	Engine *speed* (rev/min)	TKE *of* cycle (J)	FMEP (N/M^2)
Engine, 645E3B (two-stroke); peak cylinder pressure, 1.0372×10^7 N/m^2; piston weight, 275.9 N; maximum speed, 900 rev/min; connecting rod weight 370.9 N; piston speed, 7.6 m/s											
5200	3	0.34	450	1.755	5449.9		0.21	8	450	1.502	464.53
		1.99	500	1.681	5535.6		1.34		500	2.347	565.76
		1.24	550	1.674	5630.4		0.37		550	2.844	684.37
			600	1.851	5660.0		1.90		600	3.389	814.69
			650	2.100	5773.3		0.33		650	3.981	956.12
			700	2.393	5898.4		1.70		700	4.622	1108.90
			750	2.639	6029.0		1.13		750	5.310	1272.90
			800	2.922	6169.1		0.26		800	6.045	1448.30
			850	3.241	6379.1				850	6.829	1637.10
			900	3.570	6536.6				900	7.660	1835.40
Engine, RKC (four-stroke); peak cylinder pressure, 1.3837×10^7 N/m^2; piston weight, 212.2 N; maximum speed, 1000 rev/min; connecting rod weight 487.9 N; piston speed, 10.2 m/s											
8871.1	12	0.743	450	9.365	9206.5		0.920	16	450	3.651	873.28
		1.688	500	5.241	9304.7		1.713		500	4.508	1078.10
		0.650	550	5.899	9395.8		0.706		550	5.454	1304.50
		0.976	600	6.092	9522.4		1.385		600	6.491	1552.50
		0.587	650	6.661	9693.0		0.821		650	7.617	1822.00
		1.042	700	15.931	9848.3		1.351		700	8.835	2113.10
		0.857	750	17.431	10036.0		0.774		750	10.143	2425.80
		1.906	800	14.813	10254.0		1.363		800	11.540	2760.00
		0.772	850	10.697	10498.0		0.902		850	13.028	3115.80
		1.719	900	12.601	10757.0		1.713		900	14.605	3493.10
		2.973	950	14.096	11022.0		0.706		950	16.273	3892.00
		0.001	1000	13.914	11326.0		1.385		1000	18.031	4312.50
		.		.			0.821			.	.
		.		.			1.351			.	.
		.		.			0.770			.	.
		.		.			1.363			.	.

computer program output for the two engines to yield some of the following conclusions:

3.1 From Table 1, it can be seen that values of piston sidways force, kinetic energy released at impacts and the number of impacts, total cycle kinetic energy, and friction mean effective pressure are much higher for the RKC engine, suggesting higher mechanical loading than in the 645E3B engine. It should be noted that the cylinder pressures are accounted for in full when calculating piston motion parameters being considered in this context.

3.2 All the above-mentioned parameters are factors that aggravate vibration excitation, mechanical stresses, and mechanical wear, and minimize mechancial efficiency.

3.3 The inertia force is outward in the expansion and exhaust stroke. If four-stroke designs used heavy pistons to offset the gas pressures in the expansion stroke, they will be penalized in the exhaust stroke with the higher inertia from piston and with no gas pressures to offset it. This is solved in the two-stroke design since there is no exhaust stroke.

3.4 It has been shown that the severity and repetition of impacts during engine cycle produce higher vibration levels at the coolant side of the cylinder liner, substantiating the commonly observed high rate of pitting attack in these engines.

4 Thermal Loading of the Two Engines

The ultimate limit on specific power output at the present time appears to be on the basis of thermal loading. A GEC Mechanical Engineering Laboratory (MEL) computer program to predict thermal loading was used (through courtesy of Wellworthy, Ltd.) to produce thermal loading of the two engines. The MEL computer program is a cycle simulation program that calculates cyclinder gas pressure, temperature, and mass; cylinder volume; work done; heat transfer coefficients; heat loss; mass flow in and out of the cylinder; all tabulated against crank angle. Also from the numerous parameters, it calculates mean heat transfer coefficients; mean cycle temperature; trapped air mass, trapped air/fuel ratios, and total air mass flow.

In developing the program calculation methods, the existing theories have been used. Where existing theories have been shown to be uncertain, research work has been carried out to clarify them [19]. Figure 8 shows a block flow diagram of the MEL computer program [20].

Many heat transfer formulas are in use, but probably the best known and simplest formula for calculating heat transfer in diesel engines is Eichelberg's. It is the experience in GEC's Mechanical Laboratory at Whetstone (U.K.) that Eichelberg's formula gives lower temperatures and temperature gradients than the measured values. The MEL of GEC found that Eichelbeg's formula is quite satisfactory if the index for pressure is changed from 0.5 to 0.54. Again, reference [1] presents a full set of results on thermal loading for the two engines under investigation. Only typical results are discussed here.

Figure 9 is the heat flow to the piston. It indicates the higher thermal loading of the 645E3B piston. At the rated power/speed, the 645E3B has a 42 percent higher thermal loading than the RKC (see Table 2). For the heat flow of the cylinder liner and due to the change of state, as the piston uncovers parts of the cylinder liner in its motion downward, it was found satisfactory to take the mean effective heat transfer coefficient as half that of the piston [20]. The liner wall temperature is estimated at 144°C for both engines.

Figure 10 is the heat flow to the cylinder liner with heating values for the 645E3B engine. Again, at rated power speed, the 645E3B cylinder liner has 45 percent higher thermal loading than the RKC engine (see Table 2).

This computer program was also used to calculate the piston temperatures and their effect on performance and thermal stresses using a suitable finite element mesh and predetermined heat transfer for boundary conditions for the two engines.

Figures 11 and 12 show typical isotherm maps for the

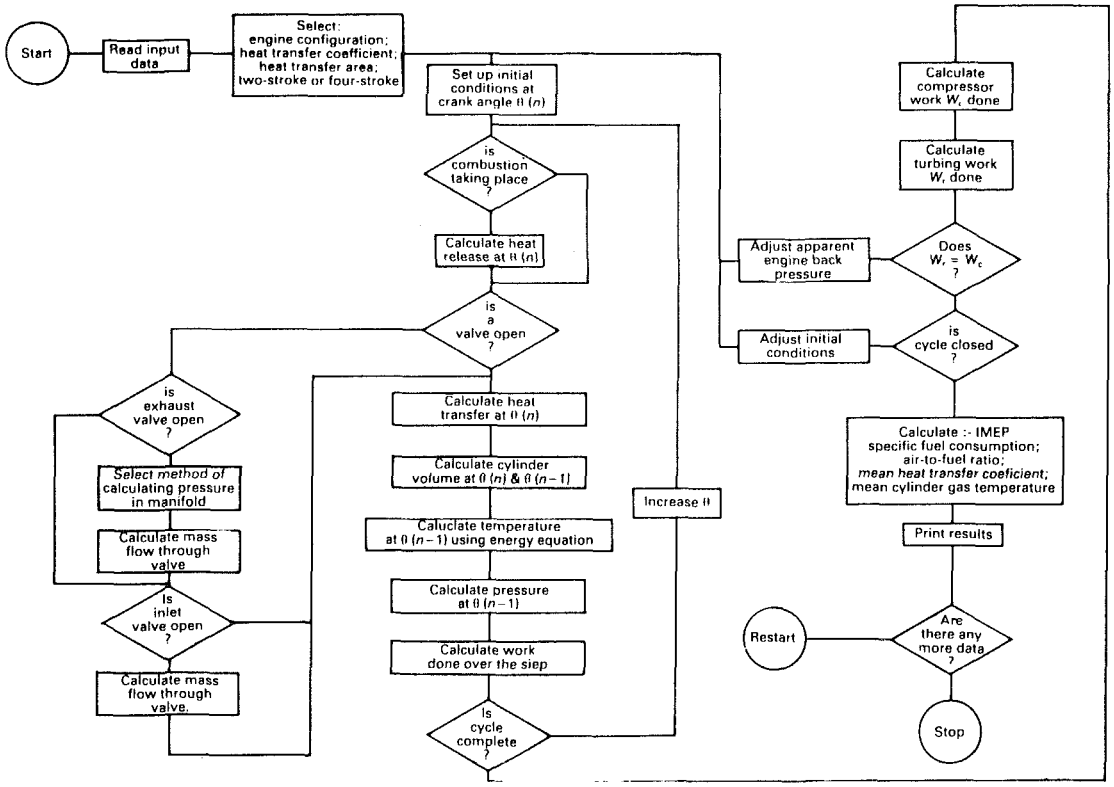

Fig. 8 Diesel engine cycle calculation block flow diagram of computer program

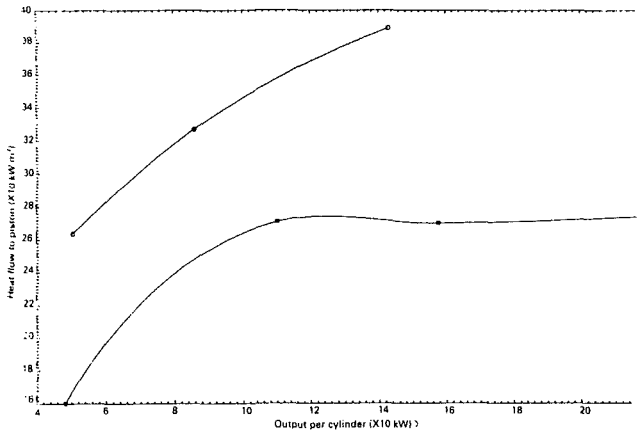

Fig. 9 Piston heat flow versus engine output per cylinder: ◯, 645E3B; ★, RKC

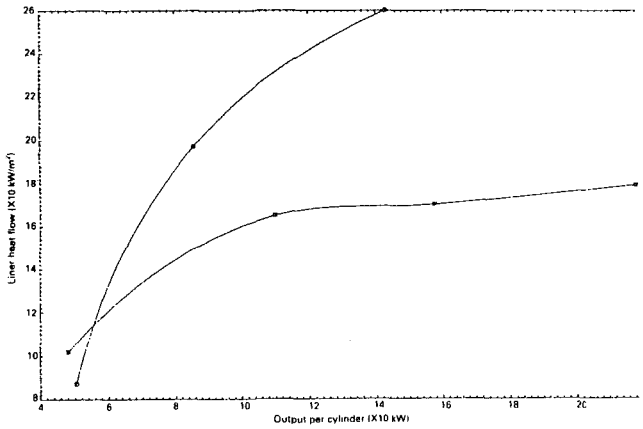

Fig. 10 Liner heat flow versus engine output per cylinder: ◯, 645E3B; ★, RKC

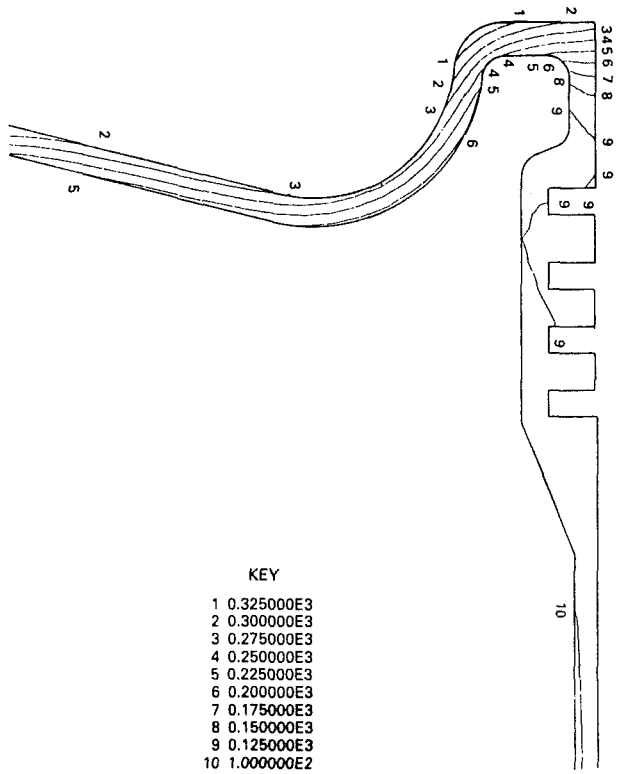

Fig. 11 Predicted temperatures (engine, 645E3B; BMEP, 960 kN/m^2; speed, 900 rpm)

645E3B and RKC pistons at rated power/speed. The maximum piston temperatures are 325°C and 275°C, respectively. The high temperatures affect lubricating oil consumption. As for the thermal stress analysis, it depends on the temperature gradient, the configuration of the component and the material used.

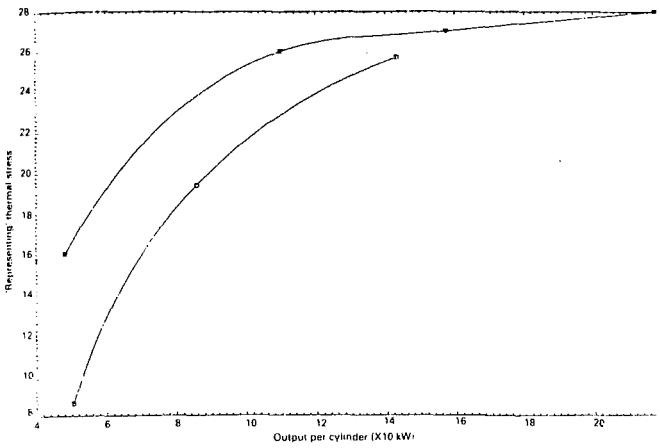

Fig. 12 "Representing" thermal stress versus engine output per cylinder: ◯, 645E3B; ★, RKC

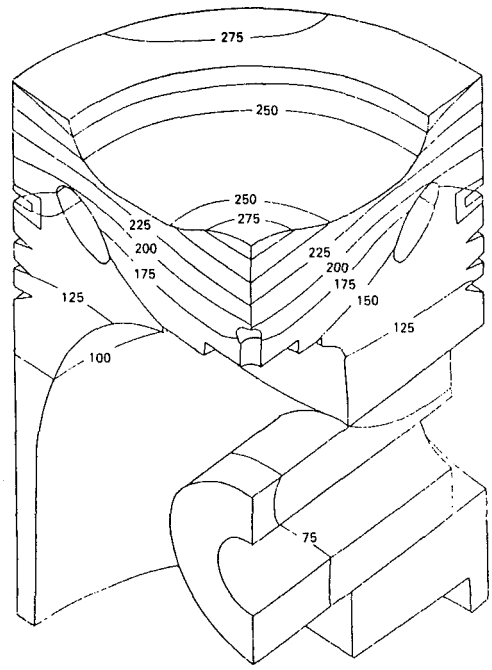

Fig. 13 Predicted temperatures (°C) (RKC piston; BMEP, 1688 kN/m^2; speed, 1000 rpm)

Higher temperatures do not mean necessarily higher thermal stresses [21]. The 645E3B engine uses a cast iron piston because of the higher temperature produced by a two-stroke engine without material property deterioration during hot operation.

Nabag's experience with EMD645E3 engines is the absence of piston failures due to thermal loading [13].

When criteria of "representing" thermal stress ($\sigma_R = q\delta$), presented in [22], are applied to compare the thermal stresses of the two engines' cylinder liners, the result is in favor of the 645E3B engine because of its 0.098-m liner thickness, as compared to a 0.157-m thickness of the RKC engine. Results of "representing" thermal stresses for both engines are shown in Fig. 13.

Table 2 presents some key results extracted from the output of the MEL computer program to compare the thermal loading of the two engines to yield some of the following conclusions.

4.1 The 645E3B engine has higher thermal loading than the RKC engine.

4.2 The piston temperatures of the 645E3B engine are higher than those of the RKC engine, which gives adverse conditions for lubrication and oil consumption.

4.3 The 645E3B engine uses cast iron as piston material, which has better hot strength than aluminum (the RKC piston is aluminum).

4.4 The thermal stress is a function of temperature gradient, type of material used, and the geomety of the component.

Even though the thermal loading of the 645E3B cylinder liner is higher than that of the RKC, its "representing" thermal stress is lower.

Table 2 RKC (four-stroke engine)

Parameter (units)	Value under the following engine conditions			
	BMEP, 1752 kN/m^2; speed, 1000 rev/min; power per cylinder 218 kW	BMEP, 1419 kN/m^2; speed, 862 rev/min; power per cylinder 157.5 kW	BMEP, 1180 kN/M^2; speed, 725 rev/min; power per cylinder 110 kW	BMEP, 637 kN/m^2; speed, 587 rev/min power per cylinder 48 kW
Mean heat transfer coefficient (kW/m^2 K)	0.6051	0.4835	0.4416	0.4089
Mean gas temperature (°C)	734.0	825	921	800
Heat lost to combustion chamber wall per cycle (kW)	5.803	6.541	7.491	5.275
Heat flow to piston (kW/m^2)	247	270	271	160
Heat flow to cylinder liner (kW/m^2)	179	170	165	102
Precent of heat lost to combustion chamber walls (%)	9	12	16	19
Air mass flow measured (kg)	0.0531	0.0412	2.0295	0.018
Air mass flow predicted (kg)	0.0538	0.0407	0.0331	0.0211
Trapped air mass predicted (kg)	0.0498	0.0356	0.0266	0.0193
Trapped air-to-fuel ratio predicted	33	29	24	31
Trapping temperature predicted (°C)	75	70	69	71

645E3B (two-stroke engine)

Parameter (units)	Value under the following engine conditions		
	BMEP, 950 kN/m^2; speed, 900 rev/min; power per cylinder 143 kW	BMEP, 713 kN/m^2; speed, 729 rev/min; power per cylinder 85.9 kW	BMEP, 535 kN/M^2; speed, 571 rev/min; power per cylinder 50.5 kW
Mean heat transfer coefficient (kW/m^2 K)	0.5814	0.4487	0.3689
Mean gas temperature (°C)	1039	1024	994
Heat lost to combustion chamber wall per cycle (kW)	389	327	264
Heat flow to piston (kW/m^2)	389	327	264
Heat flow to cylinder liner (kW/m^2)	260.3	197	87
Precentage of heat lost to combustion chamber walls (%)	12.5	15.6	19.8
Air mass flow measured (kg)	0.0219	0.0168	0.0166
Air mass flow predicted (kg)	0.0219	0.0170	0.0169
Trapped air mass predicted (kg)	0.0169	0.0124	0.011
Trapped air-to-fuel ratio predicted	27.15	25.66	29.90
Trapping temperature predicted (°C)	168	139	120

5 Conclusions

Specific conclusions have been drawn in relation to the various aspects investigated for the GM and Ruston diesel engines.

5.1 The theoretical advantage of two-stroke cycle design over four-stroke cycle is that double the power output should be produced from the same bore, stroke, and speed. In reality, there is hardly any difference in power output of the two designs, when applied in the medium power range. Because of its good breathing capabilities, the four-stroke normally

abridges the gap, but its mechanical loading would be higher due to higher mean piston speed (higher inertia) and higher BMEP (higher firing pressures).

5.2 Thermal loading of diesel engines is mainly a direct function of fuel input rate per cycle, in addition to other parameters. In reality, a two-stroke cycle engine attains higher output than its four-stroke cycle counterpart. By derating, thermal loading of the two-stroke engine can become similar to that of its four-stroke counterpart.

For comprehensive conclusions and comments comparing the two- and four-stroke diesel engines for locomotives refer to the recently published book by Haddad [23].

References

1 Nabag, E. B., "Diesel Engine Two-Stroke Versus Four-Stroke Cycle Design in Rail Traction," *M. Phil. Thesis, Loughborough University, United* Kingdom, Dec. 1983.

2 Kettering, H., "History and Development of the 567 Series General Motors Locomotive Engines," Paper before DEMA Conference, Published by Cleveland Diesel Engine Division, GMC, Oct. 13, 1953.

3 Steigher, H. A., "Two-Stroke Versus Four Stroke Cycle, a Report About Tests With Two Otherwise Absolutely Similar Experimental Trunk-Piston Diesel-Engines of 320 m Bore," presented at CIMAC Eight Congress, Brussels, 1968.

4 French, C., and Lilly, R., "The Locomotive Diesel Engine," Report published by Ricardo and Co., Ltd., 1966.

5 Schur, T., "Developing a High Powered Locomotive Engine," *Sulzer Technical Review*, Vol. 49, Part 4, 1967.

6 Schur, T., "Developing a High-Powered Diesel Engine for Railway Traction," ASME JOURNAL OF ENGINEERING FOR POWER, Vol. 90, 1968, pp. 375-383.

7 VonKienlin, M., and Maybach, G. W., "High Speed High Output Diesel Engines—35 Years of Development of Railroad and Marie Applications," *Trans. SAE*, Paper No. 367A, 1961.

8 Hermann, R., "Service Results of Pielstick 12 PA 6 V 280 Locomotive Engine," Diesel Engineers and Users Association (D.E.U.A.), Publication No. 404, 1981.

9 Ephraim, M., Jr., Kotlin, J. J., and Williams, H. S., Jr., "A Versatile Two-Cycle Diesel Engine—The EMD Model 645 Series," ASME Paper No. 76-DGP-5, 1976.

10 Kotlin, J. J., Dunteman, N. R., and Williams, H. A., "The GM/EMD Model F3, A Diesel Engine for Rail Application," I. Mech. E. Conference, York, 1982.

11 Brandshaw, T. A., "Increased Engine Output—Traction Improves the Breed," I. Mech E. Conference, York, 1982.

12 Whatam, R., and Sinha, S. K., "Enhanced Engine Design Meets the Requirements of British Rail's New Freight Locomotive," CIMAC, 1984.

13 Nabag, E. B., Private Communication.

14 Dunteman, N. R., GM Electro-Motive Division, LaGrange, IL, Private Communications, 1983.

15 Whattam, M., British Railways, Derby, Private Communication, 1983.

16 Sinha, S. K., Ruston Diesels, Ltd., Newton-le-Willows, Private Communication, 1983.

17 Haddad, S. D., and Howard, D. A., "Analysis of Piston Slap-Induced Noise and Assessment of Some Methods of Control in Diesel Engines," SAE Paper No. 800517, 1980.

18 Haddad, S. D., "Predicted Minimum Mechanically-Induced Noise Levels in Automotive Diesel Engines," Report TT 81 R04, Loughborough University of Technology, United Kingdom, Sept. 1981.

19 Polonski, Ç., "Thermal Loading of Diesel Engine Pistons," Mechanical Engineering Laboratory (GEC) Report, 1967.

20 Griffiths, W. J., Wellworthy, Ltd., Private Communication, 1983.

21 Ball, K., and Sinha, S. K., "Predicting the Temperature of Pistons of Some Highly Rated Medium-Speed Diesel Engines," *GEC Journal of Science and Technology*, Vol. 46, No. 2, 1980.

22 Steiger, A., and Aue, G. K., "The Influences of the Thermal Loading Criterion on the Design of Turbocharged Two-Stroke Diesel Engines," *I. Mech. E Proceedings*, Vol. 179, Paper No. 5, 1964-65.

23 Haddad, S. D., ed., *Advanced Diesel Engineering and Operation*, Ellis Horwood and John Wiley, Chap. 7, June 1988.

Piston Ring Thermal Transient Effects on Lubricant Temperatures in Advanced Engines

M. E. Boisclair

D. P. Hoult

V. W. Wong

Sloan Automotive Laboratory,
Massachusetts Institute of Technology,
Cambridge, MA 02139

One class of advanced diesel engines operates with low heat rejection and high operating temperatures; piston-ring/liner lubrication is a major problem for these engines. This study attempts to illustrate the time-dependent thermal environment around the top piston ring and lubricant in these advanced engines. Particular emphasis will be placed on the maximum lubricant temperature. The analysis starts with a standard cycle simulation and a global finite-element analysis of the piston and liner in relative motion. A more detailed finite-element model, which considers variable oil film thickness on the liner, focuses on the top ring and lubricant and uses the groove and liner temperatures generated in the global analysis as boundary conditions. Results for different heat rejection engine configurations are presented. We observe that because of major transient effects, high lubricant temperature is experienced not only at top ring reversal but also down the liner to bottom ring reversal.

Introduction

The demand for higher output diesel engines for commercial and military applications, together with advancements in high-temperature material technology, has pushed up engine operating pressures and temperatures. In particular, the "adiabatic" or low heat rejection (LHR) diesels [1–3] operate at elevated temperatures. These advanced engines generally feature the simultaneous use of combustion chamber insulation and efficient exhaust energy recovery systems. These engines offer the potential benefits of improved fuel economy, reduced weight, and possibly wider fuel tolerance [1, 2].

Before these potential benefits can be realized, major breakthroughs are necessary in the area of high-temperature lubrication [4, 5], and the cylinder liner interface with the piston and rings is of paramount concern. The maximum continuous operating temperature of most present-day lubricants in conventional engines approaches 300°C [4]. Above that point, deposits generated by oil degradation increase significantly [6] and cause severe engine damage. Cylinder wall temperatures at the top ring reversal (TRR) point of recent LHR engine designs will reach over 370°C and up to 600°C, according to various estimates [1, 5]. At 600°C, examination of the boiling point or oxidation temperatures of these lubricants suggests little or no lubricant remains [5]. Much work will be required before a fully formulated high-temperature lubricant is developed.

Besides lubricant stability, high-temperature operation also affects the oil film thickness. Current models seem adequate to predict the oil film thickness between piston rings and cylinder liner from lubricant rheology and engine operating parameters [7, 8]. The viscosity and film thickness of a liquid lubricant decrease rapidly with temperature; boundary lubrication and significant wear are expected in traditional LHR engines. In fact engines with 370°C TRR temperature have experienced tribology-related problems [4].

The objective of the present study is to define and illustrate the time-dependent thermal environment of the piston, rings, lubricant, and cylinder liner interface region of an operating diesel engine. This is a basic step toward characterizing the lubricant behavior around the ring/liner interface, which we need to understand and control to provide adequate engine lubrication under severe operating conditions.

Past studies of the temperature distributions focused on the piston [9–12], and in some cases, the models comprise piston and cylinder liner in relative motion [13–15]. However, detailed analyses that focus on the piston ring and lubricant temperatures have been notably absent. There is general agreement that the transient temperature behavior penetrates only to a thin surface layer on the piston and liner. Most of the piston is at steady state; however, this does not necessarily mean that the rings also are at steady state.

Examination of the temperature conditions surrounding the rings suggests that the thermal behavior would be transient. The liner surface temperature has an axial gradient from the top portion in contact with the combustion gases to the lower section in contact with the cooling oil. The ring outer radial surface will see this gradient as it traverses up and down the liner. Results that follow will illustrate this transient thermal behavior of the rings (top ring in particular) and of the oil film between the ring and liner.

Contributed by the Internal Combustion Engine Division and presented at the Twelfth Annual Energy-Sources Technology Conference and Exhibition, Houston, Texas, January 22–25, 1989. Manuscript received by the Internal Combustion Engine Division August 1988. Paper No. 89-ICE-2.

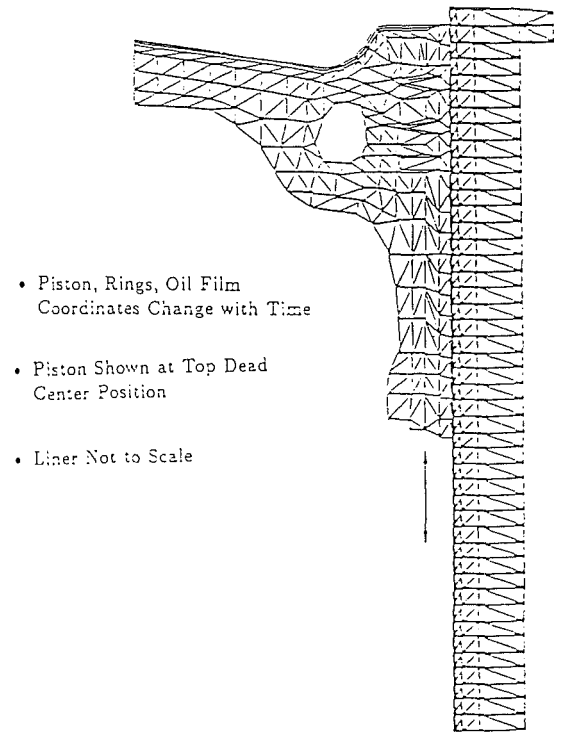

Fig. 1 Piston model finite element grid

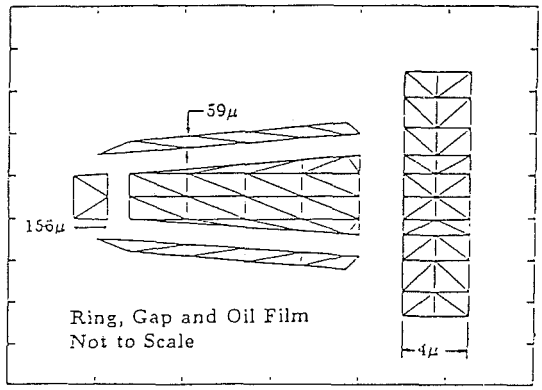

Fig. 2 Top ring, gap, and oil film finite element grids of the ring/oil film model

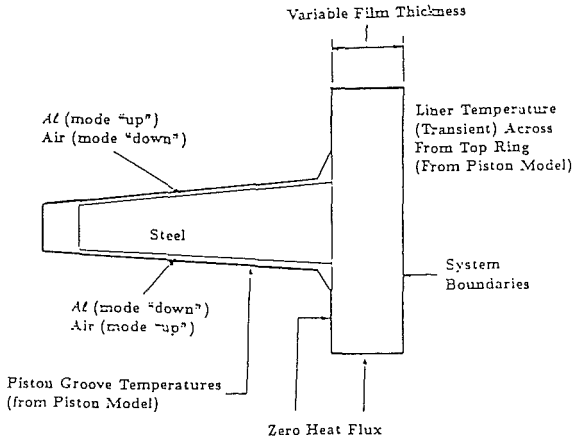

Fig. 3 Ring-lubricant model schematic (not to scale)

This paper presents results of a detailed thermal analysis of the top piston ring, in contact with the piston ring groove, and a variable-thickness lubricant film. The model combines an engine cycle analysis with component heat transfer calculations. A finite element algorithm is first applied to model the heat transfer through the piston, rings, and the cylinder liner in relative motion. A second finite element model of only the top ring and lubricant is then applied using the groove and liner temperatures generated in the first model as boundary conditions. This study will also show that thermal transient effects have a major role in the lubrication environment, and that these transients will influence the design considerations for strategic cooling or lubrication system.

Analysis

Model Formulation. Two coupled finite element axisymmetric models were developed. The first model, hereafter referred to as the piston model, included the piston, rings, gap and oil film regions, and the liner. The second model included the details of the top ring, ring groove, oil film, and liner as a submodel of the overall piston model. The second model allows a much more detailed study of the top ring region's thermal behavior than would be possible using the piston model due to the exceedingly small element sizes required to resolve the high thermal gradients. The element grids for the piston model and the top ring/oil film model are shown in Figs. 1 and 2. Figure 3 is a schematic of the ring-lubricant model showing the various boundary surfaces and applied boundary conditions.

The discretization of the transient heat conduction equation for an axisymmetric model follows the standard finite element variational formulation as developed by Segerlind [16] and Huebner [17]. The result is a set of coupled liner equations expressed in matrix notation as

$$[K]\{T\} + [W]\{\dot{T}\} = \{P\} \quad (1)$$

In equation (1), [K] is the global conductance matrix, [W] is the global capacitance matrix, both of dimension $N \times N$, where N is the number of temperature nodes. $\{P\}$ is the vector of applied heat flows and $\{T\}$ is the unknown nodal temperature vector. The boundary conditions used to calculate the applied heat flows are contained in $\{P\}$. Both the piston and top ring/

Nomenclature

d = oil film thickness, m
$[K]$ = global conductance matrix
N = total number of nodes in finite element model
$\{P\}$ = global force matrix
(Q/A) = heat flux, W/m/m
Δt = transient time step, s
ΔT = maximum temperature difference between the top ring outer radial surface and adjacent liner
t = time, s
$\{T\}$ = global temperature matrix
U = piston speed, m/s
$[W]$ = global capacitance matrix
X = heat pulse penetration distance, m
α = thermal diffusivity, m^2/s
κ = oil film thermal conductivity, W/m/K
μ = oil film viscosity, kg/m/s
ω = frequency of temperature variation, 1/s

Subscripts

1 = top ring
avg = cycle average
t = current time step
$t-\Delta t$ = previous time step

Table 1 Piston finite element model predicted temperatures compared with measured Cummins VT903 piston temperatures

Piston Temperatures Measured on Cummins VT903 Diesel Engine K	FEM Predicted Temperatures K	% Difference
376.7	387.2	2.8
398.7	402.3	0.9
484.3	483.6	- 0.1
429.7	429.6	0.0
482.5	499.1	3.4
494.9	517.7	4.6

oil film models use triangular, simplex elements to break down the region into discrete finite elements.

The basic approach used by the piston and top ring/oil film programs to solve equation (1) is to assume a finite difference approximation for $\{T\}$ of the form

$$\{\dot{T}\} \simeq (\{T\}_t - \{T\}_{t-\Delta t})/\Delta t \quad (2)$$

where ΔT is the transient time step; $\{T\}_{t-\Delta t}$ is the known temperature array calculated at the previous time step.

Correctly predicting the top ring/oil film thermal behavior requires the proper boundary conditions as seen by the piston ring. This is the primary purpose of the piston model. Similar to a finite element stress analysis done by Nurnukra et al. [18] on a connecting rod, a global model, i.e., the piston model, is used to generate the boundary conditions applied on a subregion, i.e., the ring. The subregion is then taken out of the global model and analyzed using a much finer elemental grid. The benefits are a better discretization of the specific subregion of an overall model along with a reduction in computer run time necessary to model the subregion behavior properly.

The ring submodel is defined as the top ring and groove gap and the oil film. The oil film is modeled for one ring width on either side to account for axial conduction affects. No account is taken of oil that might migrate into the groove. The ring code also models the ring radial motion in the groove by incorporating a variable oil film thickness capability as well as the axial motion from the bottom surface to the top surface of the groove. The variable oil film thickness capability is particularly important since over a cycle the film thickness can vary from 1 to 20 μm, having a significant effect on lubricant thermal resistance and hence ring to liner heat transfer. In both the piston model and the ring submodel, it is assumed that the top ring is in contact with the upper surface of the ring groove during the downstrokes and with the lower surface during the upstrokes.

The piston code treats the relative motion between the piston and liner by reconnecting the gap/oil film elements to their nearest neighbors on the liner surface for each crack angle increment. For both the piston and ring codes, six degree crank angle increments are used as the transient time step. In the piston code, as the top ring traverses the liner surface, the temperatures of the two liner surface nodes closest to the top ring are extracted. The ring code linearly interpolates between these two nodal temperatures to determine the intermediate liner surface boundary nodal temperatures of the ring model at each crank angle increment.

In the piston model, one node is placed at each corner of the top ring groove. When the piston transient calculation has converged, these four nodal temperatures are used as the basis for defining the ring model groove surface boundary conditions. The ring code linearly interpolates between these corner nodes to define the boundary temperatures at each intermediate node around the groove at each crank angle increment. For the remaining boundary nodes of the ring model not on the groove or liner surfaces, the boundary condition is assumed to be zero heat flux.

Both the piston and ring programs do not account for viscous heating effects, which are assumed to be negligible particularly at top and bottom ring reversal where piston speeds are low. More will be said about this assumption in a later section.

Model Validation. The piston model was validated by data matching predicted model temperatures with thermocouple data obtained by Facon [11] on an instrumented Cummins VT903 diesel engine piston. The heat transfer coefficient and temperature of the combustion chamber gas as a function of crank angle are generated by the MIT diesel engine cycle simulation code [19]. The remaining boundary heat transfer coefficients and environmental temperatures are determined to give a temperature match that is physically plausible. The results of the temperature match are tabulated in Table 1. The operating conditions correspond to the VT903 full load rated speed conditions (2600 rpm, 14.7 atm bmep).

The good agreement between the predicted and measured temperatures indicates that the piston model is reasonable in predicting the thermal environment within the piston and will provide valid boundary conditions for the detailed ring calculations.

Results

Description of Cases Studied. To determine the ring-lubricant thermal behavior over a range of cooling strategies, four cases were examined. Calculations were done for a simulated turbocharged, single-cylinder version of a Cummins VT903 diesel engine. In each case, the combustion chamber driving boundary conditions generated by the cycle simulation code correspond to the rated conditions of the VT903, i.e., 182 N • m torque load at 2600 rpm. All boundary conditions are represented by heat transfer coefficients and environmental temperatures as will be described in detail for each case.

Case 1. Case 1 represents a standard cooled piston, head, and liner configuration. The piston underside and oil gallery boundaries are completely cooled by oil forced convection. To model the thermal characteristics of the head, an effective heat transfer coefficient is computed assuming a 1.45-cm-thick iron head with forced convection water cooling and applied on the liner top boundary. The iron liner is water-cooled by forced convection. The gasket and metal region of the lower liner boundary is also modeled by computing an effective heat transfer coefficient assuming parallel heat conduction paths through iron and rubber. The liner surface below the piston and the bottom of the liner are cooled by an oil film.

Case 2. Case 2 represents a cooled head but uncooled liner configuration. The boundary conditions generated by the cycle simulation program are slightly different from those in Case 1 to correspond to the VT903 different operating conditions. The liner is no longer cooled by forced water convection, but is now cooled by air natural convection, resulting in an order of magnitude decrease in the heat transfer coefficient from 0.35 to 0.01 W/cm^2/K. The remaining boundary conditions are adjusted to match the data.

Case 3. Case 3 represents an uncooled head and uncooled liner configuration. The boundary conditions generated by the cycle simulation program are the same as in Case 2, except that the head is no longer cooled by water forced convection, but is now cooled by air natural convection. The liner heat transfer coefficient is also reduced to 0.001 W/cm^2/K and the coolant temperature is increased to 360 K to simulate completely uncooled conditions. The effective heat transfer coefficient of the head is decreased to account for the decreased head cooling.

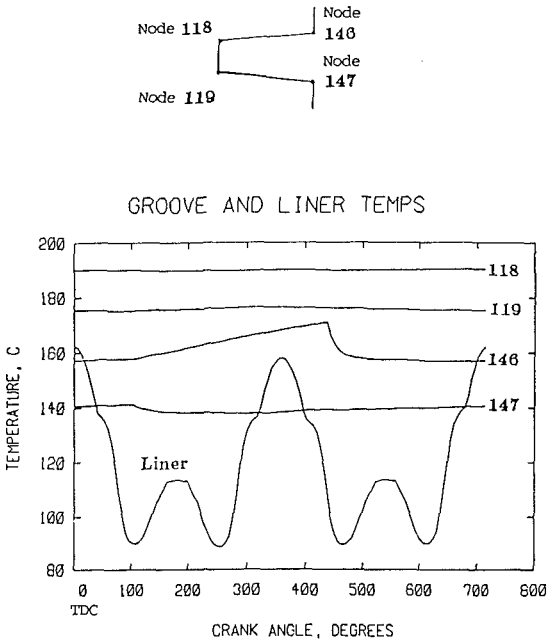

Fig. 4 Top groove, corner nodal temperatures, and liner surface temperature opposite the top ring calculated by the piston model

Case 4. Case 4 represents an insulated configuration of an uncooled piston, head, and liner. The piston underside and oil gallery are now cooled by air natural convection. The liner boundary conditions are the same as in Case 3 except for the gasket region in which the heat transfer coefficient is halved to simulate reduced cooling. Additionally, a 1-mm-thick coating of zirconium is modeled on the piston bowl and crown surface and on the liner surface facing the piston. The cycle simulation program modeled the insulated conditions in the piston and liner to reflect the higher combustion chamber temperatures expected in an insulated engine configuration.

Behavior of Liner Temperature. The nature of the top ring/oil film thermal environment depends upon the temperature of the liner surface at the top ring and the top groove surface temperature, both as functions of crank angle. The top groove surface temperature exhibits a fairly steady temperature history over a cycle, as shown in Fig. 4, where temperatures at the four numbered groove corner nodes are plotted. Conversely, the liner surface temperature seen by the top ring over a cycle exhibits a strong cyclic behavior. Understanding the causes of this transient behavior provides the basis for evaluating the overall ring/oil film/liner thermal interaction.

Figure 5 shows a composite plot of the Case 1 cyclic average liner heat fluxes generated by the piston program from various sources versus the axial distance down the liner surface. A striking characteristic of the plot is that the total heat flux curve does not monotonically decrease from liner top to bottom. From 0 to 5 cm the heat transfer is dominated by the combustion chamber hot gases. But from midstroke to bottom ring reversal, the heat transfer from the rings and piston skirt and lands begins to have a significant effect, causing a bump in the total heat flux curve. Past the bottom ring reversal position, the heat transfer is negative, indicating that heat flows from the liner to the piston skirt and the cooling oil. This plot agrees with the total liner heat flux profile along the gas side of a liner generated by ITI using a finite element analysis [13].

The result of the heat inputs and outputs to the liner surface shown in Fig. 5 is the cyclic average liner surface temperature profile shown in Fig. 6. The first peak at 0.7 cm is due directly to the combustion gas heat flux. As the input heat flux decreases away from the liner top so does the liner surface temperature. At 10 cm, even though the heat flux has increased

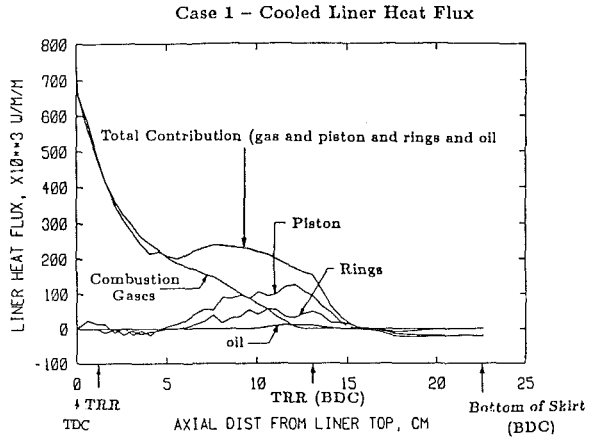

Fig. 5 Cycle-averaged heat flux to liner versus axial position on liner

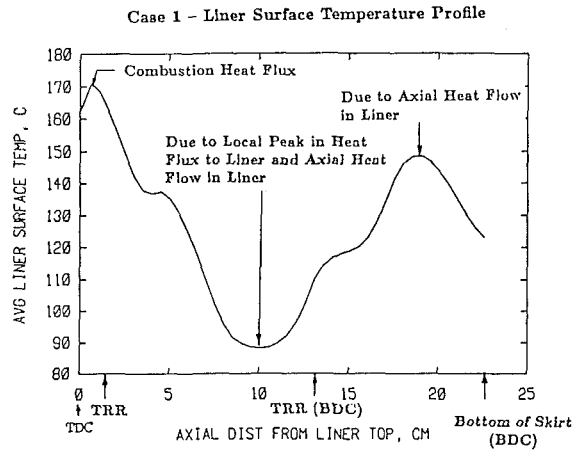

Fig. 6 Cycle-averaged liner temperature versus liner position

due to the effects of the rings and piston, the liner cooling is able to remove the excess heat causing a minimum in the liner surface temperature. Approaching the gasket and oil cooling region of the liner, axial conduction down through the liner begins to develop. But because the heat transfer coefficients of the regions are less than that of the coolant region, particularly for oil, the heat conducted down the liner cannot be convected away quickly. The result is that the liner temperature begins to increase and a second peak is reached. At 16 cm, the heat flux begins to flow out of the liner into both the cooling oil and piston skirt. Not until 19 cm, though, does the heat flux out begin to overcome the excess axial heat flux into the lower liner region causing the liner temperature to decrease.

As the top ring traverses the liner from top ring reversal to bottom ring reversal, it will see the liner surface temperature profile from 1.5 cm to 13.6 cm as shown on Fig. 6. The liner temperature profile generated by the piston program is used as a boundary condition for the top ring/oil film model.

Thermal Time Constant of the Top Ring. The thermal behavior of the top ring in relation to the thermal behavior of the liner is the key to understanding the behavior of the oil film temperature. If the top ring could react infinitely fast to changes in boundary temperature the top ring outer radial surface temperature would follow the liner surface temperature, assuming no viscous heat generation occurs within the oil. However, the top ring cannot react infinitely fast to changes in temperature.

The thermal time constant of the ring is the time required for a temperature pulse to propagate from the inside surface of the ring to the opposite side of the ring. Ingersoll et al. [20]

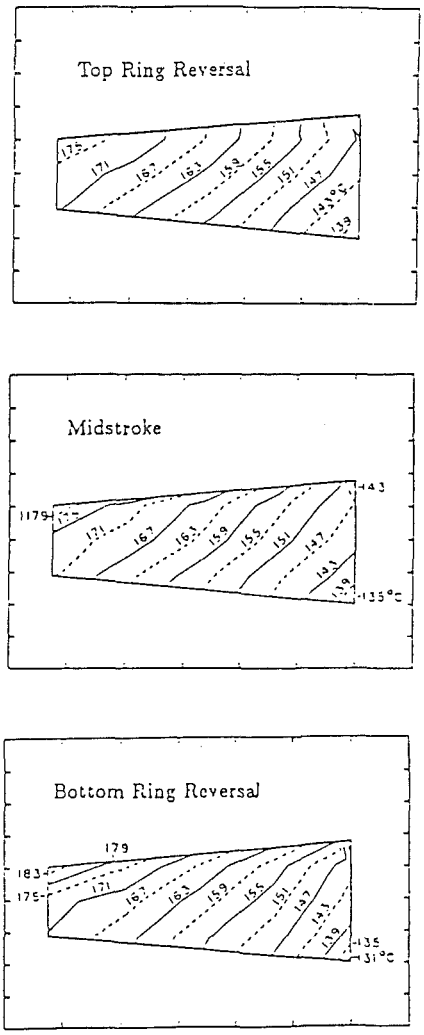

Fig. 7 Top ring temperature contours for Case 1

have shown that the thermal time constant for one-dimensional heat flow in a medium undergoing simple periodic variations in surface temperature is

$$t_1 = X\sqrt{1/2\alpha\omega} \tag{3}$$

where α is the medium's thermal diffusivity, ω is the frequency of the temperature variation, X is the distance, and t_1 is the thermal time constant. For a 1 percent carbon steel ring, we assume $\alpha = 1.2 \times 10^{-5}$ m²/s and ring width = 0.0052 m. If the engine is operating at 2600 rpm, the thermal time constant of the top ring would be

$$t = 0.045 \text{ s or } 2 \text{ revolutions}$$

It takes two revolutions for a temperature pulse to travel from one end of the ring to the opposite end.

Figure 7 shows temperature contours of the top ring at top ring reversal, midstroke, and bottom ring reversal of the power stroke for Case 1. The contours indicate that the heat flow is approximately radial from the inner ring radius to the outer ring radius. The contours also show that over the quarter cycle examined, boundary temperature variations have only penetrated a small distance from the surface. The conclusion is then that because the ring thermal lag is relatively long compared with the liner surface temperature variation seen by the top ring, the top ring thermal behavior lags behind that of the liner. As the liner temperature decreases as bottom ring reversal is approached, the top ring cannot react to the liner temperature variation and hence remains at elevated temperatures.

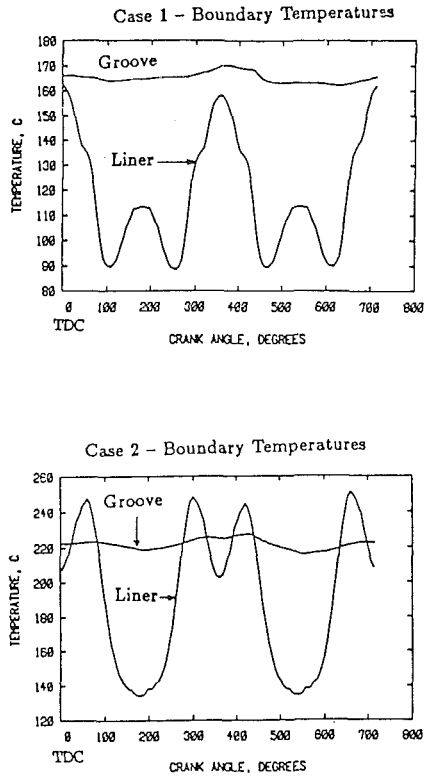

Fig. 8 Ring model boundary conditions for Cases 1 and 2

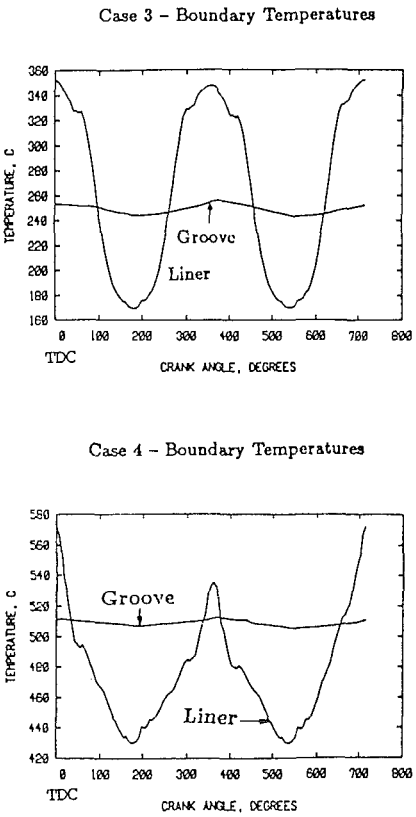

Fig. 9 Ring model boundary conditions for Cases 3 and 4

Boundary Conditions for Ring/Lubricant Model. Figures 8 and 9 show the spatially averaged boundary temperatures seen by the top ring over a complete cycle. The spatially averaged top groove temperature is fairly steady while the liner surface temperature at the top ring shows a cyclic character-

Table 2 Fraction of viscous heat generation in oil film under top ring

	U_{avg},m/s	ΔT_{avg},K	d_{avg},10^{-6} m	% Total Ring to Liner Q/A
Top Third	9.5	10	3.7	5.
Middle Third	15.5	50	7.0	7.
Bottom Third	5.7	40	4.7	1.

istic. The bump in liner temperature at bottom ring reversal for Case 1 is explained by the liner surface temperature profile on Fig. 6. At a crank angle of 100 deg and engine speed of 2600 rpm, the top ring has traversed 10 cm down the liner to the minimum surface temperature. From 100 to 180 deg, the top ring moves down the liner from 10 cm to 13.6 cm and the liner surface temperature increases for reasons explained above.

For Cases 2, 3, and 4, without liner cooling, the liner surface temperature no longer exhibits the temperature bump at bottom ring reversal characteristic of the Case 1 cooled liner. The coolant region of the liner can no longer convect away the quantities of heat necessary to minimize the liner surface temperature resulting in a liner surface temperature profile that decreases from liner top to bottom.

The decrease in liner surface temperature seen by the top ring at top ring reversal for Case 2 can be explained by the coolant side boundary conditions on the liner. For Case 2, the head is completely cooled while the liner is uncooled. The cooled head is able to convect away more heat than the uncooled liner, causing the temperature at the top of the liner to be less than the liner regions directly below it. In Cases 3 and 4 where the liner cooling is more uniformly distributed, the liner surface temperature cycles smoothly from top to bottom ring reversal.

Viscous Heating Effects. In both the piston and ring finite element models, the effect of viscous heating is neglected. The heat flux generated by viscous effects in oil under the top ring is a fraction of the cyclic average top ring to liner total heat flux

$$(Q/A)_{\text{friction}} = \mu U_{\text{avg}}/d_{\text{avg}}(U_{\text{avg}}/2) \tag{4a}$$

and

$$(Q/A)_{\text{heat conduction}} = \kappa \Delta T_{\text{avg}}/d_{\text{avg}} \tag{4b}$$

where μ is the oil viscosity, U_{avg} is the average piston speed, κ is the oil thermal conductivity, ΔT_{avg} is the average maximum temperature difference between the top ring and adjacent liner, and d_{avg} is the average oil film thickness. Integrating equation (4*b*) over the cycle, the cyclic average heat flux from the top ring to the liner is 970 κ W/m^2 for Case 1. Table 2 shows the average heat flux ratio calculated from equation (4) for a piston speed of 2600 rpm. The average velocities and oil film thicknesses are calculated over the top third, middle third, and bottom third of one complete piston rotation.

At midstroke, where the piston speeds are high, the viscous heat flux accounts for approximately 7 percent of the top ring to liner total heat flux. Since the viscous heating is at least a factor of ten less than the ring to liner heat flux, the ring temperature is expected to respond just as slowly to the viscous heating as the ring to liner heat transfer. Around top and bottom ring reversal, the fraction of total liner heat flux generated by viscous heating is negligible.

Results for Cases Studied. With the boundary conditions of Figs. 8 and 9, the top ring/oil film model was run. Of particular interest in ring lubrication theory and practice is the maximum oil film temperature between the top ring and liner. It was previously thought that the maximum oil film temperature occurred on the liner surface at top ring reversal. Results

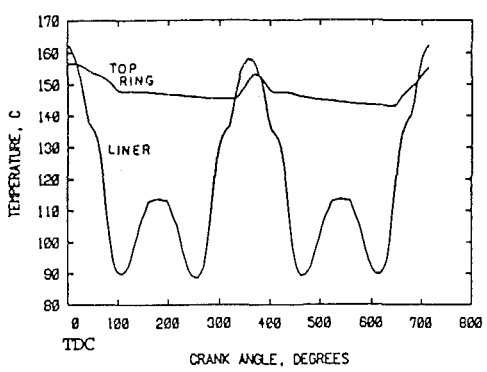

Fig. 10 Top ring outer radial surface maximum temperature and average liner surface temperature opposite the top ring for Case 1

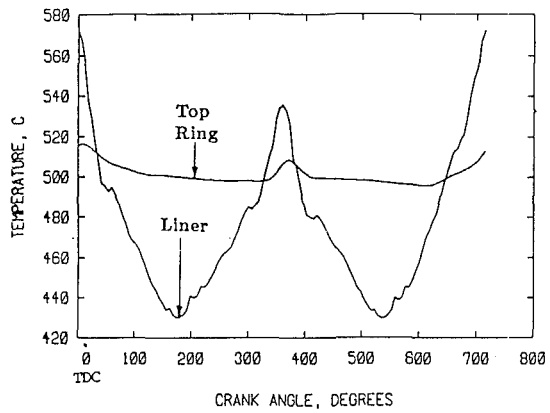

Fig. 11 Top ring outer radial surface maximum temperature and average liner surface temperature opposite the top ring for Case 4

of the ring model substantiate this hypothesis but also lead to a more complete description.

The maximum lubricant temperature must occur on either the ring or liner surfaces if no internal heat generation occurs. Figure 10 shows the top ring outer radial surface maximum temperature and the liner surface temperature at the top ring over a cycle for Case 1. The maximum oil film temperature over a cycle is the locus of the maximum of the ring face and liner surface temperatures at each crank angle. At top ring reversal, the maximum lubricant temperature does occur on the liner, but as the piston moves toward bottom ring reversal the maximum lubricant temperature switches to the top ring surface and stays there until the piston again approaches top ring reversal. Because the top ring surface stays hot throughout the cycle due to the thermal lag, the maximum lubricant temperature is prevented from decreasing to the lower liner temperature levels at bottom ring reversal.

Figures 11 through 13 show the top ring outer radial surface maximum temperature and the liner surface temperature at the top ring for Cases 2, 3, and 4. For Case 2, uncooled head and liner, the effect of the top ring keeps the maximum oil film temperature 80°C hotter than the minimum liner surface temperature at bottom ring reversal, while for Cases 3 and 4, the ring keeps the oil film temperature 90°C and 70°C hotter, respectively. For Case 1, when the minimum liner temperature seen by the top ring does not occur at bottom ring reversal due to the temperature bump, the ring keeps the oil film temperature 60°C hotter than the minimum liner temperature.

Figures 14 and 15 show the maximum oil film temperature locus for Cases 1, 2, 3, and 4. For Case 1, the maximum oil

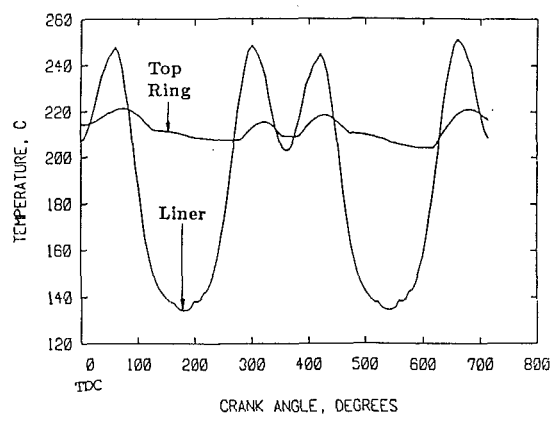

Fig. 12 Top ring outer radial surface maximum temperature and average liner surface temperature opposite the top ring for Case 2

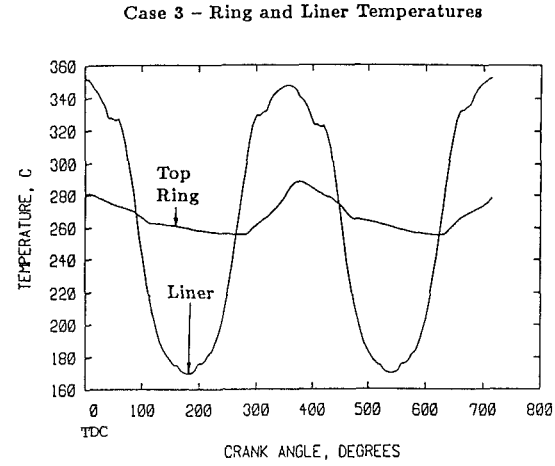

Fig. 13 Top ring outer radial surface maximum temperature and average liner surface temperature opposite the top ring for Case 3

film temperature is largely determined by the ring outer radial surface temperature. Only over a small portion of the cycle near the top ring reversal positions is the maximum oil film temperature determined by the liner surface temperature.

Note that as the liner and head cooling is decreased from Case 1 to Cases 2 to 3, the liner surface temperature determines the maximum oil film temperature over a greater part of the cycle. But, when the piston and liner surfaces are insulated for the same cooling conditions, Cases 3 and 4, the ring outer radial surface temperature determines the maximum oil film temperature over a greater part of the cycle.

For the uncooled configurations, Cases 2, 3, and 4, at top ring reversal the liner surface temperature rises substantially above the maximum ring surface temperature. The result is that the maximum oil film temperature drops sharply after top ring reversal until the temperature of the top ring surface is reached, stays relatively constant on the top ring, and rises sharply as top ring reversal is again approached. Therefore, as the liner and head cooling is decreased or in an insulated configuration, the maximum oil film temperature can experience large temperature swings. This could have a pronounced affect on the lubricant deposit rate, which, as the results of McGeehan have shown, doubles for a 10°C increase in lubricant temperature [6].

The temperature contours in the top ring for Cases 2, 3, and 4 are shown in Figs. 16 through 18. Note that the temperature distributions are highly nonlinear in both the axial

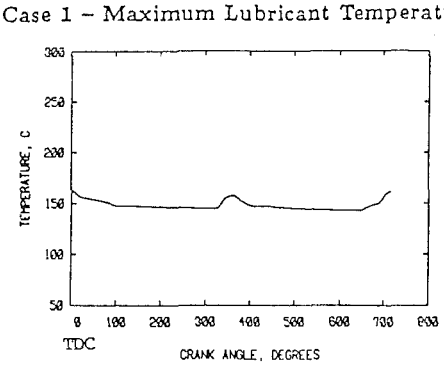

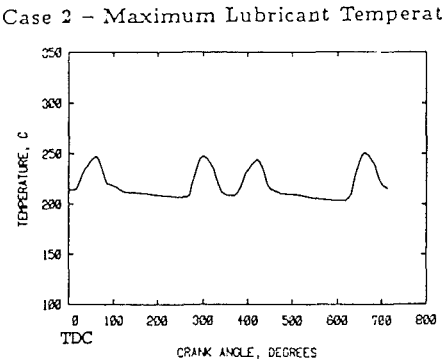

Fig. 14 Maximum lubricant temperature locus for Cases 1 and 2

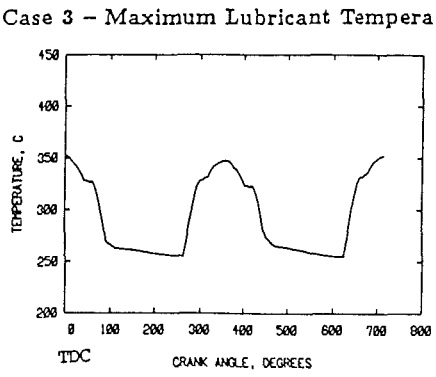

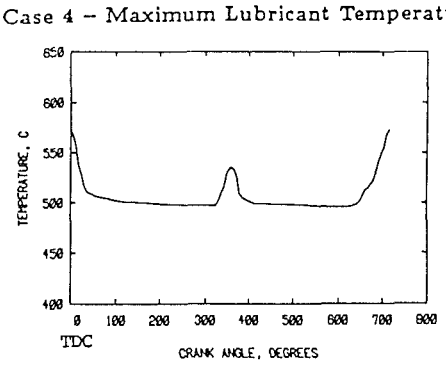

Fig. 15 Maximum lubricant temperature locus for Cases 3 and 4

and radial directions, particularly at bottom ring reversal where a steep gradient occurs at the ring outer radial surface. This result clearly shows the limitations of the piston model, which would predict a linear temperature distribution within the top ring using only two elements. The temperature contours also

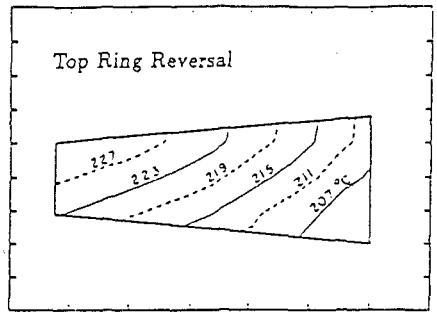

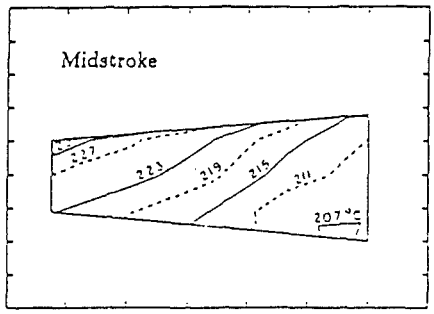

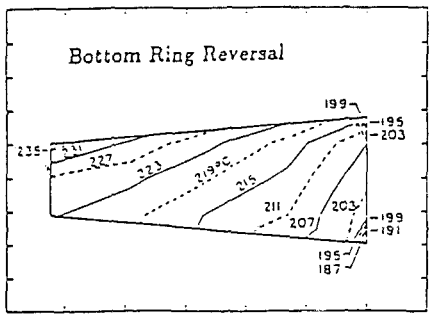

Fig. 16 Top ring temperature contours for Case 2

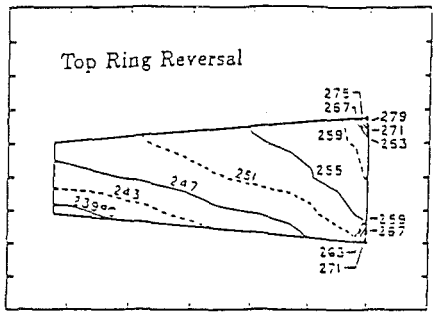

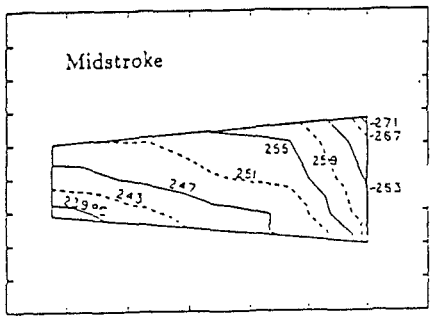

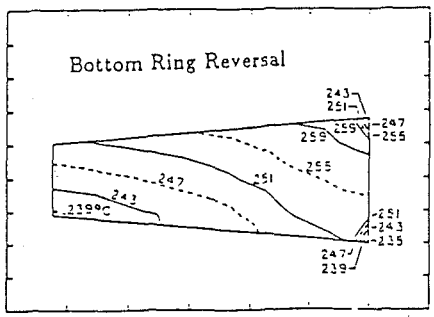

Fig. 17 Top ring temperature contours for Case 3

show that although the ring thermal time constant is long, on the order of two revolutions, transient effects do have time to penetrate slightly.

Figures 19 through 22 show the heat flow from the top ring to the liner as a function of crank angle. These plots further substantiate the conclusion that the top ring outer radial surface temperature does not follow that of the liner but remains at elevated temperatures throughout the cycle due to the long thermal time constant. To see this, compare the ring to liner heat flow plots with the liner surface temperature plots, Figs. 10 through 13. The two plots for each case are almost exactly opposite in shape. For example, when the liner surface temperature peaks, the heat flow is minimized, being negative from liner to ring. When the liner surface temperature is minimized, the heat flow peaks, being positive from ring to liner. The heat flows are a function of the liner surface temperature, indicating that the ring surface temperature remains fairly constant.

The direction of the ring to liner heat flow gives an alternate indication of the crank angle at which the maximum lubricant temperature switches from the liner to the top ring and back again. When the heat flow changes sign from negative to positive, i.e., from liner-to-ring to ring-to-liner, the corresponding crank angle is also that at which the maximum lubricant temperature switches from the liner to the ring. When the sign changes from positive to negative, i.e., from ring-to-liner to liner-to-ring, the corresponding crank angle is that at which the maximum lubricant temperature switches from the ring to the liner.

Discussion

Of particular interest in the area of piston ring lubrication is the maximum lubricant temperature. The maximum lubricant temperature determines its viscosity and whether the lubricant is close to thermal breakdown or boiling. The traditional view holds that the maximum lubricant temperature occurs on the liner surface opposite the top ring at top ring reversal. As the ring pack travels down the liner, the lubricant temperature is assumed to decrease along with the liner temperature. The implicit assumption made here is that the ring temperature follows the liner surface temperature as the piston moves up and down the liner.

The results of this study indicate that the top ring temperature does not follow the liner surface temperature but remains at elevated temperature levels throughout the cycle due to a long ring thermal time constant. The lubricant in contact with the top ring surface therefore remains at the elevated temperature levels of the ring while the lubricant temperature in contact with the liner varies continuously. The lubricant between the top ring and liner must therefore exhibit significant transient behavior over a cycle as well as a high thermal gradient.

The major implication of an elevated top ring temperature is that the maximum lubricant temperature does not decrease at bottom ring reversal but remains at elevated temperatures throughout the cycle. Because the top ring stays hot, the maximum lubricant temperature will switch from the liner to the ring surfaces as the liner surface temperature decreases below

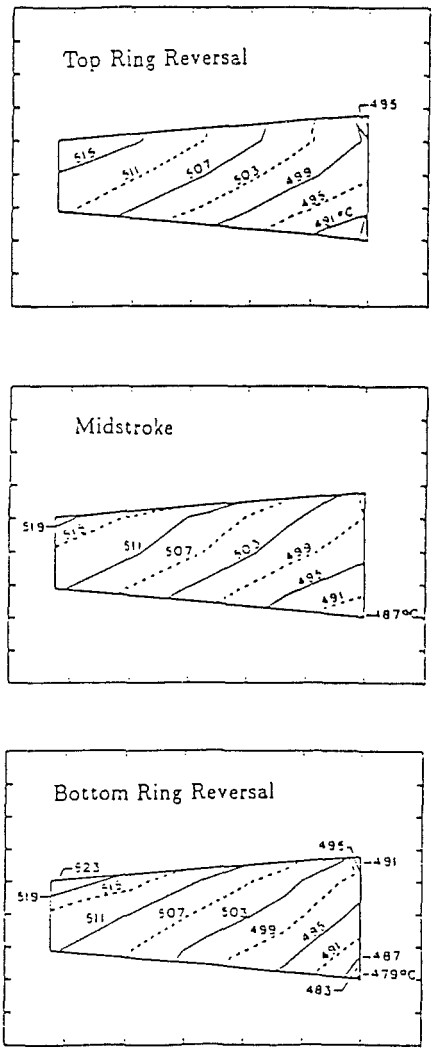

Fig. 18 Top ring temperature contours for Case 4

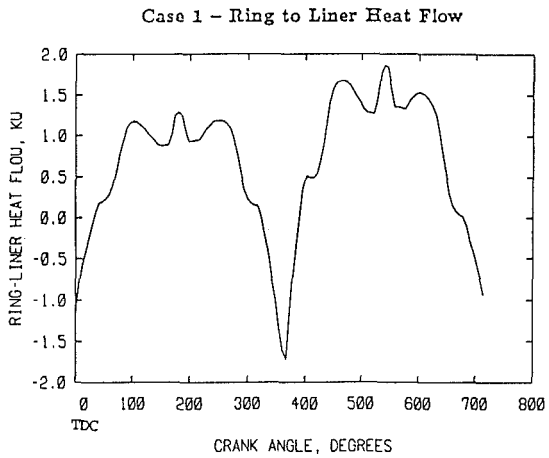

Fig. 19 Ring to liner heat flow calculated by the ring model for Case 1

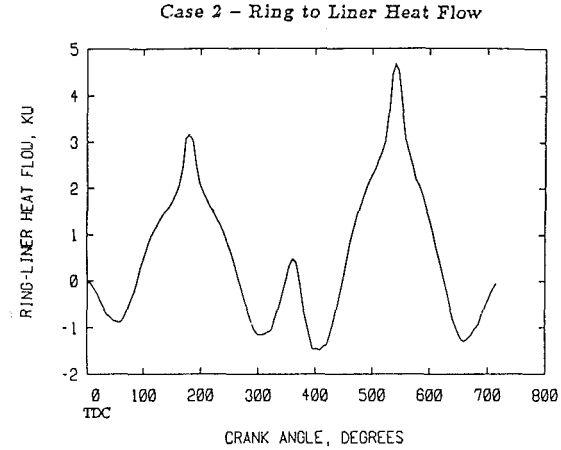

Fig. 20 Ring to liner heat flow calculated by the ring model for Case 2

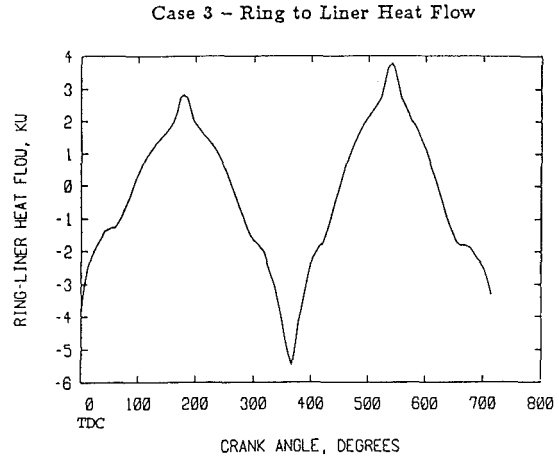

Fig. 21 Ring to liner heat flow calculated by the ring model for Case 3

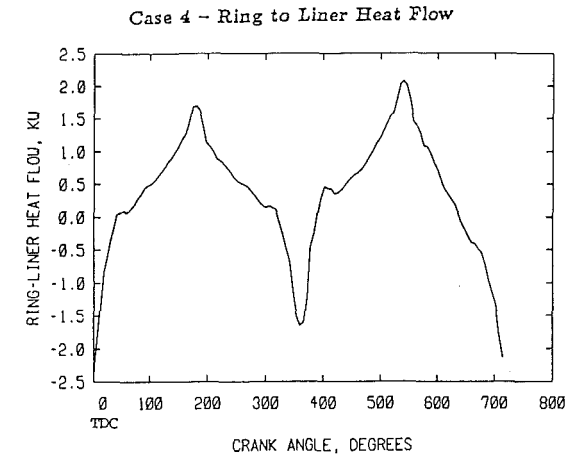

Fig. 22 Ring to liner heat flow calculated by the ring model for Case 4

that of the ring. This presents a major design problem especially in advanced engine designs utilizing high-temperature components such as in ceramic engines. The possibility of designing a lubricating scheme when the lubricant is exposed to high temperature levels over a large portion of the cycle is much more difficult than if the lubricant was only exposed over a small portion of the cycle around top ring reversal.

Another major design concern is the deposit rate of the lubricant. McGeehan [6] has shown that a 10°C change in lubricant temperature doubles the deposit rate. The maximum lubricant temperature locus shown in Figs. 14 and 15 indicates that as the cooling is decreased or insulation is increased, the maximum lubricant temperature experiences large temperature swings, which could have a major impact on lubricant deposits. The large temperature swings are due to the increased liner

surface temperature at top ring reversal. To reduce the liner temperatures, selective cooling strategies could be used that are tailored to this particular liner region.

The liner surface temperature distribution also points out an interesting conclusion regarding liner distortion. In the design of the sleeves for cooled liners, an attempt is made to minimize the thermal distortion. Previous liner design practice assumed that the liner temperature decreased monotonically from top to bottom. However, Fig. 6 indicates that the liner surface temperature decreases initially but then rises again around bottom ring reversal. The liner surface profile resulting from a nonlinear temperature distribution like Fig. 6 would be quite different from a monotonically decreasing distribution. The gradual rise in liner temperature near the bottom of the liner is due to a slower rate of axial heat transfer down the liner. It is expected that designs that promote axial liner heat conduction through the bottom of the liner will decrease the degree of liner thermal distortion.

The results show that because the top piston ring stays hot throughout most of the engine cycle, hot spots on the lubricant film are expected not only near the top ring reversal point but up and down the liner also, regardless of the liner temperature. This represents a major challenge to successfully lubricating engine systems utilizing advanced concepts, such as the application of low heat rejection materials.

Conclusions

The results of this study indicate that before the benefits of higher output diesel engines can be realized, significant technological breakthroughs must occur in piston ring/liner lubrication to handle the elevated temperatures encountered. Some of the more challenging findings of this report facing a designer are:

- The top ring and the oil film around it have major transient effects that must be accounted for in order to estimate the lubricant temperature properly.
- The maximum lubricant temperature occurs on the liner at top ring reversal but switches to the top ring surface as the piston moves toward bottom ring reversal, thereby maintaining the maximum oil film temperature at high levels throughout the cycle. The effect of the piston ring (top ring) in determining the maximum oil film temperature over a cycle varies with both the degree of cooling and the insulation configurations.
- The maximum oil film temperature can experience large swings depending on the degree of liner and head cooling and on the degree of insulation and these temperature swings could have a significant effect on the lubricant deposit rate.
- The liner surface temperature distribution for the standard cooled piston and liner, for example, decreases along the top half of the liner but increases again around bottom ring reversal. Because the temperature does not monotonically decrease from top to bottom, the liner sleeve thermal distortion will be nonuniform. This nonuniformity can be minimized by promoting better axial heat conduction through the cylinder liner.

Acknowledgments

This work is sponsored by the MIT Research Consortium on the Use of Ceramics in Internal Combustion Engines. Current or past members of this Consortium include: Caterpillar Inc., Cummins Engine Co., General Motors Corporation, John Deere, Kolbenschmidt, Rhone-Poulenc, TRW, U.S. Army/TACOM, and U.S. Department of Energy. Michael Boisclair's education during this research was supported by General Electric Co. The authors appreciate and acknowledge the funding and technical support of the sponsors.

References

1 National Research Council, "A Review of the State of the Art and Projected Technology of Low Heat Rejection Engines," National Academy Press, Washington, DC, 1987.

2 Kamo, R., Bryzik, W., and Glance, P., "Adiabatic Engine Trends—Worldwide," SAE Paper No. 870018, 1987.

3 Siegla, D. C., and Amann, C. A., "Exploratory Study of the Low-Heat-Rejection Diesel for Passenger Car Application," *SAE Transactions*, Vol. 93, 1984, pp. 259–283.

4 Sutor, P., and Bryzik, W., "Tribological Systems for High Temperature Diesel Engines," SAE Paper No. 870157, 1987.

5 Sutor, P., and Bryzik, W., "Development of Advanced High-Temperature Liquid Lubricants," SAE Paper No. 880015, 1988.

6 McGeehan, J. A., Fontana, B. J., and Kramer, D. J., "Effects of Piston Temperature and Fuel Sulfur in Diesel Engine Piston Deposits," SAE Paper No. 821216, 1982.

7 Ting, L. L., "Lubricated Piston Rings and Cylinder Bore Wear," *Wear Control Handbook*, ASME, New York, 1980, pp. 609–667.

8 Furuhama, S., "A Dynamic Theory of Piston Ring Lubrication," *JSME Bulletin*, Vol. 2, No. 7, 1957, pp. 423–428.

9 Woods, M. W., Glance, P., and Schwarz, E., "In-Cylinder Components for Higher Temperature Diesel," SAE Paper No. 870159, 1987.

10 Li, C.-H., "Piston Thermal Deformation and Friction Considerations," SAE Paper No. 820086, 1982.

11 Facon, F. J., "Temperature Distribution Measurements and Heat Flux Calculations in a Diesel Engine Piston," Department of Mechanical Engineering, Masters Thesis, MIT, Cambridge, MA, 1987.

12 Tade, T., and Furuhama, S., "On the Heat Flow From the Pistons in a Farm Gasoline Engine," *Bulletin of JSME*, Vol. 7, No. 28, 1964, pp. 784–791.

13 Morel, T., Keribar, R., Fort, E. F., and Blumbert, P. N., "Methods for Heat Transfer and Temperature Field Analysis of the Insulated Diesel, Phase II—Progress Report," Integral Technologies Incorporated report to NASA for U.S. Department of Energy under contract DEN 3-342, 1985.

14 Wong, V. W., Report to "MIT Research Consortium on the Use of Ceramics in Internal Combustion Engines," Oct. 1986.

15 Assanis, D. N., and Badillo, E., "Transient Analysis of Piston-Liner Heat Transfer in Low-Heat Rejection Diesel Engines," SAE Paper No. 880189, 1988.

16 Segerlind, L. J., *Applied Finite Element Analysis*, Wiley, New York, 1976.

17 Huebner, K. H., *The Finite Element Method for Engineers*, Wiley, New York, 1986.

18 Nurnukra, T., Yamamoto, A., and Seki, T., "A Consideration in Strength Evaluation Methodology for a Diagonally Split Connecting Rod," *Proceedings of Institute of Mechanical Engineers*, Paper No. C13/87, 1900, pp. 39–46.

19 Assanis, D. N., and Heywood, J. B., "Development and Use of a Computer Simulation of the Turbocompounded Diesel System for Engine Performance and Component Heat Transfer Studies," SAE Paper No. 860329, 1986.

20 Ingersoll, L. R., Ingersoll, A. C., and Zobel, O. J., *Heat Conduction With Engineering and Geological Applications*, McGraw-Hill, New York, 1948.

Long-Stroke Pielstick Engine Design Philosophy and Service Result Confirmation

J.-F. Chapuy
Technical Assistance and
Technical Support Sections Manager,
Licenses Division,
SEMT Pielstick,
St. Denis, France

Shipowners and diesel engine users are faced with changing fuel costs. The high price of fuel in recent years has pushed SEMT Pielstick to introduce recently a new version of its long-stroke PC engines. SEMT Pielstick worked on basic parameters of engines to reduce fuel consumption. Research was done on supercharging by adapting a new exhaust manifold, by pass arrangement and new turbo-blowers. The combustion chamber parameters have been thoroughly examined regarding firing pressure, stroke-to-bore ratio, and rotational speed. Reliability was checked by designing components of engines according to the state of art and the experience of SEMT Pielstick. The levels of stresses or temperatures were kept the same as for previous engines or even improved in order to give better reliability. This reliability has been confirmed by the results of the first long-stroke Pielstick engines put into service: the PC 20 L installed on the "Sovereign of the Sea" (RCCL) and the PC 40 L, installed on "New Hamanasu," "New Shirayuri," and "Muroto." The oldest of these has operated trouble-free for more than two years. The availability of engines is very good, and service results, such as wear of components, are even better than with the previous standard stroke engine.

Introduction

In recent years, the increasing proportion of fuel costs in operating expenses has led Diesel engine designers to make every effort to decrease the specific fuel consumption (SFC). One cannot escape from this, as SFC is given first consideration when users or shipbuilders make their choice for new engines.

The ability to burn low-quality fuel oils safely has also become a major design target. Such ability, as regards medium-speed engines, has been clearly demonstrated over the past few years. Fuel of decreasing quality has been utilized with no consequence as regards service results for our medium-speed engines.

Reduction of maintenance costs is also strongly requested by users. This can be achieved by increased reliability, one of our main goals during recent years, but before all by a reduction of the number of cylinders.

Another request, which is more and more frequent, is the ability to operate during long periods on heavy fuel at very low load.

Having all these considerations in mind, SEMT Pielstick has carried out over the last few years an extensive development program, in order to put on the market advanced engines that will meet market requirements for years to come. The most difficult task was obviously the reduction in SFC.

Contributed by the Internal Combustion Engine Division and presented at the Twelfth Annual Energy-Sources Technology Conference and Exhibition, Houston, Texas, January 22–25, 1989. Manuscript received by the Internal Combustion Engine Division August 1988. Paper No. 89-ICE-10.

I Basic Concepts Design

I.1 Supercharging Process

I.1.1 The use of our so-called MPC supercharging arrangement, based on a constant pressure piping, which receives the

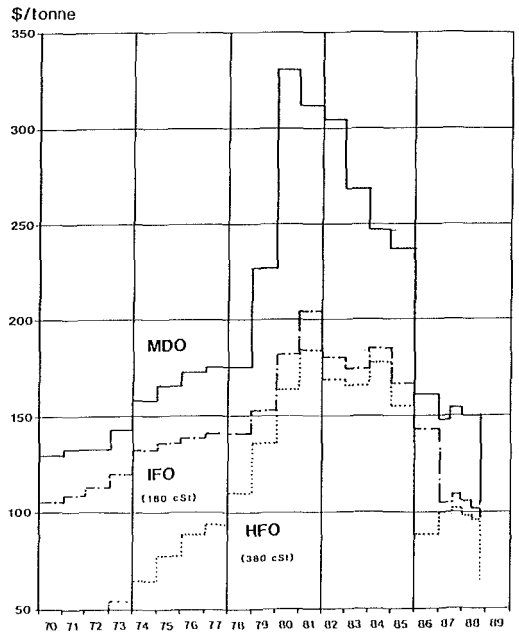

European fuel price evolution

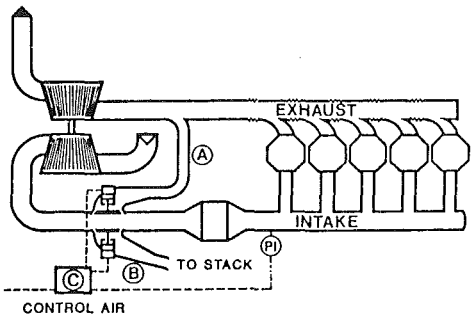

(A) Part-load "By-pass"
- Increases air excess
- Prevents surging

(B) "Waste gate" (open above 85 % MCR)
- Limits maximum pressure at full load
- Permits to optimize the engine at service rating

(C) Control panel

Fig. 1 Supercharging system

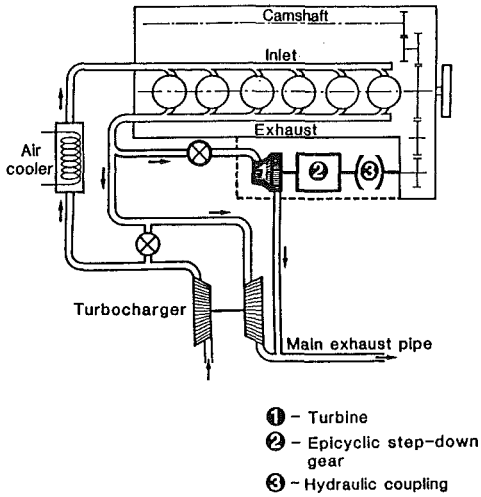

❶ - Turbine
❷ - Epicyclic step-down gear
❸ - Hydraulic coupling

Fig. 2 Recovery power turbine (RPT)

exhaust gases from all cylinders of the same bank through a pressure converter, has now become standard. The experience in service of this supercharging system applied for several years on previous PC engines has fully met expectations.

I.1.2 Advantages of the MPC system are complemented by a bypass arrangement incorporated in the turbocharging system (Fig. 1), which makes possible:

- increased excess air at part load;
- optimum adaptation for the turbocharger, with no risk of surging;
- adaptation of the turbocharger at service power, for the best performance, still permitting the use of the engine up to full power (engine operated at constant combustion pressure from optimized power to full power).

The operation of the two bypass valves A and B (A is opened at low load while B is opened at high load; both valves are closed at service power) is fully automatic, under fuel rack control.

I.1.3 Turbochargers are the latest type, B. B. C. series IV A with increased compression ratio and efficiency, incorporating uncooled casings.

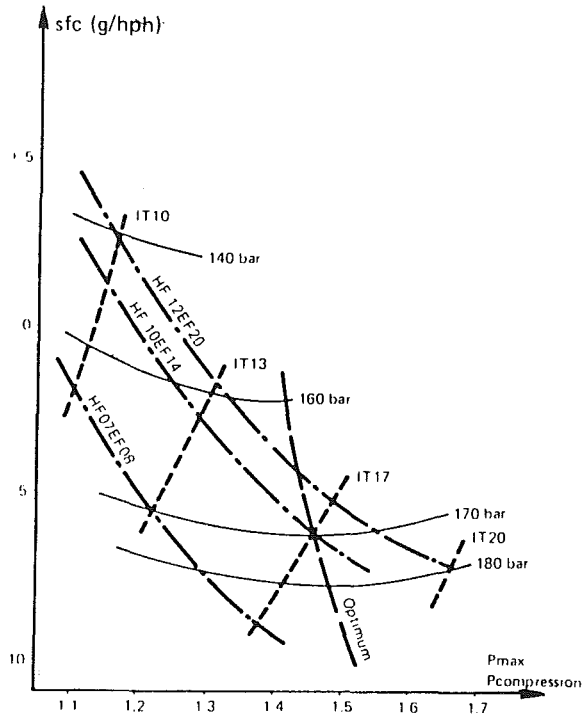

Fig. 3 Test engine 4 PC4V; $\epsilon = 15$; 1.500 hp/cyl.; 400 rpm

I.2 Recovery Power Turbine (RPT). Owing to the higher efficiency of the turbochargers, there is more air available and the pressure difference between air and gas is increased. Even with a low specific fuel consumption, the energy in the exhaust gases is more than required for the engine. It is possible to take advantage of this situation, in order to further reduce the SFC. The Recovery Power Turbine (RPT), mechanically connected to the engine, is an attractive solution (Fig. 2). The RPT does not work at part load (say below 75 percent of MCR) since the gas delivery valve at turbine inlet is closed. It is put into service at higher loads. Consequently, the turbocharger works in two different operating areas depending on engine loading:

- At part load, the air and gas pressures are at the higher level. This is similar to a special turbocharger adaptation for low output, with good efficiency and reduced SFC. In this operating range, a bypass P2-P4, as described earlier, is needed to avoid surging.
- At normal service load, the RPT is used, with two consequences: First, the power supplied by the turbine assists the main engine by feeding back mechanical energy. Second, the turbocharger works in the other range, with lower air and gas pressures, which permits one to reduce firing pressure and keep it at its normal level.

Fuel consumption is lower by 3 percent over the full range of power, i.e., 4 g/hph, and the air excess, when running at part load, is substantially increased.

I.3 Basic Combusion Chamber Parameters. Systematic investigations carried out on test engines have permitted an evaluation of what should be the basic engine parameters, in order to minimize SFC:

- Optimum firing pressure/compression pressure ratio; although it increases slightly with the firing pressure, this ratio is to be kept between 1.4 and 1.6 (Fig. 3).
- Efficiency increases together with the firing pressure and reaches its nearly optimum point when firing pressure is 170–180 bar (Fig. 4).

I.4 Cylinder Geometry—Stroke/Bore Ratio. Increasing

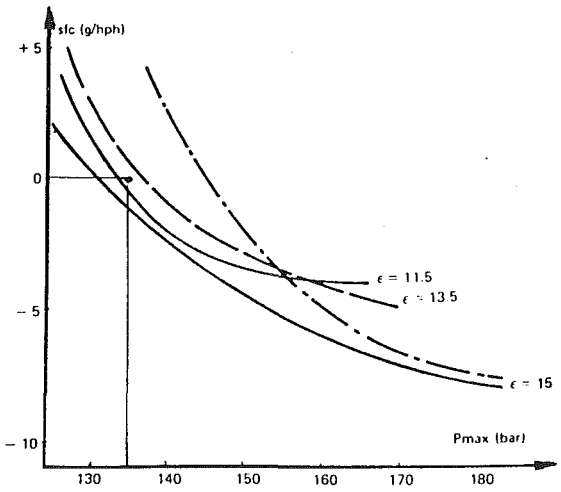

Fig. 4 Test engine 4 PC4 V SFC versus P_{max}; 1500 hp/cyl; 400 rpm

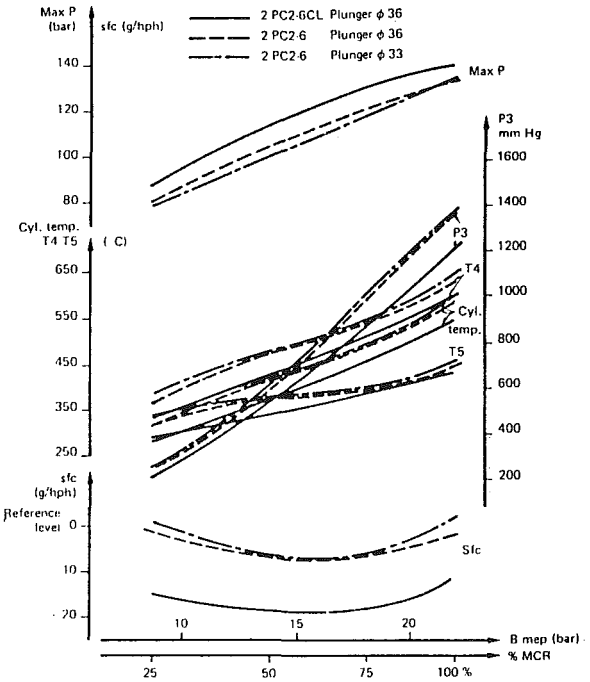

Fig. 5 Comparison between the PC2.6 and PC2.6 CL (propeller law)

the stroke/bore ratio of our engines, with a corresponding speed decrease to keep about the same piston speed, was considered several years ago. Based on the assumption that the injection time expressed in milliseconds and the combustion time are kept, there will be in the longer stroke engine running at a lower speed, less fuel consumed during the last part of the cycle, at constant temperature when its efficiency is not at its best. Therefore, one may expect better efficiency.

Successful tests were made on our PA 6 engine, normally rated at 1000 rpm, which were followed by the introduction in 1982 of a longer stroke version PA 6 CL with an SFC reduced by 9 g/Hph.

It was then decided to use a similar approach for the medium-speed engines. Our PC2.6 and PC 30 test engines, converted for that purpose, were used.

Figure 5 shows results recorded on the two-cylinder PC2.6 test engine (stroke/bore ratio increased from 1.15 to 1.37):

- SFC is reduced by 12 g/Hph with an increase in firing pressure of 7 bar. For the same firing pressure, the improvement would be 10 g/Hph or 7 percent.
- The exhaust temperature at cylinder outlet and turbine inlet is reduced by 40° C, which is consistent with the lower fuel consumption.

Table 1

	PC4-2V	PC 40L	EVOLUTION
CONN.ROD.BEAR.			
. Specific pres.(bar)	363	355	- 2 %
. Min. oil film thick-ness	10.0	14.8	+ 48 %
MAIN BEARING			
. Specific pres.(bar)	273	222	- 19 %
. Min. oil film thick-ness	9.2	15.7	+ 71 %

I.5 Main Design Features. The new PC types have in general inherited the traditional design features of their predecessors and it has been a rule to keep mechanical stresses at their safe level, whereas thermal stresses have been reduced for several components. Computer stress analysis has been used for important components, such as piston, connecting rod, and crankshaft.

The main deviations from components of previously developed engines or important design features adopted for the new engines are (Table 1):

- The crankcase remains a one-piece fabricated component carrying the crankshaft underslung from it. The crankcase for the in-line PC 20 L engine, nevertheless, is a casting similar to that for the PC2.6 engine introduced in 1980.
- The crankshaft is a one-piece forging with an important safety margin as regards mechanical stresses.
- Regarding bearing shells, the oil film thickness and specific pressure, systematically computed, are on the safe side. Oil film thickness is a general greater than values computed on previous engines.
- A three-piece construction has been retained for connecting rods, instead of the two-piece construction with oblique cut and serrations used earlier (Fig. 6). The reason for this change is double: reduced dismantling height of the pistons, and simplified machining.

Two-piece piston construction providing a large safety margin and good oil cooling has been retained for all engines. For the PC 20 and 40 engines, the piston has a steel crown and a light alloy skirt, incorporating stepped bosses and forced lubrication of the skirt (Fig. 7).

II Running Results

II.1 Test Bench Results. All expectations on fuel consumption have been met by the first industrial engines. The PC 20 showed a minimum specific fuel oil consumption of 130 g/Hph (see Fig. 8) while PC 40 showed a specific fuel oil consumption of 120 g/Hph (see Fig. 9).

So, the engines proved to be as economical as expected regarding fuel oil consumption. The efficiency of PC 20 is 48 percent and that of PC 40 is 51 percent.

II.2 Service Results. Another very important point for the shipowner is reliability. Are the new long-stroke PIELSTICK engines reliable?

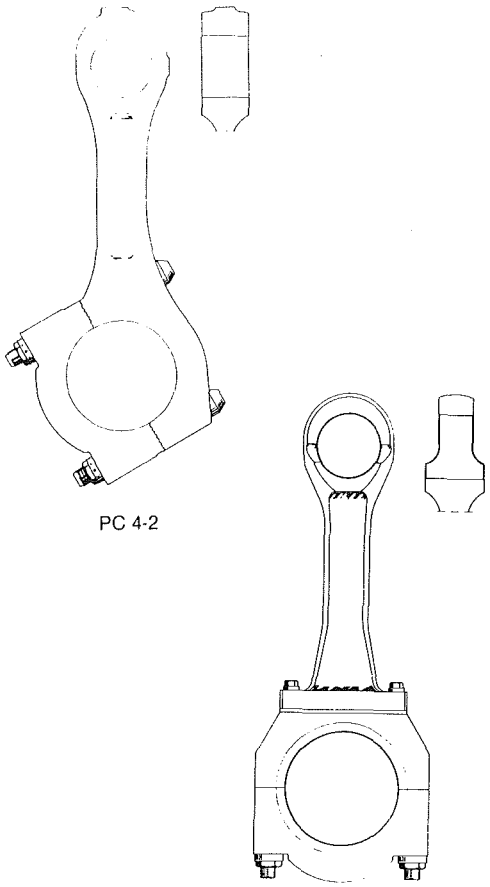

Fig. 6 Connecting Rods

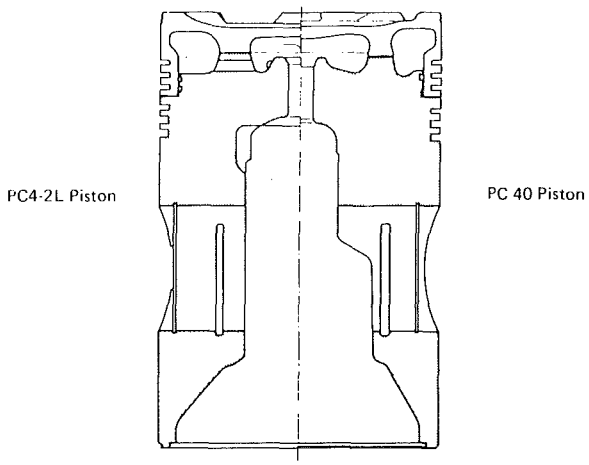

Fig. 7 Piston

(*A*) *PC 20.* There are four PC 20 9 cylinders in service on the cruise liner "Sovereign of the Seas" (RCCL) (Fig. 10). She is cruising in the Caribbean. She was commissioned at the end of 1987 and started her commercial life in the middle of January 1988.

At the time of printing of this article, it is too early to speak about results of wear and service results. In fact, the major point is that "Sovereign of the Seas" has never missed a call and was never delayed, neither at arrival nor at departure.

(*B*) *PC 40.* The first PC 40 L engines were manufactured

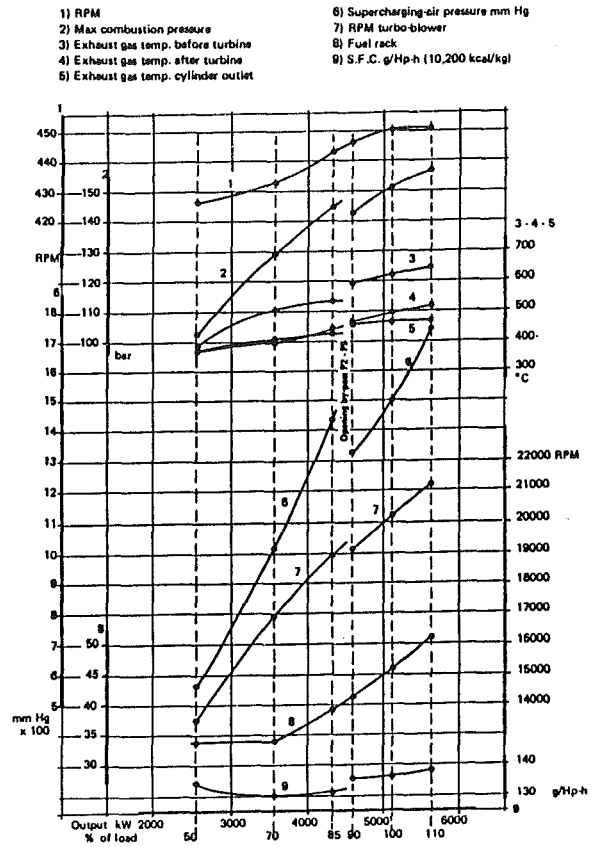

Fig. 8 PC 20 test bench results

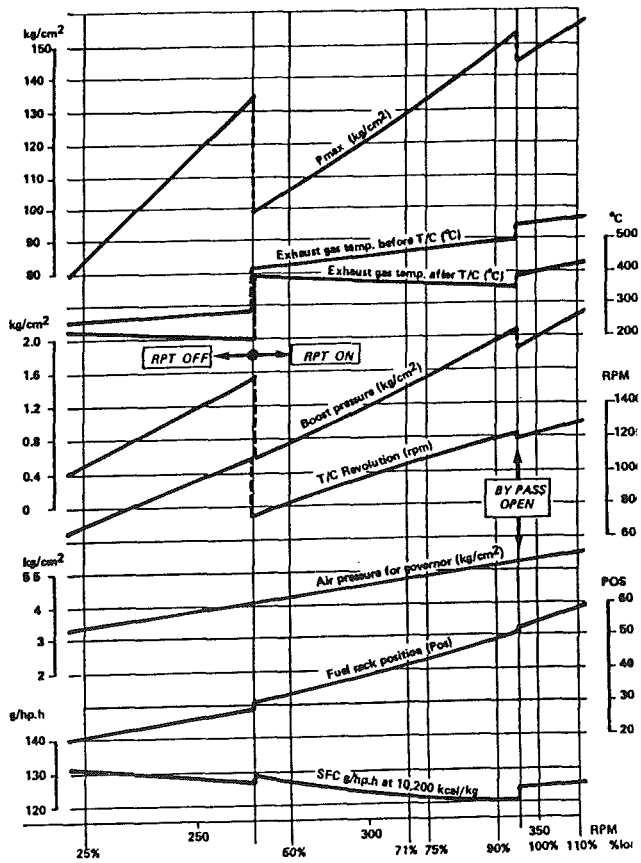

Fig. 9 PC 40 test bench results

Fig. 10 RCCL—Sovereign of the Seas

Fig. 11 New Hamanasu

by our Japanese licensees IHI and NKK and have been sailing regularly since entering service. As of Oct. 1, 1988, 19 PC 40 engines were on order or in service.

At the beginning of Jan. 1988, the first two ships completed about one year of service. These two ferries are the "New Hamanasu" (Fig. 11) and the "New Shirayuri." They are equipped with two 9 PC 40 L engines rated at 14,850 hp (1 650 hp/cyl). They were launched on Mar. 26, 1987 and on Apr. 24, 1987, respectively.

The vessels came to dry dock at the beginning of 1988 after nearly one year in service. The "New Shirayuri" ran for 4007 hours before she came to dry dock, and the "New Hamanasu," 4427 hours. During these dry docks, vital components including pistons were dismantled.

The following describes the service results during one year on the PC 40 L engines of both ships. First, the engines are run 18 hours a day 6 days a week between Niigata City and Otaru, for a total of 5500 hours a year. It should be noted that, out of 495 sailing days, there have been no stops at sea or delays due to engine trouble.

The engines proved also, when needed, to be able to recover delay due to bad weather. In fact, the shipowner is so satisfied by results that he intends to increase the speed of the ship to reduce the trip by one hour. He has also ordered a new ship equipped with a 2×8 PC 40 L engine.

The above results show a 100 percent availability of the ship and 100 percent availability for the engines, of course.

Another vessel has been overhauled after one year service. She is also a car-ferry called "Muroto." Dry dock was made in July 1988 and the engines, at that time, had accumulated 6150 hours. She is running two times 10 hours per day for a total of 6800 hours a year. The availability of the propulsion plant is 99.99 percent.

Fig. 12(*a*)

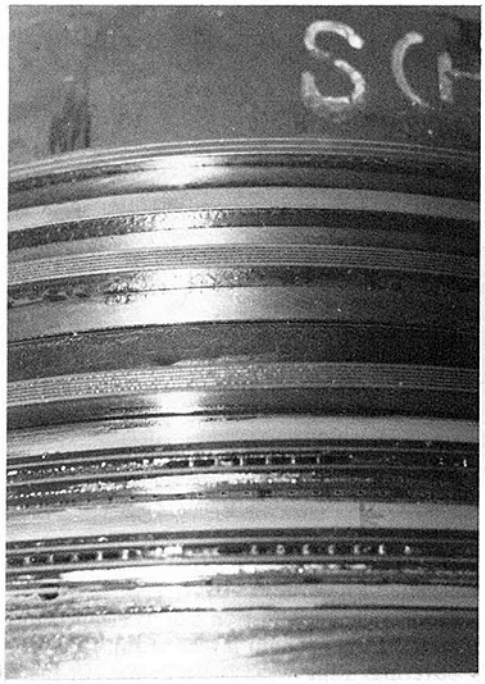

Fig. 12(*b*)

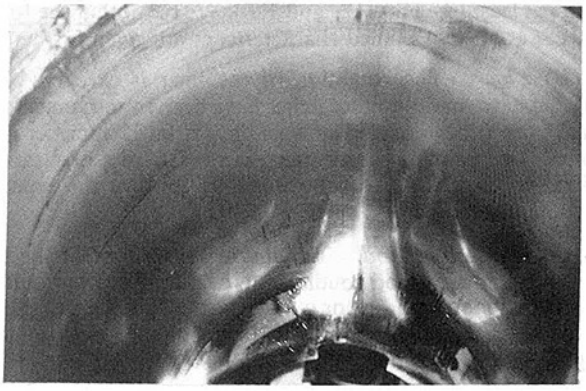

Fig. 13

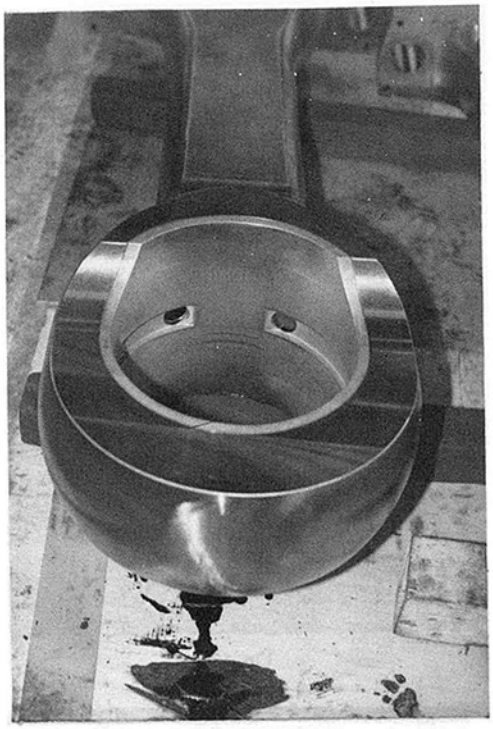

Fig. 14(a)

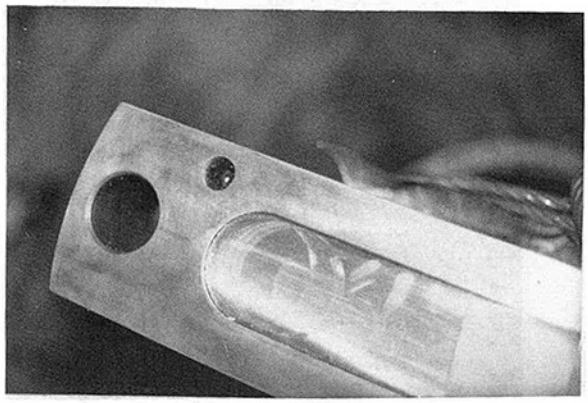

Fig. 14(b)

Fig. 15

Fig. 16

II.3 Inspection of Components

(*A*) *Piston.* The combustion side is clean; rings are free in the grooves; the chromium layers of top ring and scrapers are fully covering. Ring wear is negligible. In fact, no wear was measured; the rings were within machining tolerance. This means that MTBO can be maintained for 12,000 to 14,000 hours at least (see Figs. 12*a* and 12*b*). We recall that the fuel is 180 cSt at 50°C. Detailed characteristics are given further on.

(*B*) *Liner.* The condition of the liner is excellent (Fig. 13). No hard marks and scratches have been found; machining marks are still present. The wear rate is 0.012 mm per 1000 hours. This value is even better than the results of wear obtained on the PC 4. The above results confirm the expected lifetime of the liner.

(*c*) *Connecting Rod.* The marine three-part connecting rods were in very good condition. No fretting marks could be found on the rod landing or on the shims. The shells of the big end and the bush of the small end were in new condition (see Figs. 14*a* and 14*b*).

(*D*) *Cylinder Cover and Contents. Inlet Valves.* On three valves, we note some repeating impacts on the surface on the spindle seat (Fig. 15). The hypothesis is that deposits forming at particular load conditions are falling off the cylinder cover cavity and getting caught between stem and seat. Nevertheless, the conditions of all valves were excellent.

Exhaust Valves. Except for one valve cage, which had an imperfect tightness on the cover (we consider this as accidental), all valves were smooth and exempt from burning or wear (Fig. 16). These valves have NIMONIC spindles and water-cooled cages.

Injector. The injector is of monobloc type with hardened seat. The nozzles are checked now every 2000 hours, but due to the good results, they will be checked every 4000 hours.

(*E*) *Supercharging.* These engines are equipped with the RPT (Recovery Power Turbine). They are running on heavy fuel, as previously mentioned. The turboblower and the RPT are cleaned by a special carbon powder once a week. This system of MPC turbocharging with RPT has proved to be efficient and reliable.

II.4 Fuel Oil and Lube Oil

Heavy Fuel. As previously mentioned in this paper, these ships are running on heavy fuel of a relatively conventional quality. Below are listed some characteristics of the fuel:

Viscosity	$120 < V$	< 220 Cst
Specific gravity	$0.94 < SG$	< 0.98
Sulfur	$2 < S$	< 2.9 percent
Carbon Conradson	$9 <$ CCR	< 15 percent
Ash	$0.02 <$ Ash	< 0.05

This fuel is of a fairly good quality and is used for running at sea.

Starting, stopping, and maneuvering are made on a blended fuel, which is 90 cSt at 50°C (intermediate fuel).

Lube Oil. The oil used is an SAE 40 oil with 35 TBN. Evolution of characteristics of lube oil is such that everything is normal. Lube oil consumption is stabilized around 0.8 to 0.9 g/Hph.

Conclusions

As a general conclusion, results of the first long-stroke Pielstick engines in service confirm that these new long-stroke engines give full satisfaction, meet the requirements of a modern marine engine, and answer the expectations of the shipowner in terms of running cost, reliability, and availability.

We intend, in the future, to progress with the same validation obtained both on our test engine at SEMT Pielstick and from interpretation of service results.

Turbocharging Systems With Control Intervention for Medium Speed Four-Stroke Diesel Engines

E. Meier

J. Czerwinski

Asea Brown Boveri Ltd.,
Baden, Switzerland

The turbocharging systems of highly boosted four-stroke diesel engines (BMEP 25 bar/363 psi) have to cope with two basic problems: lack of air and compressor surge at reduced engine speed. In the case of medium speed engines for ship propulsion and stationary applications, the following three control interventions have proved to be successful solutions: (1) waste gating air or exhaust gas at full load and speed, (2) using a compounded or independent exhaust gas driven power turbine that can be shut off at part load and speed, and (3) blowing air from the compressor outlet to the turbine inlet through a controlled bypass. The effect of these control interventions on engine performance is shown by examples and analyzed by means of characteristic quantities for the efficiency of the turbocharging system and the engine. The definitions and meanings of these quantities are explained in the first part of the paper.

Introduction

Turbocharging medium-speed four-stroke diesel engines for very high BMEP requires not only high-efficiency turbochargers for high compressor pressure ratio, but suitable turbocharging systems with control interventions as well [1, 2]. For evaluation of different supercharging systems with regard to their thermodynamic quality, a number of characteristic quantities are found to be useful.

The deciding factor in a thermodynamic assessment of a supercharging system is of course the power output and specific fuel consumption that are attained within given limits of the mechanical and thermal load on the supercharged engine. But in order that the results of test-bed runs or computer simulations of the entire charging system may be better understood and possibilities for improvement recognized, it is appropriate to determine and evaluate the contribution of the gas exchange and supercharging process to the output and efficiency of the system as a whole separately from the contribution of the closed-cycle part of the engine. By dividing the overall system of the supercharged engine into appropriately limited subsystems, it becomes possible to define efficiencies and quality factors for the latter, and also a utilization factor for the exhaust-gas energy theoretically available. From the efficiencies of the subsystems it is also possible to calculate the overall efficiency of the whole system.

With the aid of the proposed characteristic quantities, some contemporary turbocharging systems are compared with one another. To illustrate individual results, flow diagrams are also used, which show the energy, the exergy, and the work potential of the fluid when isentropically expanded to ambient pressure.

Contributed by the Internal Combustion Engine Division and presented at the Twelfth Annual Energy-Sources Technology Conference and Exhibition, Houston, Texas, January 22–25, 1989. Manuscript received by the Internal Combustion Engine Division August 1988. Paper No. 89-ICE-12.

Scope and Subdivision of the Supercharging System

Every supercharging system, according to its two main tasks, can be subdivided into a compression subsystem on the air side and an expansion subsystem on the gas side (Fig. 1).

The task of the compression subsystem is, with a minimum of mechanical work, to draw in atmospheric air, and possibly gaseous fuel, to compress it, cool it, or heat it and then to feed it to the engine at any time at the right pressure and the right temperature.

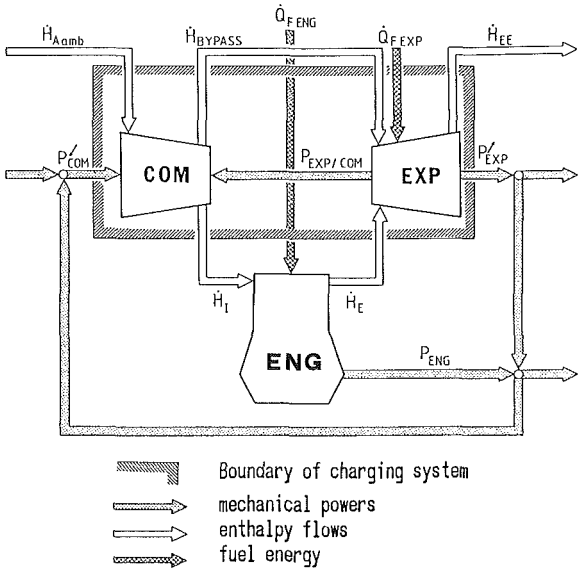

Fig. 1 Overall system of the turbocharged engine with energy flows of significance for evaluation; subsystems: engine (ENG) and supercharging system with compression (COM) and expansion (EXP)

The compression subsystem can, for instance, consist of the compressors of turbochargers, auxiliary blowers, and scavenging pumps driven by the main engine or externally, the air sides of pressure-wave chargers, tuned suction manifolds, resonance suction systems, filters, coolers, carburetors, waste gates, throttling devices, etc., and every possible arrangement of those components.

The expansion subsystem on the exhaust-gas side has to discharge the exhaust gases to the atmosphere and utilize as much of the work potential as possible, either to cover the demand for work of the compression subsystem or to supply mechanical work to the engine or some external load.

The expansion subsystem can, for instance, consist of turbines of turbochargers, power turbines driven by exhaust gas, the gas sides of pressure-wave chargers, combustion chambers, heat exchangers, blowoff and throttling devices, and all kinds of exhaust ducts in every imaginable arrangement.

Heat-recovery boilers and any subsequent steam cycles are not generally considered as belonging to the supercharged engine, but to its environment. If they exist, they may form part of the same power unit as the engine, but as a rule they are not usually from the same supplier. Distinguishing the supercharging system from subsequent systems for the utilization of waste heat means that the work potential of the exhaust gases that can be theoretically utilized in the expansion subsystem does not correspond to all the exergy, but only to the work that can be gained through isentropic expansion to ambient pressure.

In certain highly turbocharged four-stroke diesel engines air from the compressor outlet is bypassed directly to the turbine inlet. This bypass may contain not only a valve, but also a combustion chamber, a heat exchanger, or a blower. Thus, parallel to the engine, this bypass connects the compression subsystem directly with the expansion subsystem. The boundary between the two subsystems is defined by the point of maximum pressure in the bypass. Throttling elements, combustion chambers, and heat exchangers, if present, must therefore be considered as belonging to the expansion subsystem, any auxiliary blowers provided being part of the compression subsystem.

Mass and energy are exchanged between subsystems and also to and from the environment. The arrows in Fig. 1 illustrate the flows of energy, which are significant for the considerations that follow. The arrows indicate the normal direction of flow, for which a "plus" sign is used in the calculations.

Boundaries of the Supercharging System

In the region of the mechanical interconnection between the engine and the charging system, the boundary is quite clear. But it may be difficult to allocate the mechanical friction power between the engine and the charging system, as for instance in reciprocating scavenging pumps or crankcase scavenging pumps. For externally driven blowers the question arises as to what power shall be considered as being fed to the charging system from the environment: the mechanical shaft power of the blower, the electric motor power consumption, or even the mechanical power needed to generate the electric power. The answer to this question is left to the discretion of the person who carries out the comparison between different charging systems. For the comparison of the systems considered here it is immaterial.

In the region of the thermodynamic interconnection between the charging system and the engine, i.e., the region of gas exchange, several definitions of the boundaries are possible, resulting in different characteristic quantities used for evaluation.

At first sight it would appear obvious to define the boundary between the engine and its charging system by the states of the working fluid in the intake and in the exhaust manifold, i.e., immediately before and after the cylinders. In fact, turbocharger efficiency calculations are sometimes based on these gas states together with atmospheric conditions, especially for constant-pressure turbocharging. This definition of a turbocharger efficiency, however, does not do justice to either the engine or the turbocharger, as the outlet valves or ports and their control have a major influence on the work potential of the exhaust gases and must be adapted according to the type of exhaust manifolding.

Already in the first fundamental publications on the utilization of exhaust-gas energy by turbochargers [3–5] the outlet valves and ports were considered together with the exhaust ducts. Also in the latest investigations [6–9] the outlet valves and their control are treated together with the exhaust manifold as one thermodynamic system, which transmits the work potential of the exhaust gases with a specific efficiency from the interior of the engine cylinder to the turbine entry.

The inlet valves or ports and their control can also represent major features of the charging system, as for example in the Miller supercharging system [10, 11].

If one wishes to compare all known kinds of charging system with each other by means of uniformly defined quantities, the

Nomenclature

A = anergy
BMEP = brake mean effective pressure
BSFC = brake specific fuel consumption
c_m = mean piston velocity
E = exergy
H = enthalpy
$\dot{H}$ = enthalpy flow rate
h = specific enthalpy
h_u = net specific combustion heat of fuel (lower calorific value)
m = mass
$\dot{m}$ = mass flow rate
n = speed of rotation
P = power (output)
p = pressure (absolute)
Q = heat, quantity of heat
$\dot{Q}$ = heat flow rate
S = entropy
T = temperature (absolute)
V_{sw} = swept volume per cylinder
$\dot{V}$ = volume flow rate
W = work
x = proportion of stoichiometric combustion gas
z_A = utilization factor of the energy theoretically available in the exhaust gases
Δ = difference
ϵ = volumetric compression ratio of the engine
ζ = loss factor
η = efficiency
η_g = quality factor
$\bar{\kappa}$ = isentropic exponent (mean value during a change of state)
λ_s = ratio of the trapped mass of fresh charge to the total mass trapped in a cylinder
λ_z = ratio of the trapped mass of fresh charge to the total mass supplied to a cylinder for one working cycle
λ_v = ratio of the mass of air trapped in a cylinder to the stoichiometrically required mass of air for combustion of the fuel
Π_C = compressor pressure ratio

gas exchange valves and ports of the engine must be treated thermodynamically as part of the charging system. The boundary between the engine subsystem and the compression and expansion subsystems is thus defined by the cylinder pressure and the total enthalpy of the fluid flowing into or out of the cylinder.

Considering the boundary between the charging system and the environment, it is again less a question of principle than one of discretion by the user, which pressure drops may be attributed to the charging system and which may be regarded as given by the ambient conditions.

Overall Isentropic Efficiency of the Supercharging System

The symbols used in Fig. 1 to denote the three subsystems engine, compression, and expansion are meant to imply that every known charging system can be represented by an equivalent turbocharger, which may be equipped with a bypass from compressor outlet to turbine inlet, a combustion chamber, and a mechanical connection to the engine or to systems in the environment. Therefore, as a characteristic quantity for the whole charging system, it suggests itself to define an overall isentropic efficiency similar to the overall efficiency of a turbocharger.

The numerator of the overall isentropic efficiency represents energy usage, i.e., the combined energy needed for isentropic compression in the charging system together with all useful mechanical power supplied to the engine or some external load. The denominator, representing energy source, is calculated as the total of isentropic expansion power from exhaust gas and bypass air together with the mechanical power delivered by the engine or external drive power input.

For the normal directions of energy flow, as illustrated in Fig. 1 and for an engine with internal mixing, the overall isentropic efficiency of the charging system is defined by

$$\eta_{sCS} = \frac{\sum_{\text{all cyl.}} \dot{m}_I \, \Delta h_{s\ \text{com}}\left(\frac{p_{\text{cyl}}}{p_{\text{amb}}}, T_{\text{amb}}\right) + \dot{m}_{BY}\Delta h_{\text{com}}\left(\frac{p_{BY}}{p_{\text{amb}}}, T_{\text{amb}}\right) + P'_{\text{EXP}}}{\sum_{\text{all cyl.}} \dot{m}_E \, \Delta h_{s\ \text{exp}}\left(\frac{p_{\text{cyl}}}{p_{\text{amb}}}, T_{\text{cyl}}\right) + \dot{m}_{BY}\Delta h_{s\ \text{exp}}\left(\frac{p_{BY}}{p_{\text{amb}}}, T_{BY}\right) + P'_{\text{COM}}} \quad (1)$$

This equation defines the momentary value of η_{sCS} with respect to time. The mean value of one work cycle is obtained by integrating the terms in the numerator and denominator over a complete cycle. For engines with external fuel mixing, one must take into account the possible compression of the mixture or combustion gas from charging system inlet to the total pressure in the inlet valves or ports.

If there is a combustion chamber in the bypass or exhaust section, as in the Hyperbar system, then the increased work potential of the combustion chamber mass flow due to the supply of heat must be taken into account as energy supply in the denominator. If, on the other hand, the bypass air is heated in a heat exchanger by the exhaust gases, then this is a process within the expansion subsystem and as such does not appear explicitly in the calculation of the isentropic efficiency, although it naturally influences its value.

The subsystems compression and expansion can be subdivided into further subsystems, e.g., compressor, turbine, exhaust manifold, etc. Depending on the structure of the system, it is possible to calculate the overall isentropic efficiency of the supercharging system, from the efficiencies of these subsystems. Only the simplest case is illustrated here as example, in which a diesel engine is charged by a single-stage free-running turbocharger. In this case the overall isentropic efficiency of the charging system is given by

$$\eta_{sCS} = \eta_{sEM} \cdot \eta_{sT} \cdot \eta_{\text{mec}} \cdot \eta_{\text{vol}} \cdot \eta_{sC} \cdot \eta_{sAM} = \eta_{sEM} \cdot \eta_{TC} \cdot \eta_{sAM} \quad (2)$$

η_{sEM} is the transmission efficiency of the exhaust manifold including valves or ports. It corresponds to the "manifold efficiency" or "transmission efficiency" in [6, 8, 9] and is defined by

$$\eta_{sEM} = \dot{m}_{TI}\,\Delta h_{sT} \Big/ \sum_{\text{all cyl.}} \dot{m}_E \Delta h_{s\ \text{exp}}\left(\frac{p_{\text{cyl}}}{p_{\text{amb}}}, T_{\text{cyl}}\right) \quad (2a)$$

η_{sAM} is the transmission efficiency of the intake air manifold including in valves or ports and is defined by

$$\eta_{sAM} = \sum_{\text{all cyl.}} \dot{m}_I \Delta h_{s\ \text{com}}\left(\frac{p_{\text{cyl}}}{p_{\text{amb}}}, T_{\text{amb}}\right) \Big/ \dot{m}_{CO}\Delta h_{sC} \quad (2b)$$

η_{TC} is the overall or combined efficiency of the turbocharger, defined by

Nomenclature (cont.)

Subscripts

A	= air	EE	= exhaust-gas outlet from charging system	i	= indicated, internal
AC	= air cooler	eff	= effective	IO	= inlet opens
ac	= imaginary start of compression at BDC	EM	= exhaust manifold	IC	= inlet closes
AM	= air manifold	ENG	= engine, engine subsystem	id	= ideal
amb	= ambient	ENG-GE	= engine excluding gas exchange	max	= maximum
BDC	= bottom dead center	EO	= exhaust opens	mec	= mechanical
BY	= bypass	ex	= imaginary end of expansion at BDC	PT	= power turbine
C	= compressor	EXP	= expansion subsystem	S	= scavenging and charging air
c	= combustion	exp	= expansion	s	= isentropic
CO	= compressor outlet	EXP/COM	= from subsystem EXP to subsystem COM	T	= turbine
COM	= compression subsystem	F	= fuel	TC	= turbocharger
com	= compression	fr	= friction	th	= thermal
CS	= charging system	GE	= gas exchange	TI	= turbine inlet
cyl	= cylinder	I	= inlet	vol	= volumetric
E, e	= exhaust, exhaust gas energy			w	= walls of cylinder
EC	= exhaust closes			x	= arbitrary state
				$\swarrow$	= fed in
				$\nearrow$	= drawn out
				$\uparrow$	= increased

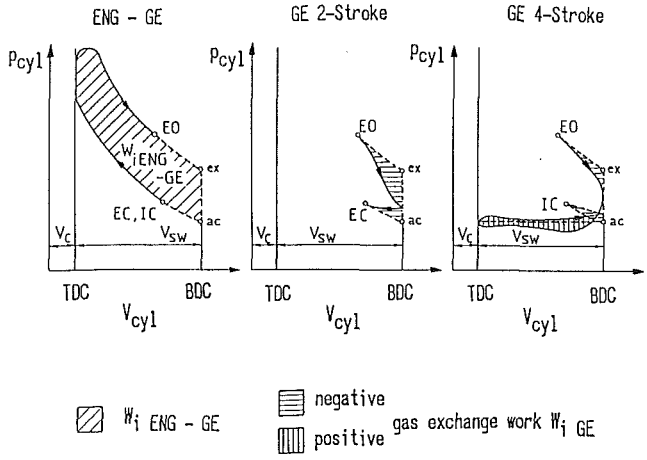

Fig. 2 Boundaries of the subsystems "engine excluding gas exchange" and "gas exchange"

$$\eta_{TC} = \eta_{sT} \cdot \eta_{\text{mec}} \cdot \eta_{\text{vol}} \cdot \eta_{sC} \qquad (2c)$$

In more complicated supercharging systems the relationship between the isentropic efficiency of the system as a whole and that of the subsystems is no longer quite so simple. Although the individual efficiencies naturally retain their significance, energy flow diagrams in such cases provide a clearer picture. Therefore, to compare the charging systems currently used on some highly turbocharged medium-speed four-stroke diesel engines, energy flow diagrams are also used in this paper.

The overall isentropic efficiency of the supercharging system, just like the overall efficiency of the turbocharger, is an important characteristic quantity for evaluation of the aerodynamic flow path quality of the particular system under given boundary conditions. Neither these efficiencies nor the energy flow diagrams say anything about the effect of the charging system on the engine. The direct influence on cylinder pressure during the gas exchange process, and thus on the indicated output and indicated efficiency of the engine, is important, though, for assessment of the charging system. Consequently, a further characteristic quantity is needed to evaluate this influence.

Reference Model for Gas-Exchange Process and Indicated Work of Gas Exchange

The direct influence of the charging system on the pressure variation in the engine cylinders during the gas-exchange process does not appear explicitly in the real engine cycle, but is contained in the indicated work. In order to determine it, the indicated work of gas exchange W_{iGE} must be defined. To do this the total engine cycle is divided into two subprocesses with respect to the variation of the cylinder pressure and the indicated work performed by the piston (Fig. 2), i.e., engine excluding gas exchange (ENG-GE), and gas-exchange process (GE). The heat transfer to the cylinder walls and the mechanical work of friction in the engine during the gas-exchange process are both regarded as belonging to the engine.

The boundary between the two subprocesses is given by an imaginary cylinder pressure curve, which also serves as reference model for the gas-exchange process and is defined by:

- Isentropic expansion from the real state *EO* (exhaust opens) to the imaginary state *ex* at bottom dead center BDC
- Imaginary gas-exchange process at BDC with the same quantities of trapped fresh charge and residual gas in the cylinder and the same scavenging mass flow as in the real gas-exchange process
- Isentropic compression from the imaginary state *ac* at BDC to the real state *IC* (inlet closes on four-stroke) or *EC* (exhaust closes on two-stroke engines)

In order to compare justly different gas-exchange processes, the states at the points *ac* and *ex* on the diagram should be completely independent from valve or port timing and valve lift curves. To satisfy this requirement, the process from *EO* to *ex* and from *ac* to *IC* or *EC* should not be calculated isentropically, but should be calculated step by step taking into account the heat exchange with the walls of the cylinder and regarding the latter as a closed system. But since the valve timing generally has very little influence on the isentropically calculated curves of state, it is permissible in practice to dispense with the tedious method of calculating in steps.

The difference between the indicated work of the real gas-exchange process and the reference model process as defined above is defined as the indicated work of gas exchange W_{iGE} (Fig. 2). For a four-stroke engine it may be either positive or negative. For a two-stroke engine it is always negative.

The gas exchange work that is positive for the engine is useful work, which is transferred from the charging system to the engine; that which is negative for the engine is an effort that has to be provided by the engine in favor of the charging system.

Model for the Ideal Charging System

For the gas exchange, which is part of the charging system, it is necessary to define a reference model in order that the direct influence on the indicated work of the engine could be explicitly determined. It is therefore a logical step also to define a comparative model for assessment of the entire charging system. Independent of the real process, it should describe an ideal charging system, but it must agree with the real process within the boundary conditions given by the engine and the environment. For the charging system of an engine in which the mixture is produced internally, the following idealized, comparative model should be suitable:

1 Same mass of residual gas, scavenging, combustion, and bypass air as in the real work process.

2 In the compression subsystem:

- Isentropic compression of the scavenging and combustion air from the ambient state to the imaginary initial pressure p_{ac} of compression in the cylinder.
- Cooling or heating of the scavenging and combustion air at the pressure p_{ac}, so that on mixing with the residual gas in the cylinder, the imaginary mean initial temperature T_{ac} of compression in the cylinder results.
- Isentropic compression of the bypass air from the ambient state to the maximum pressure in the bypass p_{BY} (generally higher than p_{ac}).

3 In the expansion subsystem:

- Isentropic expansion of the cylinder contents from the imaginary state at the end of expansion in the cylinder p_{ex}, T_{ex} to the pressure p_{ac}.
- Displacement of the combustion gas (not including residual gas) by the scavenging and combustion air at the pressure p_{ac}. The surplus scavenging air temperature is T_{ac}.
- Isentropic further expansion of the displaced combustion gas and the surplus scavenging air to atmospheric pressure.
- Isentropic expansion of the bypass air from the state p_{BY}, T_{BY} to atmospheric pressure.
- If heat from fuel is supplied to the subsystem directly, e.g., by a combustion chamber in the bypass airflow or in the exhaust flow from the engine, then the relevant isentropic expansion in the comparative model only applies as far as the pressure at which the heat was supplied. With correspondingly increased temperature and changed heat capacity and isentropic exponent the isentropic expansion is then continued to atmospheric pressure.

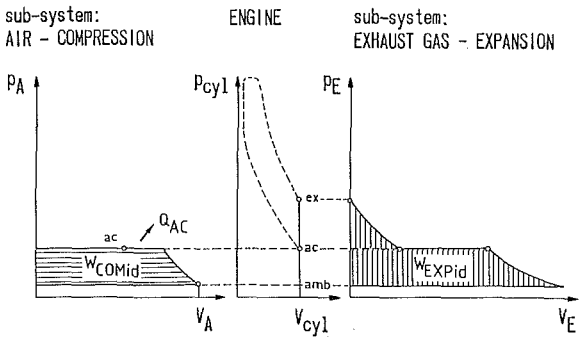

Fig. 3 Ideal supercharging and gas-exchange process

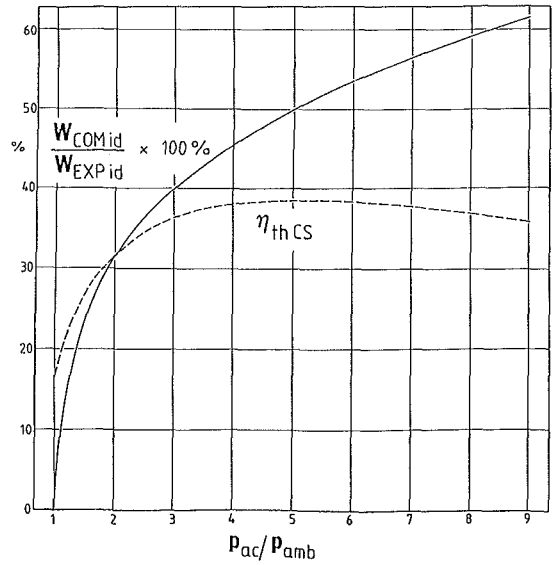

Fig. 4 Characteristic quantities of the ideal model process plotted against the compression pressure ratio

4 The surplus of the total ideal work $W'_{EXP\ id}$ performed by the gas in the expansion subsystem over the total ideal work $W'_{COM\ id}$ to be performed in the compression subsystem is entirely converted into useful mechanical energy and supplied to the engine or an outside load. The indicated work of gas exchange of the comparative process is, on the other hand, zero according to definition.

Figure 3 illustrates the changes in state and the expansion and compression work of this comparative process in the compression, engine, and expansion subsystems with the aid of pressure–volume diagrams, considering an example without bypass or combustion chamber. The formulae for calculating the changes in state and the compression and expansion work are listed in the Appendix.

As for the working cycles of engines and other thermal prime movers, a thermal efficiency can also be defined for the ideal charging system. The energy use in the numerator is the mechanical work that the ideal charging system could provide, i.e., the difference between the work of expansion and that of compression. The energy source in the denominator is the portion of the combustion heat of the fuel contained in the exhaust gas of the real engine excluding gas exchange, but including any heat that may be supplied directly to the expansion subsystem by a combustion chamber.

$$\eta_{thCS} = \frac{W'_{EXPid} - W'_{COMid}}{\zeta_{eENG-GE} \cdot Q'_{FENG} + Q'_{FEXP}} \tag{3}$$

$$\zeta_{e\ ENG-GE} = 1 - \eta_{i\ ENG-GE} - \zeta_{w\ cyl} \tag{4}$$

Here,

$W'_{EXP\ id}$ = work of expansion of the ideal charging system

$W'_{COM\ id}$ = work of compression of the ideal charging system (Fig. 3, calculation in the Appendix)

$\zeta_{e\ ENG-GE}$ = exhaust-gas energy from the real engine excluding gas exchange, referred to $Q_{F\ ENG}$

ζ_w = heat lost through the cylinder walls of the real engine, referred to $Q_{F\ ENG}$

$\eta_{i\ ENG-GE}$ = indicated efficiency of the real engine excluding gas exchange

$Q'_{F\ ENG}$ = fuel heat supplied to the engine (per cylinder and work cycle)

$Q'_{F\ EXP}$ = fuel heat supplied to the expansion subsystem (per cylinder and work cycle)

The exhaust-gas energy of the engine excluding gas exchange is $\zeta_{e\ ENG-GE} \cdot Q_{F\ ENG}$ is only dependent on the parameters specified for the high-pressure part of the engine's work cycle. For constant values of these parameters and the scavenging air surplus, the thermal efficiency of the comparative process for a charging system without bypass or combustion chamber is only a function of the pressure ratio p_{ac}/p_{amb}.

Figure 4 shows that the relationship between the thermal efficiency $\eta_{th\ CS}$ and the pressure ratio p_{ac}/p_{amb} is similar to that of an open cycle gas turbine.

If the charging system includes a bypass and/or combustion chamber, the similarity with the open gas-turbine cycle also prevails, of course, except that the number of determining variables in the comparative process is larger.

Quality Factor of the Charging System

As for the engine, it is also possible to define a quality factor for the real working process of the charging system as well as an internal efficiency. The quality factor is the ratio of the internal useful work of the real process to the useful work of the ideal model.

$$\eta_{gCS} = \frac{W_{i\ GE} + W'_{i\ EXP} - W'_{i\ COM}}{W'_{EXP\ id} - W'_{COM\ id}} \tag{5}$$

where

$W_{i\ GE}$ = work of gas exchange as per Fig. 2

$W'_{i\ EXP}$ = useful work performed by the expansion subsystem (e.g., internal useful work of the power turbine per cylinder and work cycle)

$W'_{i\ COM}$ = work supplied to the compression subsystem (e.g., internal work of an auxiliary blower or scavenging pump per cylinder and work cycle)

$W'_{EXP\ id}$ = work of expansion } of the ideal

$W'_{COM\ id}$ = work of compression } charging system

Whereas the thermal efficiency of the model process states how much useful work could be gained with the ideal charging system under the given boundary conditions, the quality factor is a quantity with which the thermodynamic quality of the actual charging system can be evaluated. It also enables different charging systems to be compared with one another, provided their boundary conditions do not differ appreciably.

Internal Efficiency of the Charging System and the Supercharged Engine

A thermodynamic characteristic quantity that, independent of the definition of an ideal charging system, enables different real charging systems to be compared and evaluated with one another under roughly equal boundary conditions, is the internal efficiency, i.e., the ratio of the internal useful work to the heat energy supplied.

$$\eta_{iCS} = \frac{W_{i\,GE} + W_{i\,EXP}' - W_{i\,COM}'}{\zeta_{e\,ENG-GE} \cdot Q_{F\,ENG}' + Q_{F\,EXP}'} \quad (6)$$

As for the engine, the internal efficiency of the charging system is the product of quality factor and thermal efficiency of the ideal charging system.

$$\eta_{i\,CS} = \eta_{g\,CS} \cdot \eta_{th\,CS} \quad (7)$$

Between the internal efficiencies of the charging system $\eta_{i\,CS}$ of the engine excluding gas exchange $\eta_{i\,ENG-GE}$ and the complete system of the charged engine $\eta_{i\,ENG}$, there is a very simple relationship

$$\eta_{i\,ENG} = \frac{W_{i\,ENG-GE} + W_{i\,GE} + W_{i\,EXP}' - W_{i\,COM}'}{Q_{F\,ENG}' + Q_{F\,EXP}'} \quad (8)$$

$$\eta_{i\,ENG} = \frac{\eta_{i\,ENG-GE} \cdot Q_{F\,ENG}' + \eta_{i\,CS}(\zeta_{e\,ENG-GE} \cdot Q_{F\,ENG}' + Q_{F\,EXP}')}{Q_{F\,ENG}' + Q_{F\,EXP}'} \quad (9)$$

$$\eta_{i\,ENG} = \left[\eta_{i\,ENG-GE} + \eta_{i\,CS}\left(\zeta_{e\,ENG-GE} + \frac{Q_{F\,EXP}'}{Q_{F\,ENG}'}\right)\right] \cdot \frac{1}{1 + \frac{Q_{F\,EXP}'}{Q_{F\,ENG}'}} \quad (10)$$

For the charging system without any direct supply of fuel heat, i.e., in by far the majority of cases, equation (10) can be simplified to

$$\eta_{i\,ENG} = \eta_{i\,ENG-GE} + \eta_{iCS} \cdot \zeta_{e\,ENG-GE} \quad (11)$$

$$\zeta_{e\,ENG-GE} = 1 - \eta_{i\,ENG-GE} - \zeta_{w\,cyl} \quad (12)$$

where ζ_w is the heat lost through the cylinder walls, referred to $Q_{F\,ENG}$.

The separate determination of the mechanical friction work in the charging system and the engine is hardly feasible in practice, since the friction work in the engine would have to be split between the high-pressure part and the gas-exchange part of the work process, and also the work to overcome friction in built-on scavenging pumps and power turbines would have to be determined separately. Therefore in most cases the mechanical friction work will be determined for the whole system and with it the mechanical and effective efficiency of the supercharged engine will be calculated.

Utilization Factor of the Energy Theoretically Available in the Exhaust Gases

The overall isentropic efficiency of the charging system is a measure of its aerodynamic flow path quality without referring to the effects on the engine. The thermal efficiency of the ideal charging system, as well as the quality factor and internal efficiency of the real charging system, are a measure of the direct influence on the indicated efficiency of the engine, but with them it is not possible to recognize how well the energy theoretically available in the exhaust gases is utilized for the primary purpose of supercharging: compressing the air. Hence, a further characteristic quantity is needed in order to judge how well a charging system utilizes the energy theoretically available in the exhaust gases. We may regard as useful work not only the coverage of the minimum work needed for compression of the air, but also the mechanical work in the form of gas exchange and power turbine work in favor of the engine respectively an external load. Since in this case we are dealing with theoretical work of an ideal charging system, but in the other case with real useful work, the characteristic quantity will not be referred to as efficiency, but utilization factor. The utilization factor of the energy theoretically available in the exhaust gases is therefore defined as follows:

$$z_A = \frac{W_{COM\,id}' + W_{i\,GE} + W_{i\,EXP}' - W_{i\,COM}'}{W_{EXP\,id}'} \quad (13)$$

This utilization factor can quite simply be referred back to the ratio of the work of compression to the work of expansion (Fig. 4) and the quality factor

$$z_A = \frac{W_{COM\,id}'}{W_{EXP\,id}'} + \eta_{g\,CS}\left(1 - \frac{W_{COM\,id}'}{W_{EXP\,id}'}\right) \quad (14)$$

Just as the overall isentropic efficiency can be resolved into the transmission efficiencies of the valves, ports, and ducts and into isentropic efficiencies of compressors and turbines (equations (2)–(2*c*)), it is also possible to break down the utilization factor of the energy theoretically available in the exhaust gases into utilization factors and efficiencies of subsystems. But then the indicated work of gas exchange must be divided into a component from the compression subsystem and one from the expansion subsystem. It is then possible to formulate a utilization factor of the energy theoretically available in the exhaust gases for the outlet valves or ports and exhaust ducts to the turbocharger turbine, in order that different exhaust systems, such as pulse, pulse converter, and constant-pressure exhaust systems may be compared with one another. For charging systems with branched mass flows, e.g., where there is a power turbine parallel to the turbocharger, a waste gate or a bypass, the relationship between the characteristic quantities of the subsystems and the whole charging system becomes complicated. In such cases it would probably be more expedient to evaluate only the system as a whole with the aid of the characteristics so far defined, but to illustrate the losses of work potential of the fluid within the charging system by means of flow diagrams.

Flow Diagrams of Energy, Exergy, and Isentropic Work Potential

Energy flow diagrams (also known as Sankey diagrams) are a known means of illustrating the transmission, utilization, devaluation, and losses of energy in any kind of installation, including charging systems. For a thermodynamic analysis to be possible, not only must the energy flows be represented by bars, the width of which is proportional to the respective amount of energy; it is also necessary to represent the exergy and anergy flows and, in the case of charging systems, the work potential by isentropic expansion to ambient pressure. When plotting a Sankey diagram, it is usual to proceed in three stages, as follows:

1 Establishment of the energy balance of the subsystems and the whole system (1st law)

2 Dividing the amounts of energy into exergy and anergy (2nd law)

3 Dividing the exergy into mechanical work or work potential for isentropic expansion to ambient pressure (the system is only in equilibrium with the ambient pressure) and remaining exergy, available outside the system for the utilization of waste heat.

The main equations of this analysis are given in the Appendix. In the examples that follow it is assumed that zero enthalpy occurs at the absolute temperature zero. All amounts of energy are related to the lower calorific value of the fuel, in order to obtain relative values that are comparable with the definitions of efficiency usual in engine building. The changes of state within the engine and the dissipation or possibly utilization of the energy in the exhaust gas and cooling water

outside the charging system are not plotted. Air intake filters and silencers are not treated separately, but as integral parts of the compressor.

Comparing Turbocharging Systems Employed on Modern Medium-Speed Four-Stroke Diesel Engines

With the aid of a model engine (for data see Appendix) the following charging systems were compared with one another, using a computer simulation program (12, 13)[1] developed and perfected in the course of many years at Asea Brown Boveri:

- Constant-pressure charging with free-running turbocharger without any ancillaries (*TC* alone)
- Constant-pressure charging with free-running turbocharger and waste gate (*WG*)
- Constant-pressure charging with free-running turbocharger and disconnectable power turbine parallel to the turbocharger turbine (*PT*)
- Ditto with bypass from the compressor outlet to the exhaust-gas receiver when the inlet to the power turbine is closed (*PT* + *BY*)
- Ditto with increased turbocharger efficiency (*PT* + *BY* + η_{TC}↑)

For all charging systems propeller operation is considered with the same full-load output and engine speed. All charging systems are dimensioned for the same charge-air state at the full-load operating point. Since in all examples the compression ratio, the valve timings, and the state of the charge air are the same, practically the same maximum pressure of combustion is obtained at full load.

Power Turbine, Waste Gate, and Turbocharger Alone. The comparison of these charging systems is illustrated with the aid of the most important engine performance data usually employed for comparisons; see Fig. 5 above. The gas inlet to the power turbine is open from full load down to 70 percent engine output, is gradually closed from 70 to 60 percent engine output in order to prevent a sudden rise in pressure, and remains closed in the part-load region below 60 percent output. The waste gate is gradually closed between full load and 80 percent engine output and remains closed at lower part loads. Since the proportion of the mass flow for the power turbine and the waste gate was made the same, i.e., 7.3 percent of the total mass flow, the operating values at part loads below 60 percent output are equal, since the dimensioning of the turbocharger is exactly the same.

As was to be expected, the system with power turbine yields the best performance data throughout the entire load range, while the system with turbocharger alone is definitely inferior at part load to the two other systems because the turbocharger turbine has a larger flow cross section, with the result that the charging pressure is lower at part load.

The characteristic quantities of the charging systems illustrated in Fig. 5 below will now help to understand the different performance data of the engine.

The efficiency of the turbocharger η_{TC} is not equal in all three cases because the operating points in the characteristic fields of the compressor and turbine are different and therefore the matching of the turbocharger has to be partly different.

Much greater differences can be seen in the overall isentropic efficiency of the charging system $\eta_{s\,CS}$. For the system with turbocharger without ancillaries a maximum is obtained at about 80 percent engine output. At higher loads the decreasing turbocharger efficiency dominates, while with decreasing load the steep drop is caused by the high transmission losses of the constant-pressure exhaust system at low turbine pressure ratios. For the other two charging systems $\eta_{s\,CS}$ is higher in the entire part-load range up to about 90 percent full load, because the turbine pressure ratio is higher and therefore the transmission losses between engine and turbine are less. That between 90 and 100 percent engine output the system with power turbine has the best efficiency, that with waste gate the worst, is not really astonishing. What is surprising, though, is that the system with the waste gate has the best isentropic system efficiency between 60 and 90 percent of the full-load output, because the waste gate is then closed, but the power turbine is open. Nevertheless, even in this load range the system with power turbine is still the best for the engine, as can be seen in the internal efficiency of the charging system $\eta_{i\,CS}$.

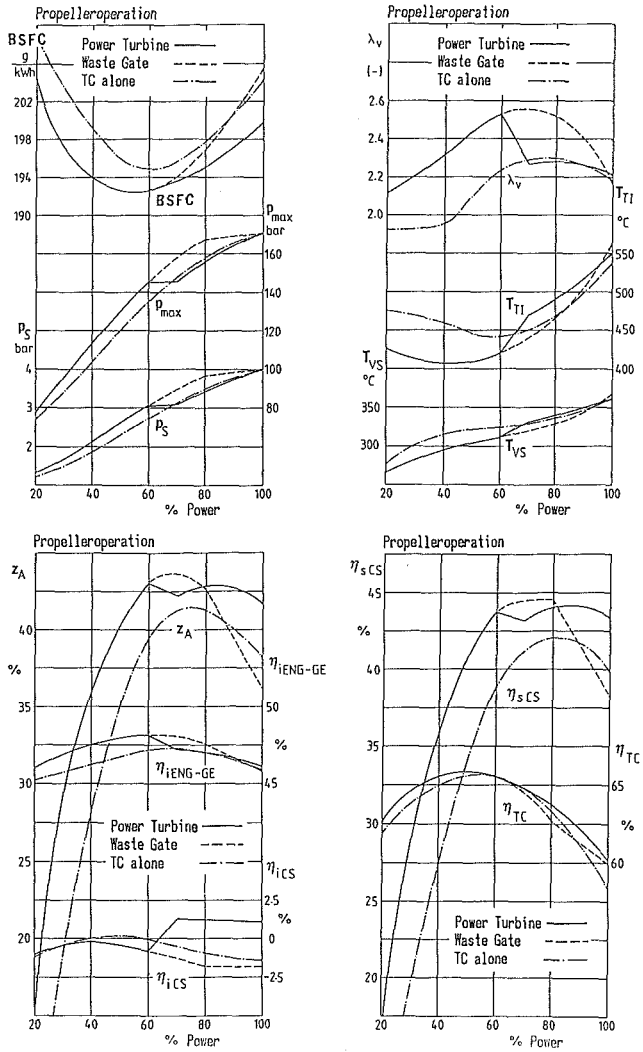

Fig. 5 Comparing turbocharging systems: turbocharger with power turbine in parallel; turbocharger with waste gate; turbocharger alone

The utilization factor Z_A for the energy available in the exhaust gases in the ideal charging system has, in the examples considered here, the same character as the isentropic efficiency of the charging system. This can be attributed, on the one hand, to the control of the gas exchange process being the same for all three systems and to the useful work (gas exchange and power turbine) being small in comparison to the isentropic work of compression.

The internal efficiency of the charging system $\eta_{i\,CS}$ shows what useful work the charging system supplies directly, i.e., what it does over and above its primary task of compressing the air charge. For many readers this may appear to be disappointingly little, since $\eta_{i\,CS}$ is nearly always negative, except

[1]The authors would like to thank Dr. Tomas Bulaty for the necessary additional programming.

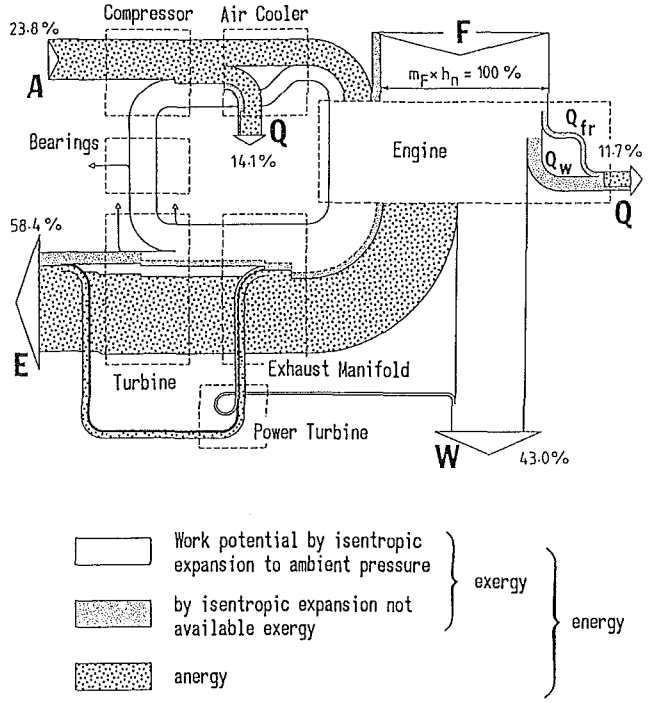

Fig. 6 Energy flow diagram of turbocharging system with power turbine: full load

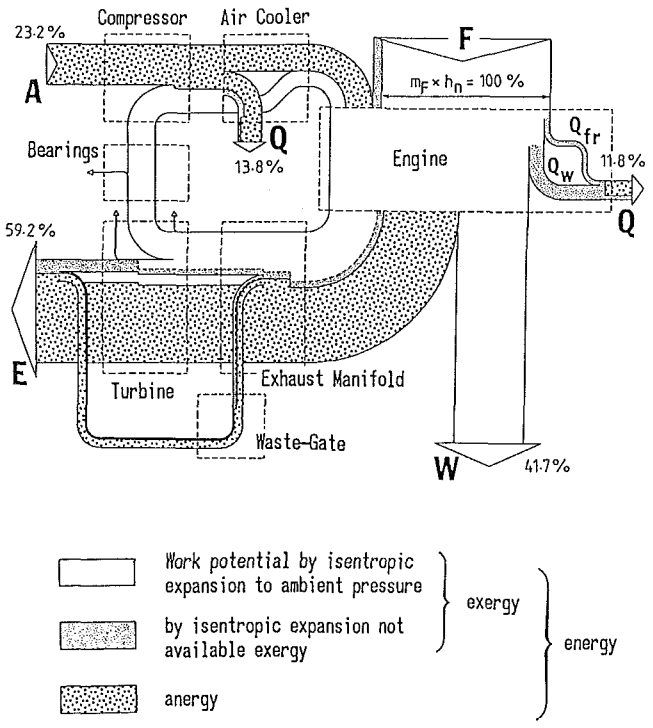

Fig. 7 Energy flow diagram of turbocharging system with waste gate: full load

when the power turbine is switched on. This means that the engine has to supply useful work to the charging system in the form of negative gas-exchange work. In the naturally aspirated engine the gas-exchange work is also negative, but with a larger absolute amount.

The indirect influence of charging on the internal efficiency of the charged engine is shown by the internal efficiency of the engine excluding gas exchange $\eta_{i\,\mathrm{ENG-GE}}$. At full load this is almost the same for all three systems since the same state of the charge air was assumed. At part load the systems with

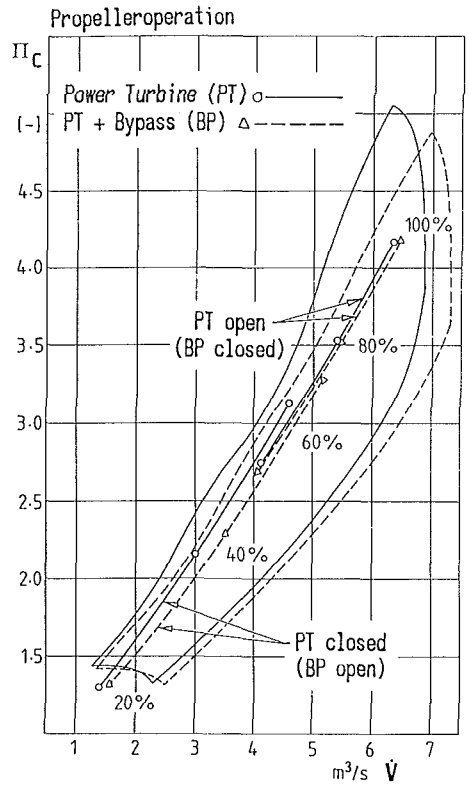

Fig. 8 Influence of power turbine and bypass on the operating curve in the compressor map

power turbine or waste gate result in a better efficiency for the engine less gas exchange because the charging pressure and with it the air–fuel ratio and maximum pressure of combustion are increased.

The different actions of the power turbine and waste gate at full load are illustrated by the Sankey diagrams in Figs. 6 and 7. In both cases part of the mass flow in the exhaust duct is diverted with corresponding components of work potential by isentropic expansion to ambient pressure, exergy, and anergy. In the power turbine the greater part of the work potential is converted into useful mechanical work and added to the useful work of the engine. In the waste gate the isentropic work potential is converted into residual exergy and anergy. In both cases residual exergy and anergy are returned to the flow of exhaust gas following the turbine, so that the gap in the diagrammatic representation of the energy flow is closed again.

Power Turbine With Bypass and Increased Turbocharger Efficiency. By closing the inlet to the power turbine at part load the operating curve in the compressor characteristic is displaced in the direction of the surge limit. To prevent surging at part load, a relatively large margin from the surge limit must be observed at full load, so that full advantage cannot be taken of the best compressor efficiency. If, when the power turbine is shut off, a bypass is opened between the compressor outlet and the inlet to the turbocharger turbine, the operating curve in the compressor characteristic shifts away from the surge limit. The compressor can now be optimally matched throughout the entire working range (Fig. 8). Under the conditions prevailing the highly charged four-stroke diesel engines and high turbocharger efficiencies, a bypass is not only a means of avoiding surging but also of increasing the charging pressure [1, 2]. Figure 9 shows what improvements are achieved when the charging system with power turbine is augmented by a bypass from the compressor outlet to the turbine inlet. Al-

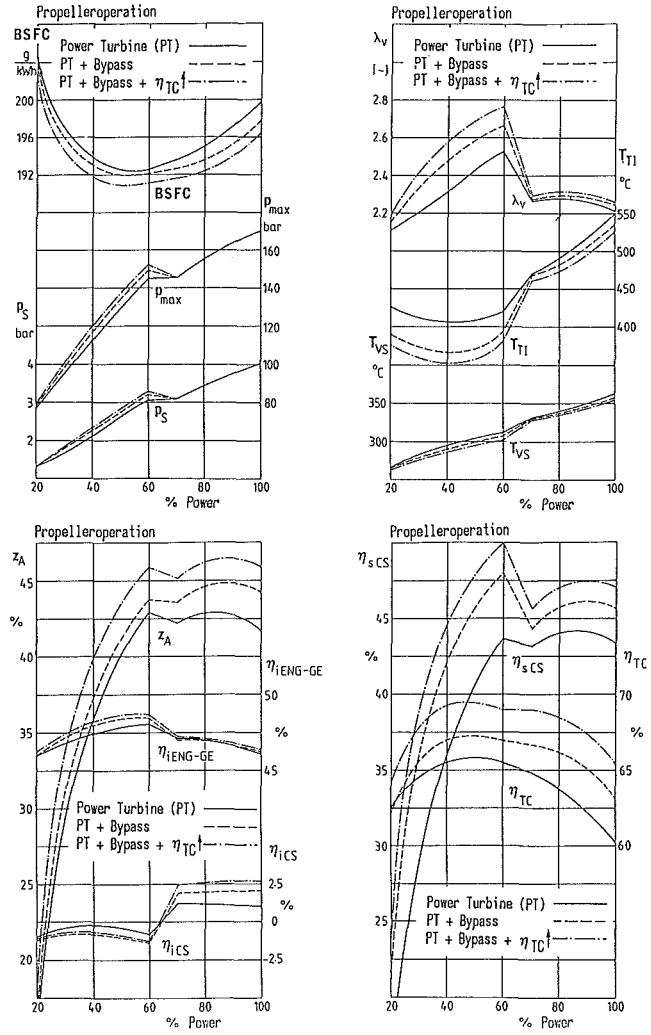

Fig. 9 Comparing turbocharging systems: turbocharger with power turbine in parallel; turbocharger with power turbine and bypass; turbocharger with increased efficiency, power turbine, and bypass

though compression and expansion of the bypass air involve loss of energy—the internal efficiency of the charging system $\eta_{i\,CS}$ is lowered—the isentropic efficiency $\eta_{s\,CS}$ and the utilization factor of the energy available in the exhaust gas in the ideal charging system, Z_A, as well as the indicated efficiency of the engine excluding gas exchange $\eta_{i\,ENG-GE}$ with open bypass are higher. The reasons for this are, on the side of the charging system, the better utilization of the energy in the exhaust gases owing to the higher pressure ratio of the turbine and, on the side of the engine, the higher charging pressure.

If turbochargers with a higher overall efficiency are available, then the proportion of the exhaust-gas mass flow that can be diverted to the power turbine can be increased. Owing to the bypass, the compressor can still be optimally matched,so that a notable improvement of all charging characteristic quantities and engine performance data can be achieved. In Fig. 9 it was assumed that the efficiency of the turbocharger could be raised by 2.2 points. If the bypass alone enables the mass flow through the power turbine to be increased from 7.3 to 9.1 percent because the operating curve in the compressor characteristic is more favorably situated, then the higher turbocharger efficiency will permit a further increase in the mass flow through the power turbine to 10.4 percent.

The effect of the bypass on the flows of energy, exergy, and work potential with isentropic expansion to ambient pressure is illustrated in Fig. 10.

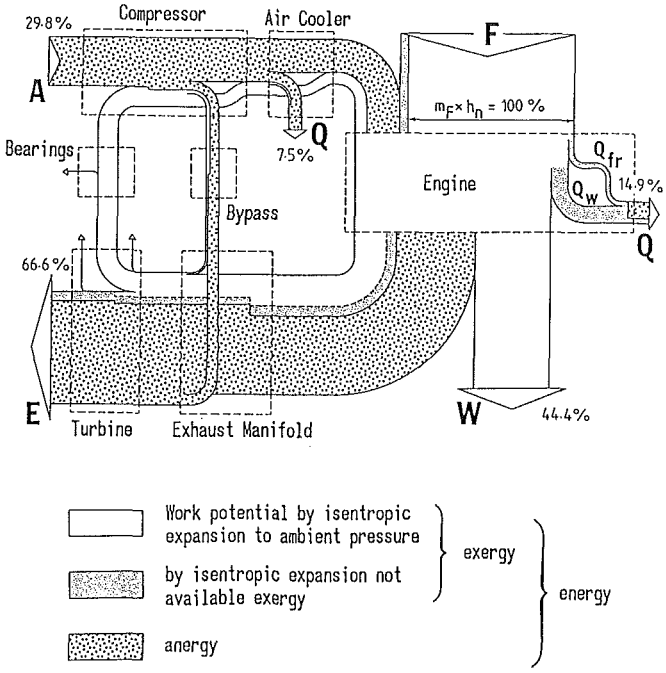

Fig. 10 Energy flow diagram of turbocharging system with power turbine and bypass: 40 percent load, propeller operation, power turbine shutoff

Conclusions

Based on various approaches expressed in the literature, characteristic quantities are proposed that permit an objective comparison and evaluation of different supercharging systems and make their thermodynamic analysis easier. The significance of these characteristic quantities is that they provide uniformly applicable criteria for the thermodynamic assessment of any supercharging system and that they are compatible with the conventional definitions of engine and turbocharger efficiencies.

As a means of illustrating the utilization of the energy in supercharging systems in a clear manner, flow diagrams can be used for the energy, exergy, and work potential by isentropic expansion to ambient pressure.

The examples analyzed with the aid of the abovementioned characteristic quantities and flow diagrams prove that turbocharging systems with constant-pressure exhaust manifolds need control interventions for highly turbocharged medium-speed four-stroke diesel engines driving propellers. They show also that power turbines or exhaust-gas waste gates are suitable means for controlling boost pressure and improving engine performance. A bypass from compressor outlet to turbine inlet of the turbocharger can further improve engine performance, especially if a turbocharger with a higher efficiency is used and the portion of the exhaust gas diverted to the power turbine is increased.

References

1 Meier, E., "Part-Load Operation of Highly Turbocharged Four-Stroke Marine Diesel Engines," CIMAC-Congress Paris, 1983, Paper No. D14.2.

2 Neth, P., and Streuli, A., "Turbocharging and Its Potential for Improving the Performance of Diesel Engines," CIMAC-Congress Warsaw, 1987, Paper. No. D39.

3 Jenny, E., "Berechnungen und Modellversuche über Druckwellen grosser Amplituden in Auspuff-Leitungen," Dissertation ETH Zürich, 1949.

4 Jenny, E., "The Utilization of Exhaust-Gas Energy in the Supercharging of the Four-Stroke Diesel Engine," *Brown Boveri Review*, Vol. 37, No. 11, 1950, pp. 433-447.

5 Baumann, G., "Increasing the Output of Two-Stroke Engines by Means of Exhaust-Gas Turbochargers," *Brown Boveri Review*, Vol. 41, No. 8, 1954, pp. 287-311.

6 Watson, N., and Oldfield, S. G., "The Influence of Exhaust Valve and

Port Design on Energy Transfer to the Turbocharger Turbine," CIMAC-Congress, Paris, 1983, Paper No. D8.4.

7 Winterbone, D. E., Nichols, J. R., and Alexander, G. I., "The Efficiency of Engine Manifolds—Application of Exergy to Unsteady Flow," *Proc. IAVD-Congress on Vehicle Design and Components*, Geneva, 1984, Vol. 4, Conference C.

8 Winterbone, D. E., Nichols, J. R., and Alexander, G. I., "Efficiency of the Manifolds of Turbocharged Engines," *Proc. IMechE*, Vol. 199, 1985, pp. 137-149.

9 Winterbone, D. E., Nichols, J. R., Alexander, G. I., and Sinha, S. K., "The Evaluation of the Performance of Exhaust Systems Equipped With Integral Pulse Converters," CIMAC-Congress Oslo, 1985, Paper No. D62.

10 Miller, R., and Lieberherr, H. U., "The Miller Supercharging System for Diesel and Gas Engines Operating Characteristics," CIMAC-Congress Zurich, 1957.

11 Meier, E., "The Miller System—a Possible Solution to Present Problems With Highly Charged Four-Stroke Engines," *Brown Boveri Review*, Vol. 64, No. 4, 1977, pp. 235-242.

12 Bulaty, T., "Special Problems Involved in Step-by-Step Calculation of the Gas-Exchange Process—Typical Applications," ASME Paper No. 88-DGP-2, 1988.

13 Bulaty, T., "The Use of Computer Simulation to Improve Turbocharging of Diesel Engines," presented at the ASME Winter Annual Meeting, Chicago, IL, 1988.

APPENDIX

Energy and Work Potential With Isentropic Expansion

Exergy in an arbitrary state x in the charging system:

$$E_x = \dot{m}_x \left[h_x - h_{amb} - T_{amb}(s_x - s_{amb})\right]$$

Exergy of the air at the inlet valve of an engine cylinder:

$$E_I = \int_{IO}^{IC} \left[h_I - h_{amb} - T_{amb}\,(s_I - s_{amb})\right] dm_I$$

Exergy of the exhaust gases at the outlet from an engine cylinder:

$$E_E = \int_{EO}^{EC} \left[h_{cyl} - h_{amb} - T_{amb}(s_{cyl} - s_{amb})\right] dm_E$$

Loss of exergy from state 1 to state 2:

$$E_L = H_1 - H_2 - T_{amb}\,(S_1 - S_2)$$

Work potential with isentropic expansion to ambient pressure:

Exhaust gas at the outlet from an engine cylinder:

$$W_{sexpE} = \int_{EO}^{EC} \Delta h_{s\,exp}\left(x_{cyl},\, T_{cyl},\, \frac{p_{cyl}}{p_{amb}}\right) dm_E$$

Work potential in the charging system in an arbitrary state x:

$$W_{sexpx} = m_x \cdot \Delta h_{s\,exp}\left(X_x,\, T_x,\, \frac{p_x}{p_{amb}}\right)$$

Work of compression of the ideal charging system (Fig. 3):

$$W_{COM\ id} = V_{sw} \cdot \frac{\epsilon}{\epsilon - 1} \cdot \frac{\lambda_s}{\lambda_z} \cdot \frac{T_{amb}}{T_{ac}} \cdot p_{ac} \cdot \frac{\bar{\kappa}_A - 1}{\bar{\kappa}_A} \cdot \left[\left(\frac{p_{ac}}{p_{amb}}\right)^{\frac{\bar{\kappa}_A - 1}{\bar{\kappa}_A}} - 1\right]$$

Work of expansion of the ideal charging system (Fig. 3)

$$W_{EXP\ id} = V_{SW} \cdot \frac{\epsilon}{\epsilon - 1} \cdot \left\{ p_{ex} \cdot \frac{\bar{\kappa}_E}{\bar{\kappa}_E - 1} \cdot \left[1 - \left(\frac{p_{ex}}{p_{ac}}\right)^{\frac{1 - \bar{\kappa}_E}{\bar{\kappa}_E}}\right] - (p_{ex} - p_{ac}) + \left[\left(\frac{p_{ex}}{p_{ac}}\right)^{\frac{1}{\bar{\kappa}_E}} - 1 + \lambda_s\right] \cdot p_{ac} \cdot \frac{\bar{\kappa}_E}{\bar{\kappa}_E - 1} \cdot \left[1 - \left(\frac{p_{ac}}{p_{amb}}\right)^{\frac{1 - \bar{\kappa}_E}{\bar{\kappa}_E}}\right] + \left(\frac{\lambda_s}{\lambda_z} - \lambda_s\right) \cdot p_{ac} \cdot \frac{\bar{\kappa}_A}{\bar{\kappa}_A - 1} \cdot \left[1 - \left(\frac{p_{ac}}{p_{amb}}\right)^{\frac{1 - \bar{\kappa}_A}{\bar{\kappa}_A}}\right] \right\}$$

Data for the Model Engine

Highly turbocharged, medium-speed four-stroke diesel engine:

18 cylinders in **V** arrangement

P_{eff} = 8000 kW BMEP = 25 bar n = 750 min^{-1}

c_m = 9 m/s p_{max} = 170 bar constant injection timing

Constant-pressure turbocharging with two BBC turbochargers VTR 354.

Variants:
- BBC power turbine NTC 214 in parallel to the turbocharger
- Waste gate
- Bypass from compressor outlet to turbine inlet
- Increased turbocharger efficiency

Material Property Evaluation of Thick Thermal Barrier Coating Systems

R. C. Brink
Caterpillar Inc.,
Peoria, IL

Coating system optimization is a critical step in the design and development of plasma-sprayed thermal barrier coatings (TBC's) for diesel engines. Physical and mechanical property measurements and bench screening tests were performed to evaluate the candidate TBC systems. Additional understanding of the material behavior and failure mechanisms of thick TBC's gained from the property measurements and bench testing was identified. A specific graded zirconia (ZrO_2)/bond (NiCrAlY) coating material system with good strain tolerance and fatigue resistance was selected for follow-on diesel engine durability testing.

Introduction

A primary purpose of insulating the combustion chamber on a diesel engine is to retain thermal energy for subsequent recovery. One insulation approach that has received a lot of attention is the use of plasma-sprayed ZrO_2 ceramic coatings [1–3]. A primary advantage of plasma-sprayed ZrO_2 is its low thermal conductivity, typically between 0.5 and 1.2 W/m°C. Based on engine cycle simulation predictions, a turbocompound engine utilizing a 2.5-mm-thick TBC (1 W/m°C) on the piston and cylinder head would lower specific fuel consumption by 2.5 percent [4].

The successful operation of certain thinner TBC's in previous turbine [5] and diesel [6] engine applications is encouraging. This method of insulation may provide a more reliable and practical alternative to monolithic ceramic design approaches. Unfortunately, the demonstration of acceptable durability with thicker TBC's, say above 1 mm, in a diesel engine environment has not yet been accomplished [2, 7]. Some of the difficulty stems from a lack of understanding of the material behavior and failure mechanisms of TBC's within a diesel engine environment. Controlled bench tests that simulate the operating environment of the diesel engine coupled with pertinent material property testing and analysis are needed.

Under DOE/NASA Contract No. DEN3-332 with Caterpillar Inc., a program to demonstrate the durability of thick thermal barrier coatings for in-cylinder diesel engine components is being conducted. The thermal conductance goal for these coatings is 408 W/m²°C (e.g., 2.5 mm coating with 1.02 W/m°C thermal conductivity). Plasma-sprayed ZrO_2 TBC systems will be applied to the piston and cylinder head fire deck for 100 hours of testing in a single-cylinder test engine that is representative of advanced on-highway truck diesel engines.

The objective of this paper is to present the results of the contract involving coating development and bench testing. In particular, material properties for ZrO_2 and ZrO_2/NiCrAlY coating mixtures were evaluated. Candidate TBC systems were screened with 1000 hour environmental contamination, thermal shock, and compressive fatigue tests. Finally, the selection of the proposed TBC design for engine component durability testing is outlined. Additional information on coating behavior and observed failure mechanisms is also reported.

Contributed by the Internal Combustion Engine Division and presented at the Twelfth Annual Energy-Sources Technology Conference and Exhibition, Houston, Texas, January 22–25, 1989. Manuscript received by the Internal Combustion Engine Division August 1988. Paper No. 89-ICE-13.

Coating Characterization

Two partially stabilized ZrO_2 powders, designated A and B, were evaluated for the ceramic top coat, and a NiCrAlY powder was used for the bond coat. Property data for the powders are listed in Table 1. Note that besides the difference in stabilizer amount the two ZrO_2 powders have a different preparation technique and particle size distribution. The spray process parameters necessary for good coating deposition will also be different as a result.

Table 1 Spray powder property data

	NiCrAlY Powder	ZrO_2 Powders A	B
Composition (% wt.):	Ni = 76.3 Cr = 17.1 Al = 6.12 Y = 0.52	ZrO_2 = 89.9 Y_2O_3 = 7.50 HfO_2 = 1.65 SiO_2 = 0.34 CaO = 0.36	ZrO_2 = 89.9 Y_2O_3 = 10.0
Preparation:		sintered & crushed	fused & crushed
Particle Size Distribution (μm):			
Mean	61.22	67.30	30.94
St. Dev.	16.38	24.40	15.53
Density (g/cm3):	7.42	5.73	5.73

Table 2 TBC systems investigated

TBC System	Coating Layer Arrangement
Duplex	ZrO_2 Ceramic NiCrAlY Bond Substrate
Graded	ZrO_2 Ceramic 75%ZrO_2/25%NiCrAlY 50%ZrO_2/50%NiCrAlY 25%ZrO_2/75%NiCrAlY NiCrAlY Bond Substrate
Strain-Isolated	ZrO_2 Ceramic NiCrAlY Bond Strain-Isolation Pad Substrate

Table 3 Anticipated component operating temperatures (°C)

	Piston	Cylinder Head
TBC Peak	738	670
Metal Peak	350	485

Table 4 ZrO_2/NiCrAlY coating properties at 400°C

Material Type	Specific Gravity (g/cm³)	Thermal Conductivity (W/mC)	Expansion[b] Coefficient (μm/mC)	Elastic Modulus (GPa)
A ZrO_2/NiCrAlY:				
0/100	—	—	12.0	61
25/75	—	3.25	11.0	57
50/50	—	1.95	9.3	49
75/25	—	—	8.8	43
100/0 (A1)	5.43 (5)[a]	1.13	8.7	44
100/0 (A2)	4.99 (13)	0.94	7.7	44
100/0 (A3)	5.02 (12)	0.93	7.7	44
B ZrO_2/NiCrAlY:				
0/100	—	4.01	—	34
25/75	—	3.33	12.5	42
50/50	—	1.53	9.3	38
75/25	—	—	8.1	28
100/0 (B1)	5.44 (5)	1.15	9.2	52
100/0 (B2)	5.04 (12)	0.80	7.2	63
100/0 (B3)	4.91 (14)	0.62	—	51
Metal Substrate:				
17-4 St. Steel	7.80	23	13.0	165
Gray Iron	7.20	37	12.7	110

Notes: a. ( ) indicates coating porosity in %.
b. Thermal expansion coefficient per 20°C reference temperature.

Duplex, graded, and strain-isolated coating systems as defined in Table 2 were evaluated. The powders were deposited using conventional air plasma spray equipment. Independent spray process parameters were selected for the NiCrAlY bond, the graded ZrO_2/NiCrAlY layers, and the ZrO_2 ceramic coating in each ZrO_2 material group (A and B). Plasma spray process parameters for the ZrO_2 ceramic coatings were varied to achieve porosities between 5 and 15 percent. This coating porosity variation was intended to achieve a range of thermal conductivities between 1.05 and 0.75 W/m°C, with the denser coatings producing the higher conductivity [8]. This allowed the trade-offs between coating porosity/thickness versus coating strength/strain tolerance and thermal fatigue resistance to be evaluated. A denser, more conductive coating would have to be sprayed thicker to meet the given conductance goal of 408 W/m²°C

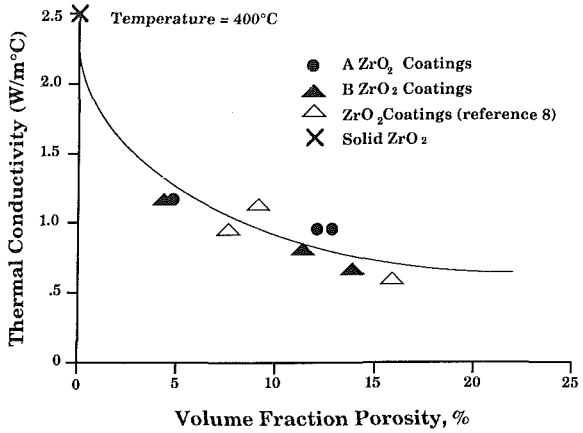

Fig. 1 Influence of coating porosity on thermal conductivity

$$C_c = k_c/t_c \quad (1)$$

where C_c = coating conductance; k_c = coating thermal conductivity; t_c = coating thickness.

Coating Property Measurement

Knowledge of coating physical and elastic properties (thermal conductivity, thermal expansion coefficient, and elastic modulus) is necessary for proper thermomechanical modeling of the TBC on the engine component. The coating mechanical properties (strength and strain tolerance) are needed to establish the coating's operating limitations and are also helpful for the TBC selection process. The coating strain tolerance has been used as the primary material parameter for comparisons of the coating's operating limitations.

Physical and Elastic Properties. Thermal conductivity and thermal expansion data were acquired from 20 through 1000°C and elastic modulus data were acquired at 400 and 700°C to provide a material data base for component finite element analysis. The anticipated component operating temperatures are listed in Table 3.

The coating porosity was determined from the coating specific gravity (weight and micrometric coating measurements) and theoretical (powder) density as outlined in a previous paper [9]. The thermal conductivity was obtained by the laser-flash measurement technique [10]. Coating thermal expansion was measured with a Theta dual push rod dilatometer. The coating elastic modulus was determined using the four-point bend method with free-standing coating specimens. The bend fixture design was derived from a previous reference [11]. Free-standing coatings were prepared by spraying on a mild steel substrate, machining the coating to a uniform thickness, and chemically etching the metal off. A more complete description and sample use of the four-point bend method for coating property determination can be found in a previous reference [12].

A characteristic sample of the coating properties measured at 400°C is shown in Table 4. The substrate materials for the piston (17-4 PH stainless steel) and cylinder head (gray iron) are also included for reference.

As can be seen in Table 4, both "dense" (5 percent porosity) and "porous" (12–14 percent porosity) straight ZrO_2 coatings were sprayed. The relationship observed between coating porosity and thermal conductivity is plotted in Fig. 1. As expected, the thermal conductivity was reduced as coating

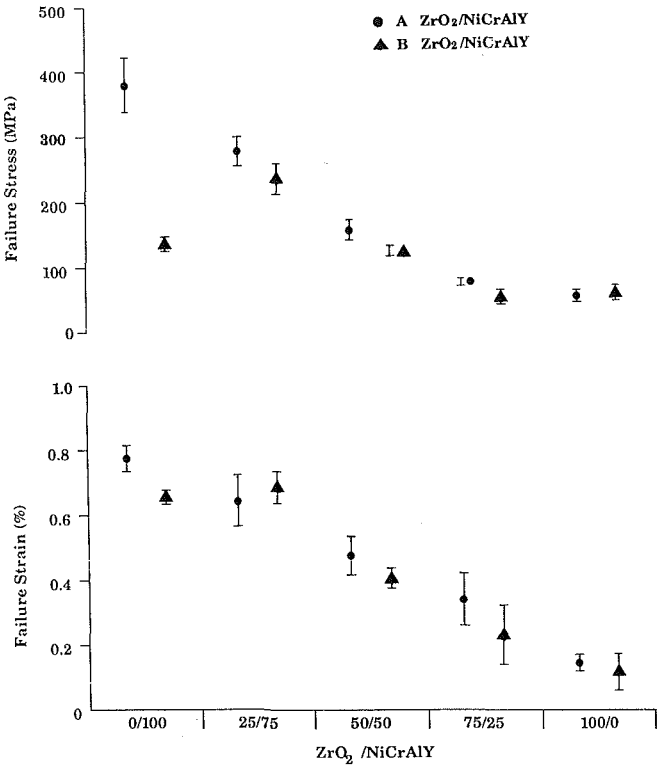

Fig. 2 Tensile strength and strain tolerance of ZrO_2/NiCrAlY coating mixtures (@ 400°C)

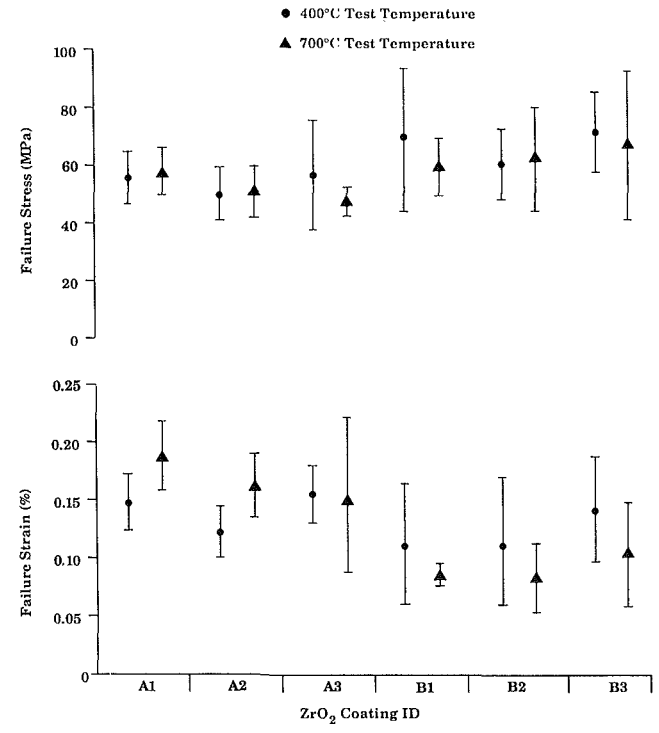

Fig. 3 Tensile strength and strain tolerance of straight ZrO_2 coatings

porosity was increased. The data are characterized reasonably well with an empirically adjusted Einstein equation ("least-squares" fit with a correlation coefficient r of 0.90)

$$k_c = k_s \times \frac{1}{1.16 + (16.8 \times P)} \quad (2)$$

where k_s = solid ZrO_2 thermal conductivity; P = volume fraction porosity.

Also, increased thermal conductivity resulted when the ZrO_2/NiCrAlY coating mixtures approached pure NiCrAlY. This is the basic reason graded ZrO_2/NiCrAlY TBC designs will require greater overall thickness than duplex TBC designs for a given thermal resistance.

With a thermal expansion coefficient of 7.2 to 9.2 μm/m°C measured for the straight ZrO_2 coatings and approximately 13 μm/m°C for the metal substrates, a significant thermal mismatch is evident. In duplex TBC designs, where a thin bond coat and the ceramic coating are directly applied to the substrate, tensile and shear thermal stresses are created in the ceramic coating at the ceramic/bond coat interface. This interface is often the site where coating delamination failures are noted. The ZrO_2/NiCrAlY coating mixtures provide a good transition of the thermal expansion coefficient between the straight ZrO_2 ceramic and the substrate. With proper selection of the graded ZrO_2/NiCrAlY layer thicknesses, the tensile and shear interface stresses can be reduced considerably.

As a result of the relatively low elastic modulus and thickness of TBC's (as compared to the metal substrate) in typical diesel engine component applications, the TBC does not contribute significantly to the overall component rigidity. Thus, the coating is operating primarily in a deflection, or strain, controlled environment. Finite element analyses of components have illustrated this in unpublished work. Under these conditions the coating operating stress is a direct function of its elastic modulus and a lower coating elastic modulus is desirable. Thus, the straight ZrO_2 coatings from group A with their lower elastic modulus would produce lower operating stresses than those from group B. The NiCrAlY bond and graded ZrO_2/NiCrAlY coating layers also exhibited different elastic moduli between the two material groups as a result of spray process and powder differences.

Mechanical Properties. The coating's strength (failure stress) and strain tolerance (failure strain) were acquired with the four-point bend test method to provide a measure of the coating's mechanical operating capabilities. Coating bend tests were conducted at 400 and 700°C with coating thicknesses of 1.25 and 2.50 mm. A minimum of three specimens per test point was used. Coating tensile property data were acquired with free-standing coating bend specimens, whereas coating compressive property data were acquired with composite coating/metal bend specimens. The composite specimens consisted of coated 17-4 stainless steel bend coupons.

The influence of the ZrO_2/NiCrAlY coating mixture on tensile strength and strain tolerance is shown in Fig. 2. Both the average and +/− one standard deviation of the data are included. The addition of NiCrAlY to ZrO_2 clearly improved the coating strength and strain tolerance. This is another key benefit (besides reduction of expansion mismatch) for graded TBC systems. Both the A and B graded ZrO_2/NiCrAlY coating layers performed well, although the B bond coat was rather weak.

A comparison of the tensile strength and strain tolerance for the straight ZrO_2 coatings is shown in Fig. 3. Although the B ZrO_2 coatings produced slightly higher tensile strength, they had lower tensile strain tolerance than the A ZrO_2 coatings. Coating strain tolerance is likely to provide a better measure of the coating durability than strength, since the coating operates in a strain-controlled environment. No overall strength or strain tolerance trend with coating thickness was observed. However, it should be noted that the B1 ZrO_2 coating suffered from some inconsistency in spray deposition, as a number of the specimens (particularly thicker specimens) fractured prematurely during routine handling. No consistent relationship

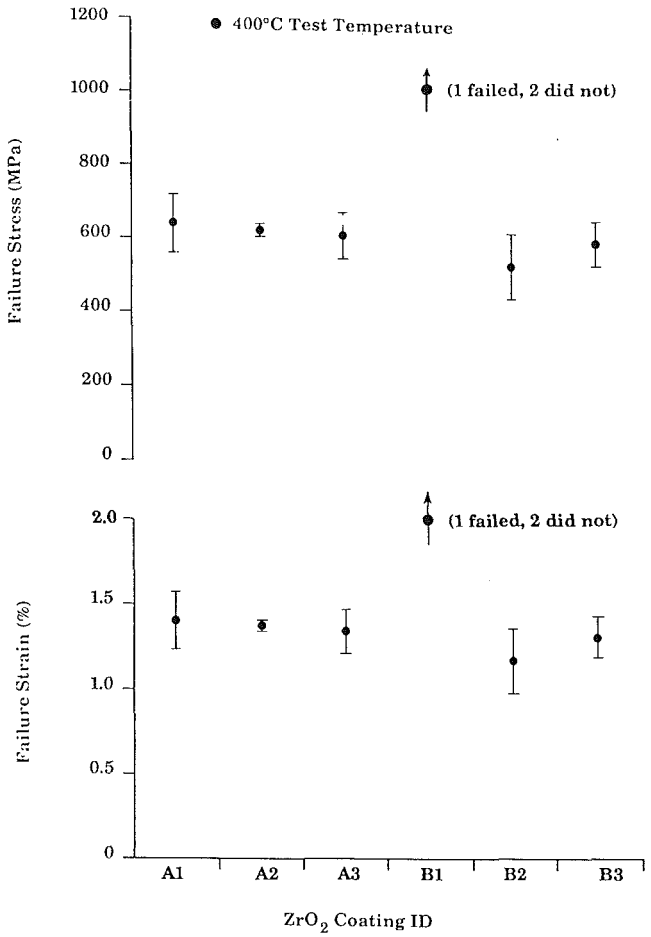

Fig. 4 Compressive strength and strain tolerance of straight ZrO_2 coatings

between coating porosity and strength or strain tolerance was found.

A comparison of the compressive strength and strain tolerance for the straight ZrO_2 coatings at 400°C is shown in Fig. 4. The B1 ZrO_2 coating was clearly stronger and more strain tolerant in compression than the other coatings. Due to bend fixture deflection limitations, two of the three B1 coating specimens produced no failure. Although substrate plasticity limited quantitative strength measurement at 700°C, coating compressive strength and strain tolerance at 700°C were at least as good as those found at 400°C.

An overall comparative summary of the coating strain tolerance for the six ZrO_2 top coat materials is shown in Table 5. The relative strain tolerance ranking takes into consideration the data average and standard deviation. The coating rank in tension and compression were somewhat consistent, with the exception of the B1 coating. Overall, the strain tolerance ranking indicated superiority for the A1 and A2 top coat materials. The best and worst coating materials were separated by almost a factor of two in strain tolerance.

Environmental Contamination Screening

The purpose of the environmental contamination test was to evaluate the long-term influence of the elevated temperature diesel combustion environment on ZrO_2 coating properties. The six ZrO_2 top coat materials were tested in composite (coated 17-4 strainless steel, cast iron, and Pyromet 31 substrates) and free-standing bend specimen configurations. The composite specimens utilized the duplex coating arrangement. A total of 48 bend specimens were placed in a 750°C furnace with a simulated diesel engine exhaust gas for 1000 hours.

Table 5 Strain tolerance comparison of the ZrO_2 top coat materials

Coating ID	Tension ε_{rel}	Rank	Compression ε_{rel}	Rank	Overall ε_{rel}	Rank
A1	1.00	1	0.67	3	1.00	1
A2	0.83	2	0.73	2	0.93	2
A3	0.78	3	0.66	4	0.86	4
B1	0.49	5	1.00	1	0.89	3
B2	0.41	6	0.53	6	0.56	6
B3	0.57	4	0.65	5	0.73	5

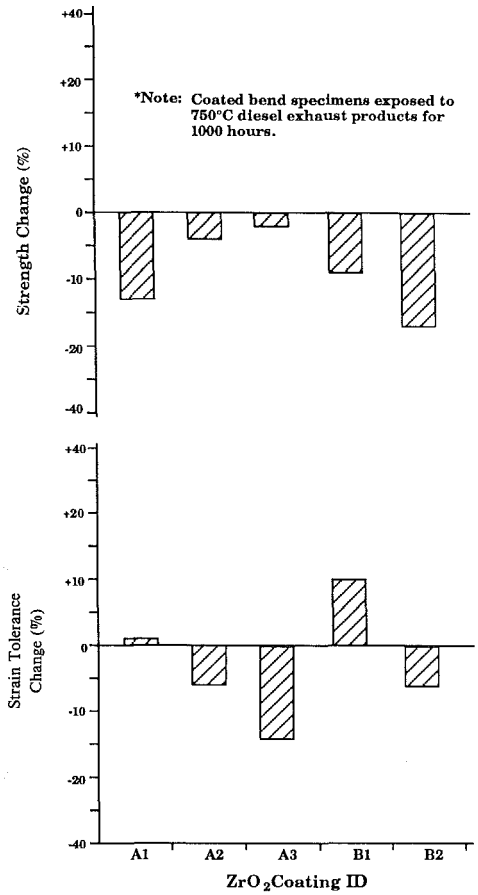

Fig. 5 Influence of environmental contamination* on coating compressive strength and strain tolerance

All the coatings survived the test without any apparent distress, with the exception of a single B2 coating specimen, which experienced partial spallation. The influence of the environmental contamination on the compressive strength and strain tolerance of the coatings is shown in Fig. 5. The small change in coating strength and strain tolerance properties suggests that these ZrO_2 coatings are relatively insensitive to the diesel combustion atmosphere.

X-ray diffraction results of pretested and posttested specimens indicated that no new phases precipitated in the A ZrO_2 coating material, whereas a monoclinic phase was observed in the B ZrO_2 coating material after exposure. Coating performance has been linked to phase distribution [13]. The large volume increase and accompanying stress associated with a tetragonal to monoclinic phase transformation is considered detrimental to the integrity of the coating.

Microscopic examination of the exposed samples revealed some oxidation of the bond coat. The cast iron substrate was severely oxidized in the exposed areas. The group B specimens showed heavy oxidation between the bond coat and the cast

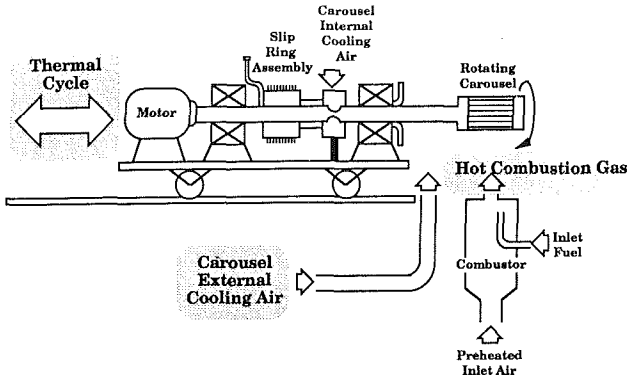

Fig. 6 Coating thermal shock rig

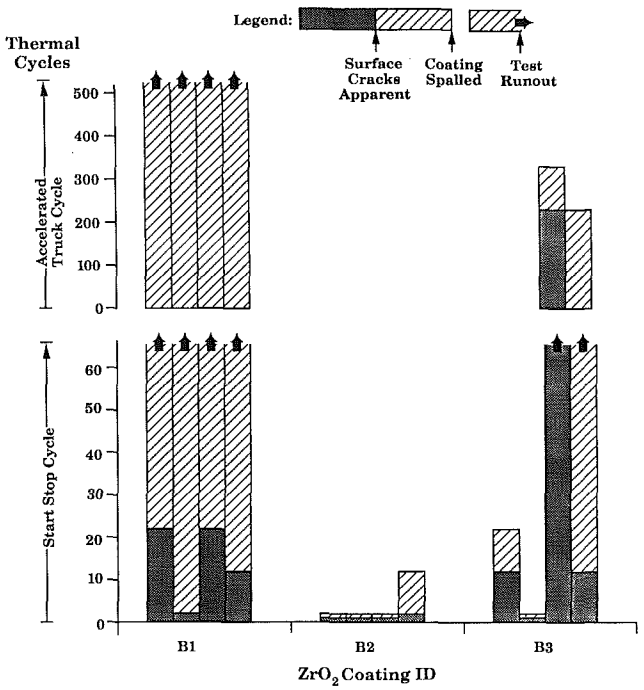

Fig. 7 Thermal fatigue life comparison of group B coating materials with duplex TBC system

iron, which was not evident on the group A specimens. This oxidation is likely a result of a thinner, more porous bond coat used for the group B specimens. Under actual engine operation bond coat oxidation should not be a problem, since much lower metal temperatures are expected.

Thermal Shock Screening

A specially designed thermal-shock rig was developed to test the thermal fatigue resistance of the candidate TBC systems. The rig consists of a rotating carousel that holds 12 coated bend specimens and is cycled between hot and cold air blasts, as shown in Fig. 6. Within the carousel, individual cooling channels were provided behind the substrate for proper control of coating temperatures and heat flux. A peak coating temperature of 750°C and metal substrate temperature of 450°C were established for the test. The coating samples were subjected to a number of "start-stop" (20/750°C) cycles followed sequentially by a larger number of "accelerated truck" (300/750°C) operating cycles. TBC thicknesses were selected for evaluation on the basis of the conductance requirement of 408 W/m²°C.

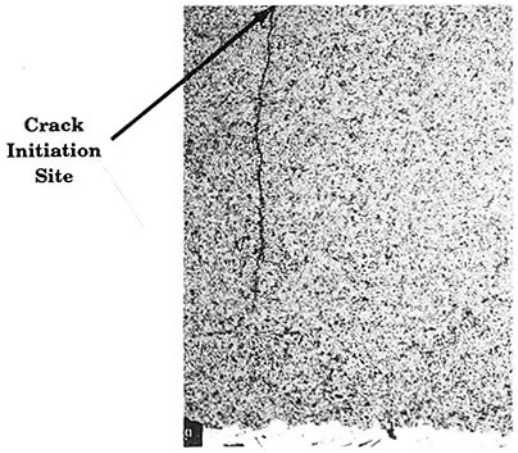

Fig. 8 Surface-initiated vertical coating crack in a B1 thermal shock specimen

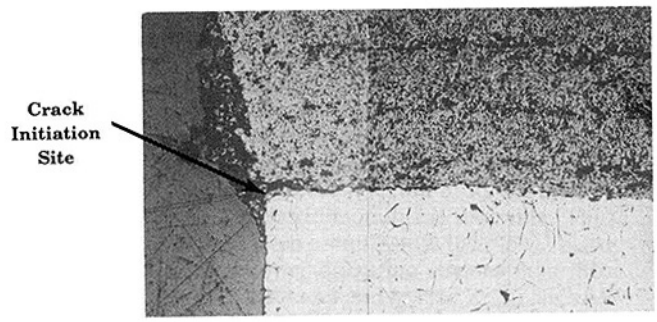

Fig. 9 Edge-initiated coating ceramic/bond interface crack in a B2 thermal shock specimen

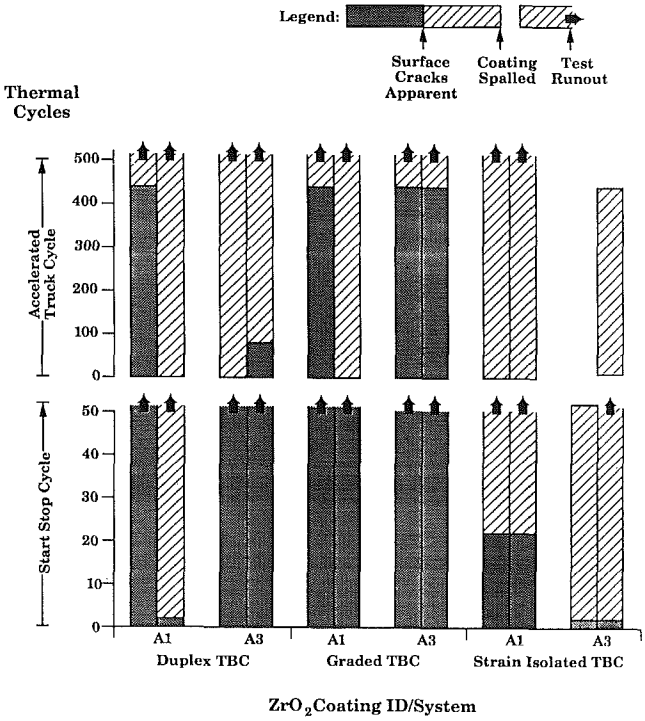

Fig. 10 Thermal fatigue life comparison of candidate TBC systems with group A coating materials

The thermal fatigue lives of the three group B duplex TBC's are shown in Fig. 7. Only surface cracking was apparent on the B1 coating specimens. A section of a B1 specimen, Fig. 8,

Table 6 Overall ZrO_2 material ranking

Coating ID	Strain Tolerance ε_{rel}	Rank	Thermal Shock Rank
A1	1.00	1	1 (no spall)
A2	0.93	2	- (not tested)
A3	0.86	4	3 (no spall)
B1	0.89	3	4 (no spall)
B2	0.56	6	6 (spalled)
B3	0.73	5	5 (spalled)

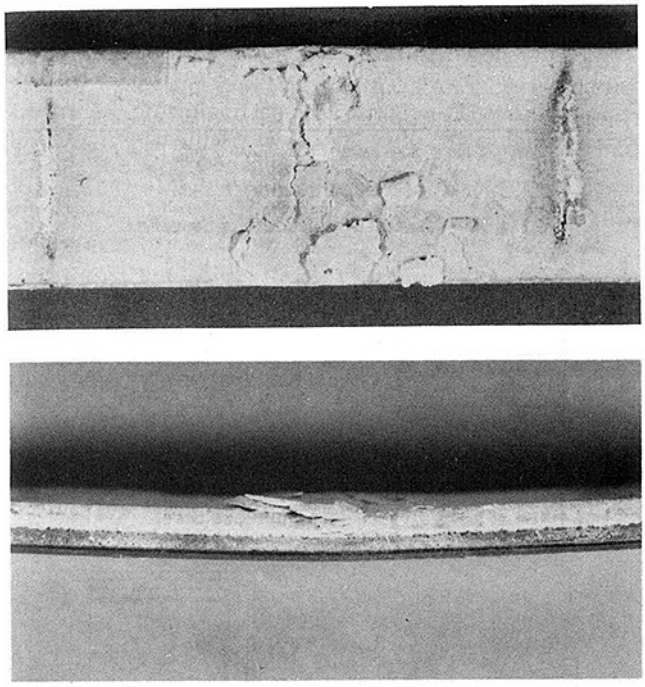

Fig. 11 Spallation fracture appearance of ZrO_2 coating fatigued in compression

shows that these vertical cracks were surface initiated. The B3 and B2 coating specimens delaminated at the bond/ceramic interface. A section of a B2 specimen, Fig. 9, illustrates that these horizontal cracks initiated at the specimen edge. Thermal tensile and shear stresses associated with the transient cycle operation are believed to be responsible for the coating crack and spallation patterns. No detrimental oxidation of the bond coat was evident on these specimens. The B1 coating material, with its higher strain tolerance, showed better adherence and superior fatigue resistance.

A thermal fatigue life comparison of duplex, graded, and strain isolated TBC systems was also conducted for two of the group A top coat materials. The graded and strain isolated systems were intended to reduce ceramic/bond interface stresses. All the coatings survived the test, with the exception of the A3 strain isolated TBC system as shown by Fig. 10. The A3 coating delaminated at the bond/ceramic interface due to poor bonding. Within this carousel the thermal fatigue resistance of the graded TBC system was found to be best, followed by the duplex and then strain-isolated TBC systems.

An overall comparative summary of the ZrO_2 top coat materials' strain tolerance and thermal fatigue resistance is shown in Table 6. Good correlation is found between the coating material parameter-strain tolerance and the thermal fatigue resistance of the coating. The A1, A2, A3, and B1 coatings showed better performance, whereas the B3 and B2 coating materials were clearly worse.

Compressive Fatigue Screening

Compressive stresses have been related to spallation failures

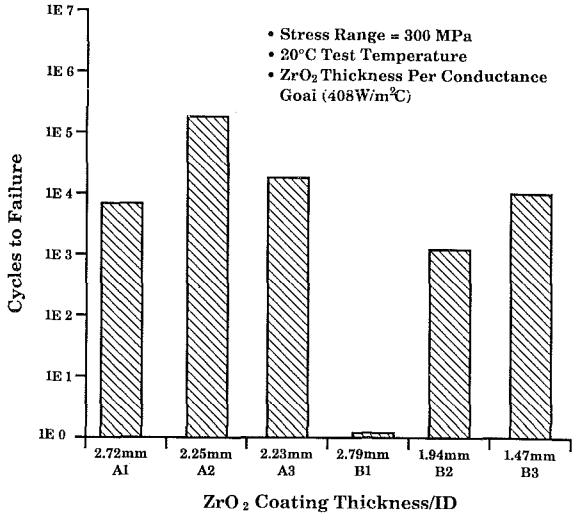

Fig. 12 Compressive bend fatigue life comparison

of ceramic coatings in turbine engine applications [14]. In a relatively high heat flux application such as an oil-cooled piston, compressive thermal stresses are generated at the TBC surface. The diesel combustion cycle also induces an additional high-cycle compressive stress component at the TBC surface during firing due to gas pressure and transient thermal loading [15, 16], which is not found in turbine engine applications. Thus, the high-cycle compressive fatigue performance of ZrO_2 coatings is likely a key material parameter for diesel engine TBC applications. The spallation failure appearance of a ZrO_2 coating cycled in compressive bend fatigue is illustrated in Fig. 11.

The compressive fatigue performance of the six ZrO_2 top coat materials was evaluated with the four-point bend test method. The coatings (four of each type) were sprayed at their conductance thickness requirement onto 17-4 stainless steel bend specimens and cycled at a constant alternating stress range. The A2 coating material gave the best compressive fatigue performance as shown in Fig. 12. The very poor performance of the B1 coatings is attributable to the spray deposition inconsistency mentioned earlier for this coating configuration. Coating "mud-flat" cracks were apparent on these B1 specimens upon spray completion, producing poor compressive coating strength.

TBC Design Summary

Based on the strain tolerance and thermal shock results, the A1, A2, A3, and B1 top coat materials were given serious consideration. No obvious coating porosity optimum was found. The "dense" (B1) coating configuration appeared the most promising within the group B candidates, whereas both "dense" (A1) and "porous" (A2) coatings appeared promising within the group A candidates. Although the relatively high compressive strength/strain tolerance observed with the B1 coating was intriguing, the deposition inconsistency with this coating was unacceptable and would require further development. The A2 top coat material was ultimately selected, based on its superior compressive fatigue performance and good overall strain tolerance. The graded ZrO_2/NiCrAlY TBC system was chosen over duplex or strain-isolated systems based on the thermal shock results. The group A graded ZrO_2/NiCrAlY coating layers showed good strain tolerance and provide a smooth transition of the thermal expansion coefficient through the TBC system.

Evaluation of the structural acceptability of the coating system is a critical step in the TBC design process. Unfortunately,

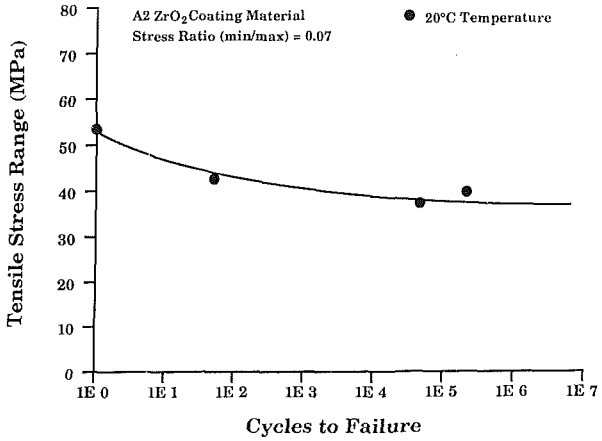

Fig. 13 ZrO_2 coating fatigue strength in tension

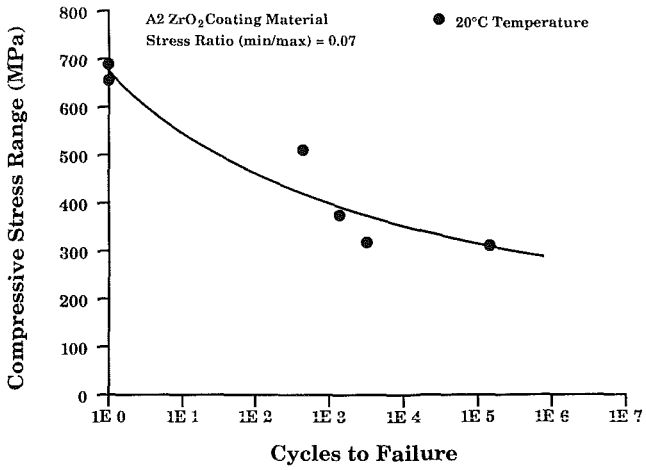

Fig. 14 ZrO_2 coating fatigue strength in compression

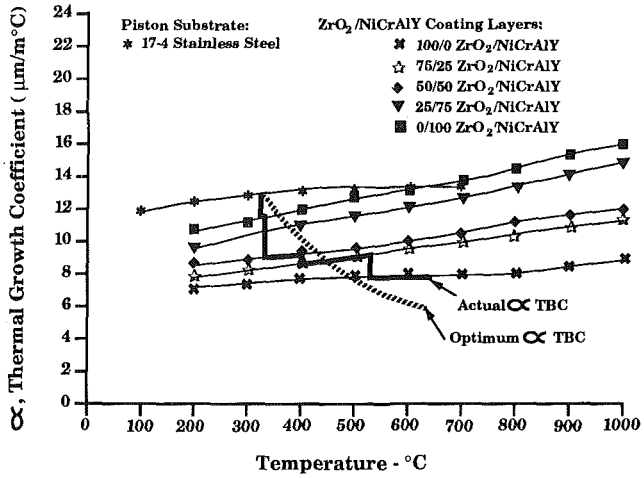

Fig. 15 Graded TBC thickness optimization

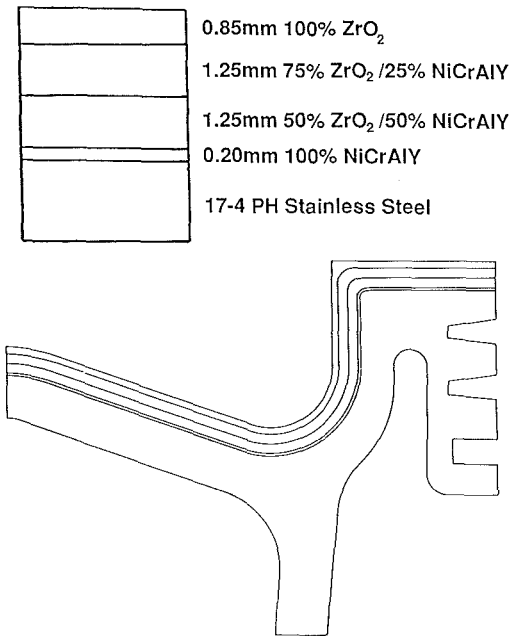

Fig. 16 Graded TBC design for piston

the basic failure mechanisms of thick TBC's operating in the diesel engine environment has not been well documented. The four-point bend method was used to quantify the effect of fatigue loading on ZrO_2 coatings. As illustrated in Figs. 13 and 14, the A2 coating material was sensitive to both tensile and compressive fatigue loading. Thus, both the static and fatigue strength of ZrO_2 coatings should be considered in the design of diesel engine component TBC's.

Component finite element analysis was used in conjunction with the TBC material property database to complete the TBC design process. The TBC thermal stresses can be minimized with proper selection of the individual ZrO_2/NiCrAlY layer thicknesses. The graded TBC thickness design optimization will depend on the thermal expansion characteristics of the substrate and the TBC system. The relationship between the "optimum" TBC thermal expansion coefficient (to produce uniform substrate/TBC thermal growth) and the "actual" TBC thermal expansion coefficient (graded layer TBC design) selected for the piston TBC is shown in Fig. 15. A graded ZrO_2/NiCrAlY TBC thickness of 3.55 mm with individual layer thicknesses as noted in Fig. 16 was ultimately selected. This TBC design was deemed structurally acceptable for the engine operating conditions and also met the thermal conductance requirement of 408 $W/m^2°C$. The 3.55-mm-thick graded ZrO_2/NiCrAlY TBC design is proceeding toward engine durability testing for the piston and cylinder head components.

Conclusions

This paper has described the test and analysis effort involved in the development of a thick thermal barrier coating system to be used in a diesel engine application. The major conclusions are:

1 The A2 top coat material and the A ZrO_2/NiCrAlY TBC system exhibited superior performance (i.e., strain tolerance, thermal shock, and compressive fatigue) among the coating material candidates investigated. A 3.55-mm-thick graded ZrO_2/NiCrAlY TBC design has been selected for the piston and cylinder head components for subsequent diesel engine durability testing.

2 Compressive fatigue coating spallation has been identified as a potential early hour failure mode for coatings operating in the diesel engine environment.

3 Coating delamination failure at the ceramic/bond coat interface was an additional failure mode observed for certain TBC's in the thermal shock rig.

4 No significant ZrO_2 coating strength degradation was observed under 1000 hour exposure to a diesel engine operating environment, although some phase change was observed for the B ZrO_2 material.

5 Graded ZrO_2/NiCrAlY coatings can be used to minimize the coating/substrate thermal expansion mismatch and minimize the likelihood of coating delamination failures.

6 An inverse relationship between the coating thermal conductivity and the coating porosity was observed.

7 The material property parameter-coating strain tolerance provided the best measure of the coating thermal shock durability.

Acknowledgments

The author is grateful to the Department of Energy for supporting this work through Contract No. DEN3-332 and to Murray Bailey and Bob Miller of the NASA-Lewis Research Center for providing technical direction. The author would also like to thank his colleagues at Caterpillar Inc. for help in making this report possible.

References

1 Holtman, R. L., Layne, J. L., and Schechter, B., "An Investigation of Enhanced Capability Thermal Barrier Coating Systems for Diesel Engine Components," NASA CR-174820, Aug. 1984.

2 Woods, M. E., Glance, P., and Schwarz, E., "Exploratory Development of Insulated Components for High Temperature Engines," SAE Paper No. 880191, 1988.

3 Toyama, K., et al., "Heat Insulated Turbocompound Engine," SAE Paper No. 831345, 1983.

4 Larson, H. J., "Thick Thermal Barrier Coatings," *Proceedings of the Twenty-Fourth Automotive Technology Development Contractor's Coordination Meeting*, SAE P-197, 1986.

5 Liebert, C. H., and Miller, R. A., "Ceramic Thermal Barrier Coatings," *I&EC Product Research & Development*, Vol. 23, No. 3, 1984, p. 344–349.

6 Levy, A. V., and MacAdam, S., "Durability of Ceramic Coatings in 14000 Hours Service in a Marine Diesel Engine," ASME Paper No. 88-ICE-19, 1988.

7 Kamo, R., et al., "Thermal Barrier Coating for Diesel Engine Piston," ASME Paper No. 80-DGP-14, 1980.

8 Batakis, A. P., and Vogan, J. W., "Rocket Thrust Chamber Thermal Barrier Coatings," NASA CR-175022, Final Report, July 1985.

9 Roode, M. V., and Beardsley, B., "Porosity Determination of Thermal Barrier Coatings," ASME Paper No. 88-GT-278, 1988.

10 Parker, W. J., et al., "Flash Method of Determining Thermal Diffusivity, Heat Capacity, and Thermal Conductivity," *J. Appl. Phys.*, Vol. 32(9), 1961, pp. 1679–1684.

11 Quinn, G. D., Baratta, F. I., and Conway, J. A., "Commentary on U.S. Army Standard Test Method for Flexural Strength of High Performance Ceramics at Ambient Temperature," AMMRC TR 85-21, 1999.

12 Shiembob, L. T., "Development of a Plasma Sprayed Ceramic Gas Path Seal for High Pressure Turbine Applications," NASA CR-135387, May 1978.

13 Miller, R. A., "Phase Distributions in Plasma-Sprayed Zirconia-Yttria," *American Ceramic Society Bulletin*, Vol. 62, No. 12, Dec. 1983.

14 Mullen, R. L., "Correlation of Compressive Stress With Spalling of Plasma Sprayed Ceramic Materials," NASA TM-83406, Jan. 1986.

15 Assanis, D. N., "Transient Heat Conduction in Low Heat Rejection Engine Combustion Chambers," SAE Paper No. 870156, 1987.

16 Hoag, K. L., "Modeling of Thick Thermal Barrier Coatings," ASME Paper No. 88-ICE-20, 1988.

Electrostatic Dispersion of Diesel Fuel Jets at High Back Pressure

E. Y. Kwack
Associate Mem. ASME

L. H. Back
Fellow ASME

C. P. Bankston
Assoc. Mem. ASME

Jet Propulsion Laboratory,
California Institute of Technology,
Pasadena, CA 91109

An experimental study of electrostatically atomized and dispersed fuel jets has been conducted in room temperature N_2 gas for various back pressures to 41.8 atm. No. 2 diesel fuel was injected through an electrostatic spray triode designed for high-pressure operation. Charge density measurements were conducted at various combinations of injection velocities, electric potentials, and back pressures. The charge density of fuel drops increased up to 1.5 C/m^3 with increasing electric potential until breakdown occurred. After breakdown the charge density was reduced by 40 to 60 percent and again increased but more slowly as electric potential increased. At higher flow rates, breakdown occurred at higher voltages. At higher back pressure, lower charge density was obtained and breakdown occurred at higher voltages. Visual observations showed that significant electrostatic dispersion was accomplished at high back pressures, and that the average drop size was about the same as the spray triode orifice diameter.

I Introduction

Diesel engines are widely used for transportation vehicles and power generation. Unfortunately, one of their important drawbacks is the fact that they produce non-negligible amounts of soot. The soot is formed in the fuel-rich regions of the spray, where a large amount of fuel vapor accumulates without burning and undergoes pyrolysis reactions that transform it to soot. Mixing and controlled atomization have good potential to reduce soot yield in spray flames (Prado et al., 1977), and many methods for improved mixing and dispersion of the spray to reduce local fuel-rich regions have been investigated for improved combustion and reduced soot formation.

In general, the breakup of fuel jets in diesel engines is accomplished by high-pressure injection in the range 20 MPa, 200 atm (for indirect injection) up to about 140 MPa, 1400 atm (for direct injection). The mechanism of breakup of a fuel jet at high-velocity injection has been investigated and was well reviewed in articles by Reitz and Bracco (1982) and Lin and Kang (1987). Swirl is imparted to the flow field in the chamber to assist the fuel–air mixing process further, and soot formation is strongly dependent upon swirl characteristics. However, fuel-rich regions apparently still persist in current engines, and methods for improved mixing and reduced soot formation continue to be of interest.

Previously, Kelly (1981, 1982) and Bankston et al. (1988) reported on an electrostatic spray breakup and dispersion technique for possible use in diesel engines or other combustion systems to enhance breakup. Those results showed that an electrostatic spray triode (EST) can effectively disperse and impart charge densities of 1.5–2 C/m^{3}to liquid hydrocarbons at flow rates relevant to diesel engines (up to 1 ml/s). However, those studies were conducted at ambient back pressure, and no experimental work has been reported for high back pressures such as those expected in diesel engines. This detailed experimental study was carried out to investigate the effects of high back pressure on the charging of fuel jets and on the behavior of breakup and dispersion of charged fuel drops.

Contributed by the Internal Combustion Engine Division for publication in THE JOURNAL OF ENGINEERING FOR GAS TURBINES AND POWER. Manuscript received by the Internal Combustion Engine Division November 1988.

II Experimental Setup

The nozzle used in the current study is an electrostatic spray triode (EST) "single-hole" injector designed for high-pressure and above-ambient temperature (up to 200°C) operation. The basic operational principle of the EST nozzle can be found in previous reports (Kelly, 1982; Bankston et al., 1988). The OMC (Oxide-Metal Composites) company manufactured the insulator-electrode (emitter) assembly and the Parker Hannifin Company assembled it into the housing. Any diesel fuel or fuel simulant can be used in this EST nozzle as long as the fluid is nonconducting and has electrical properties similar to diesel fuel. The EST nozzle has a 254-μm-dia orifice and can be operated up to fuel pressures of 205 atm, electric potentials of 20 kV, and temperatures of 200°C.

The EST was located in the top of a high-pressure chamber of 15 cm i.d., and 40 cm height, which also has a 10-cm-dia window to allow spray development to be observed (Fig. 1). The EST injects fuel vertically downward into a cylindrical glass container of 10 cm diameter and 25 cm height placed inside the high-pressure chamber. The glass container is lined with copper wire screen on the wall and has copper gauze on the bottom in order to collect the charge of the dispersed fuel spray.

The copper wire screen and gauze are connected to an electrometer to measure the electric charge carried by the fuel per unit time i_f, which when divided by the volume flow rate $\dot{Q}$ gives the mean charge density ρ_e.

$$\rho_e = i_f/\dot{Q} \tag{1}$$

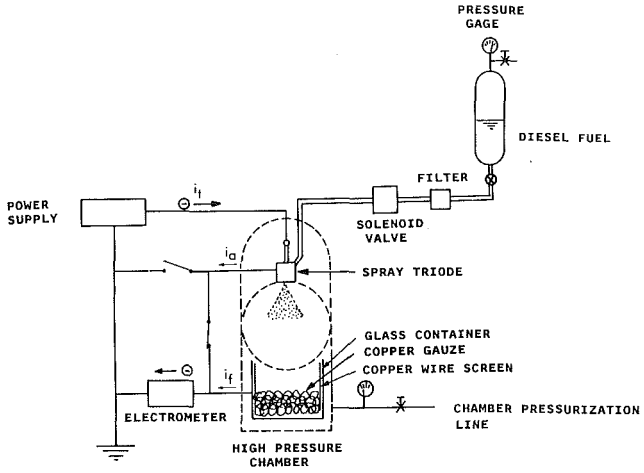

Fig. 1 Schematic diagram of high-pressure experimental setup. No. 2 diesel fuel was injected vertically downward through the electrostatic spray triode by the pressure difference between the diesel fuel tank and the chamber. Both the total charge emitted by the cathode per unit time i_t and the charge swept downstream by fuel per unit time i_f were measured using the switching arrangement.

The fuel, charged by cathode emission, either goes to the anode/orifice electrode or is swept downstream to the collector. Therefore, the total charge per unit time i_t is the sum of the charge carried to the anode and to the collector per unit time

$$i_t = i_a + i_f \tag{2}$$

The anode is connected to the electrometer as shown in Fig. 1 by a switching arrangement when the total current is measured.

The high-pressure chamber was pressurized up to 41.8 atm by room temperature N_2 gas. Fuel is supplied to the EST nozzle by the pressure difference between the fuel tank and the high-pressure chamber through a line with a 10 μm filter to remove particles that can cause the nozzle to plug or to spray erratically, which may lead to early electrical breakdown. The flow rates through the EST were calibrated as a function of pressure difference measured using a differential pressure transducer for three different chamber pressures of 0.97, 21.4, and 41.8 atm (0, 300, and 600 psig). It was found that the calibration was almost independent of the chamber pressure. Since it was planned to increase the pressure inside the chamber to 41.8 atm to simulate the pressure inside a small diesel engine cylinder before the injection of fuel, the high-pressure chamber and the fuel tank were located in one room for safety and the associated instrumentation was located in an adjacent room. For remote control, a solenoid valve was located in the fuel line between the 10 μm filter and the EST nozzle.

The test fluid was No. 2 diesel fuel with a viscosity of about 6cp. The density and the surface tension of No. 2 diesel fuel are 0.824 g/cm^3 and 30 dyne/cm, respectively. The electric charge density of the diesel spray was measured for various flow rates/injection velocities at various chamber pressures, e.g., 0.97, 21.4, and 41.8 atm, by applying different electric potentials with a power supply.

Characterization of the spray was carried out by flash illumination and photographs. Analysis of the photographs was carried out using an image processing system. A photograph was placed on a light table in view of a video camera (Model CC-65S, DAGE-MTI, Inc.). The analog signal from the video camera was fed to a digitizer, which writes the data into RAM memory using an add-on board (PCvision Frame Grabber, Imaging Technology) in conjunction with an IBM PC-AT. A computer code was developed with the aid of commerically available software (IMAGELAB/IMAGETOOL, Werner Frei Associates) for image enhancement and analysis of droplet size.

III Results and Discussion

1. Electric Charge Density. The charge per unit time i_t emitted by the cathode and the charge per unit time i_f swept downstream with the fuel were measured over a wide range of flow rates from 0.51 to 2.5 ml/s at a chamber pressure of $p_c = 0.97$ atm. The values of i_f and i_t along with i_a, the current to the anode/orifice, are shown in Fig. 2 as a function of the electric potential E from -5 to -16 kV for a particular value of the flow rate $\dot{Q} = 1.2$ ml/s. The influence of flow rate on the charge per unit time i_f carried by the fuel is also shown in Fig. 3 as a function of electric potential. The complex current-voltage characteristics of the spray triode evident in Figs. 2 and 3 are now discussed in connection with charge transport considerations.

The cathode starts emitting electrons from its surface if the local electric field is higher than the minimum value needed to extract electrons from the metallic surface, which is of the order of 10^9 V/m. The number of electrons emitted from the cathode per unit time is proportional to the strength of the local electric field above the minimum value as indicated in Fig. 2 by the increase of i_t with E. Once the electrons are injected into the fuel, they are coupled with the fuel near the cathode, forming a charged cloud or layer. Some of the charged fuel is attracted to the anode/orifice electrode (i_a) and

Nomenclature

A = geometric constant in equation (5)
B = geometric constant in equation (6)
d = drop diameter, m
d_n = spray nozzle diameter, m
d_{10} = arithmetic mean diameter, m
d_{32} = volume-surface mean diameter, m
E = electric potential across cathode and anode electrodes, V
f = function in equation (4)
i_a = charge attracted to anode per unit time, A
i_f = charge swept downstream by fuel per unit time, A
i_t = total charge emitted by cathode per unit time, A
m_f = fuel mass, g
N = number of fuel drops
p_c = chamber pressure, atm
$\dot{Q}$ = fuel flow rate, ml/s
Re = Reynolds number = $\rho_f V_i d_n/\mu_f$
T = aerodynamic breakup parameter
V_i = fuel injection velocity, m/s
We_f = Weber number based on fuel properties = $\rho_f V_i^2 d_n/\gamma$
x_{max} = function in equation (5)
x_1 = length of intact core, m
γ = surface tension of fuel, N/m
ϵ_o = permittivity of free space = 8.85×10^{-12} C/V-m
θ = spray angle, deg
μ_f = viscosity of fuel, kg/m-s
ρ_e = charge density, C/m^3
$\rho_{e,max}$ = maximum charge density, C/m^3
ρ_f = fuel density, g/cm^3
ρ_g = gas density, g/cm^3

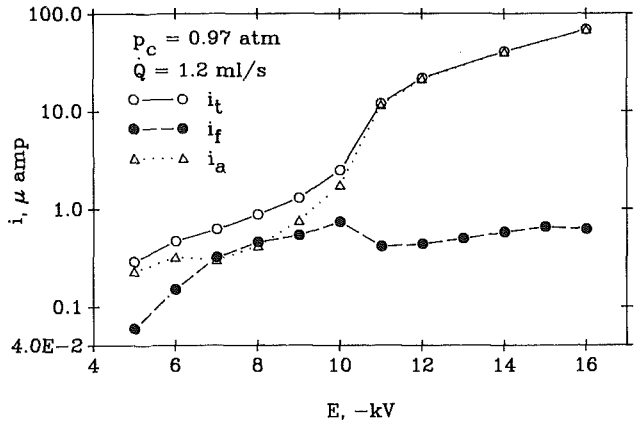

Fig. 2 Currents versus electric potential at $p_c = 0.97$ atm and $\dot{Q} = 1.2$ ml/s. The charge ratio i_f/i_t was 0.1 to 0.5 before breakdown occurred. After breakdown the ratio was reduced below 0.05.

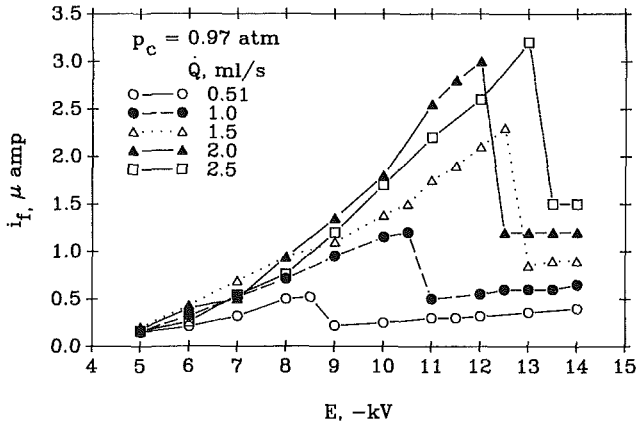

Fig. 3 Charge swept downstream by fuel per unit time i_f (for various flow rates) increases with increase of electric potential, sharply decreases at electrical breakdown, and increases slightly again with increase of electric potential. The chamber pressure was 0.97 atm.

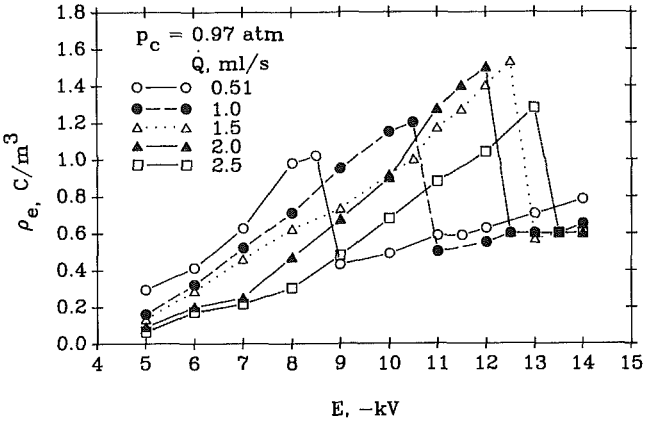

Fig .4 Charge density versus electric potential for various flow rates at $p_c = 0.97$ atm. The maximum charge densities for various flow rates were observed just before breakdown. The maximum charge density was obtained at $\dot{Q} = 1.5$ ml/s and $E = -12.5$ kV and was about 1.5 C/m^3.

the other is discharged to the collector (i_f). The amount of charge attracted to the orifice electrode depends on electron mobilities of the charged fuel, which are in the range of 10^{-7} to 10^{-8} m^2/V•s (Inuishi, 1979). Therefore, more charged fuel is attracted to the orifice electrode (i_a) as the electric field increases (Fig. 2). When the fuel velocity or flow rate $\dot{Q}$ increases (at a fixed electric potential), more charged fuel (i_f) in the layer moves downstream (Fig. 3) and the charged layer presumably becomes thinner, which results in more electrons emitted from the cathode. In other words, the total charge emitted from the cathode increases with increasing flow rate (not shown herein) as also does the charge carried downstream (i_f) indicated in Fig. 3 for flow rates up to 1.5 ml/s at the lower voltages. However, for fuel flow rates above 1.5–2 ml/s, i_f tends to decrease (Fig. 3).

At the higher voltages it is evident in Figs. 2 and 3 that another phenomenon occurs. In this case the layer of the charged fuel is believed to become thicker as the electric field increases, until it reaches the anode locally to form an electric channel or low conducting path, a so-called electric breakdown. After electric breakdown occurs, the amount of electrons emitted by the cathode (i_t) increases drastically by 5 to 10 times, as seen in Fig. 2 for the particular flow rate shown. However, since most electrons move to the anode directly (note that i_a becomes nearly equal to i_t in Fig. 2), and thus are not carried by the fuel (i_f), the amount of electrons emitted by the cathode no longer depends on the fuel flow rate. In this regime, most of the electrons are attracted to the anode/orifice, and only a small amount is swept away by the fuel, so that i_f is reduced by 40 to 60 percent after breakdown (Figs. 2 and 3). The ratio of the charge swept downstream to the total emitted charge i_f/i_t was observed to be 0.1 to 0.5 (depending on flow rate) before breakdown occurred. After breakdown, this ratio was reduced below 0.05. After breakdown, i_t and i_f again increase as electric potential increases (Figs. 2 and 3). However, i_f increases more slowly with increasing E than before breakdown (Figs. 2 and 3) while the slope of i_t remains the same. Since the growth of the charged layer is believed to decrease as the fuel velocity increases, breakdown occurs at higher voltages as can be seen in Fig. 3 (e.g., −8.5 kV at 0.51 ml/s to −13 kV at 2.5 ml/s).

Whereas the previous discussion focused on the current-voltage characteristics, the quantities that are important in the jet breakup and drop dispersion are the charge density or the charge on individual drops. The maximum amount of charge on a liquid drop is limited by the Rayleigh relation.

$$\rho_{e,\max} = 12(2\epsilon_o\gamma)^{1/2}d^{-1.5} \tag{3}$$

If the charge increased more than the maximum limit, the liquid drop would break up into several smaller drops. Therefore, the maximum size of drops for a specific charge density may be estimated from the Rayleigh relation. Kelly (1982) has utilized a statistical equilibrium end-state model to propose a charge density–drop size relationship independent of fluid properties. According to his relationship, the size of drops is inversely proportional to the square root of charge density. Hence, the charge density is a very important parameter to measure and is coupled to drop size.

The experimental results shown in Fig. 3 were converted to charge density by dividing i_f by the flow rate $\dot{Q}$; the results are shown in Fig. 4. The charge per unit time carried by the fuel to the collector, i_f, increased with increasing flow rate to 2 ml/s at a fixed voltage before breakdown occurred (Fig. 3). However, the incremental increase was not enough to give the same or larger charge density, so that the charge density monotonically decreased with increasing flow rate (Fig. 4). However, the maximum charge density, which was obtained just before electrical breakdown occurred, is 1.0 C/m^3 at the flow rate of 0.51 ml/s and increases with increasing flow rate, reaching a peak value of 1.53 C/m^3 at a flow rate of 1.5 ml/s (Fig. 4). Further increase of the flow rate resulted in a slight decrease of the maximum charge density.

Since the chamber pressure in a diesel engine before fuel injection is relatively large, the charge density of No. 2 diesel fuel was measured for high back pressures up to 41.8 atm (at 21.4 and 41.8 atm) and the results are shown in Figs. 5 and 6. The results for the high back (chamber) pressures exhibit

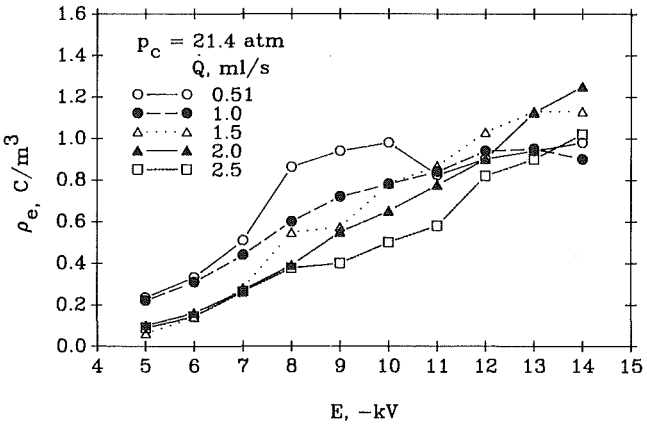

Fig. 5 Charge density versus electric potential for various flow rates at $p_c = 21.4$ atm

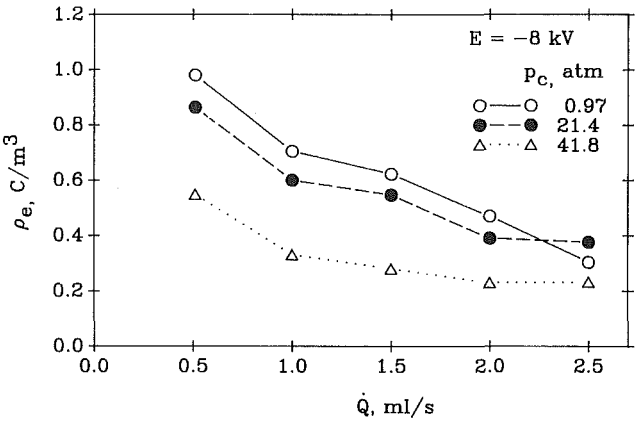

Fig. 7 Charge density versus flow rate for various back pressures. Charge density decreases with increase of flow rate and with increase of back pressure if electric potential is fixed, i.e., $E = -8$ kV.

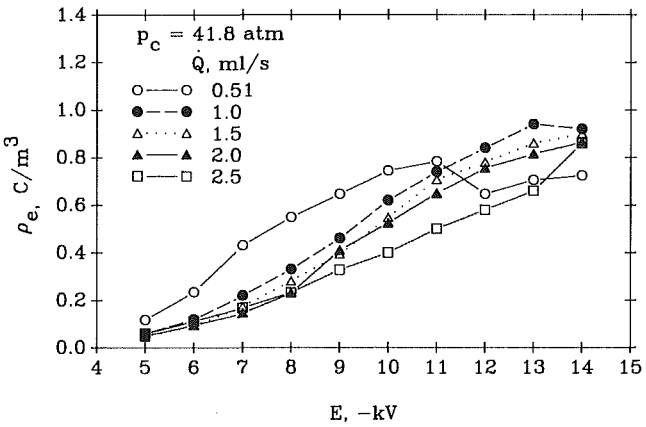

Fig. 6 Charge density versus electric potential for various flow rates at $p_c = 41.8$ atm. In general, charge density decreases with increasing back pressure. However, breakdown occurs at higher electric potential.

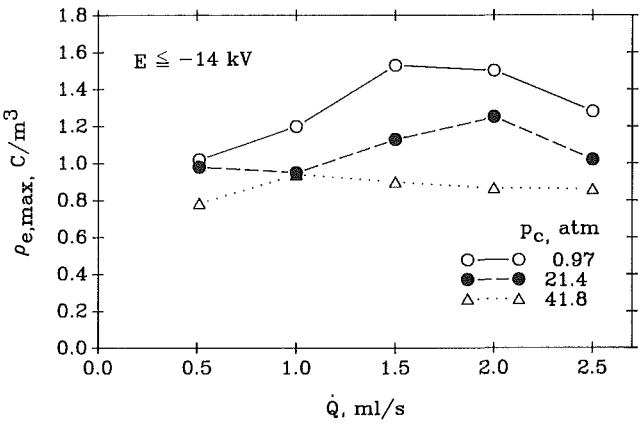

Fig. 8 Maximum charge density versus flow rate for various back pressures. Maximum charge density increases with increase of flow rate, reaches a maximum, and decreases with further increase of flow rate. It decreases with increasing back pressure when $E \leq -14$ kV.

similar behavior to those at $p_c = 0.97$ atm, i.e., the charge density increases with an increase of the applied voltage (at a fixed flow rate), and decreases with increasing flow rate at a fixed applied voltage. The chamber pressure, however, plays an important role in determining the charge density and the breakdown voltage. Breakdown seems to occur at a higher voltage (for a fixed flow rate) as the chamber pressure increases. For example, for $\dot{Q} = 0.51$ ml/s the breakdown occurs at $E = -8.5$ kV for $p_c = 0.97$ atm, at $E = -10$ kV for $p_c = 21.4$ atm, and at $E = -11$ kV for $p_c = 41.8$ atm. The decrease in the charge density right after breakdown is much smaller for higher chamber pressures. The charge density decreases by 20 percent for $p_c = 21.4$ and 41.8 atm, compared to 50 percent for $p_c = 0.97$ atm at $\dot{Q} = 0.51$ ml/s. Moreover, the charge density decreases as the chamber pressure increases before breakdown occurs, if the flow rate and the applied voltage are the same. This behavior is clearly seen in Fig. 7, which shows the charge density as a function of the flow rate at $E = -8$ kV for $p_c = 0.97$, 21.4 and 41.8 atm. The charge density at $p_c = 0.97$ atm is about 1 C/m^3 at $\dot{Q} = 0.51$ ml/s and monotonically decreases with increase of the flow rate, reaching about 0.3 C/m^3 at $\dot{Q} = 2.5$ ml/s. The charge densities at pressures of 21.4 and 41.8 atm show similar behavior but, however, are smaller than those at 0.97 atm by 10–17 percent for 21.4 atm and 40–50 percent for 41.8 atm, depending on the flow rate.

The maximum charge densities measured at three different back pressures are plotted in Fig. 8 using the results shown in Figs. 4, 5, and 6. This plot clearly demonstrates that the maximum charge density becomes smaller as the back pressure increases if the electric potential is limited, i.e., $E \leq -14$ kV. The maximum charge density is smaller by 20–26 percent at 21.4 atm and by 22–43 percent at 41.8 atm depending on flow rate, compared to that at 0.97 atm.

The detailed maximum charge density with the high-pressure spray triode was measured at two different chamber pressures p_c of 0.97 and 21.4 atm for a wider range of flow rates of 0.3 to 4.2 ml/s. In this case, the electric potential was applied to -18 kV. The maximum charge density increases with increasing the flow rate, reaching maximum values of 1.65 C/m^3 at $p_c = 0.97$ atm and 1.5 C/m^3 at $p_c = 21.4$ atm as shown in Fig. 9. It remained at the maximum value for a range of flow rates and tended to decrease with further increase of flow rate. The maximum charge density at 21.4 atm was lower than that at 0.97 atm by 10–25 percent, depending on flow rate. Using the model calculations of Bellan (1983), a charge density of 1.5 C/m^3 would result in the expansion of 0.5 cm spherical spray volume containing 54 mg of fuel by a factor of two in 0.5 ms under diesel engine conditions (Fig. 1 of Bankston et al., 1988).

The electrostatic spray triode used in the current study shows different characteristics at low flow rates compared to those used by Kelly (1982) and Bankston et al. (1988) for atmospheric pressure. For example, Kelly reported almost constant charge density of 1.5 C/m^3 for a range of flow rates from 0.25 to 1.25 ml/s. However, the charge density in Fig. 9 increases almost linearly up to flow rates of 1.5 ml/s at 0.97 atm and 2.2 ml/s at 21.4 atm, and then remains constant. In any case, the data confirm that charge densities of 1.5 C/m^3 up to a flow rate of 4.3 ml/s are definitely achievable at atmospheric pressure, and slightly lower values are found at

Table 1

Pressure, atm	$V_i = 20$ m/s	$V_i = 40$ m/s
0.97	0, −8, −10 kV	0, −8, −10 kV
21.4	0, −10, −12 kV	0, −10, −12 kV
41.8	0 kV	0 kV

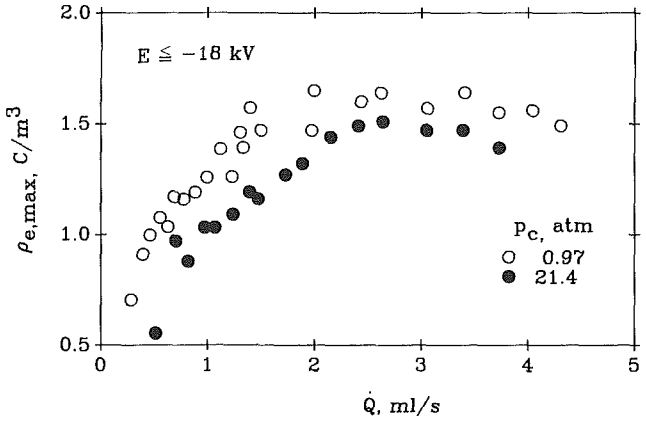

Fig. 9 More detailed maximum charge density variation with flow rate at back pressures of 0.97 and 21.4 atm and at $E \leq -18$ kV

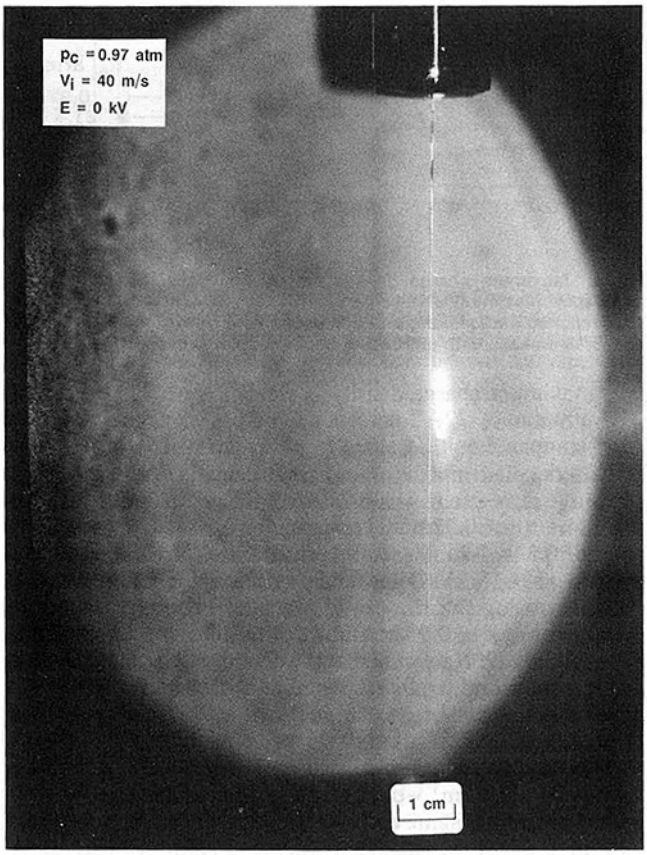

Fig. 10(*a*) Diesel fuel jet doesn't break up all the way across the window without electric charge $E = 0$ kV even at $V_i = 40$ m/s when $p_c = 0.97$ atm

high pressures. The performance at high pressure may be improved by redesigning the insulator that limits the electric potential. If an electrostatic spray triode were used in a diesel engine, the applied voltage should be varied according to the injected fuel amount or injection velocity since the maximum charge density is obtained at higher electric field as the flow rate increases.

2. Flow Visualization. Pictures were taken of diesel fuel

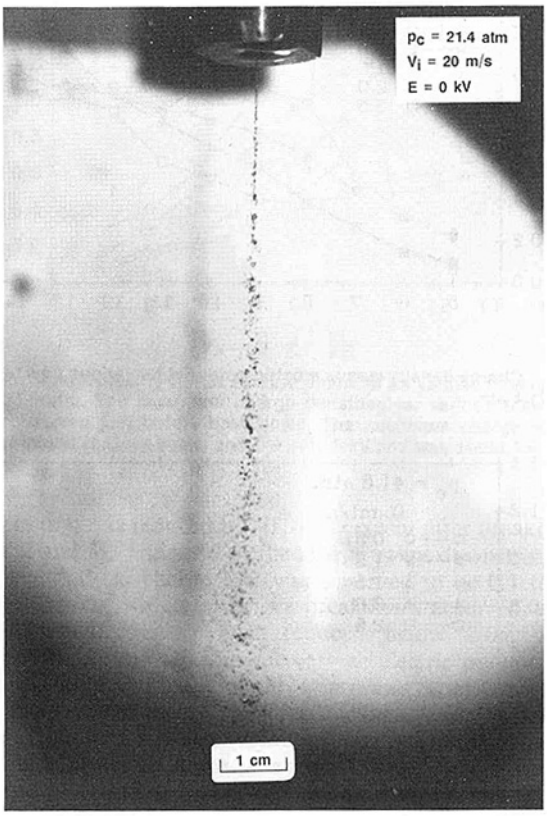

Fig. 10(*b*) Diesel fuel jet spray at $E = 0$ kv, $V_i = 20$ m/s, and $p_c = 21.4$ atm. Since the nitrogen gas density is 21 times larger than that of air at atmospheric pressure, the fuel jet begins breaking up at $x_1 = 0.75$ cm. The spray angle is 26 deg.

injected through the high-pressure spray triode. Photos were taken through the 10 cm i.d. window at various combinations of test conditions of chamber pressures, fuel injection velocities, and applied voltages as shown in Table 1. The results are discussed below, including data obtained without charging, to provide a reference basis for comparison to electrostatic charge effects and previous investigations.

Without Electric Charge. When fuel was injected into air at 0.97 atm, a single stream of fuel was observed all the way across the window without electric charge even at an injection velocity of 40 m/s (Fig. 10*a*). At $p_c = 21.4$ atm, $V_i = 20$ m/s, the fuel jet breaks up even without the applied voltage since the nitrogen density is about 21 times larger than that of air at atmospheric pressure (Fig. 10*b*). The fuel jet begins breaking up at 0.75 cm beyond the injection nozzle ($x_1/d_n = 30$) and mixes with surrounding nitrogen gas, forming a spray plume having an included angle of 26 deg. However, a dense central core exists for several centimeters beyond the injection nozzle. Many large irregular droplets were observed to remain in this dense core region. When fuel is injected at 40 m/s (Fig. 10*c*), the jet breaks up earlier, less than 0.5 cm beyond the nozzle exit, forms a narrow spray angle of 23 deg, and breaks up into much smaller droplets. The fuel was also injected into nitrogen gas having a pressure of 41.8 atm to simulate an actual diesel engine. Compared to data at 21.4 atm, spray angles are larger and the jet breaks up earlier: $\theta = 35$ deg, $x_1 = 0.5$ cm at 20 m/s (Fig. 10*d*) and $\theta = 30$ deg, $x_1 = 0$ cm at 40 m/s (Fig.

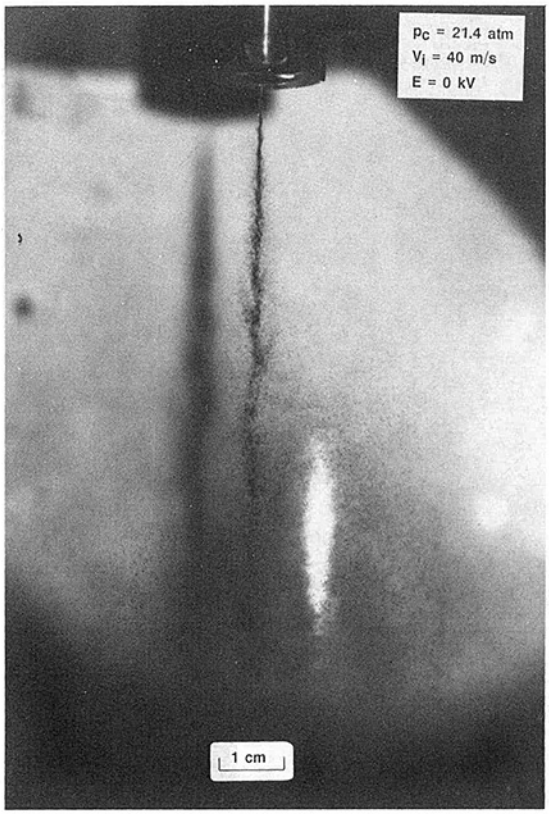

Fig. 10(c) Diesel fuel jet spray at $E=0$ kV, $V_j=40$ m/s, and $p_c=21.4$ atm. When the injection velocity is higher, the jet breaks up earlier ($x_1=0.5$ cm), forms a narrow spray angle of 23 deg, and breaks up into smaller droplets.

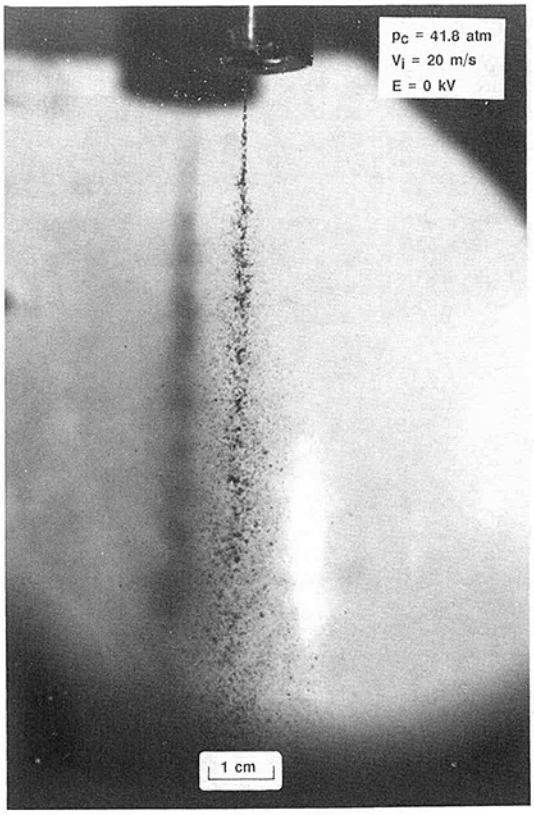

Fig. 10(d) Diesel fuel jet spray at $E=0$ kV, $V_j=20$ m/s, and $p_c=41.8$ atm. At higher back pressure, spray angle is larger, 35 deg, and the jet breaks up earlier, $x_1=0.5$ cm, compared to Fig. 10(b).

10*e*). The droplet sizes are somewhat larger at 41.8 atm if the injection velocity is the same. Despite the large spray angle at $p_c=41.8$ atm, the dense core still exists for several centimeters beyond the injector nozzle.

Atomization of fuel jets has been studied using aerodynamic interaction mechanisms (Ranz, 1958; Reitz and Bracco, 1982; Wu et al., 1986). The following relationships were proposed for initial spray angle θ, and initial average drop diameter d:

$$\tan(\theta/2)=\frac{1}{A}\,4\pi\left(\frac{\rho_g}{\rho_f}\right)^{1/2} f(T) \tag{4}$$

$$\bar{d}=B\,\frac{2\pi\gamma}{\rho_g V_i^2}\,x_{\max}(T) \tag{5}$$

where the aerodynamic breakup parameter $T=\rho_f/\rho_g$ $(\mathrm{Re}/\mathrm{We}_f)^2$. The functions f and $x_{\max}$ tend to $\sqrt{3}/6$ and 1.5, respectively, when T is greater than unity. A and B are constants whose values depend on the nozzle geometry and must be determined experimentally. Of note is that the Weber number We_f is based on the fuel properties, injection velocity, and nozzle diameter, not on the gas properties and fuel droplet size.

The spray angle is essentially linearly proportional to the square root of gas density, being independent of injection velocity if the function f is constant. This relation for spray angle was confirmed by extensive experiments by Reitz and Bracco (1982). In the current experimental results, the Reynolds numbers are 700 at 20 m/s and 1400 at 40 m/s. The values of the aerodynamic breakup parameter T are 2 at 20 m/s, and 0.5 at 40 m/s when $p_c=21.4$ atm. Since the density of nitrogen at 41.8 atm is 1.95 times larger than at 21.4 atm, those at 41.8 atm are about one half of those at 21.4 atm, being 1 and 0.25, respectively. The values of the function f from

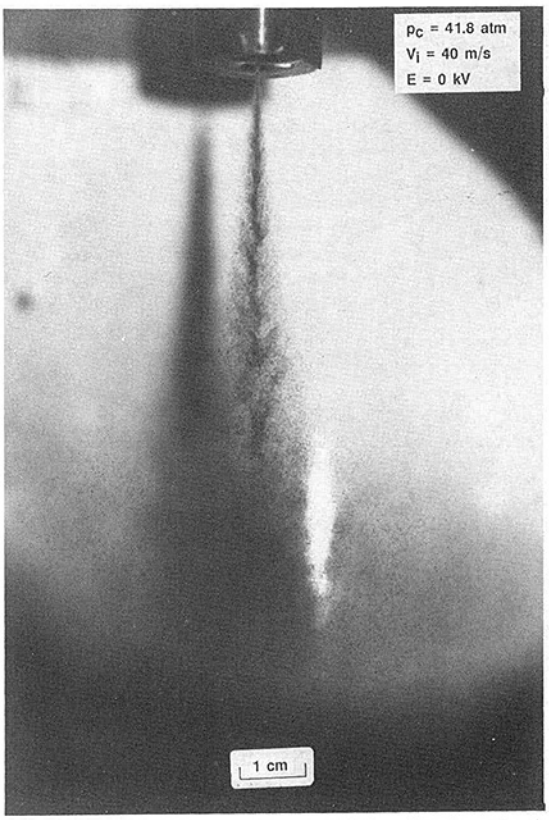

Fig. 10(e) Diesel fuel jet spray at $E=0$ kV, $V_j=40$ m/s, and $p_c=41.8$ atm. Even at these conditions, a dense core exists for several centimeters and many large irregular droplets remain in the dense core region.

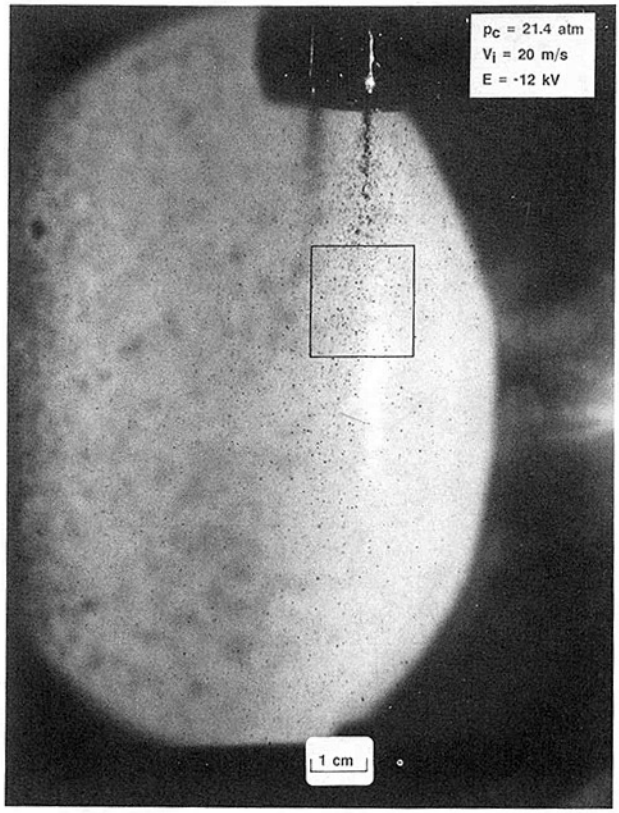

Fig. 11(*a*) Diesel fuel jet spray at $E = -12$ kV, $V_j = 20$ m/s, and $p_c = 21.4$ atm. With electric charge, fuel breaks up considerably more, especially in the central dense core region, which reduces the size of the dense core, compared to that without charge shown in Fig. 10(*b*).

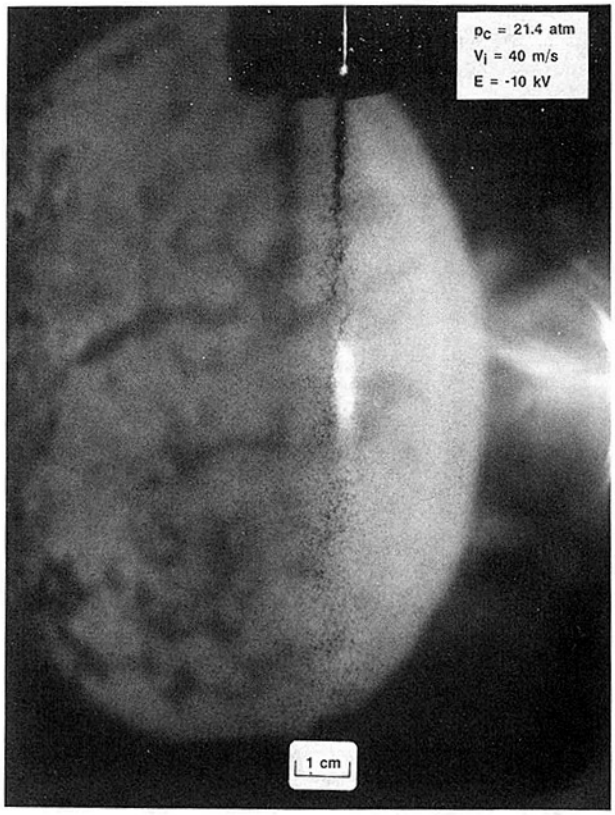

Fig. 11(*c*) Diesel fuel jet spray at $E = -10$ kV, $V_j = 40$ m/s, and $p_c = 21.4$ atm. Since the inertial force is larger at higher injection velocity, the dense core region extends further (compared with Fig. 11(*b*)).

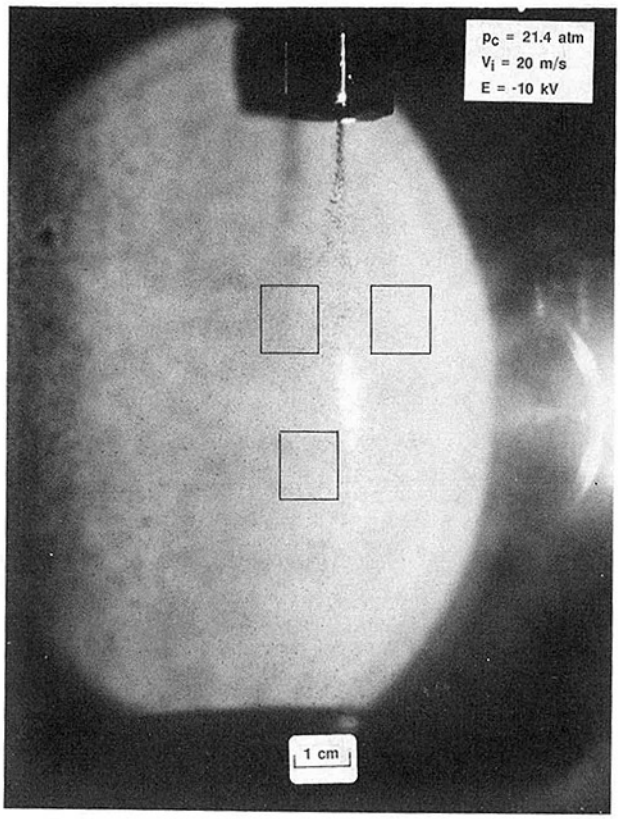

Fig. 11(*b*) Diesel fuel jet spray at $E = -10$ kV, $V_j = 20$ m/s, and $p_c = 21.4$ atm. With the lower applied voltage, the spray angle becomes smaller. However, a large number of small droplets were everywhere except in the 1.5-cm-long dense core region.

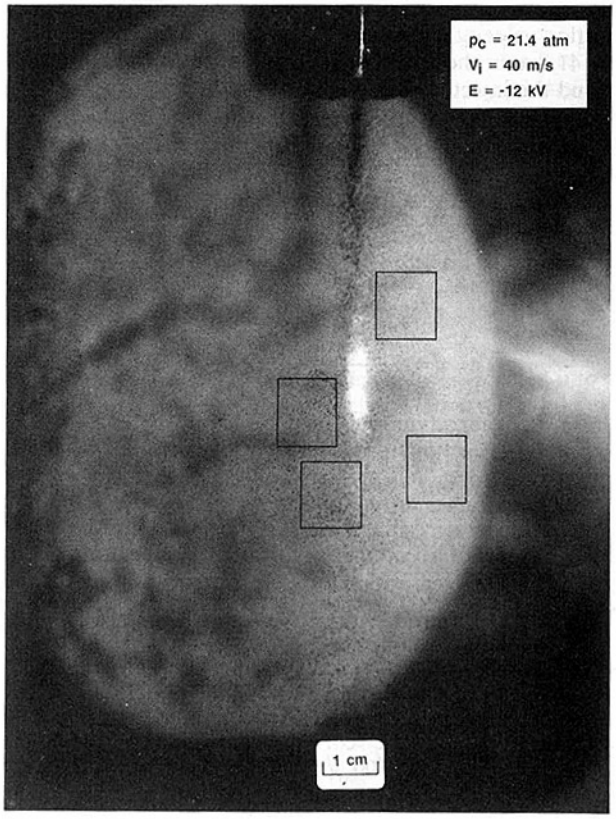

Fig. 11(*d*) Diesel fuel jet spray at $E = -12$ kV, $V_j = 40$ m/s, and $p_c = 21.4$ atm. The dense core become shorter with the higher applied voltage.

Reitz and Bracco (1982) were calculated to be 0.21 at $V_i = 20$ m/s and 0.18 at $V_i = 40$ m/s when $p_c = 21.4$ atm; and 0.20 at $V_i = 20$ m/s, and 0.18 at $V_i = 40$ m/s when $p_c = 41.8$ atm. The values of the geometric parameter A for the electrostatic spray triode were calculated to be 2.02, 1.99, 1.96, and 2.05 with an average of 2. The current data support the idea that the spray angle of the fuel jet can be predicted if the geometric parameter A is known for a particular nozzle.

The average droplet size from equation (5) is inversely proportional to the square of the injection velocity and to the density of gas into which the fuel is injected, if x_{max} is constant. Although the detailed sizes of droplets were not measured at $E = 0$ kV, Fig. 10 clearly shows that the droplet size becomes much smaller if the injection velocity is doubled at the same pressure. However, when the injection velocity is the same, the droplets tend to increase in size with increase in gas density or pressure, which is opposite to equation (5). A recent experimental study by Wu et al. (1986) reported similar behavior. Drop coalescence leads to a rapid increase in drop size, particularly at high gas density, which may be prevented by electrostatic repulsion.

With Electric Charge. When fuel was injected into air at 0.97 atm a single stream of fuel was observed all the way across the window without electric charge even at the flow injection velocity of 40 m/s (Fig. 10*a*). However, the fuel jet breaks up when the voltage is applied, not shown since similar photos were shown in an earlier paper (Bankston et al., 1988). As the charge density increased, the breakup of fluid occurred earlier, and the spray angle increased more rapidly. It seems that the droplet size becomes smaller as the charge density increases.

At $p_c = 21.4$ atm and $V_i = 20$ m/s, the fuel jet breaks up without the applied voltage (Fig. 10*b*). However, the applied voltage caused the fuel stream to break up considerably more and increases the initial spray angle to almost 180 deg at $E = -12$ kV (Fig. 11*a*). A large number of small droplets was observed everywhere except in the dense core, which extended to about 1.5 cm beyond the nozzle at $E = -10$ kV (Fig. 11*b*). At $E = -12$ kV, there was significant fuel jet breakup in the near proximity of the orifice, and large lateral dispersion of the charged droplets. Early breakup and enhanced dispersion are important in diesel engine applications. If soot is primarily formed in a fuel-rich region such as a dense core region, electrostatic dispersion should reduce the formation of soot. Similar behavior was observed for the higher injection velocity $V_i = 40$ m/s. Since the inertia force is larger, however, the dense core region extended to 3 cm at $E = -10$ kV (Fig. 11*c*) and to 2.5 cm at $E = -12$ kV (Fig. 11*d*).

The drop size distributions were obtained using image processing for Figs. 11(*a*), 11(*b*), and 11(*d*). Details on the procedure are given in the appendix. The drops in the three areas in Fig. 11(*b*) were examined. About 20 drops in each region were processed and the average diameters d_{10} were estimated to be 235, 235, and 240 μm, respectively. It was observed that the fuel drops were somewhat nonround with the ratio of major to minor axes about 1.2. Since the drop size distributions in the three regions are similar, the values of d_{10} and d_{32} for all drops in the three regions were calculated. They are 236 and 242 μm, respectively, comparable to the orifice diameter of 254 μm. The detailed distribution is shown in the bottom of Fig 12.

The average charge density of fuel drops was obtained from Fig. 5 and was plotted as solid points in Fig. 13 as a function of the drop diameter d_{10}. For comparison, the Rayleigh limit and Kelly's prediction (1982) are included as solid lines. The current averaged value is higher than Kelly's prediction but is lower than the Rayleigh limit. This is the same trend as the previously reported results at 1 atm (Bankston et al., 1988) shown as open points in Fig. 13. The same estimation of drop

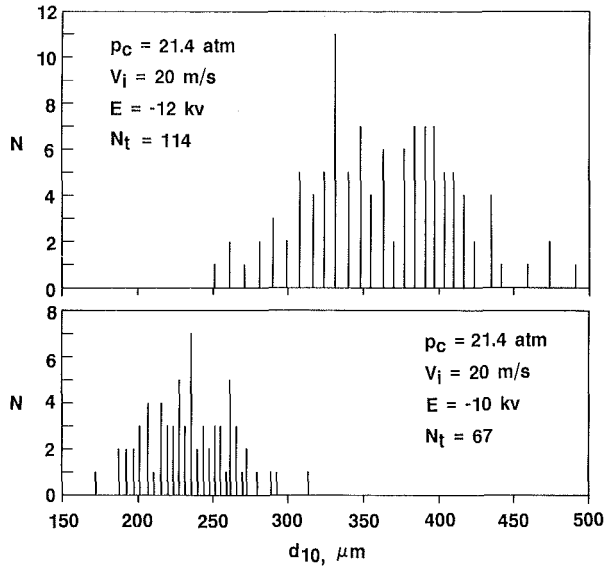

Fig. 12 Droplet size distributions of fuel sprays of Figs. 11(*a*) and 11(*b*)

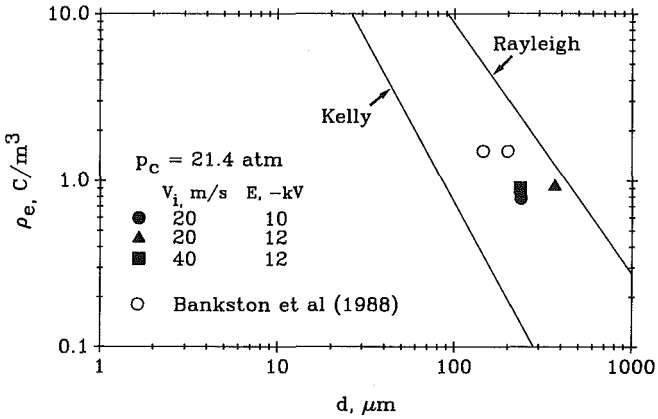

Fig. 13 Charge density versus droplet size. The measured charge densities are between the Rayleigh and Kelly predictions.

size was done for one region in Fig. 11(*a*). The drop size distribution is shown in the top of Fig. 12. Even though the charge density is higher than the previous case (Fig. 5), the drop sizes are larger. The values of d_{10} and d_{32} are 367 and 384 μm, respectively. As shown in Fig. 13, the data are close to the Rayleigh limit.

In the case of the higher injection of $V_i = 40$ m/s (Fig. 11*d*) the drop size distribution is similar to that of $V_i = 20$ m/s at $E = -10$ kV even though the aerodynamic force on the fuel jet is four times larger. The values of d_{10} and d_{32} are 234 and 241 μm, respectively (sample size, $N_t = 85$). The charge density was about 0.9 C/m^3, which is the same order of that of $V_i = 20$ m/s at $E = -10$ kV ($\rho_e = 0.78$ C/m^3). Therefore, it seems that the drop size is primarily determined by the charge density rather than by the aerodynamic forces. Since high injection of fuel tends to increase the fuel-rich or dense-core region, better performance is expected at the lower injection velocities. However, the performance of electrostatic dispersion should be optimized by adjusting various parameters such as the injection velocity, electric potential, and nozzle size to inject a certain amount of fuel in an engine to produce a suitable size of drops and fewer fuel-rich or dense-core regions. To date, flow visualization studies at the higher back pressure of 41.8 atm have not been carried out due to an insulation problem in the electrostatic spray triode.

Summary and Conclusions

The results and conclusions of this investigation are summarized as follows:

1. Charge density measurements ($p_c = 0.97$ atm)
   (*i*) The total charge emitted by the cathode per unit time increased monotonically with the electric potential until breakdown occurred. After breakdown occurred, the total current sharply increased by 5 to 10 times depending on flow rates and again gradually increased as the electric potential increased.
   (*ii*) The charge swept downstream by the fuel showed behavior similar to the total charge, but decreased by 40 to 60 percent depending on flow rate when breakdown occurred.
   (*iii*) The ratio of the charge swept downstream to the total emitted charge was 0.1 to 0.5 before breakdown and was smaller than 0.05 after breakdown.
   (*iv*) As the flow rate increased, breakdown occurred at higher voltages: -8.5 kV at 0.51 ml/s to -13 kV at 2.5 ml/s.
   (*v*) The maximum charge density increased with flow rate, reached a maximum value of 1.65 C/m^3, remained at the maixmum value for a range of flow rates, and decreased slightly with further increase of flow rate.
2. Charge density measurements ($p_c = 21.4$ and 41.8 atm)
   (*i*) The charge density at high back pressures exhibited behavior similar to those at $p_c = 0.97$ atm; the charge density increased with electric potential at a fixed flow rate and decreased with flow rate at a fixed applied voltage.
   (*ii*) The charge density decreased with increasing back pressure before breakdown occurred, being smaller than that at 0.97 atm by 10–17 percent for 21.4 atm and by 40–50 percent for 41.8 atm when $\dot{Q} = 0.51$ ml/s.
   (*iii*) The maximum charge density was also smaller by 20–26 percent for 21.4 atm and by 22–43 percent for 41.8 atm depending on flow rate when the applied voltage was limited below -14 kV.
   (*iv*) Breakdown occurred at a higher voltage as the back pressure increased; at -8.5 kV for $p_c = 0.97$ atm, at -10 kV for $p_c = 21.4$ atm, and at -11 kV for $p_c = 41.8$ atm when $\dot{Q} = 0.51$ ml/s.
   (*v*) The decrease in the charge density right after breakdown was much smaller at higher back pressures; 20 percent reduction for 21.4 and 41.8 atm, compared to 50 percent for 0.97 atm at $\dot{Q} = 0.51$ ml/s.
3. Flow visualization
   (*i*) In general, with electric charge, rapid breakup of the jet was achieved without large droplets in the core region.
   (*ii*) The spray angle increased to larger than 180 deg with increased electric potential, which enhanced dispersion of fuel near the nozzle exit and reduced the dense core region.
   (*iii*) It was observed for a given orifice diameter that the size of drops may be determined primarily by the charge density rather than by aerodynamic forces.

The present investigation has indicated significant early breakup and dispersion of charged diesel fuel jets by using an electrostatic spray triode at high back pressures compared to aerodynamic breakup and dispersion. These results are encouraging for engine injection, but demonstration of this technique under pulsed fuel injection and autoignition conditions requires subsequent investigations to evaluate the potential for improvement in combustion and reduced soot formation.

Acknowledgments

This paper describes the results of research carried out by the Jet Propulsion Laboratory, California Institute of Technology, and was supported by the U. S. Army Research Office through an agreement with the National Aeronautics and Space Administration. The authors express their appreciation to Messrs. J. J. Godley and S. Kikkert for their contributions in fabrication and assembly of the test setup, and in the conduct of the experiments. They also express their appreciation to Dr. Kenneth Harstad for his assistance in the analysis of droplet sizes and to Dr. Parthasarathy Shakkottai for discussions. The Spray Triode is used by permission of Mr. Harold Simmons of the Parker Hannifin Corporation. Valuable technical discussions with Dr. A. J. Kelly of Princeton University are also acknowledged.

References

Bankston, C. P., Back, L. H., Kwack, E. Y., and Kelly, A. J., 1988, "Experimental Investigation of Electrostatic Dispersion and Combustion of Diesel Fuel Jets," ASME JOURNAL OF ENGINEERING FOR GAS TURBINES AND POWER, Vol. 110, No. 3, pp. 361–368.

Bellan, J., 1983, "A New Approach to Soot Control in Diesel Engines by Fuel Drop Charging," *Combustion and Flame*, Vol. 51, pp. 117–119.

Inuishi, Y., 1979, "High Field Conduction and Breakdown in Dielectric Liquids," *J. Electrostatics*, Vol. 7, pp. 1–12.

Kelly, A. J., 1981, "Electrostatic Atomizing Device," U. S. Patent No. 4,255,777, Mar. 10.

Kelly, A. J., 1982, "The Electrostatic Atomization of Hydrocarbons," *Proc. 2nd Int. Conf. on Liquid Atomization and Spray Systems*, June.

Lin, S. P., and Kang, B. J., 1987, "Atomization of a Liquid Jet," *Physics of Fluids*, Vol. 30, No. 7, pp. 2000–2006.

Prado, G. P., Lee, M. L., Hites, R. A., Hoult, D. P., and Howard, J. B., 1977, "Soot and Hydrocarbon Formation in a Turbulent Diffusion Flame," *Proc. 16th Symp. (Int.) on Combustion*, pp. 649–661.

Ranz, W. E., 1958, "Some Experiments on Orifice Sprays," *Can. J. Chem. Eng.*, Vol. 36, pp. 175–181.

Reitz, R. D., and Bracco, F. V., 1982, "Mechanism of Atomization of a Liquid Jet," *Physics of Fluids*, Vol. 25, No. 10, pp. 1730–1742.

Wu, K-J., Reitz, R. D., and Bracco, F. V., 1986, "Measurements of Drop-Size at the Spray Edge Near the Nozzle in Atomizing Liquid Jets," *Physics of Fluids*, Vol. 29, No. 4, pp. 941–951.

APPENDIX

Image Processing

Drop sizes were determined in the following manner. Image frames with 512×480 pixel resolution were formed over areas approximately 2 cm on a side from a spray photograph. The corresponding pixel size (image physical resolution) is about 45 μm. Any drops of about this size or smaller would not register in the image; at most, they would add apparent "noise" to the image. Thus measurements were valid down to drop sizes of order 100 μm. Using a mouse-guided cursor, isolated, distinct drops in a frame were selected. Pixel values along two perpendicular lines through a drop center were obtained. The first and second moments of these pixel arrays were used to determine an average pixel threshold value corresponding to the rms drop extension in each direction. The image in a box of pixels surrounding the drop was thresholded and a pixel count of the drop in the threshold image made. Assuming a Gaussian pixel gray level distribution for a drop, the actual drop cross-sectional area is calculated as twice this pixel count.